Biomimetic Silk-Bioceramic Based Composites for Bone Tissue Engineering Applications

A Thesis Submitted in Partial Fulfillment of the

Requirements for the Degree of

Doctor of Philosophy

by

Joseph Christakiran Moses

Department of Biosciences and Bioengineering

Indian Institute of Technology Guwahati

Guwahati 781039, Assam, India.

September 2022

Dedicated to
my dear
Amma and Appa

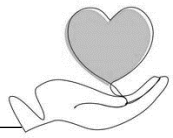

INDIAN INSTITUTE OF TECHNOLOGY GUWAHATI

DEPARTMENT OF BIOSCIENCES AND BIOENGINEERING

STATEMENT

I do hereby declare that the research findings of this thesis is the result of research work carried out by me in the Department of Biosciences and Bioengineering, Indian Institute of Technology Guwahati, Guwahati, India, under the supervision of **Prof. Biman B. Mandal**.

As per the general norms of reporting research findings, due acknowledgments have been made, wherever the research findings of other researchers have been cited in this thesis.

Joseph Christakiran. M

Date: 13.09.2022 **Joseph Christakiran Moses**

INDIAN INSTITUTE OF TECHNOLOGY GUWAHATI

DEPARTMENT OF BIOSCIENCES AND BIOENGINEERING

CERTIFICATE

It is certified that the work described in this thesis entitled "***Biomimetic Silk-Bioceramic Based Composites for Bone Tissue Engineering Applications***" by ***Joseph Christakiran Moses*** for the award of degree of Doctor of Philosophy is an authentic record of the results obtained from the research work carried out under my supervision in the Department of Biosciences and Bioengineering, Indian Institute of Technology Guwahati, India, and this work has not been submitted elsewhere for the award of any other degree.

Joseph Christakiran. M

CERTIFIED

Joseph Christakiran Moses
(Candidate)
Roll No: 156106042

Biman B. Mandal, Ph.D.
(Thesis Supervisor)
Date: 13.09.2022

Acknowledgements

'A marathon is kind of a mini-science; Running a marathon is like doing scientific research. Although the journey may be long and painful, the end goal is always worth the race.'

- Nobel Laureate, Prof. Shinya Yamanaka

I am recording my acknowledgements here drawing analogy for this PhD journey to marathon running. Being an amateur marathon runner, I found many similarities between these two facets and indeed long-distance running helped me to realise and appreciate many virtuous values which are apparently needed for scientific research.

Marathon is a test of patience, endurance, dedication, mental grit and determination. Unlike, sprinting, in marathon training a runner has to realise that it's not the short-term goals or validation but one has to commit for the long haul, and with it the satisfaction that follows in achieving the final goal.

For any marathon runner, the main driving force behind their running passion is stemmed through their coaches and mentors, who help shape their talent and realise their full potential at different passages of their life.

First and foremost, I extend my heartfelt gratitude to my PhD supervisor, Prof. Biman B. Mandal for providing me this opportunity and wonderful platform to be part of his vibrant and enterprising research group. He had always been a constant driving force in my PhD journey, through his relentless pursuit of excellence and to bring out the best out of his students' potential. I am always grateful for his guidance and mentoring which enabled me to keep pushing my limits and strive to be the best version of myself. The time spent under his tutelage during my PhD tenure helped shape me as an individual in my academic and research vocation.

I express my sincere gratitude to my Doctoral committee members; Chairperson, Prof. Siddhartha Sankar Ghosh, Dr. Rajkumar P. Thummer from Department of Biosciences and Bioengineering, IITG; and Dr. Uttam Manna from Department of Chemistry, IITG, for their valuable counsel, scientific inputs and sparing time off their busy schedule to evaluate my progress throughout my PhD tenure.

I convey my gratitude to the present and former Heads of the Department of Bioscience and Bioengineering, IITG; Prof. Rakhi Chaturvedi, Prof. Latha Rangan, Prof. Kannan Pakshirajan and Prof. V. V. Dasu for providing support through various research and academic endeavours.

I have been fortunate to have come across some exceptional teachers who also helped in moulding me as a researcher. I record my heartfelt gratitude to Dr. Sirsendu Sekhar Ray, Dr. Indranil Banerjee, without their initiation I would not have opted to start this PhD journey. Their constant encouragement and guidance during M.Tech, laid the necessary groundwork

and inspired me to take up research as a career. I am always indebted to late Mr. Roy Anand and late Mr. Stephen Chinnaswamy, two teachers who shaped me during my B.Tech, whom the student community lost due to COVID complications. They left a lasting impression on me due to their selfless teaching and their untiring efforts in uplifting students who came from humble backgrounds.

For a marathon runner or athlete, the next important aspect is the holistic support he/she receives for their training, without which one cannot improve and fuel oneself towards their goal.

In this regard, I record my heartfelt gratitude here to thank all the collaborators for providing technical and infrastructural support. I thank Prof. Jonathan Knowles and Dr. Philip J. T. Reardon from UCL Eastman Dental College (London), for providing us technical and characterization support in collaborative research project funded by UK-India Education and Research Initiative (DST, UKIERI). I express my sincere thanks to Prof. Samit K. Nandi from West Bengal University of Animal and Fishery Sciences (Kolkata) for helping us with animal experimentation. I also express my gratitude to Dr. Manoj Agarwala (Senior Resident and in-charge, A&E, GNRC Hospital (Dispur) and his team for helping in sourcing human umbilical cord and cord blood samples, which were needed for our investigation. I thank the support provided by National Institute of Pharmaceutical Education and Research (NIPER, Guwahati) for help in animal experimentation; especially Ms. Tshewuzo-u Lohe for rendering her skilful assistance during small animal experimentation.

I express my sincere thanks to Dr. Nandana Bhardwaj (Sr. Scientist STANVAC) for her kind help and enlightening inputs during my research work.

I express my sincere gratitude to the infrastructural sustenance provided by Central Instrumentation Facility (CIF), IITG; Centre for the Environment, IITG; Centre for Nanotechnology, IITG; and Departmental Central Instrumentation Facility (DCIF), Department of Biosciences and Bioengineering, IITG, through the various student operators and technical scientific personal for the high-end instrumentation support for characterization of various samples investigated in this thesis. I also acknowledge the Ministry of Education (MoE), (formerly, the Ministry of Human Resource Development), Government of India for providing me the fellowship for my PhD research.

The Race Day! It's the ultimate test where years of training and practise is reciprocated into that one marathon race, the gruelling 42.2 km where the athlete's sheer will power and patience is put to the test. This is analogous to the PhD journey itself. The initial few kilometres, you would feel the spring in your legs to surge head with all the might and finish the race in no time. However, as the race unveils itself, after 13-15 kilometres when the muscles feel fatigued, you realise the humongous task at hand. It is at this juncture you look around to find inspiration from fellow runners in this journey, those running the race alongside you, who are pushing through and campaigning their way forward.

Similarly, I would like to express my deepest gratitude to my dear lab mates who have been part of this wonderful journey starting from day one. They have been my fellow runners in this PhD journey from whom I have drawn inspiration through countless ways. I thank Dr. Rocktotpal Konwarh, Mr. Bibhas Kumar Bhunia da, Dr. Jadi Praveen Kumar, Dr. Prerak

Gupta, Ms. Janani G., Dr. Manishekar Kumar, Dr. Dimple Chouhan, Dr. Yogendra Pratap Singh, Ms. Shreya Mehrotra, Mr. Souradeep Dey, Ms. Triya Saha, Mr. Ashutosh Bandyopadyay, Ms. Bibrita Bhar and Ms. Chitra Jaiswal, whose comradery I cherished in this journey. Without their cooperative lab environment, their help, insights, and ethos, this journey would not have been so memorable. I have drawn inspiration from each of them, from their personal and professional lives, relating to dedication, work ethics, commitment, and have been directly or indirectly touched through their beautiful lives. I also record my gratitude to other former and present lab mates: Dr. Ashang Luwang Laiva, Dr. Biswajit Chakraborty, Dr. Deepika Arora, Dr. Aparjita Ghosh, Dr. Rajiv Bora, Dr. Bhaskar Birru, Dr. Chandramouli Ghosh, Dr. I Putu Mahindra, Ms. Mimi Adhikary, Mr. Omkar Majumder, Ms. Shivanshi Kumar, Mr. Sonu Rudra, Ms. Smriti Priya, Mr. Apoorv Bajpai Ms. Tarishi Gupta, Ms. Prerna Pant, Mr. Namit Dey, Mr. Suvro Kanti Chowdhury, Ms. Ayushi Mukherjee, Ms. Monisha V, Mr. Nikhil Gnanavel, Mr. Saptarshi Biswas, Mr. Rishabh Deo Singh, Ms. Sangeetha Pillai, Mr. Nakul Pai, Mr. Anupam Mishra, Ms. Priyanka Korgaonkar, Mr. Shubham Choudhari, Ms. Sayanti Shome, Ms. Ananya Das, Mr. Amit Kumar, Ms. Amritha Bhat and Mr. Rupam Khatua. I am happy that I was able to meet all these wonderful people and value their kindness, scientific discussions and company during their stay in the lab.

The darkest of times is when we lose hope, when things seem impossible and everything around seems to be shrouded by uncertainty. In a marathon, this is when the lactate threshold is reached, when lactic acid accumulates in the muscles and one's feet and arms feel heavy as boulders. Into 30-35 km of a marathon, far from the starting point but just few kilometres before the finish, this inevitable doom hits a runner. The fatigue even makes the runners to contemplate quitting. It is at this juncture, the good will and emotional support of family and friends, enables the runner not to lose hope and keep trudging forward.

My acknowledgements are incomplete until I thank my dear friends: Aashish, Ankit, Arpita, Jananee, Sohenii and Vasu who have been with me through the thick and thin, supporting me in my vulnerable times. I am forever indebted for their counsel; comforting, wise words and encouragement. I record my sincere apologies to my friends and family here for failing them at times. Despite my unavailability due to work priorities, their understanding of my shortcomings and standing by me in my low points while helping me through, was very noble of them; for which I am ever thankful. I express my sincere thanks to Pallabita ma'am for being a beacon of hope in my difficult times.

I lack words to describe the countless sacrifices and untiring love of my parents (amma and appa), without whom I could not have completed my work here. They were the primary source of my strength, inspiration and passion, whose prayers and goodwill have shepherded me through this journey.

Finally, I thank God Almighty, the Alpha and the Omega, for bestowing His blessings and Grace, from the very beginning till the very end of this beautiful journey.

- Joseph Christakiran Moses

Thesis Abstract

Bone, a structurally and functionally important organ is hierarchically built through bottom-up approach using organic - collagen biopolymer and inorganic - apatite bioceramic. Composited into a biomineralized tissue, bone is considered to be nature's most robust, nano-assembled biological structures contributing to its strength and fracture toughness. Though the bone possesses innate healing abilities, clinical interventions are necessitated for bone defect repair during pathological or degenerative conditions. In this thesis, few of the major long bone defects which arise due to degeneration, infection or trauma were identified. Biomaterials-based regenerative strategies were explored in addressing these issues through five objectives which are progressively presented in this thesis. Inspired by bone's nano-architecture, different fabrication strategies were investigated towards recreating biomimetic, cell instructive composites using resorbable and bioactive biomaterials. Silk fibroin was chosen as the bioactive biopolymer, sourced from mulberry (*Bombyx mori*) or non-mulberry (*Antheraea assama*) silk types, for development of composites along with sol-gel derived bioactive glass or wet chemical synthesized apatites (as the ceramic constituents).

In the first objective, electrospun silk-bioactive glass mats were investigated as prospective bilayered grafts for osteochondral lesion management. The hierarchically structured composite electrospun mats helped in preserving the chondrogenic and osteogenic phenotype of seeded chondrocytes and osteoblasts preferentially due to the innate physicochemical cues presented by the biomimetic mats. In the second objective, functionalised silk microfiber-reinforced freeze-dried composite silk sponges were investigated as resorbable bone grafts for volumetric bone defect management. The copper doped bioactive glass used for functionalising the microfibers, helped attribute proangiogenic traits to the scaffold, which aided in restoration of volumetric defects in rabbit femur with total resorption of implants noticed after 3 months. In the third objective, advanced additive manufacturing technique was investigated to develop 3D bioprinted cellularized osteochondral grafts, thereby circumventing drawbacks associated with conventional acellular grafts. Similarly, in the fourth objective, diaphyseal cross-sectional unit was biofabricated with an outer mechanically robust bioprinted cortical bone shell, encompassing an engineered bone marrow towards serving as orthobiologic substitute for atrophic non-union repairs. In the fifth objective, to improve implant patency of metal implants used as fixtures or prosthesis in orthopaedic reconstruction, silk-bioactive glass nanocomposites were used to create multifunctional interface on these metal surfaces. Conformal coatings of these mesoporous nanocomposites enabled in releasing antibiotics or glucocorticoids towards preventing implant associated infection and improving osseointegration of these metal implants.

Thus, the conventional and additive manufacturing strategies demonstrated in this thesis helped develop pro-regenerative, cell instructive matrices in different length scales, to suit the clinical need of the investigated bone pathology. These matrices were functionally validated under both *in vitro* and preclinical *in vivo* conditions. Thus, the positive findings from this work hold promise for the viable clinical translation of these interventions for bone tissue engineering applications.

Contents

Abbreviations

ACAN	-	Aggrecan
ASTM	-	American Society for Testing and Materials
ANOVA	-	Analysis of variance
ANGPTN1	-	Angiopoietin 1
APTES	-	3-(aminopropyl) triethoxysilane
AA or AAS or AASF	-	*Antheraea assama* silk fibroin (solution)
bFGF	-	Basic fibroblast growth factor
BM or BMS or BMSF	-	*Bombyx mori* silk fibroin (solution)
BMP	-	Bone morphogenetic protein
BSP	-	Bone sialoprotein
BTE	-	Bone tissue engineering
BSA	-	Bovine serum albumin
BET	-	Brunauer–Emmett–Teller (surface analysis)
CTSK	-	Cathepsin-K
CTAB	-	Cetyltrimethylammonium bromide
CCR7	-	Chemokine (C-C motif) receptor 7
CD	-	Cluster of differentiation (antigens) receptors
COL	-	Collagen
CDU	-	Collagen digestion units
cDNA	-	Complementary deoxyribonucleic acid
CAD	-	Computer-aided design
Cu	-	Copper (element)
CBFA1	-	Core binding factor alpha-1
CT	-	Cycle threshold
COX2	-	Cyclooxygenase-2
CXCR4	-	Receptor for the C-X-C chemokine CXCL12/ SDF1
°C	-	Degree Celsius (unit of temperature)
DNA	-	Deoxyribonucleic acid
Dex	-	Dexamethasone
ϕ	-	Diameter
DEA	-	Diethanolamine
DAB	-	3, 3'-diaminobenzidine stain
DAPI	-	4′,6-diamidino-2-phenylindole
D_e	-	Diffusion coefficient
DC	-	Direct current
DMEM	-	Dulbecco's Modified Eagle Medium
DMMB	-	1,9-dimethymethyleneblue
EPD	-	Electrophoretic deposition
eNOS	-	Endothelial nitric oxide synthase

EDX	-	Energy-dispersive X-ray spectroscopy
ELISA	-	Enzyme linked immunosorbent assay
ECM	-	Extra-cellular matrix
ERK	-	Extracellular signal-regulated kinases
FESEM	-	Field emission scanning electron microscope
FETEM	-	Field emission transmission electron microscopy
FITC	-	Fluorescein isothiocyanate
FAK	-	Focal adhesion kinase
FBS	-	Foetal bovine serum
FTIR	-	Fourier transform infrared spectroscopy
GSH	-	Glutathione
GAPDH	-	Glyceraldehyde-3-phosphate dehydrogenase
g	-	gram
nHA or HA or HAp	-	(nano) Hydroxyapatite
HSCs	-	Hematopoietic stem cells
H&E	-	Hematoxylin and eosin (stains)
HRP	-	Horseradish peroxidase
h	-	Hour (unit of time)
HLA	-	Human leukocyte antigen
hMSCs	-	Human mesenchymal stem cells (adipose tissue derived)
MG63	-	Human osteosarcoma cell line
HUVECs	-	Human umbilical vein endothelial cells
HIF-1α	-	Hypoxia inducible factor 1α
IgG	-	Immunoglobulin G
IL-1β	-	Interleukin-1β
ISO	-	International Organization for Standardization
Fe	-	Iron
k	-	Kilo (10^3)
kDa	-	kilo Dalton
kV	-	kilo Volt
LPS	-	Lipopolysaccharides
L	-	Litre
G''	-	Loss modulus
MMP	-	Matrix metalloproteinases
M	-	Mega (10^6)
m	-	Metre
µ	-	Micro (10^{-6})
mg	-	Milligram
mL	-	Millilitre
mm	-	Millimetre
mM	-	Millimolar
min	-	Minute (unit of time)

M	-	Molar
MNC	-	Mono-nuclear cells
MTT	-	3-(4,5-dimethilthiazol-2-yl)-2,5-diphenyltetrazolium bromide
ng	-	Nanogram
nm	-	Nanometre
NBF	-	Neutral buffered formalin
N	-	Newton (unit of force)
NO	-	Nitric oxide
NLPR3	-	NLR family pyrin domain containing-3 (inflammasome)
N	-	Normality
NFATc	-	Nuclear factor of activated T cells
OCD	-	Osteochondral defects
OPN	-	Osteopontin
ppm	-	Parts per million
Pa	-	Pascal (unit of pressure)
%	-	Percent
PMA	-	Phorbol-12-myristate-13-acetate
PBS	-	Phosphate buffered saline
PE	-	Phycoerythrin
PDPN	-	Podoplanin
PLGA	-	Poly(lactic-co-glycolic acid)
PVA	-	Poly(vinyl-alcohol)
PVB	-	Poly(vinyl-butyrate)
PCL	-	Polycaprolactone
PDMS	-	Polydimethylsiloxane
PDI	-	Polydispersity index
PCR	-	Polymerase chain reaction
PVP	-	Polyvinylpyrrolidone
pADSCs	-	Porcine adipose derived mesenchymal stem cells
pECs	-	Porcine endothelial cells (porcine descending aorta derived)
psi	-	Pounds per square inch
PGE2	-	Prostaglandin E2
rad	-	Radian
RAW 264.7	-	Murine macrophage cell line
RGD	-	Arginine-glycine-aspartate
rpm	-	Revolutions per minute
RNA	-	Ribonucleic acid
RUNX2	-	Runt-related transcription Factor 2
s	-	Seconds (unit of time)
SAED	-	Selected area electron diffraction

γ	-	Shear strain
SF	-	Silk fibroin
SBF	-	Simulated body fluid
K_{sp}	-	Solubility product (in dissolution)
sRANKL	-	Soluble receptor activator nuclear factor-κB ligand
SD rats	-	Sprague Dawley rats
SOX9	-	SRY-Box transcription factor 9
STL	-	Stereolithography
G'	-	Storage modulus
SDF-1	-	Stromal cell derived factor 1
Sr	-	Strontium (element)
SR0	-	Unmodified nano-apatite [$Ca_5(PO_4)_3.OH$]
SR1	-	Strontium substituted nano-apatite [$(Sr_{0.5}Ca_{0.5})_5(PO_4)_3.OH$]
THP1	-	Human monocytic cell line
TRAP	-	Tartarate resistant acid phosphatase
TEOS	-	Tetraethyl orthosilicate
3D	-	Three dimensional
TEBN	-	Tissue engineered bone marrow
TAZ	-	Transcriptional coactivator with PDZ-binding motif
TEP	-	Triethyl phosphate
TNF-α	-	Tumour necrosis factor
2D	-	Two dimensional
UV	-	Ultra-violet radiation
US FDA	-	United States of America, Food and Drug Administration
U	-	Units (enzyme)
VEGF	-	Vascular endothelial growth factors
V	-	Volt
v/v	-	Volume/volume
vWF	-	von Willebrand factor
ω	-	Angular frequency
λ	-	Wavelength
w/v	-	Weight/volume
WJMSCs	-	Wharton jelly derived mesenchymal stem cells
XRD	-	X-ray Diffraction
YAP	-	Yes-associated protein
ζ	-	Zeta potential

List of Tables

List of Figures

Chapter 2

Chapter 1

Introduction and review of literature

Conventional biomaterials used in orthopaedic reconstruction suffer from several drawbacks such as limited vascularization, variable resorption rates and poor osseointegration. Unconventional strategies employing biomimetic design principles, embed biophysical and biochemical cues akin to native bone tissue, which enable in developing biomimetic cell-instructive biomaterials that hold promise in resurrecting the personalized and precision medicine domain of orthopaedic treatment. This chapter introduces the different concepts involved in cell-instructive biomaterials domain and a progressive overview of the approaches adopted to materialize these concepts for bone tissue engineering applications.

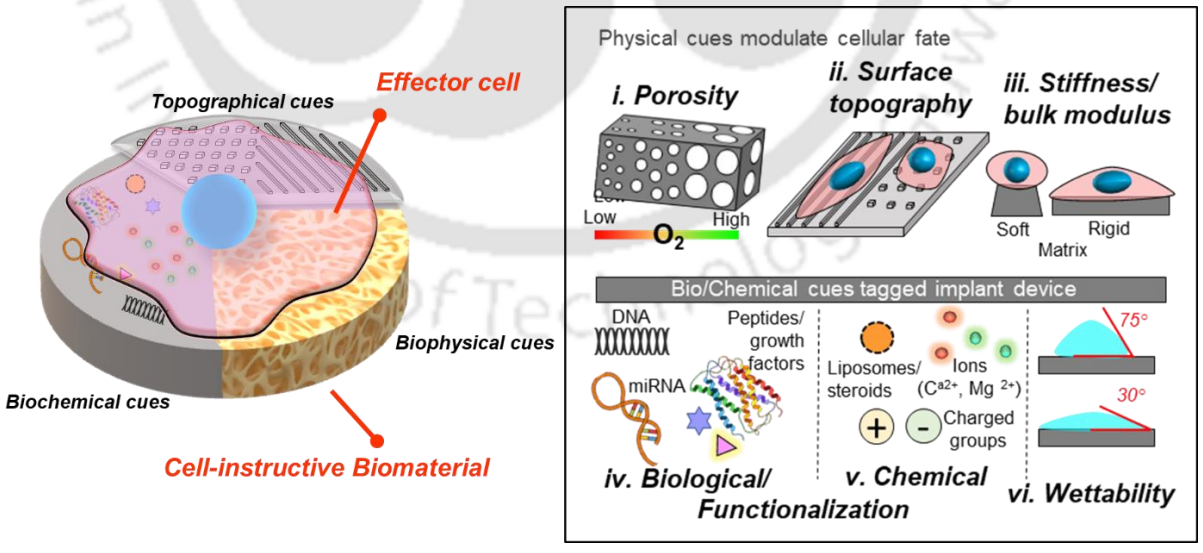

1.1 Introduction

Bone, a biomineralized tissue is a fascinating composite from an engineering standpoint, deeming it to be considered nature's arguably most robust biological structures known for its fracture toughness and strength. [1] The composite is light weight, produced under ambient conditions and composed of organic-inorganic entities (organoapatites). These organoapatites are synthesized inside the body with energy conservation principles which the 21st century manufacturing principles find hard to replicate. This fascination for bone has inspired design ideas on biomimicry, to develop lightweight yet robust structures ranging from cosmopolitan architecture to automobiles. [2] From a biological perspective, bones apart from providing structural support to the human form, is involved in plethora of functions involving mineral homeostasis, blood production, blood pH regulation and houses important progenitor cells of both mesenchymal and hematopoietic origin. In order for the bone to perform its functions, it undergoes continuous destruction termed resorption carried out by osteoclasts and bone formation carried out by osteoblasts. In the adult skeletal tissues, these two important processes are maintained in balance via *bone homeostasis*, wherein vascularization and innervation play major roles for achieving this orchestrated event. The skeletal tissue responds to dynamic mechanical loading, inflammatory, hormonal and mineral challenges. Yet the skeletal tissue is capable of acting on its own accord by secreting factors that control the function of other tissues such as kidney, pancreas and gonads, [3] behaving like an endocrine organ.

The adult human skeletal system is constituted by 206 bones, each uniquely different from the five classes: namely long bones, short bones, flat bones, irregular bones and sesamoid. Flat bones in the cranium differ from the long bone in the limbs, while short bones in carpal/ tarsal regions differ from the irregular bones of the pelvis. Regulatory mechanisms during development and evolutionary adaptation to mechanical loading regime governs the formation of these different bones present in the body [4]. This mechanosensitivity can be attributed broadly to two features. *Firstly*, the complex hierarchical structure of the bone, intricately built through a bottom-up approach is composed of ordered arrays of mineralized collagen fibrils at nanoscale with simplicity in the design language cascading across micro- and macro-scales [5]. This design, observed across these different length scales of bone help in propagation of forces and contribute to its fracture toughness. [1] *Secondly*, the forces propagated are sensed by osteogenic lineage cells (especially osteocytes) and respond to them through mechanotransductory pathways. [6] Interesting to note is the loading patterns subsequently get

trickled down across the different length scale in the hierarchical bone structure. For instance, at macro scale for a man (weighing 75 kg) the peak tibio-femoral force would be 2.8 times his body weight with an average resultant joint force of ~ 3 N. [7] On the contrary, forces experienced by osteogenic cells (osteocytes) are in the range of 1 to 10 pN, either directly through the immediate extracellular matrices' (ECM) stiffness or interstitial fluid flow in the canalicular network of the osteon [8]. The latter in turn contributes to the piezoelectric phenomenon noticed in bone due to the convective ion transport occurring as a result of streaming potentials during interstitial fluid flow. [9, 10] Thus, when the bone is dynamically loaded it exhibits distinguished electrical and magnetic fields. The mechanical loading has been found to play a crucial role in maintaining bone homeostasis, wherein if the mechanical stimulation stops, the anabolic function of bone formation ceases and catabolic function of bone resorption is initiated.

Apart from mechanosensitivity, osteogenic cells are also responsive to the physical and chemical nature of the microenvironment. Various cell types in the tissue respond to different physical and chemical cues, triggering signalling cascades within the cells which form the basis for the feedback routine for cell-fate choices. For instance, it has been well characterized that mesenchymal progenitor cells exhibit robust actin stress fibers when they encounter rigid substrates. This cytoskeletal tension is transmitted to the nucleus *via* linker of nucleoskeleton to cytoskeleton (LINC) complexes to the nuclear lamins and chromatin by mechanical coupling [11]. Focal adhesion (FAs) complexes-controlled ECM adhesion also has been found to evince similar behaviour. Cells encounter different type of ECM in the micro-milieu having adhesion peptides for anchoring different integrin complexes of the FAs. Thus, the spacing and availability of ECM adhesion sites control the cellular spreading, cytoskeletal tension, and ultimately modulating the gene expression profiling. Cells adapting osteogenic fate are influenced by these physical cues from the micro-environment, and as an outcome seen to upregulate RhoA expression to confer lineage commitment. [12] Apart from these physical cues, chemical cues also regulate the osteogenic fate. Cellular signalling is a complex orchestration of events mediated by several biomolecules such as proteins, peptides, lipids, nucleic acids and their complexes. Manipulating these cellular signalling pathways by synthetic small molecules has been a pivotal area of interest for chemical biologists to harness the enormous potential of cells towards therapeutic or disease etiology understanding. For instance, it is a well-established protocol to utilise β-glycerophosphate, ascorbic acid and dexamethasone as supplements *in vitro* for driving the osteogenic differentiation of mesenchymal stem cells

(MSCs). Here, dexamethasone is a small molecule corticosteroid which targets glucocorticoid receptors thus playing a crucial role in controlling osteogenic fate. [13]

Presently, bone biomaterials used in clinical setting (for bone and joint substitution) have traversed a long way with the fascination of mending bones with different materials. The earliest reported material as early as 1300 BC in Egypt was the use of wooden splinters for mending femur fracture and wooden prosthesis in case of amputation. [14] The orthopaedic field has evolved and so have the biomaterials alongside, and even more so in the last 50 years. It can be put into perspective and well regarded that biomaterials have evolved through three generations in these last 5 decades chronologically as follows: *first generation* (bioinert materials); *second generation* (bioactive and bioresorbable materials); and *third generation* biomaterials (smart biomaterials which trigger molecular response to harness cell's therapeutic potential) [15]. The first two generation biomaterials used in orthopaedic settings has been extensively reviewed elsewhere [15-18] and the third-generation biomaterials that have been developed and are in lab setting (yet to be clinically used extensively) have also been reviewed in the recent years [19-21]. A brief summary of the different bone graft substitutes (under broad classification) used thus far and their drawbacks are listed in **Table A1.1** (*Appendix*). The drawbacks in these current generation biomaterials serve as the driving factors to expedite further research in overcoming them. It is imperative to mention here is that there is huge disparity between the volume of scientific papers generated in the domain of bone tissue engineering and the number of new materials that have traversed into the clinical translation domain. For instance, for the search query: (["bone graft" OR "bone scaffold" OR "bone biomaterial"] AND ["bone regeneration" OR "bone tissue engineering" OR "bone defect repair"]), with limits set for year "2015 to 2021" (searched on 16, June 2021), restricting to only "articles", conference papers in SCOPUS and Web of Science, following the PRISMA's statement (http://www.prisma-statement.org). In SCOPUS, 1866 documents were listed with 96.3% of documents as research articles and 3.7% of documents as conference papers, while in Web of Science 9183 records were listed with 98.1 % of records as articles and 1.9 % of records as meeting/ conference records. On the contrary for the same search query, only 188 records were listed for clinical trials in Web of Science while only 37 records were listed in MEDLINE (through PubMed). Positive anecdotes from the recent past usher in hope that research in the right direction would eventually yield fruition, which is the hallmark in Larry L. Hench's Bioglass® episode [22]. The pressing need to aid US military surgeons during 1960s where metal/ plastic orthopaedic prosthesis available at their disposal faced severe

rejection rate. Thus, the first bone bonding biomaterial capable of forming apatite layer between the implant and bone surface was developed and since 1985, Bioglass® has been widely used in clinical setting improving the implant patency drastically. [22]

The focus of this chapter is to revisit different third generation biomaterials on the context of delineating the existing literature into three important aspects: *firstly,* as briefly introduced earlier osteogenic cells are responsive to their immediate micro-milieu and hence the different physical, chemical cues are integral part for maintaining their lineage commitment and maintenance. Therefore, it becomes pertinent to understand these cellular dynamics to harness them for therapeutic potential. *Secondly*, using the knowledge gained over the years in modulating cellular response *in vitro,* insights obtained from developmental, pathological aspects, "cell-instructive" traits can be conferred on to biomaterials to emulate structural, biochemical features inspired by biomimetics of bone. Different stratagems adopted to confer these cell-instructive traits are discussed in detail in forthcoming sections of this chapter.

The literature review presented in this chapter have been communicated as a review article and is under peer-review:

Moses, J. C., and Mandal, B. B., *'Cell-instructive biomaterials in bone tissue engineering - Cellular dynamics, engineering principles and clinical translation prospects.'*

Review of Literature

1.2. Understanding the Cellular Perspective - *Catering to the Cells*

1.2.1 Cell-Material Interaction – The Key Determinants

For the success of any implant it is imperative that it has a dynamic response with the host tissue, capable of eliciting an inflammatory response which favours cellular migration, followed by host tissue engraftment and integration. This dynamic crosstalk between the cells and the biomaterial decides the fate of the implant and subsequent performance. Thus, presentation of appropriate physical and chemical cues on the biomaterials to influence the cellular behaviour has been an integral aspect of research philosophy of the *third-generation* biomaterials development. There are four key determinants (**Figure 1.1**) which play major role in the success of engineering such cell-instructive cues: which include (i) nano/micro/macro scale molecular complexes present on cell surfaces which recognize the cues and engages further course of action; (ii) the choice of biomaterials and adapting it in "*the right form*", embedded with the appropriate cues; (iii) the spatiotemporal dimensions of local micro-environment where the cell-instructive biomaterial (CIB) is implanted; and finally (iv) the effector cells' potency to respond to the cues presented, eliciting favourable outcome.

1.2.1.1 Macromolecular Engagers

Unless the cues presented are recognised, the desired biochemical outcome from cells in response to cues from biomaterial is not guaranteed. Therefore, this is the most critical determinant in the cell-material interaction mechanism. The macromolecular complexes bridge the cell (self) and biomaterial (non-self) thus engaging the commencement process which decides the fate of the implant. In this regard, these macromolecular complexes can be broadly classified into: (i) subcellular components which are integral part of the cells itself – direct engagers and (ii) molecular components present in the local micro-environment which interrogate the new biomaterial (non-self) surface (indirect engagers), thus forming an indirect contact with subcellular complexes.

Direct engagers include cell adhesion molecules (transmembrane integrins, focal adhesion complexes), which mediate cell adhesion and cell receptors, which mediate growth factor/ ligand receptor activation. Direct engagers also include ion channels and plasma membrane which opens the putative portal for endocytosis for engulfing relevant cargoes pertinent to osteogenesis here. Cell adhesion molecules help in perceiving the surface cues pertaining to ECM ligands, topography, wettability, and material stiffness [23] (**Figure 1.1A**).

Of these three, ECM ligand-cell adhesion molecules interaction is pronounced and has been well studied [24] Integrin subunits (18 α and 8 β units; combine to form 24 known functional dimers) recognise motifs on the ECM molecules and facilitate the nascent adhesion process [24]. Some of the recognition motifs present in ECM proteins are: RGD, REDV, KQAGDV and PHSRN (in fibronectin); LRE, IKLLI, PDGSR, LRGDN, LGTIPG, IKVAV and YIGSR (in laminin); DGEA, RGD, GFOGER (in collagen I); and VAPG (in elastin). [25] RGD (arginine-glycine-aspartate) tripeptide ubiquitously present in many ECM proteins has been documented to be recognized by 8 functional integrin dimers out of the 24 discovered: namely αIIbβ3, αvβ1, αvβ3, αvβ5, αvβ6, αvβ8, α5β1 and α8β1. Once the nascent adhesion process driven by ECM interaction, the adhesion process may either disintegrate or mature into larger complexes called focal adhesion complexes (encompassing the involvement of other components such as talin, vinculin, paxillin, focal adhesion kinase (FAK) reviewed here [23, 24]). This mature focal adhesion is characterized by well-developed lamellipodium and tension generated myosin-II (in contrast nascent adhesion tension is retrograde through actin on talin). Intercellular adhesion molecules which are presented by niche cells such as cadherin (CDH2, CDH11, CDH4 in osteogenic fate [26]) also mediate cell recognition and involved in maintenance of stemness. Additionally, growth factor receptors (like BMP/TGFβ, WNT, Notch, FGF, PDGF, IGF), inflammatory mediators and their receptors (interleukins IL, TNFα, IFNγ, CD28; CD80/ CD86/ CD163, CD204, CD206, etc.), ion channels and calcium sensing receptors (CaSRs) also play critical role in sensing these biochemical stimuli and engaging them to elicit appropriate action in response.

Indirect engagement involves the first step post implantation of a biomaterial inside the body. A layer of proteinaceous coating develops over the biomaterials (**Figure 1.1A**) following blood contact which mainly includes serum proteins, fibrin dominant protein adsorption of plasma proteins which include albumin, fibrinogen, complement factors, γ-globulin, fibronectin and vitronectin. Additionally, chemoattracts from blood, growth factors such as TGFβ, PDGF, CXCL4, MCP-1 also get adsorbed on to the biomaterial surface [27] which favour further cellular interaction. These protein-based interaction forms an *intermediary step* before the actual molecular engagement between biomaterial and cells. If the biomaterial is inert, chances are favoured for granuloma/ fibrous encapsulation where implant might be rejected otherwise if biomaterial has “immuno-informed” cues embedded might lead to a different engagement improving biomaterial patency. [28]

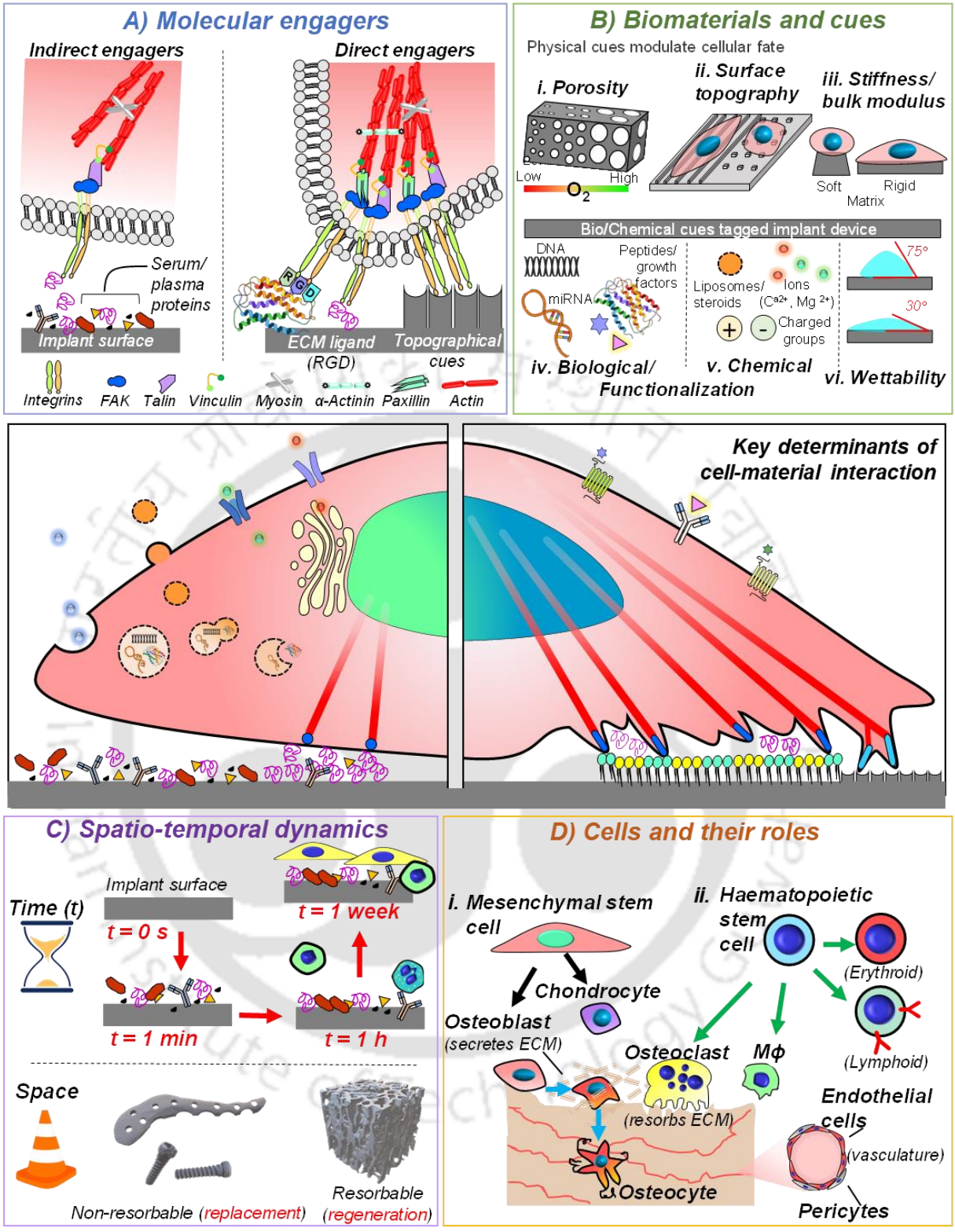

Figure 1.1. ***Key determinants that regulate cell-biomaterial interaction's fate.*** *A) Molecular engagers, which help in sensing the offered physicochemical cues such as cell receptors involved in detecting topographical cues like ECM ligands, surface patterns and biomolecules/ ions through receptor-ligand interactions (direct engagers) [23], or through serum/ plasma proteins (indirect engagers) which first interact with implant surface and forms an intermediate connect between implant and cells; B) Different types of biomaterials and*

different types of physico-chemical cues have definite, distinct impact on bringing about unique cellular behaviours; C) Spatiotemporal awareness is essential to known the predictable performance of the medical device post-implantation – Foreign body reaction (FBR) initiated within few minutes, could last weeks/ months and depending upon the utility whether a resorbable (intended for regeneration; occurs over months, years) or permanent non-degradable material (for replacement) is to be decided upon the implantation site/ space; D) Ultimately, cells are the effectors which sense the cues and react to it – typically two main effector progenitor cells are involved, namely i) mesenchymal stem cells (MSCs) which differentiate to either chondrocytes which forms the cartilage or osteoblasts which forms the bone (either directly via intramembranous ossification or through calcification of cartilaginous template by endochondral ossification); also they give rise to the vascular cells (endothelial cells) and perivascular cells; ii) haematopoietic stem cells which give rise to either erythroid/ lymphoid lineage cells that constitute the marrow, also giving rise to the tissue resident macrophages (MØ), monocytes which fuse to form the polykaryon osteoclasts (which resorb the bone matrix).

1.2.1.2 Know Thy Biomaterial; Know Thy Cue

By definition in 1987, in a European Society for Biomaterials conference, biomaterial was defined as *'a non-viable material used in any medical device intended to interact with biological systems'*. However, the definition has been amended and the meaning of the term biomaterial has changed drastically over the years and currently well accepted as opined here as *'a substance engineered to take a form which, alone or part of complex system, is used to direct (by control of interactions with components of living systems) the course of any therapeutic or diagnostic procedure'*. [29] This definition was adopted based on the consensus in the conference 'Definition in Biomaterials' (Chengdu, China 2018) [30]. Hence, it becomes pivotal here for the success of any medical device to take into considerations the choice of biomaterial from the cornucopia of materials available in fabrication of the device. Some of the materials that have been explored in this regard (as few listed in **Table A1.1** (*Appendix*) including ceramics, polymers, metals, composites and have been extensively reviewed elsewhere. [15-18, 31] Discovery of new biomaterials and its use could also be a contributing factor for achieving better clinical success. Having prior knowledge of how a particular class of biomaterial type behaves (the 'class effect') would help biomaterial scientists to fine tune its properties to overcome its limitations. A material in its macroscale totally exhibits a different characteristic in its nano-scale, paving way for nanotechnological advances [32]. It also becomes pertinent to have the knowledge of the plethora of cues that can be supplied or imparted to the biomaterial gained by studying developmental biology and pathological conditions (**Figure 1.1B**). These two aspects are reviewed in subsequent sections where few of

these biochemical/ physical cues exploited so far and the various engineering strategies employed in fabrication of medical devices towards orthopaedic applications.

1.2.1.3 Mind the Gap and Time

The space and time dimensions together constitute two important external determinants which regulate the lifecycle of a biomaterial implant. Once implanted, sequence of events termed as foreign body response/ reaction (FBR) takes place. Within minutes of implantation indirect engagers form a proteinaceous coating over the surface of biomaterial (**Figure 1.1C**), within hours immune cells (tissue resident macrophages, platelets, monocytes, neutrophils etc.) interrogate the biomaterial, and within the span of few days (1-5 days) the adhered immune cells secrete further cytokines which help in recruitment of tissue repair cells (fibroblasts, circulating MSCs, pericytes, endothelial cells) (5-15 days). This continues for weeks (3-4 weeks) wherein new ECM is secreted, [28] remodelled, the biomaterial degrades (in case or resorbable matrices) and the fate of biomaterial is decided over the course of months/ years. An orthopaedic device may be intended for replacement (as in total joint replacement prosthesis – hip/ knee arthroplasties) or regeneration (**Figure 1.1C**). In case of replacement devices, the success involves in the osseointegration of the device; avoiding periprosthetic joint infection (PJI); overcoming aseptic loosening of device. PJI could occur due to pathological bacteria residing at implant site or could be haematologically presented via circulation, leading to implant associated infection (occurs within few days to weeks). It is also essential to clarify, the terms "biodegradation" and "bioresorption" with reference to bone biomaterials. Biodegradation is the physical phenomenon of dissolution and disintegration/ fragmentation *in vivo*; whereas bioresorption is mainly mediated through cellular mechanisms (by osteoclasts, neutrophils, giant cells, remodelling enzymes secreted by macrophages and immune cells).

In case of regeneration, the rate of resorption/ degradation of biomaterial implant has to match the rate of neo-osseous tissue ingrowth (takes place 4-6 months post implantation, continues for years), such that the mechanical strength, bioactivity and osteoinductivity is not compromised in the due course. For instance, bicalcium phosphates have solubility of ~88 mg/L (at 25°C) whereas hydroxyapatite exhibits just ~0.3 mg/L (at 25°C) making it relatively stable. Similarly, biodegradable synthetic polymers poly (α-hydroxy esters) (**Table A1.1** (*Appendix*) degrade through hydrolysis of ester bonds, whereas protein biopolymers such as collagen-I, silk fibroin gets cleaved by proteolytic activity and hence might get resorbed faster than its synthetic counterparts. Additionally, factors such as crystallinity, length scale (macro/ nano) of these ceramics/ polymers also determine the rate of resorption. The size of the defect and implant site also play contributing roles here. The local pH, temperature and micro-milieu

has to be taken into consideration too. The osteoporotic bone (heightened osteoclastic activity) or the osteoarthritic exposed subchondral bone (inflamed synovium, cartilage) or osteomyelitic bone (acute infections) vary from normal homeostatic bone. The bone implants placed in such spaces have to take into considerations such hostile pathological microenvironments and the repercussions thereof for its survival. Thus, spatiotemporal dimensions are to be critically evaluated, making sure *'one size fits all'* approach does not qualify as the best option in orthopaedic defect management.

1.2.1.4 Ultimately, Cells

The clinical utility of biomaterial science is directing cells to favourably interact with the medical implant in a spatially and temporally controlled way. Thus, it can be reemphasized that cells encountering the biomaterial and the tissue surrounding it is the ultimate determining factor. Cells (**Figure 1.1D**) not just of the osteogenic lineage but immune cells involved in FBR, fibroblasts, vascular cells also play vital role in bringing out the favourable outcome. Two approaches are followed in orthopaedic management, (i) acellular approach (most widely followed) where the cells inside the body interacts with the implanted device; and (ii) cellular approach, either cells alone (scaffold-free strategy) and cells seeded on scaffolding matrix are used as grafting materials. Ever since the discovery of adult stromal cells (mesenchymal stem cells from hematopoietic niche of bone marrow) in 1960, MSCs (from bone marrow and adipose tissue derived) they have been explored through the years for their therapeutic potential with many clinical studies approved by FDA for use in non-unions of bony defect, osteonecrosis of femoral head (ONFH), and osteoarthritis (autologous/ allogenic source). [33] The original premise for use of MSCs was to harness their regeneration potential, wherein the MSCs seeded construct once implanted would differentiate and help in forming neo-osseous tissue. Alongside MSCs, notable strategies involve the use of chondrocytes either in a scaffold-free (autologous chondrocyte implantation ACI) or matrix assisted technologies (MACI – matrix assisted chondrocyte implantation) to aid in treating osteoarthritic lesions. [34] However, cell-based therapy has come into lot of scrutiny because of the paucity of adult stem cell source, and the loss of cells at the implant site as very few cells survive in the graft post implantation. Moreover, high failure rate in ACI (up to 25%) in a 10 year follow-up study indicate only cell based (scaffold-free) approaches are not clinically viable [35]. Thus, it is essential to find the right balance between engineering biomaterials and engaging the cells to biofabricate bone tissues which could enhance the clinical success. Increasing knowledge in developing immuno-informed biomaterials and embedding cell-free cues (use of exosomes) are becoming thrust areas in new generation bone graft substitutes. [28, 36, 37]

1.2.1.5. Clinical Goals of Cell-instructive Biomaterials

Bone injuries are caused as a result of various pathological conditions and traumatic accidents (**Figure 1.2A**). This could be broadly grouped under three main categories namely, (i) fractures, (ii) degeneration of tissue due to diseased conditions such as osteoarthritis, osteoporosis, and (iii) pathological conditions such as infections (osteomyelitis) or tumours. The strategies involved in treating these conditions include, repair of fractures using fixtures, which engages bone's innate healing capacity. In case of degenerated tissues, augmentation or restorative approaches are opted wherein structural supports (non-resorbable) or prosthesis are used in total knee or hip arthroplasty (**Figure 1.2B**). In case of mild osteochondral lesions, resorbable defect filling using grafts are opted. The defects resulting due to resection of tumour or infected tissue, grafting is done to restore the defect site with resorbable materials or grafts (**Figure 1.2C**). Listed in **Table 1.1** are the defect classification and the commonly adopted strategies in clinical management of these defects. The implants used in these interventions are fabricated across different length scales ranging from nano- to micro- to macro- ranges (**Figure 1.2 B-C**) to specifically augment/ restore/ replace the defective tissue. However, if imparting cell-instructive cues in current generation of biomaterials, for instance modulating the zonal mechanical profile (micro-macro range) or surface features (nano range) in metal implants could facilitate better osseointegration and implant compliance. Similarly, fabricating resorbable tissue engineered grafts embedded with cellular cues could hasten the rate of healing whilst minimizing the risk of graft rejection. For these clinical goals to be manifested in cell-instructive materials, an understanding of these cues is important, which is discussed in the forthcoming section.

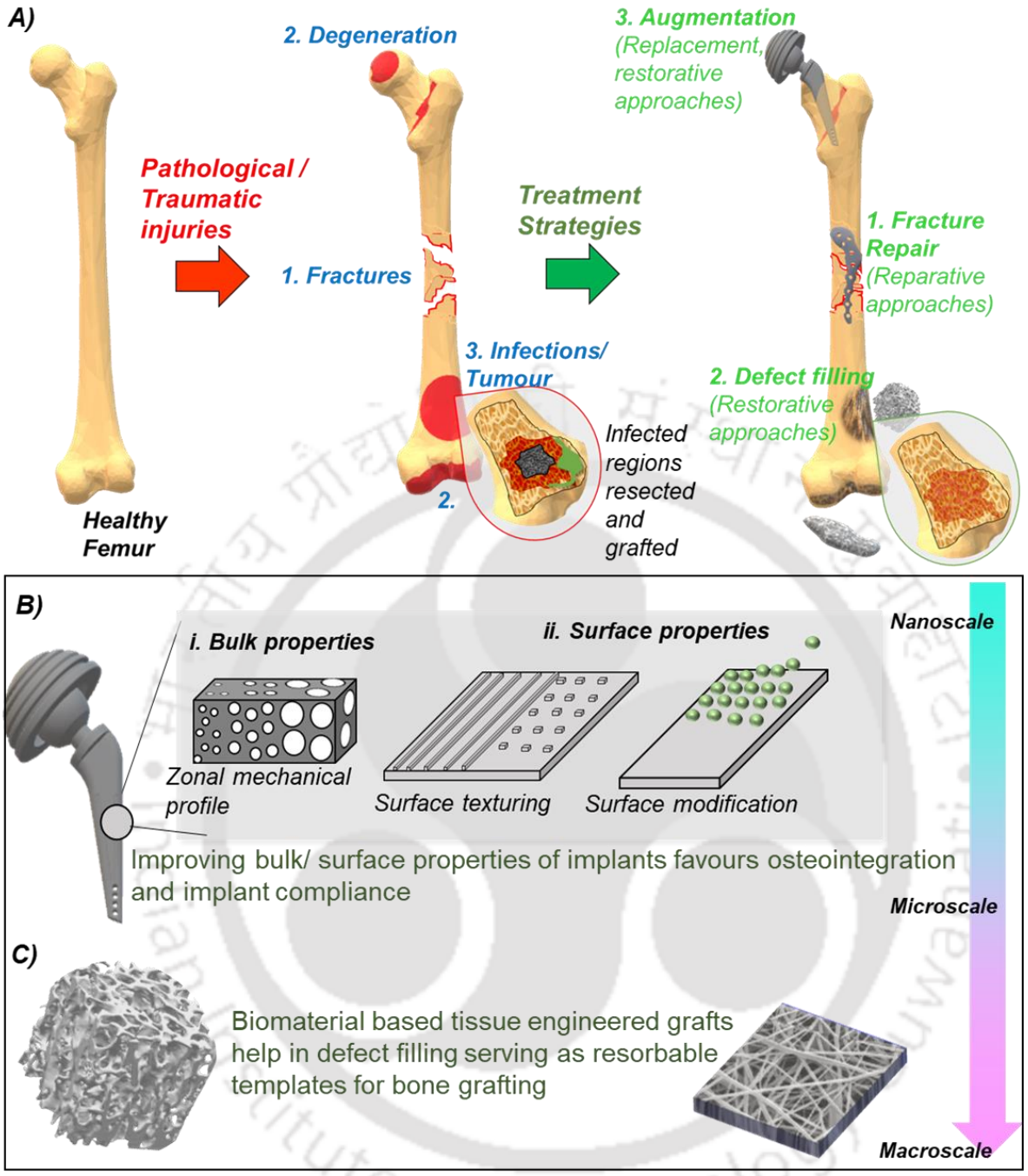

Figure 1.2. ***Clinical goals of cell-instructive biomaterials.*** *A) Depicted as an analogy is the femur for different bone injuries encountered, which involve 1) fractures as a result of trauma, 2) degenerative conditions such as osteoporosis or osteoarthritis, 3) pathological conditions as a result of osteomyelitis or osteosarcoma; B) The treatment strategies involve the 1) fracture repair using fixtures, 2) defect filling of resected infected/ tumour site or degenerated lesions with grafts and 3) augmentation in terms of replacement non-resorbable prosthesis. B) Imparting cell-instructive cues in these implants by tailoring mechanical profile, surface features and C) fabricating tissue engineered grafts with cellular cues could improve the current clinical success rate of conventionally used implants/ grafts.*

Table 1.1. *Bone defect classification system adopted by Clatworthy and Gross [38], the available treatment options and their fabrication methods*

Defect Type	Defect Size	Severity of Bone Loss Encountered	Available Treatment Options	Implant/ Graft Fabrication Method
Type-I (Contained)	< 5 mm	Contained with metaphyseal bone intact	PMMA/ Bone cement fill	Chemical synthesis
Type-I (Contained)	5 - 10 mm	Contained with damaged metaphyseal bone	PMMA/ Bone cement fill	Chemical synthesis
Type-I (Contained)	> 10 mm		Allograft/ Porous metal augments	Allografts or Demineralized bone sponges by conventional scaffolding techniques Porous metal augments
Type-II (Non-contained)	< 5 mm	Non-contained and non-circumferential defects, requiring a partial distal femur, partial proximal tibia or femoral head graft	PMMA/ Bone cement fill	Chemical synthesis
Type-II (Non-contained)	5 - 10 mm		Reinforced PMMA/ Bone cement fill	Chemical synthesis
Type-II (Non-contained)	5 - 15 mm	Non-contained and non-circumferential defects, requiring a segmental distal femur or proximal tibial graft	Total knee arthroplasty modular systems with stems (metal augments)	Injection moulding/ machining (limited customization) Metal implant surfaces are modified either by physical methods/ electro-chemical methods [39] like:

			i) Course grit blasting - SLActive (Strauman, Switzerland); Osseospeed (Astra Tech, Sweden) ii) Sol-gel deposition – Nanotite (3i Implant innovations, USA) iii)Electrochemical anodization – TiUnite (Nobel Biocare, Switzerland)
Type-II (Non-contained)	> 15 mm	Structural allografts/ mega-prostheses/ Porous metal augments	Injection moulding for polymers/ machining for metals (limited customization)

1.2.2 Biochemical Cues

1.2.2.1 Biological Cues

Biological cues regulate vast number of cellular functions, among which regulation of osteogenic fate in osseous tissue and chondrogenic fate in cartilaginous tissue is vital to maintain their homeostasis. Both these specialized cell types of the skeletal tissue originate from the mesenchymal progenitor cell (MSC) (**Figure 1.3A**). The MSCs are precursor cells which reside in specialized niches within the adult tissue, where the their stemness is tightly regulated by the niche cells. Once a cue for differentiation is received, these precursor cells transit to become specialized cells by going through stages (i) *determination phase* (early stage markers are expressed, **Figure 1.3A ii**), (ii) *commitment phase* (early-mid stage markers are expressed **Figure 1.3A ii**) and (iii) *terminal phase* (mid-late stage markers are expressed, **Figure 1.3Aii**). The differentiation follows a close route noticed in bone development process, as the key markers expressed in early, early-mid, mid and late stages of development (*in vivo*) are analogous to commitment, determination and terminal phases of differentiation observed *in vitro* [40]. Biomaterial strategies which help trigger these phases termed 'osteoinductive' approaches are intended in bone graft materials which resorb and aid in regeneration of the defect site. Each of these stages/phases are governed meticulously by wide variety of biological cues, of which few pathways are well studied and many are still debated or yet to be discovered.

Clinically growth factors (GFs) are used to supplement bone regeneration in non-union defects, to accelerate fracture healing, open tibial fractures, osteoarthritis, osteonecrosis, and spinal fusions. The well-studied GFs include bone morphogenetic proteins (BMP-2, 7), fibroblast growth factor-2 (FGF-2), insulin like growth factor-1 (IGF-1), platelet derived growth factor (PDGF) and vascular endothelial growth factor (VEGF). [41] These GFs have been identified by studying their roles through developmental biology approaches. [42]

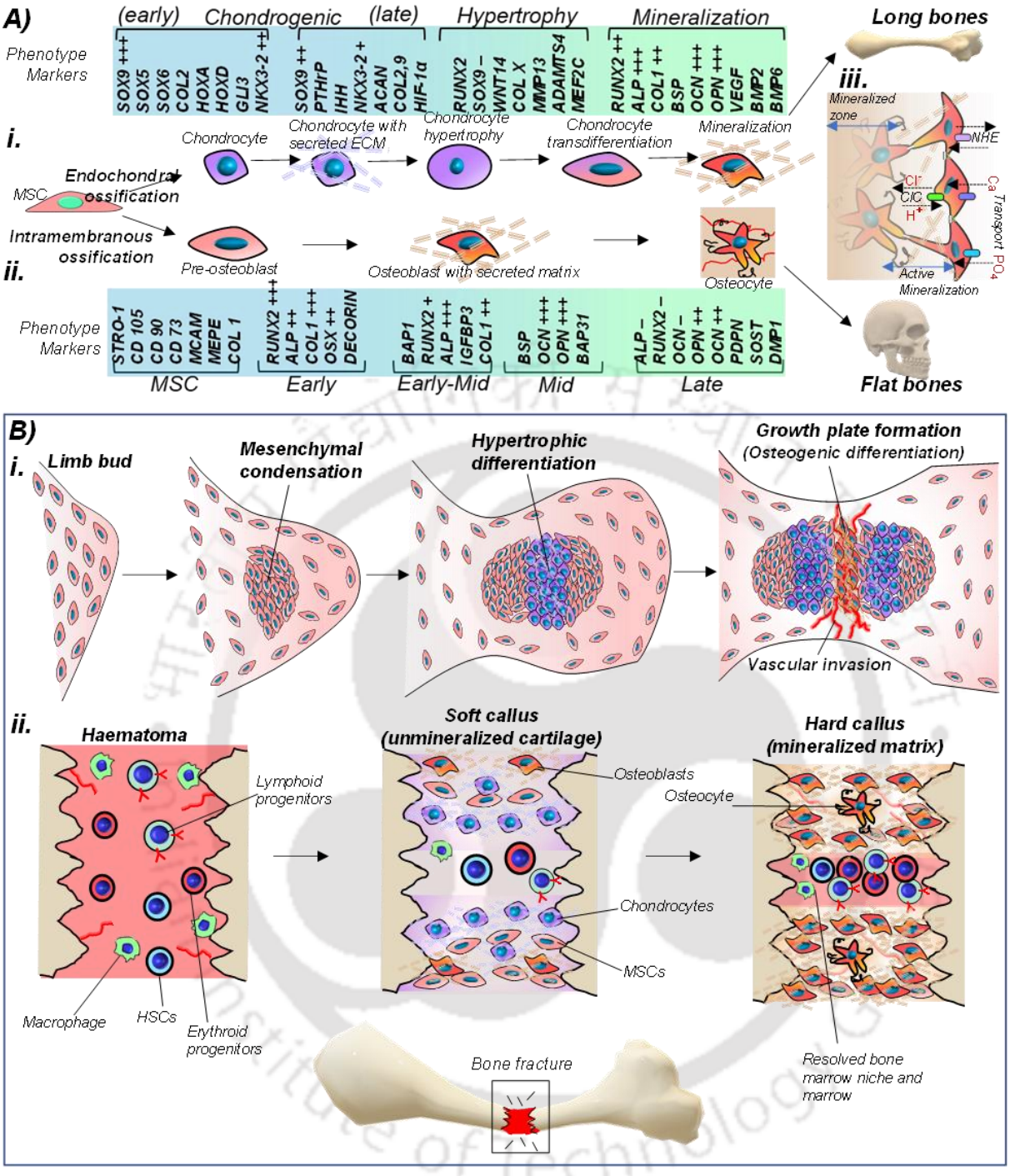

Figure 1.3. ***Cellular regulation in bone development and repair.*** *A) Scheme representing ossification pathways involved during developmental (pre-natal) and post-natal fracture healing processes; i) Endochondral ossification by which long bones are formed, involve the formation of intermediate cartilaginous template (developed by chondrocytes), which later mineralize following chondrocyte hypertrophy, chondrocyte transdifferentiation (few key markers expressed at each stage is presented); ii) Intramembranous ossification by which flat bones are formed, involve the direct conversion of MSCs to form mineralized matrix, following osteoblast matrix secretion, and terminal maturation into osteoblast (few key markers expressed at each stage is presented); iii) Ossified mineral matrix consists of tight epithelium*

formed by osteoblasts which secrete collagen-I, where active mineral deposition occurs due to ion transport mediated through ion channels and transporters, within well vascularized microenvironments; B) Analogy between pre-natal bone development and fracture healing; i) Endochondral ossification in skeletal development, where in developing limb bud, mesenchymal condensation occurs, followed by chondrocyte differentiation and hypertrophy; the cartilaginous template (indicated in purple) then experiences vascular invasion setting the ossification centre, thus establishing the growth plate [43]; ii) Fracture healing (postnatally) involves the hematoma formation (blood clot) which recruits inflammatory, progenitor cells that get resolved (4-10 days); following this cartilaginous template (soft callus indicated in purle) is formed bridging the proximal, distal ends (10-14 days), that slowly mineralizes to form the hard callus, facilitated by remodelling of the soft callus and vascular invasion [44] with resolved bone marrow niche and restored bone marrow (> 28 days).

Classically, four important (among others) signalling cascades have been demonstrated over the years to play important roles in controlling osteogenic and chondrogenic fate during developmental stages (**Figure1. 4A**). They are (i) (Wingless type) Wnt /β-catenin, (ii) receptor serine threonine kinase (RTSK) family, (iii) receptor tyrosine kinase (RTK) family and (iv) Hedgehog signalling pathways. Wnt signalling has been found to play role during the early determination phase of differentiation in MSCs, and also helps in proliferation. There are 19 Wnt receptors that have been discovered and it has two classical arms, the canonical (β-catenin dependent involved in differentiation/ proliferation) and non-canonical (β-catenin independent involved in adhesion/ migration) [45]. Wnt signalling is closely associated in osteoblast maturity, osteoclast and haematopoietic stem cell ageing [46]. RTSK and RTK family are perhaps the most widely explored ligand-receptor interaction for bone regeneration, as they include the growth factors (ligands) which important roles through the determination, commitment and terminal maturation phases of differentiation (during embryonic development and fracture healing) [42, 47]. Some of the major factors characterized to be present at fracture site are TGF β1,2; BMP 2,3,4,7; FGF 1,2 [42] and these ligands activate two distinct class of receptor kinases namely RSTK (TGF-βR, BMP R, activin -Act receptors) and RTK (FGF R, PDGF R, IGF R, VEGF R receptors) (**Figure 1.4A**). These factors play different roles at different expression levels in the role of action as mitogens, chemotactants, differentiation stimulant or together as a pleiotropic factor [47, 48].

Hedgehog (three variants namely Sonic Hedgehog (SHH), Indian Hedgehog (IHH) and Desert Hedgehog (DHH) have been found to role in skeletogenesis and moderating pre-osteogenesis (while having anti-adipogenic roles). All these signalling cascades have their own downstream signalling messengers and transcription factors which regulate the osteogenic/ chondrogenic commitment. Among them, the two major regulators are Runt related (*RUNX2*)

[49] and SRY (sex-determining region Y)-box (*Sox9)* [50] transcription factors which are master regulators of osteogenic and chondrogenic phenotype maintenance, respectively. They control the expression profile of growth factors, transcription factors and mediators which allow in differentiation by a feedback loop mechanism with respect to their immediate microenvironment cues. Their roles are interrelated, working co-operatively as their expression pattern are overlapped, both spatially and temporally [51]. They are overexpressed during initial lineage determination/ commitment stage while gradually downregulated during maturation phase. Pertinent to note here, the intramembranous ossification (**Figure 1.4Ai**) involving direct conversion of MSC progenitor to terminally differentiated osteoblast/ osteocytes involve regulation with *RUNX2* predominantly; whereas in endochondral ossification (**Figure 1.3B**) pathway where a cartilaginous template which gets mineralized, relies on the strict orchestration between *RUNX2* and *SOX9* [52], where *RUNX2* regulates chondrocyte hypertrophy, subsequent transdifferentiation into osteoblast [53]. Pertinent to note here, fracture healing in long bones (postnatally) also follows a similar route, involving endochondral ossification where soft callus ossifies to bridge the defect (**Figure 1.3B**).

1.2.2.2 Chemical Cues

Embedding chemical cues in biomaterials enable in harnessing the osteogenic cells and precursor cells chemosensitivity towards osteogenic commitment. This chemosensitivity is attributed to the ion channels and endocytosis mechanisms. In the osteon, the structural unit of cortical (compact) bone the osteoblasts which are organised as tight epithelium (**Figure 1.3Aiii**), actively transport minerals using ion channels and transporters which line the basolateral and apical surfaces [54]. The osteoblasts secrete dense collagen matrix on to which amorphous calcium phosphate precipitation occurs, which later crystalize to hydroxyapatite thus forming the bone matrix. Therefore, there is active site of mineralization, where inorganic phosphates (P_i), calcium ions are readily available to form the bone mineralization which occurs as follows: $6HPO_4^{2-} + 2H_20 + 10Ca^{2+} \leftrightarrow Ca_{10}(PO_4)_6(OH)_2 + 8H^+$. As by-products protons and chloride ions which are generated are also removed from this active site of mineralization by exchangers and transporters. Thus, the osteogenic cells are sensitive to chemical cues especially divalent ions which regulate key signalling mechanisms pertaining to osteogenic differentiation and maintenance. Broadly, the mechanisms which regulate the uptake of these chemical cues can be broadly classified into three categories namely, (i) transporters, (ii) G-protein coupled receptors (GPCRs) and (iii) endocytosis mediated mechanisms (**Figure 1.4B**). The passive transport of ions across the cell during the osteogenic

processes is regulated by ion channels (L type calcium channels) which does it across the extracellular to intracellular cytosol across an electrochemical gradient without the expenditure of energy. Active transport of essential ions against electrochemical gradient is mediated through exchangers and transporters, which include Na^+P Type II cotransporters (NaPi-IIa, b), where transport of one P_i is done at the expense of co-transport of 2 or 3 Na^+ [55] (symporters), solute carrier family 20 (SLC20a1 or P_iT-1) [56], chloride proton antiport (CLC) which allow transport of Cl^- and H^+ ions, [54] sodium hydrogen exchangers (NHE) for Na^+ H^+ transport, sodium calcium exchangers (NCX) for Na^+ Ca^{2+} transport [57] and zinc importers (ZIP) for transport of Zn^{2+} [58]. In addition to these active transporters (secondary pumps where energy expenditure is balanced by sodium), primary pumps where ATP is expended in case of ATPases for transport of calcium (Ca-ATPases), of sodium potassium (Na^+ K^+ ATPases) and of proton potassium (H^+ K^+ ATPases). [57] These transporters play crucial role in mineralization-resorption process and thus a bioactive material eluting chemical cues of essential ions involved in mineralization/resorption utilize these transporters expressed in both osteoblasts and osteoclasts for the mineral trafficking.

G-proteins, GPCRs and calcium signalling play a very important role during bone development and remodelling. [59] GPCRs (**Figure 1.4B**) after binding with its specific ligand transduces the signal to heterodimeric G proteins (after guanine triphosphate GTP binding), which then activate secondary messengers such as cyclic adenosine monophosphate (cAMP) and Ca^{2+} (activated through inositol triphosphate IP_3 receptor, a store operated calcium entry SOCE channel in endoplasmic reticulum). The transcription signals are then passed on through cAMP responsive element binding (CREB) protein. Synthetic agonists (receptors activated solely by synthetic ligands RASSLs) such as hRO-I, hRO-s (shown to enhance bone formation) which target GPCRs are becoming attractive options to modulate this cascade [60]. Of particular importance in GPCRs among several, are frizzled (Frz) which mediate Wnt signalling, parathyroid hormone (PTH) receptor, parathyroid hormone related peptide (PTHrP) (class B GPCRs) PTHR1 whose activation has inhibitory roles on TGFβ signalling [61] and calcium sensing receptors (CaSR) [62] which regulate calcium homeostasis. CaSR in addition to sensing Ca^{2+} level in the extracellular space, can also sense/ respond to other divalent or trivalent cations because of its ionic properties similar to calcium. [63, 64] Therefore, this has been exploited in many approaches where alkaline earth metals, alkali metals and transition metals ions are doped into bioceramics. The dissolution products from these bioceramics are sensed by CaSR, thus having a positive impact on osteogenic differentiation. Some of the ions

that have been investigated are boron (B^{3+}), calcium (Ca^{2+}), cobalt (Co^{2+}), copper (Cu^{2+}), magnesium (Mg^{2+}), strontium (Sr^{2+}), and zinc (Zn^{2+}) at both *in vitro* and *in vivo* animal studies [65]. It is pertinent to note here is these divalent cations also have been observed to bestow proangiogenic traits (in case of Co^{2+} Cu^{2+} Sr^{2+}) [66], which is achieved when these divalent ions stabilize HIF-1α (hypoxia inducible factor), which under normoxic conditions is destined for proteolytic degradation by prolyl-4-hydroxylase (PHD, a 2-oxoglutarate and Fe(II) dependent dioxygenase) enzyme. Stabilized HIF-1α accumulates and helps in regulating downstream proangiogenic signals which is vital for neovascularization. [67] Synergistic roles of dual doped ceramics have also been explored in this regard to aid in osteogenesis while favouring angiogenesis also, towards bone regeneration applications. [66, 68] A similar approach of stabilising the HIF-1α signalling cascade (where it binds to hypoxia response elements HRE) to trigger proangiogenic cues is the use of dimethyloxalylglycine (DMOG), a cell permeable inhibitor of PHDs (**Figure 1.4B**) [69]. Iron chelators and other synthetic chemical compounds (2-oxoglutarate analogues) also have been investigated as PHD inhibitors as hypoxia mimetic factors in upregulating HIF-1α levels [70]. Pertinent to note here, chondrocytes residing within avascular cartilage, surrounded by poorly oxygenated synovial fluid experience low oxygen tension, where this hypoxia helps in maintaining chondrocyte phenotype via HIF-1α by activating Sox-9 by unidentified regulators (as opposed to HRE). [71]

Extracellular vesicles (EVs) which are implicated with cell-cell communication, immune-regulation and transfer of genetic material, have in the recent years become an attractive approach to mediate “cell-free” approach in regenerative medicine, as opposed to stem cell therapy. EVs contains thousands of metabolites, DNA, RNA, lipids, proteins and with high heterogeneity varying in terms of size, content and cellular origin [72]. Several approaches are emerging where engineered EVs are utilised to mediate osteogenic differentiation, angiogenesis and immune-modulation. [73, 74] EVs are up taken by cells through endocytosis which is either receptor mediated (clathrin or any suitable receptor) or non-coated (small buds called caveolae) or by micropinocytosis (highly ruffled plasma membrane). [75] Synthetic liposomes (nm to μm scales) with embedded molecular cargoes such as ions, growth factors, miRNAs, peptides which mimic EVs have also garnered attention in the recent years. Depending upon the acyl chain length, degree of saturation the size and properties for encapsulation can be controlled, thereby the payload can also be planned. For instance, silencing mRNA (siRNA-STAT3), miRNA-335-5p (activator of Wnt signalling), DNA (*RUNX2*), glucocorticoids (dexamethasone) have all been investigated as payloads for delivery

through liposomes for bone regeneration [76]. Nanoparticles or degradation products from bioactive materials also tend to be up taken by this route through endocytosis and the payload is released into the cytosol after fusion with lysosome (**Figure 1.4B**). Another well explored route for triggering osteogenic commitment is the glucocorticoid receptors (GCR), where glucocorticoids (GC) (such as dexamethasone) are enter the cytosol (intermediate activation by 11β-HSD2, hydroxysteroid dehydrogenases) converts the inactivated GC to active form. The GC binds to cytoplasmic receptor (GCR) associated with chaperone proteins (HSP90, FKBP52), later this complex shuttles (**Figure 1.4B**) into the nucleus to activate genes associated with osteogenic fate (*RUNX2*, glucocorticoid induced leucine zipper - GILZ, and canonical Wnt signalling). [77] Furthermore, small molecules (naturally derived or synthetic) which target the above discussed biochemical signalling pathways have gained attention, owing to their cost-effectiveness and prolonged bioactivity in comparison to growth factors. For instance, purmorphamines, hydroxycholesterol have been found to activate Hedgehog signalling; resveratrol have been found to activate Wnt signalling; genistein and icariin have been found to activate BMP signalling pathways. [78]

1.2.3 Physical Cues

Substrate mechanics regulate cellular differentiation, migration and spreading. [79] Cells in the tissue are within a meshwork of ECM which act as physical scaffolding and also control biochemical signalling by regulating the availability of biomolecules by the virtue of the ECM makeup. Additionally, mechanical properties of this ECM matrix control cellular behaviour by elastic deformations which is transmitted from the ECM to the cell. Thus, this cell-ECM mechanical coupling is reciprocated, where cell senses them and also secretes remodelling enzymes (like matrix metalloproteinases MMPs) to remodel the surrounding enzyme. This unique form of communication, termed ‘cell mechano-sensing’ also helps in collective cell migration and multicellular organization during developmental stages. [80] The implanted biomaterial at defect site, ideally must exhibit matrix stiffness and bulk properties akin to the surrounding osseous tissue. In order for cells to probe their immediate vicinity’s mechanical property (elasticity) they must strain the substrate, which is brought about by cytoskeletal contractile forces generated through cytoskeletal actin-myosin machinery. [80] This is transmitted through the focal adhesion complexes (direct engagers, discussed previously).

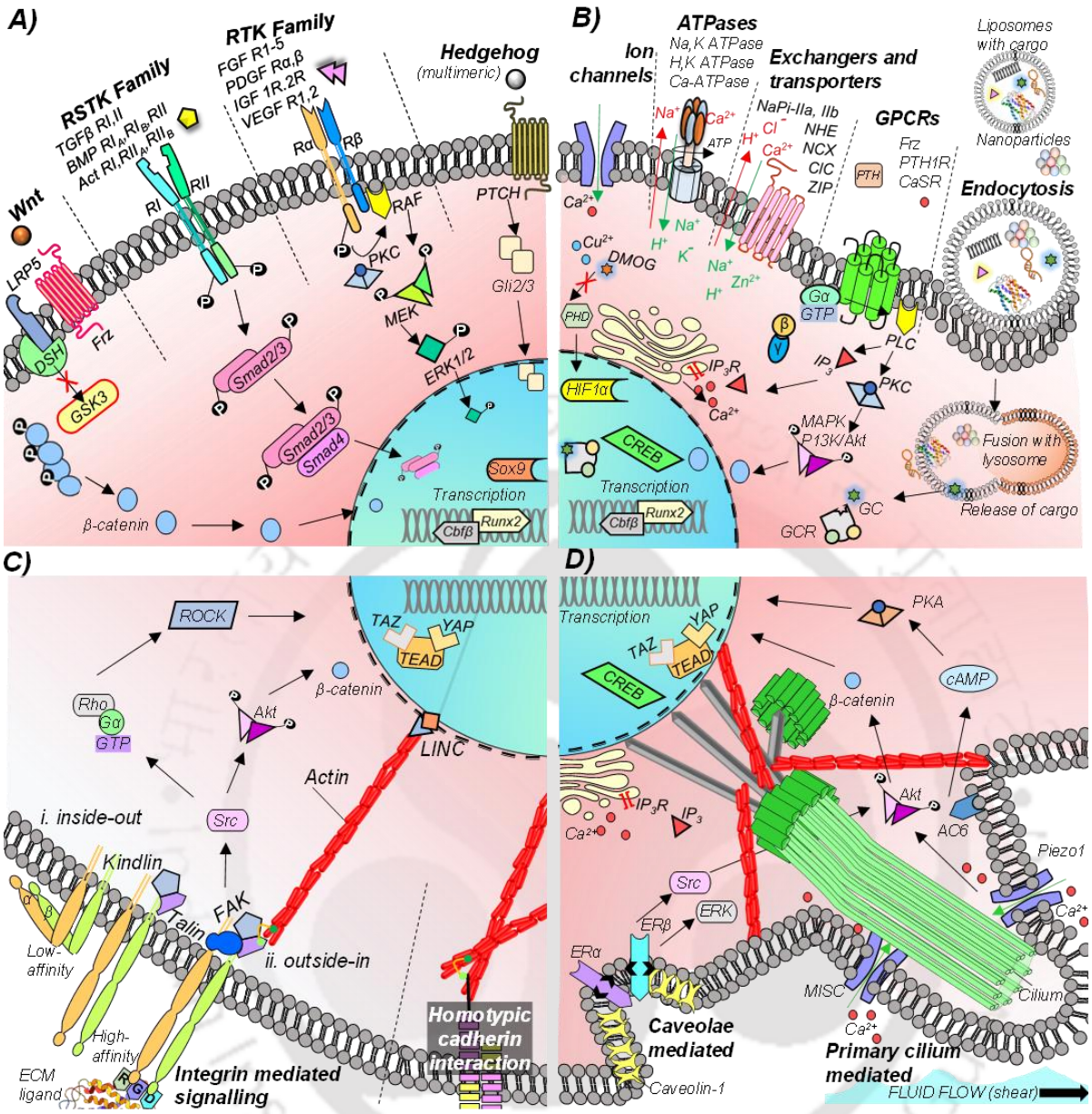

Figure 1.4. ***Biological, chemical and physical cues regulating osteogenic fate.*** *A) Biological cues mediated through growth factors involving Wnt/β-catenin signalling, serine threonine receptor kinases, tyrosine receptor kinases and Hedgehog signalling cascade; B) Chemical cues mediated through L-type ion channels, exchangers and transporters, G-protein coupled receptors, endocytosis mediated; C) Physical cues mediated through mechanical coupling of actin tension of cell with ECM (cell-ECM interaction through integrin inside-out, outside-in signalling) and cell-cell coupling through cadherins; D) Sensing of physical cues, mainly shear stress (as a result of fluid flow) through caveolae and primary cilium.*

Frz – Frizzled receptor; DSH – Dishevelled; GSK-3 – Glycogen synthase kinase 3; SMAD – "small" worm phenotype and "mothers against decapentaplegic" genes homologies; RAF – Rapidly accelerated fibrosarcoma (serine/ threonine protein kinases); PKC – Protein Kinase C; MEK – Mitogen activated protein kinase (MAPK); ERK – Extracellular signal-regulated protein kinase); PTCH – patched; Gli – glioma associated oncogene transcription factor; PLC

– phospholipase C; PI3K – phosphoionositide-3-kinase; Akt – Protein kinase B; Src – proto-oncogene tyrosine protein kinase; PI3K - Phosphatidylinositol 3-kinase

The mechanical signalling is long range too, as the native ECM exhibits non-linear force propagation, resulting in Young's modulus (E) = 20 GPa along the Haversian system (longitudinal axis) whereas in the transverse direction modulus, E = 8 GPa is witnessed [4] in cortical (compact) bone. The ECM's anisotropic makeup carries over to the spongy or trabecular bone (plate like structuring offering more porosity, larger surface area to mass), which enables it to encase the marrow, imparting modulus of E = 100 MPa. Thus, the cells residing within these compartmental quarters experience different levels of forces thus responding accordingly to the forces experienced. This is very much evident in bone mineralization where organ level mechanical loading mediates bone mass or density through pericellular mechanics [10] (Wolff's law). In osseous tissue, the transient mechanical loading also mediates interstitial fluid flow in the lacunar-canalicular (Haversian) system. Therefore, the biophysical cues experienced in the cellular and pericellular space can be attributed to (i) the stress-strain exerted via the ECM on the cells (and vice versa) which is predominantly mediated through ECM ligands, (ii) interstitial fluid flow which creates a shear stress in the pericellular space (experienced particularly by osteocytes), and (iii) streaming potential (through the gap junctions and mechanosensitive ion channels: MISC). [10, 81] These biophysical cues are translated further downstream to activate signalling pathways relating to osteogenesis, thus achieving mechano-transduction.

The ECM's non-linear force propagation is attributed to the anisotropy of the ECM make-up wherein the constituents are aligned in anisotropic manner. The immediate manifestation of this extracellular anisotropy is evident on cell behaviour, where contact guidance enables cells to occupy the ridges/ grooves, and move along the fibers – a phenomenon termed as *topotaxis* (based on topographical cues) [82]. The extracellular anisotropies presented to cells are by virtue of either physical cues (grooves/ ridges) or chemical cues (ligand mediated) [83]. In both the cases, the cell adhesion is driven by focal adhesions. Integrins play major role here, where the bidirectional signalling controls cellular fate; (i) inside-out signalling governs cell-adhesion, migration, ECM assembly while (ii) outside-in signalling dictates cell-polarity, survival and osteogenic phenotype expression (**Figure 1.4C**). [81] The low-affinity integrin hetero-subunits, after kindlin/talin binding to β-subunit undergo conformational change, which further bind to specific ligands or undergo clustering. This is the initial process whereby cells engage their substrate, thus responding to

physical cues presented (in terms of roughness, topography and wettability). [84] Ligand mediated (high-affinity states of integrins) outside-in signalling happens when the integrin heterodimers bind to the ligand and downstream cascade is triggered through focal adhesion kinases (FAKs), Src family of kinases (Src) and integrin linked kinases. FAK and Src predominantly, in this mechanical coupling based mechanostransduction trigger Rho, Rac GTPases whose transcript regulators involve Yes-associated protein-1 (YAP)/ PDZ binding motif (TAZ), β-catenin. [85] While cell-ECM interaction is mediated through integrins, cell-cell interaction (a prerequisite in stromal niche cells to maintain cellular functionality, stemness) is guided by cadherins. [83, 86] The physical mechanical coupling translates the tension from the outside through the actin to the chromatin through LINC, which again modulate nuclear chromatin reorganization noticed during cell spreading. [11]

In addition to primary mechanical coupling (through cell-ECM interaction), shear forces exerted by fluid flow is detected by primary cilia. Primary cilium (9+0 microtubule-based organelle) exhibited by osteocytes help in concentrating signalling components such as ion channels (MISCs such as Piezo1) via the solitary extensions of the plasma membrane [10]. Calcium mobilization into the cytosol is facilitated through MISCs by engaging the mechanical tension experienced at ciliary compartment through primary cilium, actin-myosin machinery. Second messenger (Ca^{2+}) through SOCE also contributes in calcium signalling mechanisms, as result of mechanotransduction. In addition, primary cilia bending along the direction of fluid flow (shear) is seen to activate adenylyl cyclase (AC6)/cAMP signalling through protein kinase A (PKA) [87] with downstream effectors in Wnt/β-catenin and CREB (**Figure 1.4D**) [81]. Caveolae in osteoblast and osteocytes also help in sensing mechanical forces through ligand independent estrogen receptor (ERα, β) by associating with caveolin-1, with downstream regulation through extracellular ligand regulated kinases (ERK) and Src family kinases (Src). [88]

1.2.4 Hematopoietic Niche and Immunoregulation

Bone marrow, a soft viscous tissue is encased within the trabecular meshwork and cavities of the axial and long bones. The bone marrow in humans accounts for 5% of bodyweight and is the major haematopoietic organ and lymphoid tissue, contributing for haematopoiesis – continuous process of blood cell production. [89] Hematopoietic stem cells (HSCs), the multipotent stem cell are the primary cells which mediate this process, giving rise to specialized blood cells. Haematopoiesis is a very dynamic process, where depending upon the homeostatic/ pathological condition of the host, volume changes in hematopoietic tissue

has been observed. The space occupying component is the adipose tissue which recedes when there is active haematopoiesis. The characteristic colour of marrow is attributed to adipose tissue presence (yellow marrow) or heme chromogen from blood cells (red marrow). Apart from being a dynamic process, haematopoiesis is a compartmentalized phenomenon, owing to its organization inside the marrow. This compartmentalization is achieved by the stromal/ supporting cells and other cell types (vascular, neural, connective), together forming the hematopoietic niche. Thus, the distinct sub-events (resulting cells in parenthesis) such as erythropoiesis (RBCs), granulopoiesis (granulocytes), lymphopoiesis (lymphocytes) and megakaryopoiesis (megakaryocytes) occur in distinct niche environments, tightly regulated by the humoral factors secreted by the niche cells. HSCs, by virtue of symmetrical and asymmetrical division, undergo specialization either by physical association with niche cells or via biochemical regulation.

The immediate point of contact of bone marrow is the endosteum, the inner surface of bone which consists of a layer of reticular connective tissue along with osteoblasts, osteoclasts and specialized osteoblasts. These specialized osteoblasts express spindle shaped N-cadherin (SNO) to which HSCs adhere and remain quiescent. Moreover, these SNO osteoblasts also have been found to express BMP, PTH, PTHr and receptor activator of NFκB ligand (RANKL) which regulate the quiescence/ recycling stage of HSCs (either short term ST-HSCs contributing for haematopoiesis for few weeks or long term LT-HSCs contributing for several months to lifetime), and also specialization into several progenies, once detached from this niche regulation. [90] This specialized niche composed of SNO osteoblasts is termed the endosteal niche (**Figure 1.5A**). Apart from cells of osteogenic lineage, the bone is innervated and profusely vascularized, and this connection is carried through into the bone marrow too.

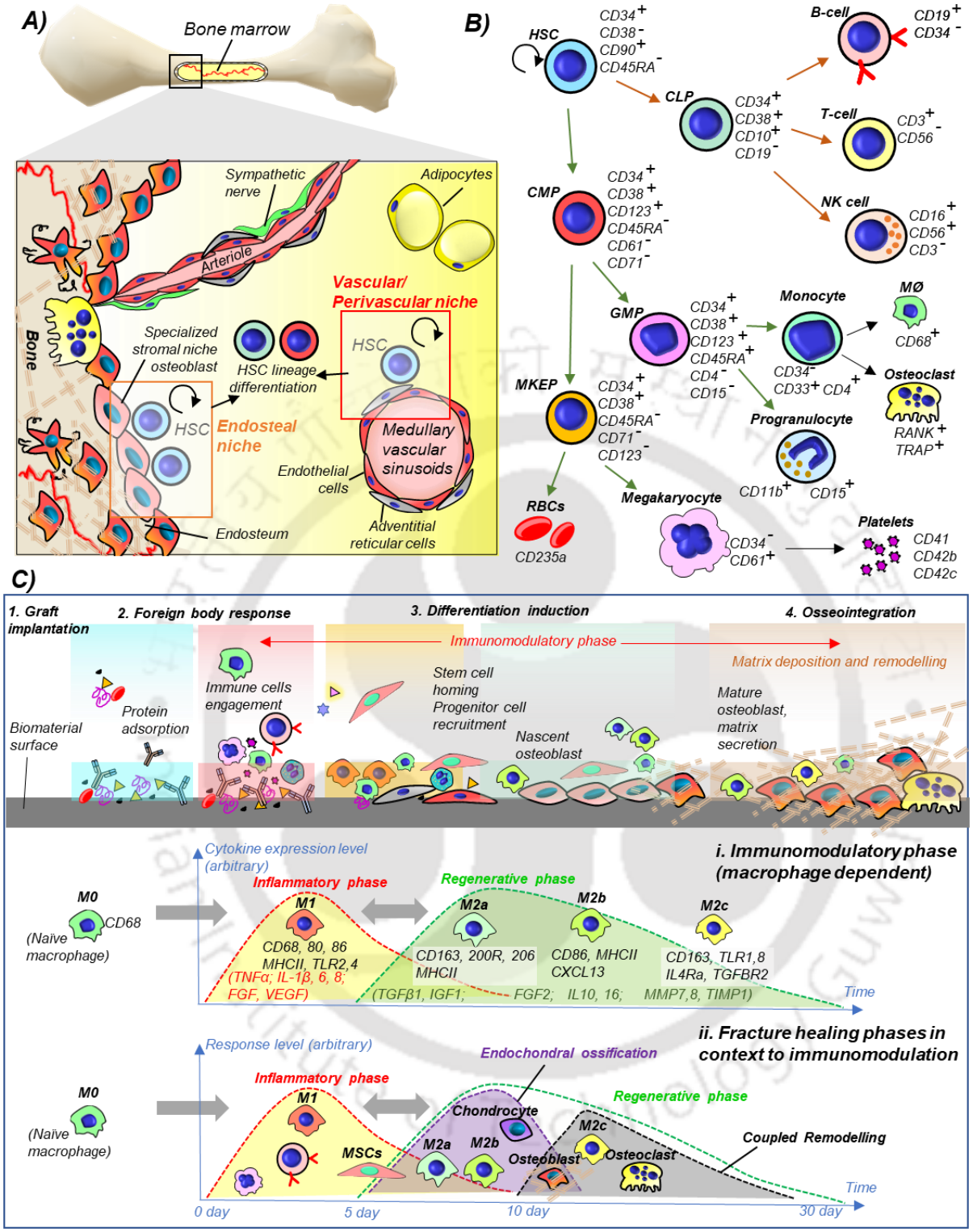

Figure 1.5. ***Bone marrow's hematopoietic niche, cells of hematopoietic origin and their roles***. *A) Bone marrow comprises of the stromal niche microenvironment (endosteal and vascular niches) where hematopoietic stem cells (HSCs) reside, renew and differentiate into precursor cells of lymphoid, myeloid and erythroid progeny; B) Progeny of HSCs, HSCs (exhibiting self-renewal traits) differentiate into specialized cells of lymphoid progeny via common lymphoid progenitor (CLP) to lymphocytes (B-cell, T-cell) natural killer (NK) cells;*

myeloid progeny via common myeloid progenitor (CMP) to either granulocyte monocyte progenitor (GMP) generating monocytes, macrophages, polykaryotic osteoclasts and granulocytes; or megakaryocyte erythrocyte progenitor (MKEP) which yields red blood cells (RBCs), megakaryocytes and platelets; C) Sequence of immunoregulatory events after biomaterial implantation in osseous defect site; after graft implantation (1), protein adsorption (2) enables immune cells engagement (macrophages, lymphocytes, granulocytes), which secretes cytokines dictating the fate of biomaterial; stem cell homing, vascular progenitor cell recruitment initiates differentiation induction (3), involving MSCs to osteogenic differentiation and macrophage plasticity switch; this immunomodulatory phase includes an initial inflammatory phase (characterized by M1 macrophage, inflammatory cytokines) which subsides, giving way for regenerative phase (characterized by M2 macrophage, corresponding cytokines, growth factors and remodelling enzymes); after the regenerative phase, osseointegration (4) is achieved where bone matrix forms over the implanted graft, ushering clinical success of the graft; i) Response intensity expressed arbitrarily for cytokine expression by different macrophages during the fracture repair phase, correlated with ii) different cells involved in fracture healing which consists of endochondral ossification which forms the cartilaginous template, which gets ossified and remodelled to form the new bone tissue.

In bone, nutrient canals (one artery; one or two veins) enter the cortical bone obliquely and disperse into fine arterioles and venous sinuses (composed of endothelial cells adventitial reticular cells) within the marrow. The nerve bundles also follow these arterioles, composed of myelinating Schwann cells encasing sympathetic autonomic neurons. It is in this vicinity of vascularized conjuncture, the niche consisting of vascular and perivascular cells is found (**Figure 1.5A**). Different perivascular cell types have been identified which express melanoma associated cell adhesion molecule (MCAM/ CD146), cell adhesion molecules (ICAM-1, VCAM-1), chemokine (C-X-C motif) ligand 12 – CXCL12, nestin, leptin, P-selectin, E-selectin and signalling lymphocytic activation molecule (SLAM). ECM proteins such as fibronectin, laminin, vitronectin and hyaluronic acid are also secreted by these associated stromal cells. These receptors help in HSC adhesion (mediated by integrins and CD receptors [91]), regulate their self-renewal and specialization. [92] Apart from this, these stromal cells of the vascular/ perivascular niche secrete stem cell factor (SCF), FGF2, IGF2, angiopoietin (ANGPT1), EGF, DHH which regulate the HSCs biochemically. [93] In addition to all these factors, chemokines and growth factors entering the marrow from circulation also regulate the specialization of HSCs, which differentiate into multiple progenies (depicted in **Figure 1.5B** with few important surface markers for identification) of myeloid, lymphoid and erythroid progeny which enter back into systemic circulation through the sinusoids. For instance, erythropoietin is crucial for erythrocyte (RBC) formation, thrombopoietin for megakaryocyte formation, macrophage-colony stimulating factor (MCF) for macrophage formation,

granulocyte colony stimulating factor for granulocyte formation, IL-7 for lymphocyte formation. [94]

The progenies from HSCs constitute the immune cells which are involved in the foreign body response (FBR). The sequence of events after a biomaterial graft is implanted at an osseous defect site is depicted in **Figure 1.5C**. Among the different immune cells, macrophages have been recognized as the primary cells of inflammatory response of FBR. Macrophages are dynamic in nature owing to their plasticity; thus from naïve macrophage (derived from infiltrating monocytes) they can switch reversibly switch between M1 (pro-inflammatory) and M2 (anti-inflammatory or regenerative) phenotypes [95] (**Figure 1.5C** representing few important surface markers of different macrophage phenotypes and the cytokines they secrete). Though precise nature of chronological progress of M1/2 switch is not understood, it has been understood that post implantation of a graft M1 macrophage mediated inflammatory phase is noticed. Naïve macrophages stimulated by helper T-cells T_H1 cytokines (such as interferon γ) to acquire the M1 phenotype, along with other antigen presenting cells in the vicinity. This inflammatory phase is very critical because a slew of factors which promote angiogenesis (vessel sprouting, pericyte differentiation via VEGF, TNF [96]) and MSCs migration/ cell recruitment (via monocyte chemoattractant protein MCP1 secreted macrophages, by stromal cell derived factor – SDF1/ CXC- chemokine CXC-4 receptor [97]). Soon after the clearance of inflammatory phase, the regenerative phase sets in marked by macrophages stimulated by helper T cell T_H2 cytokines. For instance, IL-4,13 induced M2a secrete platelet derived growth factor-BB which enhances neo-blood vessel formation, while IL-10 induced M2c secretes remodelling enzymes (MMP 7,8, tissue inhibitors of metalloproteinases – TIMPs). [96, 98] Having a good understanding of these activation phenomena of macrophages and their plasticity, helps biomaterial engineers to fine-tune biomaterial surfaces to modulate the immune response favourably. [36] This *osteoimmunomodulation*, for instance has been explored through scaffolds loaded with cytokines (IL-4) [99] and immunomodulatory drugs (dexamethasone) [100] which locally modulate the implant space thereby achieving osseointegration, without leading to fibrotic rejection.

1.3. Engineering Perspectives – Recreating the Cellular Micro-niche for Resorbable Bone Grafts

Engineering functional osseous tissue *in vitro* and achieving tissue replacement *in vivo* effectively, have been the major agenda of biomaterial research. To facilitate this, continuous

impetus has been given for decoding the crosstalk at the cell-material interface. Different materials convoke variable degree of response (in terms of strength and nature) in cell-material communication. For successful implantation of a tissue engineered bone graft, understanding cellular behaviour (the bio/chemical/physical cues that trigger them) and graft implant's physico-chemical nature is essential. Based on the cellular cues as discussed on previous section, this section focusses on some of the strategies which harness these cues in developing cell-instructive biomaterial grafts. The materials design herein involves the selection of appropriate biomimetic/ synthetic material, and adopting '*the right*' fabrication strategy to develop the graft embedded with relevant cues. Indirectly, the rationale here is to recreate the cellular micro-niche, where infiltrating host cells occupy this engineered landscape, eventually engage with the confinement and adapt to elicit a favourable response. Thus, this spatiotemporal control of the engineered micro-niche over the cells has been the crux of cell-instructive biomaterials.

1.3.1 Synthesis Standpoint – Building Blocks

To fashion a bio-template (three-dimensional/3D scaffolding) for cells to reside in, suitable building blocks has to be chosen. Bone is intrinsically built as an organo-apatite, a composite formed by mineralized type-I collagen – Col-1 (and other non-collagenous proteins - NCP), where 25% is composed of organic matter (out of which 90% is Col-1, remaining 10% is other NCP), and 65% is inorganic apatite ($Ca_{10}(PO_4)_6(OH)_2$), [101] remaining 10% comprises of water. Col-1, composed majorly by triplet amino-acids Gly-X-Y (Gly/ Pro/ Hyp) is a right-handed triple helical protein (three residues per turn) having cell attachment domains (DGEA, RGD, GFOGER) which serve as ligands for integrin ($\alpha1\beta1$, $\alpha2\beta1$), aiding cell adhesion. A single triple helical molecule is 1.5 nm in diameter interacts with another molecule based on the sidechains of X, Y residues pointing outwards per turn *via* charge/ hydrophobic interaction. Typically, through modelling experiments 5-stranded packing (3.6 nm in diameter) has been computed to form a microfibril, which eventually form macro-fibers (~ 500 nm). In this assembly, between the inter-fibrillar packing, there are overlap zones and holes which act as nucleation points (presence of COO^-) for Ca^{2+} which help in forming the amorphous calcium phosphate which later grow into apatite, strictly regulated by specific stereochemistry assemblage [102]. The size and growth of this crystal (50nm long/ 28nm wide/ 2nm thick) is regulated further by other NCPs such as γ-carboxyglutamate proteins (osteocalcin, matrix Gla proteins), proteoglycans (biglycan, decorin, asporin), glycoproteins (osteonectin, thrombospondins) and small integrin binding ligands N-linked glycoproteins – SIBLINGS

(bone sialoprotein - BSP; osteopontin - OPN, dentin matrix protein1 - DMP1) [103]. These NCPs bind to specific regions in Col-1 termed 'matrix interaction domains' which in turn regulate the fibril formation. [104] Thus, for a hierarchically structured organ like bone, these molecular building blocks are essential to recreate the bone micro-niche for effector cells to reside and execute their function.

1.3.1.2 Biomimetic Biopolymers

Biomimicry or imitating nature's design principles has enabled humans to resolve many long-standing problems, by virtue of replication either form or function of natural processes/ systems. Biomimetic strategies in bone tissue engineering (BTE) also have been attempted to recreate bone micro-niche, thereby developed bone grafts could serve as replacements with physicochemical features similar to autologous/ allogenous grafts. Native polymers present in bone/ cartilage such as collagen, hyaluronic acid, gelatin (collagen derived), proteoglycans, and demineralized matrices (from porcine/ bovine/ equine sources), listed in **Table A1.1** (*Appendix*) have been explored extensively in BTE. [18, 19, 105, 106] Though these native polymers innately have biological cues to facilitate osteogenic cell adhesion and support their growth, they have many disadvantages. Some of the major ones are the associated risk of animal-disease transmission (for animal sourced), high degree of variability, histo-incompatibility, high cost incurred in production/ purification and ethical concerns surrounding 'white boxing' (disclosure relating to sourcing). This has led to the quest for exploring 'biomimetic' polymers, which resemble collagen structurally and possess biochemical cues akin to other NCPs.

Keratin, a structural cysteine-rich fibrous protein biopolymer (obtained from wool, hair) having hierarchical structure analogous to Col-1, where single α-helical chains form left handed coils to form protofibrils, eventually combine to form intermediate filament. They also possess RGD, LDV, EDS cell attachment peptides, triggering α-4,5 integrin binding. [107] Apart from this, keratin's structural conservation across species impart them low immunogenicity and antigenicity, making an ideal biopolymer for BTE. For instance, keratin-based sponge infused with BMP-2 was assessed against Infuse™ (collagen based sponge loaded with BMP-2) in repairing segmental defects (mice femur), where keratin based sponge showed controlled release of BMP-2, suppressing adipogenesis thereby supporting osteogenesis [108]. Similarly, keratin based hydrogels also exhibited controlled degradation *in vivo* with sustained release of recombinant human BMP-2 (rh-BMP2) in critical sized rat mandibular defects, achieving higher bone mineral density (over 8 weeks) in comparison to

conventional absorbable collagen sponges (Infuse™ Medtronic). [109] Silk fibroins, have also been explored in BTE application owing to their close resemblance to Col-1. [52] Being a fibrous, structural protein spun by Lepidopteran larvae (of *Bombycidae* (mulberry silk) and *Saturniidae* (non-mulberry silk) family), has been demonstrated to be biocompatible, less immunogenic and biodegradable. Additionally, silk fibroins possess good mechanical resilience (tensile strength ~ 0.57 GPa) and strength-to-density ratio ten times greater than steel. [110] The processing feasibility enables it to be fabricated into multiple formats ranging from nanoparticles, micro-spun fibers to macro-scale scaffolds obtained through conventional processing (thermoplastic moulding to obtain interference screws [111]) and 3D printing. Moreover, the degradability can be tuned by controlling the crystallinity (imparted by the β-sheet domains GAGAGS repeats in mulberry silk and poly-(Ala) repeats in non-mulberry silk), where proteolysis by remodelling enzymes such as MMP-1,2 has been reported. [112]

Mulberry *Bombyx mori* silk fibroin has also been approve by United States Food and Drug Administration (US FDA) for use in medical devices for ligament graft (SeriACL™) and also shown promising results as an osteoconductive material in several small animal models (rats and rabbits) [113] and also in sheep humerus, tibial (critical sized) cortical defects [114]. Apart from being a good osteoconductive material, recent studies also have revealed silk matrices support vascularization and innervation when functionalized with vascular endothelial growth factor (VEGF), neural growth factor (NGF). [115] This is attributed to silk matrices ability to preserve the bioactivity of growth factors and hence also been successfully demonstrated as injectable hydrogels [116] in BTE. Moreover, similar to Col-1, silk fibroins have been found to direct the growth of apatite crystals in presence of calcium/ phosphate precursors, resulting in hierarchically mineralized composites in a bioinspired fashion [117]. The inherent presence of RGD tripeptide in non-mulberry silk fibroin (in *Antheraea pernyi, A. assama, A. mylitta, A. yammamai, Philosamia ricini*) has bestowed these wild silk varieties with enhanced osteoconductivity by virtue of improved cellular adhesion mediated through integrins [118]. *A. assama* based silk fiber reinforced scaffolds were able to facilitate apatite formation in a bioinspired manner with plate shaped apatite (~ 50 nm) deposited over silk fibroin template, and the resulting mineralized scaffold supported osteogenesis of seeded humans MSCs [119]. Mechanistic insights reveal that non-mulberry matrices (due to their biomimetic resemblance to Col-1) activates Hedgehog and PTH signalling (Gli2, Shh upregulation) in seeded human fetal osteoblasts [120]. Similarly, supplementing FGF-2 on pre-

osteoblasts seeded *A. mylitta* silk matrices aided in terminal osteocytic maturation via Wnt/β-catenin activation. [121]

Apart from protein biopolymers, biomimetic polysaccharides such as cellulose and chitin have also been explored in BTE. Cellulose, another hierarchical polysaccharide assembles into microfibrils (3.5 nm diameter) built by β-(1,4′)-D-glucopyranose monomers via intra-, inter-chain and inter-sheet hydrogen bonding, exhibiting good mechanical properties (E= 87-138 GPa). Cellulose microfibers-based scaffolds by virtue of structural guidance enabled osteoblasts to mature within these aligned matrices [122] and demonstrated guided bone regeneration in aneurysmal defects in rat cranium performing on par with collagen based membranes [123]. Among the different NCPs that associate with collagen in matrix interaction domain, are sulphated glycosaminoglycans (GAGs such as heparin sulphate, chondroitin sulphate and hyaluronic acid) which are important cartilage ECM components, enabling the chondrocytes to preserve and maintain their phenotype. Chitosan (deacetylated chitin) is an interesting anionic polysaccharide which has similarity to GAGs and has been extensively used in developing chondro-supportive matrices [124]. Natively, GAGs associate with multiple cytokines, growth factors via electrostatic interaction (presence of sulphated groups), thereby dictating the cellular phenotype of cells in immediate vicinity. Sulphated chitosan, have been found to mimic this phenomenon by binding with FGF/ BMP-2 preserving their bioactivity and aiding in osteogenesis, angiogenesis in growth factor loaded matrices [125] by triggering signalling through smad2/3 expression. [126]

1.3.1.3 Smart Synthetic Polymers

Synthetic polymers such as poly (α-hydroxy esters), poly- (aryl-ether-ketone), polyethylene (listed in **Table A1.1** (*Appendix*) are associated with poor biodegradation (non-resorbable) and are bioinert. Though these synthetic polymers possess good mechanical tenacity on par with native collagen, they lack biochemical cues which could facilitate remodelling once implanted at a defect site. Polyesters like PLA, PLGA undergo rapid hydrolytic degradation and not controlled degradation, thereby the rate of neo-tissue regeneration and rate of degradation do not match. Remodelling enzymes are secreted by cells in a planned and controlled manner, hence ECM gets remodelled spatiotemporal manner to facilitate cellular migration and infiltration. To overcome these drawbacks, synthetic polymers have been engineered with smart cues such as (i) addition of sequences which facilitate hierarchical assembly (ii) embedding cell adhesion motifs to facilitate specific cell recruitment, and (iii) inclusion of cleavage sites which MMPs/ proteases target to facilitate controlled

degradation. Hierarchical self-assembly through 3D biomimicry in synthetic polymers have been achieved by engineering peptide-amphiphiles which assemble into cylindrical supramolecular fibers [127]. Controlling the crosslinking density, thereby the viscoelastic modulus of matrices as well as the porosity could be achieved by engineering specific crosslinking chemistries, which can be adaptable/ reversible. For instance, an non-degradable matrix which is responsive to cellular stresses manipulating the reversible hydrazone linkages in PEG hydrogels have been developed. [128] These matrices are highly convenient to maintain a stable (non-degradable platform) while being covalently adaptable to cell-induced stresses by forming/ reforming elastically active crosslinks.

Engineered poly(ethylene glycol) - PEG backbone with pendant oligopeptides (GCGYGRGDSPG) for cell adhesion and linkers (GCRDGPQG↓IWGQDRCG; ↓ represents cleavage site for MMP-1) which MMPs target, were designed to make hydrogels encapsulating BMP-2 to treat defects in rat crania, which showcased localized bone regeneration [129]. Similarly, PCL functionalized with cyclic RGD (RGD(d)FK, cell adhesion motif) and MMP-2 sensitive peptide (GCRDGPQG↓IAGQDRCGC) [130] was used to develop electrsopun nanofibrous mats (resembling hierarchically aligned collagen fibrils) decorated with chitosan nanocomposite with plasmid DNA encoding BMP-2. Cationic chitosan complexes with pDNA and effectively transfects into MSCs, enabling osteogenic differentiation, circumventing the use of growth factor use directly and its drawbacks thereof. Additionally, engineered PCL matrices favoured integrin mediated binding of MSCs and controlled remodelling when implanted in rat calvarial defects. In clinical gold-standard – allografting, 60% failure rates are noticed due to poor periosteum formation, contributed due to sparse neovascularization [131, 132]. These sequences of events are tightly mediated through MMP remodelling which favours matrix degradation aiding vascular infiltration. Engineered PEG matrices with MMP-2,9 sensitive sequences GPQG↓IWGQ were found to support periosteal restoration in murine segmental defect model with 3-4 folds enhanced vascular and nerve densities in comparison to hydrolytically degradable PEG matrices. [132] This was evident from blood vessel sprouts and MSC migration within these matrices *in vitro* due to MMP responsive degradation. Presentation of integrin specific ligands have also been demonstrated to preserve MSC survival, engraftment and importantly immunomodulating the MSC's secretome. GFOGER, RGD functionalised PEG matrices enhanced the persistence of MSCs in non-healing segmental murine radial defect and also upregulated early inflammatory genes involving recruitment of lymphocytes, endothelial cells (via hypoxia factors) and recruitment of monocytes through

MCP-1 secretion. [133] In a peculiar approach, 8 arm PEG system was synthetically engineered with 20 adhesion motifs (mapped from human bone marrow protein atlas with key proteins such as laminins, tenascin C, thrombospondin, fibrinogen, fibronectin, collagen I, IX, X) to recreate a bone marrow hydrogel [134]. The hydrogel mimicked the bulk mechanics of human bone marrow viscoelastic nature and supported the MSCs as niche cells, to which HSCs can interact in a spatiotemporal manner to recreate the marrow.

1.3.1.4 Multifunctional Bioceramics and Composites

The main ceramic component in bone is a calcium deficient apatite (with Ca/P ratio less than 1.67), whereas for pure hydroxyapatite ($Ca_{10}(PO_4)_6(OH)_2$) the Ca/P is exactly 1.67. This non-stoichiometry enables the native apatite to be resorbed by osteoclasts much easily than synthetic apatites which are more crystalline and possess low solubility. The non-stoichiometry results in imperfections innately in native apatite due to regulation of the mineral homeostasis involving calcium, magnesium and phosphate ions [135]. For instance, substitutions of carbonate for hydroxyides are termed as A-type substituted carbonated-apatite ($Ca_{10}(PO_4)_6(CO_3)_X(OH_{2-2X})$) and substitutions of carbonate for phosphates are termed as B-type substituted carbonated-apatite ($Ca_{10-X/2}(PO_4)_{6-X}(CO_3)_X(OH_2)$) [136]. The structural feasibility of apatite ($M_{10}(ZO_4)_6X_2$), allows for wide variations and substitutions in its three sub lattices, i.e. (M = Ca, Sr, Pb, Na, K etc.; Z = P, CO_3, V, As, Cr, B, etc.; and X = OH, CO_3, Br, Cl, BO_2), thus achieving the regulation for mineral homeostasis. These substitutions have enabled biomaterial scientists to tweak bioceramics (such as calcium phosphates and glass-ceramics) by doping metal ions, to impart multifunctionality into them.

Large volume defects, as a result of trauma or osteosarcoma (after surgical resection) or infection (osteomyelitis) still remains a major challenge for clinicians. The implanted graft must sustain neo-osseous ingrowth, neovascularization and prevent any implant associated infection. Though these can be individually addressed by supplementing growth factors (BMPs as osteoinductive, VEGFs as proangiogenic factor) and systemic/ local delivery of antibiotics; these approaches remain inefficient. However, doping of 'therapeutic' metal ions into bioceramics have been demonstrated to mitigate these problems. For instance, copper (a known antimicrobial element) when doped/ substituted in bioceramics has been shown to enhance the osteogenesis and vascularization [137]. Mechanistic insights revealed that copper ions from dissolution products from mesoporous bioactive glasses stabilize HIF-1α (HRE are activated) and upregulate pro-inflammatory cytokine (TNF-α, involved in early sprouting, branching of blood vessels) [138]. Cobalt doping in bioactive glasses [139] and calcium phosphates [67]

also have been documented to have similar effects in endowing proangiogenic traits to these osteoconductive ceramics. Strontium doping have found to downregulate osteoclast activity while enhancing osteoblastic, angiogenic roles [140] *via* CaSR mediated uptake. This is especially useful when treating osteoporotic defects where heightened osteoclastic activity is witnessed. Strontium dualistic roles is associated with it differentially triggering (i) Wnt signalling and FGF-receptor activation in osteoblasts, while (ii) inducing apoptosis/ senescence in osteoclasts by inhibiting NFκB signalling [66] and PTH pathway. [141] The inclusion of iron doping or iron nanoparticles into ceramics [142] or polymers, [143] imparts magnetic traits to the scaffold. This is especially helpful in pre-conditioning cell seeded constructs (under dynamic or static magnetic field) to dynamic loading behaviour experienced by bones. For instance, under static magnetic field's influence, magnetic nanocomposite matrices enabled the maturation of seeded osteoblasts via activation of integrins, FAK mediated Smad 1/5/8 pathway, harnessing the mechanotransductory capabilities of osteoblasts. [143] Mesenchymal condensation is another unique feature of endochondral ossification, where MSCs condense to form a cartilaginous template. This process can be mimicked by tagging MSCs with endocytosed magnetic nanoparticle, and under the influence of magnetic field exhibit 3D cellular organization much akin to mesenchymal condensation, achieving chondrogenic commitment with enhanced sGAG secretion. [144] Meanwhile, doping of bioceramics have also been demonstrated to confer osteoimmunomodulatory effects. For instance, tricalcium phosphate-apatite (clinically used) promoted upregulation of M1 macrophage related genes while strontium doped hardystonite (calcium silicate based bioceramic) upregulated M2a, M2c related genes. [145] This has been further validated where M2 macrophages has been seen to secrete platelet derived growth factor (PDGF-BB), enhancing vascularization onset in rat calvarial defects. [146]

Composites developed from multiple components culminate in additive benefit addressing multiple problems with one solution. For instance, bone's toughness is attributed due to its composite nature which helps in fracture resilience and endure mechanical loading, which either collagen or apatite individually is not capable of handling. Composites inspired by anisotropic nature of bone have been developed using delignified wood derived cellulose exhibiting open microchannels (similar to Haversian system) into which sodium alginate is impregnated and *in situ* mineralization was done from calcium precursors used for ionic crosslinking of alginate. [147] The mineralized composite hydrogel showcased elastic modulus of 670 MPa, while the osteoconductive nature of these hydrogels *in vitro* translated *in vivo*

where rabbit femoral defects healed with neo-osseous tissue infiltration with good osseointegration between host bone and hydrogel scaffold. High strength composite polymer scaffolds with reinforced ceramic or organic fillers have been developed in this regard to facilitate reconstruction of load bearing bone tissues. [31, 68, 105] Multifunctional composites have also gained impetus in replacing bone adhesives such as PMMA, calcium phosphate cements (CPCs) **Table A1.1** (*Appendix*) which have associated drawbacks such as stability and heat generation during bone fixation procedures. In a unique approach tannic acid acting as a phenolic glue, self-assembled silk fibroin and hydroxyapatite into nanofibrils to obtain a multifunctional composite adhesive [148]. The developed adhesive possessed tensile strength of 0.22 MPa with elongation at break at 260 %, which was able to work well under wet conditions (as opposed to CPC) and did not generate any heat (as observed in PMMA) which causes thermal necrosis) and helped in repair of ruptured rat femur.

1.3.2 Fabrication Standpoint – Traversing Different Length Scales

Bone's hierarchical structure spans across several length scales, starting from the sub-nanoscale (as discussed in previous section) involving molecular building blocks of collagen (30 nm in length, 1.5 nm in diameter), other NCPs and apatite precursors (50 × 25 × 3 nm). The next level transcends into the structural components, where mineralized collagen is formed by plate shaped apatite crystals spanning the cross-section of collagen microfibril bundle, with the c-axis along the fiber axis. These mineralized collagen bundles self-assemble (microscale assembly) into arrays **(Figure 1.6A)** of different patterns, the next level. The anisotropy noticed in bone is imparted here by the arrangement of these patterns. For instance, in the lamellar (woven) bone, unidirectional arrays, with little or no preferred orientation, while in fanning pattern the orientation change in a gradational order (twisted plywood-like with angular offset 40-80°) which is also noticed in lamellar bone. [149] There is disordered pattern also, where the arrays are randomly oriented as in case of non-woven (trabecular) bone [5]. Arrays merge to form the next level of super-structures where it is essential to include the cellular components into this hierarchical make-up. The super structures consist of osteocytes embedded in the lacunae, canaliculi surrounded by bundles/ arrays interspaced by disordered material fills. The super structures then formulate the tissue elements, spanning from microscale to macro-scale range. Here, the osteonal tissue is constituted by osteons, the structural and functional units of cortical bone. They are cylindrical, concentric structures (200 µm in diameter) hosting the central Haversian canal (50 µm in diameter). These compact structures are tightly packed (3-5 % porosity) and form the secondary osteons distinguished by cement lines. The assemblage

from cortical bone when it traverses inwards, the lamellae are less dense (50-90% porosity) and form the trabecular bone which is highly anisotropic. This porosity helps house the bone marrow and associated cells, thus dynamically regulated as per need. These tissue elements combine to form the final level, the organ bone. These different levels of arrangement bestow bone with the fracture resilience, toughness and also help in regulation of homeostasis.

Reproducing these levels of hierarchical arrangement in bone implants or grafts is very difficult. However, several strategies have been adopted to mimic the different facets of bone architecture at the nano, micro and macroscale **(Figure 1.6 B-D)**. The choice of biomaterial opted and the fabrication strategy to be adopted are co-dependent. This in turn relies on the intended application, either for replacement or regeneration. For total joint replacement procedures (hip/ knee arthroplasties), metal implants with durable non-resorbable polymers are opted, which usually involve the fabrication using macro-scale techniques like injection molding of thermoplastic polymers into custom mold cavities or metals which are machined to obtain desired components. These replacement components are designed with impetus to provide structural support, with their mechanical performance matching the stress-strain trajectories with the patient's needs. Thus, the bulk properties of materials are taken into consideration, with very less importance on their microarchitecture or cellular requirements. Therefore, the problems associated with these devices such as implant associated infection, aseptic loosening, corrosion and associated toxicity issues are concerns which still plague the current orthopaedic devices and fixatives. Similarly, for regenerative applications scaffold matrices fabricated through conventional strategies such as solvent casting, freeze-drying, porogen leaching, gas foaming, foam replica and thermally induced phase separation are still being used (few listed in **Table A1.1** (*Appendix*). Precise control of micro-architecture, pore geometry and most importantly the scalability of these approaches are few well acknowledged limitations. [19] With technological improvements advanced strategies are being adopted to overcome these aforementioned drawbacks. Engineering surface features and smart interactive interfaces on bulk material surfaces help in improving osseointegration. Rapid prototyping and semi-automated strategies with superior scalability and control over scaffold microarchitecture have also been investigated in the recent past for fabricating BTE grafts.

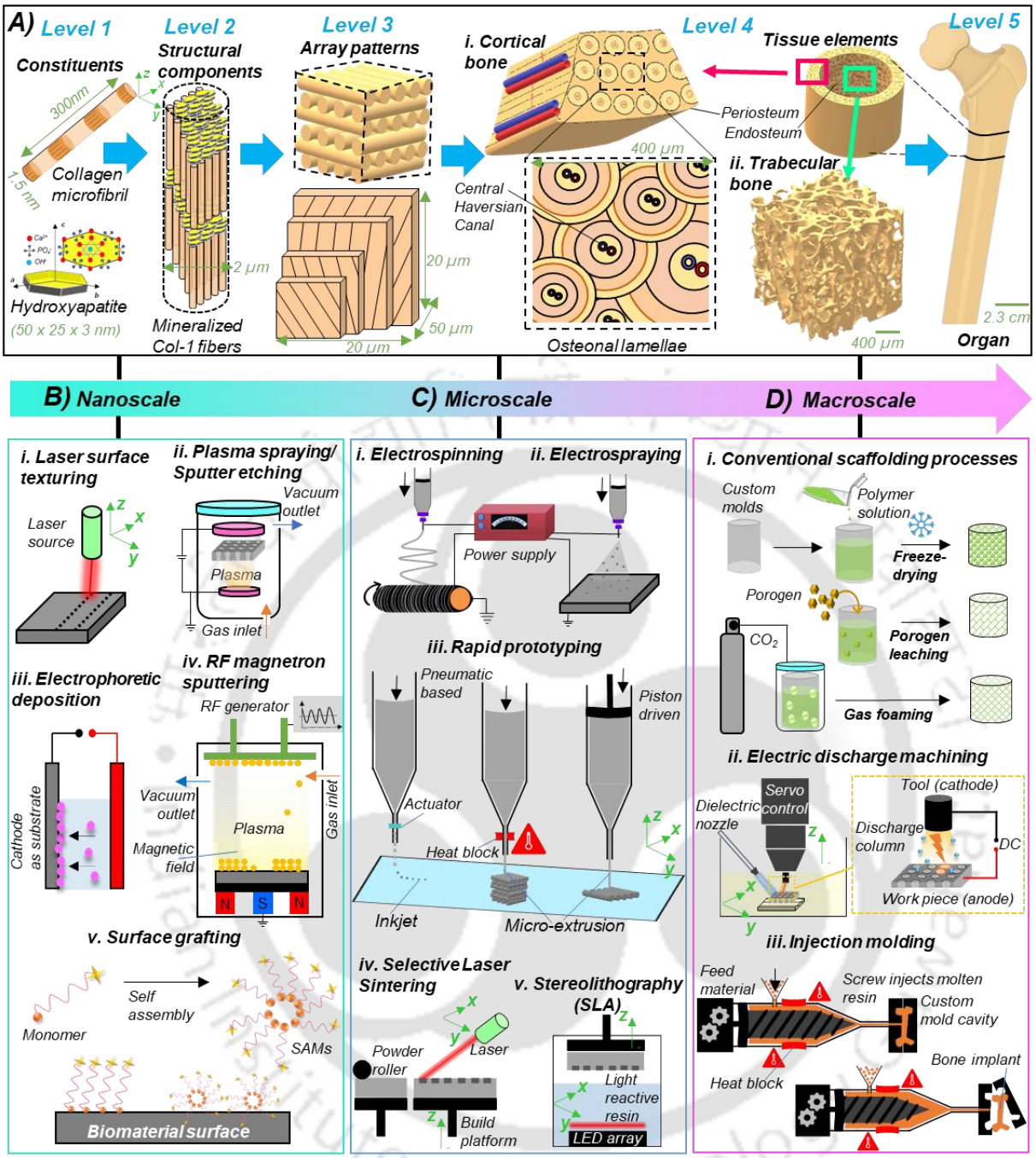

Figure 1.6. ***Traversing length scales in bone architecture and recreating it through various fabrication strategies.*** *A) Bone has been classified to possess 7 levels of hierarchical organization (Weiner and Wagner model [5]) but here for the sake of clarity to elucidate the fabrication processes, it is simplified into 5 levels. Level 1 consists the molecular building blocks collagen fibrils (other NCPs) and apatite. Level 2 consists of the structural components made up of mineralized fibers, with apatite crystals formed between hole regions along the c-axis parallel to fiber direction. Level 3 consists of the mineralized fibrils assembling into arrays (unidirectional, fanning/ twisted, disordered). Level 4 gives rise to the tissue elements consisting of superstructures, cortical and trabecular bone, which comprise the final Level 5 – organ (whole bone). Based on these observations, the structural levels can be segregated into*

B) Nanoscale level, which can be achieved by techniques such as i) laser surface texturing, ii) plasma spray/ sputter etching, iii) electrophoretic deposition, iv) radio frequency (RF) magnetron sputtering, which help in rendering nanoscale to sub-microscale surface features on to bulk materials (bone grafts); while v) self-assembly enables to formulate nanoparticles, hydrogels which by itself serve as scaffolding matrices, or they can be grafted on to surfaces to confer differences in wettability, presentation of surface ligands, antifouling/ antimicrobial features on implant surfaces. C) Microscale level can be achieved by semi-automated approaches like i) electrospinning, ii) electrospraying and automated approaches such as iii) rapid prototyping (involving inkjet, microextrusion printing), iv) selective laser sintering (SLS) and v) stereolithography (SLA); D) Macroscale level, can be achieved through i) conventional strategies which impart porosity (between microscale to sub-macro scale) using freeze-drying, porogen leaching, gas foaming techniques; while ii) electric discharge machining (EDM) helps fabricate metal implants and iii) injection molding help in fabricating thermoplastic components for replacement implants used in orthopaedic reconstruction.

1.3.2.1 Engineering Instructive Surfaces on Replacement Prosthesis/ Implants

Aseptic loosening (20.3%) and implant associated infections (20.4%) are the main drivers for revision needed in total knee arthroplasties based on epidemiological retrospective study. [150] Understandably, surface modifications of implants have found to combat these issues. Increasing the average roughness (R*a*) of implants have been found to improve osseointegration of implants via micromechanical retention of bone between peri-implant space and bone implant device [151]. This has been achieved by relatively inexpensive methods such as grit-blasting (aluminium oxide/ titanium oxide), chemical treatment (acid etching, sol-gel deposition) (R*a* = 1-5 µm). Few commercially available surface-modified products are available for orthopaedic reconstruction (**Table A1.1** (*Appendix*) which utilise these procedures. However, improving the surface roughness on the contrary also increases the chances of microbial attachment and retention. Thus, nanotopographies (R*a* ≤ 1 µm) have been found useful to minimize bacterial biofilm formation while favouring osteogenic cell attachment. Understanding cellular behaviour on nanotopographical surfaces derived through lithographical techniques [152] helped translate these findings on to metal implants. Osteoblast cells by their virtue of contact guidance and integrin mediated attachment, sense the presented biophysical cue and strive to retain the osteogenic phenotype on stiffer matrices. [153] The nanotopographies though advantageous for osteoblasts would be detrimental for bacterial cells which serve in rupturing their cell-wall (bactericidal) and act as antifouling surfaces [154] by varying the surface wettability. These sophisticated bioinspired nanotopographies (1-150 nm) are achievable using techniques like plasma-assisted etching, [155] laser texturing (pico/ femto second pulsed lasers) [156] and radio-frequency magnetron sputtering [157] over metal,

ceramic and polymer surfaces. For instance, using ion-etching titanium nanostructures were engineered which inhibited 95-98% of *Staphylococcus aureus* (a common miscreant in post-operative implant related infection), while augmenting osteogenic lineage commitment by integrin/ paxillin mediated FA formation. [158] Similarly, using glancing angle deposition magnetron sputtering (GLAD) densely packed, titanium nano-columns (40-60 nm) were formed which enabled in preventing biofilm formation by mimicking 'lotus-leaf effect' manipulating the surface wettability while not hampering osteoblast adhesion [159]. Metabolomic analysis have revealed that osteoblasts seeded on nanostructured surfaces show upregulation in protein production (histidine, serine), aminoacyl tRNA biosynthesis and osteogenic transcriptors, indicating greater metabolic demand of differentiating osteoblasts in comparison to planar surfaces [160]. These physical techniques alter the bulk implant surface to present topographical (biophysical) cues alone but do not alter the chemical nature, thereby the biochemical property of bulk material remains the same.

Improving the biochemical properties of inert biomaterials' surfaces can be achieved by grafting techniques. By self-assembling processes, colloidal particles having biomimetic, multifunctional nature help in engineering interactive biochemical cues, while presenting physical cues (by virtue of their nanoscale features). The surface grafting (mainly intended for metallic implants) is achieved either by physical colloidal interaction (weak) or covalent binding (strong). Covalent immobilization of relevant peptides or particles can be achieved using silanes, radical polymerization of (vinyl/ thiol/ phosphonate) monomers (wet chemical methods) [151] or physically by plasma assisted polymerization by radio frequency glow discharge. [161] For example, silanization of titanium surfaces enabled in grafting cell adhesion peptides (RGD) and antimicrobial peptides – AMPs (lactoferrin derived LF1-11) helped present nano-features with R*a* ~ 50 nm [162]. The functionalized Ti metal surfaces inhibited *S. aureus* (by disrupting the cell wall) while preferentially allowing osteoblast adhesion. Plasma assisted polymerization of poly(ethyl acrylate) over metal [161] or polymer (PCL [163]) surfaces to obtain nano-globular features (30 – 300 nm). Poly-(ethyl acrylate) after polymerisation was demonstrated to bind and unfold fibronectin (FN), thus enabling osteoblast adhesion mediated through integrins with vinculin expression evinced in the FA complexes. FN also sequesters BMP-2, thus loading of this growth factor was achieved and its ultra-low release made possible. High dose release of BMP-2 from conventional sponges has severe repercussions such as ectopic bone formation, risk of cancer and neurological problems. However, sequestered BMP-2 on fibronectin-functionalized metal surfaces released at a

sustained rate (at 14 days 0.25 ng, as opposed to mg in sponges) which circumvents the drawbacks of sponges but also helped in regeneration of murine critical radial defects and canine humeral defect. [163]

Contrary to the covalent surface grafting strategies, physical adsorption-based strategies involving layer-by-layer (LBL) assembly and assisted by electric field (electrophoretic deposition). These strategies are much more facile and does not involve the use of harsh chemicals. Tuning the immune response of implants are very critical since the infiltrating immune cells interact with the surface first, hence immunomodulatory modification to surfaces of implants have been investigated. For instance, medical grade poly-(etheretherketone) rods were modified by polyelectrolyte (polyacrylic acid and poly-allylamine hydrochloride) LBL self-assembly [26]. The functionalized surfaces suppressed acute inflammatory response by downregulation of NOD-like receptor (NLR) signalling pathway but also favoured differentiation of MSCs. Poly-(etheretherketone) surfaces have also been modified with MSC derived exosomes by reversible assembly through tannic acid, augmenting M2 polarization and new bone formation in rat femoral defects [37]. Demineralized bone (DBM) scaffolds, a routinely used matrix for orthopaedic reconstruction, have been also surface modified by introducing magnesium-graphene oxide nano-scrolls. It was noticed that Mg^{2+} helped in M1 polarization via NFκB pathway (initial pro-inflammatory response which recruits MSCs, neo-vascularization signals), and graphene oxide helped in repolarization into M2 phenotype in macrophages (enabling pro-healing). This harmonious orchestration of events helped in vascularized bone formation in rat cranial bone defects. [164] Implantation of bone devices in osteoporotic conditions pose special challenges, due to decreased contact surface between bone and implant, ultimately compromising osseointegration. This is further aggravated by persistent inflammation in the peri-implant site, disrupting osteoimmuno-balance. However, in an exclusive approach “burning bridges” based coatings to preferentially switch on/off macrophages on titanium surfaces were developed. [165] This was done using in a phase wise manner where Ti surfaces where conjugated to alendronate (ALN, a bisphosphonate) and then to a glycan (acetyl glucomannan, acBSP). Initially, acBSP activates pro-inflammatory M1 phenotype macrophages which secrete chemokines that help in osteoblast differentiation. After subsequent osteoblast migration and maturation, the alkaline phosphatase (ALP) secreted by osteoblasts cleaves glycan ALN which switches-off macrophages by apoptosis. This was studied in a discorded osteoimmune environment in osteoporotic rat femurs, where superior osseointegration was noticed, attributed to migration

of M1 macrophages (stained with CD68 – green, F4/80 – red) seen initially more in day 3 but receded by day 7 in Ti-acBSP-ALN group.

1.3.2.2 Engineering Cell-instructive Microstructures in Resorbable Grafts and Non-resorbable Prostheses/ Implants

Moving from nano-featured surfaces, the next level of hierarchy involves fabricating matrices in the sub-micro (≥500nm to 1µm), micro (1-750µm) and sub-macro scales (≥750µm). Here electric-field assisted technologies such as electrospinning, electrospraying and electrophoretic deposition, enable in obtaining sub-micron to micron scale featured matrices, with sufficient control over features and arrangement. Polymer solution/ melt or polymer solution composited with suitable nanoparticles is drawn out by surface tension from a needle which is subjected to an electrical field, which drives the polymer jet into fine fibers/ particles by electrostatic forces to be collected on a grounded collector [166]. The resulting fibers/ particles exhibit high surface area and are akin to the fibrillar array patterns noticed in bone hierarchy. By varying the operating parameters such as operating voltage, viscosity of solution, working distance, the process can be tuned to draw out micro/nano fibers or particles. Plethora of natural biopolymers and synthetic polymers could be easily utilised in these processes, to develop ECM-mimetic micro-featured fibers. The cortical bone as discussed earlier is made up of osteons, which are lamellae fibrillar patterns present as concentric circles (5 to 20 in number) housing the Haversian canals (enclosing the blood and nerve vessels). These intricate designs can be replicated using electrospinning effectively. For instance, an air-gap electrospinning strategy was studied where negative voltage applied polymer jet was collected between two positive voltage collector plates to obtain aligned bioactive glass/ PCL fibers, later wrapped to form microbundles mimicking the osteon like cortical bone super-elements. [167] The outermost thin connective tissue which is profusely vascularized is the periosteum. The complexity of periosteum can be easily mimicked by electrospun fibers and the electrospun mats potentially serve as periosteal membranes. Moreover, growth factors can also be incorporated into spinning solution which gets encapsulated within the fibers and zonal gradients displaying different growth factors can be achieved. For example, microfibrous hyaluronic acid (encapsulating VEGF as angiogenic stimulant) was electrospun by micro-sol electrospinning technique and subsequently coated with nanofibrous collagen-I, mimicking the outer-to-inner hierarchy in periosteum [168]. This bionic periosteal mimic induced vascularized bone growth via both endochondral and intramembranous ossification pathway in rat periosteal defect model. Furthermore, the vascularized bone niche has very explicit

hemodynamic regulation with specified venous and arterial capillary blood vessels supplying to the osteons. Reproducing these intricate vasculatures are very tedious. However, electrospun PCL/collagen/hydroxyapatite nanofibrous mesh were arrayed layer-by-layer between bone marrow derived MSCs and implanted in cranial defects [169]. The resultant neo-osseous tissue facilitated specific venous/ capillary development. $CD31^+$ and $endomucin^+$ (EMCN) blood vessels exhibited higher flow rate, partial oxygen tension than blood vessels that were $CD31^+/EMCN^-$ which were regulated by the osteoblast clusters within the nanofibrous mesh.

Macroscopic metal implants used in total hip replacements produced by conventional moulding or machining processes possess a bulk mechanical property which does not match the mechanical loading profile of native bone. It is estimated that the femoral stem in the total hip replacement implant undergoes 2 million cycles per year, which involves both tension and compression forces. The aseptic loosening occurs when implant is subjected to tension rather than to compression. These drawbacks can be overcome by designing implants which can exhibit differential/ zonal mechanical profiles, which has ushered in a multi-physics based meta-material implants. [170] These meta-material implants were simulated under physiological loads and found to sustain such loads, lowering stress-shielding effects (Hoffman's criterion) [170]. Such 3D meta-materials, though not tested in clinical models hold promise in decreasing bone-implant failure. Such complex designs are materialized with the help of rapid prototyping or additive manufacturing techniques by a bottom-up approach. The precise control of scaffold geometry by suitable designs help generate '.stl' (standard tessellation language/ stereolithography) file, which is fed into printers/ rapid prototyping units as 'gcodes' to obtain the 3D object. The most widely used rapid prototyping techniques in orthopaedics or bone tissue engineering involve micro-extrusion (pneumatic or plunger driven), stereolithography, laser sintering and inkjet printing. [19] Micro-extrusion printing utilises (biomaterial) inks which exhibit (i) shear thinning and thixotropic recovery inks (polymers such as collagen/ ECM components, [171] silk fibroin, [172] gelatin, alginate [173]) and (ii) thermoplastic polymers (such as PCL, PLA, PLGA [174]). Resolution of $\geq 100\mu m$ can be achieved by micro-extrusion printing, where nozzle diameter, ink properties dictate the final printed construct's print fidelity. On the other hand, stereolithography, laser sintering utilises light sensitive polymer resins (methacrylated polymers like gelatin, [175]silk fibroin, [176] diacrylated PEG [177]) or ceramic/ metal powder bed [178, 179] (which gets fused on laser application) respectively. The resolution ($\geq 100\mu m$) here depends upon the laser source used and its penetration depth. Introduction of cells into biomaterial inks in the above approaches

(micro-extrusion, stereolithograhy) led to the development of bio-inks, which help in obtaining 3D bioprinted (cell-laden) constructs [171]. Bioprinting enables in creating clinically viable cell laden constructs of distinct geometry akin to native tissue, mimicking it's functional and cellular heterogeneity in a scalable, high-throughput manner. [180]

Minimal interconnectivity within pores greatly hinders the host-implant integration, where subsequent neo-osseous tissue and vascular tissue infiltration is compromised. Through conventional scaffolding techniques like gas foaming/ particulate leaching heterogenous pores are obtained, 3D printing helps in obtaining ordered porosity. For instance, using micro-extrusion printing a thermoplastic ink of PCL/ nanohydroxyapatite (10:90) was rapidly used (275 cm^3/h) to print hyper-elastic cortical bone structures [174]. The constructs printed had ordered porosity (50%), with elastic modulus up to 11 MPa, with elastic strain of 67% at failure. The constructs also induced viable neo-osseous tissue ingrowth in rat posterolateral spinal defects and non-human primate calvarial defects, without the need for any biological osteoinductors. Porosity is inversely correlated to scaffold's relative density, which impacts the shear and elastic modulus as porosity of a material increases. However, using computationally designed lattices we can circumvent these drawbacks. For instance, it has been computed that lattices designed with beams aligned along the compressive loading axis, improves compressive strength, whereas lattices aligned diagonally improves the shear moduli. [181] These lattice designs can be implemented only through bottom-up approach of rapid prototyping. For instance, using selective laser melting printing and parameterization modelling, precise control of porosity-to-mechanical properties in titanium implants were realized. [182] These bionic designed Ti implants had an error rate of 2.73% to the computed designs in terms of porosity-to-mechanical properties performance. The complexity of hierarchical structures can also be replicated using 3D printing. Haversian bone-mimicking structures of the cortical bone were custom designed and printed using stereolithography, where a calcium-phosphate based ceramic (Akermanite)/ photosensitive resin composite was used as the biomaterial ink. [183] The design consisted on vertical channels (0.8 mm) mimicking the Haversian canal, while horizonal channels (0.8mm) connecting them, mimicked the Volkmann canals, thus an interconnected network was recreated. These channels were seeded with MSCs:endothelial cells in 1:1 ratios which helped in recreating the vascular-osteon micro-physiology like condition. The system also was able to integrate within the femoral defects (in rabbits) with more new bone and blood vessels formed within the Haversian canals.

1.3.2.3 Spatiotemporal Control in Biomolecule-eluting Grafts

The tissue complexity with specialized cells performing critical roles within the organ is governed by a degree of spatiotemporal control of growth factors which is presented/ encountered by these cells. Patterning these cues in scaffolds intended for regeneration is essential, as spatial distribution of biochemical cues and its temporal cues would facilitate in specialization of fate of the cells infiltrating these constructs. For instance, 3D printed molecular cages which resemble LEGO™ (interlocking building blocks) were designed which could house microgels loaded with growth factors (VEGF or PDGF) with varying compositions in each compartment, to realise growth factor patterning [184].

Circumventing non-specific release of BMP-2 locally and systemic delivery, temporal control of its delivery in a localized space was achieved in a unique approach. [185] M1 macrophages characterize the initial proinflammatory phase which secrete MMPs (gelatinases). In this study, gelatin microspheres were loaded with BMP-2, which were released in excess in the presence of M1 macrophage secreted MMPs, while minimal release was noticed in presence of M2 (non-inflammatory) macrophages, enhancing the initial osteoblast recruitment. This approach helped in synchronizing the BMP-2 release in tune with the immune response, thereby achieving spatiotemporal control of osteogenic performance. By 3D printing strategies, biochemical gradients could be realised by using biomaterial inks with encapsulated growth factors at precise positions, to bestow precise spatial control. For instance, VEGF loaded hydrogel were co-printed with calcium phosphate cement inks helped to facilitate angiogenesis within the core of 3D printed constructs. [186] 4D printing has been gaining attention recently [187], where scaffolds which respond to body's cues like strain, temperature morph back into a form which is needed to act as a structural support. This temporal control of scaffolds helps in deploying shape memory scaffolds bestowed with good creep recovery and mechanical flexibility in a minimally invasive manner [188]. In an interesting approach, culminating herringbone tessellation origami and 4D printing, PLA was used to print deformable-shape recovery scaffolds which recapitulated the natural cancellous bone [189]. The origami tessellation approach enabled in developing folding patterns, which could recover under body temperature (61% recovery) which paves way towards developing durable scaffolds as structural support, deployed via a minimally invasive manner.

1.4. Clinical Perspective of Cell-instructive Biomaterials in Bone Tissue Engineering

Biomaterials that have been employed thus far for bone tissue engineering can be historically classified as, 'bioinert' (*first generation*), 'biocompatible' (*second generation*) and 'bioactive' (*third generation*). These *third-generation* biomaterials have come into much scrutiny over the recent years, with the choice of words used in literature such as, '*smart', 'cell-instructive', 'responsive'* which has an air of ambiguity surrounding them. The word '*smart biomaterials*' was coined in 2004 to describe biomaterials that respond to specific cellular cues [21] whereas *'cell-instructive materials (CIMs)'* are engineered biomaterials with extended functionality and bioactivity which aim in regulating cellular fate (used in literature since 2012). [24] These materials are both responsive in nature. The degree of responsiveness to the implant site could be variable. For instance, rh-BMP-2 (recombinant human bone morphogenetic protein 2) was given clearance for use in collagen based scaffold (INFUSE®, Medtronic) as alternative to autologous bone graft. [190] The release of this known osteoinductive biomolecule is one-way (open-loop), where based on the level of hydrolysis/ proteolysis of scaffolding matrix, the embedded growth factor is released. The same approach is followed for dental/ bone cements with anti-microbial agents like antibiotics which release the molecules locally in a one-way/ open-loop mechanism. In contrast to this, two-way (closed-loop) responsive materials initiate a specific function on the basis of a very specific trigger. [21] These biomaterial design/ prototypes are still in the pre-clinical stage in lab settings. Few of them have been discussed in the previous sections, such as the MMP responsive PEG hydrogels which help in controlled degradation of matrix, allowing cellular migration [132] or the tactical presentation of RGD peptides for enhanced cellular adhesion. [129, 130] Controlling the release of encapsulated growth factors by cellular triggers from responsive hydrogels [185] or activating macrophages to create an osteo-immunomodulatory local microenvironment to aid in regeneration [165] are also few facets of these closed-loop responsive materials.

Though these new generation of biomaterial designs are scarce in clinics and their translation is yet to be validated, they pave the way for precision medicine. These biomaterials offer the feasibility to tailor interactions with biological processes and their immediate implant microenvironment. These programmable/ reconfigurable design principles bestow a level of autonomy to these new generation biomaterials acting on its own accord, much akin to a 'living' tissue capable of processing bio-chemical/ physical cues. This would be the epitome of success in biomaterial design philosophy and biomaterial researchers strive to reach this

level of intuitiveness. The need for such systems is necessary. For instance, rh-BMP2 with its proven clinical success for bone regeneration has severe drawbacks. Dosing discrepancies of rh-BMP2 has been associated with cancer risk, obstruction of neural and airway pathways (off-label usage). This is attributed to the current delivery scaffolds, which release 90% within 24 h and 43% in-hospital complications for rhBMP-2 augmented therapy (as opposed to 3.5% in autograft spinal fusions). [191] Similarly, antiresorptive drugs used in osteoporosis treatment such as bisphosphonates, result in systemic effects where osteoclast activity is reduced, leading to skeletal freezing and fatigue fractures. [191] These drawbacks can be circumvented by spatiotemporal controlled release of these biomolecules which has been demonstrated in preclinical/ lab settings [163, 165]. Alternatively, biomaterials which do not use growth factors but rather multifunctional ions are also being investigated in preclinical stages. For instance, cobalt doped [67] or zinc/ silicon doped [68] or copper doped [138] bioceramics have been documented to enhance osteogenesis while favouring vascularization. Moreover, these ionic dopants have also been found to modulate immune responses, [145, 164] bestowing osteoimmunomodulatory traits to grafts. Though ionic dopants have ushered in antimicrobial ceramics utilised in infectious (osteomyelitis) clinical settings (Identifier: NCT03945864, **Table A1.2** (*Appendix*), their usefulness in aiding osteogenesis/ angiogenesis/ immunomodulation in clinical trials are yet to be validated. In addition to well-established polymers (**Table A1.1** (*Appendix*), many novel polymers are being investigated in preclinical stages. [122, 123, 125, 134] Of particular interest are alternative biopolymers such as chitosan, cellulose and silk fibroin which share hierarchical similarities to collagen and can be easily sourced. Such polymer-based composites are finding its way from lab setting to animal trials, and few have been investigated in clinical trials also (Identifier: NCT02910232, **Table A1.2** (*Appendix*) holding promise for these technologies.

In addition to these responsive material properties, a thorough understanding of the patient's health and age status also needs to be accounted for in the material design process. Even though if a biomaterial exhibits spatiotemporal release dynamics, it would fall short in aging patients with compromised regenerative capacity. Similarly, immunocompromised or impaired health conditions also need to be factored in. Bone tissue engineering design principles which accommodate these facets in their design philosophy have to be investigated more and given precedence. [19] This can be addressed by designing biomaterials for 'case-specific' scenarios, rather than treating them as 'one size fits all' style (which conventionally used current clinical materials follow). In this regard, several biomaterials designs addressing

such pathological conditions such as arthritic bone microenvironment, [192] infected bone/ osteomyelitis conditions [193] [194] and bone tumour microenvironment [195] are being investigated. Few clinical trials (Identifiers: NCT03945864, NCT02879149, NCT02531100, NCT03057223 listed in **Table A1.2** (*Appendix*) also are exclusively studying bone grafts in such pathological conditions with compromised healing capacity. Employing scalable approaches such as 3D printing strategies and rapid prototyping could reduce the biofabrication timescale involved in obtaining a functional transplantable graft, while enhancing the reproducibility and confidence levels of fabricated grafts therapeutic outcomes. In an interesting development, 3D bioprinting strategy was employed for direct *in situ* bioprinting of bone marrow stem cell laden collagen inks on mouse calvarial defects, [196] which results in mature osseous tissue formation 2 months post-printing. Thus, the biofabrication of functional graft is reduced considerably and complex graft geometries can be designed and implanted based on the patient's specific needs obtained through computerized tomography scans. In this regard, 3D printed strategies have gained attention and many clinical trials using responsive materials have been initiated (Identifiers: NCT03166917, NCT03185286, NCT03185286, NCT03057223 listed in **Table A1.2** (*Appendix*).

Motivation and Objectives of the Present Investigation

Motivation and Objectives of the Present Investigation

Current clinical procedures to restore the loss of skeletal tissue due to degeneration, trauma or infection come with substantial limitations and inherent disadvantages owing to the use of biomaterials which are considered to be bio-inert. A shift in paradigm in the field of material science has enabled researchers to focus on more bio-active materials which are capable of integrating with biological molecules and cells, and help in faster regeneration. In case of bone, biomaterials should be *osteoinductive* (capable of promoting the differentiation of precuror cells towards osteogenic lineage), *osteoconductive* (capable of supporting bone cells and encourage the infiltration of surrounding bone tissue), and *osseointegration* (capable of integrating into surrounding bone) [18]. Tissue engineering and regenerative medicine, in the recent years has played a pivotal role to aid in this de novo skeletal tissue formation to address the unmet needs in clinical orthopaedic practise [197]. Some of the key drawbacks (**Figure 1.7**) that persist in the current generation (*second* and *third* generation) biomaterials used for long bone pathologies treatment/ management include:

i. Implant associated infections noticed in metal implants, generally used for fracture fixation and augmentation prosthesis which result in hampering osseointegration and implant failure.
ii. Fibrous tissue formation leading to aseptic loosening of implant contributed due to non-bone formation due to improper biomaterial signals cells, leading to graft rejection and need for revision surgery.
iii. Persistent inflammation in pathological bone microenvironment such as osteoarthritis and osteoporosis regress the survival of bone graft implanted at these defect sites, thereby compromising graft patency.
iv. Need for tissue engineered bone grafts which are resorbable in nature, with the degradation products not eliciting any adverse immune response.
v. Need for osteoinductive surfaces or grafts which could effectively induce osteogenesis in implants by recruiting progenitor stem cells and inducing osteogenesis, thereby improving graft compliance.
vi. Impaired and slow invasion of host vasculature and lack of vascularization onset severely compromises the survival of bone grafts.

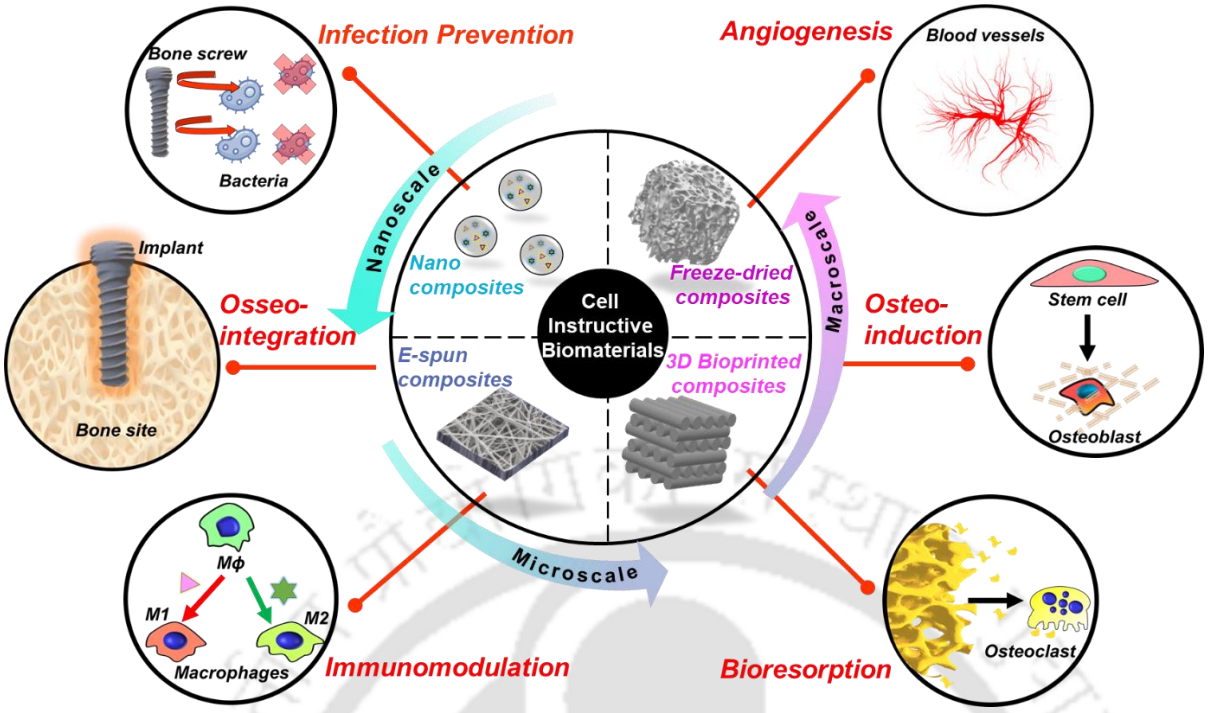

Figure 1.7. ***Scheme illustrating the various facets addressed in the present investigation****: i) infection prevention, ii) osseointegration, iii) immunomodulation, iv) bioresorption, v) osteoinduction and vi) angiogenesis through the array of cell-instructive materials developed ranging from nano-micro-macro scales towards bone and osteochondral tissue engineering applications.*

The current investigation takes into consideration these factors to develop robust biomimetic composite scaffolding matrices composed of silk fibroin (having a close resemblance to collagen-I) and sol-gel derived bioactive glass or wet chemical synthesis derived apatites (as the ceramic constituents). Silk, a structural protein represents a unique class of biocompatible, green polymer which has been in the focus of biomedical research owing to its biodegradability, low immunogenicity and processing feasibility [198]. Moreover, the greener approaches utilized to process the silk protein from the cocoon further endow it as an ideal candidate for various biomedical applications. Silk protein biopolymer is made up of two components - silk fibroin (SF) and silk sericin (SS) [199]. In silk, SF forms the central core which imparts the toughness and load bearing attributes. Based on the feeding habitat of silkworms, silk can be broadly classified into mulberry and non-mulberry silk. The variability between the different silk confer the unique bioactive, physico-chemical characteristics to the silk [199]. For instance, mulberry (*Bombyx mori*) silk fibroin has poly-(glycine-alanine) repeats (GAGAGS and GAGAGY), whereas non-mulberry silk fibroin has poly(alanine) repeats $(AAA(A)_{5\text{-}15})$, this preferential difference results in difference in fracture toughness of these silk varieties (0.1 GJ/m^3 in mulberry vs. 0.13 GJ/m^3 in non-mulberry). Moreover tensile

strength of SF (both mulberry and non-mulberry silk) range between 0.3 To 0.6 GPa [200] which are far much superior than the rat tail collagen 0.9-7.4 MPa [201], a commonly employed polymer in bone scaffolding matrices. The intrinsic physical properties in non-mulberry makes it more osteoconductive [202, 203] in comparison to mulberry silk. Non-mulberry SF scaffolds (from *Antheraea mylitta*) helped in stem cells adhesion, proliferation supporting the differentiation of stem cells to osteocyte like phenotype [203]. A relatively less explored silk variety, endemic north-east Indian non-mulberry silk (*Antheraea assama*), is also being validated here, as a potential biomaterial for BTE application (**Figure 1.8**). Recent reports have suggested that this silk variety is known to possess inherent RGD (arginine-glycine-aspartate) tripeptide sequence, enhancing the cellular performance in terms of adhesion and extra-cellular matrix turnover.

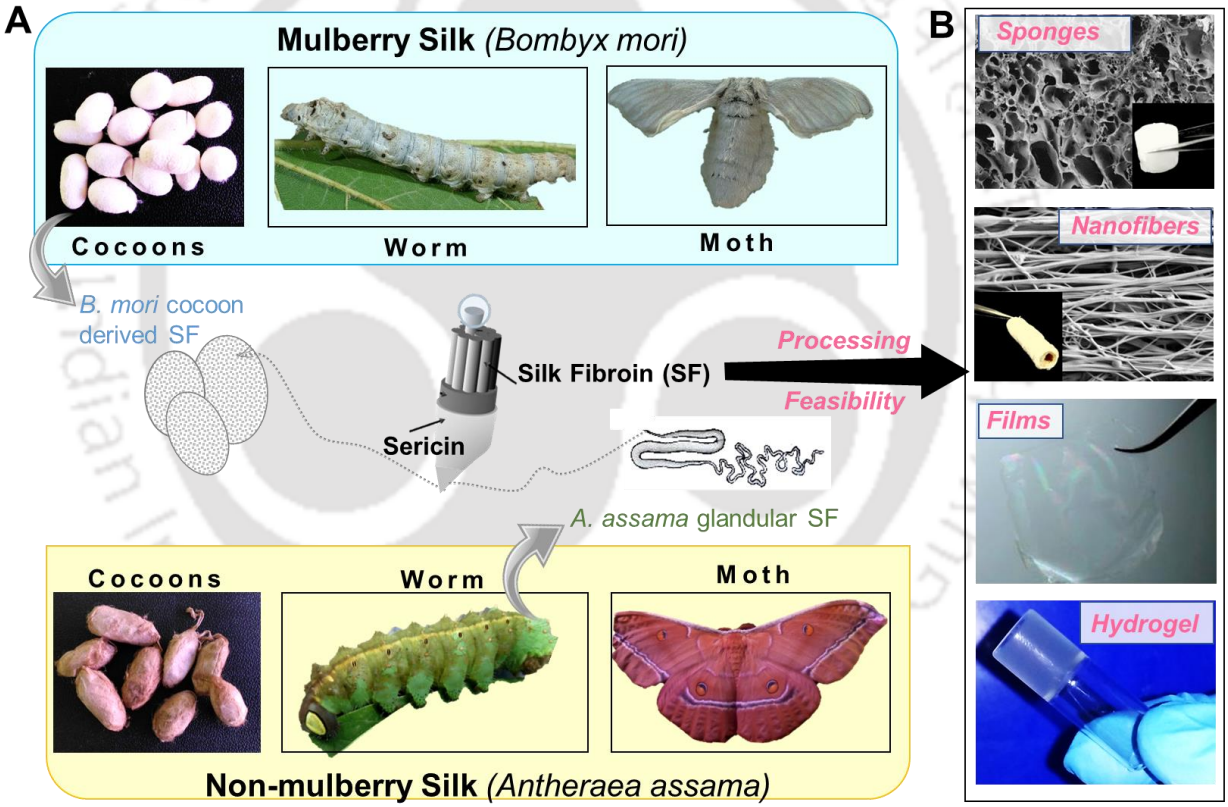

Figure 1.8. ***Sources of silk fibroin and its ease in processing into different formats***. *A) The two silk varities: mulberry (Bombyx mori) and non-mulberry (Antheraea assama) investigated in this work; B) Different scaffolding formats: sponges, nanofibers, films and hydrogels fabricated from these silk fibroins for tissue engineering applications.*

In addition to silk fibroin being used here as the biopolymer template, sol-gel derived bioactive glasses was chosen as the bioceramic for the development of composites. Conventionally, melt derived bioactive glasses are obtained by quenching oxide precursors (SiO_2, Na_2CO_3, $CaCO_3$, Na_3PO_4) which were melted at high temperatures, where silica forms the main network former in the glass formed. Whereas the sol-gel derived bioactive glasses involve the hydrolysis and polycondensation of alkoxides (tetraethyl orthosilicate – TEOS, responsible for silica network) in presence of other network modifiers in an aqueous environment. [204] The ability of bioactive glasses to allow the formation of a bioactive layer of hydroxyapatite (HCA layer) by which it bonds with the native bone is termed as *bioactivity* [205]. Sol-gel derived bioactive glasses, besides being formed at lower processing temperatures, exhibits high purity and improved homogeneity [206]. The sol-gel derived bioactive glasses exhibit mesoporosity (nano pores 20-50 nm within the particles) and ability to form macroporous structures (based on the processing technique employed to form the scaffolds) [206]. Unlike the melt derived bioactive glasses and the synthetic calcium phosphate based compound, the degradation and dissolution rates of these sol-gel derived bioactive glass can be tuned (exhibiting solubility rates of 10^{-5} to 10^{-6} $mg.cm^2.h^{-1}$) based on the chemical composition of constituents of network modifiers used [207]. Moreover, the dissolution products of these amorphous sol-gel derived bioactive glasses, owing to their faster dissolution rate, can stimulate proliferation and differentiation of bone marrow derived stem cells. Hence they are considered to be more osteoinductive in nature in comparison to other bioceramics [208]. Additionally, during synthesis of sol-gel derived bioactive glasses, they can be substituted with small amounts of extra oxides which can be of importance towards improving the biological action of the bioactive glasses [209]. For instance, inclusion of Zr, B, Mg, Fe enhances the osteogenic potential of the glasses; inclusion of Co, Cu enhances the vascularization potential; whereas inclusion of Ag, Ce, Ga has been shown to improve the antibacterial properties of bioactive glasses [208, 210].

Complying with the tissue engineering principles, the overall aim of the current work aims in developing robust yet affordable bioactive composite materials that can be employed as '*Biomimetic Cell-instructive Biomaterials'* for various bone tissue engineering (BTE) applications. The choice of these materials employed here is owing to their resorbability, osteoinductivity and versatility to be fabricated into wide array of formats for treating skeletal and associated skeletal defects of the long bone. Thus, the study takes into consideration about understanding the cell-material interaction and specific responses of osteogenic cells

(osteoblast, osteoclasts and associated immunogenic cells) to different formats (electrospun composites, 3D scaffolds, nanoparticles) for materializing improved composite material towards clinical translation. Different hypothetical strategies are defined below for addressing few commonly encountered long bone pathologies through the following objectives:

1. Mimicking hierarchical complexity of the osteochondral interface using electrospun silk-bioactive glass composites

2. Multifunctional cell instructive silk-bioactive glass composite reinforced scaffolds towards osteoinductive, proangiogenic and resorbable bone grafts

3. Chondroprotective and osteogenic effects of silk-based bioinks in developing 3D bioprinted osteochondral interface

4. Silk-based bioengineered diaphyseal cortical bone unit enclosing an implantable bone marrow towards atrophic non-union grafting

5. Mesoporous silk-bioactive glass nanocomposites as drug eluting multifunctional conformal coatings for improving osseointegration and bactericidal properties of metal implants

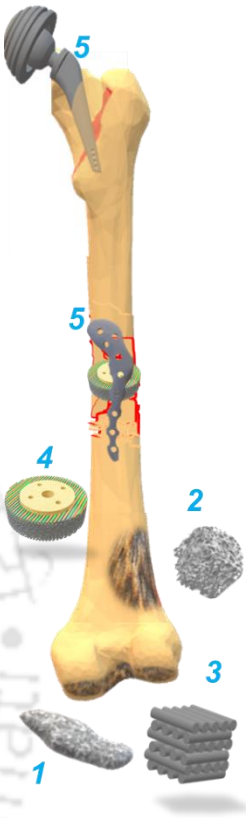

Chapter 2

Mimicking hierarchical complexity of the osteochondral interface using electrospun silk–bioactive glass composites

This chapter investigates the effect of certain biophysical and biochemical cues imparted in electrospun mats intended for osteochondral lesion repair. The biophysical cues were attributed through directional or non-directional alignment of electrospun fibers in bioactive glass mats and silk fibroin mats, respectively. The biochemical cues were attributed through the distinct gross-hydropathicity offered inherently by silk fibroins (Bombyx mori and Antheraea assama) and the compositional make-up of 70S bioactive glass. The influence of these biophysical and biochemical cues on primary chondrocytes and osteoblasts were functionally validated in vitro.

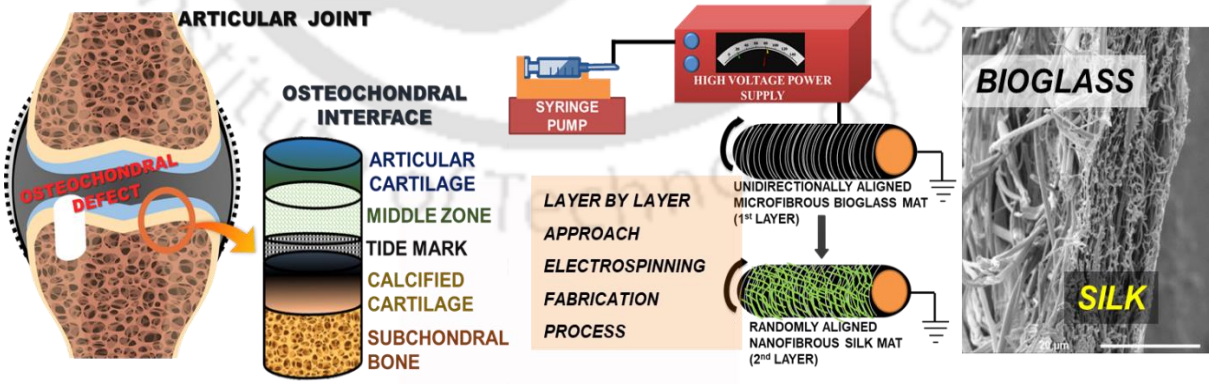

Abstract

The anatomical complexity and slow regeneration capacity of hyaline cartilage at the osteochondral interface pose a great challenge in the repair of osteochondral defects (OCD). In this study, the sol-derived 70S bioactive glass and silk fibroin (mulberry *Bombyx mori* and endemic Indian non-mulberry *Antheraea assama*) was utilized, in fabricating a well-integrated, biomimetic scaffolding matrix with a coherent interface. Differences in surface properties such as wettability and amorphousness between the two silk groups resulted in profound variations in cell attachment and extracellular matrix protein deposition. The mechanical assessment showed that the biphasic composites exhibited both an elastic region pertinent for cartilage tissue and a stiff compression resistant region simulating the bone phase. *In vitro* biological studies revealed that the biphasic mats presented spatial confinement for the growth and maturation of both osteoblasts and chondrocytes, marked by increased alkaline phosphatase (ALP) activity, osteopontin (OPN), sulphated glycosaminoglycan (sGAG) and collagen secretion in the co-cultured mats. The non-mulberry silk based biphasic composite mats performed better than their mulberry counterpart, as evidenced by enhanced expression levels of key cartilage and bone specific marker genes. Therefore, the developed biphasic scaffold shows great promise for improving the current clinical strategies for osteochondral tissue repair.

The findings of this chapter are published in a peer reviewed journal:

M. Joseph C., Reardon, P.J., Konwarh, R., Knowles, J.C. and Mandal, B.B. '*Mimicking hierarchical complexity of the osteochondral interface using electrospun silk–bioactive glass composites.*' ACS Applied Materials & Interfaces. 2017, 9 (9), 8000–8013.

2.1 Introduction

The number of orthopaedic surgeries is on the rise and it is predicted to double globally by 2030.[211] In India alone, 70000 joint replacement surgeries were performed in 2011.[212] This scenario has necessitated innovative and affordable strategies in orthopaedic care and management, particularly for defects at the osteochondral interface (OI). The OI is comprised of an anisotropic gradient of extracellular matrix and constituent cells, which includes a superficial hyaline cartilage layer, trailed by the middle transitional zone, followed by the deep zone which is in contact with the calcified subchondral bone. Osteochondral defects (OCD), a consequence of exposure of the subchondral bone,[213] if left untreated can cause pain, swelling, and eventually limited range of motion and osteoarthritis Generally, the surgical intervention for these defects utilizes reparative techniques such as autologous chondrocyte implantation (ACI) [214], matrix assisted chondrocyte implantation (MACI) or mosaicplasty.[215] However, these procedures often cause the fibro-cartilage to have poor resistance to shear and clinical durability, and are restricted by the availability of donor tissue and donor site morbidity. Recently, tissue engineered constructs have continued to gain importance for treating bone and cartilage degeneration.[216-219] However, a gold standard material which structurally, mechanically and biologically fulfils the criteria for use in OCD repair is still required. An ideal OCD scaffold will possess a chondrogenic matrix that should be flexible, resilient and possess pores small enough to mimic the hyaline cartilaginous matrix; and an osteogenic matrix that should be mechanically competent and bioactive, possessing larger pores mimicking the micro-environment of the subchondral bone.[220]

Among the different strategies studied in recent years, biphasic structures developed from a natural polymer with suitable matrices to support both osteogenic and chondrogenic cells, allowing a stable transition zone at the interface, have gained great interest. Silk fibroin (SF) based biomaterials have gained prominence in tissue engineering finding wide scale applications because of their superior cell supportive capability, excellent mechanical properties, tuneable degradability and versatile processability attributes.[216, 221] In recent years, silk based biomaterials for cartilage tissue engineering are gaining importance, as they present a conducive environment for maintaining the chondrogenic phenotype of seeded chondrocytes whilst enabling enhanced ECM secretion.[222, 223] Moreover, nanofibrous electrospun silk matrices also exhibit high surface area appropriate for maximal cell-matrix interaction, in addition to conserving the elasticity of silk fibroin which is crucial for cartilage tissue engineering [224]. The nanofibrous silk matrix thus provides the essential platform for

cell condensation and cell-cell interaction that is required for chondrogenic phenotype maintenance .Furthermore, bioactive glasses continue to play a pivotal role in bone tissue engineering (BTE) due to their ability to stimulate more regeneration than any other ceramic applied for BTE applications.[225] Sol-gel derived glasses in particular have received considerable research impetus because of their processing benefits over melt derived glasses, such as consistent purity, low temperature and reduced number of processing steps, whilst maintaining bioactivity.[226] It has been demonstrated recently that electrospinning is an attractive method for the large scale production of consistent fibres that mimic the physico-chemical milieu of native ECM. The flexibility in processing afforded by sol-gel derived bioactive glasses and SF makes them ideal candidates for electrospinning, thereby offering the exciting potential for producing replicable commercial scaffolds, which remains an elusive task for treatment in OCD repair.

Hypothesis underpinning the Objective:

Consequently, the purpose of this chapter was to develop an electrospun composite scaffolds consisting of two separate phases, one capable of supporting the osteogenic precursor cells and the other conducive to chondrogenic precursor cells that are well integrated at the interface. To achieve this, we chose 70S bioactive glass (70 SiO_2. 25 CaO. 5 P_2O_5) as the osteogenic matrix, previously reported as an excellent candidate for BTE applications owing to its unique bioactivity,[227] combined with silk fibroin from mulberry (*Bombyx mori*) and endemic North-east Indian non-mulberry (*Antheraea assama*) varieties to act as the chondrogenic matrix. These two silk varieties exhibit compositional diversity in the amino acids sequence. Recent reports on the non-mulberry silk have shown that the presence of RGD (arginine-glycine-aspartate) tripeptide and poly-alanine repeats confer unique cell supportiveness and mechanical resilience to the SF matrices, respectively.[228, 229] In this context, mulberry and non-mulberry SF were investigated to scrutinize their effect as a suitable chondrogenic matrix. The biphasic constructs were fully characterised for their physico-chemical properties such as structural conformation, wettability, degradation and swelling behaviour. Furthermore, the ability of the biphasic constructs to synergistically support the growth of chondrocytes and osteoblasts was evaluated by co-culturing porcine auricular chondrocytes and human osteoblast cell line (MG63) as a model system, and the cellular, biochemical and gene expression profile were studied to assess the suitability of the constructs as potential matrices for OCD repair.

2.2 Materials and Methods

The following analytical grade chemicals were used for the study reported here: calcium nitrate tetrahydrate (Sigma-Aldrich), Butvar-B98 - poly(vinyl-butyrate) - PVB (Sigma-Aldrich), poly(vinyl alcohol) - PVA (Himedia, India), tetraethyl-orthosilicate (TEOS) (Sigma-Aldrich), triethyl phosphate (TEP) (Sigma-Aldrich), hydrochloric Acid (HCl) (Merck, India), ethanol (Jiangsu Huaxi Int. Ltd., China); and remaining miscellaneous analytical chemicals used in the study were sourced from Himedia, India, unless otherwise noted.

2.2.1 Fabrication of the Bilayered Composites

2.2.1.1 Synthesis of 70S Bioactive Glass and Electrospinning of 70S Bioactive Glass

The 70S bioactive glass was synthesized following a previously published protocol.[227] Briefly, TEOS, calcium nitrate tetrahydrate and TEP were added in the molar ratio of 70:25:5 in ethanol/water solvent system with 2% (v/v) HCl in the molar ratio of 1:2:2 TEOS/Ethanol/Water. The sol obtained was aged for 48 h at 40 ºC. The aged sol was mixed with 10 % (w/v) PVB prepared in absolute ethanol (to enhance the rheological properties of the sol) in the ratio of 1:4 (v/v). The solution was electrospun using a blunt 21G needle in an electrospinning setup (E-spin nanotech, India) at a voltage of 16 kV, a working distance of 10 cm and a flow rate of 1 mL/h and the fibers were collected over a rotating mandrel (of diameter 40 mm and length 165 mm, rotational speed of 1550 rpm) at ambient conditions. The obtained bioactive glass **(BG)** mats were dried overnight at room temperature to remove residual solvent.

2.2.1.2 Isolation of Silk Protein and Electrospinning of Silk

For isolation of mulberry silk, *Bombyx mori* cocoons were obtained from local silk farms and the cocoons were processed based on a previously published method.[198] Briefly, the cocoons were cut into small pieces and degummed in boiling 0.02 M Na_2CO_3 and fibers obtained were dried at room temperature. The dried, degummed silk fibers were dissolved in 9.3 M LiBr (Sigma-Aldrich), followed by subsequent dialysis done extensively using a 12 kDa cut-off dialysis membrane (Sigma-Aldrich) against distilled water for 48 h. The regenerated aqueous silk fibroin solution was further used for electrospinning. For isolation of non-mulberry silk, mature fifth instar *Antheraea assama* silkworms were obtained from local silk farms. The glandular protein was isolated using a previously published protocol.[230] Briefly, the non-mulberry silk was squeezed out from silk glands of fifth instar *A. assama* silkworms and the silk protein was dissolved using 1 % (w/v) sodium dodecyl sulphate (SDS) (Himedia,

India) followed by its extensive dialysis at 4 °C. The regenerated aqueous silk solution was further used for electrospinning.

The *B. mori* silk (3 % w/v) was blended with PVA (to improve the rheological property of the silk solution) (13 % w/v) in the ratio 1:1 (v/v) and 10 mL of the blended solution was electrospun using a blunt 21G needle, at a voltage of 21 kV, at a working distance of 13 cm and a flow rate of 1 mL/h to obtain the *B. mori* silk mats **(BM)**. Similarly, *A. assama* silk (3 % w/v) was blended with PVA (13 % w/v) in the ratio 1:1 (v/v) and 10 mL of the blended solution was electrospun using a blunt 21G needle, at a voltage of 21 kV, at a working distance of 13 cm, mandrel rotational speed of 1550 rpm, and a flow rate of 1 mL/h at ambient conditions to obtain the *A. assama* silk mats **(AA)**.

2.2.1.3 Fabrication of Bilayered Composite Mats

For obtaining the composite bilayered mats, a layer by layer approach was followed, wherein the bioactive glass (volume = 5 mL) was spun over the mandrel, the silk (volume = 5 mL) was spun over the top of the spun bioactive glass mats (with parameters maintained as mentioned previously). Thus, two mats were obtained namely PVB-bioactive glass/ PVA - *B. mori* silk **(BI)** and PVB-bioactive glass/ PVA - *A. assama* **(AI)** silk which were further evaluated for their cytocompatibility. All the mats were then treated with absolute ethanol for 10 min, followed by 70 % (v/v) ethanol for 10 min and vacuum dried to induce cross-linking and also to confer insolubility within the silk matrices.

2.2.2 Physico-chemical Characterizations

Scanning Electron Microscopy (SEM)

Analysis of fiber diameter and morphology was carried out using scanning electron microscopy (XL30 FEG, Philips, Netherlands). SEM micrographs were analysed using Image-J (Wayne Rasband, National Institute of Health, USA) to determine the average diameter and standard deviation of the population of fibres (50 fibres were measured from each sample).

Fourier Transform Infrared (FTIR) Spectroscopy

The infrared spectra of all electrospun samples were recorded using an FTIR-ATR (Attenuated Total Reflectance)-Perkin Elmer 2000 spectrophotometer (USA). Sliced samples of the mats were placed on the ATR crystal, and then compressed using an axial screw. Spectra of all samples were recorded using a frequency range between 400-4000 cm^{-1}, and averaged over 4 runs.

X-ray Diffraction

The X-ray diffraction (XRD) patterns of samples were obtained from a Bruker D8 Advance X-ray diffractometer (USA) with a CuK_{α} (λ = 0.1541784 nm) radiation source.

Diffraction patterns were collected from 10° to 60° with a step size of 0.02° and 1 second per step was used.

Contact Angle Measurements

Static contact angle measurements were performed on dry films (n = 3) using a goniometer (CAM200, KSV, Sweden). Ultrapure distilled water droplets were used for measurements. Contact angle measurements were taken for monophasic electrospun mats (**BG**, **BM** and **AA**) and for biphasic composite mats (**BI** and **AI**) on bioactive glass side and silk fibroin side. The measurements are represented as mean ± standard deviation.

Mechanical Testing

The tensile mechanical properties of the electrospun fiber mats were recorded using Universal Testing Machine (Instron, Model: 5944, USA) equipped with a 100 N load cell at a crosshead rate of 1 mm/min. Electrospun mats were cut into rectangular strips of 1 cm x 3 cm, as defined in ASTMD882-02. The samples were mounted in silicon carbide paper grips prior to placement in pneumatic grips. Measurements were carried out in triplicate under ambient conditions. The Young's Modulus was calculated using an offset-yield approach.[231] A line was drawn parallel to the linear regression elastic region at an offset of 0.5 % to the initial sample gauge length; the intersection point wherein the line met the stress-strain curve was defined as the Young's modulus for the sampling.

Swelling Properties

Swelling percentage was evaluated using previously published protocols.[232] Briefly electrospun mats (n = 4) of predetermined weight (W_D) were immersed in phosphate buffered saline (PBS; pH 7.4) and at regular intervals swollen mats were weighed (W_S) after wicking off excess PBS using filter paper. The swelling percentage was calculated by applying the following equation:

$$\text{Swelling Percentage (\%)} = ((W_S - W_D)/W_D)) * 100$$

In vitro Enzymatic Degradation

The *in vitro* enzymatic degradation was carried out in presence of protease XIV (Sigma-Aldrich, ≥ 3.5 U/mg; isolated form *Streptomyces griseus*) according to earlier reports.[222] Briefly, the electrospun mats (n = 4) of predetermined weight were immersed in PBS (pH 7.4) with 2 U/mL protease XIV at 37 °C. At regular intervals the mats were retrieved, washed with PBS (pH 7.4) and dried. The mass remaining was recorded and the following equation was implied to calculate the mass remaining:

$$\text{\% Mass remaining} = (\text{mass at time } `t' / \text{ initial mass}) * 100$$

Protein Adsorption Studies

Protein adsorption studies were carried out using bovine serum albumin (BSA) (Sigma-Aldrich) following previously reported protocols.[233] Briefly, electrospun mats (10 mm diameter) were immersed in PBS (pH 7.4) with 20 mg/mL BSA for 24 h. The protein concentration in solution after incubation was estimated using Bradford's reagent (Sigma Aldrich) and the amount of protein adsorbed was estimated by subtracting from the initial protein solution. A calibration curve was plotted taking BSA as standard for protein concentration estimation.

2.2.3 *In vitro* Biological Studies

For cell culture, the mats (10 mm diameter) were sterilized using 70% ethanol followed by UV irradiation for 20 min. The sterile mats were placed in 24 well plate (n=4) while cells grown in tissue culture plate (TCP) served as control. MG63 (osteosarcoma cell line, NCCS Pune) were maintained in high-glucose DMEM (Gibco, USA) supplemented with 10% FBS (Gibco, USA). The porcine ear chondrocytes were isolated from the porcine pinna of pigs obtained from local slaughter house. The chondrocytes were isolated based on a previously published protocol.[222] Briefly, bilateral ear cartilage was harvested post stripping the perichondrium, under sterile conditions. The obtained cartilage was diced and further subjected to enzyme digestion (0.2 % (w/v) type XIV protease (Sigma-Aldrich, ≥ 3.5 U/mg) for 1 h, 0.05 % type I-A collagenase (Sigma-Aldrich, ≥ 125 CDU/mg) overnight at 37 °C, 95% relative humidity and 5 % CO_2). The resulting digestate was centrifuged at 2000 rpm for 5 min and cell pellet was washed thrice with high glucose DMEM. The chondrocytes obtained were maintained in high-glucose DMEM supplemented with 10% FBS.

2.2.3.1 In vitro Cell Proliferation Assay

For the evaluation of cell proliferation, the Alamar blue (Invitrogen, USA) assay was performed based on the manufacturer's protocol at 1, 3, 7, 11 and 14 days. Briefly the BG, BM and AA mats were seeded with MG63 – osteoblast at a density of 10^5 cells per 10 mm membrane used (n = 4); similarly, the BG, BM and AA mats were seeded with primary chondrocytes at a seeding density of 10^5 cells per 10 mm membrane used (n=4). For the composite bilayered mats, the cells were co-cultured. Initially the MG63 osteoblasts were seeded and on the bioactive glass side at a seeding density of 5×10^4 cells per 10 mm membrane, after 2 h the mats were flipped and primary porcine chondrocytes were seeded at a seeding density of 5×10^4 cells per 10 mm membrane (n=4). The cell seeded membranes were incubated with 10 % (v/v) Alamar blue dye in culture media for 3 h. Post incubation, 100 µL of the culture

media was read at 570/600 nm using microplate reader (Tecan Infinite Pro, Switzerland). The results are represented as normalized Alamar units at different time intervals. Subsequently, the cell seeded membranes were maintained for 14 days in culture in high-glucose DMEM supplemented with 10% FBS at 37 °C and 5% CO_2 with subsequent media change every 48 h.

2.2.3.2 Live/dead Imaging

The cell seeded mats (n = 4) after day-14 were visualized for the distribution of live and dead cells using calcein-AM and ethidium homodimer (Sigma-Aldrich). Briefly, the mats were washed with phosphate buffered saline (PBS, pH 7.4) and the mats were incubated at 37 °C and 5% CO_2 with 40 nM calcein-AM and 20 nM ethidium homodimer for 20 min. The dye mix was removed and washed twice with PBS and the mats were visualized under fluorescence microscope (EVOS XL Digital microscope, USA) and representative images are presented.

2.2.3.3 Cytoskeletal Architecture Assessment

In order to visualize the cytoskeletal architecture of the cells seeded on the electrospun mats, the cell seeded mats were fixed with neutral buffered formalin (NBF) (Sigma-Aldrich). The fixed constructs were treated with 0.165 µM phalloidin conjugated to rhodamine (Life technologies, USA) to stain the F-actin and counter stained with Hoechst-33342 (Sigma-Aldrich). The mats were then visualized under fluorescence microscope (EVOS XL Digital microscope, USA) and representative images are presented.

2.2.3.4 Biochemical Analysis

Alkaline Phosphatase Assay

For determining the membrane bound alkaline phosphatase (ALP), MG63 cells were seeded on BG, BM and AA electrospun mats at a seeding density of 10^5 cells per 10 mm membrane (n = 4) as control. Whereas in the bilayered composite membranes, chondrocytes and MG63 were co-cultured (5×10^4 chondrocytes and 5×10^4 MG63 per 10 mm membrane (n = 4)). At different time points the cells laden membranes were lysed using cell lysis buffer (20 mM Tris-HCl (Merck, India) (pH 7.5), 150 mM NaCl (Himedia, India), 5 mM $MgCl_2$ (Himedia, India) and 0.5% Triton-X100 (Sigma-Aldrich). The ALP activity was determined following the manufacturer's protocol (Abcam, Alkaline Phosphatase Assay Kit (Abcam, U.K.). The ALP activity expressed as U/mL was normalized with the total DNA content for both the membrane bound and soluble ALP and represented as U/µg DNA. [234]

Total Collagen Estimation

To determine the amount of collagen secreted by cells in response to the mats, BG, BM and AA mats were seeded with MG63 – osteoblast at a density of 10^5 cells per 10 mm membrane used (n = 4); similarly, the BG, BM and AA mats were seeded with primary

chondrocytes at a seeding density of 10^5cells per 10 mm membrane used (n = 4). For the composite bilayered mats, the cells were co-cultured. MG63 Osteoblasts were seeded on the bioactive glass side at a seeding density of $5*10^4$ cells per 10 mm membrane and primary porcine chondrocytes were seeded at a seeding density of $5*10^4$ cells per 10 mm membrane (n = 4). A previously published protocol utilizing Sirius red dye based colorimetric assay [235] with rat tail collagen (Sigma-Aldrich) (0 to 250 µg/mL) as standard. The cell laden mats (n=4) were digested with pepsin (Sigma Aldrich, 1 mg/mL pH 3.0). An aliquot of 100 µL from the digested sample was allowed to dry at 37 ºC in 96 well-plate overnight. The dried sample was treated with Sirius red dye solution (1 mg/mL) saturated with picric acid for 1 h, the samples were washed with 0.01 N HCl thrice. Finally, the samples were dissolved in 0.1 N NaOH (Merck, India) and the absorbance were recorded at 550 nm and the collagen content was determined with reference to rat tail collagen as standard.

Sulfated Glycosaminoglycan Content

To determine the amount of collagen secreted by cells in response to the mats, BG, BM and AA mats were seeded with primary porcine chondrocytes at a density of 10^5 cells per 10 mm membrane used (n = 4). For the composite bilayered mats, the cells were co-cultured. MG63 Osteoblasts were seeded on the bioactive glass side at a seeding density of 5×10^4 cells per 10 mm membrane and primary porcine chondrocytes were seeded at a seeding density of 5×10^4 cells per 10 mm membrane (n = 4). A previously published protocol was followed for sGAG estimation using 1,9-dimethylmethylene blue (DMMB) assay.[217] Briefly the cell seeded membranes were digested using papain digestion solution (125 µg/mL papain (Sigma-Aldrich), 5 mM L-cysteine (Sigma-Aldrich), 100 mM Na_2HPO_4 (Merck, India), 5 mM EDTA (Sigma Aldrich) at 60 °C for 16 h. The amount of sulphated glycosaminoglycan was determined using DMMB (Sigma-Aldrich), with reference to chondroitin sulphate from bovine trachea (Sigma-Aldrich) as standard, by measuring the absorbance at 525 nm using Tecan infinite-pro microplate reader.

2.2.3.5 Gene Expression Studies

For analysing the osteogenic and chondrogenic potential of cells cultured on the different mats, the relative gene expression was assessed after day-1, day-7 and day-14 for osteogenic genes namely bone sialoprotein (*BSP*), Runt-related transcription factor 2 (*RUNX2*) and for chondrogenic genes namely aggrecan (*ACAN*) and SRY-Box transcription factor 9 (*SOX9*) to housekeeping gene glyceraldehyde-3-phosphate dehydrogenase (*GAPDH*). RNA was isolated by lysing the cells using TRIzol reagent (Sigma-Aldrich). The lysate was centrifuged at 13,000 rpm (10 min, 4 °C) and the supernatant was transferred to fresh tubes.

After incubation with chloroform for 15 min, the mixture was centrifuged at 13,000 rpm (15 min, 4 °C) and upper aqueous layer was used for elution of RNA. 1µg total RNA was reverse transcribed using High Capacity Reverse Transcription Kit (Applied Biosystems, Invitrogen, USA) in a thermal cycler (TaKaRa, Japan). Expression level of genes was quantified using Power SYBR Green PCR Master Mix (Applied Biosystems, USA) in a real-time PCR machine (Applied Biosystems 7500, USA) with the sequences shown in **Table 2.1**.

Table 2.1. *Primer sequences of different genes used for gene expression studies*

Gene	Sequence	Accession Number
Human *GAPDH*	**F** 5′-GACCTGACCTGCCGTCTA-3′	NM_001289746.1
	R 5′-GTTGCTGTAGCCAAATTCGTT-3′	
Human *BSP*	**F** 5′AACCTACAACCCCACCACAA-3′	NM_004967.3
	R 5′-GTTCCCCGTTCTCACTTTCA-3′	
Human *RUNX2*	**F** 5′-GATGGGACTGTGGTTACTGTCA-3′	NM_001278478.1
	R 5′-CTCAGATCGTTGAACCTTGC-3′	
Porcine *GAPDH*	**F** 5′-TCGGAGTGAACGGATTTGG-3′	NM_001206359.1
	R 5′-CCAGAGTTAAAAGCAGCCCT-3′	
Porcine *ACAN*	**F** 5′-CCCAACCAGCCTGACAACTT-3′	NM_001164652.1
	R 5′-CCTTCTCGTGCCAGATCATCA-3′	
Porcine *SOX9*	**F** 5′-TTCCGCGACGTGGACAT-3′	NM_213843.1
	R 5′-GGCGGCAGGTACTGGTCAAACTC-3′	

2.2.3.6 In vitro Immune Response Assessment

In order to assess the immune response elicited by the mats (n = 4), murine macrophage cells (RAW 264.7, obtained from NCCS, Pune) were utilized. The TNF-α secreted by macrophages was quantified using an ELISA kit (Invitrogen, USA) based on the manufacturer's protocol. Briefly, 10^5 cells/cm^2 were seeded on 24 well plates, and after 24 h mats of diameter 10 mm were placed on the seeded wells and the spent media supernatant after 12 h and 24 h were collected and assayed for the TNF-α production. 500 ng LPS from *Escherichia coli* (Sigma-Aldrich) served as the positive control, while tissue culture plate (TCP), wells without any samples served as negative control.

2.2.3.7 Histological Assessment and Immunostaining

The cell seeded membranes were fixed with neutral buffered formalin (NBF; Sigma-Aldrich). The membranes were subjected to ethanol-xylene dehydration procedure and embedded in paraffin and sectioned using manual rotary microtome (Leica biosystems, USA) to obtain 10 μm thick slices. The slices were further stained with hematoxylin and eosin to observe cell-scaffold interaction and the distribution of cells on and within the membrane. The sections were stained with 2 % (w/v) Alizarin red (Sigma-Aldrich) to assess the extent of the calcium deposition and 1 % (w/v) Alcian blue (Sigma-Aldrich) to determine the extent of sulphated glycosaminoglycan deposition. For immunostaining, cell seeded electrospun mats were fixed with NBF overnight. The fixed constructs were permeabilized with 0.1% Triton X-100 (Sigma-Aldrich) in PBS for 15 min, followed by blocking with 1 % BSA in PBS. The mats were incubated with corresponding primary antibody, rabbit polyclonal against collagen-II (Abcam, U.K., 1:200 dilution) for chondrocytes and rabbit polyclonal against osteopontin (OPN) (Abcam, U.K., 1:1000 dilution) for osteoblasts, overnight at 4 °C. The mats were then incubated with FITC conjugated secondary antibody anti-rabbit developed in goat (Abcam, U.K., 1:2000) for 1 h at room temperature. The mats were counterstained with 0.165 μM phalloidin conjugated to rhodamine (Life technologies, USA) to stain the F-actin and with Hoechst-33342 (Sigma-Aldrich) to stain the nucleus. At each step the mats were washed with 0.1 % Tween-20 (Sigma-Aldrich) in PBS. The stained sections or mats were visualized using inverted fluorescence EVOS XL Digital microscope and representative images are presented.

2.2.4 Statistical Analysis

All the experiments were carried in quadruples unless otherwise mentioned and the data is represented as mean ± standard deviation. Data was statistically analysed using one-way analysis of variance (ANOVA) to find the significant difference among different sampling groups. Tukey's test was performed using OriginPro 8.0 software with $*p \leq 0.05$ considered as significant, while $**p \leq 0.01$ as highly significant.

2.3 Results and Discussion

2.3.1 *Microfibrous Aligned 70S Bioactive Glass Mats and Nanofibrous Randomly Aligned Silk Mats Exhibit Hierarchical Complexity*

There are two unique aspects of the composite bilayered scaffold being reported in this article. The first is the bilayer nature of the scaffold utilizing an underlying osteoinductive sol-gel derived bioactive scaffold, coupled with an upper silk layer to drive regeneration of the cartilage layer. The second aspect was the use of an endemic Indian silk variety, which possesses RGD sequences known to influence cell adhesion and proliferation.[228] The process parameters such as working distance, voltage and solution parameters were optimized to obtain fluent bead-free fibers. As can be seen from the scanning electron micrographs (**Figure 2.1 A-F**), the BM and AA fibers appeared to have smooth surfaces and a circular cross-section. The nanofibers had an average diameter of 175 ± 53 nm and 189 ± 70 nm for BM and AA mats respectively. SEM micrographs (**Figure 2.1A and 2.1B)** also revealed the porous nature of the SF electrospun mats. The SF nanofibers were deposited non-uniformly in random manner and appeared to intersect each other forming numerous small pores ranging in size up to several microns. The finely spread nanofibers may serve as a biomimetic template which recapitulates the collagen-II fibrils present in the native cartilage tissue.[236] Pore size and porosity play a crucial role in this regard. A smaller pore size is desirable for the cartilage phase of the construct, as lower oxygen tension creates a hypoxic environment suitable for maintenance of chondrogenic phenotypes,[237] and also permits adequate nutrient transfer.

The as-spun bioactive glass (BG) mat was also porous, however, the fibers had a larger average diameter of 0.97 ± 0.34 μm (**Figure 2.1D**). Importantly, the BG fibers were distributed with an aligned orientation (**Figure 2.1C**), similar to the fibrillar pattern of mineralized collagen-I found in the osteonal lamellae.[238] Interestingly, there was no devoted collector used to attain aligned bioactive glass microfibers. The fibers were oriented in the direction of motion of the rotating mandrel. We hypothesize that a physical drafting effect[239] could have contributed to this alignment, wherein a state of synchrony between the rotating mandrel speed and the jet stretching speed could have been achieved, under the applied parameters for electrospinning. As previously reported, presentation of appropriate micro-environment is crucial for effective cell-material interaction.[240-242] and larger pores have shown to facilitate faster bone regeneration.[243] Micrographs of the composite biphasic mat cross-sections (**Figure 2.1E and F**) demonstrate the significant and successful junction formation of the two different fibrous materials. These micrographs confirm the well-integrated nature of the composite mats and importantly show the maintenance of their porous structure.

Additionally, the compact features of upper SF (**Figure 2.1F**) were observed showing the small pores (as seen in **Figure 2.1F**), and the loosely connected lower BG layer (**Figure 2.1E**) due to its microfibrous nature. In earlier reports, microfibrous milieu have shown to support the growth of osteoblast like cells *in vitro* when compared to nanofibrous environments, owing to increased porosity associated with the former.[244, 245]

Compositional analyses were undertaken using FTIR, XRD and energy dispersive spectra (EDX) to understand the material's functional properties. FTIR spectra (**Figure 2.1G**) were recorded to study the molecular conformation of the silk fibroin and bioactive glass within the electrospun mats. Characteristic peaks confirming the presence of $70SiO_2.25CaO.5P_2O_5$ bioactive glass were observed at 1042 and 446 cm^{-1} (Si-O-Si stretching and bending vibrations), 808 cm^{-1} (O-Si-O stretching), and 962 cm^{-1} (P-O stretching),[246] consistent with compositional analysis evident from EDX (*Appendix* **Figure A2.1 A**). The bone phase present in the basal side of the bilayered construct (BG) would be in direct contact with the subchondral region abundant in bone marrow derived mesenchymal stem cells, therefore the presence of a suitable bioactive ceramic is important to aid differentiation into the osteogenic lineage.[219] The peak at 1378 cm^{-1} corresponds to NO_3^- stretching vibration, indicating the presence of nitrates in the bioactive glass.[247-249] The characteristic vibrational regions for silk fibroin were also present in the electrospun mats, as shown in **Figure 2.1G**. The amide-I band (corresponding to N-H deformation and C-H stretching) was seen at 1650-1600 cm^{-1}, amide-II band (corresponding to C=N stretching) at 1550-1510 cm^{-1}, and amide-III band was observed at 1260-1210 cm^{-1} (corresponding to C-N stretching).[223, 232] The C-H stretching pertaining to aldehyde, and a broad peak corresponding to the O-H group are attributed to the polymers PVA and PVB used for aiding the electrospinning of SF and bioactive glass sol respectively.[250, 251] It is pertinent to note that both PVB and PVA used in the current study to adjust the rheological properties of bioactive glass sol and SF have FDA clearance for use in finished pharmaceuticals as adhesives and components of coatings.[252] The composite biphasic mats exhibited all the conformational peaks of SF and BG, thus there appeared no alteration in conformation of these materials when spun together. However the intensity of the amide I peak at ~1660 cm^{-1} varied in intensity between the composite materials, suggesting possible differnences in interactions with the C=O groups associated with the aldehyde groups of PVB and PVA,[253] which might have led to the important well integrated interface of the biphasic composites.

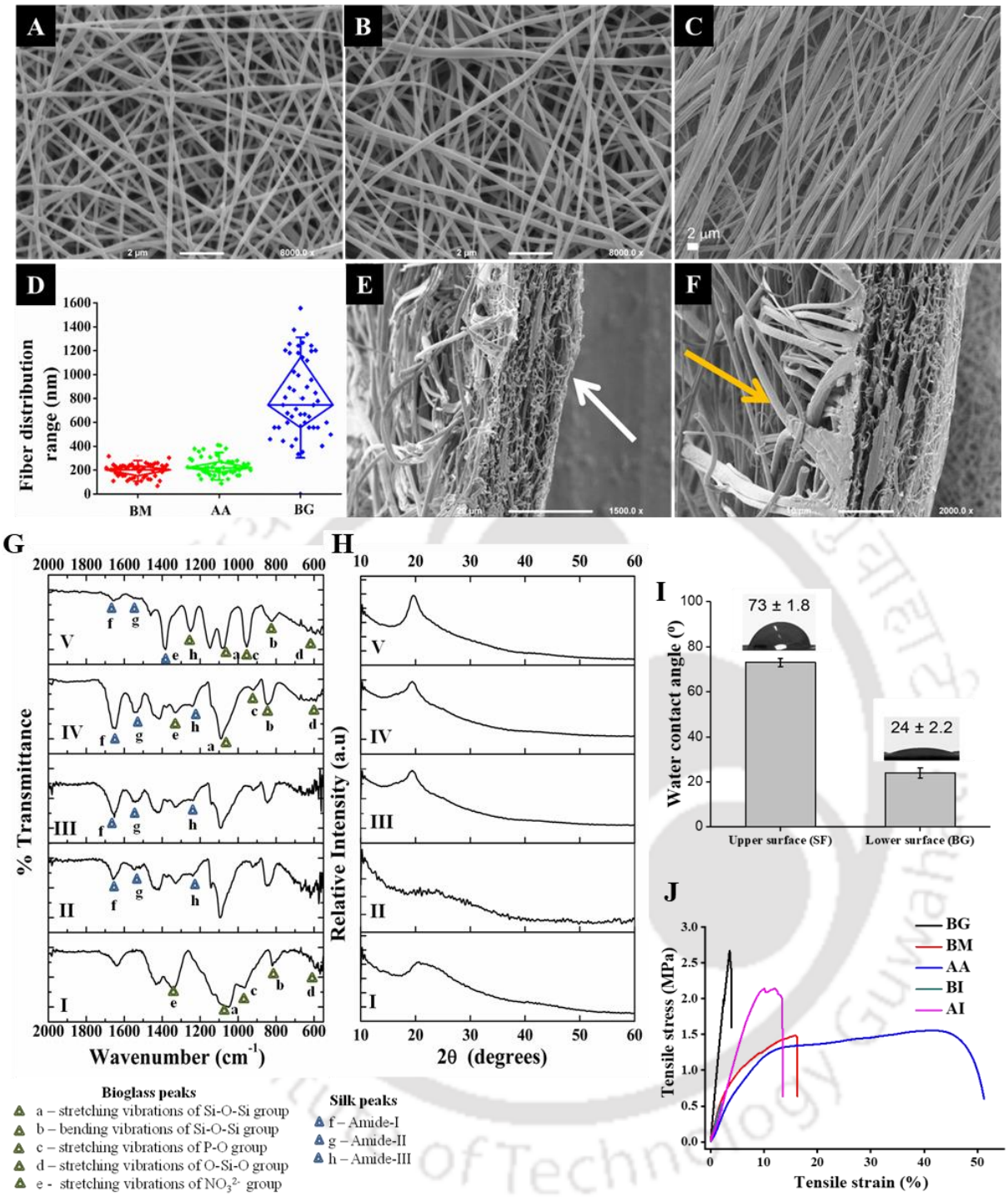

Figure 2.1. ***Physico-chemical studies on the electrospun mats.*** *Scanning electron micrographs of A) BM B) AA and C) BG mats; D) fiber distribution analysis showing nanofibrous nature of SF mats and microfibrous nature of BG mats; SEM micrograph of a cross-section of biphasic mats formed by E) electrospininning BG, followed by F) silk layer, exhibiting coherent well integrated interface. (white arrow indicating nanoporous SF layer and yellow arrow indicating microporous BG layer; G) FTIR spectra of electrospun mats; H) X ray diffractograms of electrospun mats I) BG, II) AA, III) BM, IV) BI and V) AI mats; I) contact angle measurements for BI composite mats' upper and lower surface; J) Representative stress-strain curve for electrospun mats.*

X-ray diffraction (XRD) was employed for further phase analysis of the electrospun mats (**Figure 2.1H**). The broad or weak peaks observed at ~20° corresponding to the β-sheet, indicates that the SF is amorphous in nature in the electrospun silk matrices.[254-256] The amorphous nature of the SF mats may be attributed to the rapid evaporation of the solvent, slow rate of crystallization, and the short travel time of the jet in air using electrohydrodynamic atomization.[257] Furthermore, the XRD pattern obtained for the 70S bioactive glass (BG) mat (**Figure 2.1H**) confirmed the amorphous nature of the bioactive glass, as expected for a sol-gel bioactive glass samples without thermal treatment. Sol-gel derived bioactive glasses remain advantageous over the conventionally available melt derived bioactive glasses due to their high surface area to volume ratio and faster resorption rate *in vivo*.[258] In addition, the dissolution products of amorphous bioactive glasses, owing to their faster dissolution rate, can stimulate proliferation and differentiation of bone marrow derived stem cells.[259] This was evident in the biological studies as reported in subsequent sections, thereby validating the functionality of the fabricated mats.

Hydrophobicity and/or hydrophilicity of electrospun materials are critical parameters and can be one of the main controlling factors determining the events at the cell-matrix interface. These parameters were assessed by measuring the water contact angles (**Table 2.2)**. Measurements indicated that AA mats were more hydrophilic than BM mats and this had important implications for subsequent biological measurements. Non-mulberry silk varieties belonging to the Saturniidae family (*A. assama*) are abundant in poly-alanine repeats whereas the silk belonging to the Bombycidae family contain poly-glycine-alanine repeats. These poly-alanine repeats confer more ß-sheet formation in non-mulberry than in mulberry silk.[228, 260] The poly-alanine and the poly-glycine-alanine repeats dictate the self-assembly process of the regenerated silk fibroin solution into final conformation in scaffolds. Hence the mulberry silk (BM) possesses a more hydrophobic surface when compared to the non-mulberry (AA) silk; where in the latter all the hydrophobic regions are very well embedded within the core with only hydrophilic regions exposed. There was an increase in contact angle observed upon combining SF with BG fibers for both composite mats (BI, **Figure 2.1 I** and AI); this increase was largest for the BG side of the combined mats, showing an increase from 13° for BG alone to 24° and 51° for BI and AI mats. During the electrospinning process, the biopolymer jet discharged from the needle rapidly evaporating and depositing polymer over the collecting mandrel. The resulting supramolecular assembly ensures the interaction of poly-alanine and poly-glycine-alanine repeats and subsequent condensation and molecular rearrangement into

ß-sheets. The amino-acid compositional variability between the two silks may have led to the differences in interaction with the spun primary bioactive glass layer. Furthermore, the porosity and relatively small thickness (ca. 1-2 µM) of the bioactive glass layer when in the composite material would reduce its hydrophilicity in comparison to the bulk material. This may explain the difference in the contact angles, a crucial factor for cell adhesion and growth. Importantly, the varying water contact angles of the different sides of composite mats (BI in particular) demonstrated that this material could provide both hydrophilic and hydrophobic surface functionality.

Table 2.2 *Contact angle measurements for electrospun mats*

Sample	**Monophasic**			**Biphasic**			
	BG	**BM**	**AA**	**BI**		**AI**	
Contact angle (^{0})	13 ± 2.6	71.85 ± 0.8	41.66 ± 0.6	SF Side	73.5 1 ± 1.8	SF Side	47.14 ± 2.9
				BG Side	24.2 ± 2.2	BG Side	51.23 ± 2.2

The extent of wettability possessed by a biomaterial is related to its surface property. The scaffolding material when placed inside the body must be able to absorb the body fluid, thus supporting the nutrient and metabolite transfer between the scaffolding construct and surrounding tissue in contact. The swelling profile of the electrospun mats is shown in **Figure A2.1 B (***Appendix*). All the mats attained their maximum swelling capacity within 2 h, with the BG mat exhibiting the highest swelling percentage of around 330 % while the silk mats recorded swelling percentages around 250 %, statistically significant with respect to the BG mats ($p \leq 0.05$). The composite mats exhibited swelling percentage of 300 %, with no significant difference noticed between the composite mats. The increased swelling percentage in BG mats may be attributed due to its hydrophilic nature in comparison to silk mats, which may play key roles in cell adhesion and extracellar matrix protein deposition. Though there was difference in contact angle noticed between the silk mats, there was no significant difference between the groups. This may be attributed due to the hydrophilic nature of PVA within the silk matrix which might have enhanced the water retention capacity. Similarly the swelling percentage of the composite mats ranged between that of the hydrophilic BG mats and the silk mats. The surface of the implant also mediates the adsorption of proteins when it comes in contact with physiological fluids. These adsoped proteins further regulates the cell-

matrix interaction. Bovine serum albumin (BSA) having a close likeliness to human serum proteins[233] was chosen as a model protein to study the adsorption profile (**Figure A2.1 C** *Appendix*) of the developed electrospun mats. It was noticed the silk mats exhibited higher protein adsorption, about ~ 1.3 folds higher ($p \leq 0.05$) than the BG mats. The composite mats exhibited the highest protein adsorption, about ~ 1.2 folds higher than silk mats and about ~ 1.7 folds higher than BG mats. The adsortpion was possibly mediated via electrostatic or Van der Waals interaction, proving the composite mats' potency as biologically recognizable materials.

The rate of scaffold degradation plays an important role during the regeneration process when implanted *in vivo*. The degradation process is assisted synergistically under *in vivo* conditions by various ECM modulatory enzymes such as matrix metalloproteinases.[261] In order to achieve the same functional performance offered by these enzymes, a non-specific proteolytic enzyme, protease XIV was chosen to carry out the degradation studies *in vitro*.[232] All the mats showed a time dependent mass loss as observed from **Figure A2.1 D (***Appendix*). Among the silk mats, BM exhibited a faster rate of degradation in comparison to AA. The AA retained about 87 % mass, whereas BM retained about 82 %. The slower degradation rate of AA may be attributed to the strong hydrophobic interactions of polyalainine repeats found in non-mulberry silk, rendering protease XIV inaccessible for proteolytic cleavage. The BG mats, however, retained ~94 % ($p \leq 0.05$ in comparison to silk mats) of their mass after 21 days as there was no protein component associated with it. The leaching out of inorganics may be a plausible reason for the observed mass loss. Between the composite mats there was no significant difference noticed, and they retain about ~ 87 % of the mass after 21 days.

Tensile strength investigations provided insightful inputs about the mechanical properties of the electrospun mats. Stress-strain curves representing the different electrospun mats used in this study are shown in **Figure 2.1 J**, with the data summarized in **Table 2.3**. The BG mats exhibited the highest elastic modulus of 86 MPa and the lowest strain % of ~3.8 %, characteristic of a ceramic doped polymer. In comparison, the silk mats BM and AA both exhibited higher strain % before fracture, further evidencing the ductile properties possessed by the SF biopolymer. AA exhibited significantly higher elastic modulus (23 MPa) than BM, and a higher breaking strain (55% compared to 16% for BM). This may be due to the polyalanine repeats present in the non-mulberry silk varieties, which impart superior mechanical properties for cartilage repair compared with mulberry silk (containing poly-glycine-alanine repeats).[200] There was no significant difference between elastic modulus of composite mats, both recording about 27-29 MPa. In the composite mats, the cumulative

increase in the initial elastic region (**Figure 2.1 J**) could be attributed jointly due to silk and bioactive glass. This was followed by plastic deformation, which was relatively shorter in the case of BI mats, whereas the AI mats exhibited a longer plastic deformation region consistent with the larger breaking strain exhibited by AA alone. The plastic deformation is followed by a non-linear plateau region indicating delamination of the construct and eventually failure. Thus, the composite mats, especially AI, demonstrated similar biomechanics to that seen in an osteochondral interface (consisting of the elastic hyaline cartilage) which constantly deforms under articular movement and the subchondral bone which resists the compressive force. Therefore, the silk phase should well approximate the mechanical properties for the cartilage region, and the bioactive glass to bone.

Table 2.3. *Tensile properties for electrospun mats*

	BG	BM	AA	BI	AI
Elastic Modulus (MPa)	86.66 ± 4.32 *	13.42 ± 0.16 #	22.90 ± 1.76 $	29.36 ± 1.38	27.48 ± 3.96
Elongation at break (%)	3.83 ± 0.33 *	15.98 ± 0.89 #	55.11 ± 12.84 $	2.28 ± 0.59	8.52 ± 1.43

* represents statistical significance between BG and rest of the group at $p \leq 0.05$
# represents statistical significance between BM and BG, AA at $p \leq 0.05$
$ represents statistical significance between AA and BM at $p \leq 0.05$

2.3.2 *Alignment and Inherent Physico-chemical Properties of the Electrospun mats Influences Cellular Orientation*

In vitro biological studies were carried out to investigate the differential behaviour of the seeded osteoblast and chondrocyte on the electrospun matrices. The utilization of a two cell-type culture model for the composite biphasic mats is complex but important due to the interaction that occurs between the cell types. All the tested mats supported the growth of cells seeded on them exhibiting no discernible cytotoxicity. Cell proliferation was assessed using the Alamar blue assay (shown in **Figure 2.2 A**), the chondrocytes and osteoblasts were cultured on BG, BM, AA mats separately as controls and co-cultured on the composite mats (BI and AI) for 14 days. Both the silk mats (AA and BM) aided the proliferation of the chondrocytes better than their BG counterpart (with ~1.2 folds increase with respect to BG).

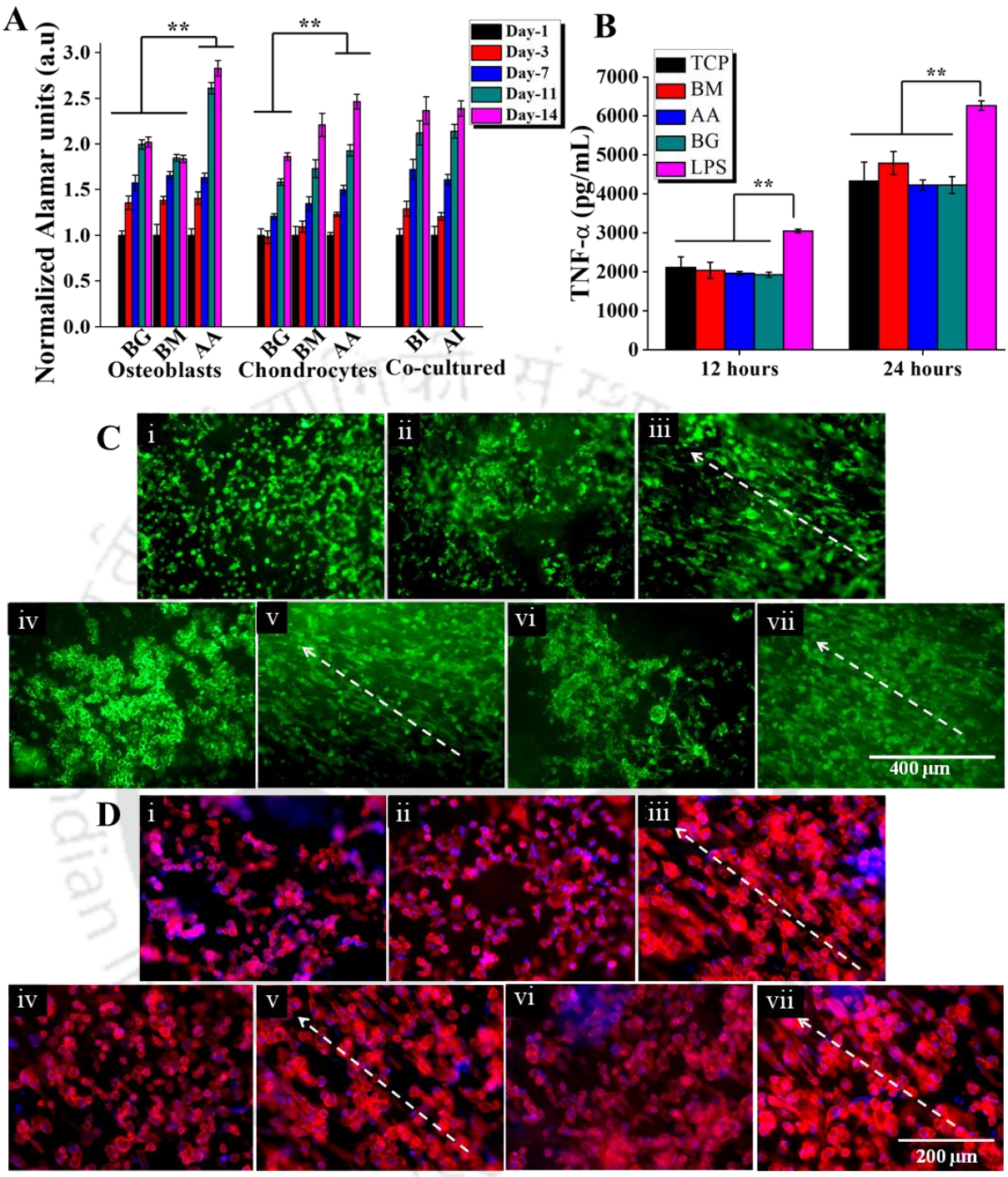

Figure 2.2. ***In vitro biocompatibility and cytoskeletal architecture assessment.*** *A) In vitro cell proliferation assessment using alamar blue cell viability assay on electrospun mats; B) In vitro immune response assessment of electrospun mats by measuring TNF-α release from murine macrophage RAW 264.7 cells; C) Live/Dead imaging and D) cytoskeletal architecture assessment of seeded cells; chondrocytes grown on i) BM and ii) AA mats, osteoblasts grown on iii) BG mats, chondrocytes grown on silk side of iv) BI, vi) AI composite mats and osteoblasts grown on bioactive glass side of v) BI and vii) AI composite mats (white dashed arrows indicating direction of alignment of cells along the fibrillar direction); (** represents statically significant difference $p \leq 0.01$).*

However, it was observed that the AA mats supported the proliferation of both chondrocytes and osteoblast cells, better; in particular displaying a ~1.3 folds and ~ 1.5 folds increase compared to BG and BM respectively for osteoblast cells. *A. assama* possesses intrinsic tripeptides – RGD (arginine-glycine-aspartate) towards the N and C terminals of glycine rich G-motif. This particular tripeptide has been widely shown to enhance cell attachment via integrin receptor mediated pathway.[262] Therefore, it can be hypothesised that the greater cell proliferation supported by the AA mats may be due to the presence of these intrinsic RGD peptides, which mediated the cell attachment and subsequently regulated the cell proliferation.[263] Importantly, the composite mats supported the growth of both the cell types in the 14 day culture, and no significant difference was seen between the composite mats. Any adverse immune reactions elicited by a biomaterial would result in acute outcomes such as inflammation, tissue destruction as well as interference in the healing process, resulting in rejection of the graft.[264] Therefore as a quantifiable precursor to *in vivo* testing, the *in vitro* immunogenicity of the mats were tested using murine macrophage cells at 12 h and 24 h using the TNF-α secretion (Figure 12). It can be seen from **Figure 2.2 B** that all the mats exhibited negligible immune response comparable to negative control, demonstrating that the mats would not induce any adverse immune response. Silk based biomaterials which have been shown to be immunocompatible *in vitro* were found to elicit negligible immune response *in vivo*.[232, 265] Therefore, these materials are expected to be applicable for successful implementation *in vivo* without further processing.

The suitability of electrospun mats as tissue engineering constructs were further evaluated using live/dead staining (**Figure 2.2 C**). It was observed that the non-mulberry silk mat (AA) showed higher live cell density compared to its mulberry counterpart, correlating with findings from the cell proliferation testing. The co-culture system on the composite mats supported the growth of both cell types with no adverse effects over the full 14 days, in keeping with the Alamar blue assay results (**Figure 2.2 A**). Furthermore, some orientation of the cell growth can be seen in these images, driven by the oriented fibrillar nature of the scaffolds. This was also evident in the cytoskeletal image measurements detailed below. In order to evaluate the cell cytoskeletal architecture, actin filaments were stained using rhodamine conjugated to phalloidin (**Figure 2.2 D**). The osteoblasts seeded on PVB-BG mats aligned themselves along the direction of the nano-fibers and spread along the fibril axis. Clusters of rounded morphology cells were observed alongside the oriented cells after 14 days, which appear to be bone-nodule like cells (**Figure 2.2 D iii**) formed from initially adherent cells. The aligned fibrillar organization is similar to the native osteonal lamellae in the cortical bone, which might

have led to this as mentioned secondary clustered pattern.[266] The chondrocytes grown on plastic (Tissue culture plastic –TCP, shown in *Appendix* **Figure A2.2**) lost their phenotype and acquired a fibroblastic phenotype, characterized by spreading-out of cells and reduction in synthesis of cartilage specific proteins.[267] In comparison, the chondrocytes grown on silk mats acquired a rounded morphology pertaining more to their native morphology. Furthermore, chondrocytes cultured on individual and composite AA mats were in clusters and well distributed throughout. This may be attributed to the hydrophilic nature of the AA mats in comparison to BM mats which exhibited a higher water contact angle.

2.3.3 *Cells Seeded on Electrospun Exhibit Preferential Cellular Phenotype Maintenance*

To assess the progression and state of chondrogenesis and osteogenesis biochemical analysis of different marker proteins and gene expression profiling of marker genes were performed. Chondrogenesis is marked by precursor cells undergoing condensation into clusters, followed by their proliferation and expression of ECM proteins. Among the ECM proteins collagen-II, glysoaminoglycan and aggrecan are the principal proteins expressed in abundance which help in forming the cartilaginous matrix.[216, 268] The hallmark feature of osteogenesis is the expression of collagen-I protein by osteoblasts on to which the calcium nucleates and apatite crystals form. This results in the mineralized matrix and followed by the expression of modulatory proteins like osteocalcin, osteopontin and BSP which regulate the crystal growth.[269] Alkaline phosphatase (ALP), a key regulatory enzyme in mineralization process was used as a marker to check the osteoconductive potential of the mats (**Figure 2.3 Ai**). The level of ALP expression peaked after 7 days with BG mats showing significantly higher levels than osteoblast seeded silk only mats (~1.6 folds higher than BM, while ~2.02 folds higher than AA), which then gradually decreased, indicating the onset of mineralization. This is concurrent with the use of amorphous 70S bioactive glass which is a potent regulator of osteogenesis,[270] and whose ionic products mediates the differentiation of osteoblasts. The ALP levels reduced at day-14 which may be an indication of terminal maturation of the osteocytes. On the composite mats, where the chondrocytes and osteoblasts were co-cultured, there was a significant increase in the ALP expression (with BI showing ~1.1 folds increase and AI showing ~1.3 folds increase in comparison to BG mats). This increase in ALP activity may be explained as the combined action of osteoblast and chondrocytes in co-culture, which has been reported previously both in micromass culture,[271] as well as in scaffold systems[272] to enhance mineralization. Furthermore, the AI mats showed significant increase

($p \leq 0.01$) in ALP expression compared to the BI composite mats, further demonstrating the excellent osteoconductive potential of the composite mats containing *A. assama* silk.

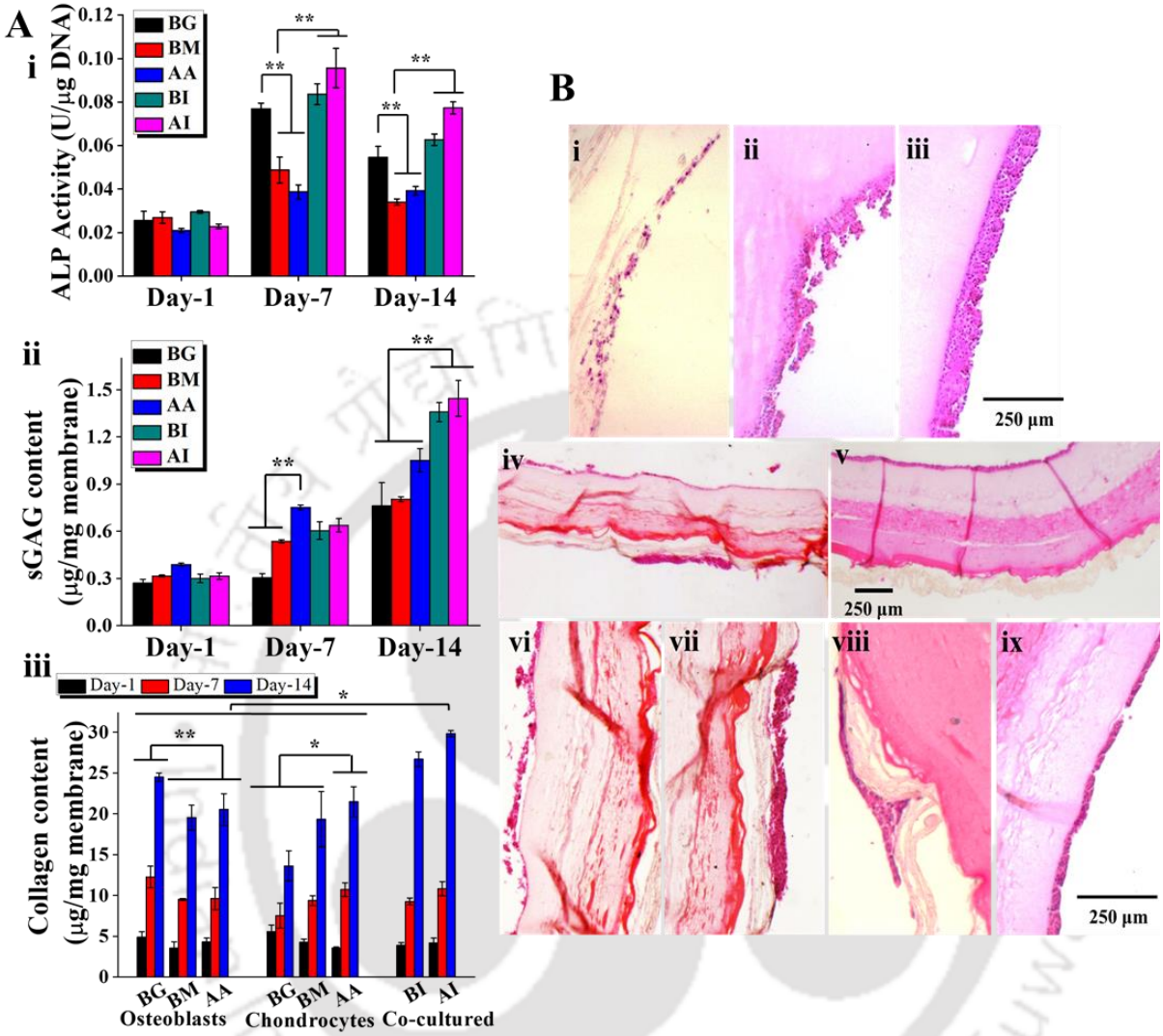

Figure 2.3. ***Biochemical assessment of key markers and cellular distribution in cell seeded electrospun mats****. A) Biochemical assessment of cell seeded mats; i) alkaline phosphatase activity estimation, ii) sulphated glycosaminoglycan estimation and iii) total collagen estimation; B) Histological assessment – Hematoxylin and eosin stained sections; i) BG mats seeded with osteoblasts, ii) AA and iii) BM mats seeded with chondrocytes; iv) AI and v) BI composite mats with chondrocytes and osteoblasts are co-cultured, while vi) and vii) are bioactive glass side with osteoblasts grown on it, viii) and ix) are silk side with chondrocytes grown on it, of BI and AI composite mats respectively; (* represents significance level at $p \leq 0.05$ and ** represents significance level at $p \leq 0.01$).*

Sulfated glycosaminoglycans (GAGs), one of the main extracellular matrix components secreted by chondrocytes were quantified within the scaffolds to evaluate their chondrogenic potential (**Figure 2.3 Aii**). The sGAG content varied significantly between the mats, with the silk mats (AA and BM) exhibiting higher levels in comparison to BG (at day-14, AA exhibited

~1.5 folds increase and BM exhibited ~1.1 folds increase). The composite mats where the cells were co-cultured also showed the greatest increase in sGAG after 14 days, in line with results seen from the ALP studies. Similarly, the AI mats exhibited the highest sGAG content (at day 14, ~1.4 folds increase in comparison to AA). This may be attributed to the hydrophilic surface provided by the AA mat. Ma *et al.*, studied the effect of chondrogenesis on hydrophobic PLLA surface and PLLA surface modified by addition of hydrophilic groups,[273] it was observed that modified hydrophilic PLLA surfaces exhibited better cell adhesion and matrix protein deposition.[274] In addition chondrocytes express several integrin receptor families which help to maintain their homeostasis. Due to the AA mats' abundance in RGD tripeptide, it may be hypothesised that integrin binding stimulates intracellular signalling and subsequent ECM production.[275]

In order to evaluate the extent of extracellular matrix (ECM) deposition on the electrospun mats, total collagen content was quantified (**Figure 2.3 Aiii**). It was observed that osteoblasts seeded on BG secreted higher collagen (~1.25 folds higher than BM and ~1.19 folds higher than AA) than silk mats. Conversely, chondrocyte seeded AA mats exhibited higher collagen (~1.57 folds increase in comparison to BG) content when compared to BG and BM mats. Among the osteoblast seeded mats BG exhibited higher collagen deposition, correlating with measured ALP activity (**Figure 2.3Ai**). The terminal maturation is characterized by an increase in mineralized matrix which is correlated with an increased collagen deposition. Collagen content was highest in the composite mats where the osteoblasts and chondrocytes are co-cultured, concurrent with sGAG and ALP results. Furthermore, after 14 days AI mats exhibited a ~1.12 folds increase in comparison to BI bilayered composite mats, correlating with the excellent osetoconductivity and retainment of chondrogenic phenotype observed for the non-mulberry silk composite mats during sGAG and ALP quantification. Due to the nature of both the scaffolds (mats) and the osteogenic-chondrogenic co-culture model, these samples readily lend themselves to histological sectioning. To assess cell attachment and distribution, transverse sections were stained with hematoxylin and eosin (**Figure 2.3B**), revealing that the cells were present on the surface of all the mats, with little infiltration. Microfibrous scaffolds have been shown to support the infiltration and survival of osteoblasts when compared to nanofibrous matrices.[245] The microfibrous nature of the bioactive glass, as discussed earlier allows for bigger pores than the nanofibrous SF. This led to better infiltration of cells in the bioactive glass mats (**Figures 2.3B i, vi and viii**) in comparison to SF mats. Sections of chondrocytes cultured on AA mats (**Figure 2.3Biii**) revealed a compact structure, and a well adherent multi-layer owing to its better surface

properties, whereas BM mats (as seen in **Figure 2.3Bii**) showed a loose adhesion profile. The composites mats supported the growth of both cell types as seen in **Figure 2.3B iv** and **v**. The chondrocytes cultured on AI (**Figure 2.3B ix**) exhibited a compact multilayer, while the chondrocytes grown on BI mats' silk side (**Figure 2.3B vii**) were loosely bound in a disrupted multilayer.

Chondrogenic marker genes aggrecan (*ACAN*) and SRY-Box transcription factor 9 (*SOX9*), and osteogenic marker genes bone sialoprotein (*BSP*) and Runt-related transcription factor 2 (*RUNX2*) were analysed to further evaluate the chondrogenic and osteogenic potential of the cell seeded constructs over a period of 14 days. Greater up-regulation of cartilage specific genes *ACAN* and *SOX9* (as seen in **Figure 2.4A i** and **ii**) was observed in chondrocytes seeded silk mats, in particular AA, further demonstrating the better suitability of these materials for chondrocyte cultivation (~2.35 folds increase in *SOX9* expression and ~3.67 folds increase in *ACAN*, in comparison to BG). Concurrent with ALP analysis results, up-regulation of bone specific gene *BSP* was found to be higher in osteoblast seeded BG mats in comparison to silk (BM and AA) mats, confirming the excellent potential for osteoblast cultivation **Figure 2.4Bi**. In the case of *RUNX2*, the expression for BG was ~2.4 folds higher than BM and ~3.4 folds higher than AA. *RUNX2*, an early differentiation marker expressed by committed osteoblast cells marks the onset of mineralization process (**Figure 2.4B ii**). High expression levels of *RUNX2* at day-7 in osteoblast seeded BG mats and co-cultured composite mats attested to the fact that the osteoblasts were moving towards acquiring osteocyte like phenotype and terminal maturation, in comparison to the osteoblasts seeded on the silk mats. Higher expression levels of *BSP* (at day-14), a non-collagenous protein which helps in nucleation and modulating the apatite crystal growth[52] concurred with the *RUNX2* experiment findings. Importantly, it was found that *SOX9*, a key early chondrogenic stage marker had a higher expression in the composite (AI) mats affirming the commitment of chondrocytes towards the chondrogenic lineage.[220] Likewise, expression of aggrecan, an important proteoglycan constituent of ECM is involved in recruitment of sGAGs and chondroitin sulphate during the condensation of chondrocytes to form functional clusters which later lay the template for the cartilaginous matrix.[222]

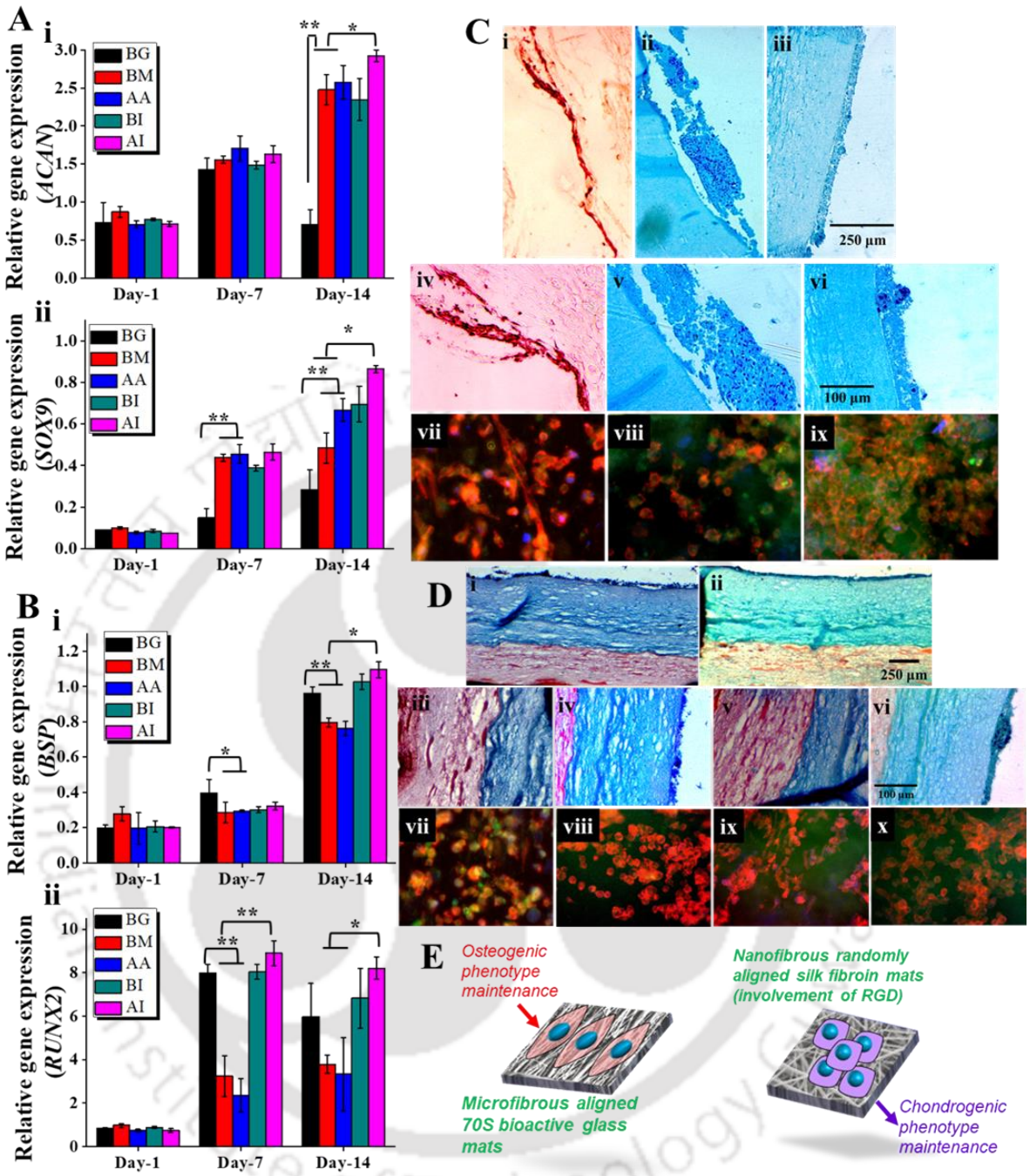

Figure 2.4. ***Gene expression assessment of key markers and funcional staining assessment of cell seeded electrospun mats***. *Real time gene expression profile for A) chondrogenic genes i) aggrecan (ACAN), ii) SRY-Box transcription factor 9 (SOX9); for B) osteogenic genes i) bone sialoprotein (BSP), ii) Runt-related transcription factor 2 (RUNX2); Histological assessment – alizarin red and alcian blue stained transverse sections of C) control group consisting of i) osteoblast seeded BG mats, ii) and iii) chondrocyte seeded BM and AA mats respectively; D) experimental group consisting of i) BI and ii) AI composites mats conducive for co-culture of iii), v) osteoblast seeded bioactive glass side retaining alizarin red and iv), vi) chondrocyte seeded silk side retaining alcian blue; Expression of marker proteins – osteoblasts were stained for osteopontin (OPN) in (C. vii) BG, (D. vii) BI and (D. ix) AI mats; chondrocytes were stained for collagen-II in (C. viii) BM, (C. ix) AA, (D. viii) BI and (D. x) AI*

mats respectively; E) Scheme illustrating the microfibrous 70S bioactive glass mats favouring osteoblasts survival and nanofibrous silk mats favouring chondrocytes in the cell-instructive composites investigated here in the study; (represents significance level at $p \leq 0.05$ and ** represents significance level at $p \leq 0.01$).*

The increased level of expression of aggrecan (involved in recruitment of sGAGs and chondroitin sulphate during the condensation of chondrocytes to form functional clusters which later lay the template for the cartilaginous matrix[222]), in line with the higher levels of sGAG recorded in the composite mats (in particular AI), attested to the maintenance of chondrogenic phenotype of the seeded chondrocytes which was marked by the clustering of cells (**Figure 2.2 C vi** and **Figure 2.2 D vi).** This observation was also in accordance with the results observed for collagen deposition, reaffirming the significant potential of these composite scaffolds for OCD treatment.

In order to further evaluate the ECM deposition on the electrospun matrices the sections were stained with alcian blue and alizarin red to differentially stain sGAG secreted by chondrocytes, and calcium deposits by osteoblasts respectively (**Figure 2.4C i** to **vi** and **9D i to vi**). The BG mats showed mineral deposits which were stained red (**Figure 2.4C i**), and appeared well infiltrated (**Figure 2.4C iv**) within the matrix. The AA mats revealed dense alcian blue accumulation over the compact multilayer cell stacks (**Figure 2.4C iii**), with clusters indicative of chondrocyte aggregates shown in **Figure 2.4C vi**, resulting from higher aggrecan expression (backed by the gene expression results). Conversely, the cells were loosely bound on the BM mats (**Figure 2.4C ii** and **v**). Both the cell types were supported on the composite mats as indicated by the differential stain uptake, the bioactive glass side taking up an intense red coloration and the SF side taking up a dense blue coloration (**Figure 2.4D i** and **ii**). Moreover, the distinguishable presence of marker proteins OPN for bone matrix and collagen-II for cartilage matrix in the electrospun mats were probed using immunostaining (**Figure 2.4C vii** to **ix** and **2.4D vii** to **x**). OPN, one of the main non-collagenous proteins involved in apatite crystal modulation during mineralization process serves as mid-late stage osteogenic marker.[52] The BG mats showed higher expression of OPN (**Figure 2.4C vii**), in unanimity with increased ALP, runx2 and BSP expression, reiterating the BG mats' osteoconductive nature. The SF mats all showed expression of collagen-II (**Figure 2.4C viii** and **ix**), with the AA mats exhibited relatively higher levels of collagen-II in comparison to BM. Similarly, expression of collagen-II was shown in the composite mats. Collagen-II is an important ECM protein responsible in giving the cartilaginous matrix the mechanical

resilience needed during mechanical stress resistance.[216] It is important to note that collagen-II expression correlated with the results observed in collagen estimation (**Figure 2.3 Aiii**), proving the composite mats' ability to sustain matrix biosynthesis.

2.4 Salient Findings of the Chapter

In this chapter, a facile, scalable and reproducible strategy was reported for the development of electrospun bilayered composite mats for osteochondral defect repair. We utilized a layer by layer approach wherein the bioactive 70S bioactive glass sol was electrospun as the first layer followed by the silk layer. The mats exhibited a coherent, well integrated interface having two distinct phases to individually support the growth and maturation of osteogenic and chondrogenic cells (**Figure 2.4 E**). The biphasic structure was shown to provide a spatially confined biomimetic micro-milieu similar to the osteochondral interface. A systematic study of physical, mechanical and biological characteristics of the electrospun composite mats revealed that non-mulberry silk-based AI mats performed better in comparison to the mulberry silk based BI mats. The former not only exhibited better tensile properties mimicking the biomechanics encountered at the osteochondral interface, but also showed superior cell supportive characteristics. Furthermore, biochemical studies indicated enhanced ALP activity, sGAG and collagen secretion with these materials suggesting phenotypic maintenance, this was corroborated by the expression of OPN and collagen-II observed in immunostaining of the seeded osteoblasts and chondrocytes, and expression profiling of bone and cartilage associated genes in cell seeded composite mats.

Limitations of the chapter

Maturation of the cell seeded construct under dynamic culture condition is needed to circumvent the cell infiltration limitations noticed during manual seeding on these developed electrospun mats. *In vitro* experiments demonstrated that the composite materials should not induce any adverse immune response; therefore, further validation of these materials *in vivo* is of great interest, which will form the basis of a future study. In conclusion, the developed novel BG/SF composites possess great promise for osteochondral graft materials amenable for OCD repair and management.

Chapter 3

Multifunctional cell instructive silk–bioactive glass composite reinforced scaffolds towards osteoinductive, proangiogenic and resorbable bone grafts

This chapter investigates the effect of doping the 70S bioactive glass with copper to attribute proangiogenic traits to the composite. Silk fibroin and 70S bioactive glass are bioresorbable in nature. Silk microfibers were coated with copper doped 70S bioactive glass sol and the functionalised microfibers were used to reinforce silk fibroin sponges to derive cell instructive bone scaffolding platforms. These matrices dictated stem cell differentiation, matrix maturation, endothelial cell migration, homing and network formation in vitro and consequently helped in complete restoration of volumetric bone defects in rabbit femurs.

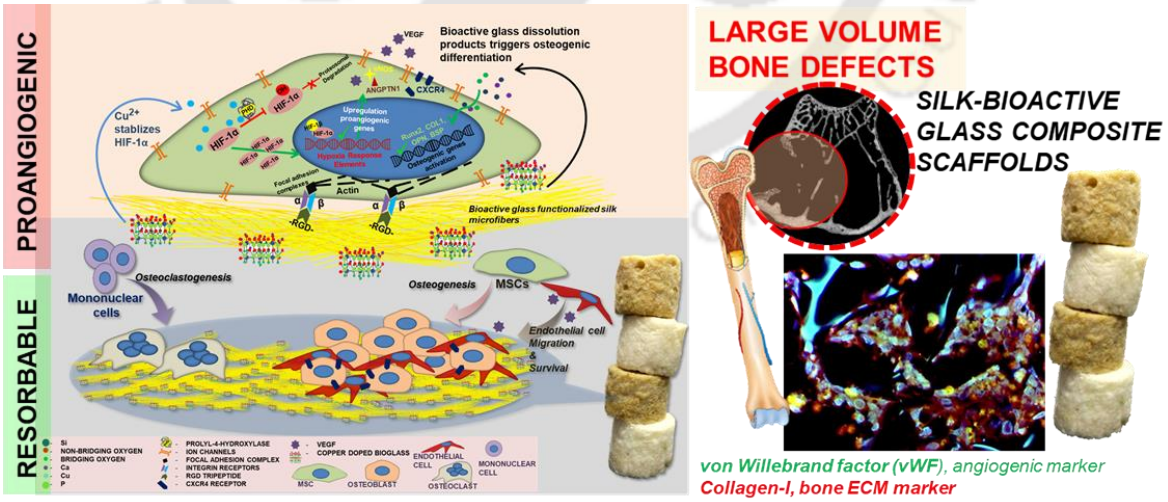

Abstract

Successful regeneration of large volume bone defects necessitates the use of proangiogenic and resorbable scaffolding matrix. Impaired and slow ingrowth of host vasculature within implanted grafts greatly compromises its effective osseointegration. Addressing this, here the use of copper doped bioactive glass functionalised silk microfiber reinforcements was demonstrated to improve the physico-chemical and osteoconductive properties of two silk scaffolding matrices (mulberry *Bombyx mor*i and non-mulberry *Antheraea assama*) employed in the investigation. The reinforced composite matrices increased the surface area and presented an open porous biomimetic micromillieu favouring stem cell and endothelial cell migration within the matrix. Biochemical results indicated the stabilisation of hypoxia-inducible factor-1α and expression of C-X-C chemokine receptor type-4 in human mesenchymal stem cells which regulated the downstream proangiogenic signalling and endothelial cell homing, respectively. Osteoinduction, matrix turnover and resorption effectiveness were favoured better in the non-mulberry silk matrices. The composite matrices significantly promoted neo-osseous tissue formation in volumetric femur defect in rabbits with periosteal restoration seen in non-mulberry silk composite matrices. Evidences of total resorption, enhanced vascular-fibrous tissue ingrowth within the scaffold, vouches for the potential clinical translation of these developed composite silk matrices.

The findings of this chapter are published in a peer reviewed journal:

Moses, J. C., Nandi, S. K., and Mandal, B. B. '*Multifunctional cell instructive silk–bioactive glass composite reinforced scaffolds toward osteoinductive, proangiogenic, and resorbable bone grafts.*' Advanced Healthcare Materials. 2018, 7(10), 1701418.

3.1 Introduction

Management of critical sized and large segmental bone defects still remains a major challenge for orthopedic clinicians, world over. With an approximated annual burden of US$ 127 billion inclusive of extended hospital outlays, there are about 1.5 million bone grafting procedures performed in USA alone. Though, autologous bone grafting still remains the benchmark for clinicians to treat large segmental bone pathological defects, donor site morbidity, pain and inadequacy of viable osseous tissue manifests to be a challenging limitation during the procedure.[276] Allografting has been to a certain extent the other clinical alternative but they encounter 30-60 % failure and 50 % mechanical strength deterioration after 10 years post-implantation.[277] Of late, to meet the huge unmet clinical demand, bone grafting procedures make use of synthetic bone grafts augmented with biological factors such as bone morphogenetic proteins (BMPs), platelet rich plasma (PRP), growth factors such as VEGF (vascular endothelial growth factors), FGFs (fibroblast growth factors) and PTH (parathyroid harmones).[44] Among them, calcium phosphate based, bioactive glass based and only limited few polymer based (bovine type-I collagen, PLGA, hyaluronic acid) grafts have been commercialized for use as bone void fillers and bone graft extenders, as identified online based on FDA 510(K) documentation.[278] Though, these synthetic grafts help in meeting the demand, they suffer from ~ 25 % failure rates and 30 – 60 % complication rates, owing to their slower osseointegration, poorer vascularization and dysregulated remodeling kinetics resulting in osteonecrosis.[279]

Bone, unlike other tissues heals via secondary or indirect bone healing process recapitulating the ontological events that occur during embryonic skeletal development, restoring the damaged tissue to its pre-injury form and structure.[44] However, in case of atrophic or hypertrophic non-unions, the critical sized defects fail to heal, where avascularity is the major contributor for the pathogenicity.[280] Vascularization plays a pivotal and integral role for both bone formation and bone remodeling orchestrating the crucial healing process.[281] Additionally, it determines the implanted graft's integration and engraftment with the host tissue. Several attempts have been strategized to promote vascularized bone regeneration, which mostly involve the use of angiogenic growth factors eluting scaffolds [279] to enable the migration of surrounding endothelial cells to facilitate neovascularization and anastomosis. The eluting efficiency of these scaffolding matrices depends on the fabrication approaches which suffer from drawbacks relating to poor release kinetics and stability of the incorporated growth factors.

Cell instructive biomaterial platforms exhibiting synergistic effect by the virtue of their physical and chemical cues that could enable better cell adhesion, enhance stem cell differentiation and migration are bringing about a paradigm shift in the domain of smart biomaterials,[282] postulating the notions for developmental reengineering. The development of such scaffolding matrices, which could closely mimic the bone's extracellular milieu and capable of osteoinduction, help in homing of stem cells and endothelial cell lineages remains prospective. The choice of biomaterials here plays a critical role; use of bioresorbable, bioactive, osteoinductive ingredients becomes an obvious discretion. Composites have proven to be viable bone graft alternatives than only polymer or only ceramic based scaffolding matrices. Though, calcium phosphate based ceramics are widely explored due to their stoichiometric similarity to bone's apatite, it suffers from drawbacks such as poor resorbability and has very low solubility product (K_{sp}) of 5.01 x 10^{-15} to 2.35 x 10^{-59}. [31] In this regard, sol-gel derived bioactive glass ceramics have carved a niche of their own, owing to their controllable resorbable rates, high surface area and superior bioactivity processing flexibility.[283, 284] Among the various polymers explored over the years, silk fibroin (SF) a unique class of biocompatible, natural polymer which has been in the prime focus in biomedical research owing to its tuneable biodegradability, low immunogenicity and processing feasibility.[285, 286] Moreover, tensile strength of SF (mulberry and non-mulberry silk) range between 0.3 To 0.6 GPa [200] which are far more superior than the rat tail collagen 0.9-7.4 MPa,[201] a commonly employed polymer in bone scaffolding matrices.

Hypothesis underpinning the Objective:

Consequently, the purpose of this chapter was to develop cell instructive, biomimetic, resorbable composite scaffolding matrices, capable of stimulating cellular processes pertaining to osteogenesis and angiogenesis. To achieve this, sol-gel derived copper doped 70S bioactive glass ($70SiO_2.22CaO.5P_2O_5.3CuO$) was chosen, to functionalize silk microfibers and exploit them as reinforcements to augment the mechanical properties of silk fibroin matrices. The incorporation of Cu^{2+} in sol derived bioactive glass is postulated to stabilize nuclear HIF-1α resulting in upregulation of angiogenic specific markers, in addition to its well documented antibacterial properties.[287] Two different silks were chosen, mulberry (*Bombyx mori*) and endemic North-East Indian non-mulberry (*Antheraea assama*) varieties to fabricate the SF matrices. These two silk varieties remarkably differ in their amino acid compositions and hence exhibit unique traits distinguishable from each other [232, 288]. Moreover, *A. assama* silk has been reported to possess inherently cell binding Arg-Gly-Asp (RGD) motifs, conferring better cell supportiveness than its mulberry counterpart. [119, 228]

The developed composite scaffolds were physico-chemically characterized. Furthermore, the scaffolds' ability to induct osteogenic differentiation of human mesenchymal stem cells (hMSCs), support angiogenesis and enable resorption was investigated holistically under *in vitro* culture. Subsequently, these matrices were clinically validated in rabbits by creating critical sized defects and studying the cortical bone regeneration.

3.2 Materials and Methods

3.2.1 Fabrication of Scaffolds

3.2.1.1 *Preparation of Degummed Silk Microfibers and Silk Fibroin Solution*

Bombyx mori and *Antheraea assama* cocoons were sourced from local silk farms and they were processed based on previously published protocols.[119, 288] Briefly the cocoons were cut into small pieces and degummed in boiling 0.02 M Na_2CO_3 (Merck, India) and the obtained silk fibers were thoroughly washed with distilled water. The microfibers were obtained based on our previously published protocol [119] by manual comminution of the dried silk fibers. Thus, obtained microfibers had a heterogeneous size distribution 500-2500 μm in length as observed by bright field microscope, were further used as reinforcements, either unmodified or surface modified with bioactive glass.

For regeneration of mulberry silk fibroin, the dried degummed *B. mori* fibers were dissolved in 9.3 M LiBr (Sigma-Aldrich) [289] and subsequently dialyzed extensively against distilled water using a 12 kDa molecular weight cut-off dialysis membrane (Sigma-Aldrich) for 48 hours. The obtained aqueous regenerated *B. mori* silk fibroin solution was further used for scaffold fabrication. The non-mulberry silk fibroin solution was obtained from the silk glands of mature fifth instar *A. assama* silkworms obtained from local silk farms following our previously published protocol.[230] The glandular protein was squeezed out of the anterior-posterior glands and dissolved in 1% sodium dodecyl sulphate (SDS) (Himedia, India), followed by extensive dialysis against distilled water at 4 °C using a 12 kDa cutoff dialysis membrane. The obtained aqueous regenerated *A. assama* silk fibroin solution was further used for scaffold fabrication.

3.2.1.2 *Synthesis of Copper Doped 70S Bioactive Glass and Modification of Silk Microfibers*

The bioactive glass sol was obtained following our previously published protocol [288], with some modifications to incorporate copper substitutions in the glass network. Briefly, tetraethyl-orthosilicate (TEOS) (Sigma-Aldrich) was hydrolysed in aqueous solvent system with HCl (Merck, India) as the catalyst in the molar ratio of 1:8:0.01 TEOS/water/HCl. After hydrolysis calcium nitrate tetrahydrate (Sigma-Aldrich), copper (II) nitrate trihydrate

(Himedia, India) and triethylphosphate (Sigma-Aldrich) were added sequentially to attain a molar ratio of 70:22:5:3 of SiO_2:CaO:P_2O_5:CuO and stirred for 24 hours at ambient conditions. The sol was further aged at 40 °C for 48 hours which was used further for modifying the silk microfibers. 40 mg of silk microfibers were packed in cylindrical Teflon® moulds (10 mm in diameter) by gently tapping the fibers till it attained a height of 10 mm. This aspect ratio of packing was maintained to maintain uniformity throughout the fabrication process. The aged sol was poured over the packed fiber column (for 40 mg of fiber, 400 µL of sol was added) and centrifuged at 3000 x g for 5 minutes to ensure the sol coats the entire packed column. The moulds were kept in 60 °C for 24 hours to further age the sol and form the bioactive glass nano-coating over the microfibers.

3.2.1.3 *Fabrication of Copper Doped Bioactive Glass Modified Silk Fibers Reinforced Composite Scaffolds*

2 % (w/v) aqueous regenerated silk fibroin was added over the bioactive glass modified silk microfiber column. For every 10 mm height, one mL of silk fibroin solution was added (a ratio of 1:2 (w/w) silk fibroin/silk fiber was maintained) and frozen at -20 °C. The frozen constructs were freeze dried in lyophilizer (Alpha 1–4 LD plus, Martin Christ, Germany) for 36 hours. The lyophilized constructs were treated with sequentially with absolute ethanol for 1 hour and followed by 80 % (v/v) ethanol for 4 hours to confer insolubility within the silk matrices through β-sheet induction and to confer glass stabilization. The composition of the scaffolds used in the current study is listed in **Table 3.1** and **Figure 3.1** presents the general schema for fabrication of the composite fiber reinforced scaffolds. The unmodified silk fiber reinforced silk fibroin scaffolds and silk fibroin scaffolds without reinforcements were used as control groups, whereas the composite scaffolds BMG and AAG served as the experimental groups.

Table 3.1. *Composition of the silk scaffolds*

Scaffold	Silk Fibroin Solution	Silk Microfibers	Scaffolding Nature
BMS	2 % (w/v) *B. mori*		Pure silk matrices without reinforcements
AAS	2 % (w/v) *A. assama*		
BMF	2 % (w/v) *B. mori*	*B. mori fibers*	Bicomposite silk matrices reinforced with unmodified silk microfibers
AAF	2 % (w/v) *A. assama*	*A. assama fibers*	

BMG	2 % (w/v) *B. mori*	Modified *B. mori fibers*	Tricomposite silk matrices reinforced with bioactive glass functionalized silk microfibers
AAG	2 % (w/v) *A. assama*	Modified *A. assama fibers*	

3.2.2. Physico-chemical Characterizations

Electron Microscopy

The microarchitecture and surface morphology of the fabricated scaffolds were examined using a field emission scanning electron microscope (FESEM) (∑IGMA, Carl Zeiss, Germany) equipped with energy dispersive X-ray analysis (LEO 1430VP®, Oxford Instruments, UK). The acquired images were analysed using Image-J (Wayne Rasband, National Institute of Health (NIH), USA) for determining the average pore size. The elemental analysis of surface modified silk microfibers was acquired for Si, Ca, P and Cu using Oxford INCA software at a working distance of 8 to 18 mm with working voltage of 15 to 20 kV. The nanogranular bioactive glass particles were examined using a transmission electron microscope (TEM) (JEM 2100, JEOL, Japan) and the selected area electron diffraction (SAED) patterns were recorded to determine its crystallinity.

Fourier Transform Infrared Spectroscopy (FTIR)

The infrared spectra of the all fabricated scaffolds were recorded in the range 400 – 4000 cm^{-1} using Nicolet iS10, Thermo Smart Omni-Transmission spectrometer (Thermo Scientific™ USA) at a scanning speed of 15 scans per second with resolution 2 cm^{-1}. Samples were prepared by making KBr pellets by mixing 2 mg of sample with 100 mg of KBr (Spectroscopy grade, Himedia, India) and pressed in a hydraulic press to form the pellet at 25 °C, which was used for analysis.

Mechanical Testing

Unconfined uniaxial compressive mechanical testing of scaffolds was carried out using a Universal Testing Machine (UTM, Instron 5944, USA) fitted with 100 N load cell under hydrated conditions in phosphate buffered saline (PBS) at 37 °C in a BioPuls bath (Instron, USA). For determining the compressive strength of the formed scaffolds, scaffolds were subjected to testing pertaining to ASTM standard D1621-04a (standard test method for compressive properties of rigid cellular plastics). Briefly, scaffolds were cut in dimensions (10 mm height and 10 mm diameter, n = 6) with a crosshead speed of 1 mm/minute and the crosshead displacement and corresponding load values are recorded till 65 % deformation is

attained. The corresponding stress-strain curves are plotted and compressive strength, compressive modulus (tangential slope of the linear region of the effective stress–strain curves) were determined. Cyclic testing of the cylindrical specimens was carried out for 15 cycles corresponding to 50 % deformation strain at a loading and unloading rate of 5 mm/minute. The Young's modulus was calculated for each loop and since the unconfined testing revealed the mechanical properties of the specimen were uniform, only three specimens of each type were tested under cyclic loading.

Scaffold Porosity and Density Measurement

The porosity of the scaffolds was determined using displacement method following a previously published protocol with modifications.[290] Briefly, the dry weight of scaffolds (W) were measured and then immersed in graduated cylinder with known volume (V_1) of hexane. In order to achieve completing of the pores, series of quick evacuation and repressurization was carried out until no further air bubble was noticed. The total volume of the hexane was recorded as V_2 post addition of the scaffold. The volume difference ($V_2 – V_1$) gives the volume of the skeleton of the scaffolds. The hexane impregnated scaffolds were removed from the graduated cylinder and the residual volume of hexane is recorded as V_3, whereas ($V_1 – V_3$) gives the volume of hexane entrapped within the pores. The total volume of the scaffold was represented as, $V = (V_2 – V_1) + (V_1 – V_3) = (V_2 – V_3)$. The density of the scaffolds was denoted as, $\rho = W / (V_2 – V_3)$. The porosity (in percentage) of the scaffolds was given as, $\varepsilon = [(V_1 – V_3) / (V_2 – V_3)] \times 100$.

3.2.3 *In vitro* Bioactivity Assessment

The *in vitro* bioactivity of the fabricated scaffolds was assessed using a protocol adopted by Kokubo *et al* [205]. Briefly, simulated body fluid (SBF), pH 7.4 and temperature 37 °C was prepared in distilled water strictly following the recipe as reported previously. The scaffolds (10 mm height and 10 mm diameter) were soaked in freshly prepared SBF at 37 °C for 14 days. The samples were retrieved and washed in deionised water and benignly dried for further examination. The dried samples' surfaces were studied using rotating anode-based powder X-ray diffractometer (Rigaku TTRAX III, Japan) using Cu K_α line (λ = 1.541 Å) radiation source (operated at 50 kV/ 100 mA) to study the apatite crystal formation on the scaffolds. Diffraction patterns were collected from 5° to 50° (2θ angles), with a step size of 0.03° and time per step of 0.5 s was used.

3.2.4 *In vitro* Degradation and Copper Release Studies

The *in vitro* degradation of the scaffolds was evaluated by monitoring the percentage of weight loss in phosphate buffered saline (PBS), pH 7.4 at 37 °C for a period of 21 days. Also enzymatic degradation of scaffolds was evaluated in presence of 2 U/mL protease XIV (Sigma-Aldrich, with specific activity ≥3.5 U/mg; isolated form *Streptomyces griseus*) in PBS, pH 7.4 at 37 °C for 21 days, based on previously published protocol.[119] Briefly the scaffolds were immersed in either PBS or in enzyme solution and at regular intervals the scaffolds were retrieved, washed with deionised water, dried and mass remaining was recorded over time for 21 days. The mass remaining percentage was calculated as, % weight remaining = (weight at time 't'/ initial weight) x 100. The buffers were changed every three days in between intervals and they were stored at 4 °C to estimate the amount of copper released over the course of the study. The copper metal leached out from the degrading composite BMG and AAG scaffolds were determined using an atomic absorption spectrometer (Varian AA240, The Netherlands) at a wavelength of λ = 217.9 nm and slit width of 0.2 nm, as per the protocols set up by the American Public Health Association (APHA).[291]

3.2.5 *In vitro* Biological Studies

Human adipose derived stem cells (hMSCs) were procured as frozen vials (passage 2) from Ansa Pvt. Ltd. (Cellspace research foundation) Bangalore, India. The hMSCs were expanded in expansion media, HiPer® high glucose Dulbecco's modified media (Himedia, India), supplemented with 10 % (v/v) foetal bovine serum (Gibco, USA), 2 ng/mL basic fibroblast growth factor (bFGF) (Sigma-Aldrich), 2 mM L-glutamine (Gibco, USA) and 1X antibiotic-antimycotic mixture (Gibco, USA; penicillin 10 units/mL, streptomycin and amphotericin B 0.25 µg/mL). The hMSCs were used within passage 6 for seeding and assessing the osteogenic potential of the fabricated scaffolds. Human monocyte cell line (THP-1) were procured from NCCS Pune, India and maintained in RPMI-1640 media supplemented with 10 % (v/v) foetal bovine serum and 1X antibiotic-antimycotic mixture, as suspension culture. Murine macrophage cell line (RAW 264.7) were also procured from NCCS Pune, India and maintained in high glucose Dulbecco's modified Eagle media (DMEM) (Gibco, USA) supplemented with 10 % (v/v) foetal bovine serum and 1X antibiotic-antimycotic mixture. For isolation of primary endothelial cells (pECs) we followed our previously published protocol [232]. Briefly, a small segment of the descending aorta was obtained from a local slaughter house and placed in ice cold sterile PBS (pH 7.4). Roughly 1 cm long aortic tube was cut open and placed in a Petridish containing 0.1 % (w/v) type I-A collagenase (Sigma-Aldrich, ≥ /125

CDU mg) for 20 minutes and the inner luminal endothelial cells were scrapped off using a sterile cell scrapper. The cell suspension was centrifuged at 1050 rpm for 5 minutes and subsequently washed with high glucose DMEM twice and maintained in high glucose DMEM supplemented with 5 % (v/v) foetal bovine serum, 100 µg/ mL endothelial cell growth supplement from bovine neural tissue (Sigma-Aldrich) and 1X antibiotic-antimycotic mix. The endothelial cells thus expanded were utilized within passage-3 for seeding and assessing the angiogenic potential of the fabricated scaffolds. The scaffolds were cut in dimensions (6 mm diameter x 2 mm thickness), sterilized by autoclaving in hydrated conditions and further used for cell culture studies. The scaffolds prior to cell seeding were conditioned in growth media overnight and subsequently used for the *in vitro* biological studies.

3.2.5.1 Osteogenic Differentiation Potential Assessment Using hMSCs

The conditioned scaffolds were statically loaded with 3×10^5 hMSCs suspended in 30 µL of expansion media per scaffold and the cell seeded scaffolds were placed in incubator (37 °C in a humid atmosphere with 5 % CO_2) for 4 hours to allow cell adhesion on the scaffolds after which the cell seeded constructs were flooded with hMSCs expansion media. After 24 hours post seeding the expansion media was replaced with osteogenic induction media (HiPer® high glucose Dulbecco's modified media supplemented with 10 % (v/v) foetal bovine serum, 10 mM β-glycerophosphate (Sigma-Aldrich), 100 nM dexamethasone (Sigma-Aldrich) and 0.2 mM ascorbic acid (Sigma-Aldrich). The osteogenic media was changed every 48 hours till 14 days.

Cell Proliferation, Cell Cycle and Viability Assessment

For evaluating the cell proliferation, Alamar blue dye (Invitrogen, USA) reduction assay was used, following the manufacturer's protocol at regular intervals. Briefly, the cell seeded scaffolds were incubated with 10 % (v/v) of the dye and incubated for 3 hours. After incubation, 100 µL of the culture media was read using a microplate reader (Tecan Infinite Pro, Switzerland) at 570/600 nm. The results are presented as the normalized value of the dye reduced, which is proportional to the number of viable cells present in the scaffolds. The viable cells within the scaffolds after 7 days were imaged using calcein-AM (Sigma-Aldrich). The cell seeded matrices were washed with PBS and incubated with PBS with 40 nM calcein-AM for 15 minutes. The dye solution was removed washed with PBS twice and cell seeded scaffolds were imaged using a fluorescent microscope (EVOS XL digital microscope, Thermo Fisher Scientific, USA) with live viable cells appearing green.

Biochemical Analysis

Alkaline Phosphatase Assay

Alkaline phosphatase (ALP) activity was assessed to determine the osteogenic differentiation fate of the seeded hMSCs using an alkaline phosphatase assay kit (Abcam, UK) following the manufacturer's protocol. At day-1, 7 and 14 the cell laden scaffolds were lysed using cell lysis buffer (20 mM Tris-HCl (Merck, India) (pH 7.5), 150 mM NaCl (Himedia, India), 5 mM $MgCl_2$ (Himedia, India), and 0.5% Triton-X100 (Sigma-Aldrich) and the cell lysate was used for membrane bound ALP estimation. Similarly, the spent cell culture media was also used for soluble ALP estimation. The ALP activity obtained as U/ mL was normalized with the total DNA content for both the membrane bound and soluble ALP and represented as U/ µg DNA.

Total Collagen Estimation

To determine the amount of collagen secreted by the hMSCs osteogenically committed on the scaffolds was estimated following a previously published protocol [288], using sirius red based colorimetric assay with rat tail collagen (Sigma-Aldrich) (0−250 µg/mL) as standard. Briefly, the cell laden scaffolds at day 1, 7 and 14 were digested in pepsin digestion buffer (0.1 M acetic acid, 0.5 M NaCl and 1 mg/mL pepsin (Sigma-Aldrich). 100 µL of the digesate from each sample was allowed to dry in 96 well plate at 37 °C overnight and treated with 100 µL of 1 mg/mL direct red 80 (Sigma-Aldrich) saturated with picric acid for 1 hour. The dye solution is removed washed with 0.01 N HCl and the samples are resolved using 100 µL 0.1 N NaOH and the absorbance were recorded using microplate reader at 550 nm. The amount of collagen determined is normalised with the amount of total DNA content and the data is presented as µg collagen/ µg DNA.

Western Blot Analysis

Immunoblots were performed to detect the expression of hypoxia inducible factor 1α (HIF-1α) on the protein level. Cell laden scaffolds were lysed using lysis buffer (50 mM Tris, pH 8, 150 mM NaCl, 1 % NP-40 (Sigma-Aldrich), 1 mM ethylene glycol-bis(2-aminoethylether)-N,N,N′,N′-tetraacetic acid (Sigma-Aldrich). The protein lysates were centrifuged and protein concentration was estimated using Bradford's reagent (Sigma-Aldrich). 50 µg of total protein per sample were loaded per lane and resolved through SDS-polyacrylamide gel electrophoresis in 10 % separating gel. The resolved proteins were electroblotted on to poly(vinylidene fluoride) (PVDF) membranes (Sigma-Aldrich) and

blocked for 1 hour using 5 % (w/v) bovine serum albumin (Himedia, India) in tris buffered saline (TBST) (0.02 M Tris, 0.9 % (w/v) NaCl, 0.05 % (v/v) Tween-20 (Sigma-Aldrich). The membranes were washed with TBST and incubated with primary mouse monoclonal antibody against human HIF-1α (Abcam, UK; 1:200 dilutions) at 4 °C overnight. The expression of HIF-1α was studied relative to GAPDH which was used as loading control (mouse monoclonal against human GAPDH, (Abcam, UK, 1:1000 dilutions). The blots were washed and incubated with horse radish peroxidase tagged secondary goat anti-mouse IgG (Abcam, UK, 1:10000 dilutions) for 1 hour. After a brief washing step, the blots were visualized using enhanced chemiluminescence method (Clarity™ Western ECL Kit, Bio-rad laboratories, USA) through a gel documentation system (Gel Doc XR+ system, Bio-rad laboratories, USA) and the densiometric analyses were carried out using Image-J software (NIH, USA).

Gene Expression Studies

For assessing the expression of osteogenic markers of the committed hMSCs, the relative gene expression of human runt-related transcription factor-2 (*RUNX2*), human bone sialoprotein (*BSP*) and human osteocalcin (*OCN*) was calculated with reference to the house keeping gene human glyceraldehyde 3-phosphate dehydrogenase (*GAPDH*) (listed in **Table 3.2)**. Total RNA content was isolated using TRI reagent (Sigma-Aldrich). One microgram of RNA was reverse transcribed using high capacity reverse transcription kit (Applied Biosystems, Invitrogen, USA) in a thermal cycler machine (Applied Biosystems Veriti, Thermo Fisher Scientific, USA). The expression level of genes was quantified using Power SYBR PCR master mix (Applied Biosystems, Invitrogen, USA) in a real-time PCR machine (Applied Biosystems 7500, Thermo Fisher Scientific, USA).

Histological Assessment and Immunostaining

The cell laden scaffolds after 14 days were fixed using neutral buffered formalin (Sigma-Aldrich). The fixed constructs were then put through to ethanol-xylene dehydration-clarification procedure and embedded in paraffin wax (Merck, India) and further sectioned using a manual microtome (Leica Biosystems, Germany) to get 10 μm sections. The slices were stained with hematoxylin and eosin (Sigma-Aldrich, USA) to assess the cell distribution within the scaffolds. For immunostaining, the sections were blocked with 5 % BSA in PBS for 1 hour, followed by incubation by primary rabbit polyclonal antibody against osteopontin (OPN) (1:1000 dilutions) (Abcam, UK) for 1 hour and finally with FITC conjugated secondary goat anti-rabbit antibody IgG (Abcam, UK, 1:2000 dilutions) for 1 hour. The sections were counterstained with 1 μg/mL Hoechst-33342 (Sigma-Aldrich, USA) and mounted. The stained

sections were visualized using a fluorescent microscope (EVOS XL digital microscope) and represented images are presented.

3.2.5.2 Induction of Osteoclastogenesis and Investigation of Remodelling Effectiveness of the Osteoclast Seeded Scaffolds

Human monocytes (THP1) were differentiated on scaffolds following a previously published protocol with modifications.[292] 5×10^5 cells were suspended in 30 µL of osteoclast differentiation media (RPMI media supplemented with 10 % (v/v) foetal bovine serum, 25 ng/mL recombinant human soluble receptor activator nuclear factor-κB ligand - sRANKL (Gibco, USA), 200 ng/mL PMA (phorbol 12-myristate 13-acetate) and seeded per scaffold. The cell seeded scaffolds were placed in incubator (37 °C in a humid atmosphere with 5 % CO_2) for 6 hours to allow cell adhesion on the scaffolds after which the cell seeded constructs were flooded with osteoclast differentiation media. The differentiation media was changed every 48 hours till 14 days.

Tartarate Resistant Acid Phosphatase (TRAP) Staining

Histological sections of cell laden scaffolds after 14 days in culture were taken and histochemical staining for TRAP was performed using leucocyte acid phosphatase (TRAP) assay kit (Sigma-Aldrich, USA) following the manufacturer's protocol. The activated osteoclasts exhibit acid phosphatase activity which appears purplish to dark granules in the cytoplasm and the images were taken using EVOS XL digital microscope.

Gelatin Zymography

The conditioned media from the cell seeded constructs were used to analyse the MMP-9 activity by using gelatin substrate gel electrophoresis following a previously published protocol.[293] Briefly the serum starved cell culture media were resolved in unreducing condition in 10 % (w/w) polyacrylamide gel with 0.1 % (w/w) gelatin (Merck, India). The resolved gel was incubated in incubation buffer [50 mM Tris-HCl, pH 7.5, 1 % (w/v) triton X-100 (Sigma-Aldrich), 5 mM $CaCl_2$ (Sigma-Aldrich) and 1 mM $ZnC_4H_6O_4$ (Sigma-Aldrich)] overnight at 37 °C. The gels were stained with 0.5 % (w/v) Coomassie Brilliant Blue R-250 (Himedia, India). The gelatinolytic activity was visualized using a gel documentation system and the densiometric analyses were carried out using Image-J software (NIH, USA).

Gene Expression Studies

The expression of osteoclast specific markers as a material response by the osteoclast laden matrices was examined by real time PCR. The relative gene expression of human

cathepsin-K (*CTSK*), human carbonic anhydrase II (*CA II*) and human nuclear factor of activated T cells (*NFATc*) was calculated with reference to the house keeping gene human *GAPDH* (listed in **Table 3.2**).

3.2.5.3 Assessing the *in vitro* Angiogenic Potential of the Scaffolds

The conditioned scaffolds were statistically seeded with 3 x 10^5 hMSCs per scaffold and cultured for 7 days in osteogenic differentiation media with media change every 48 hours. At day-7, 10^6 pECs were seeded on to the osteogenically primed hMSCs laden scaffolds. Briefly, 10^6 pECs cells were suspended in 30 µL endothelial cell culture media and seeded on to scaffolds and after 5 hours the osteogenic media were flooded and the coculture was continued till 14 days in osteogenic differentiation media with media change every 48 hours.

Gene Expression Studies

The expression of angiogenic and osteogenic markers were assessed in response to the material was assessed using real time PCR. The relative gene expression of osteogenic genes [human *RUNX2* and human podoplanin (*PDPN*)] and angiogenic genes [porcine angiopoietin 1 (*ANGPTN1*) and porcine endothelial nitric oxide synthase (*eNOS*)] was calculated with reference to the house keeping gene human *GAPDH* and porcine *GAPDH* (listed in **Table 3.2**).

Table 3.2 *Primer sequences of different genes used for gene expression studies*

Gene	Sequence	Accession Number
Human *GAPDH*	**F** 5′-GACCTGACCTGCCGTCTA-3′	NM_001289746.1
	R 5′-GTTGCTGTAGCCAAATTCGTT-3′	
Human *BSP*	**F** 5′AACCTACAACCCCACCACAA-3′	NM_004967.3
	R 5′-GTTCCCCGTTCTCACTTTCA-3′	
Human *RUNX2*	**F** 5′-GATGGGACTGTGGTTACTGTCA-3′	NM_001278478.1
	R 5′-CTCAGATCGTTGAACCTTGC-3′	
Human *OCN*	**F** 5′- CAGCGAGGTAGTGAAGAGAC -3′	NM_199173.5
	R 5′- GCCAACTCGTCACAGTCC -3′	
Human *CTSK*	**F** 5′- CAGTGAAGAGGTGGTTCAGA-3′	NM_000396.3
	R 5′- CAGTGAAGAGGTGGTTCAGA-3′	
Human *CA II*	**F** 5′- CTGAAGCCCCTGTCTGTTTC-3′	NM_000067.2
	R 5′- TCCATCAAGTGAACCCCAGT-3′	
Human *NFATc*	**F** 5′- AGAATTCGGCTTGCACAGG-3′	NM_001278675.1

	R 5′- CTCTGGTGGAGAAGCAGAGC-3′	
Human *PDPN*	**F** 5′- TTACTAGCCATCGGCTTCATTG-3′	NM_006474
	R 5′- GGCGAGTACCTTCCCGACAT-3′	
Porcine *GAPDH*	**F** 5′-TCGGAGTGAACGGATTTGG-3′	NM_001206359.1
	R 5′-CCAGAGTTAAAAGCAGCCCT-3′	
Porcine *ANGPTN1*	**F** 5′- CTTCCTCGCTGCCATTCTGA-3′	NM_213959.1
	R 5′- GACAGTTCCCGTCGTGTTCT-3′	
Porcine *eNOS*	**F** 5′- TTCCGGGGATTCTGGCAGGAG-3′	NM_214295.1
	R 5′- GCCATGGTGACGTCGCCGCAG-3′	

Flow Cytometric Analysis

Single cell suspensions from cell laden scaffolds were isolated by trypsinization and the cell suspension were strained using a sterile 40 μm cell strainer. The single cell suspension thus harvested was studied for the expression of angiogenic markers CXCR4 [receptor for the C-X-C chemokine CXCL12/SDF-1 and CD-31 (PECAM-1)] through indirect flow cytometry analysis. The cells were labelled with primary antibody [either rabbit polyclonal CXCR4 (1:2000 dilutions) or mouse monoclonal to CD31 (1:2000 dilutions)] (Abcam, UK) at room temperature for 30 minutes. Thus, primary antibody labelled cells were stained with FITC conjugated secondary antibody [goat anti-rabbit IgG (1:2500 dilutions; Abcam, UK) or goat anti-mouse IgG (1:100; Sigma-Aldrich) respectively] and incubated in room temperature for 30 minutes. The primary body unlabelled cells but labelled with secondary FITC conjugated IgG were used as control. Thus, labelled cells were analysed using BD Accuri™ C6 Plus flow cytometer (Becton Dickinson Biosciences, USA).

Western Blot Analysis

Immunoblots were performed to detect the expression of CD-31 (PECAM-1) (mouse monoclonal against porcine CD31; Abcam, UK; 1:200 dilutions). The expression of CD-31 was studied relative to GAPDH which was used as loading control (mouse monoclonal against porcine GAPDH, (Abcam, UK, 1:1000 dilutions). The blots were visualized using enhanced chemiluminescence method (Clarity™ Western ECL Kit, Bio-rad laboratories, USA) through a gel documentation system (Gel Doc XR+ system, Bio-rad laboratories, USA) and the densiometric analyses were carried out using Image-J software (NIH, USA).

Immunohistochemistry

The cell laden constructs were processed for histological assessment and immunostaining of 10 μm sections were performed to check the expression of angiogenic marker protein Von Willebrand factor (vWF) (primary rabbit polyclonal against porcine vWF, Abcam, UK; 1:400 dilutions) in relation to the osteogenic marker protein collagen-I (primary mouse monoclonal to human collagen-I, Abcam, UK; 1:1000 dilutions). To visualize the sections, DyLight®594 conjugated secondary goat anti-rabbit (Abcam, UK, 1:500 dilutions) and FITC conjugated secondary goat anti-mouse (Sigma-Aldrich, USA, 1:200 dilutions), respectively. The stained sections were visualized using a fluorescent microscope (EVOS XL Digital) and representative images are presented.

3.2.5.4 *In vitro* Immunocompatablity Assessment

To assess the *in vitro* immune response elicited by the scaffolds, murine macrophages (RAW 264.7) were used and the tumour necrosis factor - TNF-α secreted by the macrophages was quantified using an ELISA kit following the manufacturer's protocol (Invitrogen, USA). Briefly, 10^5 cells were seeded per well in 24 well plates and after 24 hours sterile scaffolds were placed on the seeded wells. The spent media after 24 hours were collected and assayed for the TNF-α release. 500 ng of lipopolysaccharides (LPS) from *Escherichia coli* (Sigma-Aldrich) served as positive control whereas tissue culture plate without any samples served as negative control.

3.2.6 *In vivo* Animal Studies

In order to assess the bone forming ability of the developed composite scaffolds, volumetric bilateral defects (4 mm in diameter and 2 mm in depth) were created at the distal epiphyseal region of femurs in white New Zealand rabbits, which served as the experimental model for the study. The protocols for animal handling and treatment were reviewed and approved by the Institutional Animal Ethical Committee (IAEC), West Bengal University of Animal and Fishery Sciences (WBUAFS), West Bengal, India (Approval No. Pharma/IAEC/166 dated 01.12.2015). Thirty healthy rabbits of either genders weighing 1.8 kg were randomized and divided into 5 groups (six rabbits per group with bilateral surgery i.e. six samples for each time point); one non-treatment group, two control groups (BMF and AAF) and two experimental groups (BMG and AAG). Prior to surgery, the rabbits were anesthetized by administering 5 mg/kg body weight xylazine hydrochloride (Xylaxin®, Indian Immunologicals, India) and 25 mg/kg body weight ketamine hydrochloride (Ketalar®, Parke-Davis, India), intramuscularly. The defects were created using a trephine dental drill and the

scaffolds were press fitted and secured by suturing the muscle, subcutaneous tissue and skin by layers. After 1- and 3-months post-surgery, the animals were euthanized and the femurs were removed from all the groups and fixed in 10 % formalin for 7 days. The tissues were decalcified and histological assessments were made. The ingrowth of osseous tissue was assessed by hematoxylin and eosin stain (H&E), Masson's trichrome staining (Sigma-Aldrich) and the extent of remodelling was assessed using TRAP staining. The stained images were visualized using a bright field microscope and the representative images are presented.

For fluorochrome (oxytetracycline dehydrate, Pfizer, India) was injected at a dosage of 25 mg/ kg body weight in 2-6-2 pattern i.e. one dose for consecutive two days and again two doses after a gap of six days and just before the sacrifice time point of 1 and 3 months. Undecalcified implanted bones were made slice of 20 mm size. Bone slices were observed under UV light with Leica DM 2000 Bright light phase contrast and fluorescence microscope. The newly formed bone fluoresced with a golden yellow colour, whereas old/host bone had a sea green hue.

3.2.7 Statistical Analysis

All the in vitro experiments were carried out in triplicates unless otherwise mentioned and the data is presented as mean ± standard derivation. The data attained between the sampling groups were analysed using one-way analysis of variance (ANOVA) by performing Tukey's test using Origin Pro-8 software (OriginLab, USA), with *$p \leq 0.05$ considered as statistically significant and **$p \leq 0.01$ as highly significant.

3.3. Results and Discussion

Decades of research in the area of bone tissue engineering has culminated in the quest for formidable yet resorbable matrices, using bioactive materials. In this regard, silk fibroin as a biopolymer has shown immense potential for bone graft applications which has been documented well in both *in vitro* and *in vivo* animal studies.[52, 285] Use of different reinforcements [294, 295] in silk matrices have been explored with the sole aim to improve mechanical performance of these silk matrices. To this end, we have explored the use of alkali hydrolysed *B. mori* silk microfibers (100 – 500 μm sized) to reinforce *B. mori* silk scaffolds [201] and use of chopped *A. assama* (0.5 – 2.5 mm sized) silk microfibers to reinforce *A. assama* scaffolds [119] to improve the mechanical properties of the silk matrices. However, an ideal bone graft does not just merely serve the purpose of providing a mechanical support but should also be able to support osteogenic cells, be amenable for remodelling and enable vascularization. Although, silk is only among the few biopolymers, which has been documented to be inherently osteoconductive similar to collagen-I but lacks the potential to induce osteogenesis.[52]

The rationale of the current study is to develop hierarchical scaffolding matrices that could modulate regulatory cellular signalling pathways, by the virtue of their topological and chemical cues and performing macro-scale functions in a synchronised manner. To address these, we resorted to functionalise silk-microfibers (both *B. mori* (BM) and *A. assama* (AA)) by a facile sol-gel coating technique using copper doped 70S bioactive glass sol (**Figure 3.1A**). The functionalised microfibers were used as reinforcements to augment the mechanical properties of the silk fibroin (SF) matrices fabricated through freeze drying. The gross morphology of the SF scaffolds is depicted in **Figure 3.1A,** representing the three groups of scaffolds (**Table 3.1**) used in the study *viz* (i) pure SF matrices without reinforcements (BMS, AAS), (ii) SF matrices reinforced with unmodified silk microfibers (BMF, AAF) and (iii) composite SF matrices reinforced with functionalized silk microfibers (BMG, AAG). The first two groups served as control groups and the third group was the experimental group, in order to delineate the effects of fiber reinforcement and functionalization on the cellular fate.

3.3.1 *Bioactive Glass Functionalization Improves Surface Properties of the Silk Microfibers*

FESEM micrographs (**Figure 3.1B**) revealed that both the silk microfibers had different fiber morphologies. BM silk microfibers appeared to have smooth and circular cross-section with an average diameter of 9.77 ± 0.25 μm (**Figure 3.1B i**) whereas AA silk microfibers appeared to be smooth, flattened and ribbon like (**Figure 3.1B iv**) with an average thickness of

3.26 ± 0.25 μm. Mesenchymal stem cells are sensitive to surface chemistry and surface roughness, which is found to control their cellular fate. Hence, improving the surface properties of any biomaterial becomes imperative. The facile sol-gel coating strategy adopted to modify the silk fibers, resulted in uniform and fine distribution of copper doped bioactive nano-granules over the silk microfibers. The bioactive glass granules were stabilized through an alternate ethanol based stabilization,[288] which also is the method generally opted to confer water insolubility in silk matrices,[119, 230] thus following an minimalistic approach in scaffold fabrication. The coating did not significantly increase the thickness of the modified fibers (**Figure 3.1B ii and v**), however the surface roughness was improved as seen through the FESEM micrographs. The compositional stoichiometry of the copper doped bioactive glass, as affirmed by the energy dispersive X-ray analysis EDX spectra was consistent with the theoretical glass composition (**Figure 3.1B iii and vi**). TEM micrographs confirmed the mesoporous nature of the nanogranules and presence of diffused selected area diffraction (SAED) patterns confirmed the amorphous nature of these granules (**Figure A3.1**, *Appendix*) and no CuO crystals were formed.

3.3.2 Functionalized Silk Microfibers Confer Functionality and Stability to the Silk Matrices

FESEM micrographs (**Figure 3.2A**) revealed interconnected porous network within the silk matrices and the pore size distribution are presented in **Figure 3.2B**. The pure silk matrices (**Figure 3.2A i and iv**) without reinforcements revealed homogenous well interconnected circular pores with AAS and BMS scaffolds exhibiting average pore size of ~175 μm and ~145 μm, respectively. The silk matrices with unmodified fiber as reinforcements (BMF and AAF), exhibited heterogeneous fibrillar pores with better interconnectivity, having average pore size of ~112 μm and ~143 μm, respectively. However, the use of functionalised silk-microfibers (BMG and AAG) in the composite matrices exhibited similar heterogeneous fibrillar pores, having average pore size of ~ 119 μm and ~ 108 μm, respectively. Enhanced viability of osteoblasts within scaffolds with pore size ranging between 40 to 135 μm is documented.[52, 294] Hence, these heterogeneous fibrillar pores observed within the tricomposite silk matrices vouches for its applicability to facilitate gaseous, nutrient and cellular transport. The porosity and the bulk density of the scaffolds were determined by volumetric displacement method; the porosities of all the silk matrices were found to be ranging between ~80 to ~93 % (**Figure 3.2C**).

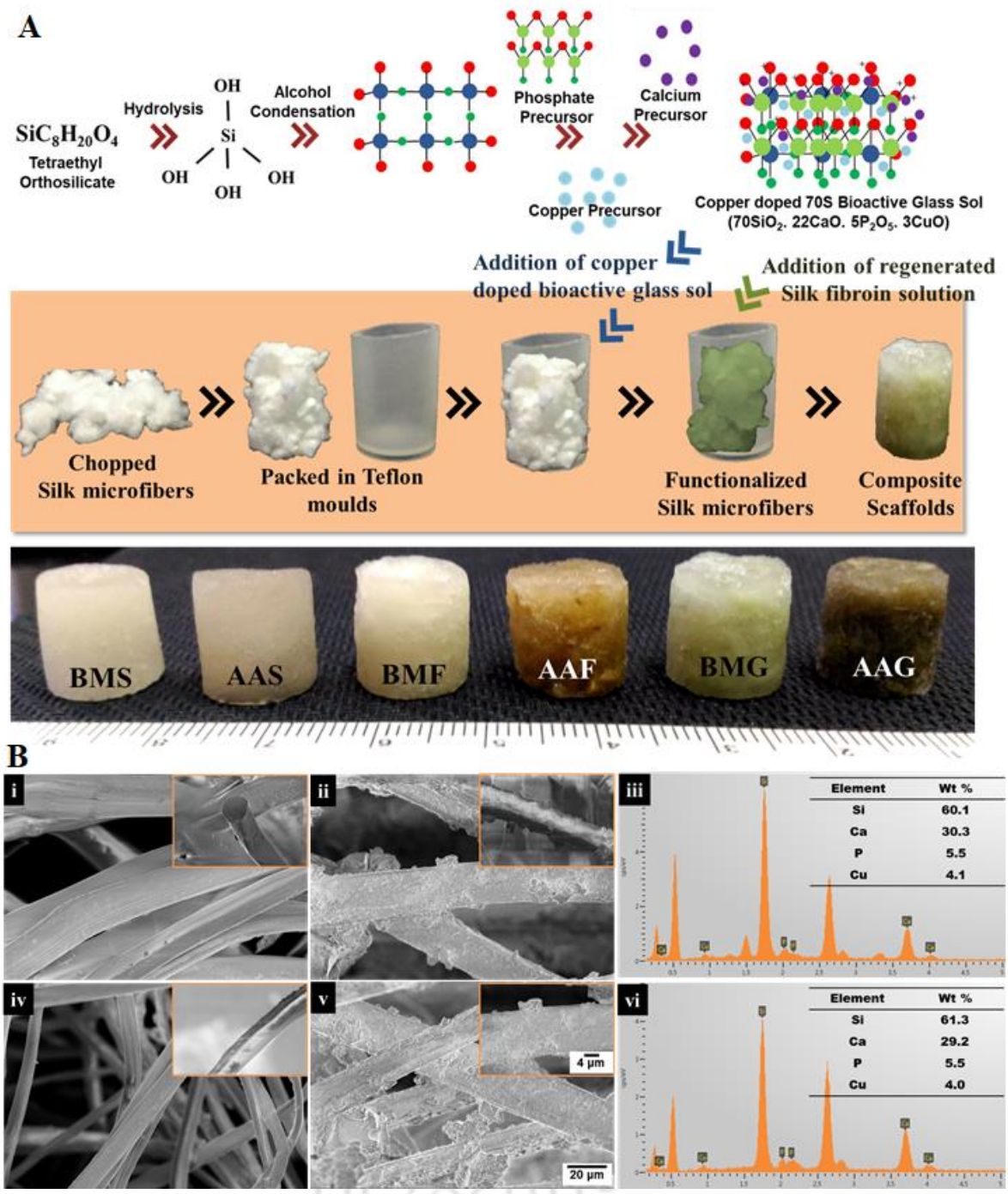

Figure 3.1. ***Strategy for modification of silk microfibers and fabrication of modified silk fiber reinforced composite silk scaffolds***. *A) Scheme for sol-gel coating of silk microfibers, fabrication of composite scaffolds, gross morphology of spongy silk scaffolds used in the study; B) FESEM micrographs of i) BM silk microfibers, ii) modified BM silk microfibers, iii) EDX spectra of modified BM silk fibers and iv) AA silk microfibers, v) modified AA silk fibers and vi) EDX spectra of modified AA silk fibers.*

Reinforcement in particular did not lower the porosity significantly and the incorporation of functionalized silk microfibers did not affect porosity of the developed matrices. However, the densities of the silk scaffolds varied significantly (**Figure 3.2D**); fiber reinforcement in BM silk matrices increased the density by ~1.31 folds and ~ 1.5 folds increment were noticed in AA silk matrices. Use of functionalized silk microfibers increased the density by ~2.09 folds and ~2.31 folds in BM and AA silk matrices, respectively (BMG and AAG).

Functional analyses in terms of composition and bioactivity assessment were undertaken. Compositional analysis using FTIR spectra were recorded to ascertain the functional conformations of silk fibroin and bioactive glass within the developed matrices (**Figure 3.2E**). In order to stabilize the bioactive glass network and for removal of unreacted nitrates, sintering is generally done. However, the strategy adopted herein utilized a greener solvent (ethanol) based strategy.[247, 288] FTIR spectral peak representing NO_3^- bending vibration at 1378 cm^{-1} in as synthesized raw bioactive glass (**Figure 3.2E i)** was remarkbly reduced in ethanol treated bioactive glass (**Figure 3.2E ii**), in addition to conferring stabiity to the glass network affirming the efficacy of the treatment. The characteristic amide peaks of SF *viz.* amide-I at 1650-1600 cm^{-1} corresponding to N-H deformation and C-H stretching, amide-II at 1550-1510 cm^{-1} corresponding to C=N stretching and amide-III band at 1260-1210 cm^{-1} corresponding to C-N stretching were observed [223] in both the silk micro-fiber reinforced matrices (BMF and AAF) (**Figure 3.2E iii and iv**). In the composite SF matrices (BMG and AAG), the finger print regions (**Figure 3.2E v and vi**) pertaining to bioactive glass were observed *viz.* spectral peak at 1042 and 446 cm^{-1} corresponding to Si-O-Si stretching and bending vibrations; spectral peak at 808 cm^{-1} corresponding to O-Si-O stretching and the band at 962 cm^{-1} corresponding to P-O stretching.[288] In addition to these bands, the characteristic amide peaks of SF (**Figure 3.2E v and vi**) were also observed but the intenisty of the peaks were subdued indicative of chemical interactions between the amide groups of SF and functional groups of bioactive glass.

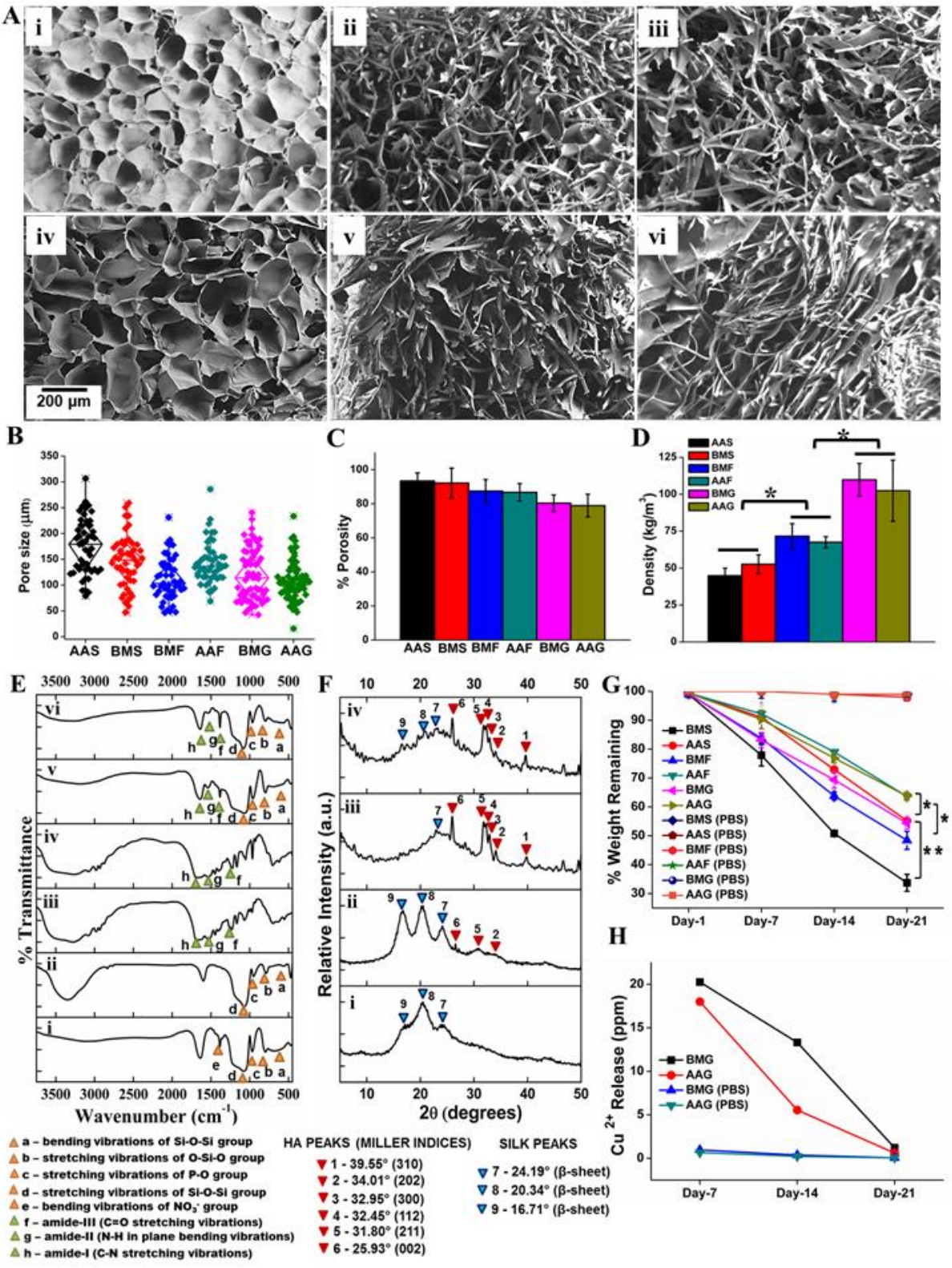

Figure 3.2. ***Fabricated silk composite scaffolds micro-architectural, functional and stability analyses.*** *A) FESEM micrographs of scaffolds i) BMS, ii) BMF, iii) BMG, iv) AAS, v) AAF and vi) AAG; B) pore size distribution, C) porosity and D) bulk density measurements of the scaffolds; E) FTIR spectra of scaffolds, i) raw bioactive glass, ii) ethanol treated bioactive glass, iii) BMF, iv) AAF, v) BMG, vi) AAG; F) in vitro bioactivity assessment, X-ray*

diffractograms of silk matrices i) BMF, ii) AAF, iii) BMG, iv) AAG; G) in vitro degradation profile and H) copper release from composite scaffolds using atomic absorption spectrometry (represents statistically significant difference ($p \leq 0.05$).*

The surface of implant determines it success in enabling osseointegration. The bone bonding ability of any bioactive material is often tested by assessing the extent of apatite formed at the surface of the material in simulated body fluid (SBF).[205] In the context of the study, fiber reinforced silk matrices immersed in SBF and after 14 days were evaluated using wide angle X-ray diffractometer for the presence of apatite phases (**Figure 3.2F**). The broad amorphous peaks noticed in the silk matrices at 16° and 24° corresponds to the β-sheets of silk-II conformation in silk fibers, whereas the broad peak at 20° corresponds to silk-II conformation of β-sheets found in silk matrices.[119, 296] In addition to these peaks, the comparatively crystalline peaks (and their corresponding miller indices) of carbonated apatite at 39.55° (310), 34.01° (202), 32.95° (300), 31.80° (211) and 25.93° (002) [297] were observed in the composite silk matrices BMG and AAG (**Figure 3.2F iii and iv**). This affirmed the composite matrices with functionalised microfibers enhanced the bioactivity of the scaffolds, wherein diffused peaks of apatite were only observed in case of unmodified silk fiber reinforced matrices (BMF and AAF) (**Figure 3.2F i and ii**). The non-mulberry silk matrices were found to be more bioactive, as evident from the better extent of apatite deposition than the mulberry silk matrices evident form the *in vitro* bioactivity assessment. This may be governed by difference in the acidic/basic amino acid ratio and the relative hydropathicity between the two silk fibroins, which differentially favour their reassembly in the β-sheet induced silk matrices.[286, 288] The functionalization further improved the bioactivity of the tricomposites by offering additional groups for the nucleation of apatite crystals contributing for better bone bonding ability.

The *in vitro* stability analyses of these scaffolds were performed under physiological like conditions, *viz* hydrolytic (in PBS without protease) and proteolytic (in PBS with protease) conditions,[119, 223] and the resultant weight loss and copper release from composite matrices was monitored. All the scaffolds maintained their integrity in PBS with no significant loss between day-1 and day-21 (**Figure 3.2G**). The copper release under hydrolytic conditions at day-1 was 0.967 ppm and at day-21 was 0.667 ppm for BMG, wherein for AAG at day-7 was 0.661 ppm and at day-21 was 0.051 ppm (**Figure 3.2H**). However, under enzymatic conditions, the silk matrices exhibited time dependent mass deterioration. Silk matrices without reinforcements (BMS and AAS) showing higher degradation rates (at day 21, ~33 % and ~55

% mass remaining, respectively, $p \leq 0.05$) than the silk matrices with unmodified and modified silk microfiber reinforcements. The reinforcements enabled in defying the enzymatic degradation and increasing the stability of the matrices. Silk matrices with reinforcements, BMF and AAF exhibited showed mass remaining percentages ~ 48 % and ~63 % respectively, at day-21 ($p \leq 0.05$). Similarly, the composite matrices, BMG and AAG showed ~54 % and ~63% mass remaining percentages respectively at day-21 ($p \leq 0.05$). Pertinent to note, is that the nonmulberry silk varieties (AAS, AAF, AAG) displayed reduced mass loss in comparison to the mulberry counterpart (BMS, BMF, BMG). This may be attributed to poly-alanine repeats $AAA(A)_{5-15}$ found in the *A. assama* silk fibroin, which reassemble into β-sheets with strong hydrophobic interaction, rendering inaccessibility for proteolytic cleavage. This throws insight in the use of suitable matrices for appropriate purposes, as neo-tissue formation and rate of graft degradation are akin to each other. These silk matrices offer prospects in controlling the rate of degradation through the type of silk used for the study, the amount of β-sheet induction,[296] and relative proportion of fibers used for reinforcements.

The copper release (**Table A3.1**, *Appendix*) under proteolytic condition was remarkably increased (**Figure 3.2H**); under proteolytic condition, the release was relatively more suggesting proteolytic degradation of silk microfibers by proteases destabilises the coating, releasing the copper ions during the *in vitro* degradation studies. Since the CuO formed is not crystalline and the extent of leachate is determined by the extent of proteolytic degradation of the silk microfiber, the release of Cu^{2+} would be closely modulated by the remodelling kinetics orchestrated by osteoclasts *in vivo* by proteases acting on the silk microfibers. It is pertinent to note, the amount of copper released even under normal hydrolytic conditions was well within the permissible limit in drinking water (1.3 ppm) as per American Public Health Association (APHA) regulation and at proteolytic condition was well within the safe dose of 65 mg/kg per day, above which initial hepatotoxic effects were noticed in rats.[298] Moreover, the use of copper as dopant in bioactive glass to endow antibacterial and proangiogenic effect has been documented before [287] and hence toxicity issues relating to its use is minimal.

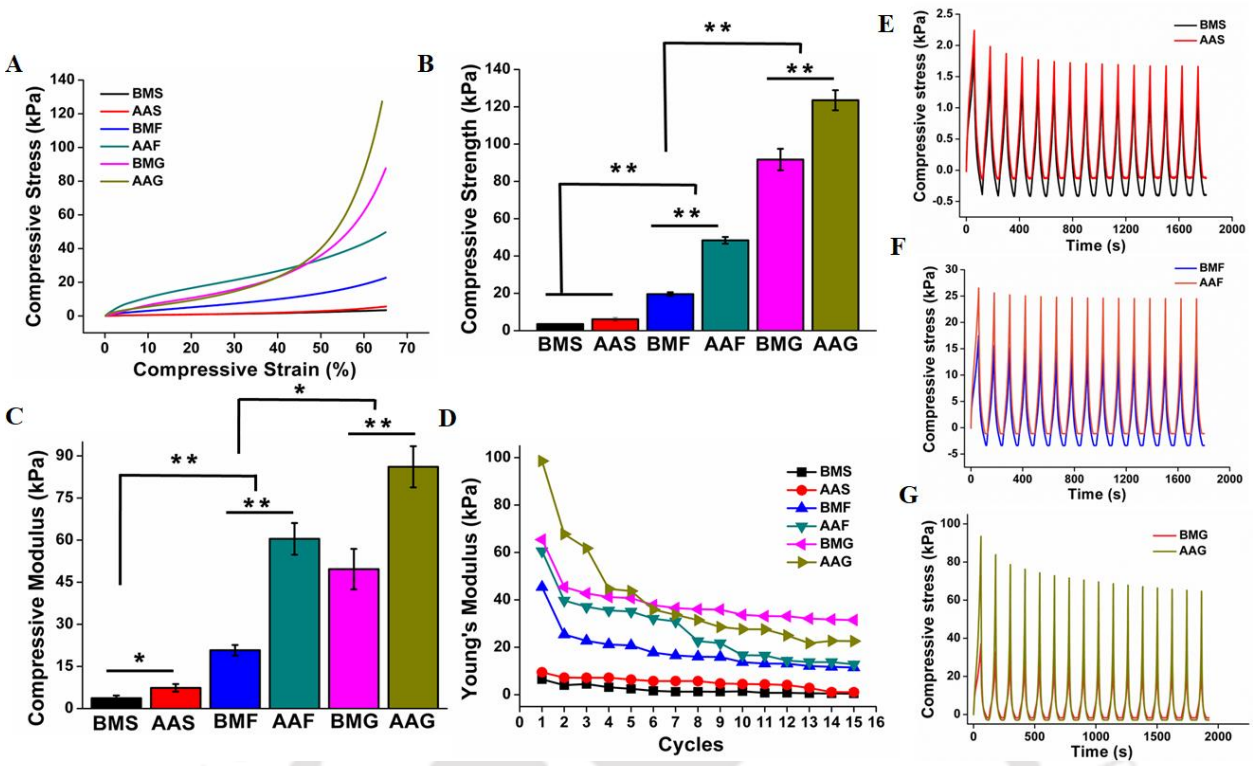

Figure 3.3. ***Mechanical properties of silk scaffolds****. A) representative stress-strain curve of silk scaffolds, and their B) compressive strength and C) compressive modulus profiles; D) Young's modulus in different cycles at cyclic compression test and stress-time curves of E) silk matrices without reinforcements, F) silk matrices with unmodified silk microfibers and G) silk matrices with functionalized silk (* represents statistically significant difference ($p \leq 0.05$), ** represents statistically significant difference ($p \leq 0.01$)).*

3.3.3 Functionalized Silk Microfibers Augment the Mechanical Properties of the Silk Matrices

Unconfined compressive testing of all the scaffolds was performed under hydrated conditions to understand the performance of the composite scaffolds under physiological load bearing conditions. The stress-strain behaviour (**Figure 3.3A**) of all the silk matrices exhibited sponge like behaviour characteristic of open celled foams [295] under uniaxial loading (up to 65 % deformation). An initial linear elastic region at the preliminary loading strains was immediately followed by a plateau region of stress indicative of pore wall buckling and crumbling in the open sponge structures. At 45 % strain, steep increase in stress is noted due to bulk densification of the sponge resultant of platen-platen contact, important to note the composite scaffolds (BMG and AAG) showed better resistance to bulk densification in comparison to other scaffolds. As expected, the mechanical properties of the silk matrices were significantly improved with the augmentation of microfiber reinforcements (**Figure 3.3 B and C**). The compressive strength and compressive modulus of the composite matrices with

modified fibers (BMG and AAG) were significantly higher than the unmodified matrices (BMF and AAF); ~1.5 folds increment (AAG > AAF) and ~2.45 folds increment (BMF > BMG) of compressive modulus was witnessed. The compressive strength strongly correlated with the bulk density of the scaffolds, with composite matrices BMG and AAG recording the highest compressive strengths 91.73 ± 5.78 kPa and 123.52 kPa, respectively among the scaffold groups. It has been observed that bulk stiffness greater than 30 kPa favours osteogenic differentiation of stem cells [119, 299] and also when bone cells are presented with a stiffer microniche, their matrix turnover is greatly enhanced.[299]

Cyclic compressive testing of the silk matrices performed under hydrated conditions exhibited good hysteresis between stress-strain (**Figure A3.2**, *Appendix*) curve with minimal loss of energy between the loading first and last loading-unloading cycles. The composite scaffolds (BMG and AAG) performed better than silk matrices with unmodified reinforcements (BMF and AAF) (~1.7 folds increase at cycle-1 and 15 between AAF vs. AAG; ~1.5 folds increase at cycle-1, ~2.9 folds increase at cycle-15 between BMF vs. BMG). The incorporation of bioactive glass coating helped in reducing residual stress (as noticed in case of other two scaffold groups, (**Figure 3.3 D-G**), due to plausible increase in elastic deformation accumulated in the composite scaffolds. Additionally, the presence of intragranular bioactive glass particles in the functionalized reinforcements might have acted as stress-contractor via generation of micro pre-cracks. Non-mulberry silk varieties are endowed with poly-alanine repeats which help in stable transitions during stress deformations, thus contributing to the non-mulberry silk's mechanical resilience,[286, 288] as opposed to the poly-(glycine-alanine) repeats of the mulberry silk. The densities (D) and the compressive modulus (E) of the composite matrices; for BMG, ~109 kg/m^3, ~50 kPa, for AAG,~102 kg/m^3, ~87 kPa respectively lies within the same limits of power law equation (Log E = -4.37 + 1.88 log D) for silk particle reinforced silk matrices correlating directly with densities and compressive modulus of cancellous bone (Log E = -4.10 + 2.47 log D).[201, 295] Though, the compressive modulus of the fabricated matrices in the current study is low, it can be increased by modulating the fiber packing density, bioactive glass coating density and protein concentration to suit the needs for high strength application without compromising on porosity and pore size.

3.3.4 Silk Scaffolds Exhibit Cytocompatibility and Immunocompatibility

The cellular viability of the seeded hMSCs was assessed after 14 days post osteogenic differentiation, using calcein-AM staining. The live cell population was detected as a bright

green calcein dye fluorescence, while the dead cells (stained with ethidium homodimer) and scaffold boundaries and silk microfibers (innate fluorescence) exhibited red fluorescence (**Figure 3.4A**). All the silk matrices used, supported the growth of cells with no discernible dead cell population noticed. The only silk matrices (BMS and AAS) showed cells attached along the pore boundaries (**Figure 3.4A i-ii**), wherein AAS showed better cell distribution and spreading. The addition of silk microfibers (in BMF, AAF) as reinforcements increased the surface area facilitating better cell adhesion; increased cell spreading was noticed in AAF, with cells firmly attached and well spread out along the silk fibers and pore boundaries. In composite scaffolds, viable cell aggregates were found, indicative of bone nodule like assembly of hMSCs going towards differentiated osteoblast phenotype (**Figure 3.4A v-vi**). The cell proliferation was assessed using Alamar blue assay, wherein the amount of Alamar blue dye reduction correlates directly to the active cellular metabolism of proliferating cells (**Figure 3.4B**). All the silk matrices supported cellular proliferation, with no significant difference noticed between groups. However, at day-14 enhanced cell proliferation in only silk matrices (BMS, AAS) than the composite matrices (BMG, AAG) was observed; ~1.17 folds increase (AAS vs. AAG) and ~1.19 folds increase (BMS vs. BMG).

Cell cycle analysis of seeded hMSCs on the silk matrices *i.e.* between only silk matrices (**Figure 3.4C i**) and composite matrices was done (**Figure 3.4C ii**) to have an insight on its cellular state. It was seen the G0 cell population in composite matrices (BMG and AAG) increased by ~1.5 folds in comparison to only silk matrices (BMS and AAS), indicating the hMSCs are acquiring a quiescent phenotype suggesting terminal differentiated state. *In vitro* immunocompatibility of the matrices were performed as a quantifiable precursor to affirm their suitability for *in vivo* applications, by using murine macrophages stimulated by the matrices (**Figure 3.4D**). Lipopolysaccharide (LPS) served as the positive control for the study, while tissue culture plate without any stimulation as the negative control. All the silk matrices, irrespective of reinforcement or functionalization exhibited negligible immune response comparable to negative control, attesting their immunocompatibility.

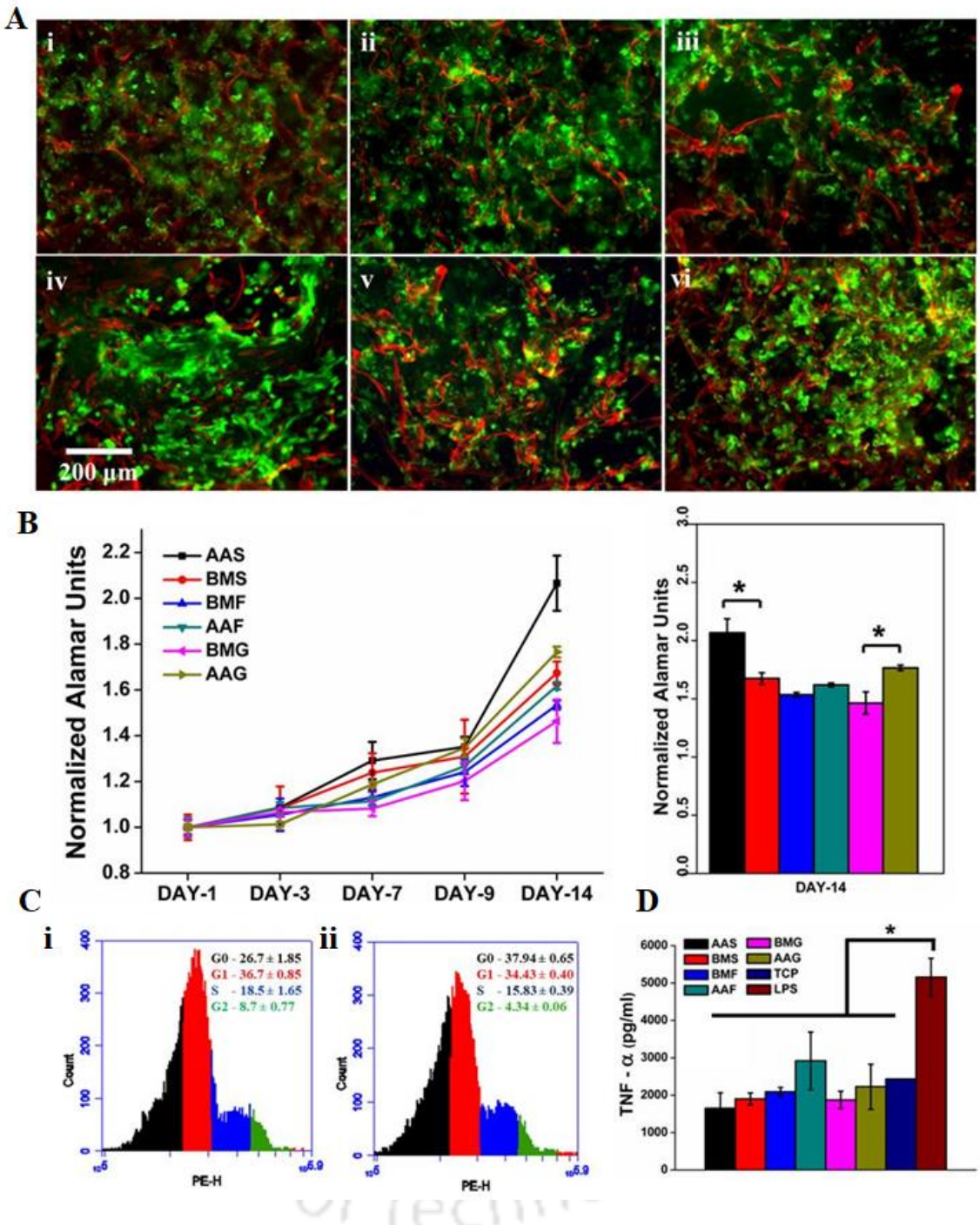

Figure 3.4. ***In vitro cytocompatibility and immunocompatibility of the silk matrices***. *A) Cellular viability assessed by A) live/dead staining of hMSCs seeded scaffolds after 14 days i) BMS, ii) AAS, iii) BMF, iv) AAF, v) BMG, vi) AAG, B) cell proliferation determined by alamar blue assay, C) cell cycle analysis of silk matrices i) only silk matrices and ii) composite matrices with functionalised silk microfiber reinforcement; D) in vitro immune response assessment by measuring murine TNF-α release from RAW 264.7 cells (* represents statistically significant difference ($p \leq 0.05$).*

3.3.5 *Silk Scaffolds with Functional Reinforcements Enable Osteoinduction and Matrix Maturation*

During osteogenesis, three distinct phases are noticed in the differentiating stem cells, *viz* a period of active cell proliferation, followed by osteoblast maturation phase characterized by extracellular matrix (ECM) secretion and terminal state of mineralisation and osteoid formation. Osteogenically primed stem cells in addition to matrix stiffness and surface roughness are responsive to the surface chemistry and chemical cues of their microniche.[52] To ascertain the progression and the state of osteogenesis of seeded hMSCs, biochemical, histological and gene expression profile of important osteogenic markers were done. Prior to these functional analyses, we verified again the cellular distribution of cells within the silk scaffolds through hematoxylin and eosin (H&E) staining (**Figure 3.5A**). The open porous structures helped in migration of hMSCs, seeded through static seeding strategy to distribute and populate well within the scaffolds. The mulberry silk scaffolds (**Figure 3.5A i, iii and v**) exhibited relatively loose adhesion profile with cells aggregating more in certain areas than an even distribution. Conversely, the non-mulberry silk scaffolds (**Figure 3.5A ii, iv and vi**) showed uniform distribution of firmly adherent cells along the pore outline and fiber. Alkaline phosphatase (ALP) is an essential regulatory enzyme that mediates the mineralization in differentiating osteoblasts. ALP expression profile (**Figure 3.5 B**) showed an overall increase at day-7 and gradual decrease in day-14 in the silk matrices, indicative of onset of differentiation and proceeding towards terminal differentiation of osteoblasts.

Reinforcements (BMF, AAF) significantly increased the ALP activity in comparison to pure silk matrices (BMS, AAS), with non-mulberry silk scaffold AAF showing ~1.2 folds increased secretion than BMF scaffolds (at day-7). However, the use of bioactive glass functionalised reinforcements remarkably increased the ALP activity, with AAG performing exceptionally better (~1.5 fold higher than BMG, ~2.08 higher than AAF). Western blot analysis to assess the expression profile of HIF-1α (**Figure 3.5 C**) revealed that there was minimal expression level of HIF-1α during the course of differentiation (day-1 to day-14) in pure silk (BMS, AAS) and silk matrices with unmodified silk fibers (BMF, AAF). This may be attributed to the static culture condition used due to a marginal hypoxic environment inside the matrices. However, an increase in expression of HIF-1α was noticed in case of composite scaffolds (BMG and AAG), suggesting the role of copper ions in stabilization of HIF-1α. The HIF-1α expression levels were maintained higher during the entire duration of differentiation period (14 days used in the current study).

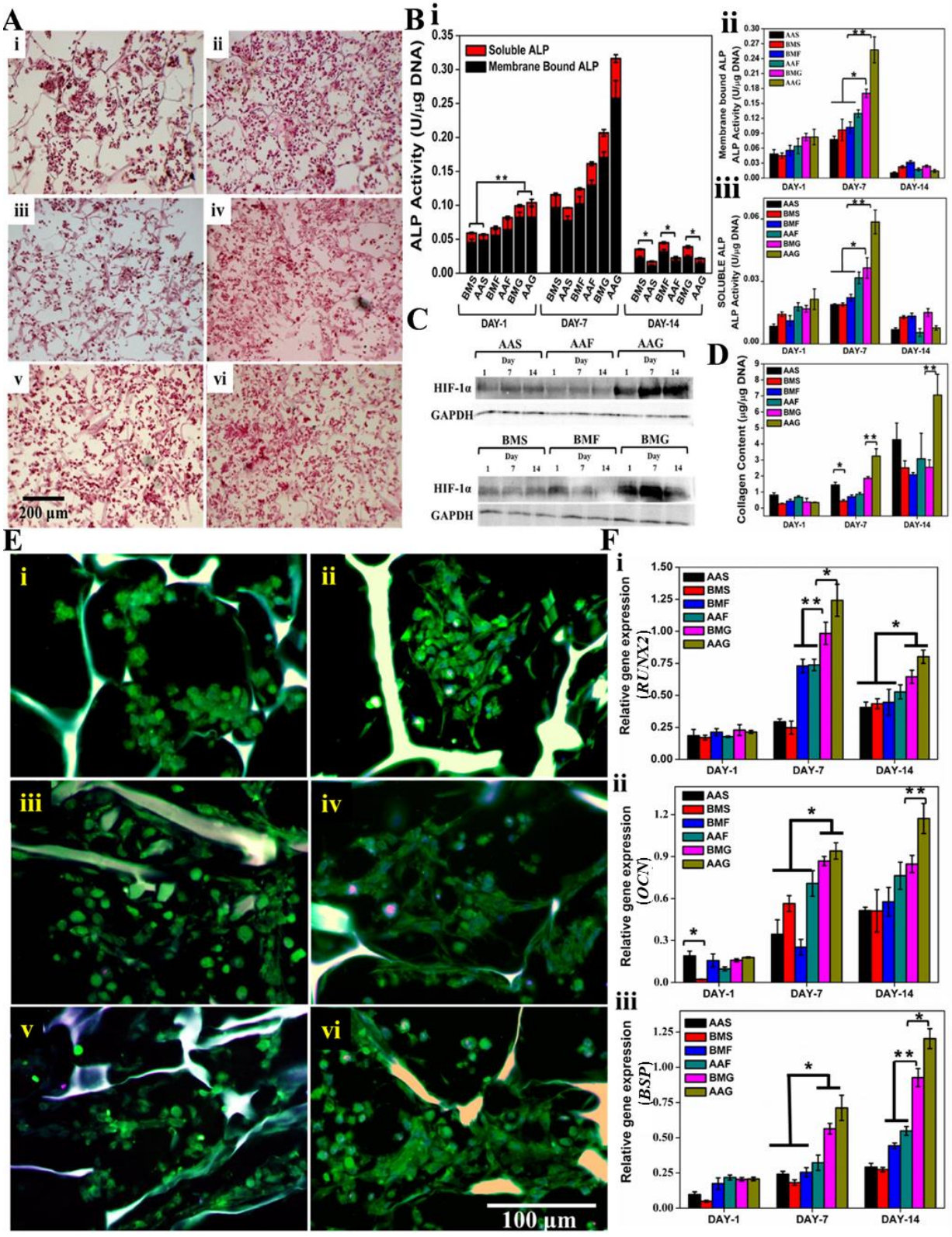

Figure 3.5. ***In vitro functional validation of osteogenesis of hMSCs seeded silk matrices***. *A) Hematoxylin and eosin stained sections, i) BMS, ii) AAS, iii) BMF, iv) AAF, v) BMG, vi) AAG; Biochemical analysis of scaffolds, B) alkaline phosphatase activity assessment, C) expression of hypoxia inducible factor 1α (HIF-1α) assessed by western blotting and D) total collagen estimation; E) Immunohistological assessment for expression of osteopontin (OPN) (stained*

*green)***,** *i) BMS, ii) AAS, iii) BMF, iv) AAF, v) BMG, vi) AAG; F) real time gene expression profile for i) runt-related transcription factor 2 (RUNX2), ii) osteocalcin (OCN) and iii) bone sialoprotein (BSP); (* represents statistically significant difference ($p \leq 0.05$), and ** represents statistically significant difference ($p \leq 0.01$)).*

Collagen-I is the most important ECM protein expressed by osteoblasts. The tricomposite scaffolds (BMG, AAG) showed significantly higher secretion of collagen (**Figure 3.5 D**) than other scaffolding types, with AAG having ~2.82 fold higher than BMG and ~2.29 folds higher than AAF. Interestingly, the non-mulberry silk scaffolds showed relatively higher secretion of collagen (~1.5 folds higher, AAF vs. BMF, ~1.68 folds higher, AAS vs BMS). The reinforcements too had a positive effect with reinforced scaffolds showing higher collagen secretion than the pure silk scaffolds. The ostegenic differentiation of hMSCs towards a terminal maturation was affirmed by the expression of osteopontin (stained green) was visualized through immunostaining (**Figure 3.5 E**). However, it was observed in the non-mulberry silk matrices, the assembly and condensation of differentiating osteoblasts was more organized, indicative of healthy bone nodules (**Figure 3.5 E ii, iv and vi**), whereas in case of mulberry scaffolds they seemed disrupted.

The state of progression of osteogenesis was assessed through real time gene expression of key marker genes (**Figure 3.5F**). *RUNX2*, an early-mid stage marker was observed to increase at day-7 and gradually decrease at day-14 in all scaffolds, indicative of commitment of differentiating osteoblasts towards maturation (**Figure 3.5F i**). At day-7, ~ 1.2 folds increase in *RUNX2* expression was noticed in tricomposite scaffolds in comparison to scaffolds with unmodified fiber reinforcements (BMF. AAF), while ~6 folds increase was noticed with respect to pure silk matrices (BMS, AAS). No significant difference between BMG and AAG was observed. Two mid-late stage markers, *OCN* and *BSP* were assessed. The hMSCs derived osteoblasts maintained their osteogenic commitment, as the expression levels increased from day-1, to day-7 and maintained till day-14. At day-14, the tricomposite scaffolds (BMG, AAG) showed significant increase in expression of *OCN*; ~1.5 folds increase with respect to BMF, AAF and ~2.2 folds increase with respect to pure silk matrices (**Figure 3.5F ii**). Similarly, at day-14 significant increase in expression of *BSP* in tricomposite scaffolds, ~1.9 fold with respect to BMF, AAF and ~4.5 fold with respect to pure silk matrices, was noticed (**Figure 3.5F iii**). Important to note, the non-mulberry silk matrices enhanced the initial cell attachment, favour better cell spreading and infiltration (as observed in live/dead imaging and H&E staining) and even regulated matrix turnover (increased collagen secretion assessed through collagen estimation). This substantiates the role of RGD mediated cell adhesion [119, 288] and

its subsequent role in matrix turnover, due to the presence of tri-peptide in the N and C termini of G_C motifs of H-chain of *A. assama* silk fibroin.[228] Also, another plausible reason for the better performance of the non-mulberry silk matrices could be the activation of Wnt/β-catenin pathway mediated through integrin/focal adhesion kinase (FAK) mechanism [300]. The non-mulberry silk matrices present a stiffer micro-milieu as evidenced from the mechanical studies, wherein the bulk compressive properties of the non-mulberry silk matrices were significantly higher than the mulberry matrices. This presentation of stiffer matrix in turn might have up regulated the ECM maturation and commitment of osteogenic fate [52, 299] as attested by the biochemical and gene expression studies.

3.3.6 *Silk Scaffolds with Functional Reinforcements Confer Proangiogenic Attributes and Mediate Endothelial Cell Migration and Homing*

The proangiogenic effect tricomposite scaffolds is attributed to the release of Cu^{2+} ions which helps in stabilization of HIF-1α. Under normoxic conditions HIF-1α is predisposed to proteolytic degradation by prolyl-4-hydroxylase enzyme. However Cu^{2+} ions leached out from the scaffolds stabilized the HIF-1α (as seen through western blotting) which further played crucial role in regulating known downstream angiogenic factors expression such as VEGF, ANGPTN and eNOS.[301] The endothelial cells (pECs) were seeded on silk matrices in which osteogenically primed hMSCs were in culture at day-7. At day-14, immunohistological assessment was done for visualization of vWF (stained green), a hallmark endothelial marker and collagen-I (stained red), an osteogenic marker (**Figure 3.6A**). It was observed that the endothelial cells migrated towards the inside of scaffold and got recruited in conjunction with osteogenically primed hMSCs. The vascular network within pure silk matrices (BMS, AAS) and bicomposite matrices (BMF, AAF), was not continuous, with vascular cells found only around the periphery of the cell clusters (**Figure 3.6A i-iv**). However, in case of composite matrices (**Figure 3.6A v-vi**), a primitive plexus-like network with pECs and hMSCs exhibiting better interaction and pECs forming discrete network like boundaries through the cell clusters attesting its proangiogenic potential.

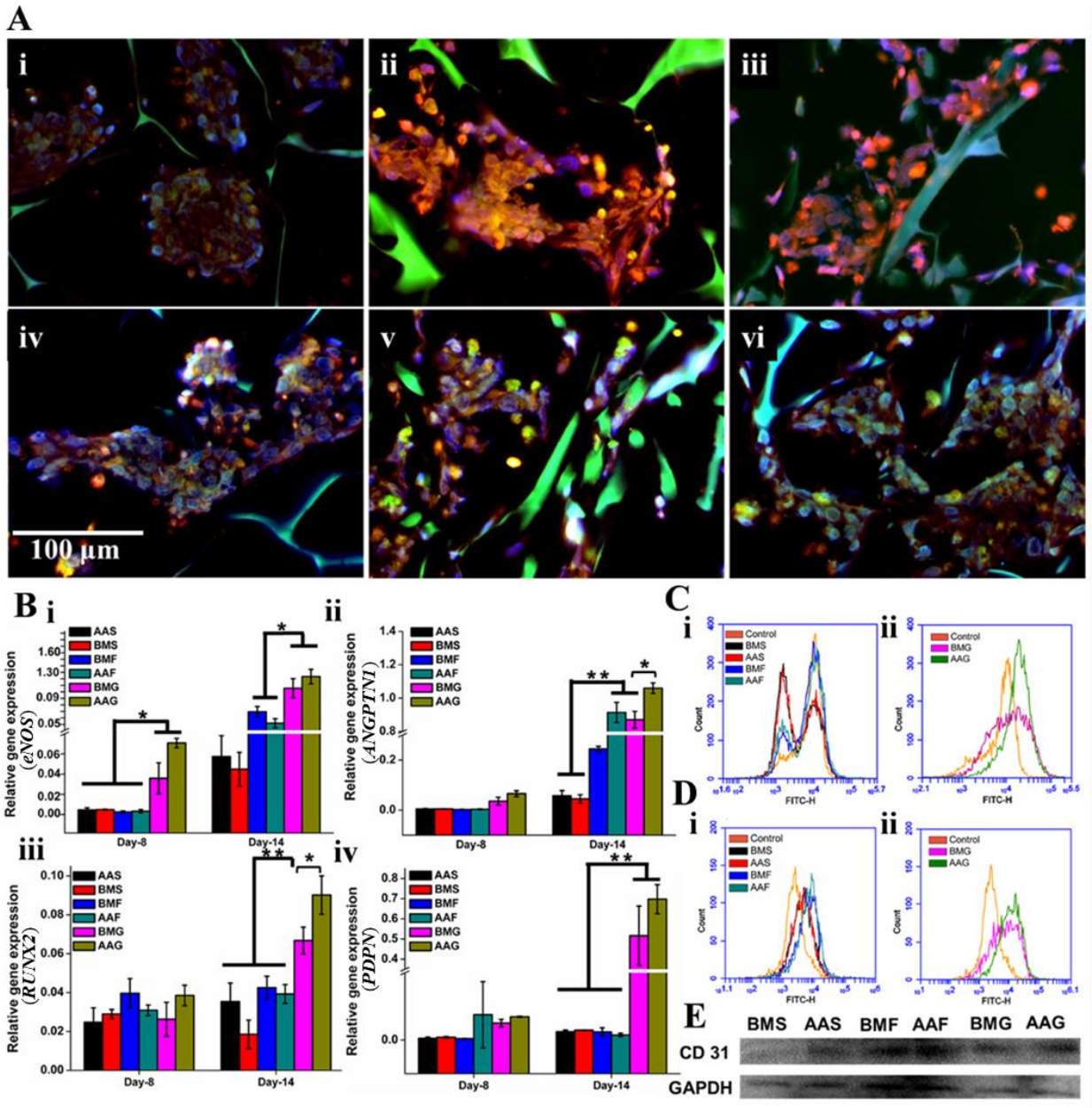

Figure 3.6. ***In vitro functional validation of proangiogenic potential of silk matrices***. *A) Immunohistological assessment for expression of Willebrand factor vWF (vWF) (stained green)and collagen-I (stained red), i) BMS, ii) AAS, iii) BMF, iv) AAF, v) BMG, vi) AAG; B) real time gene expression profile for angiogenic genes i) endothelial nitric oxide synthase (eNOS), ii) angiopoietin (ANGPTN1) and osteogenic genes, iii) RUNX2, iv) podoplanin (PDPN); Flowcytometric analysis for i) control groups, ii) experimental group, C) C-X-C chemokine receptor type 4 (CXCR-4) and D) CD-31; E) Expression of CD-31 assessed by western blotting (* represents statistically significant difference ($p \leq 0.05$), ** represents statistically significant difference ($p \leq 0.01$)).*

Moreover, we looked into the expression of angiogenic specific genes *eNOS* and *ANGPTN1*, and also osteogenic genes *RUNX2* and *OPN*, to ascertain that whether the stable co-culture of cells exist, without impairing osteogenis and concurrently assisting angiogenesis.

It was observed (**Figure 3.6B i**) that the tricomposite scaffolds (BMG, AAG) showed higher expression of *eNOS* at day-8 (~8 fold increase) and day-14 (~1.5 fold increase against BMF, AAF; ~16 fold increase against BMS, AAS), in comparison to the pure silk matrices (BMS, AAS) and bicomposites (BMF, AAF). Similarly, higher expression of *ANGPTN1* was also observed at day-14, in case of tricomposites (BMG, AAG), ~5 fold increase in comparison to BMF, ~20 fold increase in comparison to pure silk matrices (**Figure 3.6B ii**). The reinforcements, even unmodified silk microfibers increased the *ANGPTN1* expression significantly (~22.5 folds higher, in case of AAF vs. AAS; ~4 folds higher, in case of BMF vs. BMS). Interestingly, we found that the tricomposite silk matrices, maintained their osteogenic potential significanlty better than the other matrices. Commitment to osteogneic fate was noticed (**Figure 3.6B iii**), affirmed by the increased expression of *RUNX2* (~2.2 folds higher in AAG, ~1.8 folds higher in BMG) in comparison to other matrices. Podoplanin, a late stage marker expressed by osteocyte like cells, during osteoid formation was seen to increase significantly (~40 folds increase) in case of tricomposite scaffolds in comparison to other silk matrices at day-14 (**Figure 3.6B iv**). Expression of both early and late stage markers, indicate the presence of differentiating osteoblasts subpopulation and terminally mature osteocytes prelavant in the scaffold.

Further we quantified the population of hMSCs expressing CXCR4, a crucial receptor which helps in homing of endothelial cells and regulating vascularization [302]. While there was no expression of CXCR4 noticed in any of the pure silk (BMS, AAS) and bicomposite silk (BMF, AAF) matrices (**Figure 3.6C i**), an increase in expression in the tricomposite matrices was noticed (~13.8 % increase in BMG, ~12.8 % increase in AAG) (**Figure 3.6C ii**). This substantiates the plexus like primitive network (as noticed **Figure 3.6A v-vi**) formed is due to the expression of CXCR4, which enabled them to home and migrate to the differentiating hMSCs expressing the receptor. We also looked into the expression of CD-31, an important marker protein which mediates cell-cell interaction fundamentally during angiogenesis. While the silk matrices and bicomposite matrices did not significantly increase the expression of CD-31 (**Figure 3.6D i**), an increase in expression (~23.2% in BMG, 26% in AAG) was noticed (**Figure 3.6D ii**), which was substantiated by the western blot also (**Figure 3.6E**), indicative of onset of angiogenesis within the tricomposite matrices through SDF-1/CXCR4 signalling pathway.[302]

3.3.7 *Osteoclastogenesis and Resorption Effectiveness in Silk Scaffolds*

We tried to elucidate the resorbability of the silk matrices by looking into few aspects of the molecular mechanisms associated with bone remodelling, mediated through human monocyte derived osteoclasts. Extent of osteoclast differentiation was determined through tartrate resistant acid phosphatase (TRAP) staining. Overall, multinucleated cell clusters stained positively for TRAP (purplish granules, indicated by red arrows) were observed in all the silk matrices (**Figure 3.7A**). However, we observed that in case of non-mulberry silk matrices (AAS, AAF, AAG), the multinucleated osteoclasts had more cell-matrix interaction (**Figure 3.7A ii, iv, vi**), whereas in case of the mulberry silk matrices more cell-cell to matrix was preferred as opposed to cell-matrix interaction. Real time gene expression profile of osteoclast specific genes involved in resorption, reiterated the fact that osteoclast functionality was favoured better in non-mulberry matrices, with no significant difference found between AAS, AAF and AAG. The expression of *CAII* was found to increase by ~3.16 fold in AAS vs. BMS, ~2.45 fold in AAF vs. BMF, and ~1.79 fold in AAG vs. BMG (**Figure 3.7B i**). Similarly, the expression of *CTSK*, was also found to increase by ~2.78 fold in AAS vs. BMS, ~ 3.65 folds in AAF vs BMF and ~1.71 fold in AAG vs. BMG (**Figure 3.7B ii**).

Additionally, the expression of *NFATc* an important transcription factor which drives the osteoclast differentiation and maturation was found to be higher in case of the non-mulberry matrices (**Figure 3.7B iii**) (~8.4 folds increase in AAS vs BMS; ~4.5 folds increase in AAF vs. BMF and ~2 folds increase in AAG vs. BMG). MMP-9 expression, an important bone remodelling enzyme was assessed using gelatin zymography (**Figure 3.7C i**). All the silk matrices exhibited MMP-9 expression with only BMS showing relatively lesser expression than the rest of the matrices (**Figure 3.7C ii**). The resorption effectiveness in non-mulberry silk is attributed to the presence of RGD tripeptide, which has been documented to upregulate α5β1 integrins [52] which further mediates the expression of osteoclast specific markers such as TRAP, MMP-9, CTSK, CAII (resorbing enzymes) and NFATc (a transcriptional regulator governing osteoclastogenesis). **Figure 3.7D** presents the overall schema relating to the cell instructive role played by these multifunctional biomimetic scaffolds pertaining to osteoinduction, angiogenesis and osteoclastogenesis mediating resorption.

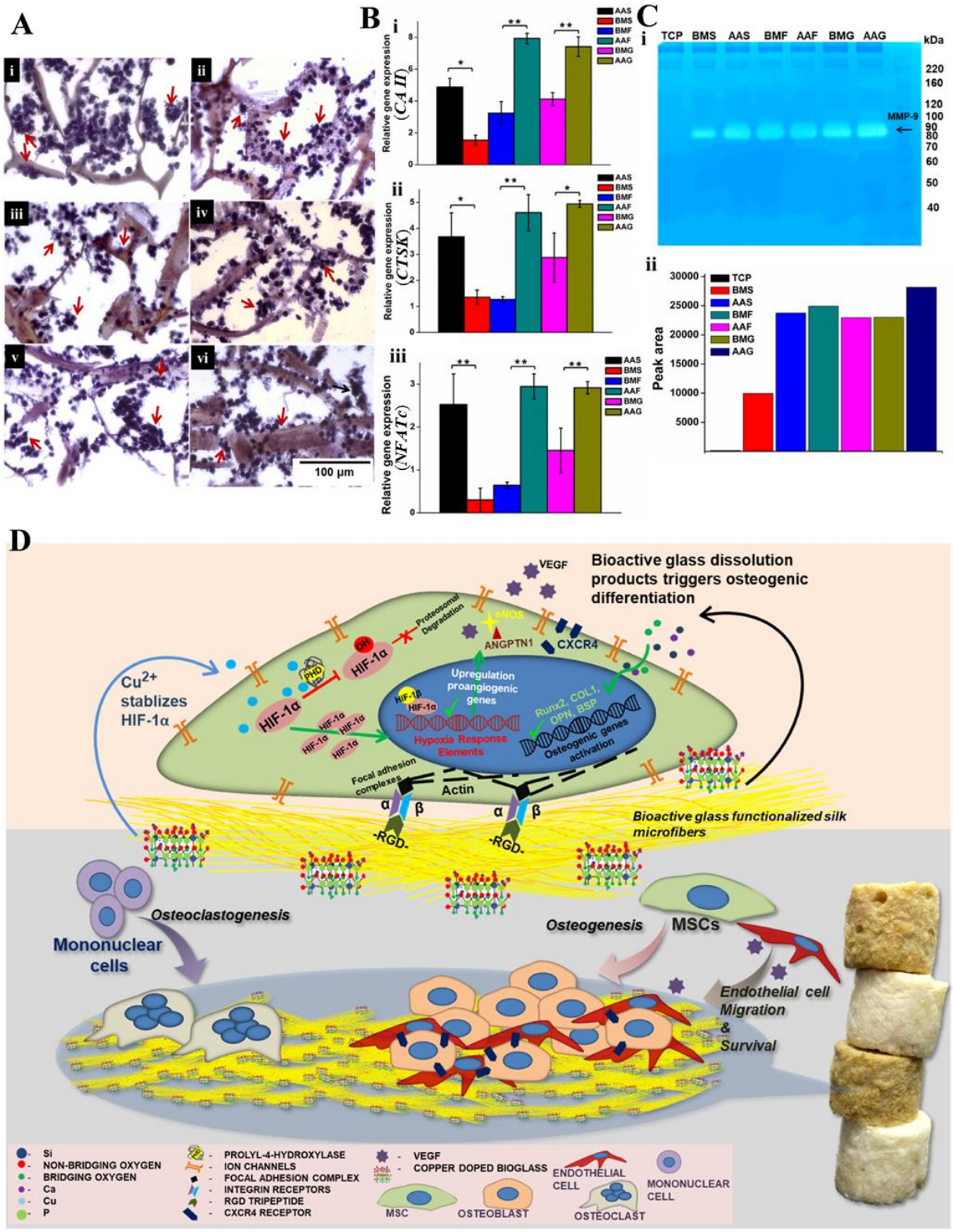

Figure 3.7. ***In vitro assessment of resorption effectiveness of silk matrices***. *A) tartrate resistant acid phosphatase (TRAP) staining, i) BMS, ii) AAS, iii) BMF, iv) AAF, v) BMG, vi) AAG; B) real time gene expression profile for osteoclastic genes, i) carbonic anhydrase II (CA II), ii) cathepsin-K (CTSK), iii) nuclear factor of activated T cells (NFATc); C) gelatin zymography to assess MMP-9 activity i) gelatinolytic bands appearing clear in blue stained gel background and its ii) densiometric profile; D) scheme representing the holistic cellular*

mechanisms involving osteogenesis, angiogenesis and resorption, regulated by cell instructive silk composite matrices (represents statistically significant difference ($p \leq 0.05$), ** represents statistically significant difference ($p \leq 0.01$)).*

3.3.8 *Non-mulberry Silk Scaffolds with Functional Reinforcements Enable Complete Restoration of Volumetric Bone Defects with Periosteal Regeneration*

Based on the *in vitro* physico-chemical and biological analyses, silk matrices with unmodified silk microfiber as reinforcements (BMF, AAF) and tricomposites with functionalized silk microfiber as reinforcemens (BMG, AAG) were chosen further to be validated preliminarily in bone defects at distal epiphyseal region of femurs in white New Zealand rabbits. Macroscopic evaluation (**Figure 3.8A; Figure A3.3**, *Appendix*), revealed inflammation, disability and deterioration were absent and a smooth exterior cover observed in the experimental group, indicating healing of defects whereas clear dents of defect created was noticed in control defect groups (even at day-30). The relative new osseous tissue formed was assessed through fluorochrome labelling (**Figure 3.8B**). Significantly higher percentage of 80.31 ± 3.01% bone formation at the end of 30 days was witnessed for experimental group AAG, while the open defect group recorded only 33.34 ± 3.89 (**Table A3.2**, *Appendix*).

The results of histological examination after 3 months by H&E staining showed the control empty defect (**Figure 3.8C i**) to have minimal newly formed bone at the defect edges, with most of the defect margin still noticeably unhealed. Whereas in case of control groups (BMF, AAF), ingrowth of new bone tissue was observed (**Figure 3.8C ii-iii**), with focal invasion of osteoblasts characterized by fibrovascular, osteocyte proliferation and scant angio-invasion. Most of the matrices were found to be resorbed, with cancellous bone like features seen with discontinuous defect margins indicative of healing. However, in case of experimental group BMG (**Figure 3.8C iv**) showed almost complete defect margin closure, with fibro-vascular invasion in the intramedullary area noticed, indicative of periosseous tissue formation and late stages of healing. While in case of AAG (**Figure 3.8C v**) complete closure of defect margins with continuous cortical bony bridge with intact periosteal regeneration was noticed. In both the experimental groups, BMG, AAG complete resorption of matrices was observed, with no remnants of scaffolds seen.

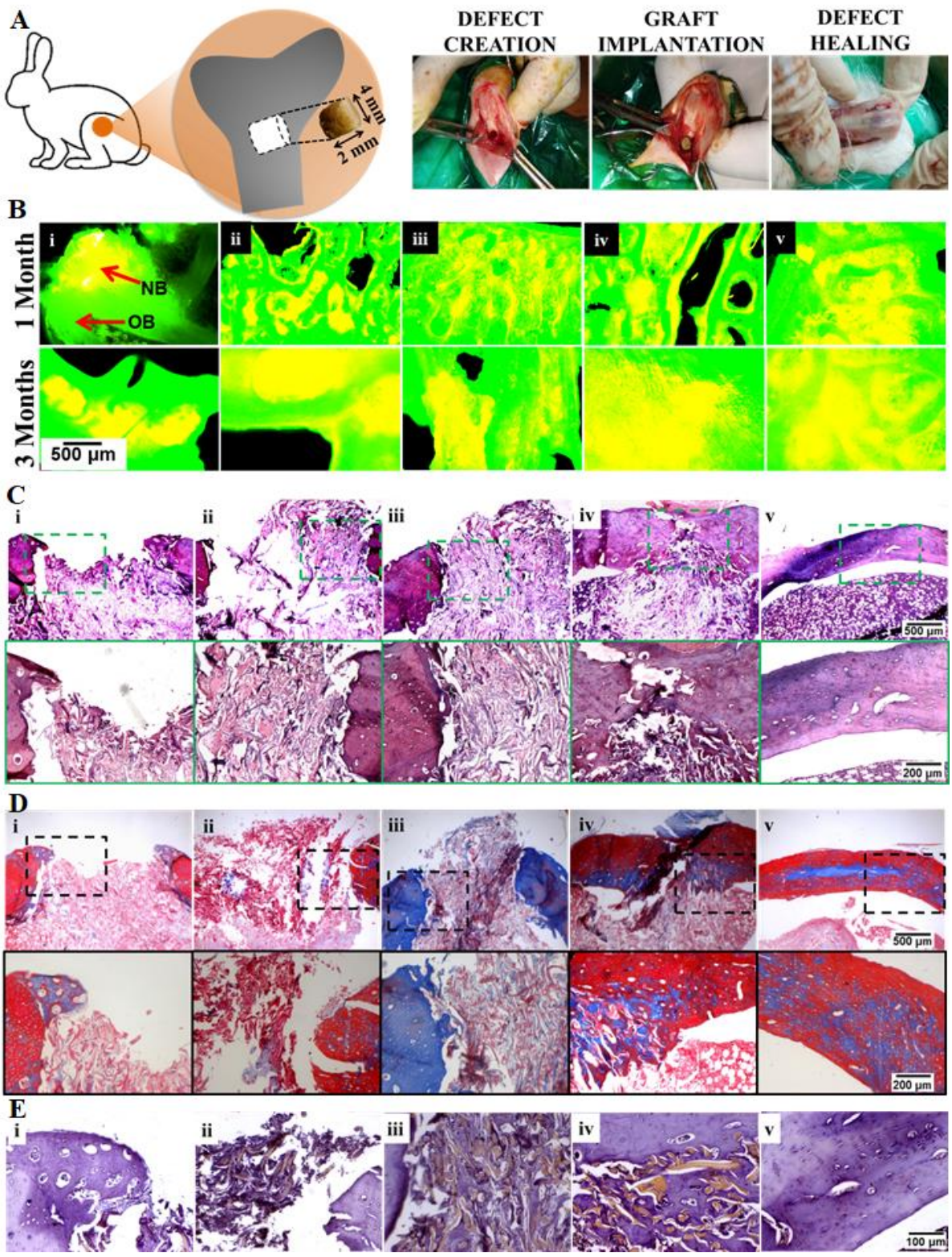

Figure 3.8. ***In vivo functional validation of silk matrices to repair volumetric bone defects***. *A) creation of volumetric bone defects, graft implantation and macroscopic observation of defect healing B) fluorochrome (oxytetracycline) labelling images 1 and 3 months post implantation red arrows indicating, bright yellow region representing the new bone (NB) formed and green region representing the old bone (OB) region; and histological validation of silk matrices 3 months post implantation; C) overview of H&E stained sections (top panel) and*

magnified images (bottom panel), D) overview of Masson's trichrome stained sections (top panel) and magnified images (bottom panel) and E) TRAP stained sections for i) non-experimental empty defect, ii) BMF, iii) AAF, iv) BMG, v) AAG.

Masson's trichrome staining was done to assess the extent of new bone formation, marked by collagen network (stained blue) and fibrous tissue, while fibrous tissue and old bone appeared red. In the empty defect group (**Figure 3.8D i**) signs of defect repair were noticed at the defect margins, with neo-osseous tissue indicated by collagen fibers seen. In case of control groups, BMF showed mostly fibrous tissue ingrowth (**Figure 3.8D ii**) whereas AAF exhibited better collagen deposition, with intramedullary cancellous bone like network noticed (**Figure 3.8D iii**). However, in case of experimental group BMG, the quantity of new woven bone like network was better than the control groups (**Figure 3.8D iv**). Membranous ossification onset was observed around about the residual fragments at the posterior side defect margins, with newly formed bone trabeculae established mostly by adipose tissue, blood vessels and haematopoietic tissue. While in AAG, compact cortical bone with Harvesian network was observed. The crevices within were filled new collagen network throughout the new lamellar bone structure formed, covering the defect margins. Evidence of osteoclast mediated resorption was observed through TRAP staining (stained brownish red) (**Figure 3.8 E**). Bone remodelling in the newly formed collagen matrix along the defect margins was seen in empty defect group (**Figure 3.8E i**), whereas TRAP positive cells were noticed alongside the resorbing matrices (**Figure 3.8E ii-iii**). In the experimental group, evidence of osteoclast activity within the intramedullary space in BMG and within the compact lamellar bone structure was noticed (**Figure 3.8E iv-v**), indicating remodelling in the neo-osseous tissue. Consistent with our *in vitro* biological studies the tricomposite non-mulberry matrices helped in defect healing, with a healthy compact cortical bone cover guided by the osteoinductive, proangiogenic and resorbable nature of the scaffolds.

3.4 Salient Findings of the Chapter

In this chapter the fabrication of multifunctional fiber reinforced silk bioactive glass composites by freeze-drying approach was shown. The facile copper doped bioactive glass-based sol-gel coating adopted by helped in efficiently functionalizing *B. mori* and *A. assama* silk microfibers in obtaining a uniform, amorphous, nanogranular coating over the silk microfibers. The functionalized silk microfibers enabled in augmenting the physical properties such as bulk density, matrix stiffness and surface roughness. The chemical cues offered by the ionic dissolution product enabled in osteoinduction and in stabilization of HIF-1α, playing pivotal role in regulating downstream angiogenic factors. Also, the enhanced osteoconductivity of wild endemic silk (*A. assama*) attributed due to its inherent RGD and polyalanine repeats was evidenced as opposed to the well explored *B. mori* silk. The composite matrices also favoured homing of endothelial cells through CXCR4/SDF-1 signalling, as noticed from the primitive endothelial plexus like network formed within the osteoid matrix. Further the resorbable nature was elucidated through *in vitro* experiments and witnessed *in vivo* defect regeneration, where the silk matrices integrated, eventually resorbed and facilitating the neo-osseous tissue formation. These positive insights vouch for the potential of these smart, cell-instructive, biomimetic composite silk matrices towards vascularized and resorbable bone grafts.

Limitations of the chapter

Skeletal growth in small animal defect models do not mimic holistically mimic the skeletal growth as noticed in larger vertebrates. Hence, assessing the efficacy of these developed composites on larger vertebrates would be needed to understand their remodelling kinetics. Moreover, the underlying mechanism involving resorption kinetics of Cu-doped bioactive glass and its effect on cellular fate have to be thoroughly investigated over a longer time line in large animal models.

Chapter 4

Chondroprotective and osteogenic effects of silk–based bioinks in developing 3D bioprinted osteochondral interface

This chapter describes the development of silk-based cartilage and bone bioinks towards 3D bioprinting osteochondral interface. Nano-hydroxyapatite synthesized through wet chemical route, either unmodified or doped with strontium was investigated for its role in modulating osteogenesis, chondroprotectiveness and osteoclastogenesis in the bioprinted constructs.

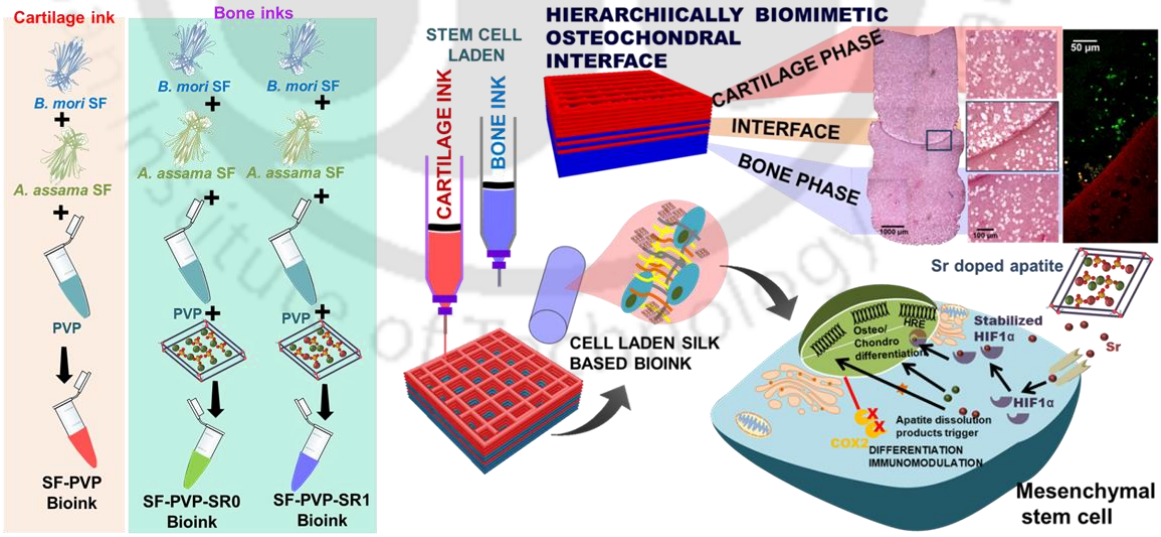

Abstract

Attributing cell instructive features and multifunctionality to biological inks (bioinks) employed for three-dimensional (3D) printing strategies is very much essential to bring about a paradigm shift in developing next generation smart intuitive 3D bioprinted constructs. Giving perspective to this notion, this chapter investigates the feasibilities in developing multifunctional silk-based cartilage and bone bioinks for recreating heterogeneous complicated tissue constructs such as the osteochondral interface. In this regard, the developed silk based bioinks exhibit shear thinning behaviour with quick thixotropic recovery (~90 % recovery) aiding in printing self-standing structures with decent print fidelity. The hydrogel network within the 3D bioprinted constructs present good permeability enabling in forming an undulating demarcation region at the bioprinted osteochondral interface. Furthermore, the cartilage and bone inks used for the microextrusion based bioprinting of osteochondral constructs facilitate the spatial maturation and differentiation of encapsulated stem cells towards osteogenic and chondrogenic lineages. The incorporation of strontium doped nano-apatites activates hypoxia inducible factor (HIF-1α) related genes, conferring proangiogenic and chondroprotective traits to the bioinks. Involvement of strontium in down regulating cyclooxygenase-2 *via* inhibiting prostaglandins (PGE2) pathway enabled anti-osteoclastic activity while favouring M2 macrophage biasness. Altogether, these findings corroborate the potential of the developed nanocomposite bioinks for fabricating clinically viable grafts for osteochondral defect repair associated with osteoporosis.

The findings of this chapter are published in a peer reviewed journal:

Moses, J. C., Saha, T., and Mandal, B. B. '*Chondroprotective and osteogenic effects of silk–based bioinks in developing 3D bioprinted osteochondral interface.*' Bioprinting, 2020, 17: e00067.

4.1 Introduction

The advent of three dimensional (3D) bioprinting approaches has enabled tissue engineers to address key drawbacks associated with conventional tissue engineering approaches such as fabrication of complex tissues, feasibility in spatial arrangement of cells or growth factors of interest with utmost precision, control over porosity for maintenance of nutritional exchange and cell survival [303]. According to an annual report (2018) by Department of Health & Human Services' (HSS, USA) Organ Procurement and Transplantation Network (OPTN), every 10 min a person is added to the donor list in need for a transplant. 3D bioprinting has the potential to mitigate this need by allowing tissue engineers to fabricate clinically viable heterogeneously distinct tissue constructs while mimicking the structural and functional integrity of tissue. In bioprinting technology, the development of suitable biological inks (bioinks) is paramount for defining its success. A wide array of biomaterials has been investigated since 1996 when the first instance of cytoscribing cells were reported [304]. Bioinks based on natural polymers such as gelatin, collagen, hyaluronic acid and synthetic polymers such as modified polyethylene glycol have been reported [303, 304]. However, some of the drawbacks concerning these conventional bioinks derived from natural extracellular matrix (ECM) based biopolymers (collagen, hyaluronic acid, fibronectin) is the cost associated in scaling up these bioinks for large scale implementation and the associated questionability surrounding crosslinkers with synthetic polymers for clinical translation. Moreover, strategies thus far have primarily focussed on developing bioinks with good flow behaviour for cell printing conducive for the encapsulated survival alone. This concerns one to look for cost effective yet multifunctional bioinks capable of attributing cell-instructive features such as control over differentiation and maturation of encapsulated cells, developed from smart intuitive biomaterials that could potentially create a paradigm shift in bioprinting technology.

Silk fibroin as a biomaterial has been in eminence in tissue engineering as an alternative biomaterial for its close likeliness to ECM components like collagen and its associated advantages involving biocompatibility, tuneable biodegradation, minimal immunogenicity and mechanical resilience [285, 305, 306]. The green aqueous processing and amenability to be processed into different formats has imparted a newer perspective of using silk fibroin as bioinks for bioprinting applications [307]. In this regard, silk fibroin based bioinks have been demonstrated to be very useful in developing self-standing structures with successful applications shown in cartilage, bone and skin tissue engineering [307]. This created an impetus

in further exploring the potential of silk in developing multifunctional bioinks by incorporating additives to enhance its biological and physico-chemical relevance in regenerating complex tissue architectures. Osteochondral interface, in particular is a heterogeneous tissue comprised of anisotropically arranged extracellular matrix and constituent cells consisting of superficial hyaline cartilage, followed by the transition interface and underlying calcified subchondral bone [308, 309]. The osteochondral interface prone for traumatic mishaps or degeneration of articular cartilage results in subsequent debridement of this intricate interface exposing the subchondral bone, leading to osteochondral defects if properly not addressed could lead to osteoarthritis. Moreover, the conditioned is worsened when such defects are associated with osteoporosis [310] where clinical treatment modalities are found severely lacking to reconstruct such defective interfacial regions. Though in previous endeavours, attempts to address these by conventional tissue engineering strategies utilising electrospinning (reported here in thesis in *Chapter-1*) [288] and freeze drying [308] techniques have been reported to develop seamless biphasic constructs, but cellularizing these constructs is an impeding task.

Hypothesis underpinning the Objective:

Consequently, the purpose of this chapter was to develop smart cell instructive bioinks, capable of exhibiting multifunctional traits addressing the shortcomings of earlier endeavours is presented. In this regard, two bioinks, namely (i) cartilage bioink and (ii) bone bioinks were obtained to recreate the intricate heterogenous osteochondral interface through microextrusion bioprinting of chondrogenically/ osteogenically primed mesenchymal stem cell laden silk based bioinks. For the silk based bioinks, we used silk blends constituted from regenerated silk fibroin solutions from two different silk varieties, *viz.* mulberry *Bombyx mori* and non-mulberry *Antheraea assama*. The rationale for using two different silk fibroins was that we found that these silk blends exhibited cumulative benefits of these two individual silk fibroins. The amino acid variability (especially the crystalline domain repeats; GAGAGS in *B. mori* and AAA(A) 5-15 in *A. assama*) confer different gross hydropathicity to these fibroins. These properties enabled in creating a conducive hydrogel network suitable for cell survival and maturation with good injectability [311]. Moreover, the presence of arginine-glycine-aspartate (RGD) tripeptide in the non-mulberry silk fibroin had profound implications in enabling chondrocyte, osteoblast maturation from our previous studies [288, 308]. In order to improve the rheological behaviour of these regenerated silk fibroin solution we included a bulking agent, polyvinylpyrrolidone (PVP) K90 (molecular weight 360,000) which has United States of America, Food and Drug Administration (FDA) approval for use in pharmaceutics.

Furthermore, to confer osteoinductive traits to the bone inks ceramic additives was incorporated, namely nano-hydroxyapatites (either unmodified or strontium doped). The potential of these strontium doped nanoapatites in downregulating osteoclast activity which is usually heightened in osteoporotic conditions, was assessed. The bioinks thus developed were then systematically characterized for their printability, rheological properties and permeability. The bioprinted osteochondral constructs were biologically validated for their multifunctionality involving osteogenesis, chondrogenesis and possible roles in mediating angiogenesis and immunomodulation.

4.2 Materials and Methods

4.2.1 Development and Optimization for Printability of Silk-based Bioinks

4.2.1.1 *Synthesis of Nano-apatite and Strontium Doped Nano-apatite*

Nano-hydroxyapatites, both doped (Sr) and undoped were synthesized based on wet ammoniacal precipitation method by modifying previously reported protocols [67]. Briefly, the calcium and phosphate precursors were taken in the stoichiometric ratio to match the Ca/P ratio of 1.67 according to the chemical reaction scheme presented below:

For unmodified nano-apatite (**SR0**):

$$\mathbf{5\ Ca(NO_3)_2.4H_2O + 3\ NH_4.H_2PO_4 \rightarrow Ca_5(PO_4)_3.OH \downarrow + 10\ NH_4NO_3 + 26\ H_2O}$$

For strontium substituted nano-apatite (**SR1**):

$$\mathbf{5\ Ca(NO_3)_2.4H_2O + 5\ Sr(NO_3)_2 + 3\ NH_4.H_2PO_4 \rightarrow 2\ (Sr_{0.5}Ca_{0.5})_5(PO_4)_3.OH \downarrow + 20\ NH_4NO_3 + 32\ H_2O}$$

Briefly, for **SR0** calcium nitrate tetrahydrate and ammonium dihydrogen phosphate were reacted under constant stirring conditions at alkaline pH (pH 10 -12) and at 60 °C for 2 h. The resulting dispersion was aged overnight and the slurry was centrifuged to get wet apatite precipitate which was repeatedly washed to remove unreacted by-products. The apatite powder was dried at 60 °C and stored in airtight containers until further use. For **SR1** a similar process was followed except along with calcium precursor, phosphate precursor and strontium precursor were also included in synthesis to obtained Sr doped nano-apatites. All chemicals were sourced from Sigma, USA unless or otherwise mentioned.

Regeneration of Silk Fibroins

The mulberry *Bombyx mori* and non-mulberry *Antheraea assama* silk fibroins were processed based on our previous protocols [288]. In brief, the mulberry silk fibroin (BMSF) was isolated from *B. mori* cocoons sourced from local silk farms, Guwahati, Assam, India. The

cocoons were degummed in boiling 0.02 M sodium carbonate for 15 min and the silk fibroin fibers thus obtained were thoroughly washed after which regenerated in 9.3 M lithium bromide. The aqueous regenerated BMSF solution was obtained after dialysis using 12 kDa cut-off membrane against MilliQ water for 48 h with intermittent changes of water. The non-mulberry silk fibroin (AASF) was isolated from the silk glands of mature 5th instar *A. assama* silkworms and regenerating them in 1 % (w/v) sodium dodecyl sulphate (SDS), followed by dialysis using 12 kDa cut-off membrane against MilliQ water with intermittent changes of water. Thus, obtained regenerated silk fibroin solutions were stored in 4 °C until further use.

4.2.1.2 *Preparation of Silk-based Bioinks*

In this study we developed two kinds of bioinks, *i.e.* (i) ***cartilage ink*** where silk blends (mixture of BMSF and AASF) along with a hydrophilic bulking agent was used; the (ii) ***bone inks*** where silk blends, bulking agent along with synthesized nano-apatites as additives served as the ingredients. The hydrophilic bulking agent used here was polyvinylpyrrolidone (PVP) K90 (molecular weight 360,000) (Sigma, USA) which has United States of America Food and Drug Administration (FDA) approval for use as binders in pharmaceutics and as plasma volume expanders. PVP stock solutions were prepared by reconstituting the same in 1X phosphate buffered saline (PBS, pH 7.4) and stored in 4 °C until use. The constituents of the bioinks used in the study are listed in **Table 4.1**.

Table 4.1 *Volume of each component in one millilitre (mL) of bioink*

Bionk	Volume from 5% (w/v) BMSF	Volume from 3% (w/v) AASF	Volume from 20% (w/v) PVP	Volume of Culture Media$^{\alpha}$	Ceramic Additive (w %)
Cartilage Ink (SF-PVP)	0.25 mL	0.25 mL	0.4 mL	0.1 mL	-
Nanocomposite Bone Ink-1 (SF-PVP-SR0)	0.25 mL	0.25 mL	0.4 mL	0.1 mL	0.5 % SR0 $^{\beta}$
Nanocomposite Bone Ink-2 (SF-PVP-SR1)	0.25 mL	0.25 mL	0.4 mL	0.1 mL	0.5 % SR1 $^{\beta}$

Note:
$^{\alpha}$*In cellular bioprinted constructs desired number of cells can be dispersed in this volume*
$^{\beta}$*The ceramic additive in case of bone-bioinks are dispersed in PVP stock solutions and sterilized by autoclaving*

The silk fibroin solutions were sterilised through UV irradiation whereas the PVP solution (in case of cartilage ink) or PVP solution with ceramic additives (in case of bone inks) were autoclaved prior to use. The ratios mentioned in **Table 4.1** can be easily scaled up to 3 mL for bioprinting which we have investigated in our studies. For crosslinking the bioink the following concentration of crosslinkers: 10 units horse radish peroxidase HRP (Sigma, USA) and 1.65 μM hydrogen peroxide H_2O_2 (Merck, India) per mL of bioink were used to initiate an enzyme mediated crosslinking [312]. After addition of all components the formulated bioinks were gelled by incubating at 37 °C for 30 min.

4.2.2 Physico-chemical Characterization of Bioinks

The synthesized nano-apatites were characterized for their dispersivity, size, morphology, conductivity, crystal parameters, elemental composition to evaluate its resemblance to native apatite crystal found in bone. Size, polydispersivity index and Zeta potential of sonicated aqueous suspensions were characterized using dynamic light scattering studies in Zetasizer NanoS (Malvern Instruments, UK). The phase identification and crystal parameters were characterized using wide angle X-ray diffraction studies. Diffraction patterns were recorded in a diffractometer (Rigaku TTRAX III, Japan) equipped with rotating 18 W anode X-ray source (λ = 1.541 Å) from diffraction angles 2θ = 10° to 60° at a step size of 0.05° per 0.5 s. For calculating the crystal parameter the following equation were used: the lattice spacing (d) = λ / 2 sinθ, using Bragg's equation; the crystallite size (D) = D = 0.9 λ / ß cosθ, using Scherrer's equation; and the crystallinity (X_c) = $(KA/ ß)^3$; where λ was the wavelength of the X-ray source (0.154 nm), KA is a constant 0.24, and ß represented the full-width half-maxima (FWHM) of the diffracting angle (θ) used [67, 313]. The morphology and elemental composition were analyzed using transmission electron microscopy equipped with energy dispersive spectrometer (JEOL 2100F, Japan).

The developed bioinks were characterized for its rheological, compositional and morphological properties. The following rheological characterizations were performed using a rheometer (MCR 302, Anton Paar, Austria), for calculation of (i) gelation point *via* dynamic oscillatory profiling (constant shear strain γ = 0.01 %, constant angular frequency ω = 10 s^{-1}); (ii) linear visco-elastic region (LVER) *via* amplitude sweep profiling (variable shear strain γ = 0.01 % to 1000 %, constant angular frequency ω = 10 s^{-1}); (iii) frequency dependant change in visco-elastic behaviour *via* frequency sweep profiling (constant shear strain γ = 2 % from LVER analysis, variable angular frequency ω = 1 rad/s to 1000 rad/s) and (iv) thixotropic nature of the inks were evaluated by a three interval thixotropic test (at alternating low shear

strain γ = 2 %, low angular frequency ω = 10 rad/s and high shear strain γ = 100 %, high angular frequency ω = 100 rad/s).

Infrared spectra of the bioinks and nano-apatites used in the study were recorded using attenuated total reflectance fourier transform infrared spectrophotometer (PerkinElmer FTIR Spectrum Two, USA) from recorded from 400 – 4000 cm^{-1} culminating from 30 scans averaged to a single spectrum with a resolution of 2 cm^{-1}. The microstructural morphological evaluation of the freeze-dried printed constructs were undertaken using field emission electron microscopy (FESEM) (∑IGMA, Carl Zeiss, Germany) using an in-lens SE detector at a working distance of 4 – 10 mm.

4.2.3 Permeability Assessment of Bionks

The permeability of the developed silk-PVP based bioinks were evaluated by encapsulating the different weight percentages (6 wt %, 9 wt % and 12 wt%) of ink hydrogels with three different molecular weight, fluorescein isothiocyanate conjugated (FITC) conjugated biomolecules. FITC-Inulin (~ 5 kDa), FITC-Dextran (~ 70 kDa) were sourced from Sigma, USA and FITC was coupled to glutathione (Sigma-Aldrich, USA) to obtain ~ 1 kDa tagged molecule following previously reported protocols [314]. 0.7 mM of the FITC-conjugated biomolecules were encapsulated in 0.5 mL of different weight percentages ink hydrogel and after gelation the release of these encapsulated FITC-biomolecules from gels in PBS (pH 7.4, 37 °C) were determined by reading the fluorescence intensity of FITC ($\lambda_{excitation}$ = 490 nm and $\lambda_{emission}$ = 525 nm) using a multiplate reader (Tecan Infinite Pro, Switzerland). The permeability of these hydrogels was correlated in terms of the diffusion properties of the different molecular weight biomolecules whose release profiles were fitted Korsmeyer-Peppas model ($M_t/M_\alpha = kt^n$), where M_t/M_α represents the cumulative fraction of drug released at time "t", with "k" denoting release rate constant and "n" denoting release exponent. The permeability was further assessed by evaluating the ability of uptake of a cell permeable dye Dil Stain (1,1'-Dioctadecyl-3,3,3',3'-Tetramethylindocarbocyanine Perchlorate) (Thermo Scientific. USA) by endothelial cell encapsulated hydrogels. Briefly, different percentages of silk hydrogels were encapsulated with 10^5 cells/mL porcine endothelial cells (isolation protocol mentioned in following sections). Post culture for 24 h, Dil stain was supplemented along with culture media (according to manufacturer's protocol) after 6 h incubation, the uptake was visualized under hydrated conditions in fluorescent microscope (EVOS XL digital microscope, Thermo Fisher Scientific, USA) with viable cells up taking the red dye.

4.2.4 *In vitro* Biological Studies on the Bioprinted Osteochondral Interfacial Constructs

Human osteosarcoma cell line MG63, murine macrophages RAW 264.7 and human monocyte cell line THP1 were obtained from National Centre for Cell Science (NCCS), Pune, India. MG63 and RAW 264.7 cells were maintained in high glucose DMEM (Gibco, Thermo Scientific Fisher, USA) supplemented with 10 % (v/v) foetal bovine serum (FBS) (Gibco, USA) and 1 X antimycotic/antibiotic solution (Gibco, USA). THP1 cells were maintained in RPMI-1640 media supplemented with 10 % (v/v) fetal bovine serum (FBS) (Gibco, USA) and 1 X antimycotic/antibiotic solution (Gibco, USA).

For bioprinting of osteochondral constructs we used adipose derived stem cells and differentiated into either osteogenic or chondrogenic lineages using our previously reported protocols [222, 305]. Porcine adipose derived mesenchymal stem cells (pADSCs) were isolated from subcutaneous fat obtained from local abattoirs in cold PBS. The subcutaneous fat was processed by separating the dermal and muscle regions and mincing the tissue finely. The minced tissue after briefly washing with cold PBS containing penicillin 100 units/mL, 100 µg/mL streptomycin and amphotericin-B 2.5 µg/mL (Gibco, USA) the tissue was digested with 0.1 % (w/v) type-IA collagenase made in incomplete DMEM (≥ 125 CDU/mg, Sigma, USA) for 2 h in 37 °C with constant mild agitation. The digested soupy consistency mixture was neutralised with equal volume DMEM media supplemented with 10 % (w/v) FBS and centrifuged at 300g for 15 min. The stromal vascular fraction (SVF) thus pelleted down was washed two times with media and plated in 90 mm Petri-dishes at a density of 5 x 10^5 cells/dish. The cells were maintained in high glucose DMEM supplemented with 10 % (v/v) FBS, 1X antibiotic/antimycotic solution, 2 mM L-glutamine (Gibco, USA) and 1 ng/mL basic fibroblast growth factor (bFGF) (Sigma, USA) and cells from passages 3 to 7 were used for experiments. To assess the differentiation potential of the isolated pADSCs they were differentiated into cardinal three lineages *via* (i) osteogenic induction media (DMEM supplemented with 5 % (v/v) FBS, 10 mM β-glycerophosphate, 100 nM dexamethasone and 0.2 mM ascorbic acid), (ii) chondrogenic induction media (DMEM supplemented with 5 % (v/v) FBS, 100 nM dexamethasone, 50 µg/mL ascorbic acid, 50 µg/mL L-proline and 1X ITS Insulin-Transferin-Selenium mix) and (iii) adipogenic induction media (DMEM supplemented with 5 % (v/v) FBS, 100 nM dexamethasone, 200 µM indomethacin and 10 ng/mL insulin). All chemicals were sourced from Sigma, USA unless or otherwise mentioned

For assessment of angiogenic potential, porcine endothelial cells (pECs) were used. pECs were isolated following our previous reports [232, 305] where porcine descending aorta obtained from local abattoirs in cold PBS were used. Briefly, small segments of aorta were cut

open and placed luminal side facing down in Petri-dishes in disassociating enzyme solution (0.1 % (w/v) type-1A collagenase made in incomplete DMEM (≥ 125 CDU/mg, Sigma, USA) for 20 min. The pECs were scrapped off using cell scraper, pelleted down and washed thrice with complete high glucose DMEM. The cells were cultured in high glucose DMEM supplemented with 5 % (v/v) FBS, 100 µg/ mL endothelial cell growth supplement from bovine neural tissue (Sigma-Aldrich, USA) and 1X antibiotic-antimycotic mix.

4.2.4.1 *Preparation of Stem Cell Laden Bioinks and Bioprinting of Osteochondral Interfacial Constructs*

Prior to bioprinting, pADSCs were primed to either osteogenic or chondrogenic lineage for 7 days in tissue culture plate in osteogenic or chondrogenic induction media. Osteogenically or chondrogenically primed pADSCs were trypsinized and resuspended in culture media volume as listed in **Table 4.1** at printing densities of 10^7 cells/mL of bone or cartilage bioinks, respectively. The scheme for bioprinting is illustrated in **Figure 4.4A**. The primed pADSCs cell suspension was gently dispersed with premixed ink suspension containing silk, PVP (either pure PVP in case of cartilage ink or PVP with dispersed ceramic additive) and crosslinkers. The cell laden bioink were transferred to 10 mL luer lock syringes and was kept in humidified 37 °C CO_2 incubator for 30 minutes for gelation. Post-gelation, the following inks (i) osteogenically primed pADSCs laden SF-PVP-SR0 bone ink, (ii) osteogenically primed pADSCs laden SF-PVP-SR1 bone ink and (iii) chondrogenically primed pADSCs laden SF-PVP cartilage ink were used to print the G-codes for geometries (designed through 3D builder software (Microsoft Corporation, USA) and STL files of the geometries sliced through Sli3r (Repetier Host software, Hot-world GmbH & Co., Germany) to get G-Codes) using using microextrusion based printer Biobot 2 (Allevi, USA) at print speeds 10 – 20 mm/s and at extrusion pressures of 13-16 psi using 21 G blunt ended stainless steel needles. The parameters of G-code are presented in **Figure A4.1** (*Appendix*).

The experimental groups consisted of osteochondral interface constructs printed through dual extrusion utilising two bioinks, (i) **ITE-1** (pADSCs laden SF-PVP-SR0 bone ink and pADSCs laden SF-PVP cartilage ink), (ii) **ITE-2** (pADSCs laden SF-PVP-SR1 bone ink and pADSCs laden SF-PVP cartilage ink). Thus, printed interfacial constructs were maintained in 1:1 ratio osteogenic:chondrogenic induction media for 14 days, with media change every 48 h. The control groups used here were monolithic structures: (i) bone group **B-SR0** (pADSCs laden SF-PVP-SR0 bone ink), (ii) bone group **B-SR1** (pADSCs laden SF-PVP-SR1 bone ink) and (iii) cartilage group (**C-SF** pADSCs laden SF-PVP cartilage ink). B-SR0 and B-SR1 (bone

groups) were maintained in osteogenic media while C-SF (cartilage group) was maintained in chondrogenic medium for 14 days, with media change every 48 h. The matured constructs were further taken forward for various biological validations.

4.2.4.2 *Live/Dead Cell Staining*

The viability of cells post printing using the three bioinks were assessed using calcein-AM and ethidium homodimer staining. The cell laden constructs were washed once with 1X PBS and incubated with 40 nM calcein-AM, 20 nM ethidium homodimer (in PBS) (Sigma, USA) for 20 min. The dye was removed and the constructs were washed twice with 1X PBS, subsequently visualized under hydrated conditions in fluorescent microscope (EVOS XL digital microscope, Thermo Fisher Scientific, USA) with viable cells appearing green and dead cells appearing red. Further to negate the autofluorescence by silk and to quantify the percentage of viable cells, we resorted to Image-J analysis. Briefly, the fluorescent image in either red or green channel was converted to 8-bit image and using *Find Maxima function* (Process> Find Maxima> Point Selection) was analysed. Noise tolerance was set at 10 for all analysed images (n =3) for each group and the number of live or dead cells appearing as green clusters or red spots, through the number of *Maxima* points obtained. Accordingly, from the ratio of live/ dead cells the cell viability percentage was calculated.

4.2.4.3 *Biochemical Assays*

Alkaline Phosphatase (ALP) Assay

ALP assay was performed to assess the osteogenic state of pADSCs within the constructs. The constructs were lysed by repeated vortexing in ice cold cell lysis buffer (20 mM Tris-HCl (Merck, India) (pH 7.5), 150 mM NaCl (Himedia, India), 5 mM $MgCl_2$ (Himedia, India), and 0.5% Triton-X100 (Sigma-Aldrich, USA). The membrane bound ALP was estimated by measuring the yellow coloured product (p-nitrophenol, λ_{max} = 405 nm) formed after hydrolysis of substrate p-nitrophenol phosphate from the active ALP enzyme present in cell lysate using a microplate reader (Tecan Infinite Pro, Switzerland). The ALP activity is presented as diethanolamine units (DEA units), where 1 DEA unit is the amount of enzyme causing hydrolysis of 1 μM of p-nitrophenol phosphate at pH 9.6 (1M diethanolamine buffer) and 25 °C. The DEA units were normalized to the DNA content present in the cell lysate to present the ALP activity as DEA units/μg DNA.

Total Collagen Content Estimation

Collagen content was estimated using Sirius red based spectrophotometric method following our previous reports [305]. Briefly, the cell laden constructs were digested in digestion buffer (0.1 M acetic acid, 0.5 M NaCl and 1 mg/mL pepsin (Sigma-Aldrich, USA) at 4 °C for 48 h. 100 µL digesate /well was dried in 96 well plate overnight, to which 100 µL Sirius red dye solution (1 mg/mL Direct red solution saturated with picric acid) was allowed to bind to collagen. The unbound dye was washed with 0.01 N HCl and the bound dye complex was resolved using 0.1 N NaOH which was read at λ_{max} = 550 nm using microplate reader. The total collagen content was estimated from a standard curve obtained from type-I rat tail collagen and the same is presented after normalization with DNA content as µg collagen/ µg DNA.

Sulphated Glycosaminoglycan (sGAG) Content

sGAG estimation was carried out using 1,9-dimethymethyleneblue (DMMB) assay following our previous reports [288]. The cell laden constructs were digested in digestion buffer (5 mM L-cysteine, 100 mM Na_2HPO4, 5 mM EDTA and 125 µg/mL papain from papaya latex, Sigma, USA) at 60 °C for 16 h. The sGAG content from the digesate was measured using DMMB (Sigma, USA) taking reference of chondroitin sulphate from bovine trachea (Sigma, USA), by reading at λ_{max} = 525 nm using multiplate reader and the same is presented after normalization with DNA content as µg sGAG/ µg DNA.

Total DNA Content Estimation

DNA estimation was performed using fluorospectrometric method using Quant-iT picogreen double stranded DNA assay kit (Thermo Fisher Scientific, USA) following manufacturer's protocol. The cell lysates after digestion or lysis were mixed with picogreen fluorescent dye and fluorescence intensity at $\lambda_{excitation}$ = 480 nm and $\lambda_{emission}$ = 525 nm was read using multiplate reader. The DNA content was estimated from a standard curve plotted using double stranded λ DNA and the same is presented as µg DNA

4.2.4.4 *Western Blotting*

Cell laden constructs were lysed using ice cold cell lysis buffer (50 mM Tris HCl, pH 8, 150 mM NaCl, 1% NP-40, 0.5 % sodium deoxycholate, 0.1 % SDS, 1 mM phenylmethylsulfonyl fluoride, 10 mM sodium fluoride, 1 mM ethylene glycol-bis(β-aminoethyl ether)-N,N,N′,N′-tetraacetic acid) *via* sonication (20 % amplitude, for 12 s with 3 s ON/ 3 s OFF cycles, Sonic Vibra-cell, Sonics & Materials, Inc. USA). Cell lysate was

centrifuged and supernatant was estimated for protein concentration using Bradford's reagent (Sigma, USA). 50 µg of the protein was resolved in reducing conditions in 10 % polyacrylamide separating gel and transferred *via* wet transfer onto 0.2 µm poly(vinylidene fluoride) (PVDF) membranes. The immunoblots were probed for the expression of proteins of interest using the following primary antibodies: mouse monoclonal antibody against human hypoxia inducible factor HIF-1α (Abcam, UK; 1:200 dilutions), rabbit monoclonal against cyclooxygenase-2 COX-2 (Abcam, UK; 1:1000 dilutions), mouse monoclonal against collagen-10 COL-10 (Abcam, UK; 1:1000 dilutions), rabbit polyclonal to collagen-2 COL-2 (Abcam, UK, 1:10000 dilutions), while mouse monoclonal against GAPDH, (Abcam, UK, 1:1000 dilutions) was used as endogenous house-keeping and loading control. The respective primary antibodies were detected with HRP conjugated antibodies either secondary goat anti-mouse IgG (Abcam, UK, 1:10000 dilutions) or secondary goat anti-rabbit IgG (Abcam, UK, 1:10000 dilutions) using enhanced chemiluminescence method (Clarity™ Western ECL Kit, Bio-rad laboratories, USA) documented by Gel Doc XR+ system, Bio-rad laboratories, USA. The densitometric profiling was done using Image-J software (NIH, USA) and the relative expression levels were normalized with respective sample's GAPDH intensity to identify upregulation or downregulation.

4.2.4.5 *Gene Expression Studies*

The cell laden bioprinted constructs were disintegrated in Tri® reagent (Sigma, USA) keeping the microfuge tubes in ice and the RNA was isolated following acidic chloroform-phenol extraction [315]. 500 ng of total RNA was reverse transcribed using high capacity reverse transcription kit (Applied Biosystems, Invitrogen, USA) in a thermal cycler (Veriti PCR, Applied Biosystem, USA). The relative gene expression of genes was quantified using Power SYBR PCR master mix (Applied Biosystems, Invitrogen, USA) in real-time PCR (Applied Biosystems 7500, Thermo Fisher Scientific, USA). The relative gene expression of osteogenic genes: core binding factor alpha-1 (*CBFA1*), podoplanin (*PDPN*) and chondrogenic genes: SRY-(sex determining region)-box-9 (*SOX9*), aggrecan (*ACAN*) were calculated with reference to endogenous house-keeping gene control glyceraldehyde 3-phsophate dehydrogenase (*GAPDH*) using the primers for cDNA amplification listed in **Table 4.2** post-confirming the single amplicons presence using melt-curves. The relative gene expression levels were calculated based on $-\Delta C_T$ method Relative expression, $R = 2^{-(C_{T\,(GOI)} - C_{T\,(GAPDH)})}$, where GOI is the gene of interest.

Table 4.2 *Primer sequences used in the study for gene expression studies*

Gene	Sequence	T_m (°C)
Human *GAPDH*	**F** 5′-GACCTGACCTGCCGTCTA-3′ **R** 5′-GTTGCTGTAGCCAAATTCGTT-3′	60
Human *CTSK*	**F** 5′- CAGTGAAGAGGTGGTTCAGA-3′ **R** 5′- CAGTGAAGAGGTGGTTCAGA-3′	60
Human *CA2*	**F** 5′- CTGAAGCCCCTGTCTGTTTC-3′ **R** 5′- TCCATCAAGTGAACCCCAGT-3′	60
Human *NFATc*	**F** 5′- AGAATTCGGCTTGCACAGG-3′ **R** 5′- CTCTGGTGGAGAAGCAGAGC-3′	60
Porcine *GAPDH*	**F** 5′-TCGGAGTGAACGGATTTGG-3′ **R** 5′-CCAGAGTTAAAAGCAGCCCT-3′	60
Porcine *ACAN*	**F** 5′-CCCAACCAGCCTGACAACTT-3′ **R** 5′-CCTTCTCGTGCCAGATCATCA-3′	60
Porcine *SOX9*	**F** 5′-TTCCGCGACGTGGACAT-3′ **R** 5′-GGCGGCAGGTACTGGTCAAACTC-3′	60
Porcine *CBFA1*	**F** 5′- GAGGAACCGTTTCAGCTTACTG-3′ **R** 5′- CGTTAACCAATGGCACGAG-3′	60
Porcine *PDPN*	**F** 5′- ACTGTAGGAAGCACAACGCA-3′ **R** 5′- CTCTTCATCTCCTTTATCGTGGG-3′	60
Porcine *PPARg2*	**F** 5′- GCGCCCTGGCAAAGCACT-3′ **R** 5′-TCCACGGAGCGAAACTGACAC-3′	60

4.2.4.6 *Immunohistochemistry*

The bioprinted constructs after 14 days culture was fixed in neutral buffered formalin (Sigma, USA) and were subjected to ethanol/xylene (dehydration/clarification) process, embedded in paraffin wax, following which the embedded constructs were sectioned using manual rotary microtome (Leica Biosystems, Germany). 8 μm sections were obtained which used for histological evaluation using hematoxylin and eosin (H&E) staining, immunostaining probed for presence of aggrecan, collagen-1. collagen-2 and collagen-10. The following primary antibodies: rabbit polyclonal to aggrecan (Abcam, UK; 1:500 dilutions), primary mouse monoclonal to collagen-1 (Abcam, UK; 1:1000 dilutions), rabbit polyclonal to collagen-2 COL-2 (Abcam, UK, 1:200 dilutions), mouse monoclonal against collagen-10 COL-10

(Abcam, UK; 1:1000 dilutions); detected through appropriate secondary antibodies: anti-mouse IgG-FITC (Sigma, USA; 1:200 dilutions) or anti-rabbit IgG-DyLight594 (Abcam, UK; 1:400 dilutions). The images were taken using fluorescent microscope (EVOS XL digital microscope, Thermo Fisher Scientific, USA) and representative images are presented.

4.2.4.7 *Angiogenic Potential Assessment Through Tube Formation Assay*

To assess the angiogenic potential of bioprinted constructs at day-7, conditioned media from cell laden 3D printed constructs were collected and used for tube formation assay following previously reported method [316]. Briefly, pECs in culture were serum starved overnight prior to the experiment. Collagen-I (rat tail) (Gibco, USA) was used as the matrix to study the angiogenic potential and collagen gel were formed following the manufacturer's protocol. pECs were trypsinized and suspended in cell density of 3 x 10^5 per mL of collagen gel, thereafter 100 µL of cell seeded gel were added to each well of a 96 well plate. To the gelled matrix endothelial culture media mixed in the ratio of 1:1 with conditioned media were added and the *in vitro* tube formation was assessed after 24 h by calcein-AM staining as mentioned earlier. The fluorescent images obtained were analysed using Image-J to calculate the tube length and representative fluorescent images are presented.

4.2.4.8 *Assessment of Osteoclastic Activity*

The effect of synthesized apatites (SR0 and SR1) on the osteoclastic activity was assessed by differentiating human monocytes (THP1) into osteoclasts in osteoclast induction media (RPMI1640 media supplemented with 10 % (v/v) foetal bovine serum, 25 ng/mL recombinant human sRANKL (Gibco, USA), 200 ng/mL PMA (phorbol 12-myristate 13-acetate) following our previous reports [305]. 5 x 10^4 THP1 cells/well in 24 well plate were seeded with osteoclast induction media, after 36 h the following concentration: 5 µg/mL, 50 µg/mL and 500 µg/mL of SR0, SR1 were dispersed in osteoclast induction media and cultured for 14 days. After 14 days the state of osteoclast activity was assessed. Untreated controls with cells grown in tissue culture plate with osteoclast induction media were also used for comparison.

Gene expression studies were carried out following the procedures mentioned earlier for primer sequences mentioned in **Table 4.2**. Relative gene expression levels within the group were calculated with reference to endogenous house-keeping control GAPDH for osteoclast genes: nuclear factor of activated T-cells (*NFATc*), cathepsin-K (*CTSK*) and carbonic anhydrase-2 (*CA2*). The relative expression levels were normalized with reference to untreated controls to assess the upregulation (>1 fold) or downregulation (<1 fold) of genes of interest

used in the study. The relative gene expression levels were calculated based on $-\Delta\Delta C_T$ method, *Fold induction or change* $F = 2^{-[(C_{T\,(GOI)} - C_{T\,(GAPDH)})_{Treated\ group} - (C_{T\,(GOI)} - C_{T\,(GAPDH)})_{Untreated\ group}]}$ where GOI is the gene of interest.

The multinucleated osteoclasts formed were identified using rhodamine-phalloidin staining and tartrate resistant acid phosphatase (TRAP) staining. The cultured cells after 14 days were washed with 1X PBS thrice to remove unbound apatites and the cells were fixed with neutral buffered formalin. The fixed cells were stained with 0.165 µM rhodamine-phalloidin dye (Sigma, USA) and counterstained with 1 µg/mL Hoechst-33342 (Sigma, USA). Similarly, the fixed cells were stained for TRAP using leucocyte acid phosphatase (TRAP) assay kit (Sigma-Aldrich, USA) following the manufacturer's protocol. The activated multinucleated osteoclasts express purplish to dark brown stained TRAP crystals in their cytoplasm.

The expression of matrix-mettaloproteinase-2 was assessed by gelatin zymography following our previous reports [305]. At day-14, cultured cells were serum starved for 12 h and RPMI1640 media (without FBS) was added and incubated for 24 h. The conditioned media was collected and protein concentration was estimated by Bradford's reagent (Sigma, USA). 50 µg of protein was resolved in 10 % polyacrylamide gel with 0.1 % (wt/wt) gelatin and subsequently incubated in buffer containing 50 mM Tris-HCl, pH 7.5, 1 % (w/v) triton X-100 (Sigma-Aldrich, USA), 5 mM $CaCl_2$ (Sigma-Aldrich, USA) and 1 mM $ZnC_4H_6O_4$ (Sigma-Aldrich, USA). The gels were stained with Coomassie Brilliant Blue R-250, where the MMP-2 activity was visualized as gelatinolytic clear bands seen in blue background documented through Gel Doc XR+ system, Bio-rad laboratories, USA. The densiometric profiling was done using Image-J software (NIH, USA).

4.2.4.9 *In vitro Immunocompatibility Assessment of Bioinks*

To assess the immunocompatibility of developed bioinks, murine macrophages RAW 264.7 were used following our previous reports [288, 305]. In brief, 10^5 cells/well were seeded in 24 well plate and cultured for 24 h. After which the media was changed and supplemented with fresh media along with 200 µL of bioink/well to elicit the macrophages. 24 h post-treatment, conditioned media were collected and tested for interleukin-1β presence using an IL-1β ELISA kit and nitric oxide (NO) produced using Griess reagent kit, following the manufacturer's protocol (Invitrogen, USA). Non-treatment controls (NTC) as negative control and 500 ng lipopolysaccharides (LPS) from *Escherichia coli* (Sigma, USA) treated cells served as positive control.

4.2.5 *In vivo* Immunocompatibility Assessment of Bioinks

In order to assess the immunocompatibility furthermore, *in vivo* macrophage response was evaluated by subcutaneous injection of bioinks in Sprague Dawley (SD) rats. The protocols for animal handling were reviewed and sanctioned by the Institutional Animal Ethical Committee (IAEC), National Institute of Pharmaceutical Education and Research (NIPER), Guwahati, India. Twelve healthy female SD rats, each weighing 170-120 g (45 – 58 days old) procured from National Institute of Nutrition, Hyderabad, India and housed/acclimatized in separate cages with *ad libitum* diet (regulated temperature and light cycles). At the day of surgery, the animals were segregated randomly into 4 groups (each group with three animals) and anaesthetized with 80 mg/kg body weight xylazine hydrochloride (Xylaxin®, Indian Immunologicals, India) and 100 mg/kg body weight ketamine hydrochloride (Ketalar®, Parke-Davis, India), intraperitoneally. Following which the hair surrounding the lateral side of thoraco-lumbar region was clipped and removed, wiped with 70 % ethanol to sterilise the area. A slender 5 mm incision was made to create a subcutaneous pocket after which 200 µL of bioinks (SF-PVP-SR0 ***n* = *6***; or SF-PVP-SR1 ***n* = *6***) per animal was injected using fine insulin syringe and the pocket was closed in place *via* surgical staples. The animals were closely monitored with superfacial wound area cleaned every day with 10 % povidone iodine and draped. At day-7 and day-14, three animals from each group were sacrificed by cervical dislocation and the tissue containing the implanted samples were retrieved and taken for histological processing.

Post-processing, 10 µm sections were probed for presence of CD-68 and CD-206 macrophage markers using primary antibodies: mouse monoclonal to CD-68 (Abcam, UK; 1:400 dilutions) and rabbit polyclonal to mannose receptor (CD-206) (Abcam, UK; 1:1000 dilutions). The primary antibodies were detected through HRP-conjugated anti-mouse/rabbit IgG and colorimetric product developed from peroxidase substrate 3,3-diaminobenzidine (DAB) following manufacturer's protocol through Vectastain elite universal ABC kit (Vector Labs, USA) and counter stained with Gill's hematoxylin. The immunohistochemical (IHC) analysis were perfomed following our previous reports [223] using Image-J IHC profiler plug-in. The stained bright field images were deconvuluted to decouple the DAB stain which was later assigned pixel intensities ranging from 0 to 255 and a histogram profiling was obtained which provided a colour scale (high positive, positive and negative). The images were analysed from each sampling group and representative images are presented.

4.2.6 Statistical Analysis

All the experiments were performed in triplicates (unless or otherwise mentioned) and the results are presented as mean ± standard deviation. The data of results from each sampling were analysed through one-way analysis of variance (ANOVA) *via* Tukey's test (Origin 2018b, OriginLabs, USA) and analysis if fulfilling the null hypothesis at $p \leq 0.05$ was considered as statistically significant, while at $p \leq 0.01$ as highly significant.

4.3 Results and Discussion

As the first building blocks needed in developing the bone bioinks, the ceramic additives to be incorporated in the bioinks were synthesized. Hydroxyapatites, a class of calcium phosphate ceramics have been highly investigated in bone tissue engineering application, due to their closeness to the bone's ceramic constituent. We explored the feasibilities of substituting the Ca lattice points with Sr substitution replacements, because of its known therapeutic consequences in mediating osteogenesis and downregulating osteoclast activity [317, 318].

4.3.1 *Hierarchically Biomimetic Nature of Synthesized Nano-apatites and Strontium Substituted Nano-apatites*

Naturally in the bone the mineral homeostasis is maintained due to substitutions in its three sub lattices of apatites ($M_{10}(ZO_4)_6X_2$), i.e. (M = Ca, Sr, Pb, Na, K etc.; Z = P, CO_3, V, As, Cr, B, etc.; and X = OH, CO_3, Br, Cl, BO_2), thus achieving the regulation for mineral homeostasis [319]. Utilising this notion we introduced Sr substitution in hydroxyapatite ($(Sr_{0.5}Ca_{0.5})_5(PO4)_3.OH$) *via* wet chemical ammoniacal precipitation method, where Sr^{2+} underwent substitutions with Ca^{2+} cations in the apatite hexagonal crystal lattice structure. The synthesized nano-apatites Sr doped (SR1) and unmodified (SR0) along with control hydroxyapatite (HA) (Sigma-Aldrich, USA) were validated with wide-angle X-ray diffraction studies where characteristic peaks (2θ) corresponding to the signature miller indices were observed (**Figure 4.1A**). The peaks 2θ = 31.86°, 32.20° and 32.90° corresponding to miller indices 211, 112, 300 in SR1 was slightly broader in comparison to SR0 and HA indicating that SR1 was less crystalline. We further calculated the crystal parameters such as crystallinity (X_c), *d* spacing and crystallite size D (**Table 4.3**) and found that Sr substitution reduced the crystallinity and increased the *d* spacing along the 002 c-axis and 300 a-axis planes. Moreover, the crystallite size (D) was determined along '*c'* and '*a'* axis and observed to be around 25-50 nm which is the same range as noticed in the native bone's apatite, thereby bearing greater

likelihood to it. Morphological analysis carried out using FETEM also corroborated this hierarchical biomimicry wherein rod-shaped crystals of individual crystallite size ~ 50 nm were noticed (**Figure 4.1 Bi-ii, 1 Ci-ii**).

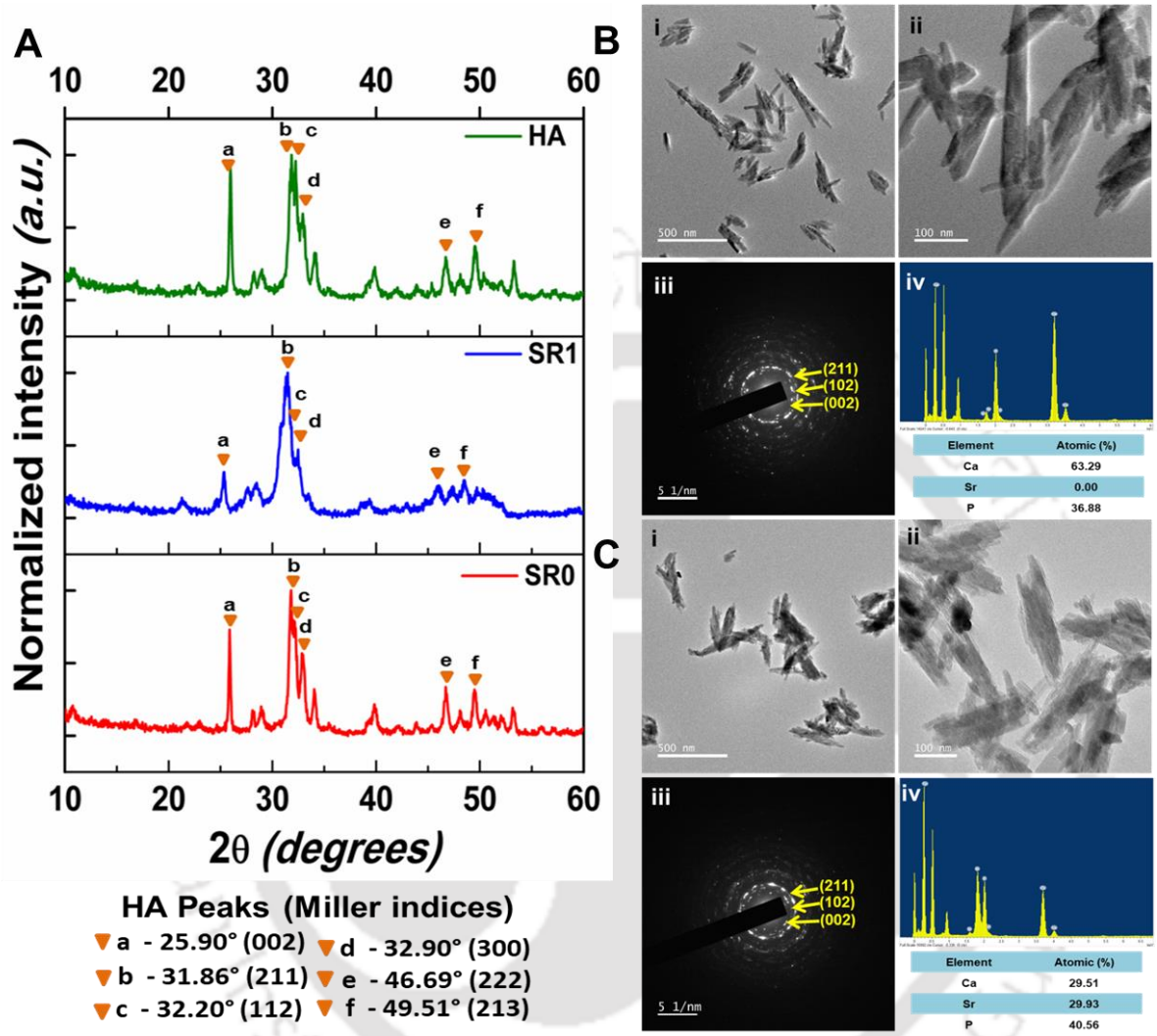

Figure 4.1. ***Hierarchically biomimetic nature of synthesized nano-apatites – physicochemical characterizations.*** *A) Wide angle X-ray diffraction analysis with corresponding 2θ (degrees) for hydroxyapatite (HA) peaks represented, followed with their miller indices in brackets: a – 25.90° (002), b – 31.86° (211), c – 32.20° (112), d – 32.90° (300), e – 46.69° (222), f – 49.51° (213); Field emission transmission electron microscopy analysis of synthesized hydroxyapatites B) i-ii SR0 apatite, iii) Selected area energy diffraction (SAED) pattern, iv) elemental analysis to confirm stoichiometry of apatite; C) i-ii SR0 apatite, iii) SAED pattern, iv) elemental analysis to confirm stoichiometry of apatite.*

Table 4.3. *Crystal parameters of synthesized hydroxyapatites*

Sample	Crystallinity	Crystal Plane (002)		Crystal Plane (300)	
	(X_C) (%)	***d* Spacing *(nm)***	**Crystallite Size (D) Along c-axis**	***d* Spacing *(nm)***	**Crystallite Size (D) Along a-axis**
HA	65.79402	0.20369	46.75786	0.154343	30.60398
SR0	63.05164	0.224185	52.13054	0.154022	37.88596
SR1	42.23993	0.785786	25.42422	0.176133	24.93892

The selected area energy diffraction (SAED) patterns also confirmed the presence of 211, 102 and 002 planes of apatite crystal with 211 plane appearing slightly diffused in SR1 than SR0 (**Figure 4.1 Biii, Ciii**) confirming its relative amorphous nature. Elemental analysis also confirmed the molar stoichiometry Ca/P ratio of ~1.6 in SR0 and SR1 whereas the experimental Sr doping values also matched with the theoretical values Ca:Sr:P (0.3:0.3:0.4) in atomic weight ratios approximately (**Figure 4.1 Biv, Civ**). Furthermore, we looked into the dispersity and Zeta potential (ζ) of aqueous dispersions of apatites (**Table A4.1**, *Appendix***)** by dynamic light scattering experiments. The hydrodynamic radius of nano-apatite agglomerates in dispersion were found to be ~800 nm, a range consistent enough to be printed and also appropriate for not invoking immune response. The incorporation of Sr however improved the polydispersity index (PDI), Zeta potential (ζ) and conductivity of the apatite whereby demonstrating that SR1 could form much stable suspensions ideal for printing applications, where sedimentation of additives always pose a great hindrance for bioinks. The synthesized apatites were hierarchically similar to the native bone's apatite in size and morphology. The hydrodynamic radius (~800 nm) of the dispersion of the apatite agglomerates were found to be appropriate for bioprinting without harming the encapsulated cells. It has also been reported that particle size and shape of apatites are few of the important factors that influence inflammatory responses, where smaller particle < 500 nm enhanced the NLPR3 inflammasome while larger particle ~1 μm did not evoke any response [320]. The introduction of Sr also decreased the crystallinity of the apatites. Crystalline apatites have very poor dissolution rates (K_d) of the order 10^{-40} to 10^{-59} [31, 321] and addressing it becomes essential, our method here shows SR1 has crystallinity % ~ 40 which desirably would have better resorption rates. It was noticed the workable range of ceramic additives in the bone bioink was found to be in range 0.1 to 0.75 w%, anything above clogged the 21 G needle used in the study.

4.3.2 *Silk-based Bioinks Exhibit Shear Thinning Behaviour and Non-Fickian Transport*

The bioink composition listed in **Table 4.1** consists of 4 (w/v) % SF, 8 (w/v) % PVP, culminating in total mass percentage of 12 % (w/v) which was found to be working optimum for bioprinting applications reported here. A range of concentrations for SF-PVP inks (**Figure 4.2A**) was assessed for printability at print speeds 10 – 20 mm/s and at extrusion pressures of 13-16 psi using 21 G blunt ended stainless-steel needles to identify ink concentrations with suitable viscosities for printing. However, it was found the ink was printable only in the ranges of mass percentages of 8 – 12 % (w/v) exhibiting shear thinning nature (**Figure 4.2B**) which is ideal for any good bioink. Concentrations of inks, anything lower resulted in lateral dispersion of the ink owing to lack of adequate viscosity of ink or anything above resulted in rigid ink with poor flow properties. Workable range of ceramic additives was found to be in range 0.1 to 0.75 wt%, anything above clogged the 21 G needle used in the study.

Factors such as permeability and associated diffusion parameters are poorly understood in hydrogel-based microenvironments, especially in bioprinted constructs which mostly rely on printing cell encapsulated crosslinked hydrogels. Better survival and extracellular matrix (ECM) turnover in chondrocytes were facilitated in hydrogel matrices with better permeability [322]. The permeability of gels was analysed in ranges 6 – 12 % (wt/v), close to our printable bioink gel's range to have an idea whether increase in concentration affected the permeability. In order to evaluate the diffusion properties, three different molecular weight, fluorescein isothiocyanate conjugated (FITC) conjugated biomolecules: FITC-glutathione (FITC-GSH ~1 kDa, FITC-Inulin ~ 5 kDa, FITC-Dextran ~ 70 kDa) was encapsulated in different weight percentages (6 w %, 9 w % and 12 w%) of ink hydrogels. The release profiles (**Figure 4.2 C,D,E i**) were correlated with their diffusion mechanism by fitting the data in Korsmeyer-Peppas model ($M_t/M_\alpha = kt^n$), where M_t/M_α represents the cumulative fraction of biomolecule released at time "t", with "k" denoting release rate constant and "n" denoting release exponent (**Figure 4.2 C,D,E ii**). All the gels exhibited a non-Fickian diffusion behaviour and the diffusion coefficient (D_e) was calculated by plotting the M_t/M_α against square of root of time "t" and the resulting slope yielded the D_e [322]. Concentration dependent release of different weight biomolecules were observed, where 70 kDa FITC-dextran's cumulative release was relatively retarded in comparison to ~1 kDa FITC-GSH (~90 % release vs. ~ 15 % release at 60 h, for 6% gel). Similarly, when comparing the low percentage gels (6%) had a better release kinetics in comparison to higher percentage gels (8 %, 12 %) owing to the micro-nano structures resulting in lesser pore sizes, albeit not significantly different between the gels.

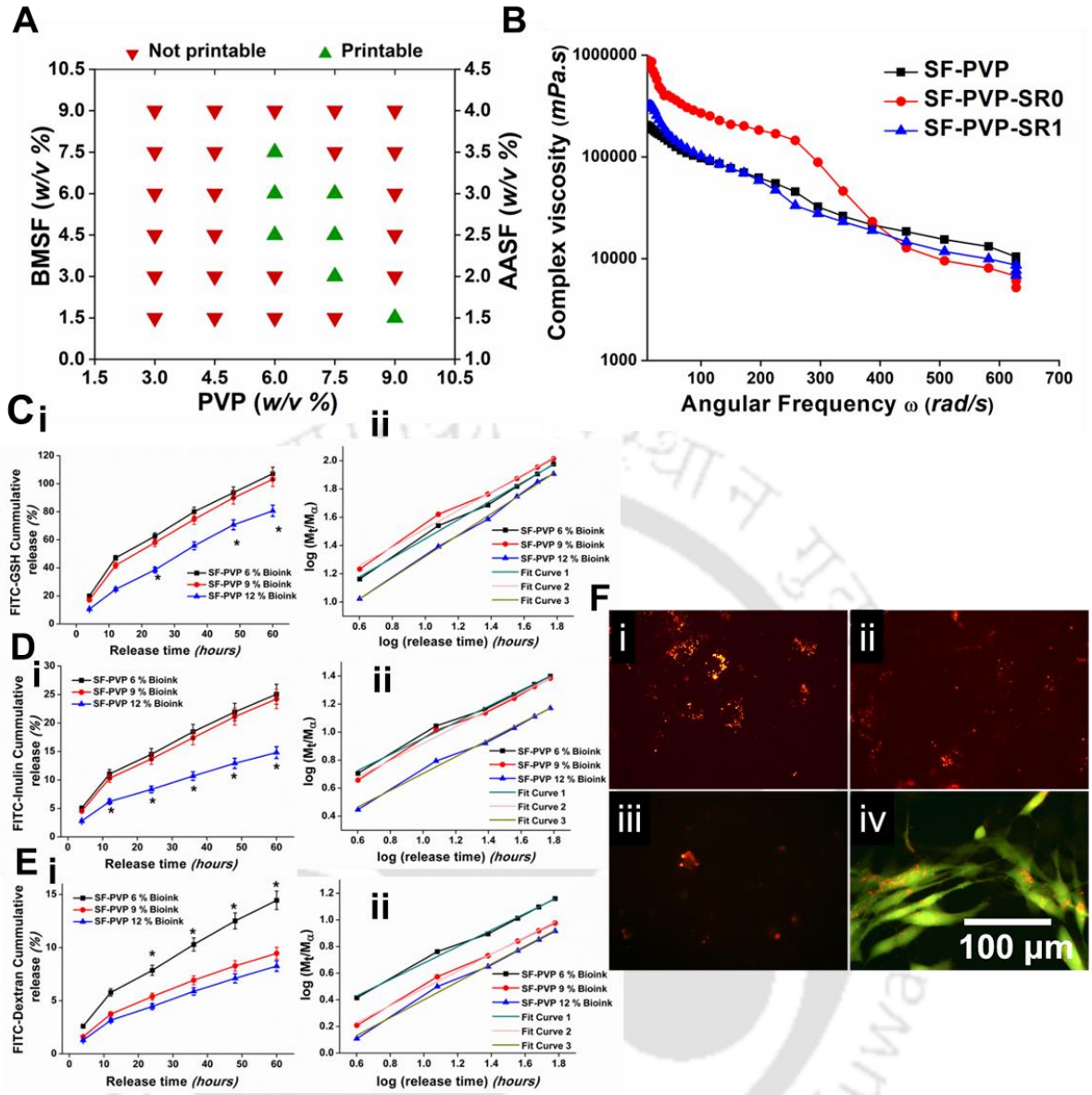

Figure 4.2. ***Characterization of developed silk-based nanocomposite bioinks.*** *A) Printabilility chart for the bioink; B) Shear thinning effect of the bioinks; complex viscosity vs. increasing angular frequency; Diffusional studies using FITC conjugated biomolecules, C) FITC-Glutathione (GSH) (~1kDa), D) FITC-Inulin (~5 kDa), E) FITC-Dextran (~70 kDa) i) cumulative percentage release and ii) respective Korsmeyer-Peppas model fitting; F) Dil C_{18} stain uptake by porcine endothelial cells to study diffusional properties on i) 6% ii) 9%, iii) 12% bioink and iv) on tissue culture plate.*

The D_e of all the gels was found to be of the order ~3 to 5 x 10^{-11} m^2/s which was close to range of few reported hyaluronic acid based hydrogels where good viability of encapsulated chondrocytes was reported earlier [322]. Similar diffusion kinetics were also noticed in polyethylene glycol based hydrogels which reported better survival of encapsulated pancreatic islet cells and exchange of secreted of insulin into outer environment from the hydrogel matrix

[323]. Moreover, the permeability of the hydrogels was ascertained through uptake of $DilC_{18}$ dye by encapsulated porcine endothelial cells within these hydrogels (**Figure 4.2F i-iii**) advocating for its good diffusion properties. Endothelial cells were used in the study because they are very susceptible to stress (nutritional diffusion constraints) and also angiogenesis is very much essential for regulating osteogenic cell fate. The bioink's (reported here) hydrogel network provided optimal diffusion properties supporting the endothelial cell survival which is supported by the uptake of $DilC_{18}$ dye by live endothelial cells within hydrogel (**Figure 4.2F i-iii)**, seen in reference with endothelial cells grown in tissue culture plate (**Figure 4.2F iv**).

4.3.3 *Silk-based Nanocomposite Bioinks Exhibit Good Flow Behaviour with Faster Thixotropic Recovery and Demonstrates Decent Shape Fidelity for Bioprinting*

For bioprinting applications, the indispensable entity is the bioink which must possess two important attributes: (i) good printability and (ii) confer biocompatibility for encapsulated cells *via* its bioactive ingredients applying cytocompatible crosslinking strategies. In the current study three bioinks were deeveloped: a cartilage bioink (**SF-PVP**) and two bone bioinks (with SF-PVP ink with either SR0 or SR1 ceramic additive), (i) **SF-PVP-SR0**, (ii) **SF-PVP-SR1**. These bioinks were crosslinked through an enzyme mediated crosslinking which has been reported earlier by us and other groups to be cytocompatible, with relatively inconceivable toxicity and having no effect on the phenotypic cellular fate [312, 324].

The printability of the developed cell-free crosslinked bioinks was assessed through rheological characterizations where the storage modulus (G') associated with elastic behaviour and loss modulus (G'') associated with viscous behaviour of hydrogel ink were recorded at different testing conditions. The gels exhibited shear thinning properties (**Figure 4.2B**) showing good extrusion at amenable extruding pressures (13 – 20 psi) and capable of printing free self-standing constructs, fulfilling the criteria of inks that print < 3 bar which ensures better cell survival post-printing [325]. Gelation time required for the crosslinking of the inks were determined through time sweep analysis through dynamic oscillatory tests at shear strain γ = 0.01% and angular frequency $\omega = 10\ s^{-1}$, where initial sol state of the inks was characterized by a phase where G'' was greater than G' (**Figure 4.3 A**). At the gelation point, where the sol-gel transition is prominent a classical G' and G'' crossover is witnessed, which is recorded as the time required for complete crosslinking to occur. All the bioinks used in the study gelled approximately around 30 min, where with the addition of ceramic additives SR0 or SR1 in the silk ink (SF-PVP) resulted in slightly prolonged gelation time in SF-PVP-SR0 and SF-PVP-

SR1 bioinks possibly due to a crowding effect which may have retarded the enzyme sites inaccessible for crosslinking. Elastic behaviour of the developed gels was assessed by performing an amplitude sweep at constant angular frequency ω = 10 s^{-1} and increasing shear strain γ 0.01% to 1000%. At lower shear strains the elastic (G' > G'') nature was evident but at higher shear strains the elastic nature was lost and a viscous nature creeped in as G'' > G' assuring in the shear thinning effect associated with viscous behaviour of hydrogel ink (**Figure 4.3B**). Linear viscoelastic range (LVER) were thus calculated for the inks and found to be decent, lying in the range 20-100 %, the workable range before it totally deforms due to applied strain. The calculated rheological parameters of the inks are tabulated in **Table A4.2** (*Appendix*). Similarly, frequency sweep was performed by keeping constant shear strain γ 2% (set from LVER data) and increasing angular frequency ω = 1 rad.s^{-1} and to 1000 rad.s^{-1}, where the developed inks resisted the angular distortion beyond 100 rad.s^{-1} (**Figure 4.3 C**) substantiating the robustness of the crosslinked hydrogel network. Furthermore, thixotropic nature of the inks was also evaluated (**Figure 4.3 D**) and the inks were found to regain their nature rapidly post deformation due to shear thinning effect in the LVER region of strain of 100 %, indicating post extrusion the inks would not tend to laterally diffuse.

Compositional features of crosslinked ink were confirmed by fourier-transform infrared (FTIR) spectroscopy. Characteristic peaks for the inks relating to their functional groups were observed at 1650 - 1600 cm^{-1} indicating presence of amide-I band denoting C=H stretching, 1550- 1500 cm^{-1} denoting C=N stretching of amide-II band and 1260 - 1210 cm^{-1} implying amide-III band corresponding to C-N stretching, along with characteristic hydroxyapatite peaks. Bands denoted by a, b, c and d indicated characteristic peaks of hydroxyapatite at 1032 cm^{-1}, 962 cm^{-1}, 574 cm^{-1} and 561 cm^{-1} respectively depicting asymmetric and symmetric stretching of P-O and bending of O-P-O as shown in **Figure 4.3 E**. Moreover, in the crosslinked silk inks a blue-shift in amide-I, amide-II and amide-III peaks was observed in comparison to silk solution, indicating that a β-sheet induction due to enzyme mediated crosslinking (**Figure A4.2** (*Appendix*). We further deconvoluted the amide-I spectra and found that an increase in β-sheet content was evident due to the shift, possibly because of di-tyrosine bridges formed due to horse radish peroxidase (HRP) enzyme mediated crosslinking of tyrosine residues present in the silk fibroins, aided by hydrogen peroxide forming an oxyferryl centre at the HRP active site catalysing the covalent bond formation [312].

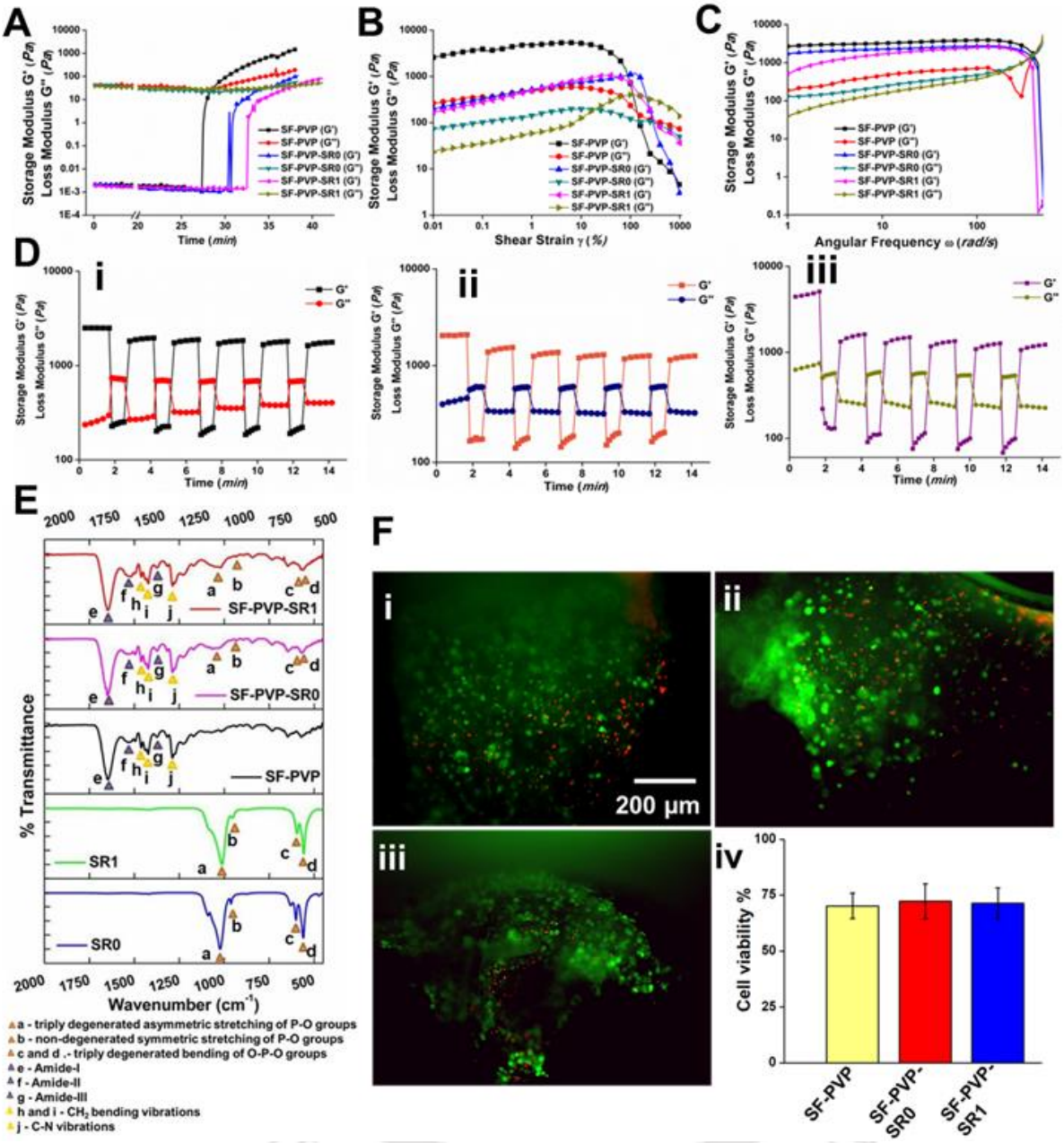

Figure 4.3. ***Characterization of developed nanocomposite silk based bioinks and its bioprinted constructs.*** *Rheological studies on bioink; A) gelation time profile, B) amplitude sweep profile, C) frequency sweep profile and D) thixotropic measurement at alternating low and high oscillating shear and angular frequency for i) SF-PVP, ii) SF-PVP-SR0 and iii) SF-PVP-SR1 bioinks; E) fourier infrared spectrographs of synthesized unmodified (SR0), strontium doped hydroxyapatite (SR1) and different bioinks used in the study; F) Cell viability assessment using calcein-AM (live cell – green clusters) / ethidium homodimer (dead cell – red spots) staining post-printing using, i) SF-PVP, ii) SF-PVP-SR0, iii) SF-PVP-SR1 bioinks and iv) the cell viability percentage calculated using Image-J analysis.*

Moreover, this also confirms that the bulking agent, PVP which improved the rheological behaviour of the ink did not hinder the crosslinking but rather formed

interpenetrating network with the crosslinked silk network. The presence of CH_2 vibrations at 1460 cm^{-1}, 1416 cm^{-1} and C-N vibrations at 1290 cm^{-1} noticed in the infrared spectra also corroborate the same. The cell viability post-printing and the shaped fidelity of the developed inks were tested. For this purpose, porcine adipose derived stem cells (pADSCs) either differentiating towards chondrogenic lineage (in SF-PVP ink) or osteogenic lineage (in SF-PVP-SR0 or SF-PVP-SR1 inks) were bioprinted in different infill patterns as shown in **Figure A4.1**, (*Appendix*) **i)** grid infill or **ii)** rectilinear infill for constructs of 10 mm x 10 mm x 5 mm in size. Cell densities as low as 6 million cells to 20 million cells per mL bioink were used for printing with viabilities maintained up to ~ 70 % post printing (**Figure 4.3F**) for the bioprinted constructs after 14 days as seen from the calcein-AM based live cell imaging. Morphological analysis of freeze-dried scaffolds also exhibited good interconnected porosity (**Figure A4.3,** *Appendix*) as visualized by electron microscopy. This may be attributed due to the good diffusion properties which was observed earlier, with a decent diffusion coefficient leading to non-Fickian transport. A good permeable hydrogel network is very much essential for nutrient transport, exchange of cytokines or growth factors from one end of the construct to other end facilitating cellular crosstalk and for extracellular matrix remodelling.

4.3.4 *Bioprinting of Hierarchically Biomimetic Osteochondral Interfacial Constructs using Silk-based Nanocomposite Bioinks Confer Chondroprotectiveness and Osteoinduction*

With incentives attributed to the silk based bioinks biofabrication of hierarchically relevant osteochondral interfacial constructs were attempted *via* microextrusion of stem cell laden inks. For this pADSCs were utilised which were either chondrogenically or osteogenically primed in tissue culture plates for 7 days prior to encapsulate in either cartilage ink (SF-PVP) or bone bioinks (SF-PVP-SR0/ SF-PVP-SR1) (**Figure 4.4 A**). For the development of interfacial constructs, a two microextruder system was used where one cartilage ink or one bone ink was housed in each extruder to print the two experimental groups: **ITE-1** (SF-PVP/SF-PVP-SR0) and **ITE-2** (SF-PVP-SR1), through a layer-by-layer approach printing the bone phase, followed by interface and finally the cartilage phase (**Figure A4.1**, *Appendix*). The control groups were monolithic constructs printed by single extruders to print cartilage phase alone (SF-PVP laden with chondrogenically primed pADSCs) - **C-SF** or bone phases (either SF-PVP-SR0 with osteogenically primed pADSCs - **B-SR0** or SF-PVP-SR1 with osteogenically primed pADSCs – **B-SR1**). Free self-standing structures with perceivable print fidelity and resolution were possible to be printed with these bioinks with no delamination at the interface region occurring during the printing process (**Figure 4.4A**).

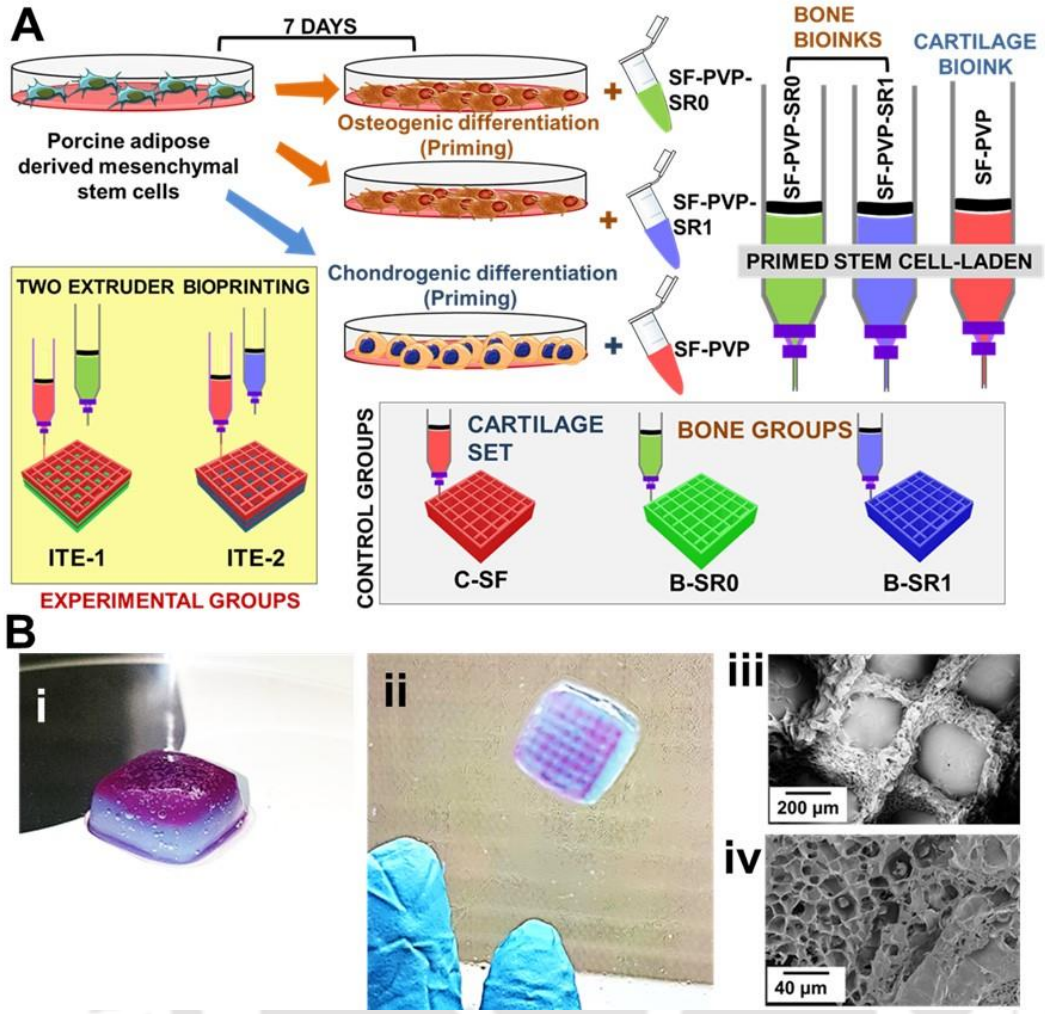

Figure 4.4. ***Bioprinting strategy followed in the study.*** *A) Scheme representing the overall work flow for developing the bioprinted osteochondral interfaces used in the study; B) i-ii) Gross morphology of self-standing bioprinted constructs with good porous network affirmed through (iii-iv) electron microscopy.*

The matured osteochondral constructs were then biochemically analysed to ascertain the pADSCs' osteogenic/chondrogenic commitment housed within the cell laden bioprinted constructs. Alkaline phosphatase (ALP), a hallmark marker expressed by differentiating osteoblasts which regulates mineralisation gave insight on the osteogenic state of the pADSCs within the constructs. It was noticed that in B-SR1 a peak in ALP activity at day-7 gradually subsided at day-14, whereas in B-SR0 an incremental rise in ALP activity was noticed even on day-14 (**Figure 4.5 A**). ALP activity generally is toned down when osteoblasts acquire a more differentiated phenotype and conceivably take up the mature osteocyte phenotype. This might be a plausible reason for B-SR1's osteoinductive state over rather more osteoconductive nature of B-SR0, where osteoblasts are still in their mineralization phase. Sulphated glycosaminoglycans (sGAG), an important ECM component expressed by condensing

chondrocytes during chondrogenesis were estimated to determine the chondrogenic fate of pADSCs. It was noticed that sGAG content was 5 folds higher in C-SF than interfacial groups ITE-1 and ITE-2 at day-7 but decreased at day-14, whereas in case of ITE-2 the sGAG content increased by ~2 folds in comparison to ITE-1 and C-SF (**Figure 4.5 B**). Chondrocytes in culture or chondrogenically differentiating pADSCs in tissue engineered constructs are finicky are mostly associated with losing their chondrogenic commitment and acquiring hypertrophic state, thus posing a great challenge in cartilage tissue engineering. This plausible reason led us in hypothesizing that the encapsulated chondrogenically primed pADSCs were undergoing hypertrophy and dedifferentiation in C-SF and ITE-1, whereas the commitment was fairly seemed to be regulated by factors secreted by either bone phase in ITE-2. In line with this, the total collagen content was estimated in the bioprinted constructs (**Figure 4.5 C**) and it was observed that B-SR1 (at day-7 and day-14) had significantly higher collagen content than the other groups, substantiating its osteoinductive role wherein the increased mineralized collagen-1 is the direct relevance of this observation. The decrease of collagen content in ITE-1 from day-7 to day-14 also is indicative of dedifferentiation and hypertrophy where these cells tend to secrete more catalytic remodelling matrix metalloproteinases (MMP-13) deteriorating the secreted ECM and disaggregating it. The cellular proliferation of encapsulated cells in terms of assessing the DNA content of the bioprinted constructs was carried out (**Figure 4.5 D**). Though no significant difference between the groups was observed the cellular DNA content gradually increased from day-1 through day-14, affirming the encapsulated cells survival within the hydrogel matrices owing to their permeable nature with adequate nutrient exchange.

Furthermore, histological examinations on the matured osteochondral constructs revealed the cells were well distributed homogenously within the hydrogel matrix of the constructs (**Figure 4.5 E,F i**) while 3 distinct phases were noticed, an upper chondral phase a transitory interface and a lower bone phase (**Figure 4.5 E,F ii,iii,iv**). It was interesting to note that an undulating demarcation at the interface which appeared to be separating the calcified bony phase from the cartilage phase (**Figure 4.5 E,F ii**). In case of ITE-2, a crisper and more coherent interface with a more intact tidemark was noticed in comparison to ITE-1. Immmunohistological staining also confirmed the spatial confinement and maturation of chondrocytes expressing aggrecan in the cartilage phase and bone specific collagen-I in the bone phase (**Figure 4.5 E,F v**).

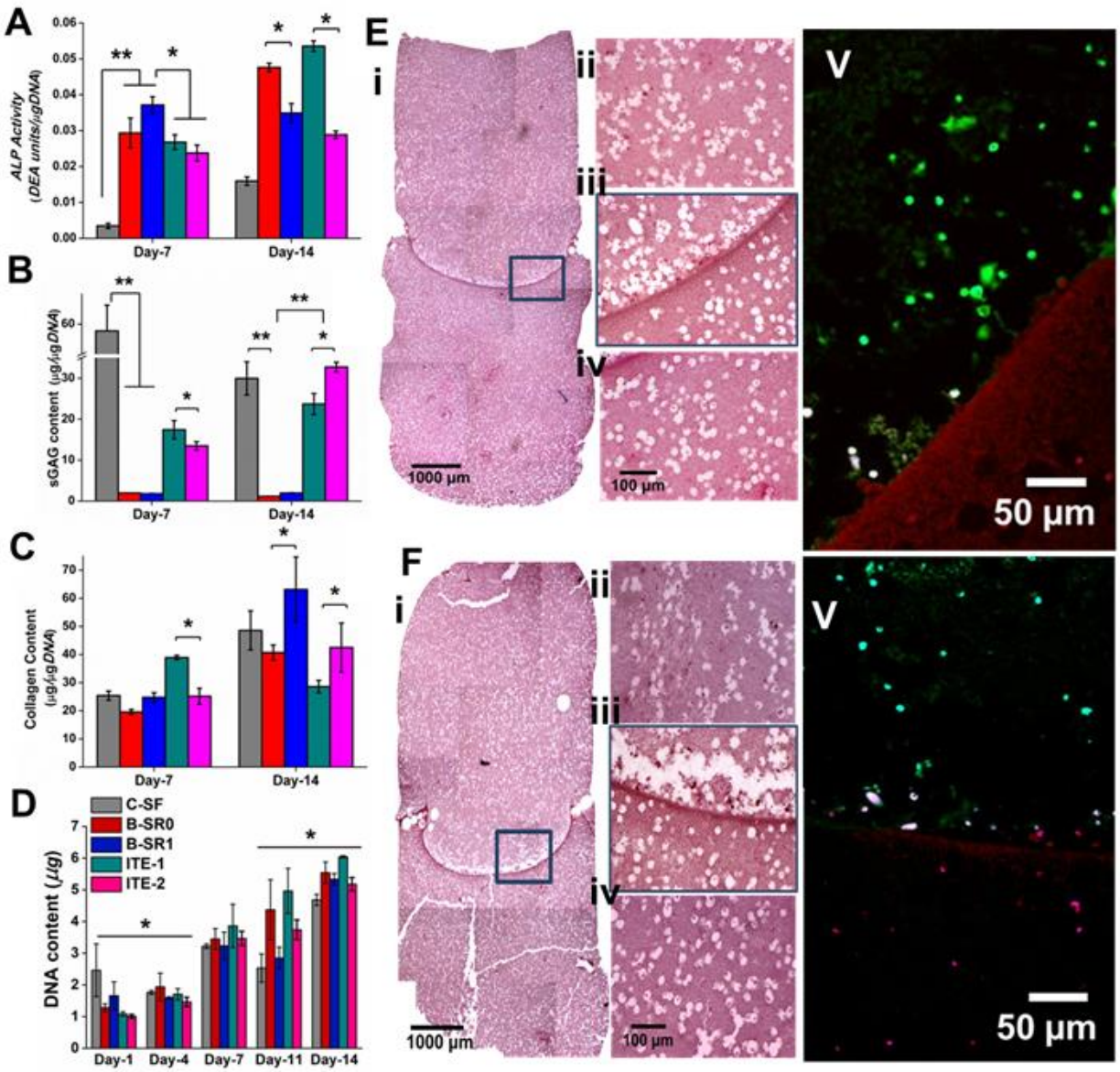

Figure 4.5. ***Biochemical analysis of 3D printed constructs used in the study.*** *A) membrane bound ALP activity; B) sulfated glycosaminoglycan content C) total collagen content D) total DNA content in 3D bioprinted constructs; Immunohistochemistry of bioprinted interfacial constructs E) ITE1, F) ITE2 post 14 days in culture; i) H&E stained image of many images stitched to reconstruct the entire construct, ii) bone phase, iii) interface, iv) cartilage phase; v) immunohistochemistry for cartilage specific marker aggrecan in green and bone specific marker collagen-I in red at the interface region (Data expressed as Mean ± S.D (n=3); *represents statistically significant difference ($p \leq 0.05$), **represents statistically significant difference ($p \leq 0.01$)*

The gene expression profile of encapsulated pADSCs pertaining to osteogenic and chondrogenic genes were studied to evaluate the cells' differentiation state. *SOX9*, a transcription factor which governs the chondrogenic commitment of chondrogenically primed pADSCs and aggrecan an important proteoglycan expressed in maturing chondrocytes were

investigated (**Figure 4.6 Ai,ii**). It was interesting to note that, both the genes were upregulated in C-SF at day-7 but drastically decreased at day-14 whereas in ITE-2 the levels were maintained consistent affirming our hypothesis that a cellular cross-talk was in tandem in this interfacial construct possibly bestowing chondroprotective traits to ITE-2. The osteogenic commitment of differentiating pADSCs were evaluated for an early stage marker core, binding factor alpha-1 *CBFA1* which is a transcription factor which acts like a master switch controlling downstream osteogenic signalling and a late stage marker, podoplanin (*PDPN*) expressed in mature osteocytes. It was noticed that *CBFA1* levels were consistently maintained in bone groups B-SR0, B-SR1 at day-7 and day-14 indicating the osteogenic potential of incorporated ceramic additives in the ink conferring spatial maturation of cells (**Figure 4.6 Bi**). Similarly, expression levels for a late stage osteogenic marker *PDPN* expressed in differentiated osteocytes, indicated that maturation of osteocytes was more directed in B-SR1, ITE-2 than B-SR0 and ITE-1 (**Figure 4.6 Bii**).

These results are concurrent with the findings from biochemical analysis where strontium doped apatite groups showcase osteoinductive traits in comparison to unmodified apatite groups. We delved into further exploring the expression of certain key proteins by immunoblotting which would provide better insight at hypertrophy, osteoinduction and proangiogenic priming of pADSCs within the bioprinted constructs. Collagen-2 is the cardinal ECM protein of differentiating chondrocytes in superficial hyaline cartilage whereas collagen-10 is expressed by dedifferentiating chondrocytes marked to be hypertrophic. The expression of collagen-2 decreased in C-SF from day-7 to day-14 whereas collagen-10 increased prominently increased in C-SF and ITE-1 from day-7 to day-14 (**Figure 4.6 Ci**). As in case of ITE-2 collagen-2 content increased from day-7 to day-14 while little expression of collagen-10 was noticed. We calculated the ratios of intensities through densitometric profiling of collagen-2 and collagen-10 and found that with C-SF the ratio at day-14 was < 1 indicating hypertrophy, whereas in ITE-2 the ratios were maintained > 1 substantiating the hypothesis that strontium incorporated bone phase indeed had a role to play in bestowing chondroprotectiveness.

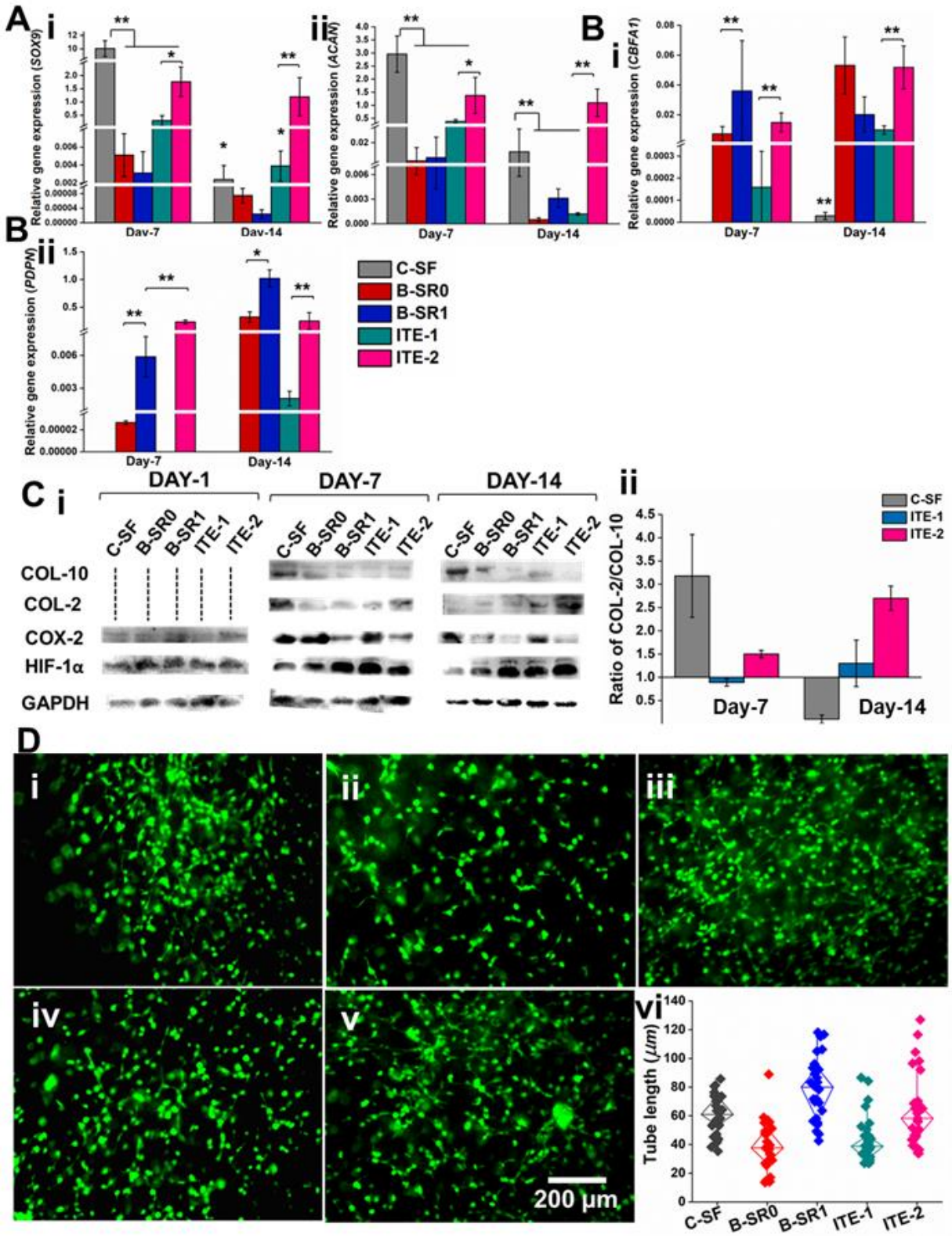

Figure 4.6. ***Functional validation of bioprinted constructs.*** *Real time gene expression studies for A) chondrogenic markers i) SOX9, ii) ACAN; B) osteogenic markers i) CBFA1, ii) PDPN; C) i) Western blot analysis of immunomoduclatory, hypertrophic markers and ii) Densitometric analysis to determine ratio of Col2/Col10; D) Angiogenic potential of bioprinted constructs; tube formation assay using calcein-AM stained ECs for conditioned media obtained from cell*

seeded constructs of i) C-SF, ii) B-SR0 iii) B-SR1, iv) ITE-1, v) ITE-2 and vi) tube length noticed per imaging field from the fluorescent micrographs.

4.3.5 *Conditioned Media from Bioprinted Constructs Bioinks Show Proangiogenic Potential*

To further understand the influence of strontium in upregulating HIF-1α and having a proangiogenic effect, we evaluated the conditioned media from stem cell laden bioprinted constructs in *in vitro* tube formation assay (**Figure 4.6 D**). If the HIF-1α upregulation has indeed set up the hypoxia response element (HRE) activation, this would enable better survival and expression of tube forming phenotype of embedded porcine endothelial cells (pECs) in collagen gels. Interestingly, it was noticed that B-SR1 and ITE-2 groups (with Sr inclusion) showcasing significantly better endothelial capillary tube formation, with a greater number of tubes and nodes noticed (**Figure 4.6 D iii, v**) in contrast to the unmodified nano-apatite (SR0) containing groups (**Figure 4.6 D ii, iv**). Relatively lengthier tubes (**Figure 4.6 D vi**) calculated from the fluorescent images in B-SR1 and ITE-2, also quantifies the same observation.

To put these cellular regulations in perspective, the incorporation of strontium in the apatite has resulted in bestowing three unique attributes to the bioprinted constructs. Firstly, strontium enabled in osteoinduction and maturation of pADSCs witnessed from the biochemical and gene expression studies. This might be due to the regulation of extracellular signal regulated kinases - *ERK1/2* signalling [318], which enhanced the *CBAF1* commitment to maintain the osteogenic fate by chemical cues and also physical cues (showing relatively higher modulus, **Table A4.2**, *Appendix*) exhibited by SF-PVP-SR1 bioink. Secondly, the strontium incorporation has been reported to have a proangiogenic effect [317] which we noticed to upregulate HIF-1α and from our previous experiences we have noticed that HIF-1α trigger ensures definitive manifestation of angiogenic signalling including secretion of chemotactic angiogenic factors which help in endothelial cell survival and homing of endothelial cells, associated cells through *CXCR4/SDF-1* signalling [305]**.** Thirdly, resulting from these two attributes the strontium incorporated groups, helped in priming the chondrogenically differentiated cells through cellular cross-talk aided by the these well diffusible gel network to exert chondroprotectiveness, probably due to the hypoxic trigger mimicking the hypoxic conditions prevalent in avascular hyaline cartilage.

4.3.6 *Downregulation of Osteoclastic Activity and Immunomodulatory Effect Conferred in Nanocomposite Bone Bioinks Due to Strontium Incorporation*

Osteochondral lesions associated with osteoporosis particularly pose a great challenge in treating for clinicians [310]. The rationale of incorporating Sr-doped apatite in bone bioink was to recapitulate the pharmacological effect of strontium ranelate, commonly used drug in inhibiting osteoclast differentiation associated with postmenopausal or senile or idiopathic osteoporosis [326]. By virtue, release of Sr ions by dissolution from matrices would inhibit the heightened osteoclast activity noticed with osteochondral lesions associated with osteoporosis enabling better regeneration while augmenting the hormonal therapies required for osteoporosis. Hence, ancillary benefits of strontium were investigated in inhibiting osteoclasts (**Figure 4.7**), that could potentially serve as added benefits to the bone bioinks in regenerating the subchondral bone, by upregulating the osteoblast survival while concomitantly toning down the osteoclast activity.

Differentiating osteoclasts were treated with different concentration of undomodified nano-apatite (SR0), Sr doped nano-apatite (SR1) and their effects on osteoclast activity at the genomic and proteomic level were studied. A dose dependent increment in osteoclast activity was noticed with increase in nuclear factor of activated T cells (*NFATc*) (**Figure 4.7 Ai**), a crucial transcription factor which drives the osteoclast differentiation with SR0 groups. The relevance of which was seen in gene expression profiles of cathepsin-K (*CTSK*) (**Figure 4.7 Aii**), a bone resorption protease and carbonic anhydrase-2 (*CA2*) (**Figure 4.7 Aiii**) involved with influx of protons into resorption pits of osteoclasts, which were significantly enhanced in SR0 groups. However, in case of SR1 treated groups a down regulation of *NFATc* was noticed and the relevance of which was seen in lower expression levels of *CTSK* and *CA2*. The same results were corroborated with proteomic expression profiles as witnessed by tartrate resistant acid phosphatase (TRAP) secretion, an enzyme expressed by active multinucleated osteoclasts (affirmed by rhodamine phallodin actin stain, **Figure 4.7 B**). The number of osteoclasts number went down and so also the associated TRAP expressing osteoclasts (**Figure 4.7 C**) in a dose dependant manner in SR1 treated groups, whereas healthy multinucleated osteoclasts were present in consistently higher in SR0 treated groups and in untreated control group grown in tissue culture plate (**Figure A4.4 A** *Appendix*). The levels in expression of a matrix remodelling enzyme secreted by active osteoclasts, matrix metalloproteinases (MMP-9) considerably reduced in SR1 treated group (**Figure A4.4 B** *Appendix*), indicating the direct relevance of Sr in downregulating osteoclast activity. This inference could be correlated with previous reports

where Sr ions have been reported to inhibit parathyroid hormone (PTH) pathway [63] in osteoclasts and subsequently activating apoptotic signalling.

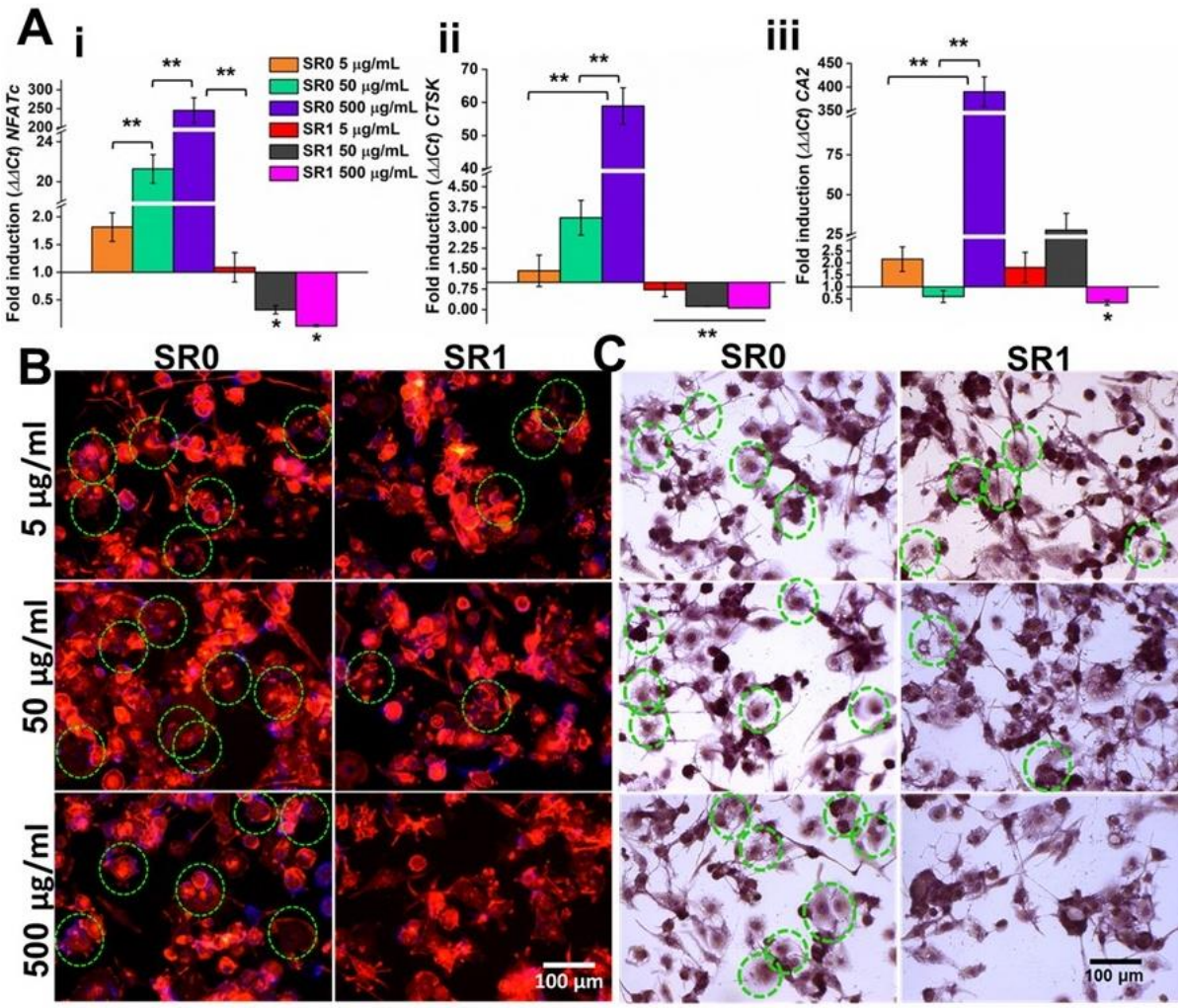

Figure 4.7. ***Effect of synthesized nano-apatites on osteoclastogenesis.*** *A) real time gene expression studies on different treatment doses of synthesized apatites i) NFATc, ii) CTSK and CA2; B) cytoskeletal architecture assessment of apatite treated osteoclasts (green circles indicate multinucleated osteoclasts)*; C) *tartarate resistant acid phosphatase (TRAP) staining for apatite treated osteoclasts (green circles indicate multinucleated osteoclasts stained for purplish TRAP granules); (Data expressed as Mean ± S.D (n=3); *represents statistically significant difference ($p \leq 0.05$).*

The treatment of the apatites if it had any negative role on osteoblasts was assessed, and the same dosage was used to evaluate the performance on osteoblasts (**Figure A4.5** *Appendix*). The concentrations used hampered neither the osteoblast cell survival, nor the osteogenic activity (ALP activity) or the cellular fate (no cell cycle arrest) was noticed for osteoblasts, confirming the nano-apatites used had osteoconductive properties while concomitantly Sr-dope apatite showcasing anti-osteoclastic activity.

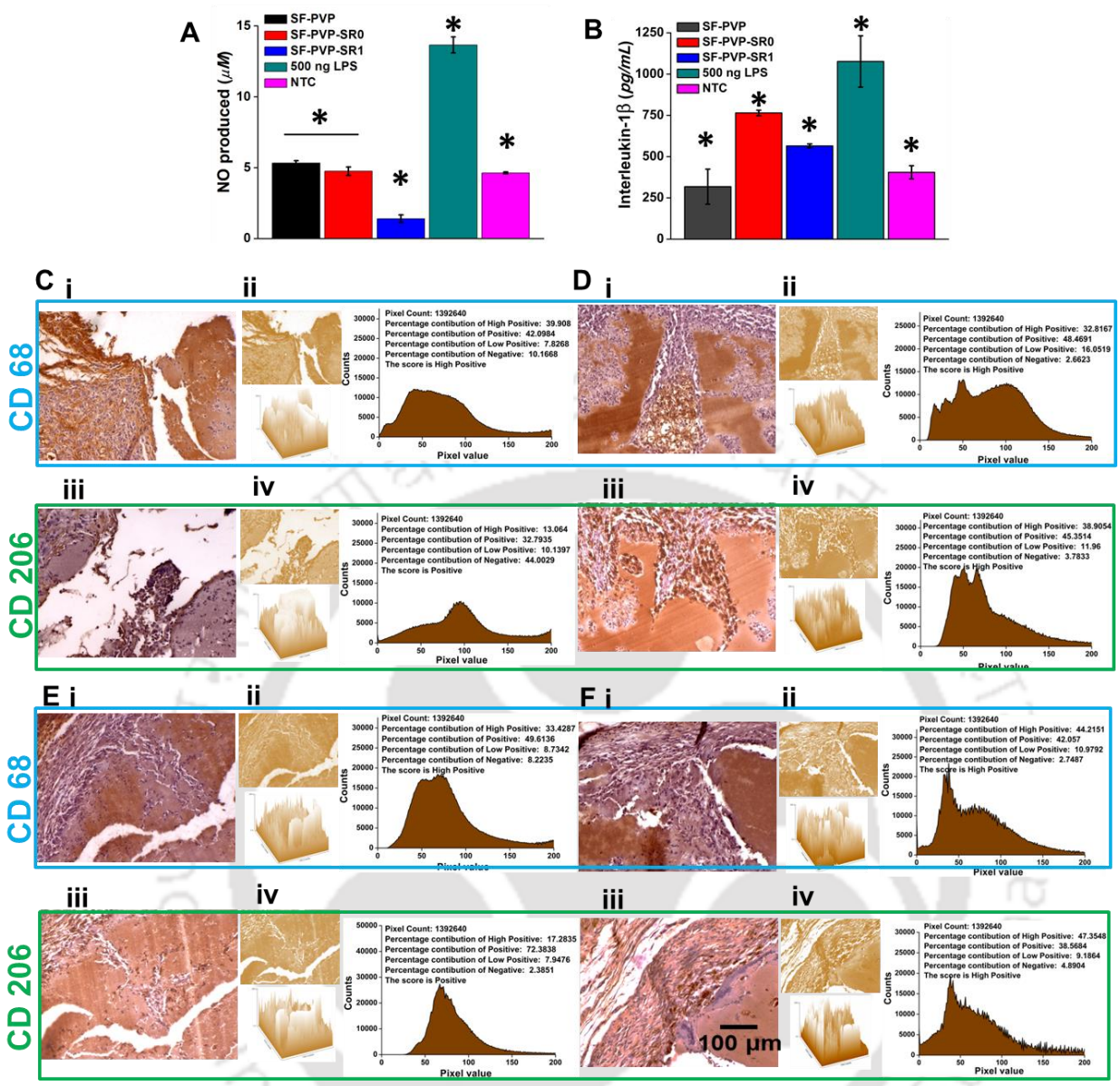

Figure 4.8. ***Evidence of immunomodulatory effect of Sr substituted nano-apatite containing silk bioinks;*** *In vitro immunocompatibility assessment through murine macrophages and estimation of pro-inflammatory A) nitric oxide (NO) and B) cytokine IL-1β through ELISA; Immunohistochemical analysis for silk bioinks from subcutaneous implantation in SD rats post 7 and 14 days for pan macrophage marker i) (CD68) and regenerative M2 macrophage marker iii) (CD206) and their respective ii), iv) deconvoluted and semi-automated image analysis of C) SF-PVP-SR0 bioink at day-7, D) SF-PVP-SR0 bioink at day-14, E) SF-PVP-SR1 bioink at day-7, F) SF-PVP-SR1 bioink at day-14; (Data expressed as Mean ± S.D (n=3); *represents statistically significant difference ($p \leq 0.05$).*

Interesting to note is that strontium has also been reported to inhibit prostaglandins (PGE2) pathway and as a materialization of the same we noticed COX-2 (proinflammatory marker) levels going down in SR1 containing groups (**Figure 4.6 Ci**). This led us in postulating that Sr has a role in immunomodulation as well, where it could potentially help us in tailoring

immune responses with biasness towards M2 macrophage polarization [324] which are associated with tissue regeneration and implanted graft compliance. *In vitro* immunocompatibility assessment using murine macrophages stimulation showed relatively lower pro-inflammatory interleukin (IL-1β) and nitric oxide (NO) secretion in strontium containing bioinks (**Figure 4.8 A-B**), reiterating our notion that it stimulates M2 macrophage biasness which however needs to be thoroughly validated further. To validate the hypothesis, further we looked into the immunocompatibility of bone bioinks (SF-PVP-SR0, SF-PVP-SR1) by subcutaneous implantation in Sprague Dawley (SD) rats. Post retrieval at day-7 the injected gels showed minimal cellular infiltration into the bulk of hydrogel, with mononuclear cells seen distinctly at the interface of gels. While on day-14, erosion and fragmentation of gels had resulted in cellular infiltration of mononuclear cells accompanied by fibroblasts into the degraded bulk of the hydrogel matrices. However, there was no evidence of any fibrous encapsulation noticed in any of the injected bioinks. The sections were stained for pan macrophage marker CD68 and it was observed that the infiltrated cells were primarily CD68 positive, which was significantly higher at day-14 in comparison to day-7 (**Figure 4.8 C-F**). The distribution of M2 macrophage expressing CD206 was also noticed amongst the infiltrating mononuclear macrophages and it was found that strontium containing bioink (SF-PVP-SR1) had significantly higher percentages of CD206 positive M2 macrophages, reaffirming the hypothesis that Sr has a role in immunomodulation. Though these are preliminary evidences of the immunomodulatory roles of Sr, they need to be studied well in detail. The current study focusses in the bioink development which potentially possesses multifunctional traits; however, understanding the other ancillary features due to Sr incorporation in immunomodulation altogether necessitates a holistic study in suitable animal models to investigate the common pathways (PGE2 or PTH) which get triggered.

4.4 Salient Findings of the Chapter

Mimicking the heterogeneity of phases and anisotropic intricacy noticed in native osteochondral interface has always limited the clinical success, while remaining to be confronting hurdle in osteochondral tissue engineering. In this chapter, the development of multifunctional silk based bioinks was carried out which exhibited shear thinning nature and rapid thixotropic recovery while demonstrating decent shape fidelity for printing. The inclusion of hierarchically biomimetic strontium doped nano-apatites as ceramic additives in bone bioink conferred osteoinduction and osteocyte maturation on the encapsulated stem cells. Moreover, the permeable nature of the silk-based hydrogel network within the bioprinted osteochondral constructs enabled better diffusion and promoted cellular cross-talk within constructs, thus achieving in formation of undulated demarcation at the interface of chondral and bone phases. The innate physico-chemical cues presented by the developed silk-based cartilage and bone bioinks established spatial confinement for differential growth, phenotypic commitment and subsequent extracellular matrix turnover of differentiating chondrocytes and osteoblasts, preferentially within the coherent bioprinted osteochondral constructs. Furthermore, the ancillary features bestowed by incorporation of strontium included better support for endothelial cell survival aiding better subchondral bone regeneration and downregulation of osteoclast activity targeting interventions for osteoporotic osteochondral lesions.

Limitations of the chapter

Evidences of strontium-based bone inks in favouring M2 macrophage biasness, opens prospective avenues for exploring the immunomodulatory effects of the developed bioinks. However, the underlying mechanism involving resorption kinetics, cellular responses and the ability of the bioprinted constructs to repair full-thickness defects *in vivo* needs to be evaluated exhaustively which are beyond the scope of the current work. Nonetheless, the promising findings from this work vouches for the potential clinical translation of these silk based bioinks for bioprinting autologous stem cell laden grafts for tissue repair and also for *in vitro* pre-clinical tissue model for drug screening applications.

Chapter 5

Silk–based bioengineered diaphyseal cortical bone unit enclosing an implantable bone marrow towards atrophic non–union grafting

Bone marrow concentrates alongside autologous spongiosa are clinical interventions used during atrophic nonunions. Paucity of viable autologous bone marrow under compromised conditions necessitates use of alternative tissue engineered solutions. This chapter describes the use of conventinal freeze-dried scaffold and 3D bioprinted constructs, in combination towards developing diaphyseal cross-sectional unit for atrophic non-union repair.

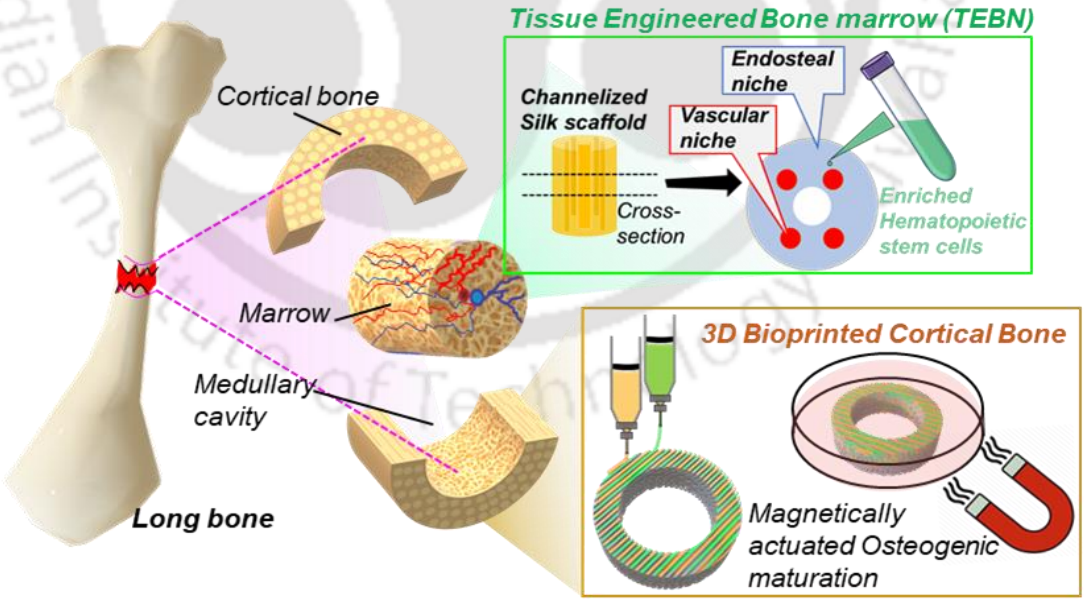

Abstract

Postnatal fracture healing of atrophic long bone diaphyseal nonunions poses a great challenge for orthopedic surgeons. Paucity of autologous spongiosa has potentiated the use of tissue engineered bone grafts to improve success rates of bone marrow engraftment frequently used in plate reosteosynthesis. In this work we report the development and *in vitro* validation of a 'sandwich type' biofabricated diaphyseal cross-sectional unit, with an outer mechanically robust bioprinted cortical bone shell, encompassing an engineered bone marrow. Channelized silk fibroin blend sponges derived from *Bombyx mori* and *Antheraea assama* help in developing compartmentalized endosteum, exhibiting specialized osteoblasts (endosteal niche) and discontinuous endothelium (vascular niche). The cellular crosstalk between these two niches triggered *via* integrin-mediated cell adhesion, enables in preserving quiescence state of $CD34^{+}/CD38^{-}$ hematopoietic stem cells and their recycling in the engineered marrow. The outer cortical bone strut is developed through multi-material micro-extrusion bioprinting strategy. Osteogenically primed mesenchymal stem cells-laden silk fibroin-nano hydroapatite bioink is bioprinted alongside paramagnetic Fe-doped bioactive glass-polycaprolactone blend thermoplastic ink, reinforcing it for mechanical stability. Pulsed magnetic field actuation positively influences the osteogenic commitment and maturation of the bioprinted constructs *via* mechanotransductory route. Therefore, the assembled engineered marrow and bioprinted cortical shell hold promise as potential orthobiologic substitutes towards atrophic non-union repairs.

The findings of this chapter are published in a peer reviewed journal:

Moses, J. C., Dey, S., Bandyopadhyay, A., Agarwala, M., and Mandal, B. B., '*Silk–based bioengineered diaphyseal cortical bone unit enclosing an implantable bone marrow towards atrophic non–union grafting.*' Advanced Healthcare Materials, 2021, 2102031.

5.1 Introduction

Delayed non-unions of long bones, especially of atrophic tibial or femoral diaphysis non-unions has an incidence rate of 9.3% [327] and poses a great challenge for orthopedic surgeons. These atrophic non-unions or pseudarthrosis, result due to infection, trauma or large osseous defects or tumor resection. These defects are characterized by severe destruction of endosteum, periosteum, damaged vascular supply and marrow depletion. [328] Therefore, these non-unions, despite repeated unsuccessful surgical interventions, lead to persistent infection (septic response) and culminates in loss of limb extremities. These repercussions (especially of femur diaphyseal non-unions) has been documented to result in high unemployment rate and early retirement, [329] affecting quality of life. The most common surgical intervention involves the treatment of impaired fracture by 'diamond concept' [330] involving cells, scaffolds and growth factors (collectively called *orthobiologics*). Autologous bone marrow grafting from iliac crest aspirates are particularly used here for atrophic non-union treatment. However, the survival of these marrow progenitor cells under the challenging wound micro-environment is poor. This has been an active area of research for decades focusing on various ways to circumvent the poor survival rates of stem cells (both hematopoietic and mesenchymal) used in cell therapy through orthobiological and tissue engineering interventions.

The human long bone is a complex organ system which can be simplified into three important parts, namely the epiphysis (distal/ proximal), the metaphysis and the diaphysis. The epiphyses composed of spongy bone meets the growth plate (epiphyseal plate) at the narrow region of metaphysis, which then connects the long shaft termed as the diaphysis. The diaphysis cross-section (**Figure 5.1Ai**) exhibits structural anisotropic heterogeneity where the outer exterior shell is composed of the compact cortical bone (having 5-10% porosity) and towards the interior housing the cancellous trabecular bone (having 50 – 95% porosity), enclosing the medullary cavity. This cross-sectional unit representing a 'sandwich type' structure, comprising the cortical bone and trabecular bone accounts for the structural support of the long bone. The cortical bone shell is sheathed by a thin layer of fibrous tissue called the periosteum which is highly vascularized and innervated, supplying the cortical bone. This vasculature (one nutrient artery and two veins) obliquely enter the cortical bone and disperses into finer arterioles and sinusoids, thus supplying the trabecular bone. Within the trabeculae and central medullary cavity is housed the bone marrow, a soft viscous hematopoietic and lymphoid tissue responsible for hematopoiesis (continuous process of blood cell formation). Hematopoietic

stem cells (HSCs) responsible for the physiologic homeostasis of blood cells are present in specialized compartmentalized niches. This compartmentalization governs their self-renewal potency, quiescent state and differentiation to committed lineages. Among the different niches, two important niches namely; (i) endosteal niche (comprised of specialized osteoblast cells) and (ii) vascular niche (comprised of vascular and perivascular cells of the vascular sinusoids arising from the dense vasculature supplying from the cortical bone) (**Figure 5.1A ii**) are well characterized and documented. [331] These niches support HSCs adhesion by presenting cell attachment ligands and secreting crucial growth factors, cytokines needed for HSC survival and differentiation.

Recapitulating the bone marrow niche has been an intense field of research over the years. Several biomaterials (such as collagen, gelatin, poly(ethylene glycol) diacrylate (PEGDA), polyethersulfone) [332-334] and different strategies to mimic these 'stromal cell support-systems', in 2D or 3D cultures have been reported in literature [335, 336]. 2D cultures of stromal cells (mesenchymal stem cells as feeder layers) have long been documented to facilitate engraftment of HSCs and helped in their *ex vivo* expansion, before HSC transplantation [337]. However, due to the inability to maintain these feeder cultures for long-term, 2D (two dimensional) functionalized biomimetic biomaterial surfaces were adopted to circumvent this issue. The functionalization strategies involved grafting with adhesion peptides or growth factors immobilization (such as, fibronectin coating [338], arg-gly-asp - RGD tripeptide grafting, [339] amine group functionalization [340], stem cell factor -SCF immobilized substrates [336]) etc. Since the bone marrow niche microenvironment is highly dynamic, these 2D strategies fail to reproduce this active cell signaling and HSC-niche interaction needed for HSC survival over extended culture periods. In this regard, perfused 3D (three dimensional) scaffolding platforms for recreating these stromal niches have shown promise. For instance, ceramic scaffolds functionalized with extracellular matrix (ECM) proteins and seeded with human mesenchymal stem cells, (typically serving as endosteal niche) aided in supporting CD 34^+ HSCs engraftment and its phenotypic number increase [335]. Silk fibroin derived from *Bombyx mori* matrices coated with cell adhesion peptides (collagen I, fibrinogen, fibronectin, laminin) and incorporating growth factors (vascular cell adhesion molecule 1 – VCAM1; vascular endothelial growth factor – VEGF) helped in megakaryocyte attachment and subsequent functional proplatelet release (typical for vascular niche microenvironment). [341] The same silk-based scaffolding platform was channelized but devoid of ECM proteins/ growth factors also aided in megakaryocyte attachment and

thrombopoiesis. [342] Conversely, microfluidic based platform developed with bone-like endosteal layer (using hMSCs) and collagen-fibrin hydrogel with endothelial cells (mimicking the vascular niche), enabled in maintenance of CD 34^{+} HSCs over 5 days studied on the chip. [343] The poor scalability of such microfluidic platforms limits its potential use for *ex vivo* expansion and clinical use. Furthermore, scaffolding platforms combining both endosteal-like niche and vascular-niche have not been studied, offering scope for such models for *ex vivo* expansion systems as well as implantable engineered bone marrow for transplantation.

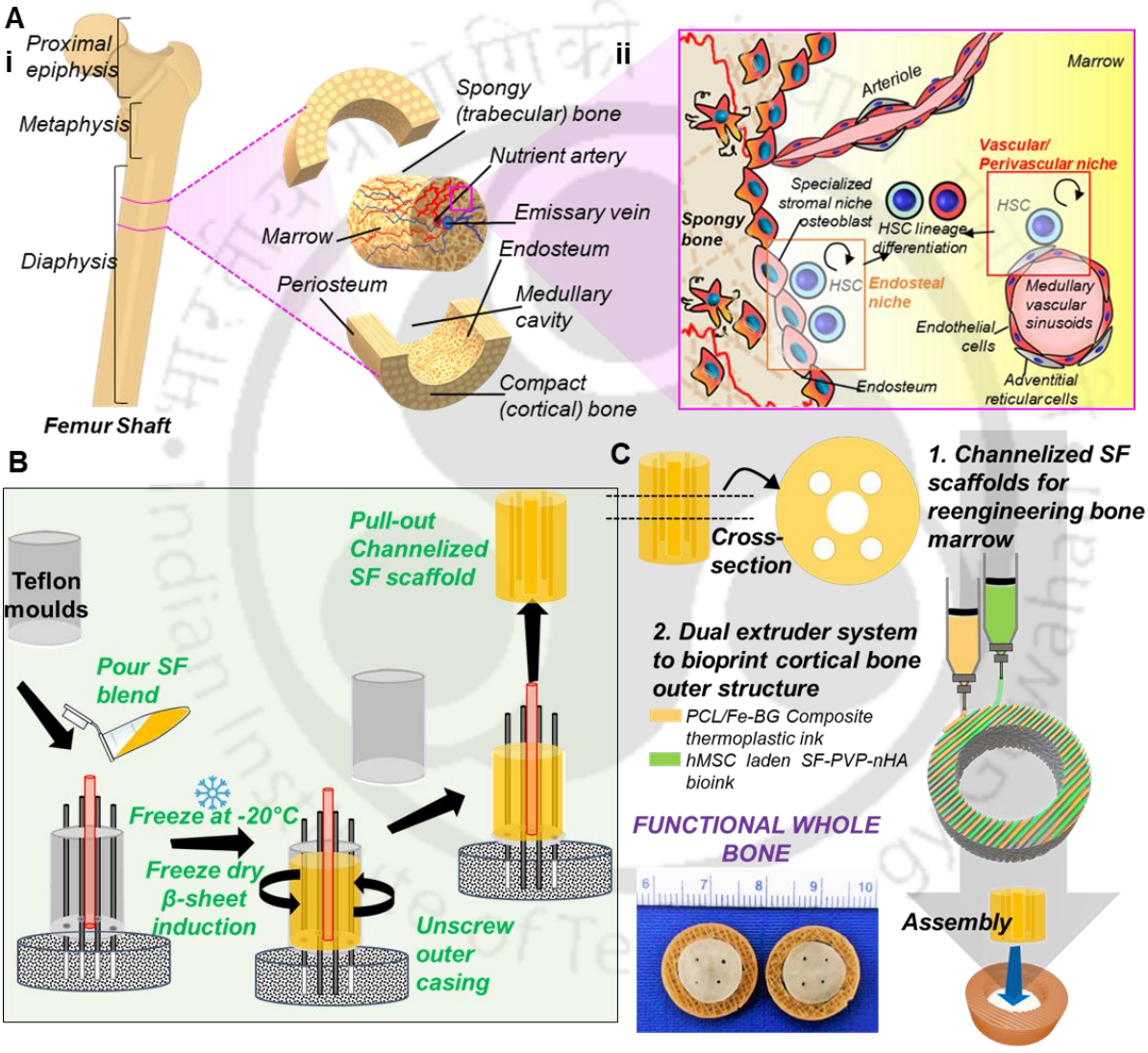

Figure 5.1. ***Scheme representing the rational of the study.*** *A) Femur long bone, i) representing the cortical bone and bone marrow components, ii) illustration showing the cellular heterogeneity of bone marrow micro-environment with endosteal and vascular niches; B). Scheme representing the development of tissue engineered bone marrow niche (TEBN); fabrication of channelized SF scaffold through freeze-drying process and C) Scheme illustrating the 3D bioprinting strategy adopted for developing cortical bone outer strut by thermoplastic magnetic PCL-FeBG ink and hMSCs laden SF-PVP-nHA bioink.*

Meanwhile, significant progress has been made in the domain of cortical bone tissue engineering with emphasis on developing high-performance biomaterials with astute mechanical properties. Rapid prototyping, especially has enabled tissue engineers to develop hierarchically bioinspired cortical bone structures at a fast, highly reproducible and reliable manner. For instance, hyperelastic composite [90 % hydroxyapatite; 10% poly(lactic-co-glycolic acid) (w%)] was used to micro-extrude femoral midshafts, exhibiting good mechanical properties (elastic modulus ~4 to 11 MPa; withstanding ~32 to 67% strain) and supported osteogenic phenotype maintenance. [174] Cortical bone shell like structures with Haversian and Volkmann channels printed *via* digital laser processing of Akermanite ceramic (with a photosynthetic resin) enabled in mimicking the osteon-vascular niche which enabled these structures to integrate well within rabbit femoral cortical diaphyseal defects. [344] Similarly, multi-material dual extrusion printing capable of dispensing biocompatible emulsion hydrogel bioinks (ECM cocktail [171], propylene fumarate [345]), reinforced with dense thermoplastic ink (PCL) have also been reported in literature. However, cellularization of these cortical structures post-printing (in case of acellular constructs [174, 344]) increases the biofabrication time; while the cost associated with ECM proteins in hydrogel bioinks for scale-up, and the use of synthetic cross-linkers in synthetic polymer bioinks limits their clinical translation. Therefore, this opens up scope for cost-effective, greener alternatives in bioprinting cortical bone structures bestowed with osteoinductive traits and desirable mechanical properties.

Hypothesis underpinning the Objective:

In this chapter, a method for recreating the diaphyseal cross-sectional unit was envisioned, encompassing two critical tissue components towards our attempt in engineering a functional whole bone (**Figure 5.1 B-C**). Firstly, reported here is a strategy for engineering compartmentalized bone marrow niches, namely the endosteal bone niche *via* osteogenically primed MSCs seeded over silk fibroin blend scaffolds which are channelized to house the endothelial cells serving as the vascular niche. This tissue engineered bone marrow niche (TEBN) was investigated for its potency to house HSCs over a three-week *ex vivo* maturation window as prospective implantable tissue engineered bone marrow. Secondly, reported here is a strategy for dual-extrusion multi-material bioprinting to biofabricate outer cortical bone shell. This was materialized by bioprinting osteogenically primed MSCs laden silk fibroin-nano hydroapatite bioink (reported in *Chapter 4* [141]) and reinforcing this with paramagnetic Fe doped bioactive glass bioceramic-PCL blend thermoplastic ink. The bioprinted cortical bone strut were magnetically actuated for osteogenic maturation *via* mechanotransduction.

It is pertinent to note here, that these two systems were studied in a delineated fashion, independently under *in vitro* conditions. The channelized TEBN studied here serves to give insights on compartmentalized niches for enabling HSCs survival under perfusion conditions *in vitro*. The outer cortical bone strut tries to elucidate the survival and osteogenic commitment of bioprinted MSCs through mechanotransduction route.

5.2 Materials and Methods

All analytical and preparatory chemicals were sourced from Sigma, USA. Cell culture reagents and molecular biology reagents were sourced from Invitrogen, USA (unless otherwise mentioned specifically in methodology section below). Cell cultureware and other consumables were obtained from Thermo Fisher Scientific, USA.

5.2.1 Development of Silk Fibroin-based Tissue Engineered Bone Marrow Niche (TEBN)

5.2.1.1 *Regeneration of Silk Fibroins*

Bombyx mori cocoons and fifth instar *Antheraea assama* silk worms were sourced from local silk farms in Guwahati, Assam, India. Silk fibroins from mulberry silk (derived from *B. mori* cocoons) and non-mulberry silk (derived from glands of fifth instar *A. assama* silk worms) were obtained based on our previously published protocols. [141] [305] Briefly, cocoons cut in small pieces were degummed in 0.02 M boiling sodium carbonate solution. The dried degummed silk fibroin (SF) fibers were dissolved in 9.3 M lithium bromide, and the obtained BMSF solution was dialysed against deionised water (18.2 MΩ; Arium ® Sartorius Ultrapure, Germany) for 48 h with several intermittent changes using 12 kDa cut-off dialysis membrane. Similarly, glandular SF from mature fifth instar silk worms were squeezed out from silk glands, and dissolved in 1% (w/v) sodium dodecyl sulphate - SDS. The AASF solution was dialysed against deionised water for 4 h in 4°C with intermittent changes using 12 kDa cut-off dialysis membrane. Thus, obtained BMSF and AASF were stored in 4°C until further use.

5.2.1.2 *Fabrication of Channelized Silk Fibroin Scaffolds*

A custom mold set-up (**Figure 5.1B; 2A**) was fabricated using a thermoplastic 3D printer (Ultimaker 3E, Netherlands), where the base was designed and printed (**Figure 5.2Ai-ii**) using acrylonitrile butadiene styrene (ABS) while the outer casing served as Teflon. The assembly was done by inserting 4 stainless steel wires (ϕ = ~ 600 μm) equidistant from the central polypropylene (food grade) hollow tube (ϕ = ~3 mm) and then placing the outer Teflon casing. 2 mL of regenerated SF solution was poured into the mold, frozen at -20 °C and freeze dried using a lyophilizer (Martin Christ, Germany). β-sheet induction was done using ethanol

treatment, after which the scaffolds were pulled out as represented in **Figure 5.1B**. Cross-section of scaffolds of 4 mm height were cut using fine razor blade and were sterilised by autoclaving (121°C, 15 psi, 15 min) under hydrated conditions. For the study, channelized scaffolds were made from BMSF (2% w/v) which served as control scaffolds (**BMC**), while experimental group (**BAC**) was made by blending BMSF (2% w/v): AASF (2% w/v) in 1:1 ratio.

5.2.1.3 *Physical Characterization*

The microstructures of the fabricated scaffold's cross-sections were examined using a field emission electron microscopy (FESEM) (∑IGMA, Carl Zeiss, Germany). Pore size distribution were calculated using Image-J (Wayne Rasband, National Institute of Health (NIH), USA) software by ND (Nearest distance) plugin [346] and 50 pores captured across n=3 samples were represented. Mechanical properties of the fabricated scaffolds along the longitudinal direction and radial direction (under diametral stress) were evaluated using universal testing machine (UTM, Instron 5944, USA with 100 N load cell, equipped with BioPuls bath) under hydrated conditions (in phosphate buffered saline, PBS (pH 7.4), 37° C). Briefly, ASTM standard D1621-04a (standard test method for compressive properties of rigid cellular plastics) was followed for assessing the mechanical properties in longitudinal direction wherein scaffolds (10 mm height; 10 mm diameter; either channelized or non-channelized sponges – as controls) were used. Cross-head speed of 1 mm/min was applied (uniaxial loading) until 80% deformation, corresponding stress-strain values were recorded. Briefly, ISO 4049 and ADA/ANSI 27 (testing polymer-based restorative materials) was followed for evaluating diametral tensile strength, where specimens (10 mm diameter - D, 5 mm thickness - T) were used. Uniaxial loading with cross-head speed of 1 mm/ min along the long axis was applied until 80% deformation, and diametral stress was calculated as $\sigma = 2F/\pi DT$, where F is the applied force in Newtons. The compressive strength at 80% and Young's modulus were calculated from the stress-strain profiles and represented.

5.2.1.4. *Cell Seeding in TEBN*

Isolation of Progenitor Cells from Umbilical Cord and Umbilical Cord Blood

Human umbilical cords (UC) from normal pregnancies and deliveries, were collected aseptically in phosphate buffered saline (PBS, pH 7.4, 4°C) and processed within 2 h after collection. Similarly, UC blood were collected in sterile centrifuge tubes with citrate-phosphate-dextrose solution as anticoagulant (Sigma, USA). The samples were obtained from

healthy donors with informed consent from GNRC Medical, North Guwahati, Assam. The collection, processing and appropriate handling protocols were reviewed and approved by Institutional Ethics Committee (Institute of Neurological Sciences Trust, GNRC Hospitals; Reference no. Inst/AS/2015/RR-2018/EC-103). UC samples were processed based on previous reports. [347, 348] Briefly, blot clots were removed by-passing ice-cold PBS through umbilical vein using blunt ended needle and syringe. For isolation of Wharton jelly derived mesenchymal stem cells (WJMSCs), UC were cut into small segments of ~ 1 cm, the epithelium was opened to expose the blood vessels which were removed, the surrounding Wharton's jelly was scraped and made into smaller ~ 1 mm pieces. These served as explants which were plated in 90 mm dishes with culture medium (DMEM (Gibco, USA); glucose 4500 mg/L supplemented with 10 % fetal bovine serum, FBS (Gibco, USA), 1X antibiotic-antimycotic mix (Gibco, USA), with first media change at 5 days and subsequent media changes every third day until 70 % confluency. After confluency, the WJMSCs were subsequently characterized for their trilineage (osteogenic/ chondrogenic/ adipogenic) potency [141], and were cultured in culture medium supplemented with 1 ng/mL basic fibroblast growth factor (bFGF), while used for experiments between passages 3 – 8. Human umbilical vein endothelial cells (HUVEC) were isolated by passing 1 mg/mL collagenase type-1A (≤125 CDU/mg; Sigma, USA) prepared in DMEM into cord (~ 7 cm long) vein, with UC clamped down in distal end, through the proximal end. The UC was incubated at 37 °C for 15 min, the enzyme solution was flushed out by passing endothelial culture medium (M199 medium supplemented with 5 % (v/v) FBS, 100 µg/mL endothelial growth supplement, ECGS (Sigma, USA). Thus, obtained neutralized enzyme digestate, was centrifuged 1000 rpm/5 min to obtain cell pellet which was plated in culture dishes with endothelial culture medium and used for experiments in passages 3 – 8.

Enrichment of human hematopoietic stem cells (HSCs) from mononuclear cells was done from collected UC blood through Ficoll-Paque density gradient method [349]. UC blood was diluted 4 times with PBS supplemented with 2mM EDTA (Sigma USA); 30 mL of this diluted blood was overlaid on top of 15 mL Ficoll-Paque Plus (GE Healthcare, USA) and centrifuged at 400g for 40 min at 20 °C. The mononuclear cell (MNC fraction) fraction from the interphase was collected using Pasteur pipette, and subsequently washed twice with PBS supplemented with 2mM EDTA, 0.5 % (v/v) FBS. The cell pellet thus obtained were cultured as suspension in T75 flasks in specific media intended for ex-vivo expansion of HSCs from the isolated MNC fraction [350]. The *ex vivo* expansion media used was, Iscove's modified Dulbecco's medium supplemented with 2 % (v/v) FBS, 1 µg/mL insulin (Sigma, USA), 10

µg/mL transferrin,1 ng/mL thrombopoietin, 2 ng/mL stem cell factor, 2 ng/mL granulocyte monocyte colony stimulating factor, where isolated MNC fraction was cultured in suspension for 5-7 days prior to seeding.

Seeding Protocol and Maturation in Perfusion Bioreactor

For engineering the stem cell niche needed to support the HSCs, a preferential seeding regimen was adopted (**Figure 5.3A**). WJMSCs were osteogenically primed in T75 flasks with osteogenic induction media (DMEM supplemented with 5 % (v/v) FBS, 10 mM β-glycerophosphate, 100 nM dexamethasone and 0.2 mM ascorbic acid) for 7 days. Channelized scaffolds (BMC, BAC) with thickness 4 mm, were sterilized by autoclaving. Sterile scaffolds were conditioned overnight in culture media (DMEM supplemented with 10% (v/v) FBS and 1X antibiotic-antimycotic mix) prior to seeding in 24-well plates. Osteogenically primed WJMSCs (Osteo-WJMSCs) were trypsinized and resuspended in cell density (10^6 cells/ 100 µL/ scaffold) in culture media. The cell suspension was seeded by a static seeding approach over scaffolds whose media was wicked off aseptically, to facilitate cell suspension permeation by capillary action. The cell seeded scaffolds were placed in in incubator (37 °C in a humid atmosphere with 5 % CO_2) for 4 h to allow cell adhesion. After 4h, osteogenic induction media was flooded over the scaffold and cultured in it with media change every 48 h. This constitutes the endosteal niche. At day-3, post-seeding Osteo-WJMSCs, injectable silk hydrogel with encapsulated HUVECs were seeded on to the 4 smaller channels, which constitutes the vascular niche. Briefly, injectable silk hydrogel by blending BMSF (1% w/v) : AASF (1% w/v) (from our previous reports [311, 351]) which forms a self-assembled hydrogel when incubated at 37°C within 30 min. After blending, at 15 min HUVECs were mixed with the pre-gelled SF hydrogel and further incubated until gelation. SF hydrogel with HUVECs in a cell density 4×10^6 cells/ mL was used to seed in the four small channels in the osteo-WJMSCs seeded scaffolds (100 µL/ channel). The endosteal and vascular niche reconstituted channelized scaffolds were then matured till 14 days (with maturation media - DMEM supplemented with 5 % (v/v) FBS, 10 mM β-glycerophosphate, 100 nM dexamethasone and 0.2 mM ascorbic acid, 50 ng/mL vascular endothelial growth factor -VEGF), thus serving as tissue engineered bone marrow niche (TEBN).

The TEBN (BMC or BAC group) served as substrates for HSC support under the influence of perfusion bioreactor. MNC fraction enriched from cord blood was seeded over the TEBN scaffold at density (5×10^5 mononuclear cells/ 100 µL ex vivo suspension media; ~ 3000 CD 34^+ cells/ scaffold) at day-15. HSC seeded TEBN scaffolds were placed in in incubator

(37 °C in a humid atmosphere with 5 % CO_2) for 12 h to allow cell adhesion, with 20 µL media added every hour after seeding. Thus, HSC seeded TEBN were matured in perfusion bioreactor (3D Biotek, USA) under operating conditions previously described [352]. Briefly, two HSC seeded TEBN (from one group either BMC or BAC) were stacked per polycarbonate chamber separated by sterile O-rings, with a flow rate of 0.5 mL/min equilibrated with 50 mL maturation media in media reservoirs, which was replenished 50% with fresh media every 7 days.

5.2.1.5 *In vitro Biological Characterization*

Biochemical Studies

Cellular proliferation of Osteo-WJMSCs seeded scaffolds was evaluated using Alamar Blue ™ assay, as per manufacturer's protocol. Briefly, cell seeded scaffolds were incubated with 10% (v/v) dye solution in culture media for 3 h and 100 µL of incubated culture media was read at 570/600 nm using a microplate reader (Multiskan Sky, Thermo Fisher Scientific, USA). The readings are normalized to day-1 and presented as normalized Alamar units (a.u) which is proportional to the viable cells in the scaffold.

Alkaline phosphatase (ALP) activity was assessed based on our previous protocols [141] [305]. Briefly, Osteo-WJMSCs seeded constructs were lysed in ice cold cell lysis buffer (20 mM Tris-HCl (pH 7.5), 150 mM sodium chloride, 5 mM magnesium chloride, and 0.5% (v/v) Triton-X100). The membrane bound ALP was estimated using a colorimetric assay formed from yellow coloured product (p-nitrophenol, λ_{max} = 405 nm) by hydrolysis of substrate p-nitrophenol phosphate (p-NPP), read using microplate reader. ALP activity is presented as DEA (diethanolamine) units, where 1 DEA unit is the amount of ALP enzyme hydrolysing 1 µM of p-NPP at pH 9.6 (1M diethanolamine buffer) and 25 °C. The ALP activity was normalised with respect to DNA content which was estimated using Quant-iT picogreen double stranded DNA assay kit. Cell lysate was mixed with fluorescent probe and fluorescence intensity ($\lambda_{excitation}$ /$\lambda_{emission}$ = 480/525 nm) was measured using a microplate reader (Tecan Infinite Pro, Switzerland), and the total DNA content was estimated from a standard curve obtained using double stranded λ DNA and the same is presented as µg DNA (as per manufacturer's protocol).

The vascular tone of HUVEC seeded TEBN was evaluated by measuring endothelial nitric oxide (NO) based on previous published protocols [68]. Briefly, at different time-points HUVEC seeded TEBN was incubated for 8 h in incomplete media, and the spent media was collected. Griess reagent (Gibco Life Technologies, USA) was used to estimate nitrite, a stable

degradation product for NO in spent media, which converts sulfanilic acid to a purple azo dye in presence of N-(1-naphthyl)ethylenediamine, read at λ_{max} = 548 nm using microplate reader. The NO produced is represented as µM by calculating from a standard curve generated from sodium nitrite.

Immunohistochemistry

Histological assessments were done on cell laden matrices after fixing them in neutral buffered formalin. The fixed constructs were then placed in 15% (w/v) sucrose made in PBS (pH 7.4) for 6h, followed by 30% (w/v) sucrose (in PBS, pH 7.4) overnight. The constructs were embedded in PolyFreeze tissue freezing medium (Sigma, USA) and using cryomicrotome (Leica CM1860 UV, Leica Biosystems, Germany) 15 µm cryosections were obtained. The sections were stained with hematoxylin and eosin to assess cellular distribution. For immunostaining, the sections were blocked with 5% (w/v) bovine serum albumin (BSA), followed by primary antibody incubation (either rabbit polyclonal against osteopontin – OPN (1:500 dilution; Abcam, USA) or rabbit polyclonal against von Willebrand factor – vWF (1:400 dilution; Abcam, USA) or mouse monoclonal against CD 34 (1:500 dilution; Thermo Fisher Scientific, USA). Appropriate secondary antibody was used – goat anti-rabbit AlexaFluor488 (1:100 dilution; Abcam, USA; for rabbit polyclonal primary antibodies) or goat anti-mouse AlexaFluor488 (1:100 dilution; Abcam, USA; for mouse monoclonal antibodies). The sections were counter stained with DAPI (4′,6-diamidino-2-phenylindole) to stain the nucleus. The stained sections were visualized and fluorescence images were captured using a fluorescence microscope (NikonECLIPSE Ti2, Japan).

Gene Expression Studies

For assessing the expression of relevant genes of cells within the TEBN, real time gene expression of genes listed in **Table 5.1** with reference to an endogenous house-keeping gene, human β-actin. Total RNA content was extracted from cell seeded TEBN constructs by TRI reagent and 1 µg of RNA was used for synthesis of cDNA by using high capacity reverse transcription kit (Applied Biosystems, Invitrogen, USA) in a thermal cycler machine (Applied Biosystems Veriti, Thermo Fisher Scientific, USA). The expression levels were estimated by Delta CT Method (-ΔCT), and represented as heat map, where relative expression level of gene of interest (GOI) is calculated based on the equation, Relative expression, $R = 2^{-(C_{T\,(GOI)} - C_{T\,(ACTB)})}$. The basal expression levels of these genes in tissue culture plates with reference to endogenous house-keeping gene was used as baseline reference against the cells seeded in scaffolds. The fluorescence signal was detected using Power SYBR PCR master mix (Applied

Biosystems, Invitrogen, USA) in a real-time PCR machine (Applied Biosystems 7500, Thermo Fisher Scientific, USA).

Table 5.1 *Primer sequences of genes investigated in the study*

Gene	Sequence	Accession Number
Human β-actin (*ACTB*)	**F** 5′- GGCATCCTCACCCTGAAGTA-3′ **R** 5′- GGGGTGTTGAAGGTCTCAAA-3′	NM_001101.5
Human Integrin αII (*ITGA2*)	**F** 5′- GGAGGAAGACTTGCGTCG-3′ **R** 5′- CACAGGTTCCCCAGTAGATG-3′	NM_001004439.1
Human Integrin α5 (*ITGA5*)	**F** 5′- GGCTTCAACTTAGACGCGGA -3′ **R** 5′- GGCCGGTAAAACTCCACTGA-3′	NM_002205.4
Human Integrin αV (*ITGAV*)	**F** 5′-AATCTTCCAATTGAGGATATCAC 3′ **R** 5′- AAAACAGCCAGTAGCAACAAT-3′	NM_001145000.2
Human Integrin α8 (*ITGA8*)	**F** 5′- CAGTTTGGACGAATCCACCT-3′ **R** 5′-TGCTGTCTGGATTGTCCTTG-3′	NM_003638.2
Human integrin β1 (*ITGB1*)	**F** 5′- GAAGGGTTGCCCTCCAGA-3′ **R** 5′- GCTTGAGCTTCTCTGCTGTT-3′	NM_002211.3
Human integrin β3 (*ITGB3*)	**F** 5′- CCGTGACGAGATTGAGTCA-3′ **R** 5′- AGGATGGACTTTCCACTAGAA-3′	NM_000212.2
Human integrin β6 (*ITGB6*)	**F** 5′- TCAGCGTGACTGTGAATATCC-3′ **R** 5′- GTGACATTTGGAGCTGTTCAC-3′	NM_000888.4
Human integrin β8 (*ITGB8*)	**F** 5′- AATTTGGTAGTGGAAGCCTATC-3′ **R** 5′- GTCACGTTTCTGCATCCTTC-3′	NM_002214.2
Human β-catenin (*CTNNB1*)	**F** 5′- GCGCCATTTTAAGCCTCTCG-3′ **R** 5′- CTGAAGCTGCTCCTCAGACC-3′	NM_001098209.1
Human C-X-C motif chemokine ligand 12 (*CXCL12*)	**F** 5′- GTGTCACTGGCGACACGTAG-3′ **R** 5′- TCCCATCCCACAGAGAGAAG-3′	NM_000609.7
Human bone morphogenetic protein receptor type 1A (*BMPR1a*)	**F** 5′-TGGGCCTTGCTGTTAAATTC-3′ **R** 5′-ATTCTTCCACGATCCCTCCT-3′	NM_004329.3

Human angiopoietin-1 (*ANGPT-1*)	**F** 5′- GCTGATAATGACAACTGTATGTGC-3′ **R** 5′- ATGGTTTTGTCCCGCAGTA-3′	NM_001314051.2
Human N-Cadherin (*NCAD*)	**F** 5′- ATTGGACCATCACTCGGCTTA-3′ **R** 5′- CACACTGGCAAACCTTCACG-3′	NM_001308176.2
Human jagged canonical Notch ligand 1 (*JAG-1*)	**F** 5′- GAAGCAGAACACGGGCGTT-3′ **R** 5′- CAGGTCACGCGGATCTGAT-3′	NM_000214.3
Human bone morphogenetic protein 2 (*BMP2*)	**F** 5′-TTTGACCAGAGTTTTTCCATGTG-3′ **R** 5′-GAAGCAGCAACGCTAGAAGA-3′	NM_001200.4
Human Wnt family member 3 (*WNT3*)	**F** 5′- CTGCCAGGAGTGTATTCGCATC-3′ **R** 5′- GAGAGCCTCCCCGTCCACAG-3′	NM_030753.5
Human endoglin (*CD105*)	**F** 5′- CCACTAGCCAGGTCTCGAAG-3′ **R** 5′- GATGCAGGAAGACACTGCTG-3′	NM_001278138.2
Human Runt-related transcription factor 2 (*RUNX2*)	**F** 5′-GATGGGACTGTGGTTACTGTCA-3′ **R** 5′-CTCAGATCGTTGAACCTTGC-3′	NM_001278478.1
Human Osteocalcin (*OCN*)	**F** 5′- CAGCGAGGTAGTGAAGAGAC-3′ **R** 5′- GCCAACTCGTCACAGTCC -3′	NM_199173.5
Human Bone sialoprotein (*BSP*)	**F** 5′AACCTACAACCCCACCACAA-3′ **R** 5′-GTTCCCCGTTCTCACTTTCA-3′	NM_004967.3

Immunoblotting

Immunoblots were developed from cell lysates of TEBN constructs extracted by ice cold lysis buffer (50 mM Tris HCl, pH 8, 150 mM NaCl, 1% (v/v) NP-40, 0.5 % (w/v) sodium deoxycholate, 0.1 % (w/v) SDS, 1 mM phenylmethylsulfonyl fluoride, 10 mM sodium fluoride, 1 mM ethylene glycol-bis(β-aminoethyl ether)-N,N,N′,N′-tetraacetic acid). Protein concentration was estimated by Bradford's reagent and 50 µg protein were resolved under reducing conditions in 10 % polyacrylamide separating gel and transferred *via* wet transfer onto 0.2 µm poly-(vinylidene fluoride) (PVDF) membranes. The blots for probed for presence of proteins of interest using the following primary antibodies: rabbit polyclonal to vinculin (1:750 dilution; Abcam, USA); rabbit polyclonal to ERK 1/2 (1:1000 dilution; Cell Signaling

Technology, USA); rabbit polyclonal to N-cadherin (1:1000 dilution; Cell Signaling Technology, USA). β-actin was used as endogenous loading control (rabbit polyclonal to β-actin; 1:1000 dilution; Novus Biologicals, USA). The primary antibody was detected using HRP conjugated secondary goat anti-rabbit IgG (1:10000 dilutions; Abcam, USA) using enhanced chemiluminescence (ECL) kit (Pierce™ ECL Western blotting substrate kit, Thermo Fisher Scientific, USA) and documented by Gel Doc XR+ system, Bio-rad laboratories, USA. The densiometric analysis was performed using Image Lab © Bio-Rad laboratories software (v 5.1, build 8).

Flowcytometry Studies

Single cell suspensions were retrieved from HSC seeded TEBN scaffolds by trypsinization and gentle physical disassociation, further passing through 40 µm cell strainer. The collected cell suspensions were subjected to indirect flow cytometry studies. The cells were sequentially labelled with primary antibodies: rabbit polyclonal to CD 38 (1:25 dilution; Thermo Fisher Scientific, USA), followed by mouse monoclonal CD 34 (1:100 dilution; Thermo Fisher Scientific, USA). Secondary antibody labelling was done after primary antibody incubation at 25°C for 30 min with DyLight594 conjugated goat anti-rabbit IgG (1:100 dilution; Abcam, USA) for 30 min followed by FITC conjugated goat anti-mouse IgG (1:100 dilution; Sigma, USA) for 30 min at 25°C. Aliquots of cell suspensions were labelled with isotype controls rabbit IgG or mouse IgG (Thermo Fisher Scientific, USA), followed by labelling with respective Dylight594 or FITC secondary antibody IgG, served as isotype controls for gating for flowcytometric analysis. The labelled cells were analysed using BD AccuriTM C6 Plus flow cytometer (Becton Dickinson Biosciences, USA) equipped with 488nm excitation laser and emission detection in FL1 channel (FITC 533/30 nm) and FL2 channel (PE 585/40 nm).

5.2.2 Fabrication of Magnetically Actuated Outer 3D Bioprinted Bone Struts

5.2.2.1 *Synthesis of Fe Doped 70S Bioactive Glass (FeBG) Nanoparticles*

A modified Stöber's method was followed for synthesis of Fe doped 70S bioactive glass nanoparticles, wherein the bioactive glass network belonging to the ternary network $70SiO_2.15CaO.5P_2O_5.10Fe_3O_4$ was chosen. For this, tetraethyl orthosilicate (TEOS) was hydrolysed in methanol/water/NH_4OH system in molar ratio as follows TEOS:methanol:NH_4OH:water 1:200:11.2:66 for 2 h. Subsequently, the precursors $CaCl_2$, $FeCl_3$, and triethyl phosphate (TEP) were added in sequence at an interval of 1 h, aged for 72

h in continuous stirring. The sol particles derived as a result was collected by centrifugation, washed thoroughly and freeze dried to obtain the FeBG nanoparticles. The FeBG nanoparticles were thermally stabilized by calcination at 700 °C for 5h (at a rate 1 °C/min in air atmosphere) to facilitate nucleation of magnetite responsible for magnetic properties [353].

5.2.2.2 *Thermoplastic FeBG-poly(caprolactone) Ink and Silk Fibroin-based Bioink Preparation*

The synthesized and calcined FeBG were physically mixed aseptically under laminar air flow on a hot plate with poly(caprolactone) pellets (MW = 80,000; Sigma, USA) in the ratio 1:10 (w/w) and the composite melt was cooled down to down obtain FeBG/PCL flakes which were used for thermoplastic extrusion printing. On the other hand, for bioprinting applications bone bioink (SF-PVP-SR0) which was reported in *Chapter 4* was used [141]. Briefly, one mL of this bioink formulation consisted of blends of 0.25 mL 5 (w/v) % BMSF, 0.25 mL 3 (w/v) % AASF, 0.4 mL of 20 (w/v) % polyvinylpyrrolidone (PVP) K90 (molecular weight 360,000) (Sigma, USA) with 0.5% (w%) $Ca_5(PO4)_3$.OH apatite and 0.1 mL of culture media containing 10^7 osteogenically primed WJMSCs.

5.2.2.3 *Physical Characterization*

The calcined FeBG nanoparticles were visualized using field emission transmission electron microscope (JEOL 2100F, Japan) equipped with energy dispersive X-ray spectrometer used for obtaining elemental analysis and mapping. The magnetic hysteresis cycle measurements of the calcined FeBG nanoparticles and FeBG/PCL composite was performed using vibrating scanning magnetometer (Lake Shore Cryotronics Inc., model 7410; USA) at room temperature. Coercivity (H*ci*), saturation magnetization (M*s*) and remnant magnetization (M*r*) were calculated from the hysteresis loop. Mechanical properties of the outer cortical bone struts (made by PCL alone or FeBG/PCL) were evaluated by following ISO 4049 and ADA/ANSI 27 (testing polymer-based restorative materials) standards. Briefly, for evaluating diametral tensile strength, specimens (10 mm outer diameter - D, 5 mm thickness - T) were used. Uniaxial loading with cross-head speed of 1 mm/ min along the long axis was applied until failure, and diametral stress was calculated as $\sigma = 2F/\pi DT$, where F is the applied force in Newtons. The Young's modulus was calculated from the stress-strain profiles and represented.

5.2.2.4 *3D Bioprinting Outer Cortical Bone Struts and Magnetic Actuation Regimen*

A dual extruder/ dual ink-based 3D bioprinting approach (**Figure 5.1C**) was followed to develop strutted bone model wherein one filament of FeBG/PCL was alternately printed next to silk fibroin bone bioink containing osteogenically primed WJMSCs. 3D object (**Figure 5.6Ci**) was designed by AutoCAD (Autodesk, USA) and the generated .STL file of the geometries were sliced through Slic3r (Repetier Host software, Hot-world GmbH & Co., Germany) to get G-Codes fed for printing in microextrusion based bioprinter Bio X™ (CELLINK, Sweden). For this, PCL-FeBG flakes were loaded in 3 mL thermoplastic cartridges with 0.2 mm metal tapered precision tip (acting as extruder-1; print temperature = 160°C, print speed = 4 mm/s, print pressure = 225 kPa) and 3 mL of gelled bone bioink was loaded in sterile 3 mL plastic cartridges with tapered 27G precision needle (acting as extruder-2; print temperature = 20°C, print speed = 5 mm/s, print pressure = 25 kPa) and the strutted structure was bioprinted. The FEBG/PCL flakes obtained were fed into thermal extrusion cartilage and maintained at 160°C for 30 min, prior to printing. Pertinent to note here, the bioink used here was reported from previous *Chapter-4* (**PVP-SF-SR0**) [141], wherein the BMSF and AASF were sterilized by UV irradiation (λ_{max} = 302 nm, 15 min) and the PVP with dispersed hydroxyapatite was sterilized by autoclaving. The sterile bioink formulation was then used to disperse the cells in aseptic manner and allowed for gelation. then bioprinted under sterile conditions using bioprinter Bio X™ (CELLINK, Sweden) alongside the thermoplastic PCL-FeBG ink.

Culture media was added post printing and the constructs were matured *in vitro* with media change every 48 h for 14 days. Maturation in magnetic actuators were done by following our previous reports where a custom magnetic actuator device (MAD) consisting of control unit, motor driving unit connected to electromagnet (Type 58, 24V DC operated capable of outputting 140 N). The magnetic actuation regimen employed was followed based on the strategy used for the device in our previous report [354], where pulsed magnetic field was applied (t_{ON}/t_{OFF} = 1s/1s) for 2 h/day inside the incubator till 14 days (**Figure 5.7A**).

5.2.2.5 *Biological Characterization*

Cellular viability post-printing at day-7 and day-14 was evaluated using live/dead stain. Briefly, the bioprinted constructs were incubated in 40 nM calcein-AM (stains live cells green) and 20 nM ethidium homodimer (stains dead cell red) in PBS for 15 min. The dye solution was removed and the constructs were visualized using a fluorescence microscope (NikonECLIPSE Ti2, Japan). Biochemical analysis for total DNA content using Quant-iT picogreen double

stranded DNA assay kit and ALP activity using p-NPP method (as described in previous sections) was performed on 3D bioprinted constructs. Total collagen content was estimated using Sirius red dye based colorimetric assay [305] with rat tail collagen used to develop the standard curve. Briefly, 3D bioprinted constructs were minced in pepsin digestion buffer (0.1 M acetic acid, 0.5 M NaCl and 1 mg/mL pepsin), and 100 µL of digesate was dried overnight in 96 well plate. 100 µL of 1 mg/mL direct red 80 saturated with picric acid was added to it later and incubated for 1 h. The dye solution was removed, unbound dye was rinsed with 0.01 N HCl, and the bound dye was resolved in 100 µL 0.1 N NaOH, which was read at 550 nm in microplate reader. The total collagen content was normalised with respect to the total DNA content and the results are presented as µg collagen/ µg DNA.

Gene expression studies for osteogenic genes (*RUNX2, OCN, BSP*) – gene of interest (GOI) with reference to endogenous house-keeping gene (*ACTB*) was performed using protocols described in previous sections for 3D bioprinted constructs. The expression levels were estimated by Delta-Delta C_T method ($-\Delta\Delta C_T$), where fold change $F = 2^{-[(C_{T\,(GOI)} - C_{T\,(ACTB)})_{Day3\ or\ 7\ or\ 14} - (C_{T\,(GOI)} - C_{T\,(ACTB)})_{Day1}]}$. The fluorescence signal was detected using Power SYBR PCR master mix (Applied Biosystems, Invitrogen, USA) in a real-time PCR machine (Applied Biosystems 7500, Thermo Fisher Scientific, USA). Immunoblotting studies were carried out on 3D bioprinted constructs after cell lysis using protocols as discussed in previous section and probed for proteins using: rabbit polyclonal to Yes-associated protein 1 (YAP) (1:1000 dilution; Abcam, USA) and rabbit polyclonal to focal adhesion kinase (FAK) (1:1000 dilution; Abcam, USA). β-actin was used as endogenous loading control (rabbit polyclonal to β-actin; 1:1000 dilution; Novus Biologicals, USA). The primary antibody was detected using HRP conjugated secondary goat anti-rabbit IgG (1:10000 dilution; Abcam, USA) using enhanced chemiluminescence (ECL) kit (Pierce™ ECL Western blotting substrate kit, Thermo Fisher Scientific, USA) and documented by Gel Doc XR+ system, Bio-rad laboratories, USA. The densiometric analysis was performed using Image Lab © Bio-Rad laboratories software (v 5.1, build 8).

5.2.3 Statistical Analysis

All the experiments were carried out in experimental or biological triplicates (unless or otherwise noted) and the results from the analysis are presented as mean ± standard deviation, for the parametric data set, with normal and F-distribution. Statistical significance was analysed by one-way analysis of variance (ANOVA) *via* Tukey's test (Origin 2018b, OriginLabs, USA) for F-distribution dataset; while Student's t-test for normal distribution dataset and results between two groups were considered statistically significant if p-value was found to be less than 0.05.

5.3 Results and Discussion

Treatment of noninfected aseptic diaphyseal nonunions with autologous bone marrow aspirates from iliac crest has been a successful clinical practise. [355] The procedure involves two surgical steps; wherein a typical noninfected (> 2 cm, non-contained defect) is stabilised with a plate osteosynthesis in first step, bridging the proximal and distal ends of non-union with bone cement spacers (~ 6-8 weeks). The second step is carried out, if no infection is noticed or gap healing has initiated. In the second step, previous osteosynthesis plate is removed along with spacer and replaced with bone marrow aspirate (by Reamer-Irrigator-Aspirator) followed by reosteosynthesis with optimal stability [327] while the secondary gap healing is monitored over 12-18 months post-operation. However, in case of infections, or patients with compromised immunity, or age-related risk the first step is repeated as often as necessary. Under such pathological conditions, there is total destruction of endosteum, vascular disruption and depletion of marrow, impairing the fracture healing further. In these scenarios, the use of suitable orthobiologic which could serve as a bridging callus is necessitated. The poor survival and engraftment of autologous bone marrow as local biological enhancement, opens scope for tissue engineered bone marrow encompassed around a cortical support, which could facilitate osteonal migration, endosteal callus formation while replenishing the marrow. In this regard, the rationale here was addressing this clinical problem involving secondary gap healing in atrophic long bone nonunions. Presented here is an orthobiological intervention, where a 'sandwich type' biofabricated diaphyseal cross-sectional unit encompassing engineered bone marrow could potentially aid in contact guidance healing in secondary reosteosynthesis procedures.

5.3.1 *Channelized Silk Fibroin Blend Scaffolds Biomimics Cancellous Endosteum Niche*

Silk fibroin (SF) has garnered attention in bone tissue engineering applications due to its well documented biocompatibility, mechanical properties and tuneable biodegradability. *Bombyx mori* SF (BMSF) in this regard has been well explored in BTE [52, 356] because of the aforementioned advantages and additionally due to its cost-effective large-scale batch production for medical device fabrication. Similarly, with our experience with endemic non-mulberry SF (*A. assama*) – AASF has proven to be a good osteoconductive bone graft material [119, 308]. This osteoconductive trait is attributed due to the presence of intrinsic RGD tripeptide which favours cell adhesion and subsequent integrin mediated osteogenic phenotype maintenance [52]. In this study, a blend of BMSF:AASF (2% w/v) solutions was used for fabrication of channelized silk SF blend scaffolds (**Figure 5.1B**) by freeze drying. It was hypothesized that the gross-hydropathicity presented by the crystalline domains (GAGAGS repeats in *B. mori* and $AAA(A)_{5\text{-}15}$ repeats in *A. assama*) together with RGD tripeptide, would favour stromal cells adhesion, survival and maturation for bone marrow engineering. Channelized BMSF sponges had earlier been reported for megakaryocyte *ex vivo* production. [342] Herein, a different strategy was adopted to mimic the spongy trabecular endosteum with a central medullary cavity and peripheral vascular channels via the assembly setup shown in **Figure 5.2A**. The channelized scaffolds derived from BMSF solution were termed BMC (devoid of RGD tripeptide; control group), while the experimental group derived from blend SF solutions (BMSF + AASF) were termed BAC, hitherto in the study.

The strategy adopted to fabricate the channelized scaffold is modular and could be easily scaled by either increasing or decreasing the number of channels or cavity size by opting for suitable custom 3D printed molds. From our previous experiences, such freeze-dried scaffolds have been replicated with good reproducibility for *in vitro* experimentation and *in vivo* small animal bone defect models. [68, 305, 308] 4 channels were chosen here arbitrarily, to aid in preferential seeding of cells and thereby achieving compartmentalization within these channelized freeze-dried constructs. Thus, freeze-dried derived BAC channelized sponges exhibited open-porous, well interconnected microstructures (**Figure 5.2Bi**) similar to the bone trabeculae exhibiting average pore size of 140-160 µm (**Figure 5.2Bii**) with no remarked change in pore size (**Figure 5.2B iii-iv** for BAC against **Figure 5.2B v-vi**) near the vascular channel region (marked red) or away (marked yellow in **Figure 5.2Bi**). Similarly, there was no difference in porosity between the group as assessed by hexane displacement method (~95%; **Figure A5.1**, *Appendix*).

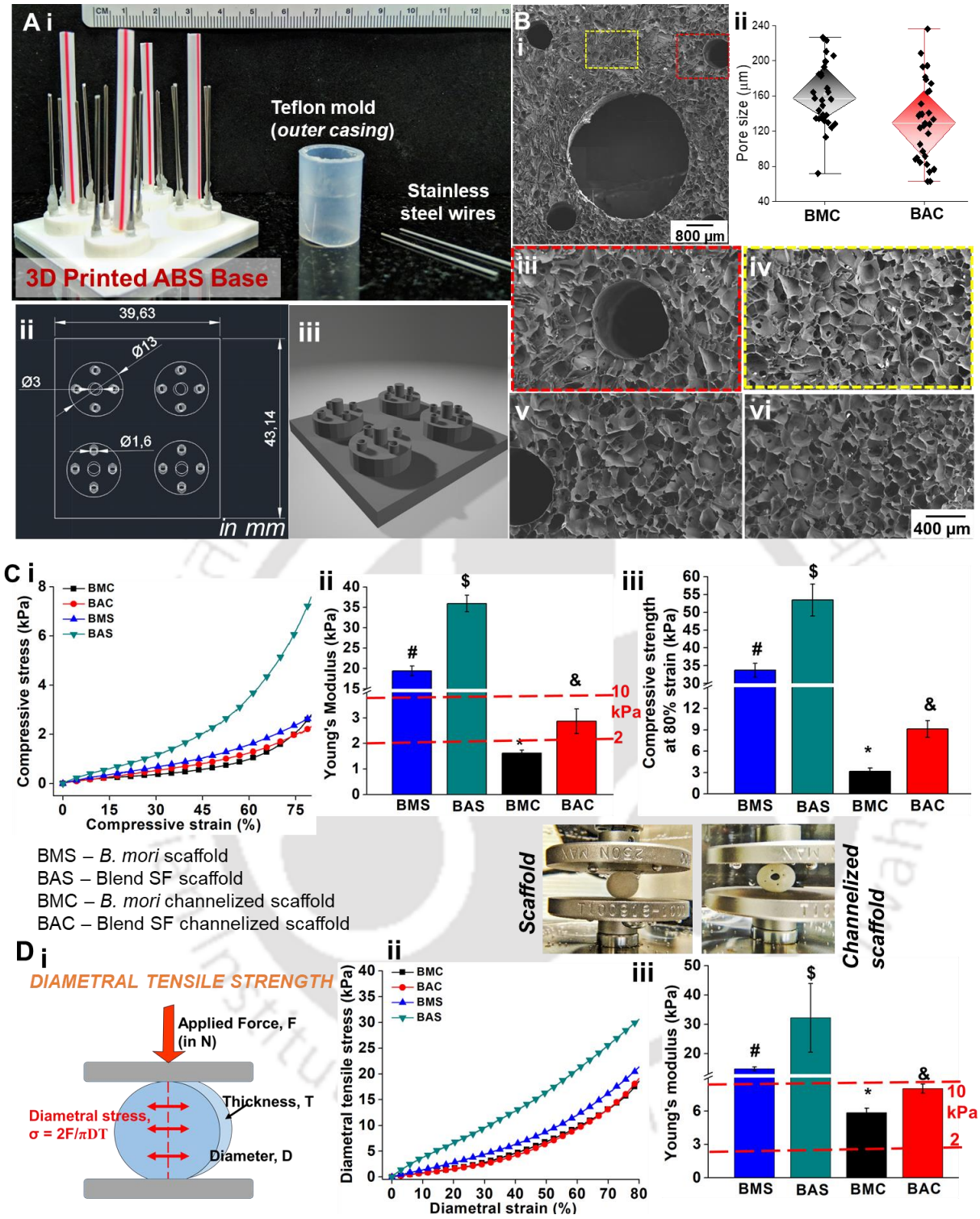

Figure 5.2. ***Fabrication and physical characterization of channelized scaffolds for TEBN matrices.*** *A) Custom molds 3D printed for channelized SF scaffolds fabrication, ii) CAD design, iii) post-assembly; B) i) FESEM images of fabricated scaffolds (BAC group), ii) pore size distribution, iii), iv) BAC scaffolds, v), vi) BMC scaffolds (red box indicating regions for endosteal niche, while yellow box indicating vascular niche); C) Mechanical characterization of fabricated scaffolds - i) Compressive stress-strain curve along longitudinal direction, ii) Young's modulus, iii) compressive strength at 80 % strain; D) Diametral tensile strength*

*calculated as represented from the lateral surface to mimic the tensile forces acting on the scaffold, ii) representative stress-strain curve and iii) Young's modulus of the scaffold types used in the study. (Data presented as Mean ± S.D (n=3); *, $, #, & represents statistically significant difference at p ≤ 0.05, same symbols indicate no significance while different symbols indicate statistical significance between the groups tested; parametric Student's t-test).*

Mechanical studies on the scaffolds were performed to understand their biophysical behaviour under load bearing conditions (**Figure 5.2C-D**). Compressive strength when evaluated along longitudinal direction revealed that the sponges had a stress-strain relationship, typical of open-celled foams. [68, 305] An initial elastic region (linear region up to 20% strain) (**Figure 5.2Ci**) followed by a steep increase in stress in relationship to applied strain, representing pore collapse and densification of sponge. The scaffolds without channels (BMS and BAS) exhibited higher Young's modulus (E) and compressive modulus at 80% strain (**Figure 5.2Cii-iii**; ~20-36 kPa, ~35-60 kPa respectively). The incorporation of channels and medullary cavity in channelized scaffolds (BMC, BAC used in the study) brought down the mechanical properties by ~8 folds, where the BAC group had an E = ~3 kPa. Though typically this is quite low for load bearing applications, the human bone marrow is elastic having E ranging between 0.25 to 24.7 kPa. [357] Therefore, our intention was that this channelized matrix would serve as suitable niche with appropriate biophysical (in terms of bulk modulus) to host the HSCs, which might not survive a stiffer matrix presentation. Similarly, the mechanical properties along the diametral direction (cross-sectional unit) were also assessed (**Figure 5.2 D**), which had similar elastic regime (stress-strain relationship) (**Figure 5.2Dii-iii**), with E ~ 6 kPa, ideal for bone marrow niche reconstruction. In our model, the actual mechanical reinforcements would be provided by the outer bioprinted cortical bone constructs (FeBG/PCL). Together with microstructure resembling open-porous trabeculae like network that would be adequate for cellular infiltration and nutrient transport. Meanwhile, the conducive bulk mechanical property would enable HSC survival and reengineering the bone marrow.

5.3.2 Stromal Cells Survival and Recreating the Compartmentalized Niche Microenvironment in Channelized Silk Fibroin Scaffolds

Cellularization of the channelized SF scaffold was done by a preferential seeding technique (**Figure 5.3A**). Cross-sections of the channelized scaffolds were conditioned and seeded with osteogenically primed Wharton's jelly derived mesenchymal stem cells (osteo-WJMSCs). The open-porous network enabled the cells to get distributed within the open-celled

sponges. After 3 days, the peripheral channels were seeded with silk-fibroin blend hydrogel containing human umbilical vein endothelial cells (HUVECs). This strategy was adopted such that we could develop two compartments: (i) osteo-WJMSCs serving as endosteal niche stromal cells and (ii) HUVECs within the channels mimicking the vascular niche. It has been documented that the endosteal niche and the vascular niche are essential for HSC survival, and its specific lineage commitment. The endosteal niche is the primary osteoblastic niche comprising mainly of osteoblast cells and help in regulating a subpopulation of HSCs known as LT-HSCs (long term HSCs) which are quiescent low-cycling cells involved in haematopoiesis [358]. In addition to this, osteoblastic cells associate with vascular cells (particularly the endothelial cells and pericytes) to form the vascular niche. The HSCs interacting with this niche, differentiates and regulates a subpopulation of HSCs involved in transendothelial migration, megakaryopoiesis and thrombopoiesis. [359]

Cell viability of seeded Osteo-WJMSCs cultured in channelized scaffold showed good survival over the 21-day culture period, as assessed by Alamar blue assay (**Figure 5.3Bi**). The growth curve depicting the active metabolism of proliferating cells (from the normalized Alamar blue assay) between the BMC and BAC groups was not significantly different till day-14. However, at day-21 enhanced cellular proliferation in BMC group (~1.13 folds) in comparison to BAC group. Biochemical analysis for alkaline phosphatase (ALP) activity, a key mineralizing enzyme was assessed to determine the state of osteogenesis of seeded osteo-WJMCs (**Figure 5.3Bii**). ALP expression profile in BMC scaffold was relatively constant till day-14, with a slight decrease at day-21 (~1.5 folds), whereas in BAC group the ALP activity peaked at day-7 (~2 folds increase in comparison to days 1, 14) and subsided by day-21. This peak in ALP activity and the relatively slower growth profile in BAC, suggests that the Osteo-WJMSCs retained their osteogenic commitment much better, possibly indicating the role of RGD and integrin mediated signalling. [52, 305]

The endothelial cell survival was evaluated in channelized scaffolds seeded with Osteo-WJMSCs, wherein the HUVECs were seeded in the channels at day-3 (following seeding regimen as depicted in **Figure 5.3A**). NO is secreted by endothelial cells which represents their vascular tone [360] and it was noticed that BAC group showed significantly higher NO secretion in day-7 (~1.8 folds), day-14 (~2.2 folds) in comparison to BMC group (**Figure 5.3Biii**). We hypothesized that cellular cross-talk within the matrices enabled this better survival of endothelial cells in the BAC group. Hence, we labelled the cells with cytotracker dyes (**Figure A5.2** *Appendix*) WJMSCs labelled green and HUVECs labelled red).

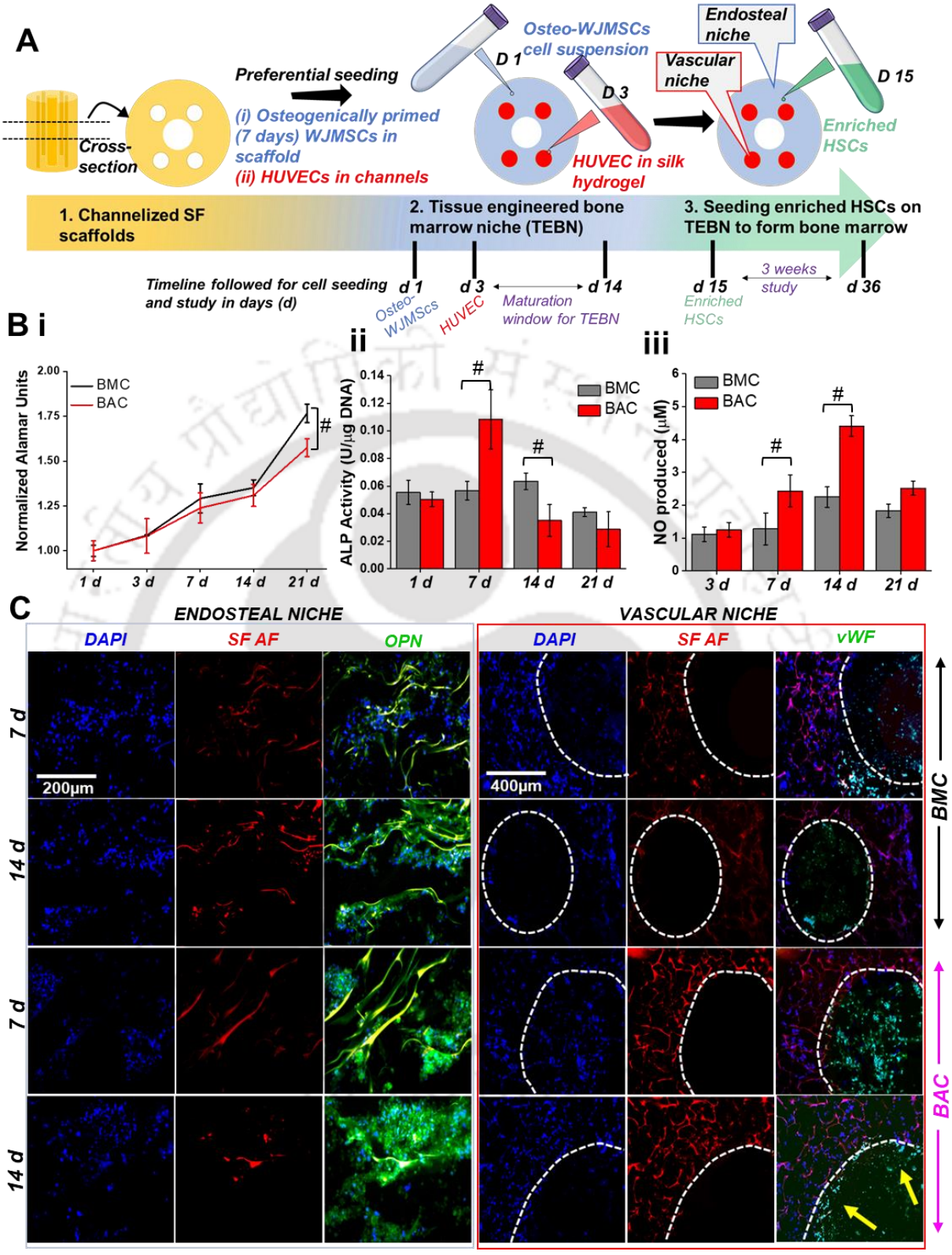

Figure 5.3. ***Development of tissue engineered bone marrow niches (TEBN).*** *A) Scheme representing the development of tissue engineered bone marrow niche, the time-line and the seeding regimens followed; B) Biochemical assessment i) Cellular proliferation of osteo-WJMSCs in scaffolds, and ii) their respective ALP activity, iii) post-seeding HUVECs, vascular tone assessed by NO assay; C) Immunohistological staining for characterization of Osteo-*

WJMSCs and HUVECs seeded TEBN groups (BMC, BAC), for nucleus stained blue with DAPI, red channel indicating silk fibroin autofluorescence as indicator of scaffold boundaries (SF AF) and protein of interest in OPN (for endosteal niche) and vWF (for vascular niche), where yellow arrow indicating migration and assembly of HUVECs to form discrete discrete endothelium lining. (Data presented as Mean ± S.D (n=3); # represents statistically significant difference at p ≤ 0.05; parametric ANNOVA Tukey's test.

Interestingly, at day-7, the migration of Osteo-WJMSCs was noticed towards the vascular niche and vice versa (**Figure A5.2** *Appendix*) when compared to day-1 in the BAC scaffolds, proving the involvement of cellular cross-talk, possibly involved in maintaining better vascular tone in BAC scaffolds in comparison to BMC group. Immunohistological analysis (**Figure 5.3C**) for a key osteoblastic marker (osteopontin - OPN) and endothelial marker (von Willebrand factor - vWF) was assessed. The BAC scaffold group showed qualitatively higher expression of OPN in comparison to BMC group (at day-7 and day-14). Similarly, the vWF expression was predominant in BAC group where by day-14 the endothelial cells migrated to the walls of the channel, assembling into discrete vascular channels; whereas in BMC group the endothelial cells still remained largely dispersed across the channel cross-section. This compartmentalization of vascular niche and osteoblastic endosteal niche by day-14, enabled us to use this TEBN to be used as support for HSCs and further maturation in perfusion bioreactor.

5.3.3 Upregulation of Key Cellular Ligands Mediates HSCs Adhesion and Survival in Tissue Engineered Bone Marrow Niche

Before seeding the HSCs, molecular characterization on Osteo-WJMSCs and HUVEC seeded TEBN were carried out (at different timepoints) for expression of key cellular ligands and molecules which enabled in this compartmentalization and reconstitution of vascularized endosteum *in vitro*. Endosteum mirconiche is a complex system exhibiting cellular heterogeneity with spatiotemporal specificity arising due to several factors. Some of the key factors include the biophysical presentation of cues, biochemical cues regulated by growth factors and cytokines, oxygen tension. The niche cells which support the multipotent stromal progenitor cells (mesenchymal) and hematopoietic progenitor cells are regulated by these signals. Thus, the niche microenvironment dictates the lineage commitment and self-renewal of these multipotent cells. In this regard, we investigated few important cell adhesion ligands (importantly the integrin family), which get upregulated. Since AASF is bestowed with intrinsic RGD tripeptide, the BAC group greatly benefits with this advantage. Real-time gene expression profiles (**Figure 5.4A**) revealed that integrins α5, αV, β3, β6, β8 were upregulated

in BAC group in comparison to BMC group. At day 14, *ITGA5* ~3.3 folds; *ITGAV* ~3.2 folds; *ITGB3* ~3 folds; *ITGB6* ~9 folds increase in BAC group in comparison to BMC, while at day-7 *ITGB8* ~2.5 folds increase in BAC in comparison to BMC was noticed ($p \leq 0.05$; n=3).

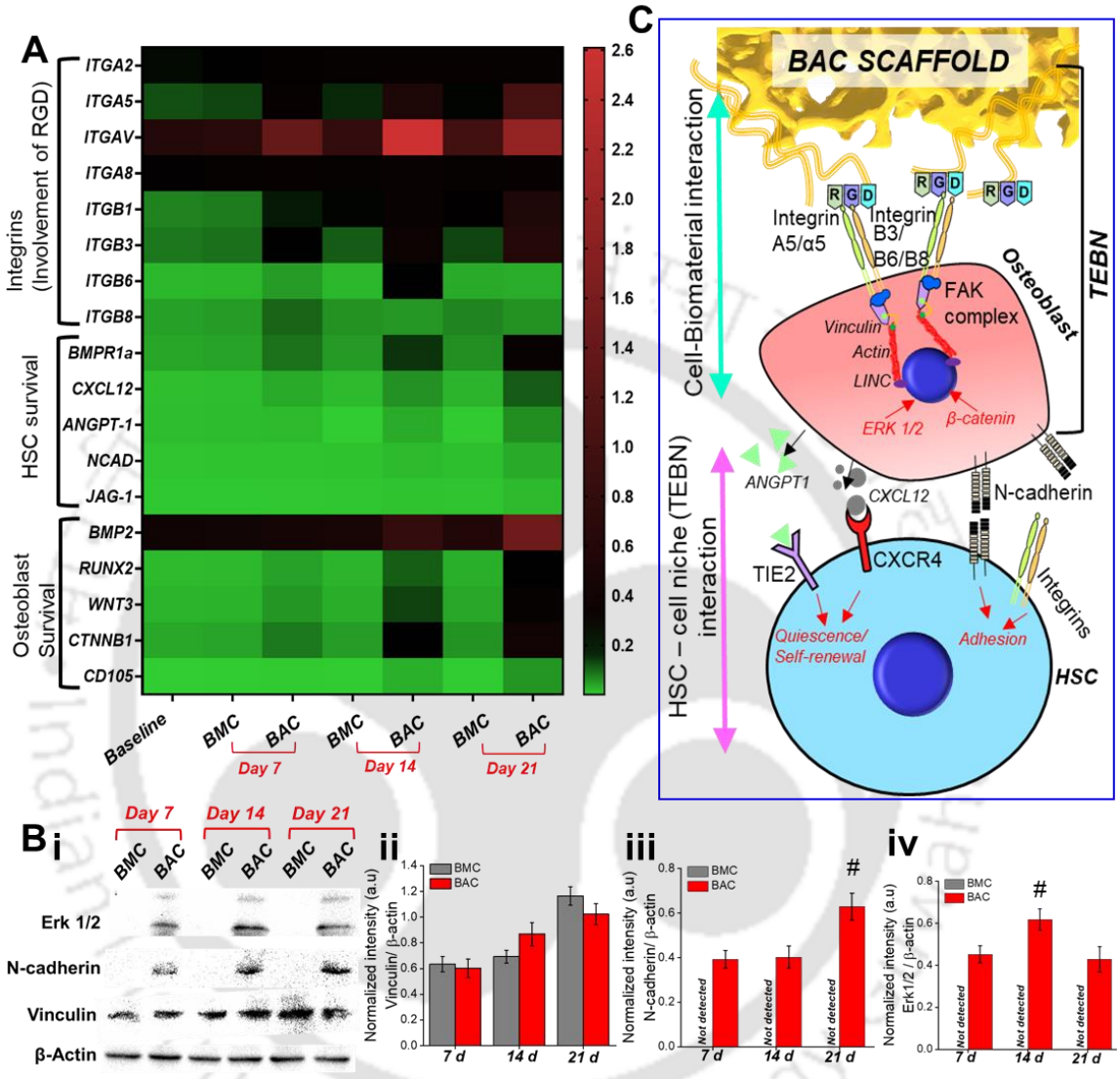

Figure 5.4. ***Molecular characterization of tissue engineered bone marrow niches.*** *A) Real time gene expression heat-map profiles for genes pertaining to integrin mediated cell adhesion, hematopoietic stem cells (HSC) survival and osteogenic survival; B) Western blot analysis i) for Erk1/2 (endosteal osteoblast survival), N-cadherin and vinculin (key proteins involved in mediating cell adhesion), and ii-iv respective densiometric profiles; C) Scheme representing the pathways activated in TEBN, mainly involving integrins for cell-matrix interaction and N-cadherin, angiopoietin-1 and CXCL12 (niche-HSC interaction). (Data presented as Mean ± S.D (n=3); # represents statistically significant difference at $p \leq 0.05$; parametric ANNOVA Tukey's test).*

Integrins play crucial role in cell adhesion and several ECM proteins such as collagens, fibronectin, laminin, vitronectin possess cell adhesion peptides which act as ligands for integrin

binding. Of the many cell adhesion peptides, RGD in particular has been documented to bind with 8 functional integrin dimers namely: αIIbβ3, αvβ1, αvβ3, αvβ5, αvβ6, αvβ8, α5β1 and α8β1 [361]. In confirmation with our hypothesis, the upregulation of the integrin (α5, αV, β3, β6, β8) helped the seeded Osteo-WJMSCs recognise the RGD cell adhesion presented in BAC. Once the integrin mediated cell adhesion is initiated, further downstream regulation is initiated which involves the involvement of focal adhesion complexes comprising talin, vinculin, focal adhesion kinases. [23] Integrin signalling (outside-in) mediates cell-polarity, survival and osteogenic commitment [81] through several secondary cascades; of which Wnt/β-catenin is a crucial pathway. [362] Interestingly, the osteogenic commitment in BAC was affirmed by the expression of key osteogenic transcription factors: runt-related transcription factor 2 (*RUNX2*) (~ 4 folds increase at day 14 in comparison to BMC); and β-catenin (*CTNNB1*) (~ 5 folds increase at day 14 in comparison to BMC) (**Figure 5.4A**). This in turn was noticed to upregulate associated osteogenic ligands such as bone morphogenetic protein 2 (*BMP2*) (~ 1.7 folds increase at day 14 in comparison to BMC) and Wnt family member 3 (*WNT3*) (~ 4 folds increase at day 14 in comparison to BMC) in BAC group. Furthermore, expression of key receptors bone morphogenetic protein receptor type 1A (*BMPR1a*, an important endosteal niche marker) (~ 3.75 folds increase at day 14 in comparison to BMC) and endoglin (*CD105*, an important vascular niche marker) (~ 11 folds increase at day 14 in comparison to BMC) was also enhanced in BAC group. These positive findings reiterate the involvement of RGD as an important cell adhesion peptide whose incorporation has implications in maintenance of osteogenic phenotype (for endosteal niche) as well as vascular niche, as reported in other studies. [333, 335, 341, 363]

Furthermore, other key cellular mediators expressed by the stromal cells in reported TEBN model were investigated that are needed for HSC mobilisation and adhesion. These included N-cadherin (*NCAD*), stromal cell-derived factor (SDF)-1α ligand (*CXCL-12*), bone morphogenetic protein receptor type 1A (*BMPR1a*). BAC scaffolds exhibited ~ 1.5 folds increase in *NCAD*, ~ 3 folds increase in *CXCL-12*, and ~ 3 folds increase in *BMPR1a* in comparison to BMC at day-14 (**Figure 5.4A**). In the endosteum, osteoblasts expressing N-cadherin serve as important stromal niche cells to which HSCs adhere and remain quiescent (HSC survival) and these osteoblasts also secrete BMPs which help in recycling of HSCs (ST-HSCs contributing for haematopoiesis for few weeks or long term LT-HSCs contributing for several months to lifetime). [90] Similarly, CXCL-12 expressing stromal cells of the vascular niche are integral part of retaining HSCs in perivascular niche [91]. While, BMPR1a, is an

important receptor serine/ threonine kinase (RSTK) which mediates the BMP signalling cascade through smad 2/3 transcription factor [52] needed for osteogenic survival of the seeded stromal cells. In addition to gene expression, the protein level expression was assessed, for key mediators involved in cell adhesion (N-cadherin, vinculin in focal adhesion complex *via* integrins) and mitogen activated protein kinases (Erk 1/2) involved in maintenance of osteogenesis (**Figure 5.4Bi**). There was not any significant difference in expression of vinculin (**Figure 5.4Bii**; n=3; $p > 0.05$) between BMC and BAC. However, there was expression of N-cadherin (**Figure 5.4Biii**) and Erk 1/2 (**Figure 5.4Biv**) in BAC group whilst it was not detected in BMC group, substantiating the results from gene expression studies. Taken into consideration all these findings, we postulate **(Figure 5.4C**) that BAC scaffold by virtue of its RGD and biophysical properties (porosity, bulk modulus) holistically presents a much scaffolding matrix which favoured cell-biomaterial interaction mediated through integrins, activating transcription factors (RUNX2, ERK1/2, β-catenin) for maintenance of osteogenic endosteal niche survival. Consequently, the cellular cross-talk enabled expression of key mediators such as angiopoietin-1 (*ANGPT-1*), *CXCL-12*, N-cadherin, which would favour HSC survival for reconstituting the bone marrow, establishing the HSC cell-niche interaction. We validated this by seeding the enriched HSCs isolated from human umbilical cord blood at day-14 on TEBN and further matured it in perfusion bioreactor for 3 weeks and assessing its performance at different timepoints.

Paucity of bone marrow donors and in case of patients with compromised immune systems, the unavailability of viable bone marrow for use in bone marrow engraftment procedures in atrophic non-union reconstruction, necessitates alternative sources. In this regard, umbilical cord blood derived hematopoietic stem cells and umbilical cord derived stromal cells (MSCs and HUVECs) presents a viable option even for HLA-mismatched transplantation. [364, 365] However, the low cell dose available from cord blood and poor survival of HSCs during cell transplantation procedures remain major roadblocks for successful clinical outcome. In this regard, *ex vivo* expansion of CD 34^+ HSCs by various strategies have been documented. [332, 334, 336, 337, 339, 340]

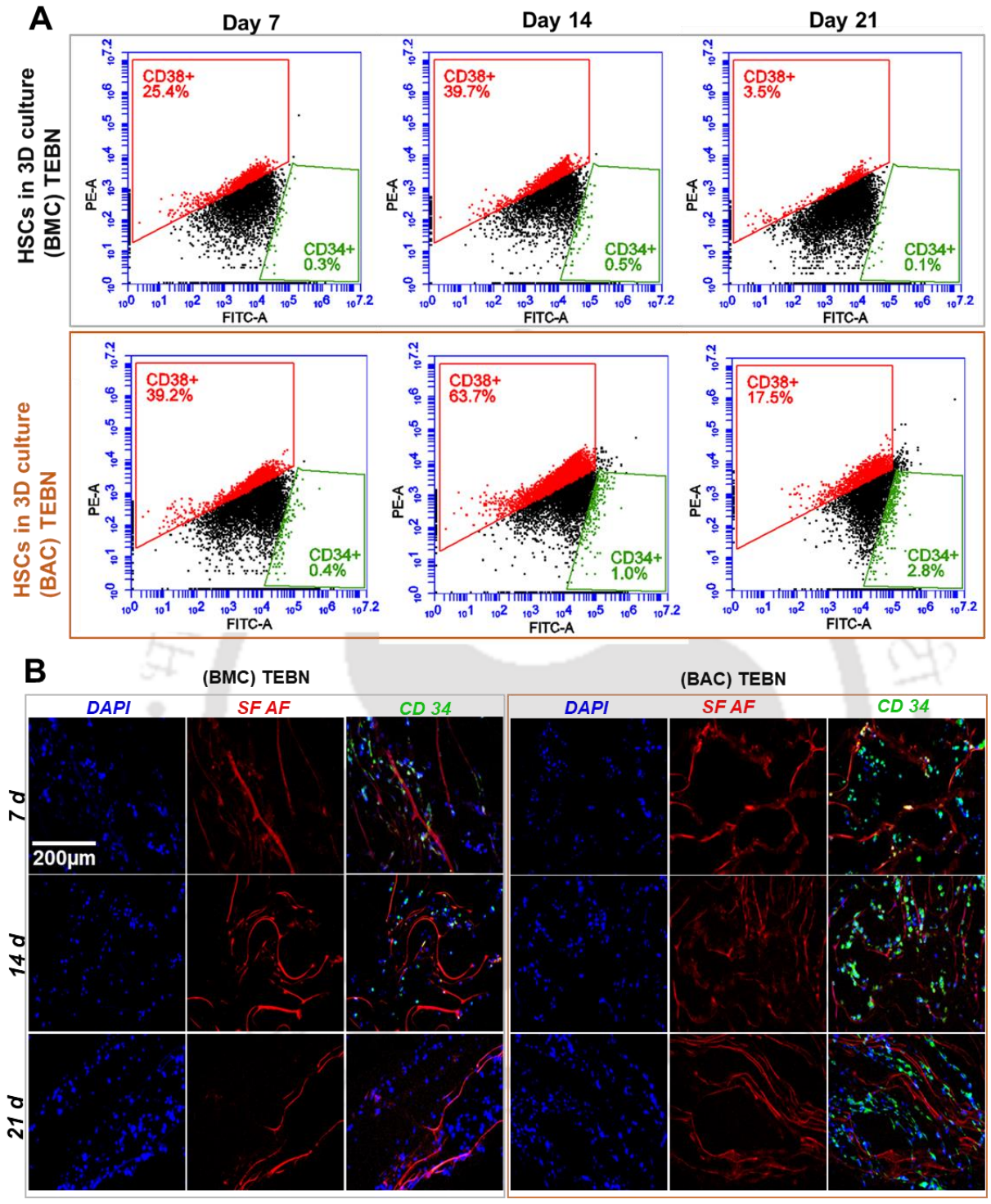

Figure 5.5. ***Survival of hematopoietic stem cells (HSCs) in TEBN***. *A) Flow cytometric analysis for CD34 (HSC marker)/ CD38 (mononuclear cell marker) for 21day study period; B) Immunohistological analysis for CD 34 in HSC seeded TEBN groups (BMC, BAC), nucleus stained blue with DAPI, red channel indicating silk fibroin autofluorescence as indicator of scaffold boundaries (SF AF) and protein of interest in CD34.*

In the approach reported here, a compartmentalised set-up was attempted, encompassing both the endosteal and perivascular niche like microenvironment noticed in bone endosteum for successful grafting of HSCs and survival. Conventionally, under *ex vivo* expansion HSCs from mononuclear fraction of cord blood are grown in suspension culture by various concentrations of early acting cytokines. [340] However, HSCs without proper stromal support or microniche do not survive *in vitro* (**Figure A5.3** *Appendix*). Typically, HSCs expressing CD 34 (an integral glycoprotein membrane receptor) are described as early multipotent cells [350] which commit to myeloid or lymphoid progeny. As the multipotency decreases, HSCs committed to become common lymphoid progenitor (CLP) or common myeloid progenitor (CMP) start to express CD 38 [94]. Flowcytometric analysis (**Figure 5.5A**) revealed that, HSCs in BAC TEBN group survived better over the 21 day in perfusion reactor, with ~7 folds increase in $CD34^{+}/CD38^{-}$ cell population (from day-7 to day-21; n=3; $p \leq 0.05$). Conversely, in BMC TEBN group ~2.5 folds decrease in $CD34^{+}/CD38^{-}$ cell population (from day-7 to day-21; n=3; $p \leq 0.05$). This was further substantiated in immunohistological staining for CD 34 (**Figure 5.5B**), where BMC TEBN showed lesser CD34 expressing cells by day-14; whereas BAC TEBN group showcased presence of CD34 cells up to day-21. The survival of CD34 HSCs within the BAC TEBN can be credited to the holistic presentation of biophysical cues and chemical ligands needed for the preservation of quiescence state of HSCs and their recycling. Thus, these findings point toward a positive direction wherein the developed BAC TEBN could be successfully applied as an implantable bone marrow for reconstruction of atrophic nonunions.

5.3.4 Osteoinductive and Paramagnetic Cortical Bone Struts Exhibit Good Mechanical Properties

The second component in the current study is the biofabrication of outer cortical bone strut with good mechanical properties which would encase the tissue engineered bone marrow. Through rapid prototyping cortical bone structures have been developed, cellularizing these cortical structures post-printing (in case of acellular constructs [174, 344]) increases the biofabrication time; while the cost associated with ECM proteins in hydrogel bioinks for scale-up, and the use of synthetic cross-linkers in synthetic polymer bioinks limits their clinical translation. Thus, in our approach we bioprinted osteogenically primed MSCs laden silk fibroin-nano hydroxyapatite bioink (reported in *Chapter 4* [141]) but here it was reinforced with paramagnetic Fe doped bioactive glass bioceramic-PCL blend thermoplastic ink. For development of this paramagnetic thermoplastic ink, sol-derived 70S bioactive glass

($70SiO_2.15CaO.5P_2O_5.10Fe_3O_4$) was used. From previous reports, 70S bioactive glasses was found to be bioactive and osteoinductive, while exhibiting resorbable traits. [305, 366] Hence, this ternary glass composition but doped with Fe to bestow paramagnetic traits by synthesizing it as nanoparticles *via* a modified Stöber's method.

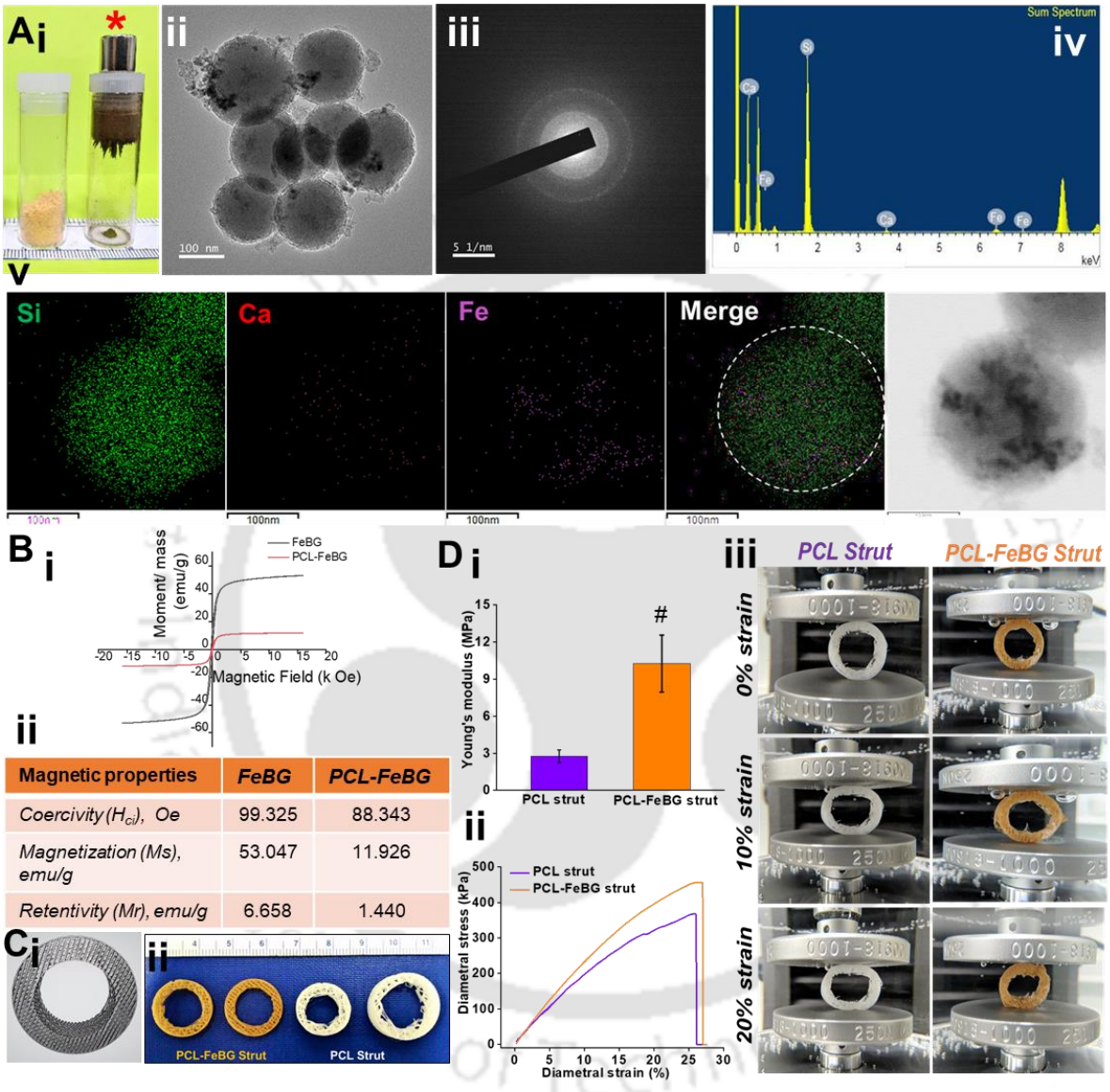

Figure 5.6. ***Development of outer cortical bone struts***. *A) Characterization of sintered nano Fe doped bioactive glass (FeBG) nanoparticles i) image showing magnetic property of FeBG (* indicating calcined nanoparticle attracted to a permanent magnet), ii) FETEM micrograph, iii) SAED pattern, iv) EDX spectra and v) EDX mapping of synthesized FEBG nanoparticles; B) Magnetic properties assessed by vibrating sample magnetometer showing i) hysteresis loop and ii) magnetic parameters; C) i) CAD model for outer strut, ii) printed struts and D) their mechanical properties assessment i) Young's modulus and ii) stress-strain curve with iii) representing figures showing deformation at various diametral strain. (Data presented as*

Mean ± S.D (n=3); # represents statistically significant difference at p ≤ 0.05; parametric Student's t-test).

The nanoparticles (**Figure 5.6Ai**) synthesized were heat stabilized by calcination at 700°C to facilitate nucleation of magnetite, responsible for paramagnetic properties (FeBG). The calcined FeBG nanoparticles were morphologically spherical with a mean size of ~100 nm (**Figure 5.6Aii**), having a slightly crystalline nature as assessed by selective area energy dispersion (**Figure 5.6Aiii**). The stoichiometric properties were attested using energy dispersal spectra (**Figure 5.6Aiv**) and mapped (**Figure 5.6Av**), which confirmed with the theoretical glass composition. The magnetic properties were assessed by vibrating scanning magnetometer and from the magnetization curve (**Figure 5.6Bi**), calcined FeBG exhibited a narrow hysteresis loop characteristic of soft magnetic material, which was reciprocated to in PCL/FeBG composite. The magnetic properties calculated from the magnetization curve (**Figure 5.6Bii**) revealed that FeBG exhibited paramagnetic traits with magnetization (M*s*) 53.047 emu/g and coercivity (H*c*) 99.325 Oe. This was achieved because of the nanoscale size (~100 nm) which helps to attain higher coercivity [367]. When FeBG was blended with PCL (a commonly used thermoplastic polymer used in bone tissue engineering), the paramagnetic property was retained (H*c* = 88.34 Oe), however the magnetization (M*s*) reduced to 11.92 emu/g which is because of the low incorporation (1:10 w/w, FeBG/PCL). Similarly, the magnetic retentivity (M*r*), an essential property for actuation purposes which denotes the residual magnetic property left after magnetic property is removed, also reduced in FeBG/PCL (M*r* = 1.44 emu/g). This implies that once the magnetic field is removed the magnetic field is not retained, thus serving as an ideal paramagnetic material for actuation under pulsed magnetic field. Moreover, the outer cortical struts [printed with PCL (control) and FEBG/PCL composite (experimental groups)] (**Figure 5.6C**) were evaluated for their mechanical properties. The incorporation of FeBG in PCL improved its mechanical property (**Figure 5.6Di**) with ~5 folds increase in Young's modulus (achieving ~11 MPa), and withstanding ~22% diametral strain (**Figure 5.6Dii-iii**) suitable for atrophic non-union reconstruction applications. [174, 344]

5.3.5 Bioprinted Magnetically Actuated Cortical Bone Struts Osteogenically Mature by Mechanotransductory Route

Bone is a mechanosensitive tissue where organ level mechanical loading facilitates mineralization (Wolff's law). This is achieved when forces applied on load bearing bones, gets transmitted through non-linear force propagation due to the ECM anisotropy seen in osseous tissue. The osteogenic cells residing within the osseous tissue detect these forces *via* cell

receptors from the ECM by physical mechanical coupling, activating mechanotransductory pathways pertaining to osteogenesis and osteogenic phenotype maintenance. [81] We tried to exploit this phenomenon by bioprinting Osteo-WJMSCs in our previously developed bioprinting osteogenically primed MSCs laden silk fibroin-nano hydroxyapatite bioink (reported earlier by us [141]) and reinforcing this with paramagnetic FeBG/PCL blend thermoplastic ink. The bioprinted constructs were then actuated in magnetic actuation device [354] where pulsed magnetic field was applied (t_{ON}/t_{OFF} = 1s/1s) for 2 h/day inside the incubator till 14 days (**Figure 5.7A**). The actuated constructs (termed Dynamic) were experimental group while, unactuated free-standing constructs (termed Static) served as control groups, to study the effects of actuation on osteogenic maturation.

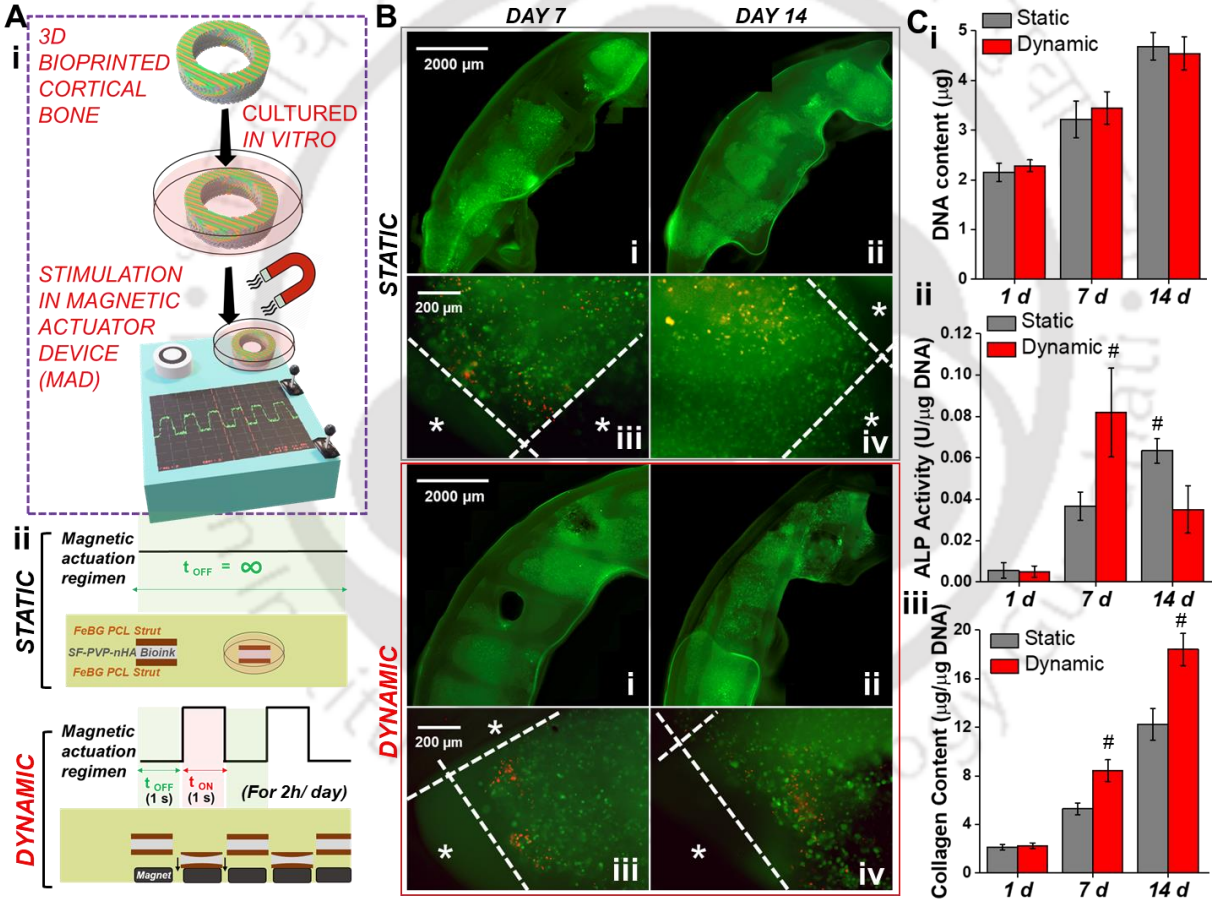

Figure 5.7. ***Bioprinting of outer cortical bone struts.*** *A) i) Scheme showing the maturation of 3D bioprinted outer cortical bone, ii) magnetic actuation regimen for 14 days period; (* and dotted white lines indicating FeBG/PCL strut) B) Live/Dead images for static and dynamic groups i-ii) lower magnification at day-7 and day-14, iii-iv) higher magnification at day-7 and day-14; C) Biochemical characterization of bioprinted constructs – i) DNA content, ii) ALP activity and iii) collagen content assessment of bioprinted constructs under static and dynamic*

regimens. (Data presented as Mean ± S.D (n=3); # represents statistically significant difference at p ≤ 0.05; parametric ANNOVA Tukey's test).

The viability of cells post-printing at day-7 and day-14 were assessed by calcein-AM (stains live cells green) and ethidium homodimer (stains dead cells red) (**Figure 5.7B i-ii**) under the aforementioned actuation regimen. The cells appear as rounded clusters within the silk based-bone bioink reinforced between the FeBG/PCL struts marked with * in **Figure 5.7B iii-iv**. The cellular viability of ~ 80% was retained, while few red dead cell populations was noticed towards the proximity of FeBG/PCL strut which might be possibly be due to the temperature differences between the thermoplastic ink extrusion and the bioink extrusion. This is a common drawback associated with such multi-material thermoplastic microextrusion bioprinting technique which could not be avoided. Bioprinted constructs exhibit soft-elastic mechanical features and not suitable for load bearing applications, hence reinforcements with a good load bearing polymeric strut is needed which results in a compromise. Biochemical analyses were performed on the bioprinted constructs (**Figure 5.7C**), where DNA content was quantified as an indirect marker for cellular proliferation (**Figure 5.7Ci**). Though, there was not significant difference between the groups (static and dynamic), cells encapsulated within the bioink gradually increased from day-1 and day-14 (~ 2 folds increase between day 1 and 14), typical of cells within encapsulated silk hydrogel systems [141, 306, 351]. We assessed the ALP activity (**Figure 5.7Cii**) and we noticed that in static groups, the ALP activity increased from day-1 through day-14; whereas in actuated, dynamic group ALP activity day-7 and toned down by day-14 (~ 2.5 folds increase between dynamic and static group at day-14). This might be attributed to early onset of mineralization and osteogenic commitment in actuated, dynamic group. Collagen content (**Figure 5.7Ciii**) also was expressed significantly higher in dynamic group in comparison to static group (~1.7 folds higher at day-14), indicating the positive effect of actuation on maturation of encapsulated hMSCs in the bioprinted constructs.

Furthermore, the gene expression profiles of key osteogenic markers: *RUNX2*, osteocalcin (*OCN*), and bone sialoprotein (*BSP*) (**Figure 5.8A**) were assessed. *RUNX2* is an important master transcription factor required for osteogenic commitment (early-mid stage marker), which was noticed to be upregulated through day-3 to day-14 of the study (**Figure 5.8Ai**), and found to be enhanced in dynamic group (~2.6 folds increase in day 7; ~1.5 folds increase in day 14) in comparison to static group. Two mid-late stage osteogenic markers namely: *OCN*, *BSP* were assessed (**Figure 5.8Aii-iii**). Both the markers showed upregulation

in expression from day-3 to day-14, while dynamic groups showed higher expression (~2.3 folds increase in *OCN* at day-14; ~1.8 folds increase in *BSP* at day-7) in comparison static group. This substantiates our hypothesis that indeed actuation had a positive influence in osteogenic commitment and maturation of bioprinted constructs. Key regulators of mechanotransduction were investigated by western blotting analysis (**Figure 5.8B**), namely focal adhesion kinase (FAK) and Yes-associated protein (YAP). It was observed that FAK expression was higher in dynamic group (~3 folds increase at day-3, ~ folds increase at day-7, ~3 folds increase at day-14) in comparison to static group. Similarly, YAP expression was predominantly upregulated in dynamic group which was detected as early as day-3 (not detected in static group), while ~12 folds and ~9 folds increase at day-7, day-14 respectively was noticed in comparison to static group.

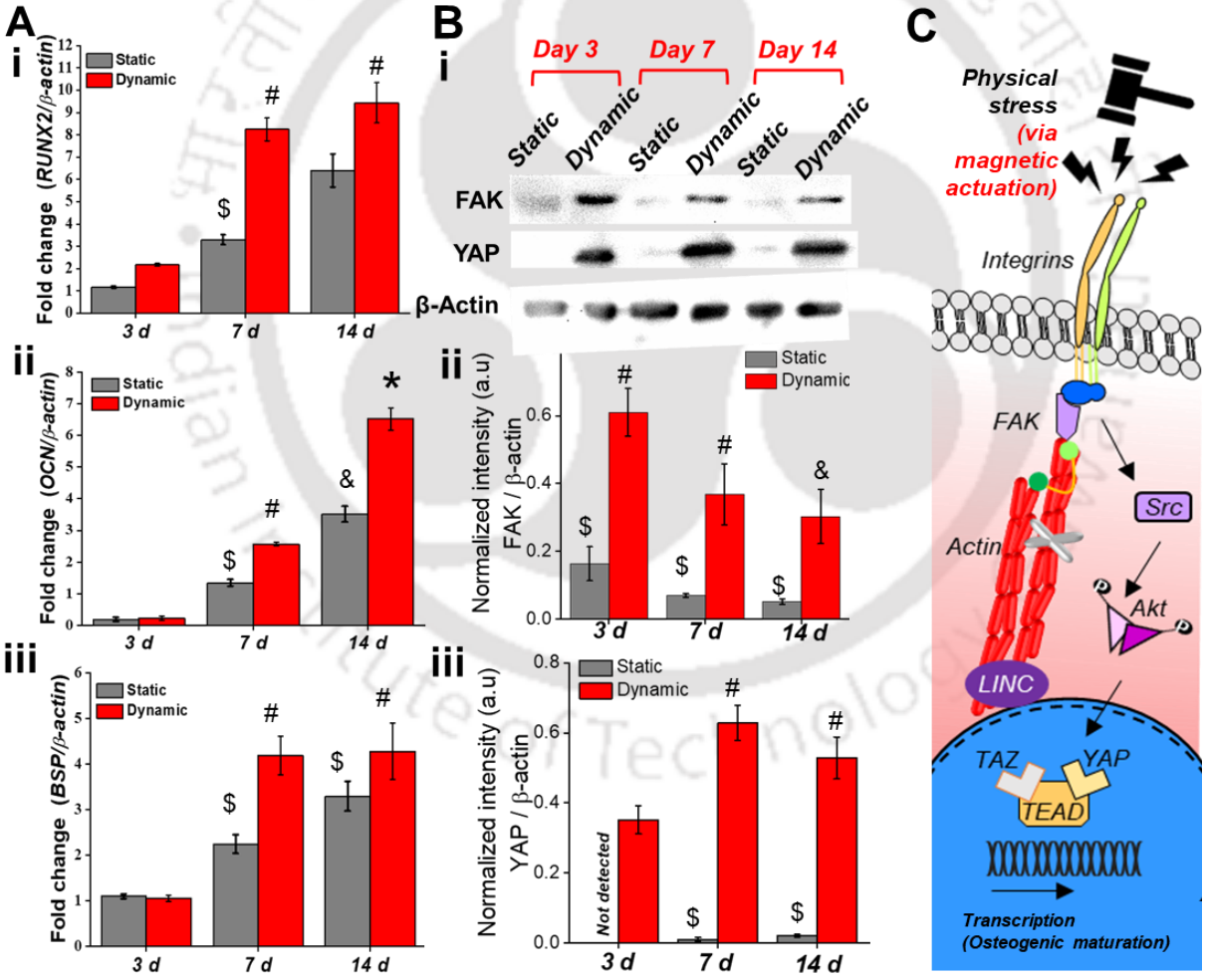

Figure 5.8. ***Molecular characterization of outer bioprinted cortical bone struts.*** *A) Real time gene expression for osteogenic markers i) RUNX2, ii) OCN, iii) BSP; B) i) Western blot analysis for FAK, YAP (key proteins involved in mechanotransduction), ii-iii) and their respective densiometric profiles; C) Scheme representing possible mechanotransductory pathway activated by magnetic actuation for osteogenic maturation in dynamic group*

*involving YAP/TAZ signalling cascade. (Data presented as Mean ± S.D (n=3); *, $, #, & represents statistically significant difference at p ≤ 0.05, same symbols indicate no significance while different symbols indicate statistical significance between the groups tested at p ≤ 0.05; parametric ANNOVA Tukey's test).*

The mechanical forces are perceived by cells *via* cell surface receptors like integrin which get physically coupled through actin-myosin filaments to linker of nucleoskeleton to cytoskeleton (LINC) complexes to chromatin in nucleus (**Figure 5.8C**), affecting transcription [85]. Similarly, in this cascade, focal adhesion kinases (FAK) in focal adhesion complexes especially Src family kinases regulate downstream transcription factors, namely Yes-associated protein-1 (YAP)/ PDZ binding motif (TAZ), which mediate osteogenic commitment and maturation [368]. In our outer cortical bone struts, we were able to successfully bioprint osteogenically primed WJMSCs, which were matured by actuation showing osteogenic commitment and phenotype maintenance with adequate mechanical properties and responsive to actuation (*via* mechanotransductory route). This outer strut could encompass the bioengineered bone marrow by a facile assembly, forming a functional diaphyseal cross-sectional unit, which could be used as a prospective orthobiological intervention for atrophic long bone non-union reconstructive procedures. The scalable facet of the techniques applied here could help upscale for large animal model or downscale for smaller animal models easily. Though here cord blood derived MNCs enriched with HSCs were used, use of sorted HSCs would be ideal. However, the BAC TEBN system could also serve as ideal scaffolding platform to support autologous bone marrow (used conventionally in atrophic nonunions [327]) or HLA mismatched cord blood [364] derived HSCs, which needs to be validated. 70S bioactive glass compositions and PCL are well studied bone tissue engineering materials, but the biofabricated cortical struts developed in the study needs to be validated for their long-term resorption kinetics, ability to support vascularization and innervation and periosteal regeneration.

5.4 Salient Findings of the Chapter

In this chapter, a prospective strategy was presented for fabricating a diaphyseal cross-sectional unit, encompassing a tissue engineered bone marrow and bioprinted cortical bone strut as graft substitute to treat atrophic long bone nonunions. The rationale of the current study involved developing a biomimetic endosteum to house marrow, which was materialized by using a channelized silk fibroin blend scaffold. The channelized scaffold presented two compartmentalized niches; namely the endosteal niche consisting of specialized osteoblasts expressing N-cadherin, *CXCL-12*, mediated through BMP-2 signalling cascade critical for its survival and vascular niche consisting of HUVECs expressing *ANGPT-1*, endoglin. The cellular cross-talk between these two niches aided in survival of $CD34^{+}/CD38^{-}$ HSCs (cord blood derived MNCs fraction) in perfusion bioreactor over the 21-day culture period. The preservation of quiescent state and recycling of these $CD34^{+}/CD38^{-}$ HSCs is attributed to the holistic biophysical cues and biochemical cues offered by the channelized silk fibroin scaffolds. Furthermore, bioprinted paramagnetic cortical bone struts helped in maturation of encapsulated osteogenically primed MSCs under magnetic actuation. The encapsulated cells maintained their viability in the 14 days study period, with upregulation of osteogenic markers under magnetic actuation following a mechanotransductory route *via* YAP/TAZ pathway. The two components could be assembled to form a functional diaphyseal unit, which could serve as a prospective orthobiological intervention for aiding atrophic long bone nonunions.

Limitations of the chapter

The current work is a proof-of-principle study wherein the developed systems have been validated *in vitro*, independently (in a delineated approach), which shows positive results. However, the assembled cortical unit needs to be validated in suitable segmental defects (long bone) small animal and large animal models which would enable us in understanding the system better. The channelized TEBN served in providing compartmentalized niches for *in vitro* maturation of HSCs, which later could be used as implantable tissue engineered bone marrow. The vascular channels do not actually dictate the orientation of angiogenesis when implanted *in vivo*. The vascular ingrowth could happen in a random manner, allowing ECM deposition and resorption of silk sponges while integrating with the cortical bone strut. This further opens research questions relating to integration, bonding of TEBN with outer cortical strut. These are not addressed in this current work and needs to be validated in animal defect models to conclusively ascertain the structural issues of the developed system.

Chapter 6

Mesoporous silk–bioactive glass nanocomposites as drug eluting multifunctional conformal coatings for improving osseointegration and bactericidal properties of metal implants

Traumatic accidents and other pathological conditions leading to fractures necessitate the use of orthopaedic devices and joint replacement prosthesis. Inevitably metals, owing to their mechanical performance are used in these orthopaedic applications under such circumstances. This chapter describes the use of mesoporous silk-bioactive glass nanocomposites to surface modify metal implants towards creating a multifunctional interface for improving osseointegration and circumventing implant associated infections.

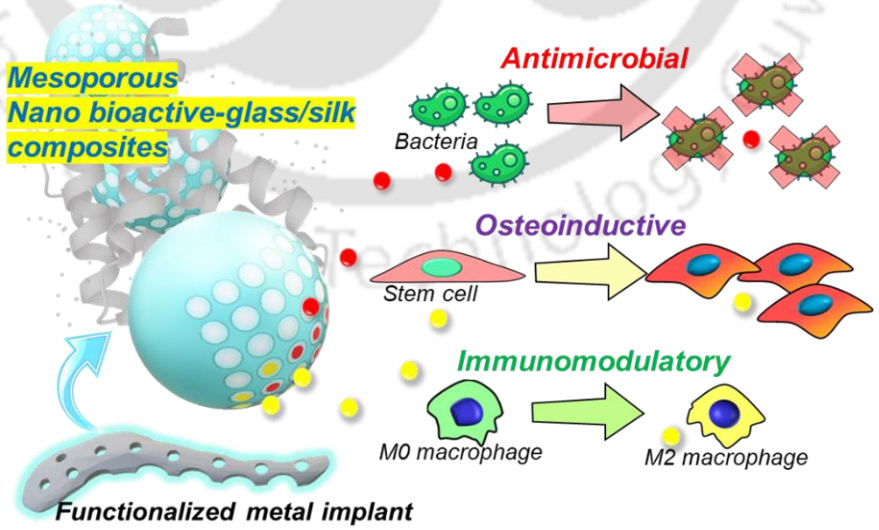

Abstract

Endowing multifunctional traits in metal implants to prevent implant associated infections and improve osseointegration have become pivotal facets in orthopaedics and dental fixation. Herein, we report the synthesis of mesoporous 70S bioactive glass-silk fibroin nanocomposites inspired by the biomimetic organo-apatites of mineralized collagen. The mesoporous, biomimetic nanocomposites enabled in loading of antibiotics (gentamicin and doxycycline) and favoured their release in a fast-acting, rapid manner, whilst preserving their bioactivity. Ease in modification of the mesoporous nanocomposites enabled in tailoring 3-(aminopropyl)-triethoxysilane to the silanol network of bioactive glass, which improved the loading capacity of hydrophobic drug (dexamethasone). The modification favoured the slow and sustained release of dexamethasone from the modified mesoporous nanocomposites, which is desired for mediating osteogenesis and immunomodulation. Conformal coatings of these drug loaded nanocomposites were materialized on stainless steel implants through facile electrophoretic deposition (EPD) technique, wherein the deposition yield can be controlled by applied parameters. Antibiotic coatings exhibited antibacterial efficacy with bioactivity retained up to 28 days, while dexamethasone loaded coatings favoured mesenchymal stem cell adhesion and osteoinduction. The immunomodulatory roles were also ascertained, wherein M2 macrophage biasness was favoured in dexamethasone loaded coatings. The versatility of these mesoporous biomimetic nanocomposites vouches for loading of scenario-specific drugs in aiding their local delivery through the conformal EPD coatings developed over metal implants towards improving implant patency.

The findings of this chapter are published in a peer reviewed journal:

Moses, J. C., and Mandal, B.B. '*Mesoporous silk–bioactive glass nanocomposites as drug eluting multifunctional conformal coatings for improving osseointegration and bactericidal properties of metal implants*' ACS Applied Materials & Interfaces. 2022, 14 (13), 14961–14980.

6.1 Introduction

Traumatic accidents and other pathological conditions leading to fractures necessitate the use of orthopaedic devices and joint replacement prosthesis. Inevitably metals, owing to their mechanical performance are used in these orthopaedic applications in load bearing prosthesis. In this regard, millions undergo restorative surgeries involving metal fixtures for musculoskeletal pathologies. By 2030, the demand for total hip arthroplasties is estimated to grow by 174%, with numbers reaching 572,000; similarly, for knee arthroplasties is estimated to grow by 67% with numbers reaching 3.48 million procedures [369]. However, in these metal implants used in orthopaedics there is considerable drawbacks involving limited rates of osseointegration and chances of implant associated infections which compromises the clinical success of these procedures [370]. . For instance, in case of knee arthroplasties, failure rates of 40-70 % are encountered. The failure mechanisms involved is loosening (39.9 %), infection (27.4%), fixture instability (7.5%), peri-prosthetic fracture (4.7%) and arthrofibrosis (4.5%) [363]. Similarly, dental implants also at large face risk of failure though considerably lesser than bone implant failures, with smoking, post-menopausal conditions and infections contributing to 6.32% of higher chances for dental implant failure [371]. The failure of a prosthesis/ implant inevitably requires a secondary revision surgery, which has serious effect on patient's mental psyche and quality of life.

Metals such as titanium and its alloys in dental implants, cobalt and chromium alloys, stainless steel is currently available for dental, bone and joint prosthesis which are chosen clinically depending upon the bulk properties of the metal [151, 372, 373]. In addition to the bulk mechanical properties of the metals, it is the surface of the implants that alters the *in vivo* bone response and fixation. In an ideal scenario (**Figure 6.1 A**), post-implantation the osseous wound bed is prepared and the metal implant is inserted where the implant surface interacts with the blood components and protein adsorption occurs. This is followed by the foreign body response where immune cells (leucocytes and macrophages) infiltrate initiating the cell mediated immune response which gets resolved in a controlled manner. Classically activated macrophages mediate this, where initially inflammatory (M1) macrophages clear any debris, apoptotic bodies, bacteria through phagocytosis This is followed by regenerative (M2) macrophages which secrete remodelling enzyme and provisional matrix aiding in fibroblast, precursor stem cell migration aiding in integration of implant with the surrounding osseous tissue [95, 98].

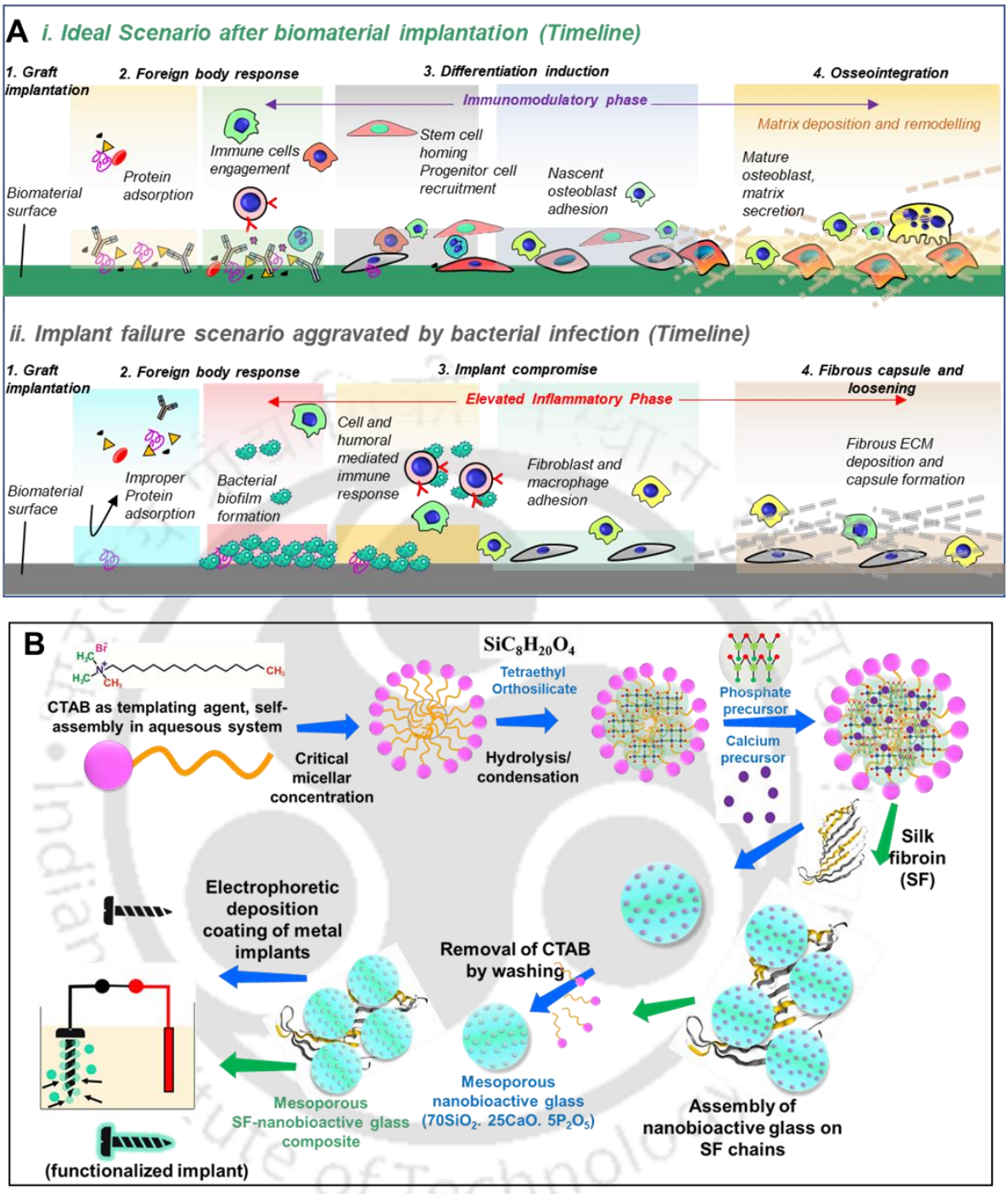

Figure 6.1. ***Schemes illustrating the rationale and methodology for modifying the bone metal implant surface.*** *A) Scheme illustrating the timeline after i) an ideal biomaterial implantation and ii) implant failure scenario aggravated by bacterial infection; B) Scheme for synthesis and electrophoretic deposition of silk-bioactive glass nano-composites on metal implants.*

However, in case of any infections or pathological conditions this synchrony is affected leading to improper protein adsorption, elevated inflammatory response due to presence of microbes and activation of pathogen associated molecular patterns (PAMPs), danger associated molecular patterns (DAMPs), leading to thick fibrous capsule formation leading to loosening

and implant failure [374] (**Figure 6.1 A**). The prevalence of such adverse conditions such as peri-implant mucositis was noted in 63.4% individuals and 30.7% of implants, while peri-implantitis was noted in 18.8% of individuals and 9.6% of implants [375]. To overcome these complications, several strategies have been adopted to improve the surface of metal implants to confer antimicrobial properties (circumventing implant associated infections) and attributing functional properties to improve osseointegration [151, 376]. Conventionally, modifying the surface topography of implant grit blasting, acid etching, ion implantation, plasma spray and self-assembled monolayer have reduced the reduced the implant failure rate less than 2% over a span of 10 year, yet there is no clear predictive model for assessing the survival rate of implants in biologic complications [375]. Some of the recent advancements involve the use of metal-organic-frameworks (MOFs) to from stable covalent coatings in titanium implants to release drugs which facilitate osteogenic differentiation or immunomodulation [373]. Use of plasma sprayed coatings to present growth factors or cell adhesion peptides [161] to enhance osteogenic cell adhesion and survival, use of covalently grafted biologic peptides [370] to facilitate antimicrobial effects whilst favouring osteoblast adhesion also has been found beneficial. Use of electrospinning and 3D texturing techniques to accommodate combinatorial release of antibiotics from coatings have also warranted to improve the early, delayed implant associated infections [377]. However, the use of these complex fabrication strategies needs sophisticated instrumentation which indirectly increases the cost incurred on the medical device.

Hypothesis underpinning the Objective:

In this chapter, electrophoretic deposition (EPD) a facile, scalable technique was resorted to develop multifunctional drug-eluting conformal coatings on stainless-steel implants. EPD is well-established solution based technique which utilises the electrophoretic mobility of charged species to form homogenous coatings of polymer/ ceramics/ composites on to metals of complex geometries under mild operating conditions without affecting the bioactivity of drugs [378, 379]. The drug-eluting vehicle was designed from a mesoporous 70S nanoparticulate bioactive glass composited with silk fibroin biopolymer. 70S bioactive glass was chosen for its innate ability to facilitate osteoconductivity [225, 305], while silk fibroin (from *Bombyx mori* and *Antheraea assama*) was chosen due to its bioactive nature and resemblance to collagen-I [52]. The nanocomposite developed was intended to mimic the native organo-apatite of mineralized collagen-I noticed in bone. Particularly, endemic non-mulberry silk fibroin from *Antheraea assama* has intrinsic RGD (arg-gly-asp) tripeptides which has been demonstrated to improve cell adhesion and survival [52, 118, 305, 311].

The mesoporosity was hypothesized to load case-specific drugs to function as drug-eluting platform, while the biomimetic nanocomposite serving to improve the osteogenic cell adhesion and survival. The ease in modifying the silanol surface in bioactive glass, with alkylamines would favour loading hydrophobic drugs. Thus, these mesoporous nanoparticle vehicles were evaluated for their utility in loading antibiotics and modified nanoparticle vehicles for their loading glucocorticoids. The loaded vehicles were assembled into conformal coatings on stainless-steel implants and assessed for versatility in acting as antibacterial coatings or osteoinductive or immunomodulatory surfaces towards improving implant survival and compliance in orthopaedic applications.

6.2. Materials and Methods

6.2.1 Synthesis of Nanoparticles and Nanocomposites

6.2.1.1 *Regeneration of Silk Fibroins*

Mulberry, *Bombyx mori* silk cocoons and fifth instar non-mulberry *Antheraea assama* silkworms were sourced from local silk farms in Guwahati, Assam, India. Silk fibroins were isolated and regenerated based on our previously reported protocols [141, 305]. Briefly, *B. mori* silk cocoons were cut into small pieces and degummed in 0.02 M boiling sodium carbonate to obtain silk fibroin fibers which were regenerated in 9.3 M lithium bromide, and the silk fibroin solution was dialysed against deionised water (18.2 MΩ; Arium ® Sartorius Ultrapure, Germany) using 12 kDa cut-off membrane for 48 h with intermittent changes of water to obtain BMSF solution. *A. assama* glandular silk fibroin was squeezed from silk glands of mature fifth instar silk worms, regenerated in 1% (w/v) sodium dodecyl sulphate – SDS and dialysed against deionised water using 12 kDa cut-off membrane for 4 h in 4°C with intermittent changes of water to obtain AASF. The BMSF and AASF were stored in 4°C until further use.

6.2.1.2 *Synthesis of Mesoporous Nano-bioactive Glass and Silk-bioactive Glass Nanocomposites*

A modified Stöber's method was followed for synthesis of 70S bioactive glass nanoparticles, wherein the bioactive glass network belonging to the ternary network $70SiO_2.255CaO.5P_2O_5$ was chosen. To impart mesoporous nature, surfactant-based sacrificial templating was resorted where Cetyltrimethylammonium bromide – CTAB was used [380]. For this, tetraethyl orthosilicate (TEOS) was hydrolysed in 10mM CTAB in pH 8 Tris-HCl (10mM) solution for 1 h. Subsequently, the precursors calcium nitrate tetrahydrate, and triethyl phosphate (TEP) were added in sequence at an interval of 1 h, aged for 48 h in continuous stirring in molar ratio corresponding to the 70S bioactive glass network. The resultant sol

particles were collected by centrifugation (19000*g* for 30 min), refluxed thoroughly three times in warm ethanol (45 °C), followed by washing with deionised water to remove CTAB imparting mesoporous nature to the nanoparticles. Thus, obtained mesoporous nano-bioactive glass (**nBG**) was lyophilized (Freeze drier - Martin Christ, Germany) and stored in ambient temperature until further use. Similarly, following a similar route, silk fibroin solution (*B. mori* – BMSF or *A. assama* – AASF) were added during synthesis. Fine droplets of 5 mL 2% (w/v) silk solution (either BMSF or AASF) (0.1 g silk fibroin per 1g of bioactive glass synthesis batch) are added to the reaction mixture after addition of calcium precursor. The sol was stirred for 48 h at ambient temperature and then resulting nanoparticles are collected by centrifugation (19000*g* for 30 min) and washed extensively with deionised water to remove residual unreacted reactants. The nanocomposites thus obtained (either **nBMBG** or **nAABG** respectively) were lyophilized and used for further studies.

6.2.1.3 *Modification of Mesoporous Nanoparticles for Hydrophobic Drug Loading*

The mesoporous nBG and nanocomposites (nBMBG, nAABG) were surface modified with 3-(aminopropyl) triethoxysilane – APTES to improve the loading efficiency of hydrophobic drugs, by virtue of alkylamines groups presented by APTES. For this, 1 g of synthesized nBG or nBMBG or nAABG were incubated under stirring conditions in 0.02 % (v/v) APTES in ethanol:water (95:5) mixture for 1 h. The particles were collected by centrifugation (19000*g* for 45 min) and washed with absolute ethanol, air dried at 37°C. The obtained modified nanoparticles were denoted as **nBG+P**, **nBMBG+P**, **nAABG+P** and used for further studies.

6.2.2 Characterization of Synthesized and Modified Nanoparticles

Synthesized and modified nanoparticles were investigated for their size, morphology, elemental, functional composition and porosity. Size, polydispersivity index, conductivity and Zeta potential of sonicated suspensions (in 30% v/v ethanol) of the synthesized and modified nanoparticles were analysed by Zetasizer NanoS (Malvern Instruments, UK). Infrared spectra of the same were obtained by attenuated total reflectance fourier transform spectrometer (PerkinElmer FTIR Spectrum Two, USA) from 400 – 3500 cm^{-1} culminating from 30 scans averaged to a single spectrum with a resolution of 2 cm^{-1}. Nitrogen adsorption-desorption isotherms were recorded at 77 kelvin using surface area and pore size analyser (Autosorb-IQ MP, Quantachrome, USA), after degassing the samples at 400 kelvin for 8 h under vacuum. The morphology and elemental composition, mapping of synthesized nanoparticles was

analysed using field emission transmission electron microscope (JEOL 2100F, Japan) equipped with energy dispersive X-ray spectrometer.

6.2.3 Electrophoretic Deposition of Nanoparticles on to 316L Stainless Steel Foils and Screws

AISI 316L stainless steel foils (alloy - FeCr18Ni10Mo3; 150 mm × 150 mm × 0.1 mm) were obtained from Sigma, USA. The foils were cut into 1 cm × 0.8 cm strips, each strip having surface area of 0.98 cm^2. They were then rinsed in acetone, followed by cleaning in ultrasonic bath in absolute ethanol and deionised water. Commercial stainless-steel dental screws (Safex, Inc., India) were used post similar cleaning procedures. In order to coat the metal surfaces, a custom electrophoretic deposition (EPD) cell was set-up using a 25 mL borosilicate glass beaker (Borosil®), with two parallel 316L steel strips serving as deposition and counter electrodes separated by fixed distance of 10 mm. The electrodes were connected to a constant DC power source to supply a constant voltage supply at different operating conditions, where voltage (10-45 V) and time intervals (5 to 100 s) were varied per run. 10 mL of electrolyte bath consisting of 30 % (v/v) ethanol/water suspension to which 0.5 g/L nanoparticles (synthesized - nBG or nBMBG or nAABG; modified nBG+P or nBMBG+P or nAABG+P) were added and briefly sonicated to disperse them. Chondroitin sulphate (0.05% w/v) was added as binder to the above sonicated suspension to improve coating adhesion. The electrodes were submerged inside this electrolyte bath in the custom EPD setup and a constant voltage was supplied using the DC source. The voltage and deposition time were varied and optimised. Post-deposition, the substrates were air dried at 37°C for 24 h and subjected for further analysis.

6.2.4 Coating Characterization and Integrity Assessment

The morphology of the coated surfaces was visualized using a using a field emission electron microscopy (FESEM) (∑IGMA, Carl Zeiss, Germany). The surface roughness was evaluated using atomic force microscope (Bruker, Innova series, USA) at a scan rate 0.7-0.8 Hz in tapping mode. The quality of coating deposited was also tested by a custom screw pull-out test, wherein the coated dental screws where fix/unfixed thrice in a PDMS (polydimethylsiloxane) negative mold under hydrated conditions (in phosphate buffered saline with phenol red, PBS (pH 7.4) at 37°C). The extent of delamination was visualized under a field emission electron microscope. Integrity of coating were evaluated based on ASTM C633 testing protocol, wherein the coating-to-substrate adhesion is evaluated. Briefly, two coated 316L strips (2 cm × 1cm) were glued using epoxy, cured and the prepared specimen were placed under tensile load until failure. The tensile stress-strain were recorded using universal

testing machine (UTM, Instron 5944, USA with 100 N load cell, equipped with BioPuls bath) under hydrated conditions (in phosphate buffered saline, PBS (pH 7.4), 37° C) under uniaxial loading rate 1 mm/min. The adhesive strength was calculated from the stress-strain curves from the linear region before failure.

6.2.5 Evaluation of Drug Loading Capacity and Release Kinetics

Drug loading and its subsequent release from nanoparticles and drug-loaded nanoparticles coated metal implant surfaces were evaluated by UV-visible spectroscopy. 10 mg/mL sonicated aqueous suspensions of synthesized/ modified nanoparticles were loaded with gentamicin sulphate (antibiotic drug) by simple adsorption for 12 h in ambient condition in a w/w ratio 1:3 (nanoparticle: drug). The unbound drug from nanoparticle suspensions were collected by centrifugation (19000*g* for 30 min) from the supernatant. Gentamicin sulphate had a characteristic absorption maximum at λ_{max} = 308 nm, with a calibration curve made from known standards the unknown concentration from supernatants were determined using microplate reader (Multiskan Sky, Thermo Fisher Scientific, USA). The loading capacity (*mg* drug loaded/ *mg* nanoparticle) was calculated as follows in equation (6.1):

$$\text{Loading capacity} = \frac{(Total\ drug\ loaded, mg - \text{Free drug detected in supernatant}, mg)}{\text{Total weight of nanoparticles}, mg} \quad \textbf{(1)}$$

Similarly, for assessing the loading capacity of doxycycline hyclate (antibiotic drug), 10 mg/mL sonicated aqueous suspensions of synthesized/ modified nanoparticles were loaded with doxycycline hyclate by simple adsorption for 12 h in ambient condition in a w/w ratio 1:3 (nanoparticle: drug). The unbound drug from nanoparticle suspensions were collected by centrifugation (19000*g* for 30 min) from the supernatant. 100 µL of supernatant of doxycycline hyclate was mixed with 100 µL 0.2M NaOH, the mixture had a characteristic absorption maximum at λ_{max} = 375 nm, with a calibration curve made from known standards the unknown concentration from supernatants were determined using microplate reader. The loading capacity was calculated based on equation (1). For assessing the loading capacity of dexamethasone (corticosteroid drug), 10 mg/mL sonicated ethanolic suspensions of synthesized/ modified nanoparticles were loaded with dexamethasone (in absolute ethanol) by simple adsorption for 12 h in ambient condition in a w/w ratio 1:3 (nanoparticle: drug). The unbound drug from nanoparticle suspensions were collected by centrifugation (19000*g* for 30 min) from the supernatant. Dexamethasone had a characteristic absorption maximum at λ_{max} = 242 nm [311], with a calibration curve made from known standards the unknown concentration

from supernatants were determined using microplate reader. The loading capacity was calculated based on equation (1). For a particular concentration of drug loading in subsequent experiments, the efficiency of drug loading was calculated as follows in equation (2):

$$\text{Loading efficiency (\%)} = \frac{(Total\ drug\ loaded, mg - \text{Free drug detected in supernatant}, mg)}{Total\ drug\ loaded, mg} \times 100 \quad \textbf{(2)}$$

After loading the aforementioned drugs, drug release kinetics were evaluated for the drug loaded nanoparticles. Briefly, 5 mg of drug loaded nanoparticles were suspended in 2 mL of phosphate buffered saline (PBS, pH 7.4) in microfuge tubes and kept in Roto-Therm™ incubated tube rotator (Benchmark Scientific, USA) at 37°C. At regular intervals the drug released was evaluated by UV-visible spectroscopy using microplate reader as mentioned before, after centrifugation (19000g for 30 min) from the supernatant. Fresh buffer was replenished after each evaluation and the cumulative drug released was calculated as follows in equation (3):

$$\text{Drug release (\%)} = \frac{Released\ amount\ of\ drug, mg}{Total\ amount\ of\ drug\ loaded, mg} \times 100 \quad \textbf{(3)}$$

Drug release kinetics were evaluated by fitting the cumulative drug release data in following models: zero order, first order, Higuchi model and Korsmeyer-Peppas model as reported previously [381]. Korsmeyer-Peppas model described the release behaviour well as reflected by the R^2 higher than 0.9 and the fitted data was presented as follows in equation (4):

$$F = \frac{M_t}{M_\infty} = K_m\ t^n \quad \textbf{(4)}$$

In equation (4), F is the fraction of drug released at time 't', where M_t is the amount of drug released at time 't', M_α is the total amount of drug loaded, while K_m is the kinetic constant and 'n' is the release exponent, if $n \leq 0.45$ it follows Fickian diffusion, if $0.45 < n < 0.89$ it follows non-Fickian diffusion, if $n = 0.89$ it follows case-II transport and if $n > 0.89$ Super case-II transport.

6.2.6 Assessment of Antibacterial Efficacy of Antibiotics-loaded Nanoparticles Deposited on 316L Stainless Steel Foils

6.2.6.1 *Disc Diffusion Assay*

Circular discs of 6 mm diameter were punched off from the AISI 316L stainless steel foils and were used as electrodes for electrophoretic deposition of antibiotic loaded

nanoparticles (synthesized/ modified). Thus, coated circular discs with a particular concentration of drug (calculated based on the yield of deposition) were subsequently used for assessing the antibiotic susceptibility by using direct zone of inhibition assay (Kirby-Bauer disc diffusion method). Whatman® 6mm assay discs (cellulose based) were used as controls for assessing the active antibiotic release. Bacterial cultures obtained from obtained from Microbial Type Culture Collection and Gene Bank (MTCC, India) – Gram negative (*Escherichia coli* MTCC 40) and Gram positive (*Staphylococcus aureus* MTCC 3160) were maintained in nutrient broth. Overnight inoculated cultures (Optical Density, $OD_{600\ nm}$ = 0.8 to 1) having viable count of 10^7 – 10^8 CFU/mL were used to test the antibiotic susceptibility. 100 µL of culture was plated (spread-plate method) uniformly in 90 mm solidified nutrient agar Petri dishes to obtain bacterial lawns (at 37°C). Coated 316L stainless steel discs (with antibiotic loaded nanoparticles) were placed and with reference to Whatman® discs wetted with known concentration of antibiotic (as control/ standard), the zones of clearance were visualized and recorded after 24h. Similarly, gentamicin loaded nBG/ nBMBG/ nAABG coated stainless steel discs were evaluated in a continuous culture method, wherein discs were transferred to freshly plated cocultures (100 µL – 1:1 of overnight cultures of *E. coli* and *S. aureus*) every 12 h, until the clearance halo was not noticed to study the extent of active release of antibiotic over 108 h.

6.2.6.2 *Bacterial Growth Inhibition Assay*

Bacterial growth inhibition was assessed by measuring turbidity $OD_{600\ nm}$ in presence of drug loaded and non-loaded coated nBG/ nBMBG/ nAABG coated stainless steel discs. Overnight inoculated cultures $OD_{600\ nm} = 0.8 \pm 0.07$ were used, where 1 mL of microbial culture were incubated with coated discs for 6 h in microfuge tubes in Roto-Therm™ incubated tube rotator (Benchmark Scientific, USA) at 37°C. 100 µL of suspension were measured for turbidity at 600nm using microplate reader, indirectly ascertaining the bacterial growth inhibition [382].

6.2.6.3 *Hydrogen Peroxide Scavenging Activity*

Hydrogen peroxide (a strong oxidiser) scavenging activity of doxycycline loaded nanoparticle suspension was assessed by a previously reported protocol [383]. 0.3 mg doxycycline/ mg nanoparticle (1.3 mg) was suspended in PBS with 0.02% H_2O_2 and incubated over 144 h at 37°C in Roto-Therm™ tube rotator incubator. At regular intervals, suspensions were centrifuged at 19000 *g* 30 min, 100 µL of supernatant was taken to which 0.8 ml of 0.1 M phosphate buffer (Na_2HPO_4:KH_2PO_2) and 100 mM NaCl were added and incubated for 10

min at 37°C. To this reaction mixture, 1 mL of 0.1 mg/mL horse radish peroxidase and 0.2 mg/ML phenol red (made in 0.1 M phosphate buffer) and further incubated for 15 min. Reaction was stopped by adding 50 µL of 1M NaOH and the absorbance was recorded at 610 nm. Similarly, the aforementioned reaction was carried out, in presence of 0.05 mg/mL tannic acid (phenolic compound – positive control). The hydrogen peroxide scavenging (H_s) activity was calculated as follows in equation (5):

$$H_S\ (\%) = \frac{(C_0 - C_{0.05})}{C_0} \times 100 \qquad \textbf{(5)}$$

In equation (5), C_0 is the absorbance without tannic acid, $C_{0.05}$ is the absorbance with 0.05mg/mL tannic acid.

6.2.7 Assessment of Osteogenic Potential and Immunomodulatory Effect of Dexamethasone-loaded Nanoparticles Deposited on 316L Stainless Steel Foils

AISI 316L stainless steel foils cut into 1 cm × 0.8 cm strips, and coated by electrophoretic deposition with dexamethasone loaded nBG+P or nBMBG+P or nAABG+P, while non-loaded nanoparticles were used as controls. Adipose derived human mesenchymal stem cells (hMSCs) were sourced as frozen vials in passage-2 from Ansa Pvt. Ltd. (Cellspace research foundation) Bangalore, India. The hMSCs were cultured in HiPer® Dulbecco's modified media (Himedia, India), supplemented with 10 % (v/v) foetal bovine serum, 2 ng/mL basic fibroblast growth factor (bFGF), 2 mM L-glutamine and 1X antibiotic-antimycotic mixture (penicillin 10 units/mL, streptomycin and amphotericin B 0.25 µg/mL) – expansion media and were used within passage 8 for the cellular studies for assessing the osteogenic potential of the coated stainless-steel foils. Human monocyte cell line (THP-1) were sourced from the National Centre for Cell Science (NCCS) cell repository, Pune, India in passage-10. THP-1 cells were cultured as suspension in RPMI-1640 media supplemented with 10 % (v/v) foetal bovine serum and 1X antibiotic-antimycotic mixture and were differentiated into macrophages (within passage 20) for assessing the immunomodulatory effect of coated stainless-steel foils.

6.2.7.1 *Cellular Viability and Proliferation*

3-(4,5-dimethilthiazol-2-yl)-2,5-diphenyltetrazolium bromide (MTT) assay was used to assess the viability of cells seeded on coated stainless-steel surfaces. For this, 5×10^4 hMSCs were seeded on UV-sterilized stainless-steel surfaces (with different dexamethasone concentrations) placed in 24 well plates, seeded cells were allowed to adhere for 2h after which was flooded with DMEM expansion media and cultured for 72 h. Similarly, 10^5 THP-1

monocytes were stimulated by 200 ng/mL PMA (phorbol 12-myristate 13-acetate) to differentiate into M0 macrophages and seeded on UV-sterilized stainless-steel surfaces (with different dexamethasone concentrations) placed in 24 well plates, seeded cells were allowed to adhere for 8h after which was flooded with RPMI expansion media and cultured for 72 h. After 72 h, the cell seeded surfaces were assessed for viability with MTT (yellow compound) reduced by mitochondrial dehydrogenases of viable cells to form purple coloured formazan crystals. The formazan crystals were solubilized by dimethyl sulfoxide (DMSO) and the absorbance was read at 570 nm. hMSCs and M0 macrophages derived from THP-1 cell stimulation seeded on similar cell densities on standard tissue culture plate were used as non-treated assay controls. Cellular viability was normalized to non-treated controls and represented as cellular viability percentage. Viable cells were also visualized using calcein-AM dye, where after 72 h the cell seeded surfaces were briefly washed with PBS (pH 7.4), incubated with 40 nM calcein-AM dye for 15 min. The green fluorescence of calcein dye by viable cells was visualized under fluorescence microscope (Nikon ECLIPSE Ti2, Japan) and represented.

Cellular proliferation was assessed for hMSCs seeded coated surfaces by using Alamar blue™ (Invitrogen, USA) dye reduction assay as per manufacturer's protocol. Briefly, hMSCs seeded surfaces were incubated with 10% (v/v) of dye in DMEM expansion media for 3h. After incubation, 100 µL of culture media was read at 570/600 nm. The results are presented as normalized Alamar units (with reference to day-1) and presented. Subsequently, cell seeded surfaces were maintained for 14 days with media change every 48 h, and cellular proliferation assessed at regular intervals.

6.2.7.2 *Biochemical Analysis*

Alkaline phosphatase (ALP) activity was determined using our previously described method [141]. Briefly, hMSCs seeded surfaces were lysed with ice cold lysis buffer (20 mM Tris-HCl (pH 7.5), 150 mM sodium chloride, 5 mM magnesium chloride, and 0.5% (v/v) Triton-X100). The cell lysate consisting of membrane bound ALP was determined by a colorimetric method, wherein ALP enzyme hydrolyses the substrate p-nitrophenol phosphate (p-NPP) to obtain an yellow coloured product, p-nitrophenol having absorbance maxima at λ_{max} = 405 nm. ALP activity thus determined was presented as DEA (diethanolamine units), where 1 DEA unit (U) corresponds to the amount of ALP enzyme hydrolysing 1 µM of p-NPP at pH 9.6 (1M diethanolamine buffer) and 25 °C. The ALP activity was normalized to total DNA and represented as U/µg DNA. The DNA content was quantified from the cell lysate

using DNA binding picogreen dye ($\lambda_{excitation}$ /$\lambda_{emission}$ = 480/525 nm), Quant-iT picogreen double-stranded DNA assay kit (as per manufacturer's protocol).

Collagen secreted by hMSCs on coated surfaces were estimated based on our previously reported method [305] using Sirius red dye based colorimetric assay. Briefly, cell seeded surfaces were digested in pepsin digestion buffer (0.1 M acetic acid, 0.5 M NaCl and 1 mg/mL pepsin) and 100 µL of digesate from each sample was allowed to dry at 37°C overnight in 96 well plate. The dried wells were treated with 1 mg/mL direct red 80 (Sigma-Aldrich, USA) saturated with picric acid for 1 h. The dye solution is removed and any unbound dye is washed with 0.01 N HCl and the bound dye solution is resolved with 100 µL 0.1N NaOH whose absorbance is read at 550 nm. The collagen content was estimated from a standard curve obtained by using standard rat tail collagen, and the collagen content is represented as µg collagen/ µg DNA, after normalising it with the DNA content estimated from the digesate.

Nitric oxide (NO) secreted by macrophages seeded on coated surfaces as result of inducible nitric oxide synthase response to cell-material interaction was determined by using Griess reagent. Briefly, after 72 h culture of macrophages (derived by PMA stimulated THP1 monocytes) in coated surfaces, they were incubated with incomplete RPMI-1640 media and the spent media was used for estimation of nitrate, a stable degradation product of NO by using Griess reagent which converts sulfanilic acid to a purple azo dye in presence of N-(1-naphthyl)-ethylenediamine. The absorbance was measured at λ_{max} = 548 nm using microplate reader and the NO produced (µM) was calculated from a standard curve generated with sodium nitrite. Interleukin (IL) -1β secreted by macrophages seeded on coated surfaces were estimated by an ELISA (enzyme linked immunosorbent assay) kit following the manufacturer's protocol (Invitrogen, USA). Conditioned media after 72 h culture was collected and assayed for IL-1β and presented as pg/mL.

6.2.7.3 *Gene Expression Studies*

For assessing the expression level of relevant osteogenic or immunogenic genes (listed in **Table 6.1**) with reference to endogenous house-keeping gene, human β-actin, total RNA content was extracted from cell seeded surfaces using TRI reagent and 1 µg of RNA was reverse transcribed to obtain cDNA using high capacity reverse transcription kit (Applied Biosystems, Invitrogen, USA) in a thermal cycler machine (Applied Biosystems Veriti, Thermo Fisher Scientific, USA). Relative expression levels of gene of interest (GOI) were quantified by Delta-Delta C_T method (-ΔΔC_T), where fold change $F = 2^{-[(C_{T\,(GOI)} - C_{T\,(ACTB)})}{}_{coated}$

$_{\text{surfaces}}$ $^{-(C_{T\,(GOI)} - C_{T\,(ACTB)})}{}_{\text{tissue culture plate control}}$]. The fluorescence signal was detected by Power SYBR PCR master mix Applied Biosystems, Invitrogen, USA) in a real-time PCR machine (Applied Biosystems 7500, Thermo Fisher Scientific, USA).

Table 6.1. *Primer sequences of genes investigated in the study*

Gene	Sequence	Accession Number
Human β-actin (*ACTB*)	**F** 5′- GGCATCCTCACCCTGAAGTA-3′ **R** 5′- GGGGTGTTGAAGGTCTCAAA-3′	NM_001101.5
Human Runt-related transcription factor 2 (*RUNX2*)	**F** 5′-GATGGGACTGTGGTTACTGTCA-3′ **R** 5′-CTCAGATCGTTGAACCTTGC-3′	NM_001278478.1
Human Osteocalcin (*OCN*)	**F** 5′- CAGCGAGGTAGTGAAGAGAC-3′ **R** 5′- GCCAACTCGTCACAGTCC -3′	NM_199173.5
Human Bone sialoprotein (*BSP*)	**F** 5′AACCTACAACCCCACCACAA-3′ **R** 5′-GTTCCCCGTTCTCACTTTCA-3′	NM_004967.3
Human *CD 163*	**F** 5′-TGTGGCCTGCATAGAGAGTG-3′ **R** 5′-TTCCCCAAAATGAGCAGAAC-3′	NM_004244.6
Human tumour necrosis factor-α (*TNF-α*)	**F** 5′- GAGGCCAAGCCCTGGTATG-3′ **R** 5′- CGGGCCGATTGATCTCAGC-3′	NM_000594.4
Human interleukin-6 (*IL-6)*	**F** 5′-ACTCACCTCTTCAGAACGAATTG-3′ **R** 5′-GTCGAGGATGTACCGAATTTGT-3′	NM_001371096.1

6.2.7.4 *Immunocytochemistry*

hMSCs seeded substrates were fixed with neutral buffered formalin overnight and then permeabilized with 0.1 % Triton X-100 in PBS (pH, 7.4) for 15 min, followed by blocking with 5% bovine serum albumin (BSA) for 1 h. These substrates where probed for the presence of osteogenic marker, Osteopontin (OPN) using rabbit polyclonal against OPN (Abcam, USA; Dilutions 1:1000), detected with FITC-conjugated secondary goat-antirabbit Ig (appearing green) (Abcam, USA; Dilutions 1:2000). The same was co-stained with 0.165 µM phalloidin conjugated-rhodamine (appearing red) to stain F-actin and nucleus stained with DAPI (4′,6-diamidino-2-phenylindole) (appearing blue).

Macrophage seeded substrates were fixed, permeabilized and blocked with BSA. These substrates were probed for the presence of macrophage markers, namely pan macrophage marker CD 68 (mouse monoclonal to CD 68; Abcam, USA; Dilutions 1:400) detected with FITC conjugated goat anti-mouse IgG (Sigma, USA;1:100 dilution) (appearing green). CD 68 stained samples were co-stained with either M2 marker rabbit polyclonal to mannose receptor CD 206 (Abcam, USA; Dilutions 1:1000) or M1 marker rabbit polyclonal to CCR7 (Abcam, USA; Dilutions 1:250), detected with DyLight594 conjugated goat anti-rabbit IgG (Abcam, USA; Dilutions 1:100) (appearing red) with nucleus stained with DAPI (4′,6-diamidino-2-phenylindole) (appearing blue). The stained samples were visualized under fluorescence microscope (Nikon ECLIPSE Ti2, Japan) and represented.

6.2.8 Statistical Analysis

All the experiments were performed in biological or experimental triplicates (unless or otherwise noted) and the results from analysis are presented as mean ± standard error. For parametric data set with F-distribution, one-way analysis of variance (ANOVA) *via* Tukey's test (Origin 2018b, OriginLabs, USA) were performed for analysing statistical significance and results between two groups were considered statistically significant if p-value was found to be less than 0.05.

6.3. Results and Discussion

Towards the first step in developing a multifunctional, biomimetic coating the selection of appropriate nanoparticle system is essential. 70S bioactive glass network was chosen for its imperative bioactive bone bonding nature and its ease to be synthesized into nanoparticulate form *via* sol-gel technique [384]. Additionally, silk fibroin owing to its well documented biocompatibility, mechanical properties and tuneable biodegradability was chosen as the biopolymer for forming the nanocomposite [385]. Imparting mesoporosity is an ideal choice in nano-delivery systems, which offers high surface area for drug loading [386, 387]. Moreover, in silicate networks the presence of silanol groups helps in ease of surface modification of such nanoparticulate systems, to tailor chemical groups of interest which has some pharmacokinetic or biological role [387].

6.3.1 *Synthesized Nanoparticles Exhibit Mesoporous Nature with Physico-chemical Properties Conducive for Electrophoretic Deposition*

Based on these design considerations, cetyltrimethylammonium bromide (CTAB) based templating was opted in the facile synthesis reported here to obtain mesoporous 70S nano-bioactive glass by a modified Stöber method. Here, the hydrolysis of TEOS and subsequent condensation of silanol monomers (**Figure 6.2 B**) occurs over the CTAB micelles for the growth of silica nanoparticle network, where positively charged amino groups of CTAB help in nucleation of negatively charged silanol groups of TEOS. Critical micelle concentration (CMC) of CTAB is 1mM in water and at this concentration earlier reports have suggested the formation of relatively non-porous silica nanoparticles [380]. However, at concentration of 10mM CTAB reported here smaller sized micelles [380] are obtained which aggregate and silanol nucleation occurs spontaneously by electrostatic interaction and aides in growth of the chosen glass network. The aged sol precipitates are washed (warm ethanol refluxing [388, 389]) to remove the templating agent which imparts mesoprosity in the synthesized nanobioactive glass (nBG). Utilising the same synthesis route, nanocomposites were developed by introducing silk fibroin (either *B. mori* or *A. assama*), wherein nucleated yet developing bioactive glass particles get incorporated in the protein template resulting in nano-composites – nBMBG or nAABG. Pertinent to note here, the synthesis of nanocomposites reflects a bioinspired route where organoapatites in bone is formed, where calcium hydroxyapatite nucleates and mineralizes in collagen-I template [102].

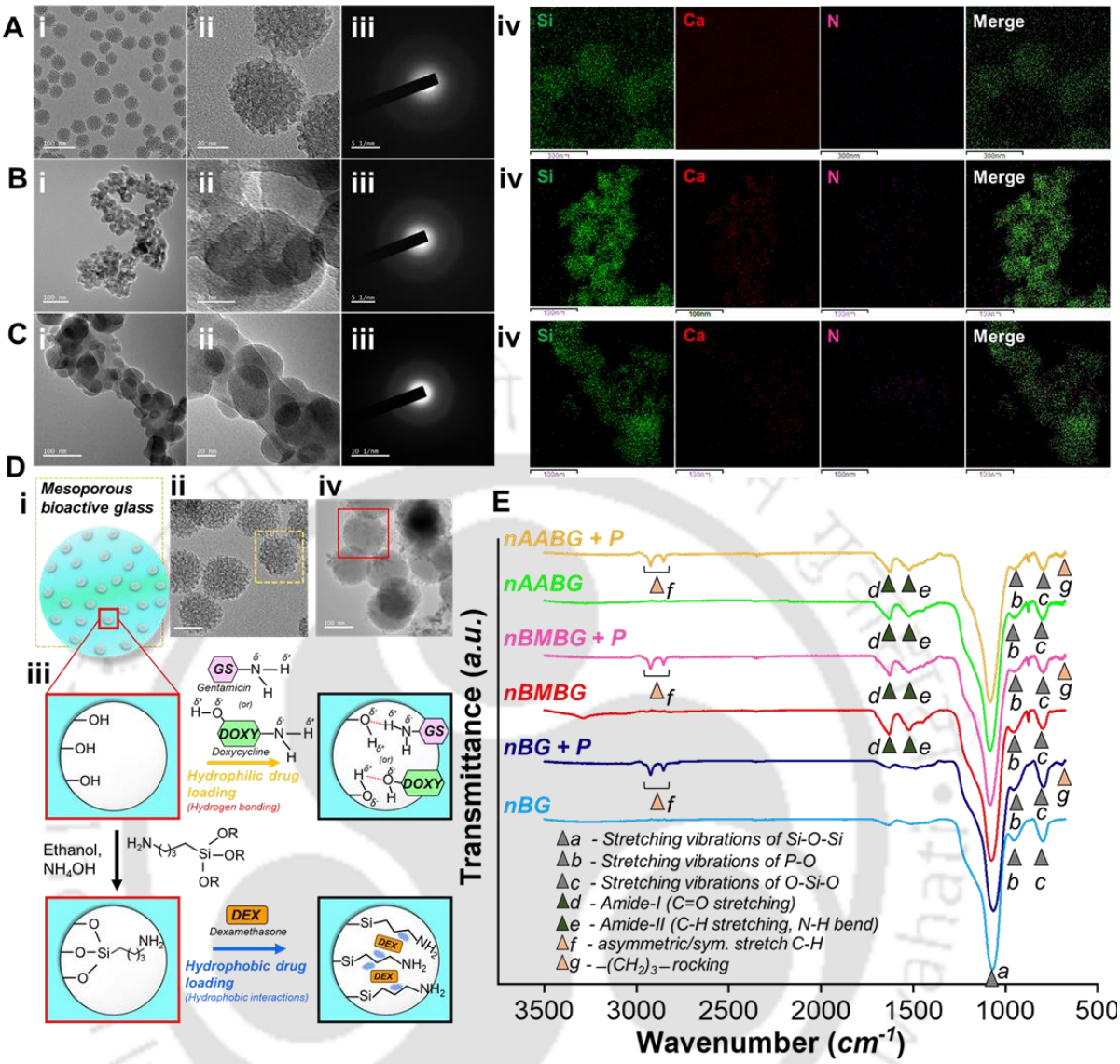

Figure 6.2. ***Characterization of synthesized nanoparticles***. *FETEM analysis (i) imaging (ii) magnified images, (iii) SAED patterns, (iv) energy dispersal X-ray spectroscopic mapping of A) nBG, B) nBMBG, C) nAABG; D) Route for obtaining (i-ii) mesoporous nBG particles and (iii-iv) modification using APTES by ethanol condensation method (+P) and proposed drug interaction between unmodified nBG and modified nBG+P for loading hydrophilic and hydrophobic drugs respectively; E) FTIR spectra of the as synthesized nanoparticles and surface modified nanoparticle (+P).*

Field emission micrographs revealed the nBG had a spherical morphology with a mean diameter 50 ± 17 nm (**Figure 6.2A i-ii**). However, with the incorporation of silk fibroin the nanocomposites nBMBG (**Figure 6.2B i-ii**) and nAABG (**Figure 6.2C i-ii**), bioactive glass nanoparticles (45 ± 8 nm) having ovoid morphology impregnated within the polymer template, resembling beads in a string were obtained. The slight reduction in size and change in circularity of bioactive glass particles within the nanocomposites could be attributed to the

influence of polymer template hindering the growth of bioactive glass network post-nucleation in CTAB template. All the groups (**Figure 6.2A-C, iii**) exhibited amorphous nature as inferred from the selected area diffractogram with the diffused rings. Mesoporous bioactive glass nanoparticles are generally calcined (>500 °C) to remove organic templating agents used to impart porosity which confers crystallinity to the bioactive glass. However, we resorted to use warm ethanol refluxing, which had two-fold advantages - stabilized the silk fibroin (inducing β-sheet), while removing the templating agent without causing any local structural damage of nanoparticle microarchitecture noticed during calcination. The stoichiometric composition of the bioactive glass used here was affirmed by using energy dispersal spectra and mapped representation of important elements Si, Ca from bioactive glass; N from organic silk fibroin template is represented in **Figure 6.2A-C, iv**.

Dynamic light scattering studies (**Table 6.2**) revealed that nBG suspensions (pH 6-7) had a hydrodynamic radius of 187.3 ± 73.92 nm with a Zeta potential ζ = -14.4 mV. Isoelectric point of silica is at pH 2 [390], and beyond pH 2 it is negatively charged due to hydroxylation of silica surfaces. The nanocomposites nBMBG and nAABG in correlation with electron microscopy images exhibited a greater hydrodynamic radius 538.4 ± 249.3, 484.7 ± 166.8, respectively while exhibiting ζ -13.8 mV and -17.1 mV (**Table 6.2**). The theoretical isoelectric point of silk fibroin is 4.53 [385], and thus at pH 6-7 they are negatively charged, which contributes to the observed Zeta potential without impeding the nanobioactive glass charge distribution. Thus, the stability of the suspensions attributed by decent Zeta potential and polydispersity index is conducive for electrophoretic deposition application. Synthesized nBG and nanocomposites nBMBG, nAABG by virtue of their porosity enable in loading of drugs, here we explored the feasibility of loading antibiotics – gentamicin sulphate and doxycycline hyclate. The drug loading can be attributed to the electrostatic interactions and (**Figure 6.2D i-ii**), where amino groups of aminoglycosides class (gentamicin) and tetracycline class (doxycycline) interact with the hydroxyl groups *via* hydrogen bonding [391]. However, in case of loading hydrophobic drugs the efficiency of such system is compromised. Therefore, we opted to introduce a facile surface modification by 3-(aminopropyl) triethoxysilane – APTES, which incorporates alkylamines (n=3) modification in the hydroxyl groups in the silanol network (**Figure 6.2D iii-iv**). The alkylamines (hydrophobic moieties) was hypothesized to improve the drug loading efficiency of hydrophobic drugs (dexamethasone) [392]. The modification increased the hydrodynamic radius of the composites and decreased the Zeta potential, though not significantly. The modified (+P) nanoparticles – nBG+P, nBMBG+P,

nAABG+P exhibited hydrodynamic radius of 207.3 ± 87.92 nm, 638.4 ± 289.1 nm, 584.7 ± 176.2 nm respectively; while exhibiting ζ -10.4 mV, -10.8 mV and -11.1 mV respectively (**Table 6.2**), where the amine groups probably contributing to the overall reduction in Zeta potential in modified groups. The same could be affirmed from electron micrographs (**Figure 6.2 B-C i**) wherein the surface morphology of bioactive glass was altered due to modification.

Infrared spectroscopy (**Figure 6.2E**) confirmed the characteristic peaks for bioactive glass in all composites relating to stretching vibrations of Si-O-Si (at 1092 cm^{-1}), stretching vibrations of P-O (962 cm^{-1}), and stretching vibrations of O-Si-O (at 808 cm^{-1}) [384]. The presence of protein templates in the nanocomposites (nBMBG, nAABG, nBMBG+P, nAABG+P) was confirmed by the presence of amide-I bands (C=O stretching vibrations at 1650-1600 cm^{-1}) and amide-II bands (C-H stretching, N-H bend at 1550-1510 cm^{-1}) [393]. The modification was confirmed by the appearance of two small signature peaks between 2923-2848 cm^{-1} due to the stretching of C-H and a very weak shoulder peak at 687 cm^{-1} probably due to $–(CH_2)_3-$ rocking from the alkylamine moieties of APTES [387] present in modified groups (nBG+P, nBMBG+P, nAABG+P). Nitrogen sorption isotherms analysis (**Table 6.2**) revealed that the synthesized nanoparticles – nBG, nBMBG, nAABG exhibited surface area (m^2/g) of 432, 552, 532 respectively, with mean pore diameter ~ 9 nm. The modified nanoparticles – nBG+P, nBMBG+P and nAABG+P had surface area (m^2/g) of 367, 491, 462, with ~ 15% reduction in surface area (m^2/g), while maintaining mean pore diameter of ~ 8 nm. The surface modification has been reported to reduce the textural properties of mesoporous silica networks [394]. However, ethanol condensation of APTES opted here and the results indicate that by maintaining a low APTES concentration (0.8 mM for 1h reaction time), the modification did not hinder the mesoporous network without hampering the surface area. Similar observations were reported in mesoporous silica nanoparticles wherein surface functionalisation with APTES with lower APTES concentration, resulted in modified silica nanoparticles without hampering the textural properties needed for drug loading [387].

Table 6.2. *Hydrodynamic radius, Zeta potential, surface area and pore size analysis of synthesized and modified nanoparticles*

Sample	Hydrodynamic Radius (*nm*)	Polydispersity Index	Zeta potential ζ (*mV*)	Conductivity (*mS/cm*)	BET Surface Area (m^2/g)	Pore Diameter (*nm*)	Pore Volume (cm^3/g)
nBG	187.3 ± 73.92	0.295	-14.4 ± 0.34	0.0639	432	9.8	0.61
nBMBG	538.4 ± 249.3	0.250	-13.8 ± 0.57	0.184	552	9.1	0.58
nAABG	484.7 ± 166.8	0.245	-17.1 ± 0.42	0.0948	532	9.2	0.59
nBG+P	207.3 ± 87.92	0.305	-10.4 ± 0.21	0.0617	367	8.3	0.52
nBMBG+P	638.4 ± 289.1	0.265	-10.8 ± 0.67	0.172	491	8.01	0.50
nAABG+P	584.7 ± 176.2	0.255	-11.1 ± 0.33	0.09	462	8..03	0.51

6.3.2 *Electrophoretic Deposition Renders Uniform Conformal Coating on Metals Surfaces with Decent Coating Integrity*

The custom electrophoretic deposition (EPD) set-up with 10 mL of electrolyte bath consisting of 30 % (v/v) ethanol/water suspension to which 0.5 g/L nanoparticles was added and sonicated briefly to disperse the particles, which resulted in colloidal suspensions. The conductivity of these suspensions from Zeta Potential analysis (**Table 6.2**) for synthesized nBG, nBMBG, nAABG nanoparticles were found to be 0.0639 mS/cm, 0.184 mS/cm and 0.0948 mS/cm respectively; whereas for modified nBG+P, nBMBG+P and nAABG+P nanoparticles were found to be 0.0617 mS/cm, 0.172 mS/cm and 0.09 mS/cm respectively. The observed values exhibit decent ionic strength for electrophoretic deposition application in accordance to previously reported values (~ 0.4 mS/cm) [395]. The operating voltages were optimized (**Figure 6.3A**) with 15 V, 30 V, 45 V and the deposition yield were recorded for different deposition time. It is pertinent to note here that electrophoretic deposition technique enables in creating ceramic laminates/ coatings in metal surfaces, there is no particle/ electrode reaction involved. Therefore, the charged colloidal particles can be easily striped off the deposited metal surface if electric field is reversed. Hence, to improve the coating similarly charged species (polymers as binders) are incorporated to improve the binding of these coatings [396]. Previously, chitosan [397] or silk fibroin [378] as charged polymer species have been reported to enhance the binding of electrophoretically deposited species. In this study, we opted to use chondroitin sulphate (a negatively charged polymer) as a binder which was added to the colloidal suspension to compliment the negatively charged nanoparticles/ nanocomposites to deposit on metal surfaces.

The synthesized nanoparticles reflect a bioinspired composite similar to bone's organoapatite (collagen-I mineralized with hydroxyapatite), where here mesoporous 70S nanobioactive glass is templated within silk fibroin protein polymer. The inclusion of chondroitin sulphate, a glycosaminoglycan (GAG) here as a binder was hypothesized to compliment the nanocomposite make-up in the EPD coatings. It is well-known that in bone extracellular matrix (organic content), apart from the predominant collagen-I (90%), the other non-collagenous proteins (10%) (NCPs) include γ-carboxyglutamate proteins, glycoproteins and proteoglycans [103]. GAGs also play a crucial role by associating with collagen-I, where they have been reported to foster osteogenesis by improving the bioavailability and activity of osteoclastic and osteogenic factors through modulating Wnt signalling [398].

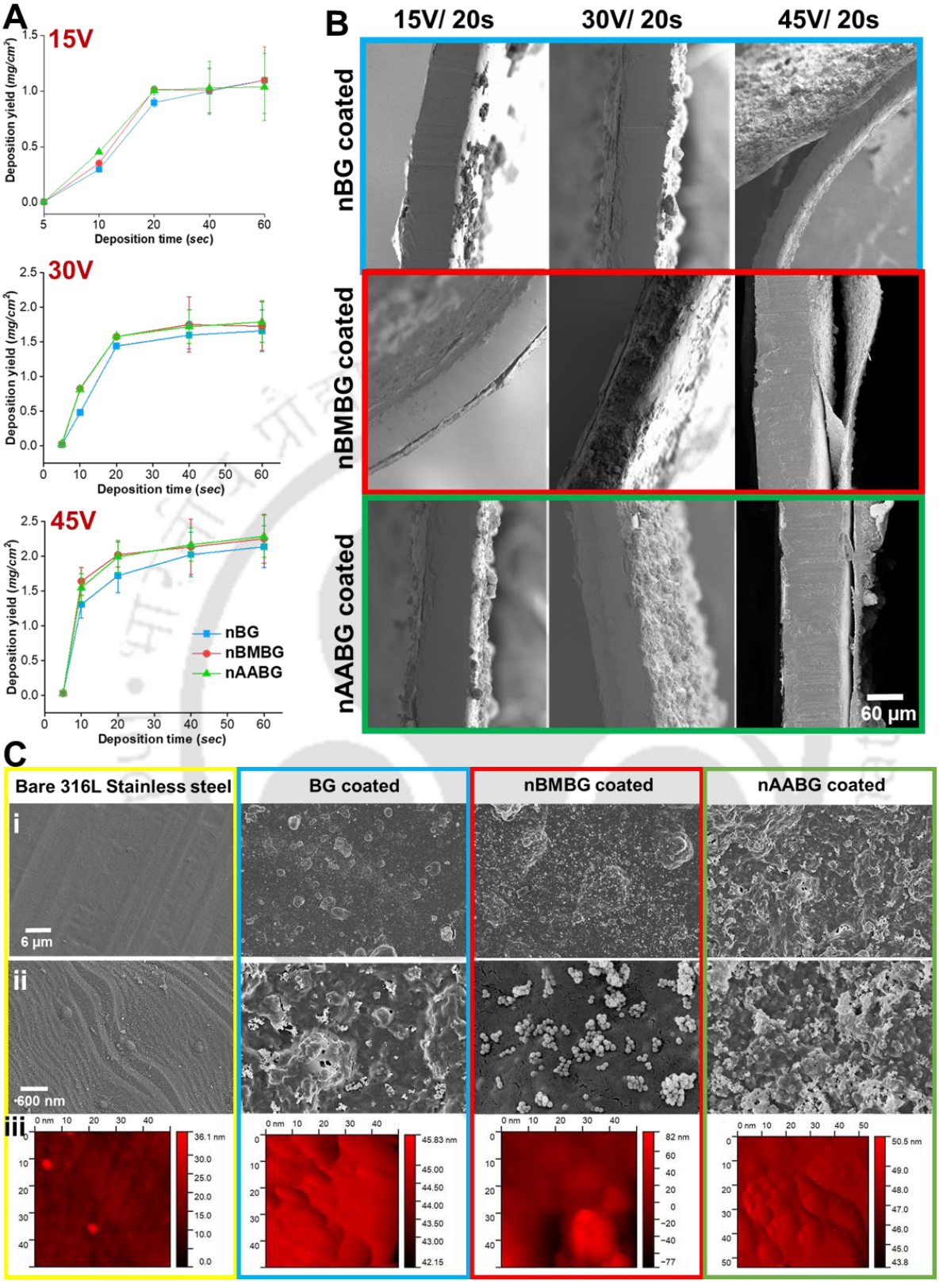

Figure 6.3. ***Characterization of electrophoretic coatings on 316 L medical grade stainless steel.*** *A) Deposition yield for different operating voltages, B) respective field emission scanning electron microscopy (FESEM) images; C) Characterization of electrophoretic coatings on 316*

L medical grade stainless steel at 30V/20s; i-ii) FESEM and iii) atomic force microscopy (AFM) analysis. (Data presented as Mean ± S.D (n=3).

In EPD, under an applied voltage negatively charged species migrate to the anode (the target metal surface), where water is electrolysed locally around the anode resulting in increase in pH (alkaline conditions). The negatively charged species gets neutralized and adhere to the anode resulting in a coating around the immersed surfaces in the electrolyte bath [378, 391]. The deposition takes place in a layer-by-layer manner wherein at an operating voltage, with increase in time the deposition yield increases linearly until a saturation plateau is reached (**Figure 6.3A**). The linear region of deposition depends on various factors such as concentration of charged particles in colloidal suspension, viscosity and permittivity of electrolyte solvent, Zeta potential of species, electric field applied, distance between the electrode and time of deposition [396] which is given by Hamaker's equation. Herein, the working distance (10 mm between electrodes) and concentration (0.5 g/L nanoparticles) was optimised until viable coating was noticed to deposit at the anode. At concentrations below 0.5 g/L and operating voltage less than 15 V, viable and homogenous coatings were not obtained, probably due to poor electric charge density at the electrode vicinity resulting in interparticle repulsion and aggregation [379]. At operating voltages above 15V, viable coatings were observed (**Figure 6.3B**) with deposition yield increasing linearly till 20 s and after which a saturation was reached (1.1 mg/ cm^2). No discernible difference in coating yield was noticed within the groups (nBG, nBMBG, nAABG). However, while increasing the operating voltage the deposition yields increased ~ 1.6 folds and ~ 2 folds at deposition time of 20 s. Beyond 20 s, the saturation in yield could be attributed to the decrease in electric field influencing the electrophoresis due to the coating acting as an insulating layer [379] self-limiting the deposition process. These observations were affirmed by cross-sectional scanning electron images (**Figure 6.3B**) where coating thickness at same deposition time (20 s) increased from 15 V to 30 V to 45 V, wherein at 45 V delamination was also observed in the coatings due to the insulation layer hampering further deposition, resulting in loosely bound laminates deposited by layer-by-layer fashion.

The operating voltage of 30 V and 20 s which resulted in a viable confluent coating without delamination was thus chosen to be carried forward for further studies. It must be noted here, the deposition yield and coating phenomena for modified (nBG+P, nBMBG+P, nAABG+P) also followed a similar trend to unmodified groups and hence the same operating conditions were opted for those groups also. Top layer of coated surfaces revealed a confluent coating of spherical nanoparticles embedded over the surface (**Figure 6.3C i-ii**), though not

homogenously distributed owing to the lack of control in EPD, as opposed to laser assisted sintering or microwave assisted co-precipitation methods. However, EPD does not need such sophisticated instrumentation and offers the advantages of being cost-effective, controlled deposition rates with predictable and scalable deposition kinetics, operating temperatures conducive for depositing drug/ biomolecule loaded vehicles [378, 391, 396, 397]. Topographic analysis (**Figure 6.3 Ciii**) by atomic force microscopy revealed average roughness (R_a) was comparable between the groups – nBG, nBMBG, nAABG, R_a (nm) = 40.23 ± 5.24, 47.82 ± 7.12 and 45.67 ± 6.32 respectively. Increasing the surface roughness has been documented to favour osseointegration by micromechanical retention of osseous tissue between peri-implant site and bone [151]. However, increasing surface roughness also could increase chances of microbial attachment and harbouring. Nanotopographies with R_a < 0.2 µm have been found to reduce chances of bacterial biofilm formation while improving osteogenic cell attachment [159, 376]. Thereby, the coated implants reported here with R_a ~ 45 nm was hypothesized to positively influence the osteogenic cell survival and osseointegration.

Integrity of the coatings were evaluated by delamination tests (**Figure 6.4 Ai**) where dental bare stainless-steel screws (**Figure 6.4 Aii**) were coated and observed pre and post-delamination under hydrated conditions. Coated screws (**Figure 6.4A iii-v**) revealed evenly deposited laminates along the shank and ridges (crest) regions with no uneven deposits noticed in between the grooves. This affirms the suitability of the nanoparticles/ nanocomposites through EPD for executing conformal coatings on metal implants intended for orthopaedic applications. After delamination, discernible delamination was noticed particularly along the threads which could be attributed to the absence of strong chemical bonding between the metal surface and ceramic laminates. To improve the adhesion strength of EPD coatings, metal surfaces are either pre-treated by etching (chemical treatment) or sand blasting (physical methods) which enhances the surface roughness and eventually improving mechanical interlocking [399]. Chemical bonding is enhanced by sintering the coated surfaces, which results in coatings with adhesion strengths > 50 MPa. However, the downside to sintering increases production costs, thermal coefficient mismatch leading to coating cracking [400], and inability to coat ceramics loaded with drugs/ biomolecules. Ceramic-polymer composite coating enables in avoiding this sintering step which helps in forming nanocomposite laminates with decent mechanical strengths suitable for orthopaedic and dental fixation applications. In this regard, lap-shear tensile adhesion tests (**Figure 6.4 Bi**) were performed to assess the adhesion strengths of coatings (**Figure 6.4 Bii**), which showed the nBG, nBMBG and nAABG

coatings had adhesion strength of ~ 5 MPa. These values were comparable to other ceramic nanocomposite coatings (~ 3 MPa) [400], vacuum sintered apatite coatings (~ 6.8 MPa) [372] and polymer coatings (5 to 6 MPa) [378] reported for orthopaedic applications.

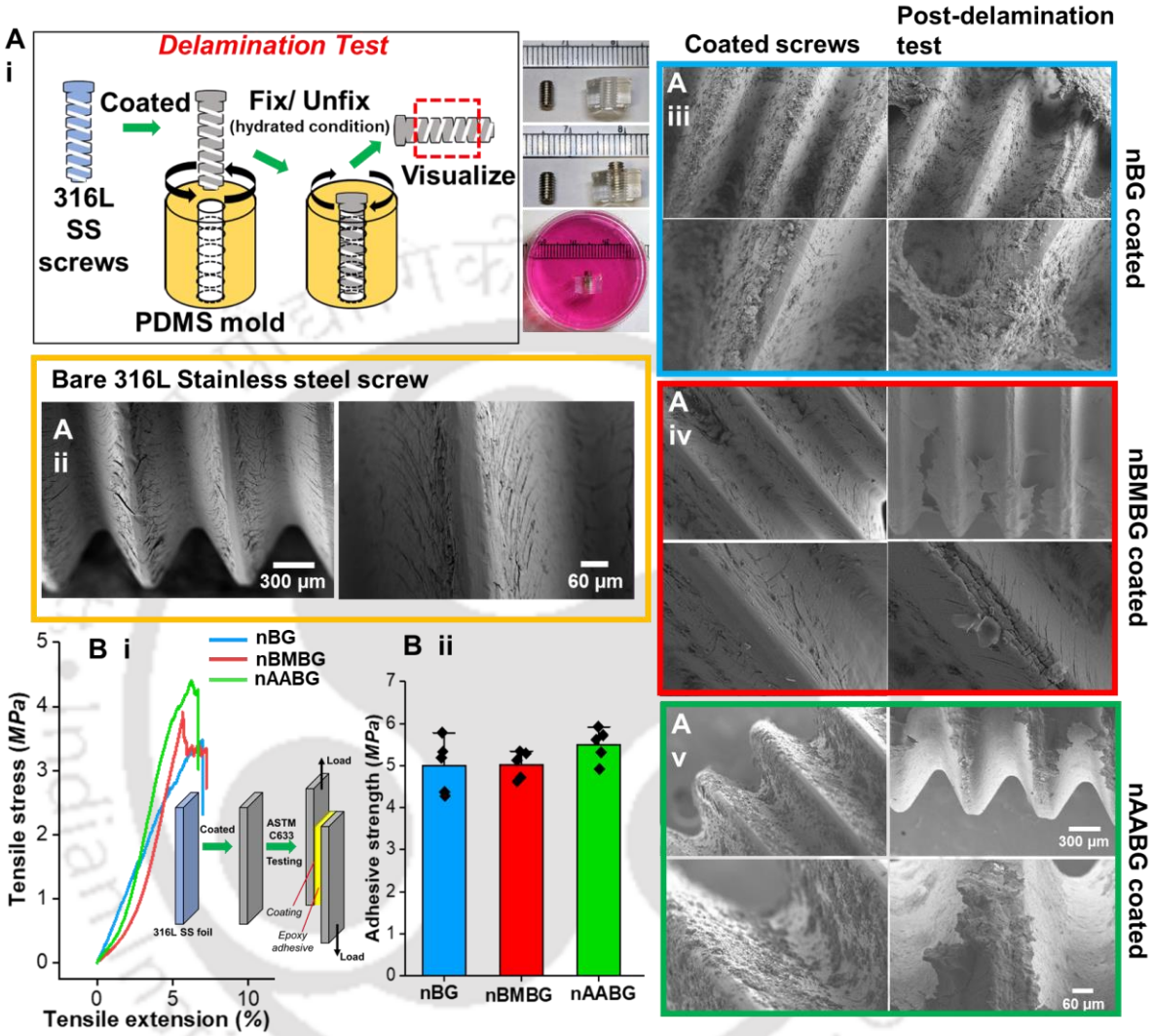

Figure 6.4. ***Characterization of electrophoretic coatings on 316 L medical grade.*** *A) stainless steel screws at 30V/20s; i) FESEM analysis post delamination tests ii) bare uncoated SS screw, iii) nBG, iv nBMBG coated, v) nAABG coated screws; B) adhesion strength determination (ASTM C633 test) – i) representative stress-strain curves and ii) adhesive strength of coated 316L SS foils. (Data presented as Mean ± S.D (n=5).*

6.3.3 *Antibiotics Loaded Mesoporous Nanocomposites Enhance the Antibacterial Effect of the Coatings*

Implant associated infections can be overcome by antibacterial coatings. Several strategies have been adopted to materialize the same, which include imparting anti-fouling topographies [151], grafting antimicrobial agents to metal surfaces [370] and coating delivery vehicles on metal implants loaded with drugs [391, 397]. In this study, mesoporous nanoparticle/ nanocomposite was synthesized as vehicle for loading drugs/ antibiotics of interest to design antimicrobial coatings. To attest the vehicle's capability to load case-scenario antibiotics two model drugs - gentamicin (aminoglycosides class) and doxycycline (tetracycline class), were chosen. Gentamicin loading capacity for nBG, nBMBG, nAABG was found to be ~ 0.45, ~72, ~ 0.7 mg/ mg nanoparticle (**Figure 6.5Ai**). The drug-nanoparticle interaction could be attributed to the electrostatic interactions between the amino groups of aminoglycosides and the hydroxyl groups of silanol of bioactive glass (**Figure 6.5Diii**). This was reflected in the reduction of ζ potential for gentamicin loaded nBG, nBMBG, nAABG groups -6.4, -5.9, -6.3 mV respectively. The *in vitro* drug release studies performed showed (**Figure 6.5Aii**) a rapid release noticed up to 36 h, with nBG group achieving ~96% release by 48 h while nBMBG showcased ~83% release and nAABG ~77 % release at 48 h. Though the release was not slow and sustained, the relatively rapid release is desirable as implant associated infections can be curtailed with such rapid release locally preventing early infection complications [377]. Moreover, slow and sustained release of antibiotics could lead to development of antibiotic resistance when local antibiotic concentration is not sufficiently high [401]. The drug release profile was fitted in drug release models and it was found to follow Korsmeyer-Peppas model (R^2 = 0.93 – 0.97) indicating release was mediated by diffusion processes with release exponent (from slope, n < 0.45), specifically Fickian diffusion (**Figure 6.5Aiii**). This could be attributed to the hydrolytic environment wherein the hydrophilic drug (gentamicin) from mesoporous nanoparticles gets released into the release media (PBS, pH 7.4, 37 °C), to a certain extent though not entirely mimics the physiological conditions.

Similarly, loading capacity of doxycycline in synthesized and modified nanoparticles (**Figure 6.5Bi**) was assessed. Unmodified groups showed higher loading capacity with ~ 0.38, 0.53 and 0.54 mg/ mg nanoparticle of nBG, nBMBG and nAABG respectively; while modified groups showed lesser loading capacity with ~ 0.05 mg/ mg nanoparticle. The higher loading capacity in unmodified group could be attributed to the electrostatic interactions between

amino groups of doxycycline with hydroxyl group as affirmed by similar trends noticed in gentamicin, with the ζ potential analysis (**Table A6.1** *Appendix*).

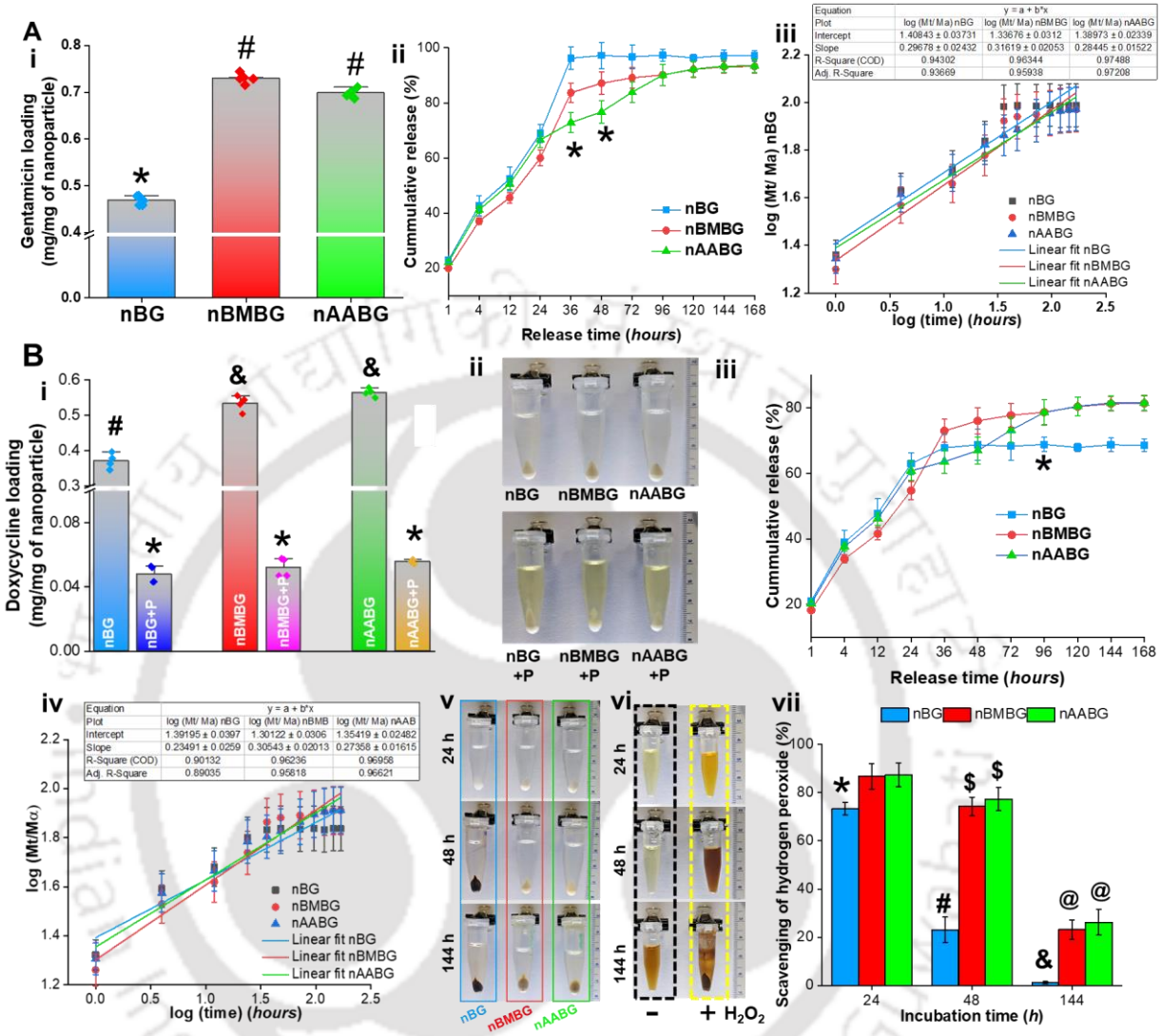

Figure 6.5. ***Loading model antibiotics on to synthesized nanoparticles****. A) Gentamicin sulphate i) loading efficiency represented as (mg drug loaded/ per mg nanoparticle), ii) drug release kinetics (at 37°C) – cumulative release iii) and release profile fitted in respective Korsmeyer-Peppas model (Mt/Mα = ktn), where exponent n (from slope) follows Fickian diffusion for release; B) Doxycycline on to synthesized nanoparticles; i) loading efficiency represented as (mg drug loaded/ per mg nanoparticle) ii) representative images of pellet (nanoparticle) and supernatant (drug suspension); iii) drug release kinetics (at 37°C) – cumulative release, iv) release profile fitted in respective Korsmeyer-Peppas model (Mt/Mα = ktn), where exponent n (from slope) follows Fickian diffusion for release; v) representative images of pellet (nanoparticle) at 24, 48, 144h; vi) representative images of doxycycline solution without/ with 0.02% H_2O_2; vii) hydrogen peroxide scavenging activity of nanoparticles. (Data presented as Mean ± S.D (n=5); *, #, & represents statistically significant difference at $p \leq 0.05$, same symbols indicate no significance while different symbols indicate statistical significance between the groups tested; parametric ANNOVA Tukey's test).*

In contrast, the presence of bulky alkylamine in modified groups (+P) might have resulted in steric hindrance preventing the electrostatic interaction. Doxycycline has a pale-yellow colour in suspension and in case of unmodified groups (**Figure 6.5 Bii**) the loaded particles took up the drug efficiently, hence acquiring pale yellow colour as noticed in the pellet. However, in case of modified group supernatant remained yellow while the pellet consisting of nanoparticles remained white, indicating relatively poor loading in modified groups. Thus, unmodified groups could serve as vehicles for loading hydrophilic antibiotics more efficiently. The doxycycline release profile (**Figure 6.5 Biii**) also exhibited a rapid release similar to gentamicin with nBG group achieving ~69% release by 96 h while nBMBG showcased ~80% release and nAABG ~81 % release at 96 h. The drug release profile was fitted in Korsmeyer-Peppas model having R^2 = 0.89 (nBG); = 0.95 (nBMBG); = 0.96 (nAABG), indicating release was mediated by diffusion processes with release exponent (from slope, n < 0.45), specifically Fickian diffusion (**Figure 6.5 Biv**). Doxycycline solution is yellow in colour and post drug-loading the white coloured nanocomposites take up this yellowish hue. During the course of release, it was noticed that the doxycycline loaded nanoparticles exhibiting slightly pale-yellow colour turned into reddish-brown colour, especially with doxycycline loaded nBG (**Figure 6.5 Bv**). In the silk composite groups, nBMBG and nAABG this discoloration was not that prominent. Doxycycline is susceptible for oxidation and it was noticed that in presence of a strong oxidiser like hydrogen peroxide (**Figure 6.5 Bvi**), doxycycline solution (5mg/mL) precipitated and formed reddish brown precipitates, whereas the same was retarded in its absence.

Tetracyclines undergoes oxidation by many processes such as presence of oxidant, photo-catalysis etc., where oxygen is acquired by tetracycline to become a new molecule 4α,12α-anydro-4-oxo-4-dedimethylaminotetracycline, changing from yellow to red-purple colour [402]. It was hypothesized that silk fibroin exhibited antioxidant traits retarding the oxidation rate of doxycycline in composite groups (nBMBG and nAABG). This was confirmed by hydrogen peroxide scavenging (**Figure 6.5 Bvii**), whereas in nBG groups the percentage dropped from ~85 % to ~ 20% within 48 h, while in composite groups it dropped from ~90% to ~ 85% only. Reactive oxygen radical-scavenging activity, thereby limiting rate of oxidation could be attributed to basic amino acids arginine, lysine and histidine which has been reported to act as antioxidants. Moreover, silk fibroin has been reported to stabilize biomolecules in different formats such as nanoparticles, fibers, films and sponges. Silk fibroin protein

assembles into a stabilizing microenvironment exhibiting protective barrier effects, increasing the bioactivity and shelf-life of entrapped, adsorbed biomolecules [403].

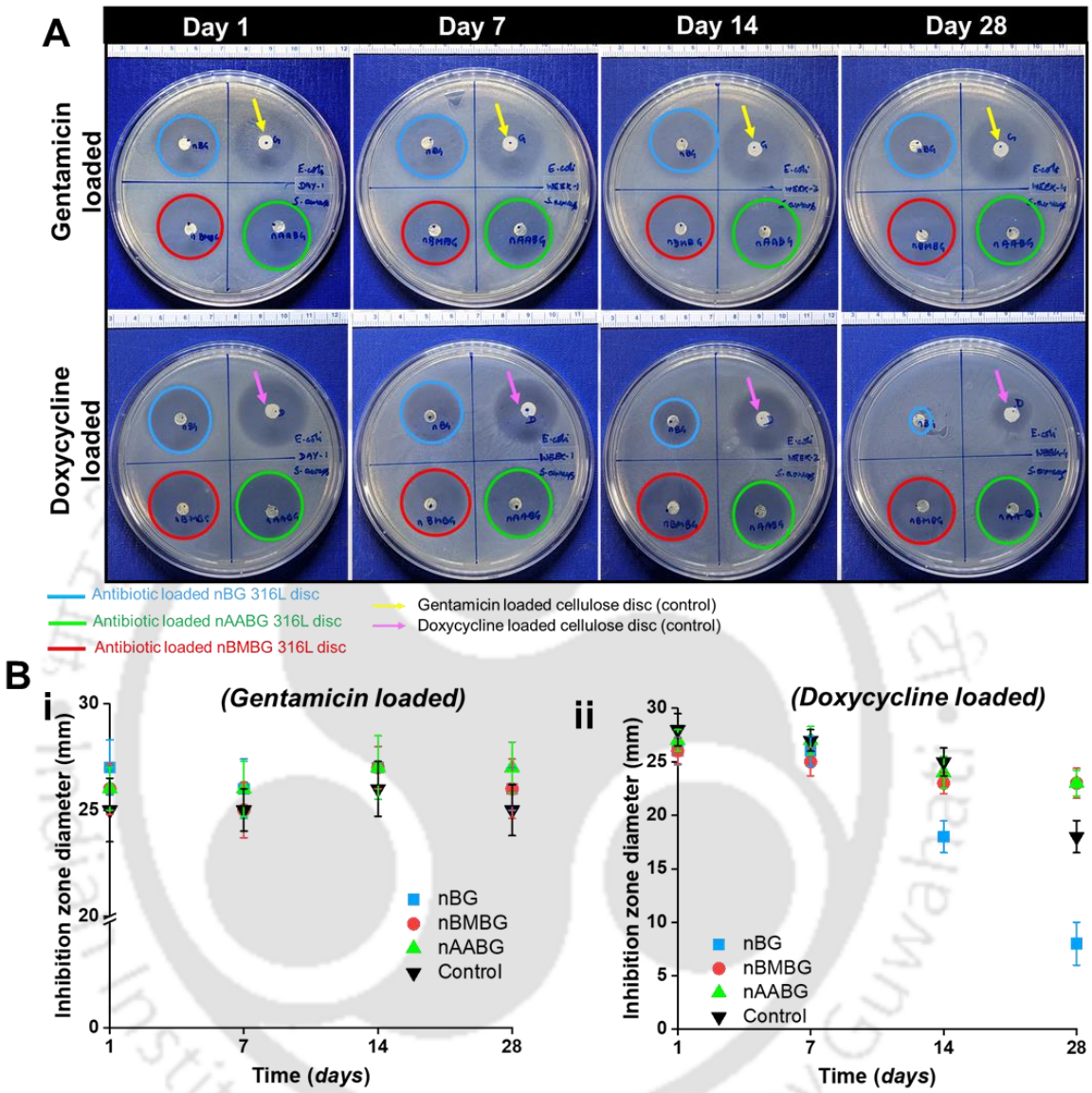

Figure 6.6. ***Antibiotic susceptibility test using Disc diffusion assay for assessing stability of drug at 37°C****. A) Gentamicin, Doxycycline (100 µg) and coated 316L discs, representative agar plates (S. aureus and E. coli co-culture) at different time points and B) Inhibition zone diameter plot of i) Gentamicin ii) Doxycycline coated 316L stainless-steel discs. (Data presented as Mean ± S.D (n=3).*

The antibacterial potency of coated stainless-steel discs was evaluated using disc diffusion method for antibiotic loaded nanoparticles. 250 µg of gentamicin was loaded per disc and gentamicin susceptibility was affirmed by the clearance halo noticed in nBG, nBMBG, nAABG coated discs (with gentamicin) against Gram-negative *E. coli* and Gram-positive *S. aureus* bacteria (**Figure A6.1 A** *Appendix*) on par with control gentamicin discs. The noncoated

metal discs and non-loaded but coated discs exhibited minimal clearance halo. Moreover, coated discs with different concentration of gentamicin were evaluated by bacterial growth inhibition assay (**Figure A6.1 B** *Appendix*). When compared to non-loaded controls, gentamicin loaded groups (nBG, nBMBG, nAABG) exhibited concentration dependent decrease in bacterial population reduction (reflected by the decrease in turbidity). These results indicate the developed system, enables in coating metal implants with mesoporous nanoparticles loaded with antibiotics of particular concentration, to combat implant associated infections in orthopaedic settings. It is pertinent to note here that periprosthetic joint infections, particularly early cases (< 3 months after surgery) can be treated with implant retention but if persistence of microbial load is noted then it leads to chronic altercations which needs the implant removed [404]. Diagnostic criteria for such cases include the presence of virulent microorganisms (*E. coli* and *S. aureus*) in synovium and removed implant [404]. Therefore, a continuous co-culture of *E. coli* and *S. aureus* in disc diffusion method of coated implants were assessed (**Figure A6.2** *Appendix*), where the coated discs were continuously challenged with fresh co-cultures until clearance halo was not observed. It was noticed that in control discs (gentamicin loaded cellulose discs) the susceptibility and zones of inhibition was noticed for 24 h only, whereas in coated stainless-steel discs with gentamicin loaded nBG group it was noticed till 36 h, while in nBMBG for 72 h and nAABG for 84 h. This preservation of bioactivity of gentamicin loaded nBMBG and nAABG could be attributed to the stabilisation of the antibiotic in the composites due to the presence of silk fibroin [403].

The antibacterial potency of coated stainless-steel discs for doxycycline loading was also evaluated using disc diffusion method for antibiotic loaded nanoparticles. 200 µg of doxyxyxline was loaded per disc and doxycycline susceptibility was affirmed by the clearance halo noticed in nBG, nBMBG, nAABG coated discs (with doxycycline) against *E. coli* and *S. aureus* bacteria (**Figure A 6.3** *Appendix*) on par with control doxycycline discs. Similarly, coated discs with different concentration of doxycycline were evaluated by bacterial growth inhibition assay (**Figure A 6.3 B** *Appendix*) which revealed concentration dependent reduction in bacterial population, similar to gentamicin loaded groups. These results affirm the possibility of using the developed system to load different antibiotics as per clinical need for coating orthopaedic metal implants to exhibit antibacterial property locally avoiding systemic dosing for implant associated infection prevention. Stainless-steel discs were coated with nanoparticles loaded with either gentamicin or doxycycline (100 µg/ disc) and stored at 37°C for 28 days and the storage stability of coated discs were evaluated (**Figure 6.6 A**). It was

observed that gentamicin coated discs preserved their bioactivity over the 28 days study period with no significant loss in bactericidal activity as assessed by the clearance halo in disc-diffusion assay with *E. coli* and *S. aureus* co-culture lawns (**Figure 6.6 Bi**). However, in case of doxycycline coated discs, with nBG and control cellulose discs, there was loss in bactericidal activity by day-28 storage (**Figure 6.6 Bii**), whereas in case of nBMBG and nAABG groups the bioactivity loss was minimal in comparison to day-1 storage. Doxycycline, being susceptible to oxidation might have lost its activity during the 28-day storage in 37°C with nBG and control discs whereas the silk fibroin groups enabled in extending the bioactivity of these coated discs, vouching for their stability during extended storage of these nanocomposite loaded antibiotic coated implants before implantation.

Conformal coatings on metal implants to impart bactericidal activity by embedding antibiotics either in form of polymers films or nano-systems or ceramics [391] have enabled in controlling infections [405]. Polymers such as silk fibroin, poly-(lactide-co-glycolide), polylactic acid which are degradable polymers help in stabilising the embedded antibiotics and the degradation helps in the release of their entrapped cargo [403]. However, the release dynamics are altered when nanoscale systems are utilised, where controlled and tuneable release can be obtained. For instance, vancomycin loaded silk fibroin nanospheres [406] exhibited controlled and sustained release in comparison to conventional silk fibroin coatings. Similar observations were reported in polycaprolactone nano-systems for vancomycin and rifampicin sustained release for preventing implant associated infections [377]. Here, we opted to use a mesoporous nanoparticle system composited with silk fibroin to develop a nanocomposite which can mimic the organoapatite niche of the bone to enable in creating an interface with good bone bonding ability. Bioactive glasses are well documented for their bioactivity and bone bonding traits [225] and with the mesoporosity imparted here allows them to be loaded with scenario specific drugs, either antibiotics or other biomolecules in orthopaedic implants. The advantages of current system serve in two ways: i) high specific surface area enables loading and release of antibiotics in a diffusion dependent manner attributed due to the mesoporous network; ii) mesoporous nanocomposites enables in preserving and stabilising the bioactivity of loaded antibiotics, thereby bettering the efficiency of such coatings that are already reported.

6.3.4 *Dexamethasone Loaded Mesoporous Nanocomposites Attribute Osteoinductive Traits to the Coatings*

In addition to improving the antibacterial property of bone metal implants to combat implant associated infections, conformal coatings on them were perceived to be passive in nature. However, active surfaces which evoke biological responses after implantation such as modifications which decrease non-specific protein adsorption, functionalisation which encourage specific cell recruitment have garnered special interest lately. It is also essential that these biological cues imparted on the surfaces must not interfere with the bulk properties of the metal, compromising the utility of the device. Immunomodulation and osteoinduction are two key factors which enhance the long-term patency of endosseous implants. In this regard, dexamethasone a corticosteroid drug has been documented for its pleiotropic roles in promoting osteoblast differentiation [386] and immunomodulation [311].

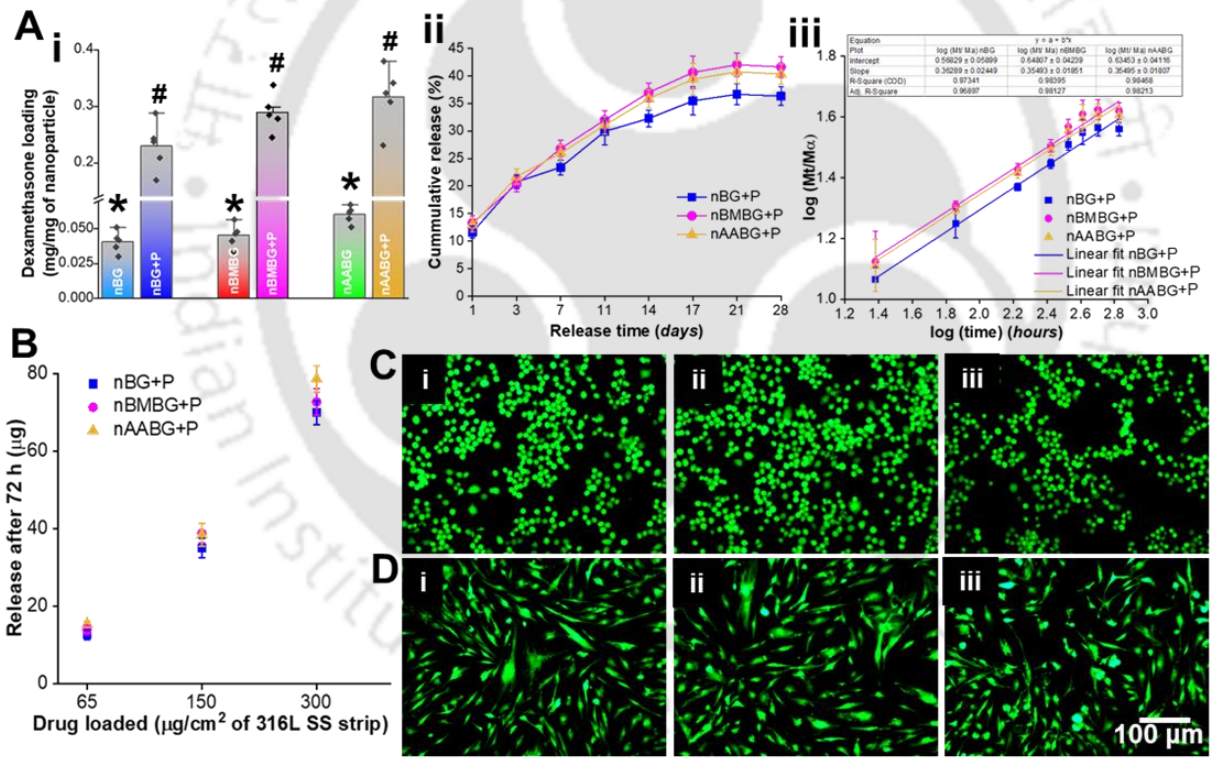

Figure 6.7 ***Loading model drug, Dexamethasone (immunomodulatory drug) on to synthesized nanoparticles and modified nanoparticles (+P).*** *A) loading efficiency represented as (mg drug loaded/ per mg nanoparticle); ii) Drug release kinetics (at 37°C) – cumulative release and iii) release profile fitted in respective Korsmeyer-Peppas model (Mt/Mα = ktn), where exponent n (from slope) follows Fickian diffusion for release; B) Release of dexamethasone (after 72 h) from different drug loading concentrations from modified nanoparticle system; Cellular viability after 72 h of seeded cells C) PMA treated THP1 monocytes (M0 macrophages), D) adipose derived human mesenchymal stem cells (hMSCs)*

*on to 316L SS discs coated with 150 µg drug concentration loaded nanoparticles (+P) for i) nBG+P, ii) nBMBG+P, iii) nAABG+P using calcein-AM staining. (Data presented as Mean ± S.D (n=5); *, # represents statistically significant difference at p ≤ 0.05, same symbols indicate no significance while different symbols indicate statistical significance between the groups tested; parametric ANNOVA Tukey's test).*

The loading capacity of dexamethasone in synthesized and modified nanoparticles (**Figure 6.7 A**) was assessed. The unmodified groups (nBG, nBMBG, nAABG) exhibited a loading capacity of ~ 0.050 mg/mg nanoparticle, while modified groups (nBG+P, nBMBG+P, nAABG+P) exhibited loading capacity of ~ 0.3 mg/ mg nanoparticle. This higher loading efficiency in modified groups could be attributed to the alkylamine modification by APTES, enhancing the retention of hydrophobic dexamethasone interacting with the alkylamines. Correlation of this differential loading was reiterated in the ζ potential (**Table A6.1** *Appendix*) analysis where in unmodified groups, the ζ potential remain unaltered similar to unloaded groups (**Table 6.2**). However, in case of modified groups (nBG+P, nBMBG+P, nAABG+P) the ζ potential decreased two folds indicating the dexamethasone loading in these mesoporous vehicles. The *in vitro* drug release studies performed showed a sustained release of dexamethasone payload from the modified groups (nBG+P, nBMG+P, nAABG+P) up to 14 days (**Figure 6.7 Bii**). Cumulative release of ~ 41%, ~ 39% and ~ 34% were realised for nBG+P, nBMBG+P and nAABG+P groups, where the release kinetics (**Figure 6.7 Biii**) followed Korsmeyer-Peppas model (R^2 = 0.97 – 0.98) indicating release was mediated by diffusion processes with release exponent (from slope, n < 0.45), specifically Fickian diffusion model. The sustained release behaviour could be attributed to the hydrophobic nature of dexamethasone and its hydrophobic interaction with the aminopropyl chains decorating the modified mesoporous bioactive glass (**Figure 6.2 Diii**). In contrast, the hydrophilic antibiotics exhibited a rapid release while hydrophobic dexamethasone exhibited a sustained release behaviour. This sustained release is desirable in case of glucocorticoids, especially from a local delivery site ameliorating the drawbacks associated with systemic delivery which include induction of abnormal blood glucose via hepatic/ peripheral insulin resistance [407] and other complications such as renal, cardiac toxicities and gastrointestinal ulcerations [408]. However, with a local sustained release from the mesoporous coatings, the intended role of dexamethasone for regulating osteogenesis and immunomodulation at the peri-implant endosseous space could be achieved.

In this regard, different loading concentration were evaluated for their release (**Figure 6.7 B**) which showed concentration release, wherein ~20% release was noticed corresponding

to the loading after 72 h, which was sufficient for orchestrating osteogenesis and immunomodulation of mesenchymal stem cells (hMSCs) and macrophages. Cell viability at different loading concentration were not hampered (**Figure A 6.4** *Appendix*) with no discernible dead cell population noted at 65, 150 and 300 µg dexamethasone/cm^2 loaded coatings of nBG+P, nBMBG+P and nAABG+P (**Figure 6.7 C-D; Figure A 6.4** *Appendix*) for the macrophages and hMSCs seeded on top of these coated stainless-steel strips. Stainless-steel strips with coatings of nBG+P, nBMBG+P and nAABG+P with 150 µg dexamethasone (Dex) loaded per stainless-steel strip, were further evaluated for their potency to modulate osteogenesis. Cellular proliferation of seeded hMSCs on these coatings (**Figure 6.8A**) assessed by Alamar blue assay showed the hMSCs were viable and proliferated on both drug-loaded (Dex) and non-loaded groups in the 14-day culture period of the study. Though no significant change was observed in the proliferation rate till day-7, at end of day-14 non-loaded loaded groups revealed a higher proliferative index (~ 1.25 folds more) than the dexamethasone loaded groups. Biochemical estimation for alkaline phosphatase (ALP) activity (**Figure 6.8Bi**) revealed that the dexamethasone loaded groups exhibited higher ALP activity in comparison to non-loaded groups, where composites [nBMBG+P (Dex) and nAABG+P (Dex)] showed ~ 1.4 folds increased activity than nBG+P (Dex) group at day-14. Similarly, collagen content estimated (**Figure 6.8Bii**) revealed that the dexamethasone loaded groups exhibited higher collagen secretion in comparison to non-loaded groups at day-7 and day-14. Osteogenesis onset is marked by secretion of collagen by osteoblasts on to which apatite nucleates whose crystal growth is regulated by non-collagenous proteins such as osteocalcin, osteopontin and osteocalcin. ALP plays a major role in this mineralization process by acting as a key mineralising enzyme. The relatively slower proliferation index in dexamethasone loaded groups, and increased collagen content and ALP activity affirm the hMSCs seeded on these stainless-steel strips were undergoing osteogenic differentiation. The morphology of the seeded hMSCs were evaluated by staining for F-actin (appearing red) (**Figure 6.8C, Figure A 6.5** *Appendix*), where in nBG+P(Dex) groups cells appeared more spindle shaped and clustered at day-7 and day-14. While in the composite groups [nBMBG+P(Dex) and nAABG+P(Dex)] spread-out morphology was observed indicating well organised cytoskeletal organisation. In nAABG+P (unloaded group, control) and nAABG+P(Dex) group cytoskeletal organisation was more developed with good cell-cell interconnections with more filopodia formation (**Figure 6.8C, Figure A 6.5** *Appendix*). Expression of a key osteogenic marker osteopontin (OPN) was evaluated (appearing green) by immunostaining and dexamethasone loaded groups

showed increased expression observed in the cytoplasm in comparison to non-loaded groups, reiterating the osteogenic commitment, correlating with biochemical estimation results.

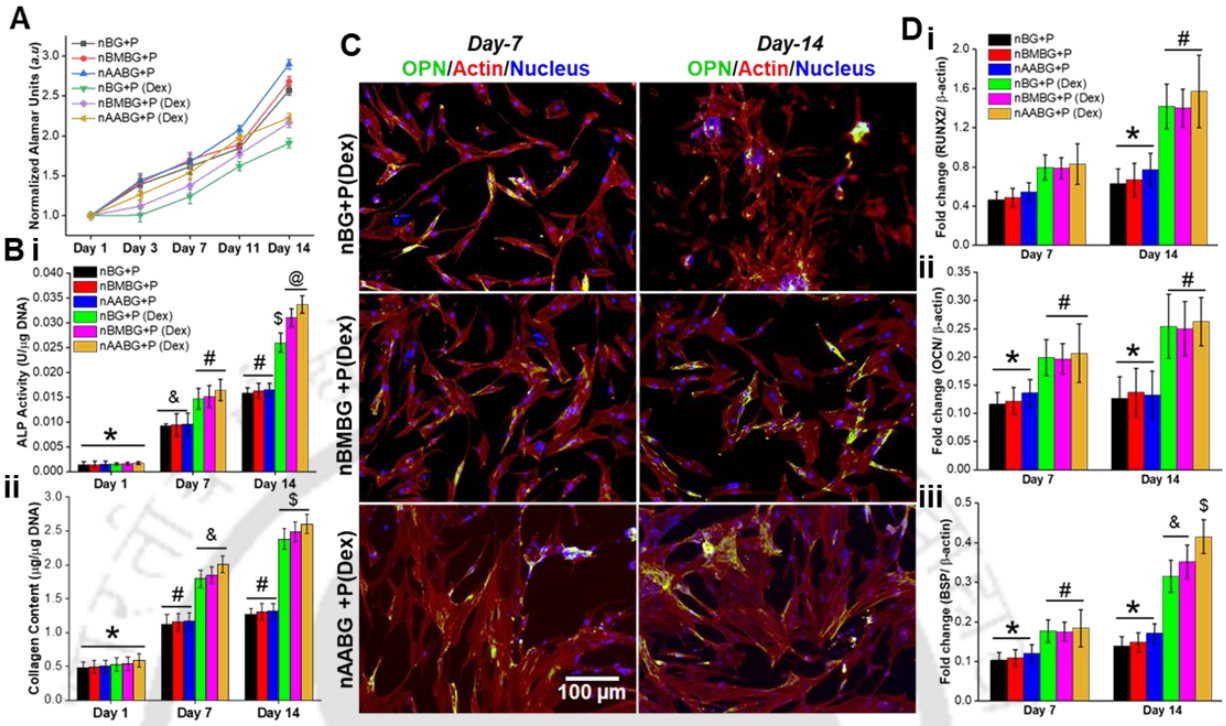

Figure 6.8. ***Assessing the osteogenic potential of hMSCs seeded on to 316L SS discs coated with dexamethasone loaded nanoparticles (+P).*** *A) Cellular proliferation by Alamar Blue assay; Biochemical estimation, i) alkaline phosphatase activity (ALP), ii) Total collagen content; C) Immunostaining to evaluate cellular morphology (red –actin) and presence of osteopontin (OPN); D) Gene expression studies for assessing osteogenic genes, i) runt-related transcription factor (RUNX2), ii) osteocalcin (OCN) and iii) bone sialoprotein (BSP). (Data presented as Mean ± S.D (n=3); *, $, #, &, @ represents statistically significant difference at $p \leq 0.05$, same symbols indicate no significance while different symbols indicate statistical significance between the groups tested; parametric Student's t-test).*

Quantitative expression of key osteogenic genes namely runt-related transcription factor 2 (*RUNX2*), osteocalcin (*OCN*), and bone sialoprotein (*BSP*) (**Figure 6.8D**) were evaluated. *RUNX2*, a master regulatory transcription factor involved in controlling osteogenesis was upregulated in dexamethasone loaded groups (**Figure 6.8Di**) with a ~2 folds increase at day-14 in comparison to non-loaded groups (nBG+P, nBMBG+P, nAABG+P) which maintained similar levels through day-7 and day-14. Similar expression profile was noticed for *OCN* (**Figure 6.8Dii**) with dexamethasone loaded groups exhibiting ~2.2 folds increase at day-14 in comparison to unloaded controls. *BSP* levels (**Figure 6.8Diii**) were upregulated at day-7 (~ 2 folds increase) and day-14 (~2.7 folds increase) in dexamethasone loaded groups in comparison to non-loaded controls. At day-14, nAABG+P(Dex) group

exhibited ~1.3 folds increase in comparison to nBMBG+P(Dex) and ~1.5 folds increase in comparison to nBG+P(Dex) group. The positive influence of dexamethasone loading is clear from these results which has triggered osteogenic differentiation of seeded hMSCs on these coated stainless strips. Dexamethasone, a glucocorticoid enables osteogenic differentiation when it binds with the cytoplasmic glucocorticoid receptor complex (GCR and chaperone proteins HSP90/ FKBP52). This activated ligand-receptor complex shuttles inside the nucleus to activate key transcriptions factors such as RUNX2, glucocorticoid induced leucine zipper (GILZ) which controls osteogenic commitment [77]. Hence, dexamethasone has been explored in numerous bone tissue engineering applications to aid in osteogenic differentiation in different formats such as scaffolds [386], electrospun fibers [409] and even through nanoparticles systems [373]. Conformal coatings through the mesoporous composites reported here also has shown to be able to load and release dexamethasone in a sustained manner, thereby aiding osteogenesis. Additionally, the biomimetic composite coatings [nAABG+P and nAABG+P(Dex)] by virtue of their physical cues (R_a = ~ 50 nm) and chemical cues presented by bioactive glass, RGD tripeptides in *A. assama* silk fibroin, enabled hMSCs in two ways. Firstly, the RGD-tripeptides enabled in forming well spread out morphology, filopodia and secondly with higher expression levels of *BSP* attesting the osteogenic commitment. This could be attributed to the possible activation of integrin linked kinases by Wnt/β-catenin pathway [305, 362]. Thus, conformal coatings capable of delivering osteoinductive molecules while presenting a biomimetic template would favour osteogenic cells migration, adhesion and integration in the peri-implant endosseous space.

6.3.5 *Dexamethasone Loaded Mesoporous Nanocomposites Confer Immunomodulatory Traits to the Coatings*

In addition to osteoinduction, dexamethasone has pleiotropic role in mediating immunomodulation. It has been reported to play a crucial role in acting as an anti-inflammatory corticosteroid by reducing leucocyte recruitment and modulating the surface adhesion molecules such as CD54 and CD 86 [407]. Moreover, dexamethasone favours anti-inflammatory (M2) biasness in macrophages (without compromising their migratory roles) [311, 410] reducing instances of elevated inflammatory phases which is detrimental for implant compliance. When a metal implant is inserted, necrosis of surrounding osseous tissue is prevalent due to preparation of implant bed [374]. Post-implantation, reparative granulation tissue and osseous tissue forms around the implant and in case of well-fixed implants, there is minimal intervening fibrous tissue while in case of unstable implants the degree of fibrous

capsule is far greater leading to aseptic loosening [374]. Inflammatory macrophages are critical in controlling the extent of fibrosis thereby governing the fate of implant patency and survival [408]. In this regard, glucocorticoids have been useful in reducing this abnormal fibrosis by reducing fibroblast proliferation and collagen deposition, while enabling M2 biasness in macrophages in the vicinity of implant space [408]. Hence, the utility of locally releasing dexamethasone is advantageous circumventing systemic administrative drawbacks. Stainless-steel strips coated with dexamethasone loaded mesoporous nanoparticle were evaluated for their ability to influence macrophages (**Figure 6.9**). Inducible nitric oxide synthase (NOS-2) responsible for production of nitric oxide (NO), a key indicator of the status of inflammation was seen to be reduced in dexamethasone loaded groups (**Figure 6.9Ai**). Interleukin-1β, an important inflammatory chemokine was also significantly reduced in dexamethasone loaded groups, indicative of the anti-inflammatory roles of the dexamethasone loaded coatings. Staining the macrophages seeded on these surfaces with CD 68 (a pan macrophage marker, appearing green), alongside either chemokine (C-C motif) receptor-7 (CCR7) (M1 proinflammatory marker, appearing red) or CD 206 (M2 anti-inflammatory marker, appearing red) revealed dexamethasone dependent macrophage biasness (**Figure 6.9Bi, Figure A6.6** *Appendix*). In the non-loaded controls (nBG+P, nBMBG+P, nAABG+P) the CCR7/CD68 population was 55-58%, slightly more prevalent in comparison to CD206/CD68 populations (**Figure 6.9Bii**). However, in case of dexamethasone loaded controls ~ 2 folds decrease in CCR7/CD68 population was noticed with 76-79% CD206/CD68 population prevalence. This clear M2 macrophage biasness in dexamethasone loaded groups were further confirmed by quantitative gene expression studies for inflammatory markers (*TNF-α, IL-6*) and anti-inflammatory marker (*CD 163*) (**Figure 6.9C**). Downregulation of proinflammatory markers, *TNF-α* (**Figure 6.9Ci**), *IL-6* (**Figure 6.9Cii**) and upregulation of anti-inflammatory marker, *CD 163* (**Figure 6.9Ciii**) in dexamethasone loaded groups was noticed in comparison to non-loaded controls, indicating a macrophage biasness attributed to dexamethasone release from the coatings.

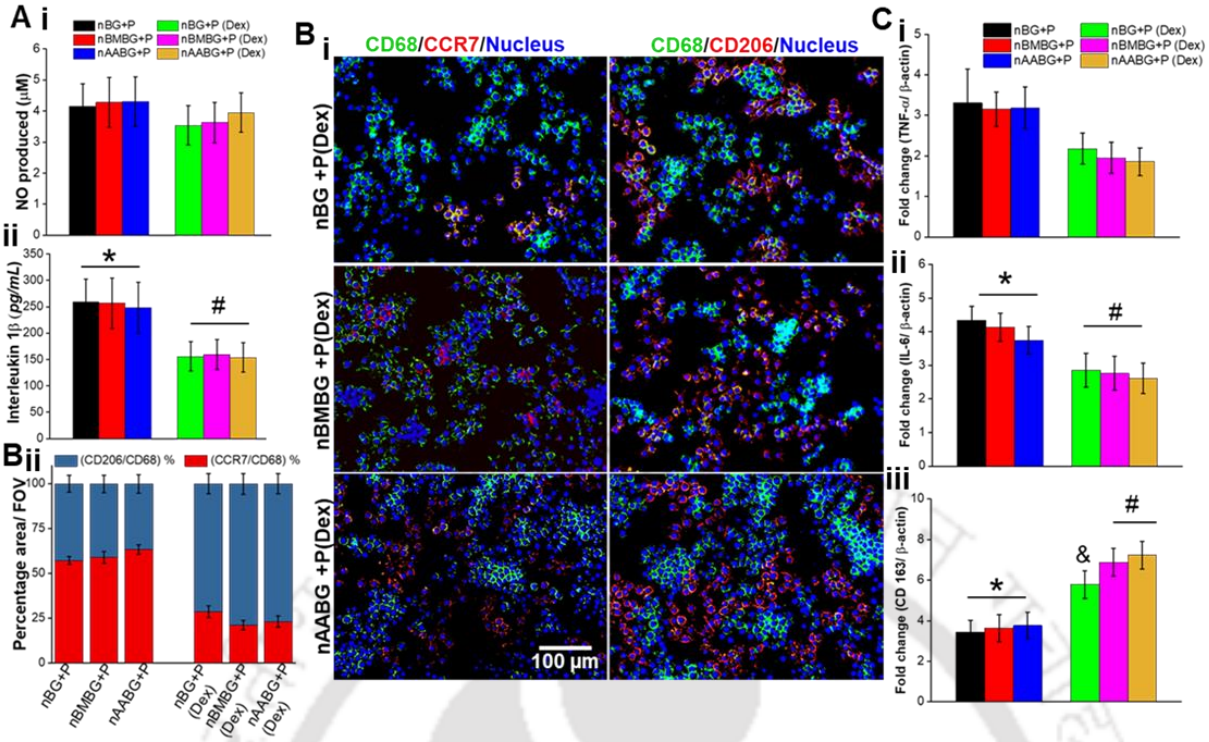

Figure 6.9. ***Assessing the immunomodulatory effect of functionalized 316L SS discs coated with dexamethasone loaded nanoparticles (+P) on PMA treated THP1 monocytes (M0 macrophages).*** *A) Biochemical estimation, i) Nitric oxide estimation n by Greiss assay, ii) Interleukin-1β by ELISA; B) i) Immunostaining to evaluate presence of M1 macrophage marker (CCR7), M2 macrophage marker (CD206) in presence of pan macrophage marker (CD 68); ii) representative image based analysis to quantify distribution of M1, M2 cell population; D) Gene expression studies for assessing immunomodulatory genes, M1 markers i) tumour necrosis factor (TNF-α); ii) interleukin-6 (IL-6) and M2 marker iii) CD 163. (Data presented as Mean ± S.D (n=3); *, #, & represents statistically significant difference at $p \leq 0.05$, same symbols indicate no significance while different symbols indicate statistical significance between the groups tested; parametric Student's t-test).*

Conformal coatings in metal implants have gained interest to act as prophylactic antibacterial strategies to prevent implant related infections [151, 377, 400]. Several strategies have been adopted in this regard which include delivery of antibiotic molecules via encapsulation in a delivery matrix [391, 400], or through direct conjugation or adsorption [370]. Additionally, improving the implant surface by imparting topographical cues to aid in osseointegration is also in practise by chemical/ physical modifications [159, 372, 376, 399]. Despite these critical advancements, a multi-pronged approach to improve sup-optimal efficacy, tuneability of drug release, osseointegrative instability is sought in orthopaedic/dental implant application. In this current work, a mesoporous nano-delivery vehicle was showcased. The utility of this system was in its ease to load antibiotics or osteoinductive molecules in

aiding local delivery while serving as a biomimetic nano-template favouring osteogenic cell or precursor stem cell adhesion. The silk-fibroin used in developing the mesoporous nanocomposites helped in preserving the bioactivity of loaded antibiotics and also served in providing biochemical cues in enabling cell adhesion via presenting RGD tripeptide. These multifunctional facets of the coatings reported here, provide an advantage and incremental advancement to conventional coatings. To overcome drawbacks associated with single antibiotic related bacterial resistance, combinatorial drug release platforms are being explored. For instance, differential coatings on titanium implants *via* direct metal printing and electrospinning where polycaprolactone (PCL)-(vancomycin) and poly(lactic-co-glycolic acid) PLGA-(rifampicin) coatings found to achieve differential release aiding combinatorial delivery of drugs [377]. In this regard, the facile approach of EPD coating reported here enables in obtaining conformal coatings without the need of any sophisticated instruments. EPD also provides an opportunity in creating multi-layered coatings wherein metal implants could be coated with mesoporous composites loaded with dexamethasone, and followed by immersion in another electrolyte bath to be coated with mesoporous composites loaded with antibiotics. The differential release profiles in such multi-layered coatings would enable in releasing fast-acting antibiotics to prevent implant associated infections, while slow sustained dexamethasone release modulate fibrosis and facilitate implant stability via osseointegration. Though positive findings from the current proof-of-concept *in vitro* studies are encouraging, the performance of these coatings under challenging *in vivo* scenarios such as infected wound beds in osteomyelitic models and immunologically dysregulated wound beds in osteoporotic models needs to be investigated.

6.4. Salient Findings of the Chapter

In summary, a facile CTAB based templating method was opted to synthesize mesoporous 70S bioactive glass nanoparticles. The addition of bioactive biopolymer – silk fibroin derived from *B. mori* and *A. assama*, enabled in obtaining biomimetic mesoporous nanocomposites analogous to bone's organo-apatite. The utility of the mesoporous network in these nano-delivery systems helped in loading antibiotic drugs, namely gentamicin and doxycycline with decent encapsulation efficiency while exhibiting fast-acting rapid release profiles. The ease in surface modification with alkylamines (APTES) enabled in loading hydrophobic drug - dexamethasone, while exhibiting slow sustained release. By adopting the facile technique of electrophoretic deposition, conformal coatings of these drug loaded mesoporous coatings on stainless-steel implants were achieved. The antibiotic loaded coatings exhibited antibacterial activity with silk fibroin in nanocomposites preserving the bioactivity of loaded antibiotic. While the dexamethasone loaded coatings conferred pleiotropic functionality by aiding in osteoinduction and favouring M2 macrophage biasness. Thus, these multifunctional coatings hold promise in functionalising metal implants used in dental and bone applications towards reducing implant associated infections and improving osseointegration.

Limitations of the chapter

Though positive findings from the current proof-of-concept *in vitro* studies are encouraging, the performance of these EPD-based coatings under challenging *in vivo* scenarios such as infected wound beds in osteomyelitic models and immunologically dysregulated wound beds in osteoporotic models needs to be investigated. Moreover, EPD based coatings have demonstrated to have weaker coating integrity which could be overcome by switching to electrochemical based coatings.

Summary and Future Perspectives

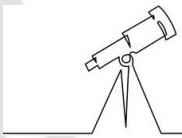

Summary and Future Perspectives

Some of the major concerns related to current generation biomaterial-based intervention for orthopaedic management involve; i) need for resorbale, osteoconductive/ osteoinductive grafts; ii) need for improving graft/ implant patency by osteo-immunoregulation; iii) need for proangiogenic grafts capable of mediating remodelling and iv) prevention of implant associated infections. The thesis identified these key drawbacks and tried to address them through the various approaches discussed in *Objectives* 1 to 5, presented in *Chapters* 2 to 6, progressively. Silk fibroin, served as an ideal biopolymer which enabled in fabricating composites in different formats as required for each pathology/ clinical problem addressed in these *Objectives*. The processing feasibility and innate bioactive properties of mulberry and non-mulberry silk fibroin helped in addressing the problem statements defined in this thesis. Each strategy was devised in a bioinspired manner, where either physical or chemical cues were imparted on to the developed composites to rationalise *cell-instructive* traits in the scaffolding formats investigated in this dissertation work.

In *Objective-1*, electrospun mats made from silk fibroin and sol-derived 70S bioactive presented physical cues and chemical cues which enabled in preserving the chondrogenic/ osteogenic phenotype of seeded chondrocytes/ osteoblasts. The composite mats mimicked the hierarchical complexity and could serve as prospective bilayered grafts for osteochondral lesion management. The favourable outcomes from this objective enabled us in further exploring these two biomaterials (silk fibroin and sol-derived 70S bioactive glass) due to their resorbable nature as resorbable bone grafts. In *Objective*-2, freeze-dried composite scaffolds were fabricated to attest their suitability for volumetric bone defect management. Here, 70S bioactive glass was doped with Cu to attribute proangiogenic traits, wherein Cu enabled in stabilizing the HIF-1α, thereby triggering hypoxia response elements, leading to better vascular ingrowth. The resorbable nature of these composites were also verified in rabbit volumetric femur defects, where after 3 months total resorption of implants with periosteal regeneration was noticed.

Advanced biofabrication strategies such as 3D printing enable us to circumvent drawbacks noticed in conventional scaffold fabrication techniques. For instance, obtaining cellularized grafts with spatial specificity in desired/ requisite format is tedious using conventional f abrication tools. 3D printing, especially micro-extrusion bioprinting

enables to bioprint grafts/ constructs with ease and in a scalable and automated manner. Circumventing the drawbacks of cellularising osteochondral grafts developed in *Objective-1*, bioprinting strategy was adopted to develop cellularized osteochondral interfaces. Silk-based bioinks (cartilage and bone inks) were developed in *Objective-3* which enabled in bioprinting chondrogenically/ osteogenically primed stem cells with good cellular viability. Similar to Cu doping in 70S, here Sr substituting in nano-apatite used in bone ink (SF-PVP-SR1) enabled in attributing osteoinductive and chondroprotective traits to the 3D bioprinted osteochondral grafts. The Sr-doped apatite also demonstrated immunoregulation and regressed osteoclast activity, which is advantageous in scenarios pertaining to osteoporosis.

In *Objective-4*, a combination of conventional and 3D bioprinting strategies was used to recreate the diaphyseal cross-sectional unit. The channelized freeze-dried blend silk fibroin scaffolds aided in compartmentalization of two bone marrow niches; namely (i) endosteal and (ii) vascular niches. This compartmentalization enabled the seeded hematopoietic stem cell survival in the blend (BAC) tissue engineered bone marrow niche (TEBN), recreating the bone marrow space. The outer cortical bone was bioprinted using the bone ink (SF-PVP-SR0). A multimaterial bioprinting strategy was used here, where Fe doped 70S bioactive glass-PCL composite was used to reinforce the bioprinted outer cortical bone shell. The paramagnetic bone cortical shell thus was matured under the magnetic field, where mechanotransduction favoured the osteogenic commitment of encapsulated stem cells within the paramagnetic cortical bone shell. In case of metal implants used as fixtures or prosthesis in orthopaedic reconstruction procedures, implant failure due to infection or aseptic loosening are major contributors for implant failures. These necessitate revision surgeries which compromise the patient's health status. In this regard, a multifunctional interface at the metal implant surface was hypothesised to overcome these clinical problems. In *Objective-5*, mesoporous nanocomposites from silk fibroin and 70S bioactive glass were synthesized and used for coating metal implants by electrophoretic deposition. The conformal coatings enabled in releasing antibiotics or glucocorticoids towards preventing implant associated infection and improving osseointegration of metal implants used in orthopaedic fixtures.

Modern orthopaedic treatment strategies have incrementally grown and has reached a sound technological standard for fracture fixation, regeneration and replacement procedures. However, there are still some unanswered questions surrounding 10-20% of cases relating to non-unions resulting from traumatic/ pathological conditions. [411] Though a cornucopia of

biomaterials is investigated each year for bone tissue engineering (BTE) applications, only a handful of them reach the clinics.

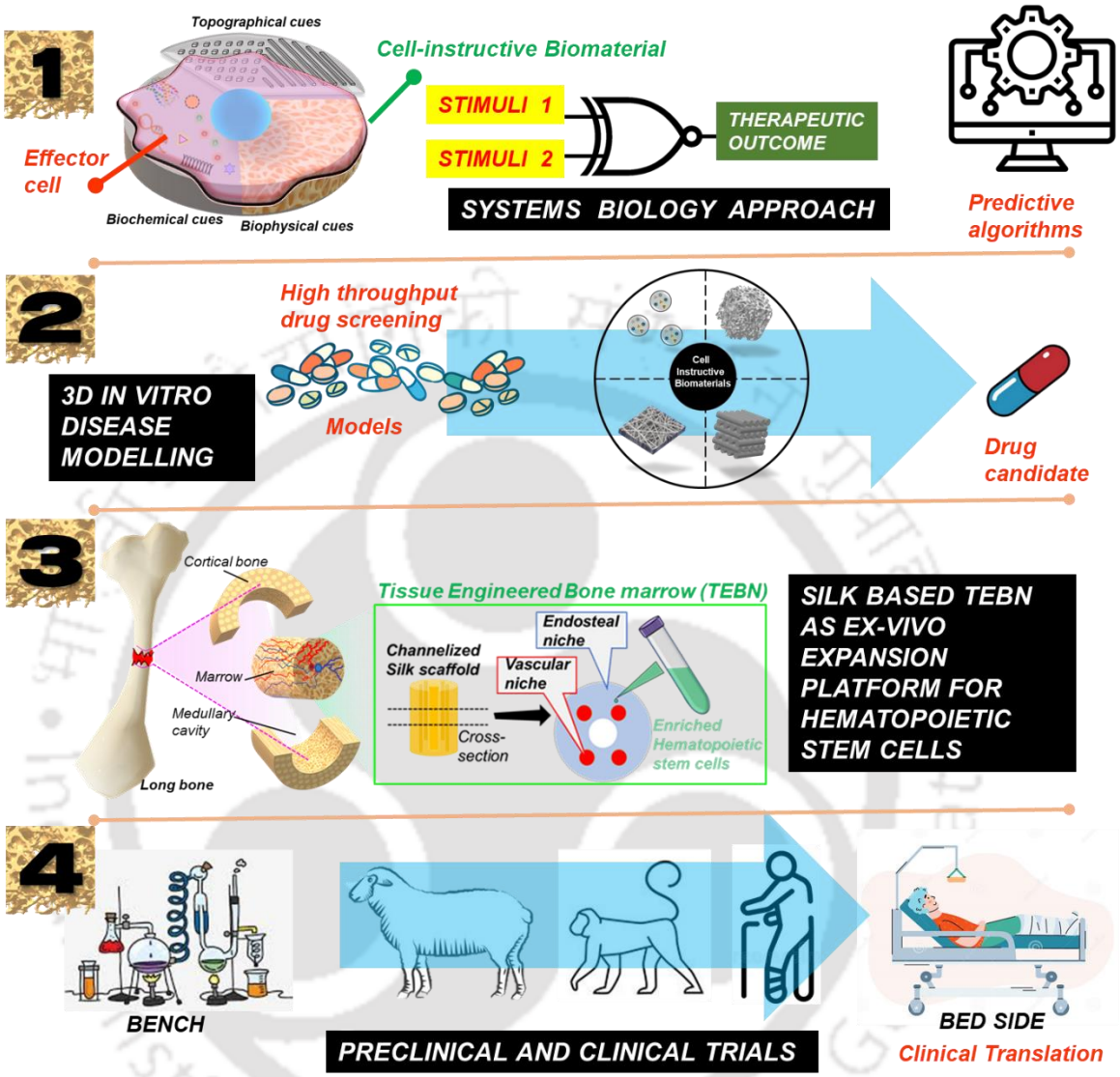

Figure 6.10. ***Four future prospects that emulate from the basis of the outcomes from the dissertation.*** *1. Utilising 'Systems Biology', holisitic understanding of cell-material interaction can be obtained using machine learning, artificial intelligence based predictive algorithms for finetuning the cell-instructive materials that are intended to be developed; 2. The prospect of utilising these biomimetic 3D composites towards 3D in vitro disease modelling and developing high-throughput drug screening platforms; 3. The compartmentalized tissue engineered bone marrow niche (TEBN) hold prospect in developing ex-vivo expansion platforms for hematopoietic stem cells conducive for clinical transfusion; 4. Designing animal preclinical studies in larger vertebrates such as sheep, dogs and pigs whose skeletal growth matches that of humans/ primates is warranted before their clinical translation.*

The roadblocks for the translation of these novel biomaterials are many, but few of them are major contributors. A fundamental understanding of the nature of biomaterials

employed for a purpose in BTE and its underlying effects on cellular behaviour needs to be thoroughly studied. A design hypothesis clearly stating the intended clinical application and the set of validation experiments to prove the same needs to be drawn with the emphasis of regulatory clearance. [19] This cell-material interaction must be holistically studied *in vitro* under stimulated (native like mechanical loading, perfusion) conditions as well as under *in vivo* conditions. In this thesis, each investigation presented tried to adopt these parameters where cell-material interaction was validated through extensive *in vitro* functional validation. However, opting a 'systems biology' route here would enable biomaterial researchers to decipher/ delineate signalling pathways more precisely *in vitro* under controlled environments. This generation of quantitative omics data (generated from genomics, transcriptomics, proteomics and metabolomics) is essential because it portrays a holistic molecular perspective on the studied biomaterial systems (**Figure 6.10** - 1). For instance, most BTE biomaterials studies focus on the osteogenic profile/ commitment of progenitor cells in the developed matrices. This is critical as it establishes whether the material could serve as a suitable osteoinductive/ osteoconductive material or not. However, it is also essential to study the vascularization, immunological aspects of the developed material to have a better idea of its prospective performance when implanted at the defect site. Moreover, multi-omics approach in the recent years have garnered attention. This is achieved by integration of omics data from multiple centres, across labs and across platforms to validate the confidence levels. Though this might seem as laborious and expensive, following such an approach would benefit the scientific community at large, by reducing the repetitive work amongst groups [412]. Ultimately, these steps would help in predicting the clinical outcome and performance by fusing system-level computational modelling (such as physico-chemical models; Bayesian networks; partial least square networks) to omics data for obtaining meaningful details from mechanistic/ molecular pathways. [413]

Prospective biomaterials for BTE are preclinically screened within subcutaneous pockets of small animal models (rodents or rabbits) for studying *in vivo* performance. In *Objective-3,* the biocompatibility or immunocompatibility of bone bioinks was studied in subcutaneous pockets in SD rats. Though it provides preliminary understanding of the biocompatibility and immunocompatibility of the implanted material, it does not reflect the complexities involved in the bone formation seen in long bone or fracture defect site [414]. Orthotopic models are more suitable defect models to predict its clinical outcome. Small animal defect models such as those studied in *Objective-2* also suffers from drawbacks, where they do

not mimic the skeletal growth as noticed in larger vertebrates, with drawbacks such as open epiphyseal growth plates (for a life time in rats), minimal cortical remodelling and minimal ratio of cancellous bone to bone mass [415]. These drawbacks could be circumvented by designing animal clinical studies in larger vertebrates such as sheep, dogs and pigs whose skeletal growth matches that of humans/ primates (**Figure 6.10** - 4). However, the slow bone turnover rate and the added maintenance costs associated with longer study duration, with the ethical concerns greatly hamper such fruitful translation of lab scale prospects to clinics. Moreover, the frequent use of healthy young animals for studies also does not resemble the diseased condition, which is generally associated with comorbidities, compromised immune/ regenerative conditions as a result of old age or pathological condition. Thus, accounting all these factors in clinical settings would be tedious, but it is necessary for fruitful translation of the biomaterial to the clinics. In this thesis work, several interventions were portrayed and were validated *in vitro*. However, these interventions need to be validated in suitable *in vivo* models to gauge its suitability for use in clinics, which serve as future scope of the works presented here.

Another facet that could be explored from this thesis is utilising the composite scaffolds developed here by conventional techniques and bioprinting strategy for 3D *in vitro* human bone or disease models for drug screening applications (**Figure 6.10** – 2-3). Drug discovery pipeline is a very laborious and time-consuming process amounting up to one or two decades of research. The initial process of screening is very vital and crucial step, as it involves identification of biomolecules/ hits for a therapeutic target and scrutinizing it from a large database of available molecules. Among the screening approaches, the two vastly followed approaches are, (i) virtual screening (VS) and (ii) high-throughput screening (HTS) strategies [416]. With the power of computational programs and rapid growth of computational biology, VS strategy has gained huge momentum in the pharma industry for scrutinizing vast libraries of molecules *via* (a) structure based – which rely on molecular docking on proteins (structural information is known) and (b) ligand based – which does not need structural information of proteins (examples include 2D/3D similarity searches, pharmacophore screening and quantitative structure activity relationships QSAR) [417]. VS strategy adopts either a 'hierarchical' route or 'parallel' route for screening. In the former, a vast available library of molecules is screened sequentially for structure/ ligand similarity, followed by pharmacophore matching and docking; while in the latter a parallel screening is put forth rather than sequential route. Thus, a vast library (up to 10^6) is screened and few hundred molecules (potential drug

candidates) could be generated that can be either cherry-picked or screened by HTS strategies. HTS involves testing hundreds of compounds in 96 or 384 or 1536 well formats by various automated assays. The success of an HTS strategy relies on the 'assay design'. Assay designs may include primary scan (less quantitative, but screens vast array of compounds), followed by accurate secondary assays (more quantitative and suited for few hundred promising 'hit' compounds from primary scan). The primary scans take in account only one/ narrow concentration range (say 1-10μM), and may include standard assays such as ELISA (enzyme linked immunosorbent assays), cytotoxicity, reporter/binder assays for expression on 2D cell cultures grown on multi-well plates. ELISA could be designed for a single parameter for pathological protein which is highly expressed or biochemical assays for expression of key regulatory enzymes. Secondary assays may include very comprehensive assays like real time gene expression studies, immunostaining/ flowcytometry of various biomarkers (pathological/ healthy) through high content analysis platforms [418]. Additionally, in secondary assays a wide concentration range (pM to mM) can be screened for a molecule and its effect can be studied. Moreover, multi-parametric ELISA or biochemical assays can also be set up at this stage. However, the success of HTS depends on the model cells; if they cultured in 2D tissue culture multi-well plates, then the results would not recapitulate the disease pathology entirely. Hence the use of miniaturized 3D *in vitro* disease models in such HTS platforms [419] would greatly benefit the screening process, in addition to choosing the right therapeutic targets in downregulating the disease condition [420].

Bibliography

1. Wegst, U.G., et al., *Bioinspired structural materials.* Nature Materials, 2015. 14(1): p. 23-36.
2. Lurie-Luke, E., *Product and technology innovation: What can biomimicry inspire?* Biotechnology Advances, 2014. 32(8): p. 1494-1505.
3. Elefteriou, F., P. Campbell, and Y. Ma, *Control of bone remodeling by the peripheral sympathetic nervous system.* Calcified Tissue International, 2014. 94(1): p. 140-151.
4. Katsamenis, O.L., et al., *Load-bearing in cortical bone microstructure: Selective stiffening and heterogeneous strain distribution at the lamellar level.* Journal of the Mechanical Behavior of Biomedical Materials, 2013. 17: p. 152-165.
5. Reznikov, N., R. Shahar, and S. Weiner, *Bone hierarchical structure in three dimensions.* Acta Biomaterialia, 2014. 10(9): p. 3815-3826.
6. van Hove, R.P., et al., *Osteocyte morphology in human tibiae of different bone pathologies with different bone mineral density — Is there a role for mechanosensing?* Bone, 2009. 45(2): p. 321-329.
7. Taylor, W.R., et al., *Tibio-femoral loading during human gait and stair climbing.* Journal of Orthopaedic Research, 2004. 22(3): p. 625-632.
8. Wu, D., et al., *Matrix-dependent adhesion mediates network responses to physiological stimulation of the osteocyte cell process.* Proceedings of the National Academy of Sciences USA, 2013. 110(29): p. 12096-12101.
9. Minary-Jolandan, M. and M.-F. Yu, *Uncovering nanoscale electromechanical heterogeneity in the subfibrillar structure of collagen fibrils responsible for the piezoelectricity of bone.* ACS Nano, 2009. 3(7): p. 1859-1863.
10. Jacobs, C.R., S. Temiyasathit, and A.B. Castillo, *Osteocyte mechanobiology and pericellular mechanics.* Annual evRiew of Biomedical Engineering, 2010. 12: p. 369-400.
11. Davidson, P.M. and B. Cadot, *Actin on and around the Nucleus.* Trends in Cell Biology, 2020.
12. Huang, C., J. Dai, and X.A. Zhang, *Environmental physical cues determine the lineage specification of mesenchymal stem cells.* Biochimica et Biophysica Acta (BBA)-General Subjects, 2015. 1850(6): p. 1261-1266.
13. Emre, N., R. Coleman, and S. Ding, *A chemical approach to stem cell biology.* Current Opinion in Chemical Biology, 2007. 11(3): p. 252-258.
14. Blomstedt, P., *Orthopedic surgery in ancient Egypt.* Acta Orthopaedica, 2014. 85(6): p. 670-676.
15. Navarro, M., et al., *Biomaterials in orthopaedics.* Journal of the Royal Society Interface, 2008. 5(27): p. 1137-1158.
16. Yu, X., et al., *Biomaterials for bone regenerative engineering.* Advanced Healthcare Materials, 2015. 4(9): p. 1268-1285.
17. Bose, S., M. Roy, and A. Bandyopadhyay, *Recent advances in bone tissue engineering scaffolds.* Trends in Biotechnology, 2012. 30(10): p. 546-554.
18. Stevens, M.M., *Biomaterials for bone tissue engineering.* Materials Today, 2008. 11(5): p. 18-25.

19. Koons, G.L., M. Diba, and A.G. Mikos, *Materials design for bone-tissue engineering.* Nature Reviews Materials, 2020. 5(8): p. 584-603.
20. Guarino, V., et al., *Bio-inspired composite and cell instructive platforms for bone regeneration.* International Materials Reviews, 2012. 57(5): p. 256-275.
21. Montoya, C., et al., *On the road to smart biomaterials for bone research: definitions, concepts, advances, and outlook.* Bone Research, 2021. 9(1): p. 1-16.
22. Hench, L.L., *The story of Bioglass®.* Journal of Materials Science: Materials in Medicine, 2006. 17(11): p. 967-978.
23. Ventre, M. and P.A. Netti, *Engineering cell instructive materials to control cell fate and functions through material cues and surface patterning.* ACS Applied Materials & Interfaces, 2016. 8(24): p. 14896-14908.
24. Ventre, M., F. Causa, and P.A. Netti, *Determinants of cell–material crosstalk at the interface: towards engineering of cell instructive materials.* Journal of the Royal Society Interface, 2012. 9(74): p. 2017-2032.
25. Rahmany, M.B. and M. Van Dyke, *Biomimetic approaches to modulate cellular adhesion in biomaterials: A review.* Acta Biomaterialia, 2013. 9(3): p. 5431-5437.
26. Chen, S., et al., *Tuning surface properties of bone biomaterials to manipulate osteoblastic cell adhesion and the signaling pathways for the enhancement of early osseointegration.* Colloids and Surfaces B: Biointerfaces, 2018. 164: p. 58-69.
27. Anderson, J.M., A. Rodriguez, and D.T. Chang. *Foreign body reaction to biomaterials*. in *Seminars in immunology*. 2008. Elsevier.
28. Sridharan, R., et al., *Biomaterial based modulation of macrophage polarization: a review and suggested design principles.* Materials Today, 2015. 18(6): p. 313-325.
29. Williams, D.F., *On the nature of biomaterials.* Biomaterials, 2009. 30(30): p. 5897-5909.
30. *II - Biomaterials and biomedical materials*, in *Definitions of Biomaterials for the Twenty-First Century*, D. Williams and X. Zhang, Editors. 2019, Elsevier. p. 15-23.
31. Bose, S. and S. Tarafder, *Calcium phosphate ceramic systems in growth factor and drug delivery for bone tissue engineering: A review.* Acta Biomaterialia, 2012. 8(4): p. 1401-1421.
32. Zhang, L. and T.J. Webster, *Nanotechnology and nanomaterials: Promises for improved tissue regeneration.* Nano Today, 2009. 4(1): p. 66-80.
33. Grayson, W.L., et al., *Stromal cells and stem cells in clinical bone regeneration.* Nature reviews. Endocrinology, 2015. 11(3): p. 140-150.
34. Huang, B.J., J.C. Hu, and K.A. Athanasiou, *Cell-based tissue engineering strategies used in the clinical repair of articular cartilage.* Biomaterials, 2016. 98: p. 1-22.
35. Minas, T., et al., *The John Insall Award: a minimum 10-year outcome study of autologous chondrocyte implantation.* Clinical Orthopaedics and Related Research®, 2014. 472(1): p. 41-51.
36. Lee, J., et al., *Current advances in immunomodulatory biomaterials for bone regeneration.* Advanced Healthcare Materials, 2019. 8(4): p. 1801106.
37. Fan, L., et al., *Exosome-functionalized polyetheretherketone-based implant with immunomodulatory property for enhancing osseointegration.* Bioactive Materials, 2021. 6(9): p. 2754-2766.

38. Clatworthy, M. and A. Gross, *Management of bony defects in revision total knee arthroplasty.* The adult knee. Philadelphia: Lippincott Williams & Wilkins, 2003: p. 1455-64.
39. Bosco, R., et al., *Surface engineering for bone implants: a trend from passive to active surfaces.* Coatings, 2012. 2(3): p. 95-119.
40. Franz-Odendaal, T.A., B.K. Hall, and P.E. Witten, *Buried alive: how osteoblasts become osteocytes.* Developmental Dynamics: an official publication of the American Association of Anatomists, 2006. 235(1): p. 176-190.
41. Kuroda, Y., et al., *Clinical application of injectable growth factor for bone regeneration: a systematic review.* Inflammation and Regeneration, 2019. 39(1): p. 1-10.
42. Barnes, G.L., et al., *Growth factor regulation of fracture repair*. Journal of Bone and Mineral Research, 1999. 14(11): p. 1805-1815.
43. Ornitz, D.M. and P.J. Marie, *FGF signaling pathways in endochondral and intramembranous bone development and human genetic disease.* Genes & Development, 2002. 16(12): p. 1446-1465.
44. Einhorn, T.A. and L.C. Gerstenfeld, *Fracture healing: mechanisms and interventions.* Nature Reviews Rheumatology, 2015. 11(1): p. 45-54.
45. Lerner, U.H. and C. Ohlsson, *The WNT system: background and its role in bone.* Journal of Internal Medicine, 2015. 277(6): p. 630-649.
46. Florian, M.C., et al., *A canonical to non-canonical Wnt signalling switch in haematopoietic stem-cell ageing.* Nature, 2013. 503(7476): p. 392-396.
47. Marie, P.J., *Fibroblast growth factor signaling controlling bone formation: An update.* Gene, 2012. 498(1): p. 1-4.
48. Al-Kharobi, H., et al., *The role of the insulin-like growth factor (IGF) axis in osteogenic and odontogenic differentiation.* Cellular and Molecular Life Sciences, 2014. 71(8): p. 1469-1476.
49. Liu, T.M. and E.H. Lee, *Transcriptional regulatory cascades in Runx2-dependent bone development.* Tissue engineering. Part B, Reviews, 2013. 19(3): p. 254-263.
50. Akiyama, H., *Control of chondrogenesis by the transcription factor Sox9.* Modern Rheumatology, 2008. 18(3): p. 213-219.
51. Cheng, A. and P.G. Genever, *SOX9 determines RUNX2 transactivity by directing intracellular degradation.* Journal of Bone and Mineral Research, 2010. 25(12): p. 2680-2689.
52. Midha, S., S. Murab, and S. Ghosh, *Osteogenic signaling on silk-based matrices.* Biomaterials, 2016. 97: p. 133-153.
53. Qin, X., et al., *Runx2 is essential for the transdifferentiation of chondrocytes into osteoblasts.* PLoS Genetics, 2020. 16(11): p. e1009169.
54. Blair, H.C., et al., *Osteoblast differentiation and bone matrix formation in vivo and in vitro.* Tissue Engineering Part B: Reviews, 2017. 23(3): p. 268-280.
55. Lundquist, P., H. Murer, and J. Biber, *Type II Na+-Pi cotransporters in osteoblast mineral formation: regulation by inorganic phosphate.* Cellular Physiology and Biochemistry, 2007. 19(1-4): p. 43-56.

56. Shih, Y.R.V., et al., *Calcium phosphate-bearing matrices induce osteogenic differentiation of stem cells through adenosine signaling.* Proceedings of the National Academy of Sciences USA, 2014. 111(3): p. 990-995.
57. Francis, M.J., et al., *ATPase pumps in osteoclasts and osteoblasts.* The International Journal of Biochemistry & Cell Biology, 2002. 34(5): p. 459-476.
58. Fu, X., et al., *Runx2/Osterix and zinc uptake synergize to orchestrate osteogenic differentiation and citrate containing bone apatite formation.* Advanced Science, 2018. 5(4): p. 1700755.
59. Keinan, D., et al., *Role of regulator of G protein signaling proteins in bone.* Frontiers in Bioscience (Landmark edition), 2014. 19: p. 634.
60. Conklin, B.R., et al., *Engineering GPCR signaling pathways with RASSLs.* Nature Methods, 2008. 5(8): p. 673-678.
61. Atfi, A. and R. Baron, *PTH battles TGF-β in bone.* Nature Cell Biology, 2010. 12(3): p. 205-207.
62. Chang, W., et al., *The extracellular calcium-sensing receptor (CaSR) is a critical modulator of skeletal development.* Science Signaling, 2008. 1(35): p. ra1-ra1.
63. Tan, S., et al., *Deregulation of bone forming cells in bone diseases and anabolic effects of strontium-containing agents and biomaterials.* BioMed Research International, 2014. 2014.
64. Pi, M. and L.D. Quarles, *A novel cation-sensing mechanism in osteoblasts is a molecular target for strontium.* Journal of Bone and Mineral Research, 2004. 19(5): p. 862-869.
65. O'Neill, E., et al., *The roles of ions on bone regeneration.* Drug Discovery Today, 2018. 23(4): p. 879-890.
66. Bose, S., et al., *Understanding of dopant-induced osteogenesis and angiogenesis in calcium phosphate ceramics.* Trends in Biotechnology, 2013. 31(10): p. 594-605.
67. Kulanthaivel, S., et al., *Cobalt doped proangiogenic hydroxyapatite for bone tissue engineering application.* Materials Science and Engineering: C, 2016. 58: p. 648-658.
68. Moses, J.C., et al., *Synergistic effects of silicon/zinc doped brushite and silk scaffolding in augmenting the osteogenic and angiogenic potential of composite biomimetic bone grafts.* ACS Biomaterials Science & Engineering, 2019. 5(3): p. 1462-1475.
69. Zhou, B., et al., *Dimethyloxalyl Glycine Regulates the HIF-1 Signaling Pathway in Mesenchymal Stem Cells.* Stem Cell Reviews and Reports, 2020. 16(4): p. 702-710.
70. Davis, C.K., et al., *Hypoxia mimetic agents for ischemic stroke.* Frontiers in Cell and Developmental Biology, 2019. 6(175).
71. Stegen, S., et al., *HIF-1α metabolically controls collagen synthesis and modification in chondrocytes.* Nature, 2019. 565(7740): p. 511-515.
72. Teng, F. and M. Fussenegger, *Shedding light on extracellular vesicle biogenesis and bioengineering.* Advanced Science, 2021. 8(1): p. 2003505.
73. Yan, H.-C., et al., *The Delivery of Extracellular Vesicles Loaded in Biomaterial Scaffolds for Bone Regeneration.* Frontiers in Bioengineering and Biotechnology, 2020. 8: p. 1015.
74. Kang, M., et al., *Bone regeneration is mediated by macrophage extracellular vesicles.* Bone, 2020. 141: p. 115627.

75. Doherty, G.J. and H.T. McMahon, *Mechanisms of endocytosis.* Annual Review of Biochemistry, 2009. 78: p. 857-902.
76. Monteiro, N., et al., *Liposomes in tissue engineering and regenerative medicine.* Journal of the Royal Society Interface, 2014. 11(101): p. 20140459.
77. Han, L., et al., *The shift in the balance between osteoblastogenesis and adipogenesis of mesenchymal stem cells mediated by glucocorticoid receptor.* Stem Cell Research & Therapy, 2019. 10(1): p. 1-14.
78. Wang, Y., et al., *Small molecules and their controlled release that induce the osteogenic/chondrogenic commitment of stem cells.* Biotechnology Advances, 2015. 33(8): p. 1626-1640.
79. Buxboim, A., I.L. Ivanovska, and D.E. Discher, *Matrix elasticity, cytoskeletal forces and physics of the nucleus: how deeply do cells 'feel'outside and in?* Journal of Cell Science, 2010. 123(3): p. 297-308.
80. Sapir, L. and S. Tzlil. *Talking over the extracellular matrix: How do cells communicate mechanically?* in *Seminars in cell & developmental biology*. 2017. Elsevier.
81. Qin, L., et al., *Molecular mechanosensors in osteocytes.* Bone Research, 2020. 8(1): p. 1-24.
82. Yao, X., R. Peng, and J. Ding, *Cell–material interactions revealed via material techniques of surface patterning.* Advanced materials, 2013. 25(37): p. 5257-5286.
83. Le Saux, G., et al., *Cell–Cell Adhesion-Driven Contact Guidance and Its Effect on Human Mesenchymal Stem Cell Differentiation.* ACS Applied Materials & Interfaces, 2020. 12(20): p. 22399-22409.
84. Nguyen, A.T., S.R. Sathe, and E.K. Yim, *From nano to micro: topographical scale and its impact on cell adhesion, morphology and contact guidance.* Journal of Physics: Condensed Matter, 2016. 28(18): p. 183001.
85. Shen, B., M.K. Delaney, and X. Du, *Inside-out, outside-in, and inside–outside-in: G protein signaling in integrin-mediated cell adhesion, spreading, and retraction.* Current Opinion in Cell Biology, 2012. 24(5): p. 600-606.
86. Yap, A.S., K. Duszyc, and V. Viasnoff, *Mechanosensing and Mechanotransduction at Cell-Cell Junctions.* Cold Spring Harbor Perspectives in Biology, 2018. 10(8): p. a028761.
87. Kwon, R.Y., et al., *Primary cilium-dependent mechanosensing is mediated by adenylyl cyclase 6 and cyclic AMP in bone cells.* The FASEB journal, 2010. 24(8): p. 2859-2868.
88. Aguirre, J.I., et al., *A novel ligand-independent function of the estrogen receptor is essential for osteocyte and osteoblast mechanotransduction.* Journal of Biological Chemistry, 2007. 282(35): p. 25501-25508.
89. Travlos, G.S., *Normal structure, function, and histology of the bone marrow.* Toxicologic Pathology, 2006. 34(5): p. 548-565.
90. Yin, T. and L. Li, *The stem cell niches in bone.* The Journal of Clinical Investigation, 2006. 116(5): p. 1195-1201.
91. Kulkarni, R. and V. Kale, *Physiological cues involved in the regulation of adhesion mechanisms in hematopoietic stem cell fate decision.* Frontiers in Cell and Developmental Biology, 2020. 8(611).

92. Mendelson, A. and P.S. Frenette, *Hematopoietic stem cell niche maintenance during homeostasis and regeneration.* Nature Medicine, 2014. 20(8): p. 833-846.
93. Wei, Q. and P.S. Frenette, *Niches for hematopoietic stem cells and their progeny.* Immunity, 2018. 48(4): p. 632-648.
94. Janowska-Wieczorek, A., et al., *Autocrine/paracrine mechanisms in human hematopoiesis.* Stem Cells, 2001. 19(2): p. 99-107.
95. Spiller, K.L. and T.J. Koh, *Macrophage-based therapeutic strategies in regenerative medicine.* Advanced Drug Delivery Reviews, 2017. 122: p. 74-83.
96. Graney, P., et al., *Macrophages of diverse phenotypes drive vascularization of engineered tissues.* Science Advances, 2020. 6(18): p. eaay6391.
97. Mulholland, B.S., M.R. Forwood, and N.A. Morrison, *Monocyte chemoattractant protein-1 (MCP-1/CCL2) drives activation of bone remodelling and skeletal metastasis.* Current Osteoporosis Reports, 2019. 17(6): p. 538-547.
98. Witherel, C.E., et al., *Macrophage and fibroblast interactions in biomaterial-mediated fibrosis.* Advanced Healthcare Materials, 2019. 8(4): p. 1801451.
99. Jin, S.-S., et al., *A Biomimetic hierarchical nanointerface orchestrates macrophage polarization and mesenchymal stem cell recruitment to promote endogenous bone regeneration.* ACS Nano, 2019. 13(6): p. 6581-6595.
100. Gao, A., et al., *Tuning the surface immunomodulatory functions of polyetheretherketone for enhanced osseointegration.* Biomaterials, 2020. 230: p. 119642.
101. Porter, J.R., T.T. Ruckh, and K.C. Popat, *Bone tissue engineering: a review in bone biomimetics and drug delivery strategies.* Biotechnology Progress, 2009. 25(6): p. 1539-1560.
102. Cui, F.-Z., Y. Li, and J. Ge, *Self-assembly of mineralized collagen composites.* Materials Science and Engineering: R: Reports, 2007. 57(1): p. 1-27.
103. Lin, X., et al., *The Bone Extracellular Matrix in Bone Formation and Regeneration.* Frontiers in Pharmacology, 2020. 11: p. 757.
104. Twardowski, T., et al., *Type I collagen and collagen mimetics as angiogenesis promoting superpolymers.* Current Pharmaceutical Design, 2007. 13(35): p. 3608-3621.
105. Fukuba, S., et al., *Alloplastic bone substitutes for periodontal and bone regeneration in dentistry: Current Status and Prospects.* Materials, 2021. 14(5): p. 1096.
106. Tan, L., et al., *Biodegradable materials for bone repairs: A Review.* Journal of Materials Science & Technology, 2013. 29(6): p. 503-513.
107. Rouse, J.G. and M.E. Van Dyke, *A review of keratin-based biomaterials for biomedical applications.* Materials, 2010. 3(2): p. 999-1014.
108. de Guzman, R.C., et al., *Bone regeneration with BMP-2 delivered from keratose scaffolds.* Biomaterials, 2013. 34(6): p. 1644-1656.
109. Kowalczewski, C.J., et al., *Reduction of ectopic bone growth in critically-sized rat mandible defects by delivery of rhBMP-2 from kerateine biomaterials.* Biomaterials, 2014. 35(10): p. 3220-3228.

110. Bandyopadhyay, A., et al., *Silk: a promising biomaterial opening new vistas towards affordable healthcare solutions.* Journal of the Indian Institute of Science, 2019. 99(3): p. 445-487.
111. Guo, C., et al., *Thermoplastic moulding of regenerated silk.* Nature materials, 2020. 19(1): p. 102-108.
112. Brown, J., et al., *Impact of silk biomaterial structure on proteolysis.* Acta Biomaterialia, 2015. 11: p. 212-221.
113. Melke, J., et al., *Silk fibroin as biomaterial for bone tissue engineering.* Acta Biomaterialia, 2016. 31: p. 1-16.
114. Uebersax, L., et al., *Biocompatibility and osteoconduction of macroporous silk fibroin implants in cortical defects in sheep.* European Journal of Pharmaceutics and Biopharmaceutics, 2013. 85(1): p. 107-118.
115. Fitzpatrick, V., et al., *Functionalized 3D-printed silk-hydroxyapatite scaffolds for enhanced bone regeneration with innervation and vascularization.* Biomaterials, 2021. 276: p. 120995.
116. Cheng, W., et al., *Injectable hydrogel systems with multiple biophysical and biochemical cues for bone regeneration.* Biomaterials Science, 2020. 8(9): p. 2537-2548.
117. Jin, Y., et al., *Bio-inspired mineralization of hydroxyapatite in 3D silk fibroin hydrogel for bone tissue engineering.* Colloids and Surfaces B: Biointerfaces, 2015. 134: p. 339-345.
118. Janani, G., et al., *Insight into silk-based biomaterials: from physicochemical attributes to recent biomedical applications.* ACS Applied Bio Materials, 2019. 2(12): p. 5460-5491.
119. Gupta, P., et al., *Biomimetic, Osteoconductive Non-mulberry Silk Fiber Reinforced Tricomposite Scaffolds for Bone Tissue Engineering.* ACS Applied Materials & Interfaces, 2016. 8(45): p. 30797-30810.
120. Midha, S., et al., *Differential Regulation of Hedgehog and Parathyroid Signaling in Mulberry and Nonmulberry Silk Fibroin Textile Braids.* ACS Biomaterials Science & Engineering, 2018. 4(2): p. 595-607.
121. Midha, S., et al., *Nonmulberry silk braids direct terminal osteocytic differentiation through activation of wnt-signaling.* ACS Biomaterials Science & Engineering, 2017. 3(6): p. 1062-1074.
122. Shi, Q., et al., *The osteogenesis of bacterial cellulose scaffold loaded with bone morphogenetic protein-2.* Biomaterials, 2012. 33(28): p. 6644-6649.
123. Lee, Y.-J., et al., *The effect of thickness of resorbable bacterial cellulose membrane on guided bone regeneration.* Materials, 2017. 10(3): p. 320.
124. Islam, M.M., et al., *Chitosan based bioactive materials in tissue engineering applications-A review.* Bioactive Materials, 2020. 5(1): p. 164-183.
125. Pan, Y., et al., *Enhancement of BMP-2-mediated angiogenesis and osteogenesis by 2-N, 6-O-sulfated chitosan in bone regeneration.* Biomaterials Science, 2018. 6(2): p. 431-439.

126. Büttner, M., et al., *Over-sulfated chondroitin sulfate Derivatives induce osteogenic differentiation of hMSC independent of BMP-2 and TGF-β1 signalling.* Journal of Cellular Physiology, 2013. 228(2): p. 330-340.
127. Shah, R.N., et al., *Supramolecular design of self-assembling nanofibers for cartilage regeneration.* Proceedings of the National Academy of Sciences USA, 2010. 107(8): p. 3293-3298.
128. McKinnon, D.D., et al., *Biophysically Defined and Cytocompatible Covalently Adaptable Networks as Viscoelastic 3D Cell Culture Systems.* Advanced Materials, 2014. 26(6): p. 865-872.
129. Lutolf, M.P., et al., *Repair of bone defects using synthetic mimetics of collagenous extracellular matrices.* Nature Biotechnology, 2003. 21(5): p. 513-518.
130. Malek-Khatabi, A., et al., *In situ bone tissue engineering using gene delivery nanocomplexes.* Acta Biomaterialia, 2020. 108: p. 326-336.
131. Colnot, C., *Skeletal cell fate decisions within periosteum and bone marrow during bone regeneration.* Journal of Bone and Mineral Research, 2009. 24(2): p. 274-282.
132. Li, Y., M.D. Hoffman, and D.S.W. Benoit, *Matrix metalloproteinase (MMP)-degradable tissue engineered periosteum coordinates allograft healing via early stage recruitment and support of host neurovasculature.* Biomaterials, 2021. 268: p. 120535.
133. Clark, A.Y., et al., *Integrin-specific hydrogels modulate transplanted human bone marrow-derived mesenchymal stem cell survival, engraftment, and reparative activities.* Nature Communications, 2020. 11(1): p. 1-14.
134. Jansen, L.E., et al., *A synthetic, three-dimensional bone marrow hydrogel.* bioRxiv, 2018: p. 275842.
135. Palmer, L.C., et al., *Biomimetic Systems for Hydroxyapatite Mineralization Inspired By Bone and Enamel.* Chemical Reviews, 2008. 108(11): p. 4754-4783.
136. Vallet-Regí, M. and D. Arcos, *Biological apatites in bone and teeth.* Biomimetic nanoceramics in clinical use. From Materials to Applications. Cambridge: RSC Publishing, 2008: p. 1-24.
137. Wu, C., et al., *Copper-containing mesoporous bioactive glass scaffolds with multifunctional properties of angiogenesis capacity, osteostimulation and antibacterial activity.* Biomaterials, 2013. 34(2): p. 422-433.
138. Dai, Q., et al., *3D printing Cu-doped bioactive glass composite scaffold promote bone regeneration through activating HIF-1α and TNF-α pathway of hUVECs.* Biomaterials science, 2021.
139. de Laia, A.G.S., et al., *Cobalt-containing bioactive glass mimics vascular endothelial growth factor A and hypoxia inducible factor 1 function.* Journal of Biomedical Materials Research Part A, 2021. 109(7): p. 1051-1064.
140. Weng, L., et al., *Binary Doping of Strontium and Copper Enhancing Osteogenesis and Angiogenesis of Bioactive Glass Nanofibers while Suppressing Osteoclast Activity.* ACS Applied Materials & Interfaces, 2017. 9(29): p. 24484-24496.
141. Moses, J.C., T. Saha, and B.B. Mandal, *Chondroprotective and osteogenic effects of silk-based bioinks in developing 3D bioprinted osteochondral interface.* Bioprinting, 2020. 17: p. e00067.

142. Perez, R.A., K.D. Patel, and H.-W. Kim, *Novel magnetic nanocomposite injectables: calcium phosphate cements impregnated with ultrafine magnetic nanoparticles for bone regeneration.* RSC Advances, 2015. 5(18): p. 13411-13419.
143. Yun, H.-M., et al., *Magnetic nanocomposite scaffolds combined with static magnetic field in the stimulation of osteoblastic differentiation and bone formation.* Biomaterials, 2016. 85: p. 88-98.
144. Son, B., et al., *Physical Stimuli-Induced Chondrogenic Differentiation of Mesenchymal Stem Cells Using Magnetic Nanoparticles.* Advanced Healthcare Materials, 2015. 4(9): p. 1339-1347.
145. Graney, P.L., et al., *In vitro response of macrophages to ceramic scaffolds used for bone regeneration.* Journal of the royal society interface, 2016. 13(120): p. 20160346.
146. Zhao, F., et al., *Promoting in vivo early angiogenesis with sub-micrometer strontium-contained bioactive microspheres through modulating macrophage phenotypes.* Biomaterials, 2018. 178: p. 36-47.
147. Wang, X., et al., *Bioinspired Highly Anisotropic, Ultrastrong and Stiff, and Osteoconductive Mineralized Wood Hydrogel Composites for Bone Repair.* Advanced Functional Materials, 2021. 31(20): p. 2010068.
148. Bai, S., et al., *Bioinspired Mineral–Organic Bone Adhesives for Stable Fracture Fixation and Accelerated Bone Regeneration.* Advanced Functional Materials, 2020. 30(5): p. 1908381.
149. Varga, P., et al., *Investigation of the three-dimensional orientation of mineralized collagen fibrils in human lamellar bone using synchrotron X-ray phase nano-tomography.* Acta Biomaterialia, 2013. 9(9): p. 8118-8127.
150. Delanois, R.E., et al., *Current epidemiology of revision total knee arthroplasty in the United States.* The Journal of Arthroplasty, 2017. 32(9): p. 2663-2668.
151. Mas-Moruno, C., B. Su, and M.J. Dalby, *Multifunctional coatings and nanotopographies: toward cell instructive and antibacterial implants.* Advanced Healthcare Materials, 2019. 8(1): p. 1801103.
152. Lord, M.S., M. Foss, and F. Besenbacher, *Influence of nanoscale surface topography on protein adsorption and cellular response.* Nano Today, 2010. 5(1): p. 66-78.
153. Fiedler, J., et al., *The effect of substrate surface nanotopography on the behavior of multipotnent mesenchymal stromal cells and osteoblasts.* Biomaterials, 2013. 34(35): p. 8851-8859.
154. Fisher, L.E., et al., *Bactericidal activity of biomimetic diamond nanocone surfaces.* Biointerphases, 2016. 11(1): p. 011014.
155. Karazisis, D., et al., *The influence of controlled surface nanotopography on the early biological events of osseointegration.* Acta biomaterialia, 2017. 53: p. 559-571.
156. Valle, J., et al., *Evaluation of surface microtopography engineered by direct laser interference for bacterial anti-biofouling.* Macromolecular Bioscience, 2015. 15(8): p. 1060-1069.
157. Mo, S., et al., *Dimensional-dependent antibacterial behavior on bioactive micro/nano polyetheretherketone (PEEK) arrays.* Chemical Engineering Journal, 2020. 392: p. 123736.

158. Hasan, J., S. Jain, and K. Chatterjee, *Nanoscale topography on black titanium imparts multi-biofunctional properties for orthopedic applications.* Scientific Reports, 2017. 7(1): p. 1-13.
159. Izquierdo-Barba, I., et al., *Nanocolumnar coatings with selective behavior towards osteoblast and Staphylococcus aureus proliferation.* Acta Biomaterialia, 2015. 15: p. 20-28.
160. Greer, A.I., et al., *Nanopatterned titanium implants accelerate bone formation in vivo.* ACS Applied Materials & Interfaces, 2020. 12(30): p. 33541-33549.
161. Alba-Perez, A., et al., *Plasma polymerised nanoscale coatings of controlled thickness for efficient solid-phase presentation of growth factors.* Materials Science and Engineering: C, 2020. 113: p. 110966.
162. Hoyos-Nogués, M., et al., *Regenerating bone via multifunctional coatings: the blending of cell integration and bacterial inhibition properties on the surface of biomaterials*. ACS Applied Materials & Interfaces, 2017. 9(26): p. 21618-21630.
163. Cheng, Z.A., et al., *Nanoscale coatings for ultralow dose BMP-2-driven regeneration of critical-sized bone defects.* Advanced Science, 2019. 6(2): p. 1800361.
164. Zheng, Z., et al., *The "Yin and Yang" of immunomodulatory magnesium-enriched graphene oxide nanoscrolls decorated biomimetic scaffolds in promoting bone regeneration.* Advanced Healthcare Materials, 2021. 10(2): p. 2000631.
165. Wang, Z., et al., *Switching on and off macrophages by a "bridge-burning" coating improves bone-implant integration under osteoporosis*. Advanced Functional Materials, 2021. 31(7): p. 2007408.
166. Bhardwaj, N. and S.C. Kundu, *Electrospinning: A fascinating fiber fabrication technique*. Biotechnology Advances, 2010. 28(3): p. 325-347.
167. Linder, H.R., et al., *Manipulating air-gap electrospinning to create aligned polymer nanofiber-wrapped glass microfibers for cortical bone tissue engineering.* Bioengineering, 2020. 7(4): p. 165.
168. Wu, L., et al., *Hierarchical micro/nanofibrous membranes of sustained releasing VEGF for periosteal regeneration.* Biomaterials, 2020. 227: p. 119555.
169. Zhai, Y., et al., *Spatiotemporal blood vessel specification at the osteogenesis and angiogenesis interface of biomimetic nanofiber-enabled bone tissue engineering.* Biomaterials, 2021. 276: p. 121041.
170. Kolken, H.M., et al., *Rationally designed meta-implants: a combination of auxetic and conventional meta-biomaterials.* Materials Horizons, 2018. 5(1): p. 28-35.
171. Kang, H.-W., et al., *A 3D bioprinting system to produce human-scale tissue constructs with structural integrity*. Nature Biotechnology, 2016. 34(3): p. 312-319.
172. Rodriguez, M.J., et al., *3D freeform printing of silk fibroin.* Acta Biomaterialia, 2018. 71: p. 379-387.
173. Luo, Y., et al., *3D printing of concentrated alginate/gelatin scaffolds with homogeneous nano apatite coating for bone tissue engineering.* Materials & Design, 2018. 146: p. 12-19.
174. Jakus, A.E., et al., *Hyperelastic "bone": A highly versatile, growth factor–free, osteoregenerative, scalable, and surgically friendly biomaterial.* Science Translational Medicine, 2016. 8(358): p. 358ra127-358ra127.

175. Irmak, G.l., T.r.T. Demirtaş, and M.e. Gümüşderelioğlu, *Highly methacrylated gelatin bioink for bone tissue engineering.* ACS Biomaterials Science & Engineering, 2018. 5(2): p. 831-845.
176. Kim, S.H., et al., *Precisely printable and biocompatible silk fibroin bioink for digital light processing 3D printing.* Nature Communications, 2018. 9(1): p. 1-14.
177. Hann, S.Y., et al., *Dual 3D printing for vascularized bone tissue regeneration.* Acta biomaterialia, 2021. 123: p. 263-274.
178. Barui, S., et al., *Microstructure and compression properties of 3D powder printed Ti-6Al-4V scaffolds with designed porosity: Experimental and computational analysis.* Materials Science and Engineering: C, 2017. 70: p. 812-823.
179. Bandyopadhyay, A., I. Mitra, and S. Bose, *3D printing for bone regeneration.* Current Osteoporosis Reports, 2020: p. 1-10.
180. Mehrotra, S., et al., *3D printing/bioprinting based tailoring of in vitro tissue models: Recent advances and challenges.* ACS Applied Bio Materials, 2019. 2(4): p. 1385-1405.
181. Egan, P.F., et al., *Computationally designed lattices with tuned properties for tissue engineering using 3D printing.* PloS One, 2017. 12(8): p. e0182902.
182. Zhao, L., et al., *Bionic design and 3D printing of porous titanium alloy scaffolds for bone tissue repair.* Composites Part B: Engineering, 2019. 162: p. 154-161.
183. Zhang, M., et al., *3D printing of Haversian bone–mimicking scaffolds for multicellular delivery in bone regeneration.* Science Advances, 2020. 6(12): p. eaaz6725.
184. Subbiah, R., et al., *3D Printing of Microgel-Loaded Modular Microcages as Instructive Scaffolds for Tissue Engineering.* Advanced Materials, 2020. 32(36): p. 2001736.
185. Annamalai, R.T., et al., *Harnessing macrophage-mediated degradation of gelatin microspheres for spatiotemporal control of BMP2 release.* Biomaterials, 2018. 161: p. 216-227.
186. Ahlfeld, T., et al., *Design and fabrication of complex scaffolds for bone defect healing: combined 3D plotting of a calcium phosphate cement and a growth factor-loaded hydrogel.* Annals of Biomedical Engineering, 2017. 45(1): p. 224-236.
187. You, D., et al., *4D Printing of Multi-Responsive Membrane for Accelerated In Vivo Bone Healing Via Remote Regulation of Stem Cell Fate.* Advanced Functional Materials, 2021: p. 2103920.
188. Kim, M., Y. Choe, and G. Kim, *Injectable hierarchical micro/nanofibrous collagen-based scaffolds.* Chemical Engineering Journal, 2019. 365: p. 220-230.
189. Langford, T., et al., *4D printing of origami structures for minimally invasive surgeries using functional scaffold.* Applied Sciences, 2021. 11(1): p. 332.
190. Cicciù, M., *Real opportunity for the present and a forward step for the future of bone tissue engineering.* Journal of Craniofacial Surgery, 2017. 28(3): p. 592-593.
191. White, K.A. and R.M. Olabisi, *Spatiotemporal control strategies for bone formation through tissue engineering and regenerative medicine approaches.* Advanced Healthcare Materials, 2019. 8(2): p. 1801044.
192. Hayder, M., et al., *A phosphorus-based dendrimer targets inflammation and osteoclastogenesis in experimental arthritis.* Science Translational Medicine, 2011. 3(81): p. 81ra35-81ra35.

193. Jin, X., et al., *Self-Adaptive Antibacterial porous implants with sustainable responses for infected bone defect therapy.* Advanced Functional Materials, 2019. 29(17): p. 1807915.
194. Li, J., et al., *Balancing bacteria–osteoblast competition through selective physical puncture and biofunctionalization of ZnO/polydopamine/arginine-glycine-aspartic acid-cysteine nanorods.* ACS Nano, 2017. 11(11): p. 11250-11263.
195. Zhao, H., et al., *Antitumor effect by hydroxyapatite nanospheres: Activation of mitochondria-dependent apoptosis and negative regulation of phosphatidylinositol-3-kinase/protein kinase B pathway.* ACS Nano, 2018. 12(8): p. 7838-7854.
196. Keriquel, V., et al., *In situ printing of mesenchymal stromal cells, by laser-assisted bioprinting, for in vivo bone regeneration applications.* Scientific Reports, 2017. 7(1): p. 1-10.
197. Black, C.R.M., et al., *Bone tissue engineering.* Current Molecular Biology Reports, 2015. 1(3): p. 132-140.
198. Rockwood, D.N., et al., *Materials fabrication from Bombyx mori silk fibroin.* Nature Protocols, 2011. 6(10): p. 1612-1631.
199. Kundu, S., et al., *Nonmulberry silk biopolymers.* Biopolymers, 2012. 97(6): p. 455-467.
200. Malay, A.D., et al., *Relationships between physical properties and sequence in silkworm silks.* Scientific Reports, 2016. 6: p. 27573.
201. Mandal, B.B., et al., *High-strength silk protein scaffolds for bone repair.* Proceedings of the National Academy of Sciences USA, 2012. 109(20): p. 7699-7704.
202. Mandal, B.B. and S.C. Kundu, *Osteogenic and adipogenic differentiation of rat bone marrow cells on non-mulberry and mulberry silk gland fibroin 3D scaffolds.* Biomaterials, 2009. 30(28): p. 5019-5030.
203. Mandal, B.B. and S.C. Kundu, *Non-mulberry silk gland fibroin protein 3-D scaffold for enhanced differentiation of human mesenchymal stem cells into osteocytes.* Acta Biomaterialia, 2009. 5(7): p. 2579-2590.
204. Tilocca, A. *Structural models of bioactive glasses from molecular dynamics simulations*. in *Proceedings of the Royal Society of London A: Mathematical, Physical and Engineering Sciences*. 2009. The Royal Society.
205. Kokubo, T. and H. Takadama, *How useful is SBF in predicting in vivo bone bioactivity?* Biomaterials, 2006. 27(15): p. 2907-2915.
206. Montazerian, M. and E. Dutra Zanotto, *History and trends of bioactive glass-ceramics.* Journal of Biomedical Materials Research Part A, 2016.
207. Franks, K., I. Abrahams, and J. Knowles, *Development of soluble glasses for biomedical use Part I: In vitro solubility measurement.* Journal of Materials Science: Materials in Medicine, 2000. 11(10): p. 609-614.
208. Bielby, R.C., et al., *Time-and concentration-dependent effects of dissolution products of 58S sol–gel bioactive glass on proliferation and differentiation of murine and human osteoblasts.* Tissue Engineering, 2004. 10(7-8): p. 1018-1026.
209. Salinas, A.J. and M. Vallet-Regí, *Glasses in bone regeneration: A multiscale issue.* Journal of Non-Crystalline Solids, 2016. 432: p. 9-14.

210. Gunawidjaja, P.N., et al., *Local structures of mesoporous bioactive glasses and their surface alterations in vitro: inferences from solid-state nuclear magnetic resonance.* Phil. Trans. R. Soc. A, 2012. 370(1963): p. 1376-1399.
211. Kurtz, S., et al., *Projections of primary and revision hip and knee arthroplasty in the United States from 2005 to 2030.* J Bone Joint Surg Am, 2007. 89(4): p. 780-5.
212. Pachore, J.A., et al., *ISHKS joint registry: A preliminary report.* Indian Journal of Orthopaedics, 2013. 47(5): p. 505-509.
213. Getgood, A., T. Bhullar, and N. Rushton, *Current concepts in articular cartilage repair.* Orthopaedics and Trauma, 2009. 23(3): p. 189-200.
214. Guettler, J.H., et al., *Osteochondral defects in the human knee influence of defect size on cartilage rim stress and load redistribution to surrounding cartilage.* The American Journal of Sports Medicine, 2004. 32(6): p. 1451-1458.
215. Vijayan, S., et al., *Cartilage repair: a review of Stanmore experience in the treatment of osteochondral defects in the knee with various surgical techniques.* Indian Journal of Orthopaedics, 2010. 44(3): p. 238.
216. Bhardwaj, N., D. Devi, and B.B. Mandal, *Tissue-Engineered Cartilage: The Crossroads of Biomaterials, Cells and Stimulating Factors.* Macromolecular Bioscience, 2015. 15(2): p. 153-182.
217. Mandal, B.B., et al., *Multilayered silk scaffolds for meniscus tissue engineering.* Biomaterials, 2011. 32(2): p. 639-651.
218. Martin, I., et al., *Osteochondral tissue engineering.* Journal of biomechanics, 2007. 40(4): p. 750-765.
219. Panseri, S., et al., *Osteochondral tissue engineering approaches for articular cartilage and subchondral bone regeneration.* Knee Surgery, Sports Traumatology, Arthroscopy, 2012. 20(6): p. 1182-1191.
220. Li, J.J., et al., *A biphasic scaffold based on silk and bioactive ceramic with stratified properties for osteochondral tissue regeneration.* Journal of Materials Chemistry B, 2015. 3(26): p. 5361-5376.
221. Kundu, B., et al., *Silk fibroin biomaterials for tissue regenerations.* Advanced drug delivery reviews, 2013. 65(4): p. 457-470.
222. Singh, Y.P., N. Bhardwaj, and B.B. Mandal, *Potential of agarose/silk fibroin blended hydrogel for in vitro cartilage tissue engineering.* ACS Applied Materials & Interfaces, 2016. 8(33): p. 21236-21249.
223. Bhardwaj, N., et al., *Potential of silk fibroin/chondrocyte constructs of muga silkworm Antheraea assamensis for cartilage tissue engineering.* Journal of Materials Chemistry B, 2016. 4(21): p. 3670-3684.
224. Zhang, F., et al., *Mechanisms and control of silk-based electrospinning.* Biomacromolecules, 2012. 13(3): p. 798-804.
225. Jones, J.R., *Review of bioactive glass: from Hench to hybrids.* Acta Biomaterialia, 2013. 9(1): p. 4457-4486.
226. Li, R., A.E. Clark, and L.L. Hench, *An investigation of bioactive glass powders by sol-gel processing.* Journal of Applied Biomaterials, 1991. 2(4): p. 231-239.

227. Kim, H.W., H.E. Kim, and J.C. Knowles, *Production and Potential of Bioactive Glass Nanofibers as a Next-Generation Biomaterial.* Advanced Functional Materials, 2006. 16(12): p. 1529-1535.
228. Gupta, A., et al., *Molecular architecture of silk fibroin of Indian golden silkmoth, Antheraea assama.* Scientific Reports, 2015. 5.
229. You, R., et al., *Comparison of the in vitro and in vivo degradations of silk fibroin scaffolds from mulberry and nonmulberry silkworms.* Biomedical Materials, 2014. 10(1): p. 015003.
230. Mandal, B.B. and S. Kundu, *A novel method for dissolution and stabilization of non-mulberry silk gland protein fibroin using anionic surfactant sodium dodecyl sulfate.* Biotechnology and Bioengineering, 2008. 99(6): p. 1482-1489.
231. Gil, E.S., et al., *Mechanical improvements to reinforced porous silk scaffolds.* Journal of Biomedical Materials Research Part A, 2011. 99(1): p. 16-28.
232. Gupta, P., et al., *Mimicking form and function of native small diameter vascular conduits using mulberry and non-mulberry patterned silk films.* ACS Applied Materials & Interfaces, 2016.
233. Kaur, T. and A. Thirugnanam, *Tailoring in vitro biological and mechanical properties of polyvinyl alcohol reinforced with threshold carbon nanotube concentration for improved cellular response.* RSC Advances, 2016. 6(46): p. 39982-39992.
234. Rawadi, G., et al., *BMP-2 controls alkaline phosphatase expression and osteoblast mineralization by a Wnt autocrine loop.* Journal of Bone and Mineral Research, 2003. 18(10): p. 1842-1853.
235. Park, S.-H., et al., *Annulus fibrosus tissue engineering using lamellar silk scaffolds.* Journal of Tissue Engineering and Regenerative Medicine, 2012. 6(Suppl 3): p. s24-s33.
236. Prein, C., et al., *Structural and mechanical properties of the proliferative zone of the developing murine growth plate cartilage assessed by atomic force microscopy.* Matrix Biology, 2016. 50: p. 1-15.
237. Schipani, E., et al., *Hypoxia in cartilage: HIF-1α is essential for chondrocyte growth arrest and survival.* Genes & Development, 2001. 15(21): p. 2865-2876.
238. Schrof, S., et al. *Three-dimensional investigation of the relationship between orientation and microelastic properties of mineralized collagen fibrils in human osteonal bone*. in *Ultrasonic Characterization of Bone (ESUCB), 2015 6th European Symposium on*. 2015. IEEE.
239. Peng, C., et al., *Preparation of uniaxially aligned mullite ceramic fibers by electrospinning.* Colloids and Surfaces A: Physicochemical and Engineering Aspects, 2014. 457: p. 1-7.
240. Matrix, E., *Osteoblast and chondrocyte interactions during coculture on scaffolds.* IEEE Engineering in Medicine and Biology Magazine, 2003: p. 28.
241. Oliveira, J.M., et al., *Novel hydroxyapatite/chitosan bilayered scaffold for osteochondral tissue-engineering applications: Scaffold design and its performance when seeded with goat bone marrow stromal cells.* Biomaterials, 2006. 27(36): p. 6123-6137.

242. Angele, P., et al., *Engineering of osteochondral tissue with bone marrow mesenchymal progenitor cells in a derivatized hyaluronan-gelatin composite sponge.* Tissue Engineering, 1999. 5(6): p. 545-553.
243. Hutmacher, D.W., *Scaffolds in tissue engineering bone and cartilage.* Biomaterials, 2000. 21(24): p. 2529-2543.
244. Badami, A.S., et al., *Effect of fiber diameter on spreading, proliferation, and differentiation of osteoblastic cells on electrospun poly(lactic acid) substrates.* Biomaterials, 2006. 27(4): p. 596-606.
245. Pham, Q.P., U. Sharma, and A.G. Mikos, *Electrospun poly(ε-caprolactone) microfiber and multilayer nanofiber/microfiber scaffolds: Characterization of scaffolds and measurement of cellular infiltration.* Biomacromolecules, 2006. 7(10): p. 2796-2805.
246. Salinas, A.J., A.I. Martin, and M. Vallet-Regí, *Bioactivity of three CaO–P2O5–SiO2 sol-gel glasses.* Journal of Biomedical Materials Research, 2002. 61(4): p. 524-532.
247. M. Mukundan, L., et al., *A new synthesis route to high surface area sol gel bioactive glass through alcohol washing: A preliminary study.* Biomatter, 2013. 3(2): p. e24288.
248. Pereira, M.M., et al., *Preparation of bioactive glass-polyvinyl alcohol hybrid foams by the sol-gel method.* Journal of Materials Science: Materials in Medicine, 2005. 16(11): p. 1045-1050.
249. Cacciotti, I., et al., *Sol–gel derived 45S5 bioglass: synthesis, microstructural evolution and thermal behaviour.* Journal of Materials Science: Materials in Medicine, 2012. 23(8): p. 1849-1866.
250. Bhattacharjee, P., et al., *Nanofibrous nonmulberry silk/PVA scaffold for osteoinduction and osseointegration.* Biopolymers, 2015. 103(5): p. 271-284.
251. Peer, P., et al., *The storage stability of polyvinylbutyral solutions from an electrospinnability standpoint.* Polymer Degradation and Stability, 2014. 105: p. 134-139.
252. U.S. Food and Drug Administration (US FDA), *CFR-code of federal regulations title 21.* Current good manufacturing practice for finished pharmaceuticals (http://www.accessdata.fda.gov/scripts/cdrh/cfdocs/cfcfr/cfrsearch.cfm?fr=175.105) (accessed February 2017).
253. Mansur, H.S., R.L. Oréfice, and A.A. Mansur, *Characterization of poly (vinyl alcohol)/poly (ethylene glycol) hydrogels and PVA-derived hybrids by small-angle X-ray scattering and FTIR spectroscopy.* Polymer, 2004. 45(21): p. 7193-7202.
254. Zhou, J., et al., *In vitro and in vivo degradation behavior of aqueous-derived electrospun silk fibroin scaffolds.* Polymer Degradation and Stability, 2010. 95(9): p. 1679-1685.
255. Amiraliyan, N., M. Nouri, and M.H. Kish, *Structural characterization and mechanical properties of electrospun silk fibroin nanofiber mats.* Polymer Science Series A, 2010. 52(4): p. 407-412.
256. Lai, G.-J., et al., *Composite chitosan/silk fibroin nanofibers for modulation of osteogenic differentiation and proliferation of human mesenchymal stem cells.* Carbohydrate Polymers, 2014. 111: p. 288-297.
257. Wang, M., et al., *Mechanical Properties of Electrospun Silk Fibers.* Macromolecules, 2004. 37(18): p. 6856-6864.

258. Arcos, D., D. Greenspan, and M. Vallet-Regí, *A new quantitative method to evaluate the in vitro bioactivity of melt and sol-gel-derived silicate glasses.* Journal of Biomedical Materials Research Part A, 2003. 65(3): p. 344-351.
259. Bielby, R.C., et al., *Time-and concentration-dependent effects of dissolution products of 58S sol-gel bioactive glass on proliferation and differentiation of murine and human osteoblasts.* Tissue Engineering, 2004. 10(7-8): p. 1018-1026.
260. Acharya, C., S.K. Ghosh, and S.C. Kundu, *Silk fibroin film from non-mulberry tropical tasar silkworms: A novel substrate for in vitro fibroblast culture.* Acta Biomaterialia, 2009. 5(1): p. 429-437.
261. Lutolf, M. and J. Hubbell, *Synthetic biomaterials as instructive extracellular microenvironments for morphogenesis in tissue engineering.* Nature Biotechnology, 2005. 23(1): p. 47-55.
262. Shin, H., S. Jo, and A.G. Mikos, *Biomimetic materials for tissue engineering.* Biomaterials, 2003. 24(24): p. 4353-4364.
263. Hersel, U., C. Dahmen, and H. Kessler, *RGD modified polymers: biomaterials for stimulated cell adhesion and beyond.* Biomaterials, 2003. 24(24): p. 4385-4415.
264. Vishwakarma, A., et al., *Engineering Immunomodulatory Biomaterials To Tune the Inflammatory Response.* Trends in biotechnology, 2016. 34(6): p. 470-482.
265. Meinel, L., et al., *The inflammatory responses to silk films in vitro and in vivo.* Biomaterials, 2005. 26(2): p. 147-155.
266. Mandal, B.B., et al., *Laminar silk scaffolds for aligned tissue fabrication.* Macromolecular Bioscience, 2013. 13(1): p. 48-58.
267. Tew, S.R., et al., *Cellular methods in cartilage research: primary human chondrocytes in culture and chondrogenesis in human bone marrow stem cells.* Methods, 2008. 45(1): p. 2-9.
268. Puetzer, J.L., J.N. Petitte, and E.G. Loboa, *Comparative review of growth factors for induction of three-dimensional in vitro chondrogenesis in human mesenchymal stem cells isolated from bone marrow and adipose tissue.* Tissue Engineering Part B: Reviews, 2010. 16(4): p. 435-444.
269. Kundu, B. and S.C. Kundu, *Osteogenesis of human stem cells in silk biomaterial for regenerative therapy.* Progress in polymer science, 2010. 35(9): p. 1116-1127.
270. Xynos, I.D., et al., *Gene-expression profiling of human osteoblasts following treatment with the ionic products of Bioglass® 45S5 dissolution.* Journal of Biomedical Materials Research, 2001. 55(2): p. 151-157.
271. Jiang, J., S.B. Nicoll, and H.H. Lu, *Co-culture of osteoblasts and chondrocytes modulates cellular differentiation in vitro.* Biochemical and Biophysical Research Communications, 2005. 338(2): p. 762-770.
272. Cao, T., K.-H. Ho, and S.-H. Teoh, *Scaffold design and in vitro study of osteochondral coculture in a three-dimensional porous polycaprolactone scaffold fabricated by fused deposition modeling.* Tissue Engineering, 2003. 9(4, Supplement 1): p. 103-112.
273. Ma, Z., et al., *Chondrocyte behaviors on poly-l-lactic acid (PLLA) membranes containing hydroxyl, amide or carboxyl groups.* Biomaterials, 2003. 24(21): p. 3725-3730.

274. LiVecchi, A., R. Tombes, and M. Laberge, *In vitro chondrocyte collagen deposition within porous HDPE: substrate microstructure and wettability effects.* Journal of Biomedical Materials Research, 1994. 28(8): p. 839-850.
275. Loeser, R.F., *Chondrocyte integrin expression and function.* Biorheology, 2000. 37(1, 2): p. 109-116.
276. Gómez-Barrena, E., et al., *Bone fracture healing: Cell therapy in delayed unions and nonunions.* Bone, 2015. 70(Supplement C): p. 93-101.
277. Delloye, C., et al., *Bone allografts: What they can offer and what they cannot.* J Bone Joint Surg Br, 2007. 89(5): p. 574-9.
278. NaPier, Z., et al., *Demineralized Bone Matrix Bone Biology and Clinical Use.* Seminars in Spine Surgery, 2016. 28(4): p. 196-216.
279. Almubarak, S., et al., *Tissue engineering strategies for promoting vascularized bone regeneration.* Bone, 2016. 83: p. 197-209.
280. Roddy, E., et al., *Treatment of critical-sized bone defects: clinical and tissue engineering perspectives.* European Journal of Orthopaedic Surgery & Traumatology, 2017: p. 1-12.
281. Lafage-Proust, M.-H., et al., *Assessment of bone vascularization and its role in bone remodeling.* BoneKEy Rep, 2015. 4.
282. Pacelli, S., et al., *Strategies to develop endogenous stem cell-recruiting bioactive materials for tissue repair and regeneration.* Advanced Drug Delivery Reviews, 2017.
283. Hench, L.L., D.L. Wheeler, and D.C. Greenspan, *Molecular Control of Bioactivity in Sol-Gel Glasses.* Journal of Sol-Gel Science and Technology, 1998. 13(1): p. 245-250.
284. Vallet-Regí, M., A.J. Salinas, and D. Arcos, *Tailoring the structure of bioactive glasses: from the Nanoscale to Macroporous scaffolds.* International Journal of Applied Glass Science, 2016. 7(2): p. 195-205.
285. Vepari, C. and D.L. Kaplan, *Silk as a biomaterial.* Progress in polymer science, 2007. 32(8): p. 991-1007.
286. Konwarh, R., B.K. Bhunia, and B.B. Mandal, *Opportunities and Challenges in Exploring Indian Non-mulberry Silk for Biomedical Applications.* Proceedings of the Indian National Science Academy, 2017. 83(1): p. 85-101.
287. Rahaman, M.N., et al., *Bioactive glass in tissue engineering.* Acta Biomaterialia, 2011. 7(6): p. 2355-2373.
288. Joseph, C.M., et al., *Mimicking Hierarchical Complexity of the Osteochondral Interface Using Electrospun Silk-Bioactive Glass Composites.* ACS Applied Materials & Interfaces, 2017. 9(9): p. 8000-8013.
289. Rockwood, D.N., et al., *Materials fabrication from Bombyx mori silk fibroin.* Nature Protocols, 2011. 6(10): p. 1612-31.
290. Zhang, Y. and M. Zhang, *Synthesis and characterization of macroporous chitosan/calcium phosphate composite scaffolds for tissue engineering.* Journal of Biomedical Materials Research Part A, 2001. 55(3): p. 304-312.
291. Water Environment Federation, and A.P.H. Association, *Standard methods for the examination of water and wastewater.* American Public Health Association (APHA): Washington, DC, USA, 2005.

292. Flecher, X., et al., *Local and systemic activation of the mononuclear phagocyte system in aseptic loosening of total hip arthroplasty.* Journal of clinical immunology, 2009. 29(5): p. 681-690.
293. Sundaram, K., et al., *RANK ligand signaling modulates the matrix metalloproteinase-9 gene expression during osteoclast differentiation.* Experimental cell research, 2007. 313(1): p. 168-178.
294. Naskar, D., et al., *Dual growth factor loaded nonmulberry silk fibroin/carbon nanofiber composite 3D scaffolds for in vitro and in vivo bone regeneration.* Biomaterials, 2017. 136(Supplement C): p. 67-85.
295. Gil, E.S., et al., *Mechanical improvements to reinforced porous silk scaffolds.* Journal of Biomedical Materials Research. Part A, 2011. 99(1): p. 16-28.
296. Wang, H.-Y. and Y.Q. Zhang, *Effect of regeneration of liquid silk fibroin on its structure and characterization.* Soft Matter, 2013. 9(1): p. 138-145.
297. Koutsopoulos, S., *Synthesis and characterization of hydroxyapatite crystals: a review study on the analytical methods.* J Biomed Mater Res, 2002. 62(4): p. 600-12.
298. Gaetke, L.M. and C.K. Chow, *Copper toxicity, oxidative stress, and antioxidant nutrients.* Toxicology, 2003. 189(1): p. 147-163.
299. Reilly, G.C. and A.J. Engler, *Intrinsic extracellular matrix properties regulate stem cell differentiation.* Journal of Biomechanics, 2010. 43(1): p. 55-62.
300. Du, J., et al., *Extracellular matrix stiffness dictates Wnt expression through integrin pathway.* Scientific reports, 2016. 6.
301. Rath, S.N., et al., *Bioactive Copper-Doped Glass Scaffolds Can Stimulate Endothelial Cells in Co-Culture in Combination with Mesenchymal Stem Cells.* PLoS ONE, 2014. 9(12): p. e113319.
302. Petit, I., D. Jin, and S. Rafii, *The SDF-1–CXCR4 signaling pathway: a molecular hub modulating neo-angiogenesis.* Trends in immunology, 2007. 28(7): p. 299-307.
303. Moroni, L., et al., *Biofabrication strategies for 3D in vitro models and regenerative medicine.* Nature Reviews Materials, 2018. 3(5).
304. Ozbolat, I.T., W. Peng, and V. Ozbolat, *Application areas of 3D bioprinting.* Drug Discovery Today, 2016. 21(8): p. 1257-1271.
305. Moses, J.C., S.K. Nandi, and B.B. Mandal, *Multifunctional Cell Instructive Silk-Bioactive Glass Composite Reinforced Scaffolds Toward Osteoinductive, Proangiogenic, and Resorbable Bone Grafts.* Advanced Healthcare Materials, 2018. 7(10): p. 1701418.
306. Zheng, Z., et al., *3D Bioprinting of Self-Standing Silk-Based Bioink.* Advanced Healthcare Materials, 2018. 7(6): p. 1701026.
307. Chawla, S., et al., *Silk-based bioinks for 3D bioprinting.* Advanced Healthcare Materials, 2018. 7(8): p. 1701204.
308. Singh, Y.P., et al., *Hierarchically Structured Seamless Silk Scaffolds for Osteochondral Interface Tissue Engineering.* Journal of Materials Chemistry B, 2018. 6(36): p. 5671-5688.
309. Nukavarapu, S.P. and D.L. Dorcemus, *Osteochondral tissue engineering: current strategies and challenges.* Biotechnology Advances, 2013. 31(5): p. 706-721.

310. Durur-Subasi, I., A. Durur-Karakaya, and O.S. Yildirim, *Osteochondral Lesions of Major Joints.* The Eurasian Journal of Medicine, 2015. 47(2): p. 138-144.
311. Kumar, M., et al., *Immunomodulatory injectable silk hydrogels maintaining functional islets and promoting anti-inflammatory M2 macrophage polarization.* Biomaterials, 2018. 187: p. 1-17.
312. Partlow, B.P., et al., *Highly Tunable Elastomeric Silk Biomaterials.* Advanced Functional Materials, 2014. 24(29): p. 4615-4624.
313. Priya, B.A., et al., *Nickel doped nanohydroxyapatite: vascular endothelial growth factor inducing biomaterial for bone tissue engineering.* RSC Advances, 2015. 5(89): p. 72515-72528.
314. Landino, L.M., et al., *Fluorescein-labeled glutathione to study protein S-glutathionylation.* Analytical biochemistry, 2010. 402(1): p. 102-104.
315. Chomczynski, P. and N. Sacchi, *The single-step method of RNA isolation by acid guanidinium thiocyanate-phenol-chloroform extraction: twenty-something years on.* Nature Protocols, 2006. 1(2): p. 581-5.
316. Pitzler, L., et al., *miR-126-3p promotes matrix-dependent perivascular cell attachment, migration and intercellular interaction.* Stem Cells, 2016. 34(5): p. 1297-1309.
317. Lin, K., et al., *Enhanced osteoporotic bone regeneration by strontium-substituted calcium silicate bioactive ceramics.* Biomaterials, 2013. 34(38): p. 10028-10042.
318. Aimaiti, A., et al., *Low-dose strontium stimulates osteogenesis but high-dose doses cause apoptosis in human adipose-derived stem cells via regulation of the ERK1/2 signaling pathway.* Stem Cell Research & Therapy, 2017. 8(1): p. 282.
319. Wopenka, B. and J.D. Pasteris, *A mineralogical perspective on the apatite in bone.* Materials Science and Engineering: C, 2005. 25(2): p. 131-143.
320. Lebre, F., et al., *The shape and size of hydroxyapatite particles dictate inflammatory responses following implantation.* Scientific Reports, 2017. 7(1): p. 2922.
321. Fulmer, M.T., et al., *Measurements of the solubilities and dissolution rates of several hydroxyapatites.* Biomaterials, 2002. 23(3): p. 751-755.
322. Fan, C. and D.A. Wang, *Effects of Permeability and Living Space on Cell Fate and Neo-Tissue Development in Hydrogel-Based Scaffolds: A Study With Cartilaginous Model.* Macromolecular bioscience, 2015. 15(4): p. 535-545.
323. Weber, L.M., C.G. Lopez, and K.S. Anseth, *Effects of PEG hydrogel crosslinking density on protein diffusion and encapsulated islet survival and function.* Journal of Biomedical Materials Research Part A: An Official Journal of The Society for Biomaterials, The Japanese Society for Biomaterials, and The Australian Society for Biomaterials and the Korean Society for Biomaterials, 2009. 90(3): p. 720-729.
324. Kumar, M., et al., *Immuno-informed 3D silk biomaterials for tailoring biological responses.* ACS Applied Materials & Interfaces, 2016. 8(43): p. 29310-29322.
325. Kesti, M., et al., *Bioprinting complex cartilaginous structures with clinically compliant biomaterials.* Advanced Functional Materials, 2015. 25(48): p. 7406-7417.
326. Kaufman, J.-M., et al., *Efficacy and safety of strontium ranelate in the treatment of osteoporosis in men.* The Journal of Clinical Endocrinology & Metabolism, 2013. 98(2): p. 592-601.

327. Moghaddam, A., et al., *Treatment of atrophic femoral non-unions according to the diamond concept: results of one-and two-step surgical procedure.* Journal of Orthopaedics, 2017. 14(1): p. 123-133.
328. Palombella, S., et al., *Bone marrow-derived cell therapies to heal long-bone nonunions: A systematic review and meta-analysis—which is the best available treatment?* Stem Cells International, 2019. 2019.
329. Zeckey, C., et al., *The aseptic femoral and tibial shaft non-union in healthy patients–an analysis of the health-related quality of life and the socioeconomic outcome.* The Open Orthopaedics Journal, 2011. 5: p. 193.
330. Giannoudis, P.V., T.A. Einhorn, and D. Marsh, *Fracture healing: the diamond concept.* Injury, 2007. 38: p. S3-S6.
331. Wilson, A. and A. Trumpp, *Bone-marrow haematopoietic-stem-cell niches.* Nature Reviews Immunology, 2006. 6(2): p. 93-106.
332. Choi, J.S., B.P. Mahadik, and B.A. Harley, *Engineering the hematopoietic stem cell niche: Frontiers in biomaterial science.* Biotechnology journal, 2015. 10(10): p. 1529-1545.
333. Nelson, M.R. and K. Roy, *Bone-marrow mimicking biomaterial niches for studying hematopoietic stem and progenitor cells.* Journal of Materials Chemistry B, 2016. 4(20): p. 3490-3503.
334. Bello, A.B., H. Park, and S.-H. Lee, *Current approaches in biomaterial-based hematopoietic stem cell niches.* Acta Biomaterialia, 2018. 72: p. 1-15.
335. Bourgine, P.E., et al., *In vitro biomimetic engineering of a human hematopoietic niche with functional properties.* Proceedings of the National Academy of Sciences USA, 2018. 115(25): p. E5688-E5695.
336. Mahadik, B.P., et al., *The use of covalently immobilized stem cell factor to selectively affect hematopoietic stem cell activity within a gelatin hydrogel.* Biomaterials, 2015. 67: p. 297-307.
337. Robinson, S., et al., *Superior ex vivo cord blood expansion following co-culture with bone marrow-derived mesenchymal stem cells.* Bone marrow transplantation, 2006. 37(4): p. 359-366.
338. Mousavi, S.H., et al., *Expansion of human cord blood hematopoietic stem/progenitor cells in three-dimensional Nanoscaffold coated with Fibronectin.* International journal of Hematology-Oncology and Stem Cell Research, 2015. 9(2): p. 72.
339. Cuchiara, M.L., et al., *Covalent immobilization of stem cell factor and stromal derived factor 1α for in vitro culture of hematopoietic progenitor cells.* Acta Biomaterialia, 2013. 9(12): p. 9258-9269.
340. Chua, K.-N., et al., *Functional nanofiber scaffolds with different spacers modulate adhesion and expansion of cryopreserved umbilical cord blood hematopoietic stem/progenitor cells.* Experimental Hematology, 2007. 35(5): p. 771-781.
341. Di Buduo, C.A., et al., *Programmable 3D silk bone marrow niche for platelet generation ex vivo and modeling of megakaryopoiesis pathologies.* Blood, The Journal of the American Society of Hematology, 2015. 125(14): p. 2254-2264.
342. Tozzi, L., et al., *Multi-channel silk sponge mimicking bone marrow vascular niche for platelet production.* Biomaterials, 2018. 178: p. 122-133.

343. Nelson, M.R., et al., *A multi-niche microvascularized human bone marrow (hBM) on-a-chip elucidates key roles of the endosteal niche in hBM physiology.* Biomaterials, 2021. 270: p. 120683.
344. Zhang, M., et al., *3D printing of Haversian bone–mimicking scaffolds for multicellular delivery in bone regeneration.* Science advances, 2020. 6(12).
345. Sears, N., et al., *Fabrication of biomimetic bone grafts with multi-material 3D printing.* Biofabrication, 2017. 9(2): p. 025020.
346. Haeri, M. and M. Haeri, *ImageJ plugin for analysis of porous scaffolds used in tissue engineering.* Journal of Open Research Software, 2015. 3(1).
347. Beeravolu, N., et al., *Isolation and characterization of mesenchymal stromal cells from human umbilical cord and fetal placenta.* JoVE (Journal of Visualized Experiments), 2017(122): p. e55224.
348. Davis, J., S.P. Crampton, and C.C. Hughes, *Isolation of human umbilical vein endothelial cells (HUVEC).* JoVE (Journal of Visualized Experiments), 2007(3): p. e183.
349. Jaatinen, T. and J. Laine, *Isolation of mononuclear cells from human cord blood by Ficoll-Paque density gradient.* Current protocols in stem cell biology, 2007. 1(1): p. 2A. 1.1-2A. 1.4.
350. Yao, C.-L., et al., *A systematic strategy to optimize ex vivo expansion medium for human hematopoietic stem cells derived from umbilical cord blood mononuclear cells.* Experimental Hematology, 2004. 32(8): p. 720-727.
351. Bhunia, B.K. and B.B. Mandal, *Exploring Gelation and Physicochemical Behavior of in Situ Bioresponsive Silk Hydrogels for Disc Degeneration Therapy.* ACS Biomaterials Science & Engineering, 2019. 5(2): p. 870-886.
352. Janani, G. and B.B. Mandal, *Mimicking physiologically relevant hepatocyte zonation using immunomodulatory silk liver extracellular matrix scaffolds toward a bioartificial liver platform.* ACS Applied Materials & Interfaces, 2021. 13(21): p. 24401-24421.
353. Wu, C., et al., *Multifunctional magnetic mesoporous bioactive glass scaffolds with a hierarchical pore structure.* Acta Biomaterialia, 2011. 7(10): p. 3563-3572.
354. Chouhan, D., et al., *Magnetic actuator device assisted modulation of cellular behavior and tuning of drug release on silk platform.* ACS Biomaterials Science & Engineering, 2019. 5(1): p. 92-105.
355. Kawaguchi, H., et al., *A local application of recombinant human fibroblast growth factor 2 for tibial shaft fractures: A randomized, placebo-controlled trial.* Journal of Bone and Mineral Research, 2010. 25(12): p. 2735-2743.
356. Farokhi, M., et al., *Silk fibroin/hydroxyapatite composites for bone tissue engineering.* Biotechnology Advances, 2018. 36(1): p. 68-91.
357. Jansen, L.E., et al., *Mechanics of intact bone marrow.* Journal of the Mechanical Behavior of Biomedical Materials, 2015. 50: p. 299-307.
358. He, N., et al., *Bone marrow vascular niche: home for hematopoietic stem cells.* Bone Marrow Research, 2014. 2014.
359. Kopp, H.-G., et al., *The bone marrow vascular niche: home of HSC differentiation and mobilization.* Physiology, 2005. 20(5): p. 349-356.

360. Gupta, P., et al., *Functionalized silk vascular grafts with decellularized human Wharton's jelly improves remodeling via immunomodulation in rabbit jugular vein.* Advanced Healthcare Materials. n/a(n/a): p. 2100750.
361. Labat-Robert, J., *Cell–matrix interactions, the role of fibronectin and integrins. A survey.* Pathologie Biologie, 2012. 60(1): p. 15-19.
362. Du, J., et al., *Extracellular matrix stiffness dictates Wnt expression through integrin pathway.* Scientific reports, 2016. 6(1): p. 1-12.
363. Sharkey, P.F., et al., *Why are total knee arthroplasties failing today—has anything changed after 10 years?* The Journal of Arthroplasty, 2014. 29(9): p. 1774-1778.
364. Brunstein, C.G., et al., *Alternative donor transplantation after reduced intensity conditioning: results of parallel phase 2 trials using partially HLA-mismatched related bone marrow or unrelated double umbilical cord blood grafts.* Blood, The Journal of the American Society of Hematology, 2011. 118(2): p. 282-288.
365. Rocha, V. and E. Gluckman, *Clinical use of umbilical cord blood hematopoietic stem cells.* Biology of Blood and Marrow Transplantation, 2006. 12(1): p. 34-41.
366. Zhang, J., et al., *The incorporation of 70s bioactive glass to the osteogenic differentiation of murine embryonic stem cells in 3D bioreactors.* Journal of tissue engineering and regenerative medicine, 2009. 3(1): p. 63-71.
367. Peng, J., et al., *Magnetic materials in promoting bone regeneration.* Frontiers in Materials, 2019. 6: p. 268.
368. Chen, J.C. and C.R. Jacobs, *Mechanically induced osteogenic lineage commitment of stem cells.* Stem cell research & therapy, 2013. 4(5): p. 1-10.
369. Sharkey, P.F., et al., *Why are total knee arthroplasties failing today?* Clinical Orthopaedics and Related Research®, 2002. 404: p. 7-13.
370. Hoyos-Nogues, M., et al., *Regenerating bone via multifunctional coatings: the blending of cell integration and bacterial inhibition properties on the surface of biomaterials.* ACS Applied Materials & Interfaces, 2017. 9(26): p. 21618-21630.
371. Keenan, J.R. and A. Veitz-Keenan, *The impact of smoking on failure rates, postoperative infection and marginal bone loss of dental implants.* Evidence-based Dentistry, 2016. 17(1): p. 4.
372. Kwok, C.T., et al., *Characterization and corrosion behavior of hydroxyapatite coatings on Ti6Al4V fabricated by electrophoretic deposition.* Applied Surface Science, 2009. 255(13): p. 6736-6744.
373. Ran, J., et al., *Rational design of a stable, effective, and sustained dexamethasone delivery platform on a titanium implant: An innovative application of metal organic frameworks in bone implants.* Chemical Engineering Journal, 2018. 333: p. 20-33.
374. Athanasou, N., *The pathobiology and pathology of aseptic implant failure.* Bone & joint Research, 2016. 5(5): p. 162-168.
375. Daubert, D.M., et al., *Prevalence and predictive factors for peri-implant disease and implant failure: a cross-sectional analysis.* Journal of Periodontology, 2015. 86(3): p. 337-347.
376. Damiati, L., et al., *Impact of surface topography and coating on osteogenesis and bacterial attachment on titanium implants.* Journal of Tissue Engineering, 2018. 9: p. 2041731418790694.

377. Jahanmard, F., et al., *Bactericidal coating to prevent early and delayed implant-related infections.* Journal of Controlled Release, 2020. 326: p. 38-52.
378. Cheng, X., et al., *Electrophoretic deposition of silk fibroin coatings with pre-defined architecture to facilitate precise control over drug delivery.* Bioactive Materials, 2021. 6(11): p. 4243-4254.
379. Diba, M., et al., *Electrophoretic deposition of graphene-related materials: A review of the fundamentals.* Progress in Materials Science, 2016. 82: p. 83-117.
380. Gupta, N., D. Santhiya, and A. Aditya, *Tailored smart bioactive glass nanoassembly for dual antibiotic in vitro sustained release against osteomyelitis.* Journal of Materials Chemistry B, 2016. 4(47): p. 7605-7619.
381. Somu, P. and S. Paul, *Bio-conjugation of curcumin with self-assembled casein nanostructure via surface loading enhances its bioactivity: An efficient therapeutic system.* Applied Surface Science, 2018. 462: p. 316-329.
382. Duarah, R., et al., *High performance bio-based hyperbranched polyurethane/carbon dot-silver nanocomposite: a rapid self-expandable stent.* Biofabrication, 2016. 8(4): p. 045013.
383. Sroka, Z. and W. Cisowski, *Hydrogen peroxide scavenging, antioxidant and anti-radical activity of some phenolic acids.* Food and Chemical Toxicology, 2003. 41(6): p. 753-758.
384. Román, J., S. Padilla, and M. Vallet-Regí, *Sol−Gel Glasses as Precursors of Bioactive Glass Ceramics.* Chemistry of Materials, 2003. 15(3): p. 798-806.
385. Lammel, A.S., et al., *Controlling silk fibroin particle features for drug delivery.* Biomaterials, 2010. 31(16): p. 4583-4591.
386. Qiu, K., et al., *Electrophoretic deposition of dexamethasone-loaded mesoporous silica nanoparticles onto poly (L-lactic acid)/poly (ε-caprolactone) composite scaffold for bone tissue engineering.* ACS Applied Materials & Interfaces, 2016. 8(6): p. 4137-4148.
387. Wang, Y., et al., *Charge-Reversal APTES-Modified Mesoporous Silica Nanoparticles with High Drug Loading and Release Controllability.* ACS Applied Materials & Interfaces, 2016. 8(27): p. 17166-17175.
388. Kleitz, F., W. Schmidt, and F. Schüth, *Calcination behavior of different surfactant-templated mesostructured silica materials.* Microporous and Mesoporous Materials, 2003. 65(1): p. 1-29.
389. Tanev, P.T. and T.J. Pinnavaia, *Mesoporous silica molecular sieves prepared by ionic and neutral surfactant templating: a comparison of physical properties.* Chemistry of Materials, 1996. 8(8): p. 2068-2079.
390. Schwarz, S., et al., *Adsorption and stability of colloidal silica.* Colloids and Surfaces A: Physicochemical and Engineering Aspects, 2000. 163(1): p. 17-27.
391. Pishbin, F., et al., *Electrophoretic Deposition of Gentamicin-Loaded Bioactive Glass/Chitosan Composite Coatings for Orthopaedic Implants.* ACS Applied Materials & Interfaces, 2014. 6(11): p. 8796-8806.
392. Ristroph, K.D. and R.K. Prud'homme, *Hydrophobic ion pairing: encapsulating small molecules, peptides, and proteins into nanocarriers.* Nanoscale Advances, 2019. 1(11): p. 4207-4237.

393. Matsumoto, A., et al., *Mechanisms of silk fibroin sol− gel transitions.* The Journal of Physical Chemistry B, 2006. 110(43): p. 21630-21638.
394. Rahman, I.A., M. Jafarzadeh, and C.S. Sipaut, *Synthesis of organo-functionalized nanosilica via a co-condensation modification using γ-aminopropyltriethoxysilane (APTES).* Ceramics International, 2009. 35(5): p. 1883-1888.
395. Mehdipour, M. and A. Afshar, *A study of the electrophoretic deposition of bioactive glass–chitosan composite coating.* Ceramics International, 2012. 38(1): p. 471-476.
396. Besra, L. and M. Liu, *A review on fundamentals and applications of electrophoretic deposition (EPD).* Progress in materials science, 2007. 52(1): p. 1-61.
397. Song, J., et al., *Electrophoretic deposition of chitosan coatings modified with gelatin nanospheres to tune the release of antibiotics.* ACS Applied Materials & Interfaces, 2016. 8(22): p. 13785-13792.
398. Mansouri, R., et al., *Osteoblastic heparan sulfate glycosaminoglycans control bone remodeling by regulating Wnt signaling and the crosstalk between bone surface and marrow cells.* Cell Death & Disease, 2017. 8(6): p. e2902-e2902.
399. Oh, I.-H., et al., *Microstructures and bond strengths of plasma-sprayed hydroxyapatite coatings on porous titanium substrates.* Journal of Materials Science: Materials in Medicine, 2005. 16(7): p. 635-640.
400. Farrokhi-Rad, M., A. Fateh, and T. Shahrabi, *Electrophoretic deposition of vancomycin loaded halloysite nanotubes-chitosan nanocomposite coatings.* Surface and Coatings Technology, 2018. 349: p. 144-156.
401. Hall-Stoodley, L., J.W. Costerton, and P. Stoodley, *Bacterial biofilms: from the natural environment to infectious diseases.* Nature Reviews Microbiology, 2004. 2(2): p. 95-108.
402. Athanassiadis, B., P.V. Abbott, and L.J. Walsh, *Mechanisms of staining with demeclocycline and doxycycline root canal medicaments.* European Endodontic Journal, 2018. 3(2): p. 66.
403. Pritchard, E.M., et al., *Physical and chemical aspects of stabilization of compounds in silk.* Biopolymers, 2012. 97(6): p. 479-498.
404. Zimmerli, W., *Clinical presentation and treatment of orthopaedic implant-associated infection.* Journal of Internal Medicine, 2014. 276(2): p. 111-119.
405. Pritchard, E.M., et al., *Antibiotic-releasing silk biomaterials for infection prevention and treatment.* Advanced Functional Materials, 2013. 23(7): p. 854-861.
406. Cheng, X., et al., *Electrodeposited Assembly of Additive-Free Silk Fibroin Coating from Pre-Assembled Nanospheres for Drug Delivery.* ACS Applied Materials & Interfaces, 2020. 12(10): p. 12018-12029.
407. Weaver, J.D., et al., *Controlled release of dexamethasone from organosilicone constructs for local modulation of inflammation in islet transplantation.* Tissue Engineering Part A, 2015. 21(15-16): p. 2250-2261.
408. Farah, S., et al., *Long-term implant fibrosis prevention in rodents and non-human primates using crystallized drug formulations.* Nature Materials, 2019. 18(8): p. 892-904.
409. El-Fiqi, A., J.-H. Kim, and H.-W. Kim, *Osteoinductive Fibrous Scaffolds of Biopolymer/Mesoporous Bioactive Glass Nanocarriers with Excellent Bioactivity and*

Long-Term Delivery of Osteogenic Drug. ACS Applied Materials & Interfaces, 2015. 7(2): p. 1140-1152.

410. Jiang, K., et al., *Local release of dexamethasone from macroporous scaffolds accelerates islet transplant engraftment by promotion of anti-inflammatory M2 macrophages.* Biomaterials, 2017. 114: p. 71-81.
411. Winkler, T., et al., *A review of biomaterials in bone defect healing, remaining shortcomings and future opportunities for bone tissue engineering: The unsolved challenge.* Bone & Joint Research, 2018. 7(3): p. 232-243.
412. Pinu, F.R., et al., *Systems biology and multi-omics integration: viewpoints from the metabolomics research community.* Metabolites, 2019. 9(4): p. 76.
413. Cosgrove, B.D., L.G. Griffith, and D.A. Lauffenburger, *Fusing tissue engineering and systems biology toward fulfilling their promise.* Cellular and Molecular Bioengineering, 2008. 1(1): p. 33-41.
414. Armiento, A.R., et al., *Functional biomaterials for bone regeneration: a lesson in complex biology.* Advanced Functional Materials, 2020. 30(44): p. 1909874.
415. Roseti, L., et al., *Scaffolds for Bone Tissue Engineering: State of the art and new perspectives.* Materials Science and Engineering: C, 2017. 78: p. 1246-1262.
416. Kumar, A. and K.Y.J. Zhang, *Hierarchical virtual screening approaches in small molecule drug discovery.* Methods, 2015. 71: p. 26-37.
417. Melville, J.L., E.K. Burke, and J.D. Hirst, *Machine learning in virtual screening.* Combinatorial Chemistry & High Throughput Screening, 2009. 12(4): p. 332-343.
418. Li, L., et al., *High-throughput imaging: Focusing in on drug discovery in 3D.* Methods, 2016. 96: p. 97-102.
419. Foster, N.C., N.M. Hall, and A.J. El Haj, *Two-dimensional and three-dimensional cartilage model platforms for drug evaluation and high-throughput screening assays.* Tissue Engineering Part B: Reviews, 2021.
420. Liu, J., et al., *Synthesis and high-throughput screening of N-acetyl-β-hexosaminidase inhibitor libraries targeting osteoarthritis.* The Journal of Organic Chemistry, 2004. 69(19): p. 6273-6283.

Appendix

Table A1.1. *Features and limitations of currently used clinical orthopaedic graft materials*

Bone Graft Materials Type	Commercial/ Clinical Product Used Since	Features	Limitations
1. Autologous Bone Grafts	Widespread use since centuries. First documented in modern science literature (Wolff, 1863; Seydel, 1889) (Meeder and Eggers 1994) Iliac crest bone grafts	• 'Gold standard' for bone defect repair, with over 100 years of documented clinical success • No risk of immune rejection • Highest degree of osteoconductivity, graft acceptance, remodelling and vascularization; patient specific	• Donor site morbidity • Limited volume of tissue needed in case of large bone defects • Need for additional surgery for harvest and grafting • Longer operating times (if repeated procedures are warranted)
2. Allogenic Bone Grafts	First documented report by MacEwen (1863) and widespread use for over 100 years (Schmidt 2021)	• Also considered as 'Gold standard', with well documented clinical success • Minimal or negligible of immune rejection if histocompatible • Highest degree of osteoconductivity, osteoinductivity, remodelling and vascularization potential	• Donor site morbidity and limited quantity of donor tissue • Need for additional surgery for harvest and rehabilitation (of donor and recipient) • Risk of disease transmission
3. Xenogenic Bone Grafts			
Direct, unprocessed xenografts	First medical report of use of canine calvarium to soldier's skull (van Meekeren, 1668) (Schmidt 2021) but discontinued in practise now (all xenogenic sources). Replaced by decullarized/ processed xenografts where mineral structure is left intact.	• Hierarchical structure and chemical makeup similar to human bone • Predictable clinical outcome • Preservation of augmented bone volume	• Severe rejection rate due to histo-incompatibility • Risk of disease/ prion transmission • Ethical concerns

Processed xenografts [Bovine source] [Porcine source]	Bio-oss® (Geistlisch Pharmaceutical)	1995	• Predictable clinical outcome • Preservation of augmented bone volume	• Possibility of / prion/ bovine spongiform encephalopathy/ Creutzfeldt–Jakob disease transmission • Variable resorption rate, vascularization onset delay/ absence • Lack of biological cues to help hasten regeneration • Stringent manufacturing procedures need to be maintained; cost incurring
	RESORBA® Xenogenic Bone Graft	2007		
	MinerOSS™ (BioHorizons)	2014		
	Creos™ Xenogain (Nobel Biocare)	2017		
[Equine source]	Osteoplant®, osteOXeon (BiOTECK)	2009 2017	• Risk of transmission of bovine spongiform encephalopathy is averted (in equine source)	
	Bio-Graft™, (Geistlich Pharma AG)			
[Coral exoskeleton source]	Biocoral® (Biocoral Inc.)	1996	• No risk of human/ animal pathogen disease transmission • Bioactive, porous, sturdy • Exhibits osteoclast remodelling • Ethically compliant	• Chemical make-up not similar to bone's composite • Lacks biological cues for rapid regeneration
	CoreBone	2019		
	Coross Coral bone graft (Dental Solution Israel)	2020		
4. Natural Biomaterials Based				
Demineralized bone matrix (allogenic source)	Grafton DBM (Osteotech Inc.)	2005	• Lesser risk of disease transmission • Osseointegrative, osteoinductive (as demineralization exposes BMPs in organic framework), osteoconductive	• Cost of 1 cm^3 DBM exceeds $100 USD, making the reconstructive procedure cost prohibitive • Reduced mechanical stability, mostly used as fillers/ extenders
	Allofuse® (Allosource)	2008 2008		

	Accell TBM® (Isotis/ Integra™ Orthobiologics)	2009	• Favourable handling property (putty, gels, particulates, along with use of carriers)	• Variability in product • White-boxing of disclosure relating to donor source (living/ deceased/ domestic/ international) (Shehadi and Elzein 2017)
	Intergro® DBM (Zimmer)	2015		
	Osteosponge (Bacterin)			
Natural polymer based Extensively used for chondral or osteochondral repair since 1999, augmented with autologous cells (Huang, Hu et al. 2016) in cell therapy	Collagen based: MACI (Verigen/ Vericel)	1999	• Bioactive, excellent scaffolding materials • Highly biocompatible	• Cost-incurring procedures involved in stringent regulatory/ GMP • Biodegradability not controllable • Poor mechanical performance
	INFUSE® Bone graft (Medtronic)	2002		
	DeNovo NT (Zimmer®)	2007		
	Hyaluronic acid based: Hyalograft® C (Anika Therapeutics)	1999 (now withdrawn)		
	Biocart™II (ProChon Biotech)	2011		
	Agarose based: Cartipatch®	2013		
	Chitosan based: BST-CarGel (Piramal Healthcare)	2013		

5. Synthetic Ceramic Based

The class of bone graft biomaterials with widespread use since 1996 (over more than two decades) to 2020, with 87 products approved by US Food and Drug Administration (FDA) – 510k certified (Fukuba, Okada et al. 2021). Few of the class categories are listed below:

Hydroxyapatite (HA) based	Frios Algipore (Friadent GMBH)	2003	• Calcium phosphates (CaPs) such as HA, TCP, BCPs are the widely used ceramics in dental and orthopaedic reconstructive procedures (Bose and Tarafder 2012); because of their versatility in fabrication and ease in manufacturing processes • Chemical composition similar to bone • Bioactive, osteoconductive and osteoinductive	• Slow resorption rates • Brittle (mostly available as filler-based application) • Devoid of biological cues to facilitate vascularization onset and neo-osseous tissue ingrowth
	OsteoGen SBRG (Impladent)	2004		
	BonGros HA (BioAlpha Inc.)	2009		
β-tricalcium phosphate (TCP)	Blue Sky Bio TCP	2000		
	CALC-I-OSS (Ultradent)	2005		
	Medtronic TCP (Medtronic)	2009		
Bicalcium phosphate, BCP (used in formulation with HA and TCP)	MBCP (Biomatlante)	2005		
	BioActys Granules (Graftys)	2009		
	Mastergraft resorbable ceramic (Medtronic)	2009		
Calcium sulphate	$CaSO_4$ (ACE Surgical)	2005	• Most commonly used bone filler (bone cement) in bone defect, barrier in guided bone regeneration (GBR) procedures, periodontitis (Thomas and Puleo 2009) • Easy to incorporate antimicrobial agents to treat bone infections like osteomyelitis	• Rapid resorption leading to time-limited osteoconductive properties • Calcium sulphate alone is not a viable grafting material, leads to structural instability at implant site
	Nanogen (Orthogen)	2011		

Glass-ceramic	Novabone BBG (NovaBone Products) A/W CeraBone ® PerioGlas (NovaBone Products) Inion BioRestore (Inion Oy)	2000 2000 2004 2007	• Bioglass and Apatite-Wollastonite (A/W) glass ceramics ushered in the third- generation biomaterials. • First bone bonding material, bioactive, osteoconductive • Ability of dissolution products of glass to mediate cellular responses	• Low mechanical strength (poor ductility) and fracture toughness • Poor machinability of conventional melt-derived glass-ceramics
6. Synthetic Polymer Based				
Poly- (methyl methacrylate) PMMA	PMMA has been in use in orthopaedic, dental reconstruction for over 60 years, with its use in bone cement for fixtures and total joint replacement procedures to secure the acetabular/ femoral components (Webb and Spencer 2007). Variety of PMMA products are available in different markets since 1960s. Molecular weight of PMMA varies (low/ medium/ high) based on the proprietary brands along with further additives to make it radio-opaque.		• PMMA based cements are preferred for its variable viscosity and ease in handling • Easy to incorporate antibiotics during preparation	• Non resorbable, associated with aseptic loosening of implants • Heat production during setting leading to thermal necrosis of surrounding tissue • Volumetric shrinkage • Bio-inert
Ultra-high molecular weight polyethylene (UHMWPE)	UHMWPE is widely used in manufacturing of hip/ knee/ shoulder prosthesis for over 40 years. (Jin and Chu 2019) In acetabular components (1962) In total hip replacements (1970)		• High impact/ wear resistant • Elastic modulus similar to bone, thus prevents stress-shielding effects	• Non resorbable, bio-inert, needs to be composited with other additives to improve bone bonding • Aseptic loosening/ need for revision surgeries

Poly- (aryl-ether-ketone) PAEKs	PAEKs has been used in manufacture of orthopaedic and spinal implants since 1980s. Two important subtypes include poly-(ether etherketone) – PEEK and poly-(ether ketone ether ketoneketone) -PEKEKK (now discontinued) (Kurtz and Devine 2007)		• High impact/ wear resistant	• Non resorbable, bio-inert, need for bioactive fillers as reinforcements to improve properties
Poly (α-hydroxy esters) This class includes polymers such as: poly-(lactic acid) chiral forms L - PLLA, D – PDLA; poly(lactide-co-glycolide) PLGA; poly-(caprolactone) PCL (Woodruff and Hutmacher 2010)which all have US FDA approval	PLA has been used fixation devices in orthopaedic/ dental applications PLLA-PLGA based - LactoSorb (BioMet Inc.) Arthrex Chondral dart (Arthrex) PLLA based RapidSorb (Synthes)	 1997 2000 2009	• Ease in processing feasibility by variety of fabrication techniques	• Degradation by-products which are acidic • Poor mechanical properties for bone applications • Non resorbable
7. Hybrid or Composites				
Hybrid composites by amalgamating the polymers and	BoneGen-TR (calcium sulphate/ PLLA); Bio-Lok Inc.	2006	• Overcomes the poor mechanical properties of either neat polymer/ ceramic based grafts	• Biodegradability not controllable • High costs associated with graft manufacture

ceramics listed above (which have either FDA/ European Medical Agency (EMA) clearances have resulted in many clinical products (Bicho, Pina et al. 2018; Fukuba, Okada et al. 2021)	PerioGlas Putty (Bioglass/ gelatin); NovaBone Products	2007	• Biocompatible, bioactive, osteoconductive • Third generation biomaterials which has resulted in considerable improvement in clinical patency	
	SynOss (Carbonate apatite/ Collagen-I); Collagen Matrix Inc.	2009		
	Osseofit plug (Collagen-I/β-TCP/PLGA) DSM Biomedical Inc.	2009		
	ReOss Putty (HA/PLGA); Intra-lock	2009		
	Healos (HA/ bovine collagen-I); Depuy Spine	2010		
8. Metallic Implants				
Non-resorbable (permanent implants)	Metals have been in practice in modern medicine for orthopaedic reconstruction since the early 19th century. Various metals such as stainless steel (and its alloys), cobalt (and its alloys), titanium (and its alloys), tantalum and nickel-titanium		• Most commonly used bulk material in screws, fixtures, prosthesis of joints owing to the superior mechanical strength as load-bearing implant (Young's modulus ranging between 55 to 240 GPa) • Superior tensile strength and ductility	• Mismatch between elastic moduli and density between bone and implant results in stress-shielding a major reason for aseptic loosening • Bioinert and failure of osseointegration

	have used in this regard, reviewed thoroughly elsewhere (Andani, Shayesteh Moghaddam et al. 2014)	• Ease in handling, manufacturing processes, sterilization	• Need for revision surgery after few years
Biodegradable metal implants	Resorbable Mg based implants have been in the infancy since early 1900s (Han, Loffredo et al. 2019), but translational hurdles associated with its toxicity, degradation control has restricted its large scale use. Mg (and its alloys) based bone screws are available now (Han, Loffredo et al. 2019), but not extensively used as non-resorbable counter parts.	• Elastic modulus similar to native bone, stress-shielding effects could be averted • Density similar to bone (density of Mg based implants – 1.7-2 g/cm^3; while that of bone 1.8-2.1 g/cm^3; whereas non-resorbable metals, stainless steel – 7.8 g/cm^3; titanium alloys 4.42 g/cm^3) (Tan, Yu et al. 2013)	• Clinical data on long-term patency, performance and toxicity are not well-understood • Controlling the degradation rate *in vivo* is still a major hurdle

References for <u>Table A1.1</u>

Andani, M. T., N. Shayesteh Moghaddam, et al. (2014). "*Metals for bone implants. Part 1. Powder metallurgy and implant rendering.*" Acta Biomaterialia 10(10): 4058-4070.

Bicho, D., S. Pina, et al. (2018). "*Commercial products for osteochondral tissue repair and regeneration.*" Osteochondral Tissue Engineering: 415-428.

Bose, S. and S. Tarafder (2012). "*Calcium phosphate ceramic systems in growth factor and drug delivery for bone tissue engineering: A review.*" Acta Biomaterialia **8**(4): 1401-1421.

Fukuba, S., M. Okada, et al. (2021). "*Alloplastic bone substitutes for periodontal and bone regeneration in dentistry: Current status and prospects.*" Materials 14(5): 1096.

Han, H.S., S. Loffredo, et al. (2019). "*Current status and outlook on the clinical translation of biodegradable metals.*" Materials today 23: 57-71.

Huang, B. J., J. C. Hu, et al. (2016). "*Cell-based tissue engineering strategies used in the clinical repair of articular cartilage.*" Biomaterials 98: 1-22.

Jin, W. and P. K. Chu (2019). *Orthopedic implants*. Encyclopedia of Biomedical Engineering, Elsevier**:** 425-439.

Kurtz, S. M. and J. N. Devine (2007). "*PEEK biomaterials in trauma, orthopedic, and spinal implants.*" Biomaterials 28(32): 4845-4869.

Meeder, P. J. and C. Eggers (1994). "*1. The history of autogenous bone grafting.*" Injury 25: SA2-SA4.

Schmidt, A. H. (2021). "*Autologous bone graft: Is it still the gold standard?*" Injury 52: S18-S22.

Shehadi, J. A. and S. M. Elzein (2017). "*Review of commercially available demineralized bone matrix products for spinal fusions: A selection paradigm.*" Surgical Neurology International **8**: 203-203.

Tan, L., X. Yu, et al. (2013). "*Biodegradable materials for bone repairs: A review.*" Journal of Materials Science & Technology **29**(6): 503-513.

Thomas, M. V. and D. A. Puleo (2009). "*Calcium sulfate: Properties and clinical applications.*" Journal of Biomedical Materials Research Part B: Applied Biomaterials 88(2): 597-610.

Webb, J. and R. Spencer (2007). "*The role of polymethylmethacrylate bone cement in modern orthopaedic surgery.*" The Journal of Bone and Joint Surgery. British volume 89(7): 851-857.

Woodruff, M. A. and D. W. Hutmacher (2010). "*The return of a forgotten polymer—Polycaprolactone in the 21st century.*" Progress in Polymer Science 35(10): 1217-1256.

Table A1.2. *List of recent clinical trials used as bone graft substitutes for orthopaedic and dental reconstruction (assessed from https://www.clinicaltrials.gov/ on Aug 19, 2021)*

Identifier	Study	Intervention/ Treatment	Phase	Sponsor
NCT03008538	Socket preservation using Autogenous Bone Graft versus MPM (mineralized plasmatic matrix)	MPM as alternative for autologous bone grafting in bone graft complications	Completed (Phase -1, Phase 2) Dec, 2017	Cairo University, Egypt
NCT03945864	Antimicrobial synthetic bone grafts	Silver ion doped calcium phosphate based synthetic grafts in chronic osteomyelitis bone defect	Primary completion (Phase 1, 2) Sept, 2020	Eskisehir Osmangazi University Hospital, Turkey
NCT02714829	Clinical study of injectable ceramics bone graft substitute containing rhBMP-2	Injectable calcium phosphate based ceramic gel/ putty with rh-BMP2 for alveolar bone preservation	Completed, April, 2018	BioAlpha Inc. (Excel-OS-inject)
NCT03777735	Human one graft for fixation of osteochondral defects in the knee joint	Use of Shark Screw® grafts as alternative for metal screws conventionally used in osteochondral graft fixation	Ongoing, Estimated completion April, 2022	LKH-Univ.Klinikum Graz, Graz, Austria General Hospital Vienna, Vienna, Austria
NCT03601130	Assessment of HydroxyColl (synthetic) bone graft substitute in high tibial osteotomy wedge grafting	Synthetic bone graft substitute for osteoarthritic knee graft substitutes	Ongoing, April 29, 2020	SurgaColl Technologies Limited Basingstoke & North Hampshire Hospital, United Kingdom
NCT02613663	Immediate implant using "Nanobone" versus "Autogenous Bone" for	Synthetic NanoBone for tooth restoration	Completed, May 2018	Faculty of Oral and Dental

	treatment of patients with unrestorable single tooth			Medicine. Cairo University, Egypt
NCT01911819	A comparison of bone formation with three different bone graft materials following sinus graft	Use of synthetic bone grafts (calcium phosphate based) Equimatrix, OSSIF-i and Bio-oss for restoring inadequate height maxillary posterior defects	Completed, June 2016	Loma Linda University School of Dentistry, California, USA
NCT01728844	GUIDOR® growth factor enhanced bone graft substitute for the treatment of periodontal defects 6-months post-surgery	Recombinant human basic fibroblast growth factor (rh-bFGF) encapsulated β-tricalcium phosphate based synthetic grafts for alveolar bone loss	Completed, Aug 2020	Sunstar Americas University of Alabama at Birmingham, Birmingham, Alabama, USA University of Michigan, Ann Arbor, Michigan, USA
NCT01771302	Efficiency of PRGF-Endoret in combination with a bone graft in lateral sinus floor elevation	Synthetic bone calcium phosphate-based graft (Bio-Oss) in conjunction with plasma rich in growth factors (PRGF-Endoret) for sinus floor augmentation	Completed, Jan 2015	Fundación Eduardo Anitua Clinica Eduardo Anitua, Spain
NCT02879149	Long-term safety and effectiveness of AUGMENT® bone graft compared to autologous bone graft	Synthetic bone graft with platelet derived growth factor (PDDGF-BB) for ankle/ hindfoot arhtrodesis	Ongoing, Jan 2018	BioMimetic Therapeutics Tucson Orthopedic Institute, Tucson, Arizona, USA
NCT04960722	OIF/β-TCP in patients with open tibial fractures in need of bone grafting	Osteoinductive factor (OIF) in combination with β-TCP	Not yet recruiting,	BioGend Therapeutics Co.Ltd

		synthetic grafts for tibial fractures and non-unions	Primary completion expected by July 2023	
NCT03166917	Clinical application of personal designed 3D printing implants in bone defect restoration	Use of 3D printing approach for prosthetic device	Recruiting, Primary completion expected by Aug, 2021	Shenzhen Hospital of Southern Medical University, Shenzhen, China
NCT02531100	BonyPid-500TM bone graft substitute study	Synthetic bone graft substitute with antibiotic doxycycline for peri-implantitis	Completed, June 2018	PolyPid Ltd. Rambam Health Care Campus, Haifa, Israel
NCT04693559	Assessment of nanocrystalline hydroxyapatite versus autogenous bone grafts: A comparative clinical study in alveolar cleft grafting	Synthetic nanomaterial as secondary alveolar bone graft	Not yet recruiting, Primary completion expected by March, 2023	Assiut University, Egypt
NCT03265795	Validity of PEEK PSI containing autogenous bone graft for maxillary reconstruction following lesion enucleation	Patient specific implants (PSI) designed by rapid prototyping for reconstructing defects as a result of surgical removal of large maxillary cysts	Not yet recruiting	Cairo University, Egypt
NCT04297813	Efficacy in alveolar bone regeneration with autologous MSCs and biomaterial in comparison to autologous bone grafting	Advanced medicinal Therapy (MSC combined with biomaterial) for bone grafting	Recruiting, Primary completion by Aug 2022	University of Bergen, Norway

NCT02910232	In vivo clinical trial of porous starch – hydroxyapatite composite biomaterials for bone regeneration	Biomimetic bone fillers for open fractures of foot	Completed, Jan 2016	Biomedical Materials and Ceramic Industrial Research Unit, Chiang Mai, Thailand
NCT02751125	Reconstruction of jaw bone using mesenchymal stem cells	Bicalcium phosphate with autologous MSCs to treat bone atrophy	Completed, March 2020	Institute of Clinical Dentistry, University of Bergen, Norway
NCT04069923	OsteoCrete in filling bone voids in participants with bone voids or defects	Use of magnesium-based bone void fillers	Recruiting, Primary completion Sept 2022	UCLA / Jonsson Comprehensive Cancer Center, Los Angeles, California, USA
NCT02375750	Treatment of peri-implantitis lesions by using biomaterial	Use of Geistlich Bio-Oss® and Geistlich Bio-Gide® (calcium phosphate-based) biomaterials for bony peri-implant defects	Completed, April 2017	Kristianstad University, Department of Health Sciences, Kristianstad, Sweden
NCT03103295	3D tissue engineered bone equivalent for treatment of traumatic bone defects	Tissue-engineered bone-like construct transplantation with autologous MSCs	Ongoing, First completion Dec 2018	A.A. PARTNERS (Medical company ilaya®), Kiev, Ukraine
NCT04998058	Autogenous mesenchymal stem cell culture-derived signalling molecules as enhancers of bone formation in bone grafting	Synthetic bone graft substitutes with MSC derived exosomes for maxillary sinus floor elevation	Not yet recruiting, Primary completion Sept 2023	Pontificia Universidade Católica do Rio Grande do Sul, Porto Alegre, Brazil
NCT03166917	Clinical application of personal designed 3D printing implants in bone defect restoration	3D printed constructs as internal prosthetic devices	Recruiting, Primary completion Aug 2021	Shenzhen Hospital of Southern Medical University, Shenzhen, China

NCT03185286	3D-printed personalized metal implant in surgical treatment of ankle bone defects	Use of titanium alloy for 3D printing personalized prosthetics	Recruiting, Primary completion Dec 2019	Southwest Hospital, Chongqing, China
NCT03057223	Three-Dimensional printing of patient-specific titanium plates in jaw surgery: a pilot study	Use of 3D printed titanium plates for mandibular neoplasms	Completed, April 2021	The University of Hong Kong

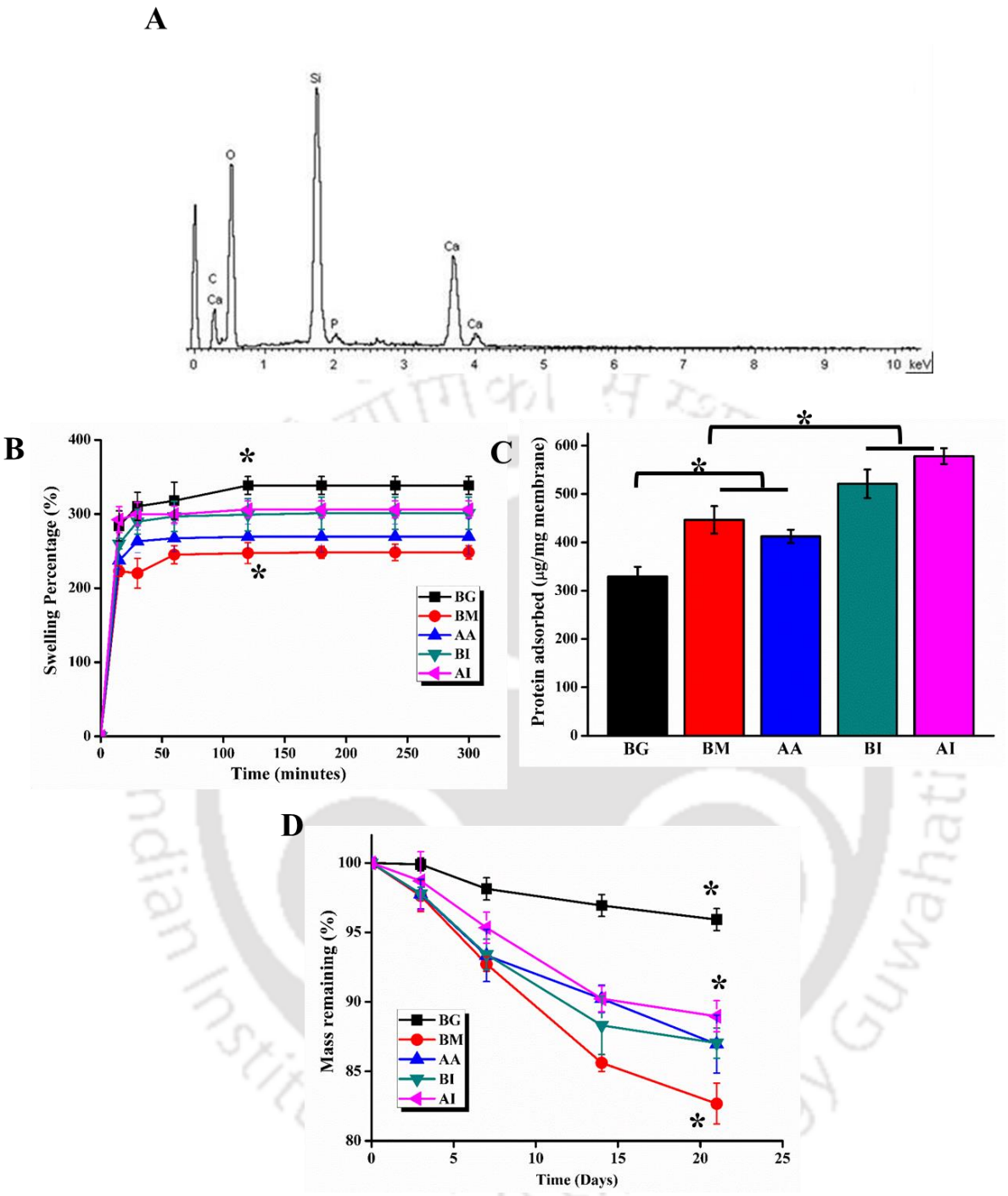

Figure A2.1. *A) Energy dispersive spectra (EDX) spectra for BG mats, showing 70:25:5 ratio of 70S bioglass used in the study; B) Swelling profile C) Protein adsorption profile and D) In vitro degradation profile of electrospun mats; (* represents statistically significant difference ($p \leq 0.05$).*

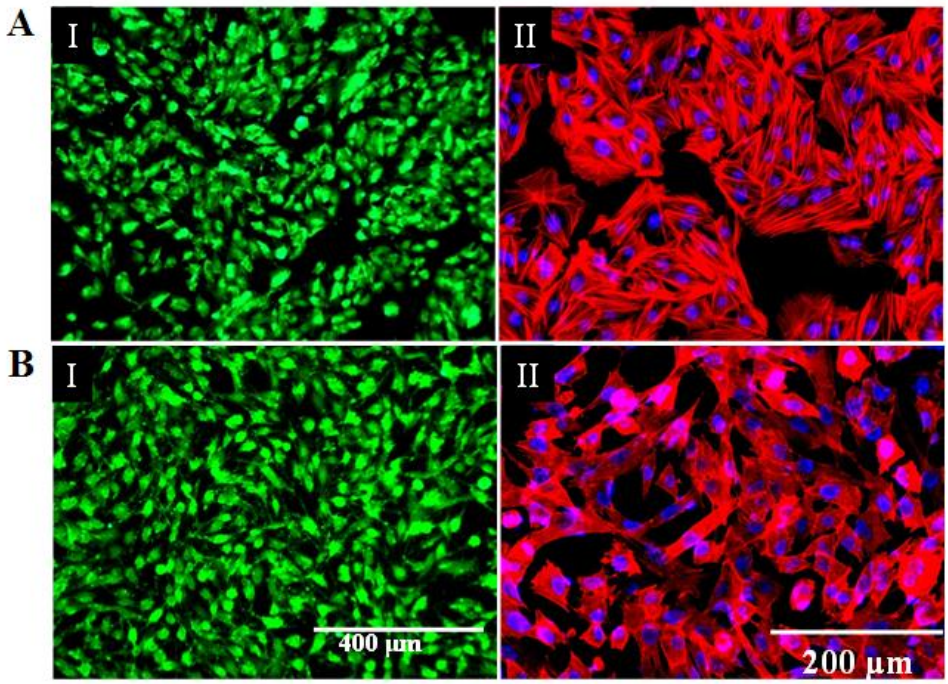

Figure A2.2. *Cells cultured in tissue culture plate (TCP); I) live/dead staining and II) rhodamine phalloidin stained actin and Hoechst-3342 stained nuclei of A) porcine primary chondrocytes and B) MG63 osteoblast like cells.*

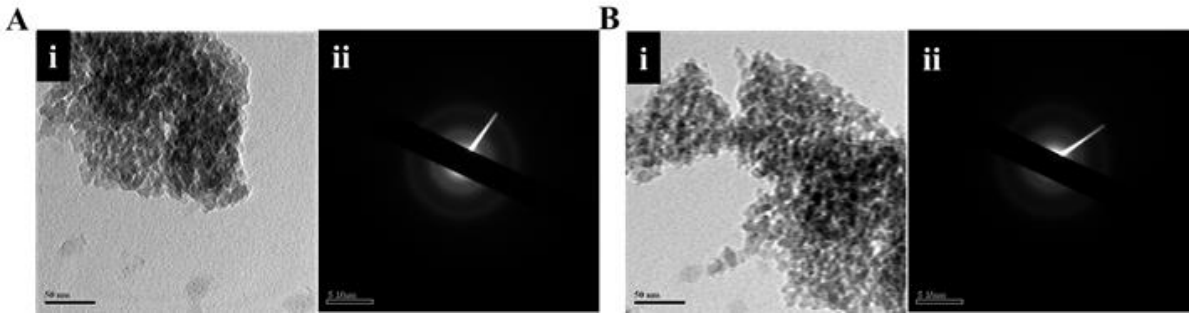

Figure A3.1. *Nanogranular and amorphous nature of copper doped 70S bioactive glass nanogranules formed over A) Bombyx mori silk microfiber and B) Antheraea assama silk microfibers, examined through i) transmission electron micrographs, ii) selected area energy diffraction patterns showing diffuse rings indicating amorphousness*

Table A3.1 *Extent of copper release determined by atomic absorption spectrometry, with measured release (ppm) and cumulative release percentage (%) presented below*

Sample	Experimental Ratio of CuO (mg/ 600 mg of silk matrix used)	Copper Release in Day-7		Copper Release in Day-14		Copper Release in Day-21	
		(ppm)	(%)	(ppm)	(%)	(ppm)	(%)
		In PBS (without protease)					
BMG	36	0.967	2.68	0.371	3.71	0.061	3.87
AAG	36	0.661	1.84	0.231	2.48	0.051	2.62
		In PBS (with protease)					
BMG	36	20.256	56.26	13.319	93.26	1.21	96.62
AAG	36	18.004	50.01	5.54	65.39	0.61	67.08

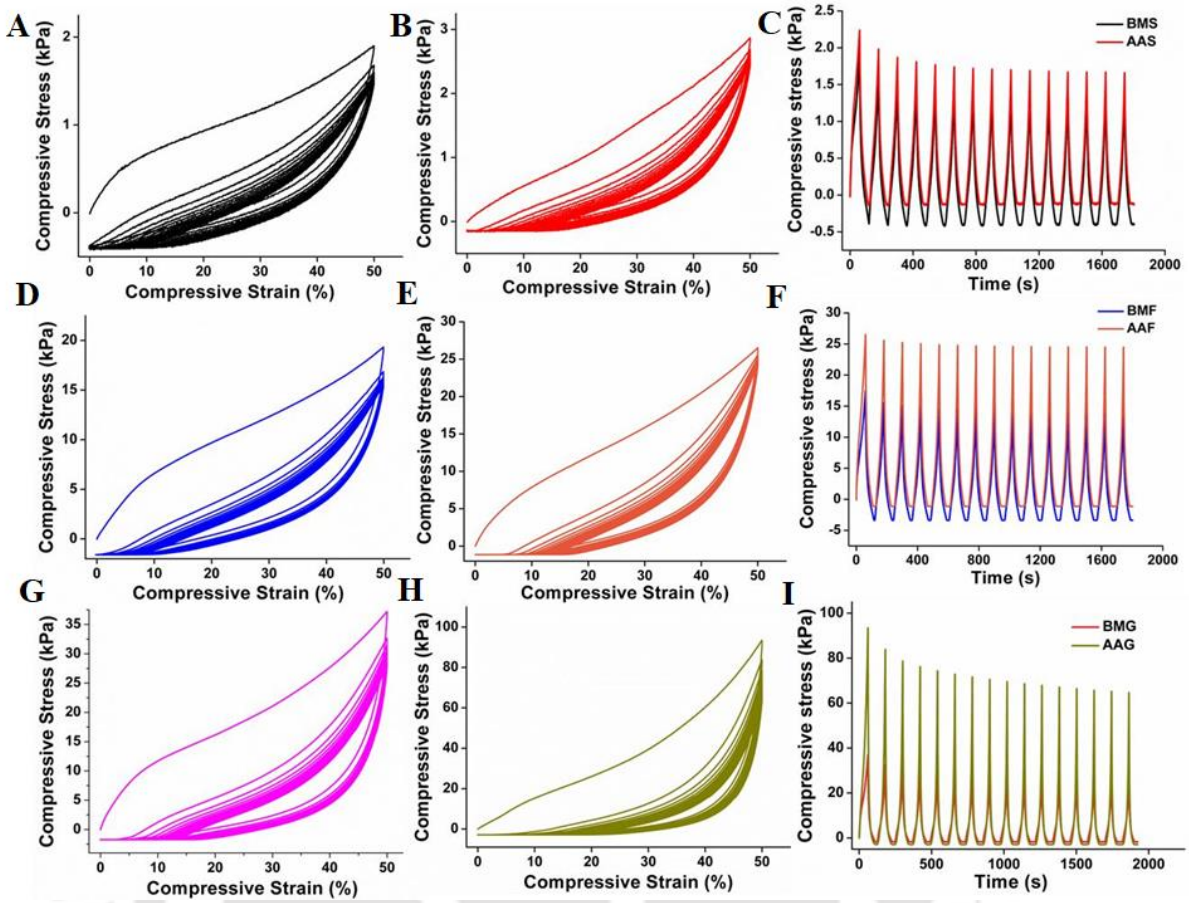

Figure A3.2. *Cyclic mechanical assessment of the silk matrices; stress-strain curves for pure silk matrices without reinforcements A) BMS, B) AAS and their strain vs. time plot; for silk matrices with unmodified silk microfibers, D) BMF, E) AAF and F) their strain vs. time plot; for silk matrices with functionalized silk microfibers, G) BMG, H) AAG and I) their strain vs. time plot*

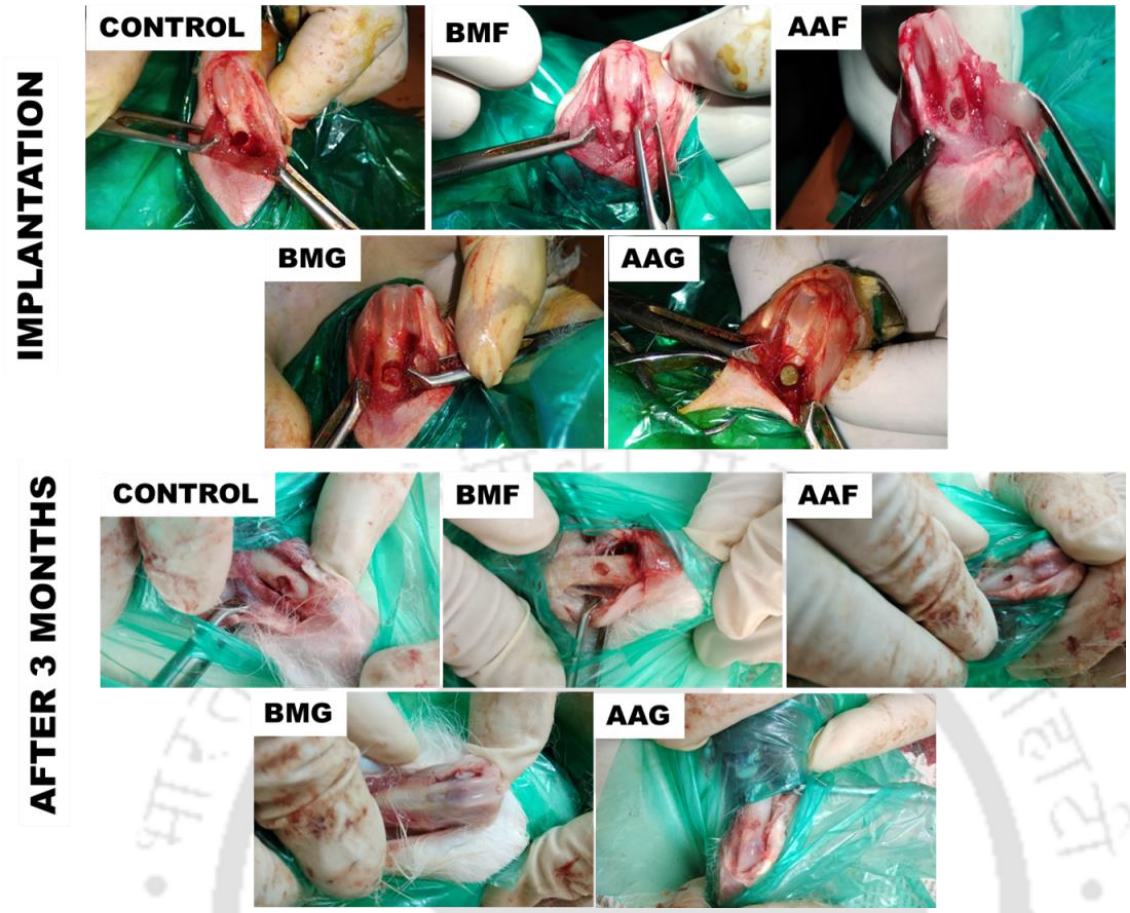

Figure A3.3. *In vivo implantation of silk matrices and the gross morphology and observation of defect site after 3 months post implantation*

Table A3.2. *Extent of new bone formed calculated from fluorochrome labelling*

Experimental Groups	New Bone Formed Percentage (%)	
	1 Month	3 Months
BMF	26.7± 5.04[a]	41.66± 2.03[a,#]
AAF	28.30± 1.93[a]	43.72±4.01[a]
BMG	43.77±4.05[b]	70.22±3.94[b]
AAG	47.58±2.92[b]	80.31±3.01[c]
Empty Defect	20.66±2.8[a]	33.34±3.89[#]

Means with standard deviation (Mean ± SD) along with different letters (a, b, c, #) above each value differs significantly ($p \leq 0.05$) among groups (One-way ANOVA) (data are shown as mean ± SD)

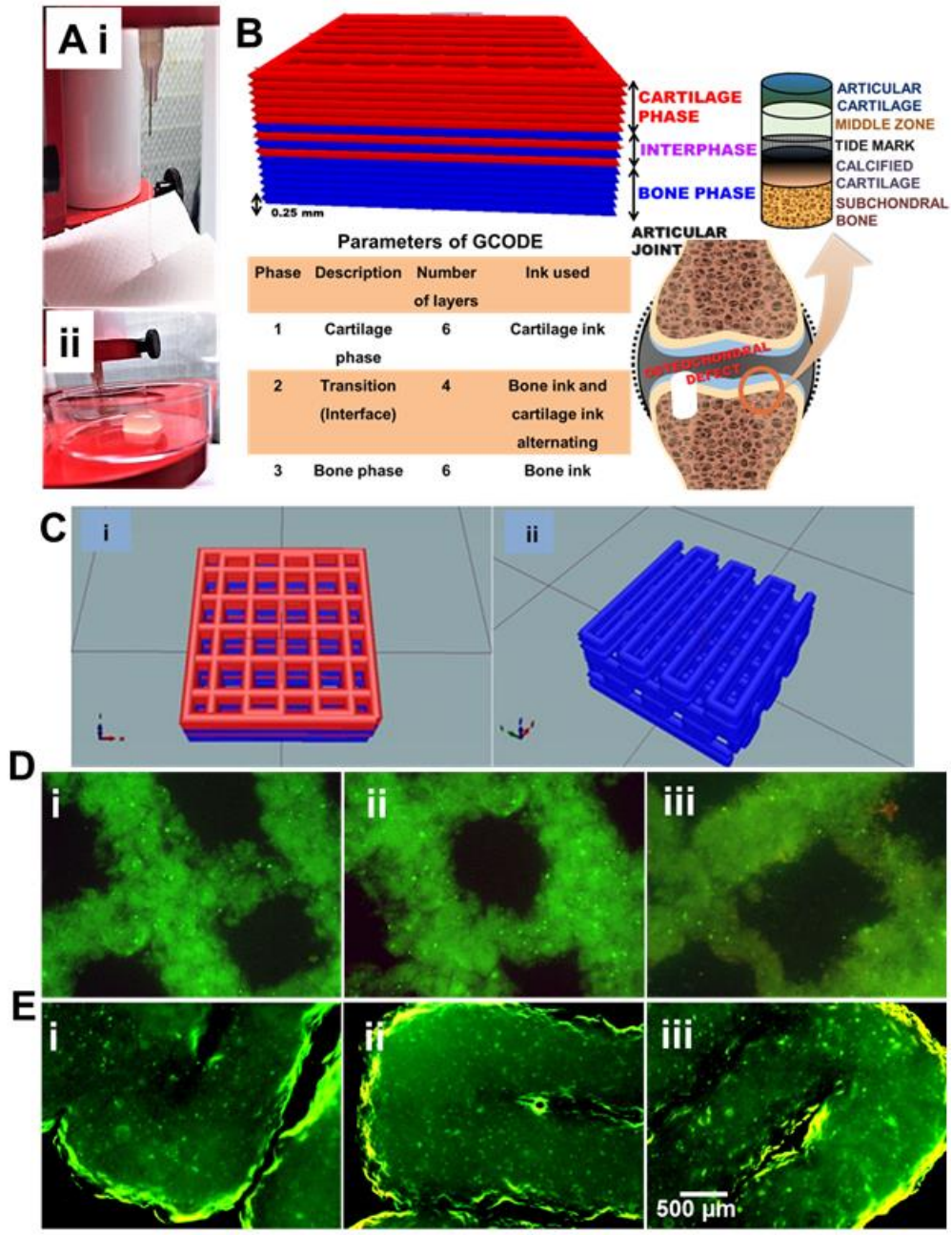

Figure A4.1. *Rheological behaviour of the silk bioinks exhibiting i) shear thinning property and quick thixotropic recovery to ii) print self-standing structures; B) GCODE parameters for the osteochondral interface constructs inspired by the native interface's anisotropic arrangement; Live/dead imaging and print fidelity of different bioinks used in the study; C i) Grid infill, ii) rectilinear infill and corresponding bioprinted constructs after 14 days D) grid infill and E) rectilinear infill using i) SF-PVP, ii) SF-PVP-SR0 and SF-PVP-SR1 bioinks.*

Table A4.1 *Dynamic light scattering and zeta potential analysis of synthesized hydroxyapatites*

Sample	Hydrodynamic Radius *(nm)*	Polydispersity Index	Zeta Potential *(mV)*	Conductivity *(mS/cm)*
SR0	707.4 ± 89.31	0.521	-14	0.0290
SR1	979.2 ± 187	0.294	-16.2	0.0602

Table A4.2 *Rheological parameters of bioinks used in the study*

Bioink	Yield Stress (τ) *(Pa)*	LVER (γ) *(%)*	Maximum Storage Modulus (G') *(Pa)*
SF-PVP	366.4	17.86	1065
SF-PVP-SR0	851	53.6	2734
SF-PVP-SR1	1302	33.34	2065

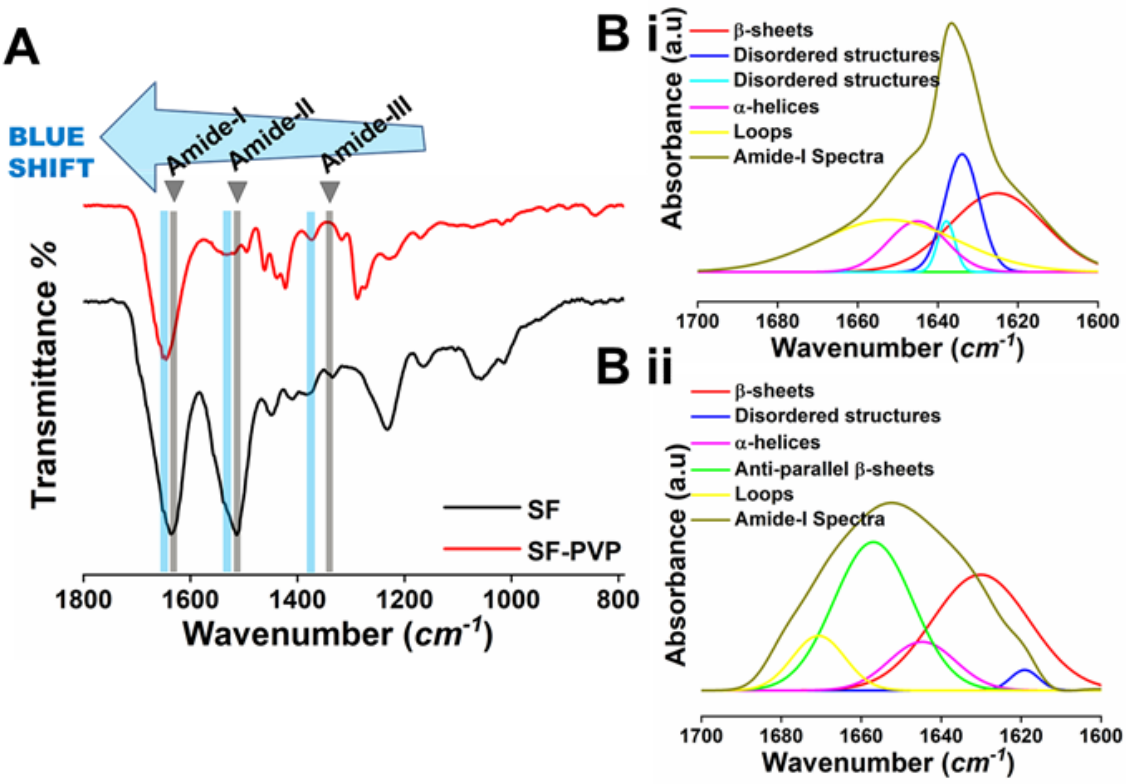

Figure A4.2. *Infrared spectra of regenerated silk fibroin blends and the crosslinked SF-PVP bioink showing A) a blue shift in Amide-I, Amide-II and Amide-II peaks and B) deconvuluted*

spectra via taking the second order derivative of amide-I spectra of i) regenerated silk fibroin blends and ii) SF-PVP bioink, showing cross-linking due to increase in β-sheet content

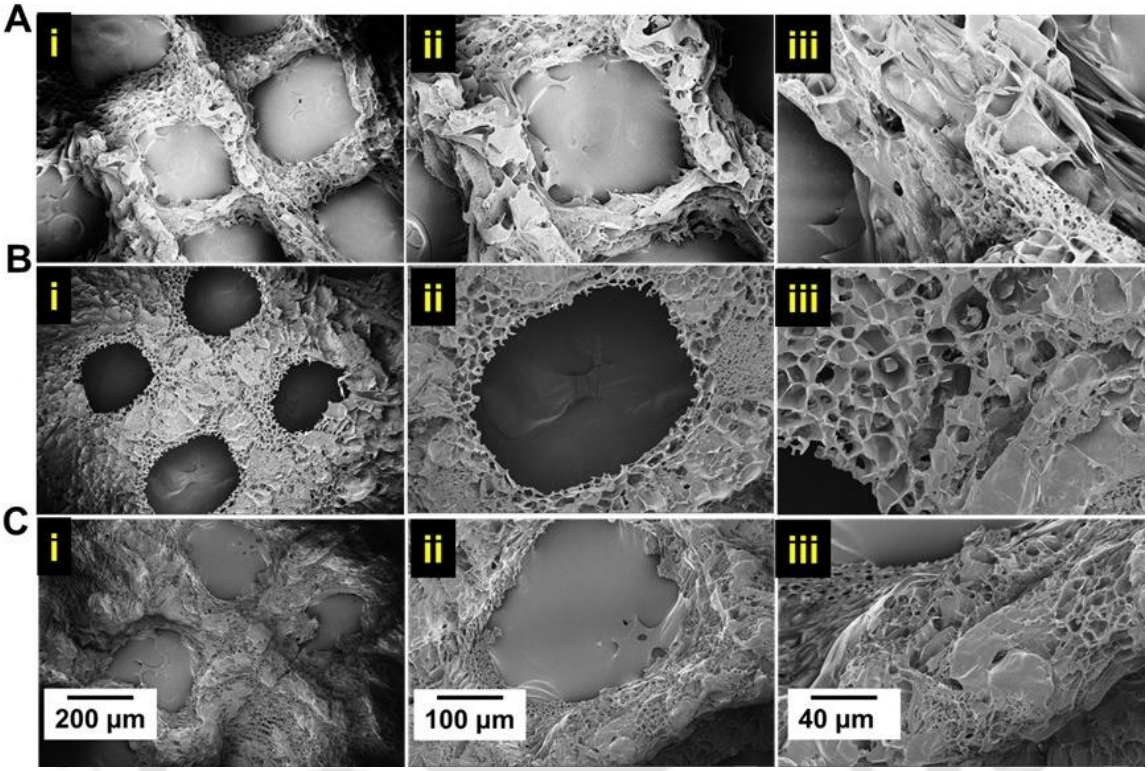

Figure A4.3. *Field emission scanning electron microscopy images of 3D printed constructs; A) SF-PVP bioink for cartilage layer, B) SF-PVP-SR0 bioink for bone layer, C) SF-PVP-SR1 bioink for bone layer, at increasing i) 84x, ii) 200x and iii) 500x magnification.*

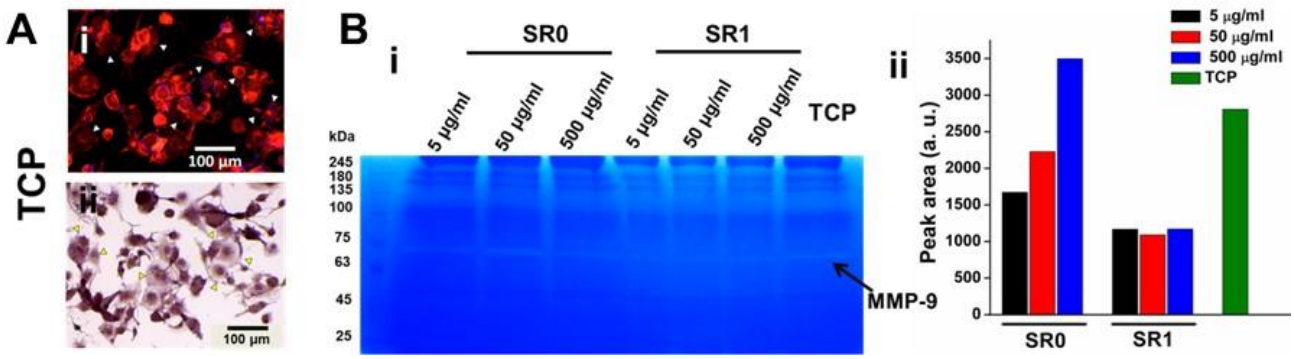

Figure A4.4. *A) Osteoclast grown on TCP i) cytoskeletal staining, ii) TRAP staining; B) (i) gelatin zymography and its (ii) densiometric profiling to assess MMP-9 activity.*

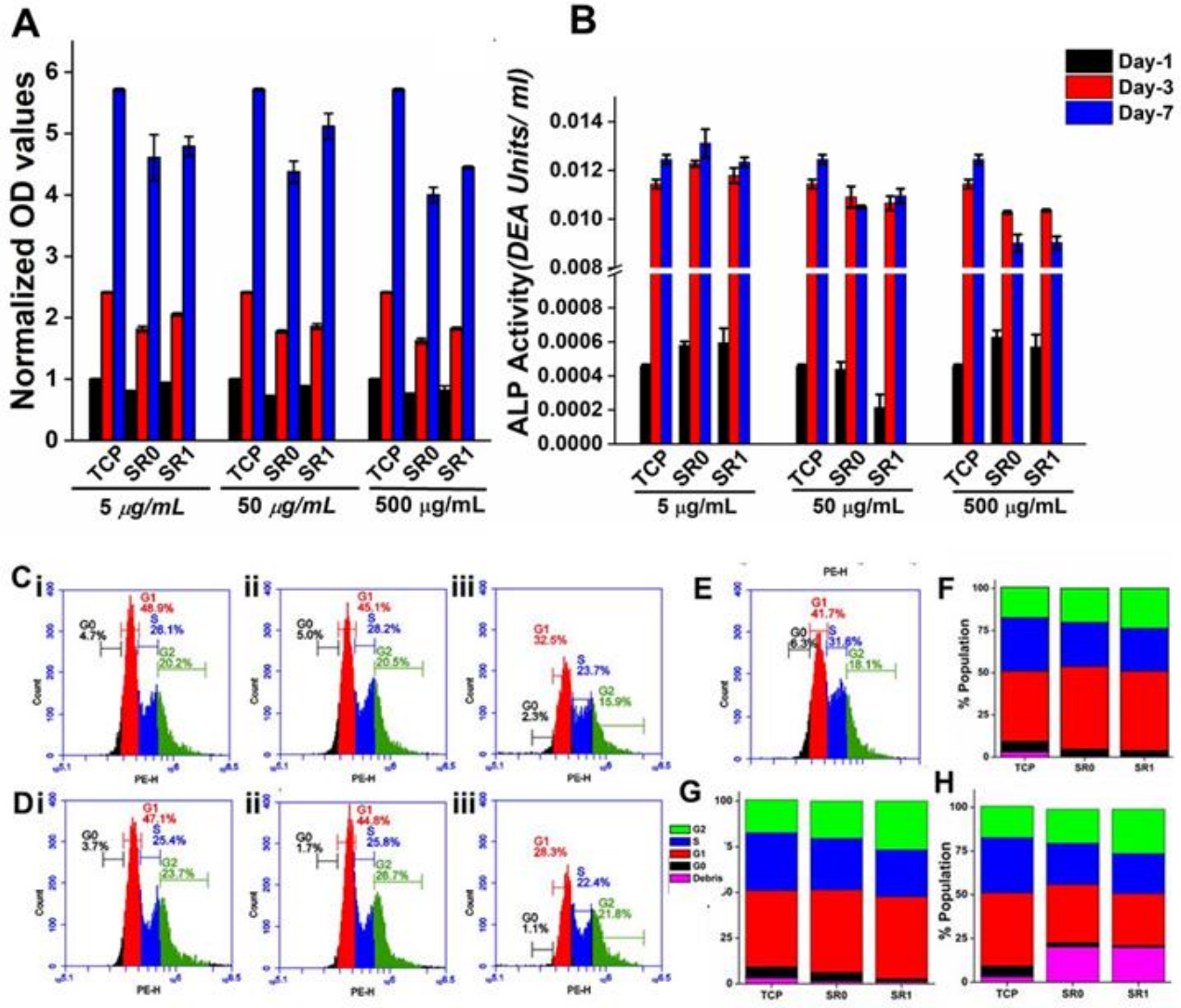

Figure A4.5. *Effect of synthesized hydroxyapatites on osteogenesis A) MTT assay and B) ALP activity assessment using MG63 cells; Cell cycle analysis of C) SR0, D) SR1 for (i) 5 µg/ml, (ii) 50 µg/ml, (iii) 500 µg/ml, E) TCP (Tissue Culture Plate control); Population percentage statistics for F) 5 µg/ml, G) 50 µg/ml, H) 500 µg/ml with respect to TCP control. Data expressed as Mean ± S.D (n=3)*

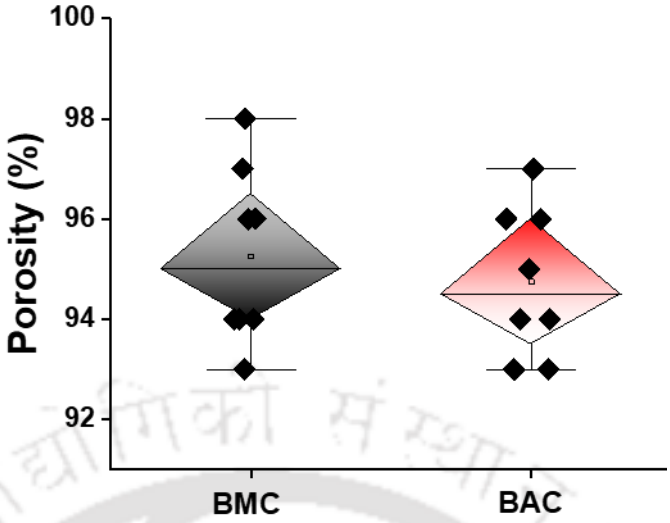

Figure A5.1. *Percentage porosity assessed by hexane displacement method for BMC and BAC scaffolds used in study.*

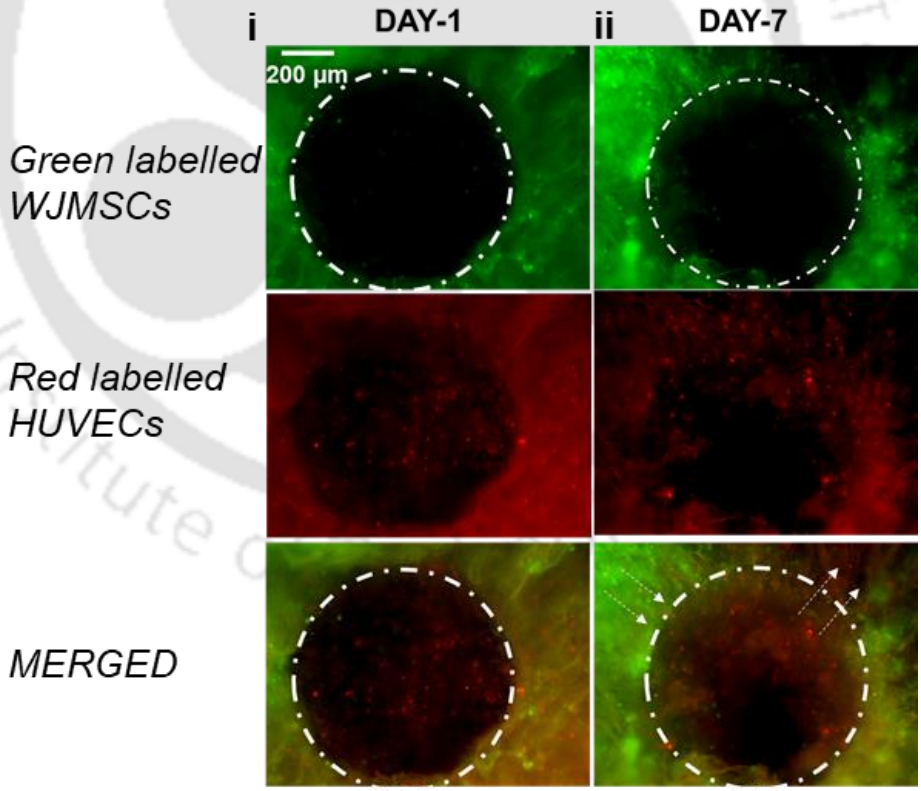

Figure A5.2. *Migration of cells within silk fibroin blend scaffold for red labelled HUVECs (low density acetylated Dil, Thermo Fisher Scientific, USA) and green cytotracker labelled WJMSCs (5-chloromethylfluoroscein diacetate; Thermo Fisher Scientific, USA; as per manufacturer's protocol) (white and green dotted lines demarcating the endosteal niche from*

the vascular channelized niche, white arrows indicating migration of cells) for i) BMC and ii) BAC scaffolds.

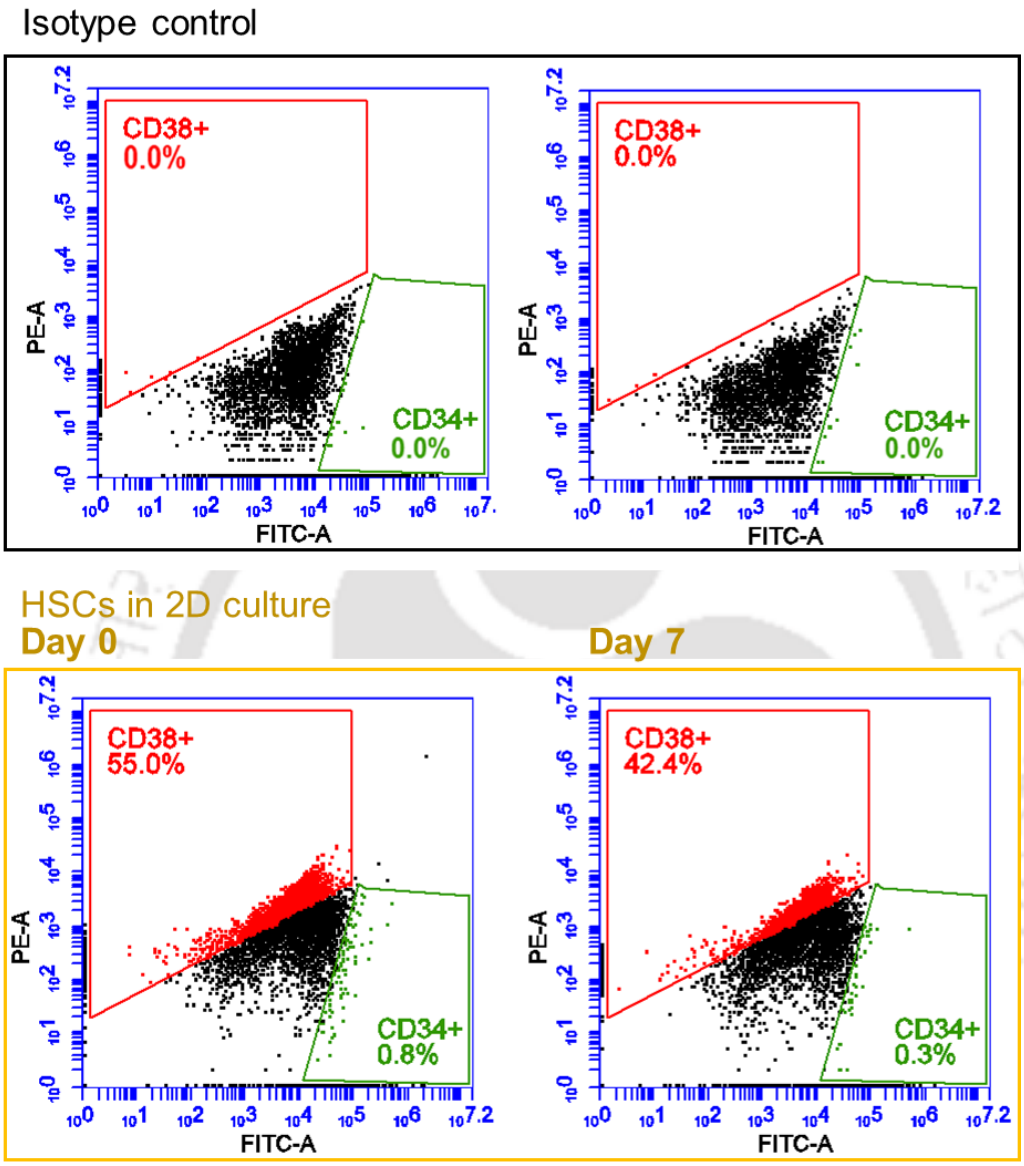

Figure A5.3. *Flow cytometric analysis for CD34 (HSC marker)/ CD38 (mononuclear cell marker); Isotype controls used for gating and HSCs in ex vivo suspension culture at Day-0 and Day-7.*

Table A6.1. *Hydrodynamic radius, Zeta potential analysis of drug loaded nanoparticles*

Sample	Hydrodynamic Radius (*nm*)	Polydispersity Index	Zeta Potential ζ (*mV*)	Hydrodynamic Radius (*nm*)	Polydispersity Index	Zeta Potential ζ (*mV*)
	(for doxycycline loading)			*(for dexamethasone loading)*		
nBG	289 ± 63.2	0.375	-6.2 ± 0.11	205.9 ± 65.7	0.332	-10.2 ± 0.46
nBMBG	671.32 ± 153.21	0.365	-5.8 ± 0.16	512.3 ± 167.8	0.278	-11.1 ± 0.34
nAABG	592.17 ± 178.23	0.328	-6.5 ± 0.28	523.7 ± 177.5	0.268	-13.2 ± 0.42
nBG+P	253.7 ± 67.2	0.345	-8.2 ± 0.17	269.5 ± 73.8	0.341	-5.2 ± 0.15
nBMBG+P	698.5 ± 193.7	0.315	-8.9 ± 0.19	691.7 ± 179.4	0.369	-5.8 ± 0.19
nAABG+P	613.8 ± 183.2	0.365	-8.3 ± 0.23	678.5 ± 142.8	0.358	-5.1 ± 0.21

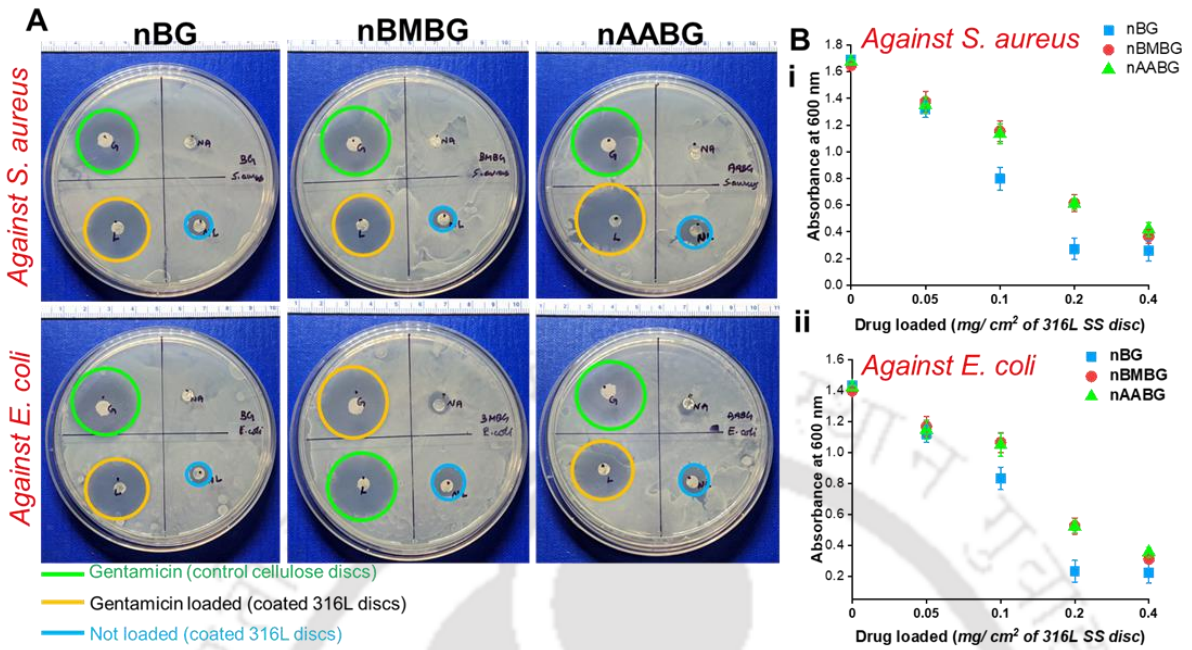

Figure A6.1. *Gentamicin susceptibility test using Disc diffusion assay; A) Gentamicin (250 µg) and coated 316L discs, representative agar plates and B) Growth inhibition studies for different drug loading concentrations and efficacy against (i) S. aureus and (ii) E. coli.*

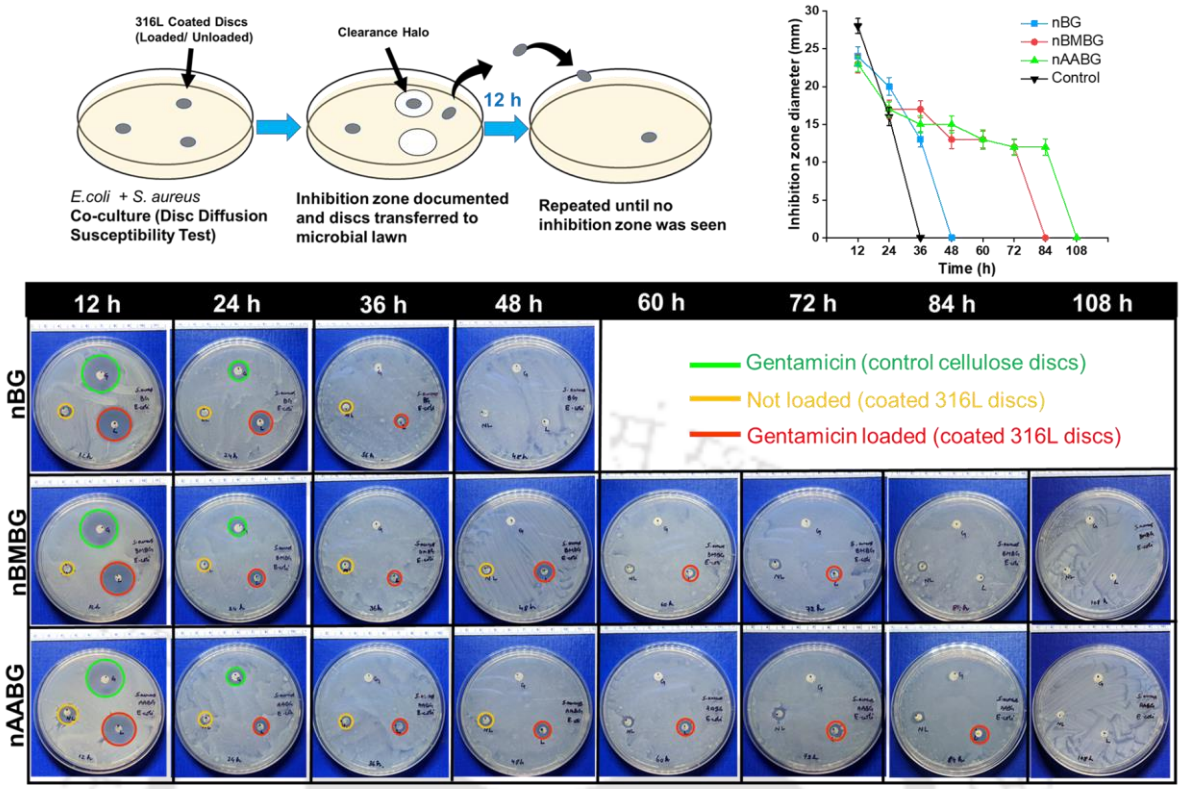

Figure A6.2. *Gentamicin susceptibility test using Disc diffusion assay; Gentamicin release (100μg) using continuous co-cultures of S. aureus and E. coli; methodology, representative agar plates and inhibition zone diameter plot.*

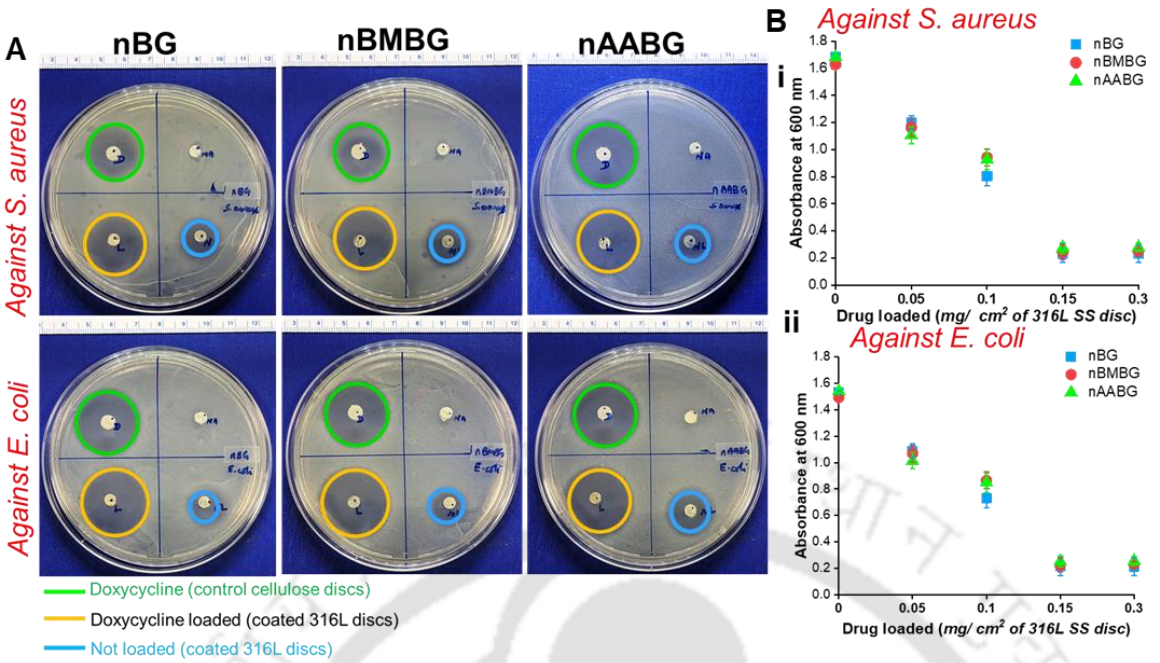

Figure A6.3. *Doxycycline susceptibility test using Disc diffusion assay; A) Doxycycline (200 µg) and coated 316L discs, representative agar plates and B) Growth inhibition studies for different drug loading concentrations and efficacy against (i) S. aureus and (ii) E. coli.*

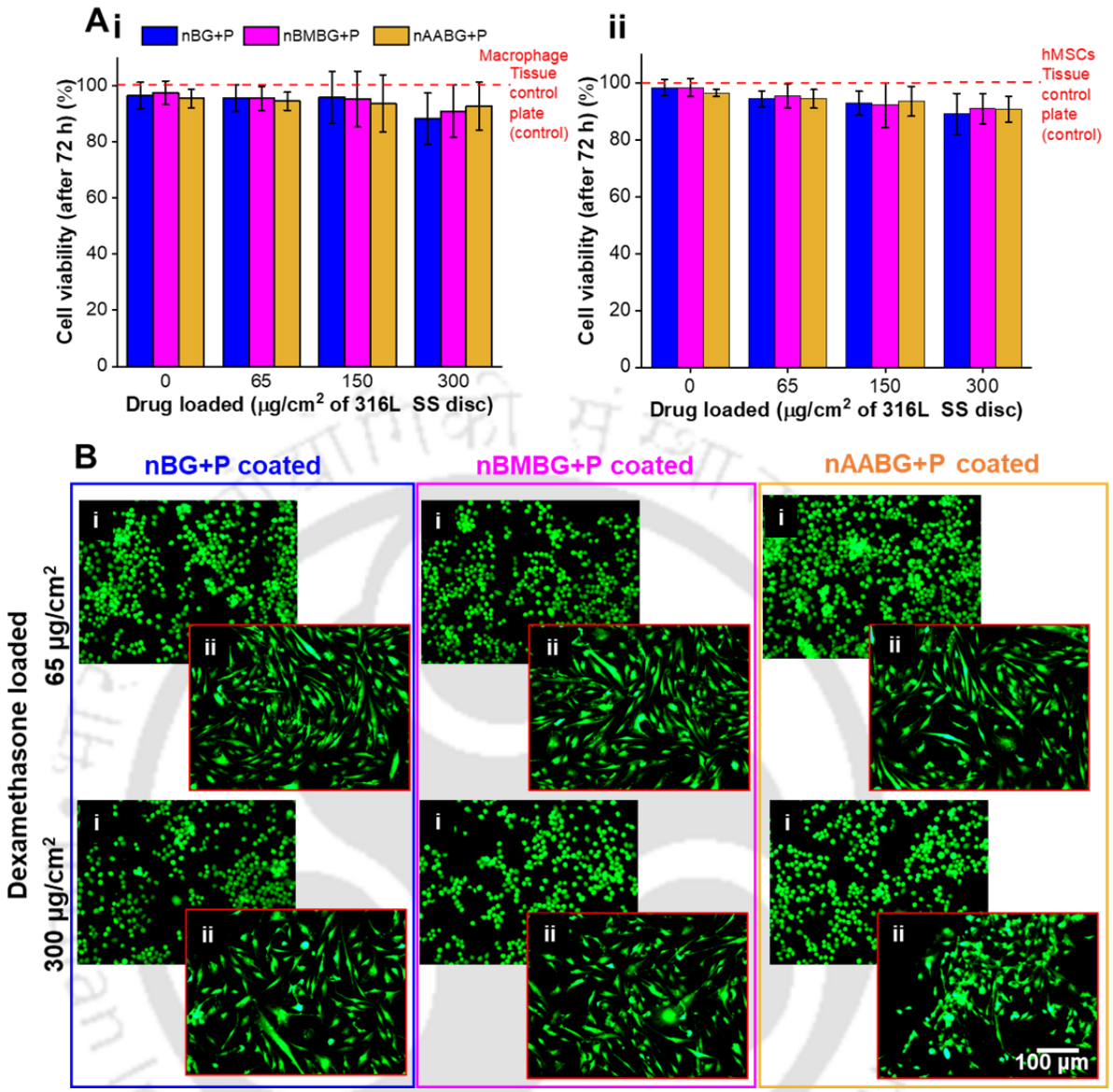

Figure A6.4. *A) Cellular viability after 72 h of seeded cells i) PMA treated THP1 monocytes (M0 macrophages), ii) adipose derived human mesenchymal stem cells (hMSCs) on to 316L SS discs coated with 65, 300 µg drug concentration loaded nanoparticles (+P); Live cell staining with calcein-AM (appearing green) nBG+P, nBMBG+P, and nAABG+P (dexamethasone laoded) for i) PMA treated THP1 monocytes (M0 macrophages), ii) adipose derived human mesenchymal stem cells (hMSCs) on to coated 316L SS discs.*

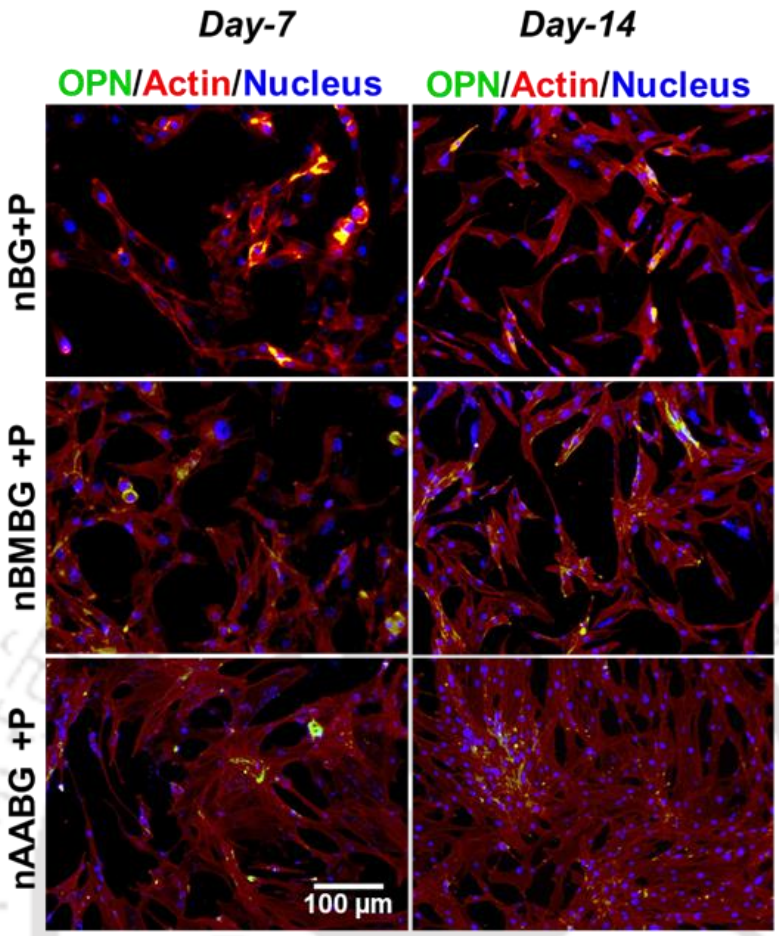

Figure A6.5. *Immunostaining to evaluate cellular morphology (red –actin) and presence of osteopontin (OPN) for hMSCs seeded on to 316L SS discs coated without dexamethasone loaded nanoparticles (+P).*

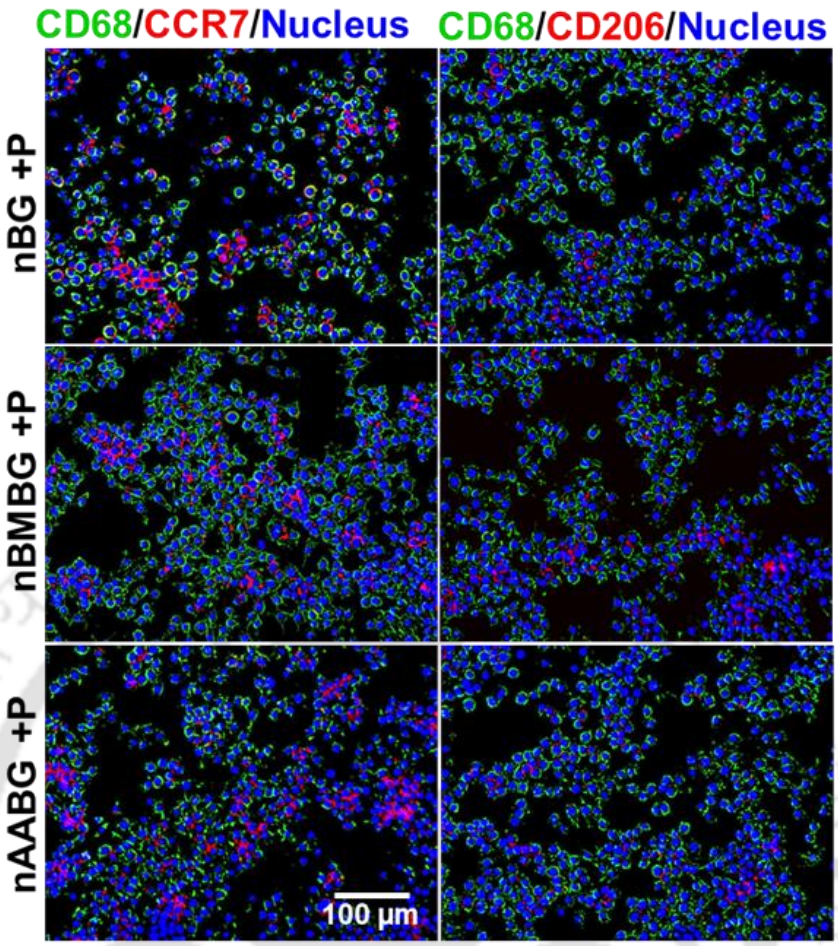

Figure A6.6. *Immunostaining to evaluate presence of M1 macrophage marker (CCR7), M2 macrophage marker (CD206) in presence of pan macrophage marker (CD 68) for PMA treated THP1 monocytes (M0 macrophages) seeded on to 316L SS discs coated without dexamethasone loaded nanoparticles (+P).*

List of Publications

I. Publications from Ph.D. Thesis

(A) Journal Publications

1. **Joseph Christakiran M.**, Philip James Thomas Reardon, Rocktotpal Konwarh, Jonathan C Knowles, and Biman B. Mandal. *Mimicking hierarchical complexity of the osteochondral interface using electrospun silk-bioactive glass composites*, ***ACS Applied Materials & Interfaces***. 2017, 9 (9), 8000-8013.

2. **Joseph Christakiran Moses**, Samit K. Nandi, and Biman B. Mandal. *Multifunctional cell instructive silk-bioactive glass composite reinforced scaffolds towards osteoinductive, proangiogenic and resorbable bone grafts*, ***Advanced Healthcare Materials***. 2018, 7.10: 1701418.

3. **Joseph Christakiran Moses**, Triya Saha, and Biman B. Mandal. *Chondroprotective and osteogenic effects of silk-based bioinks in developing 3D bioprinted osteochondral interface*, ***Bioprinting***. 2020, 17: e00067.

4. **Joseph Christakiran Moses**, Souradeep Dey, Ashutosh Bandyopadhyay, Manoj Agarwala, and Biman B. Mandal. *Silk based bioengineered diaphyseal cortical bone unit enclosing an implantable bone marrow towards atrophic non-union grafting*, ***Advanced Healthcare Materials***. 2021, 2102031. DOI: 10.1002/adhm.202102031.

5. **Joseph Christakiran Moses**, and Biman B. Mandal. *Mesoporous silk-bioactive glass nanocomposites as drug eluting multifunctional conformal coatings for improving osseointegration and bactericidal properties of metal implants*, ***ACS Applied Materials & Interfaces***. 2022, 14 (13), 14961–14980.

6. **Joseph Christakiran Moses**, and Biman B. Mandal. *Cell-instructive biomaterials in bone tissue engineering – cellular dynamics, engineering principles and clinical translation prospects*. (Manuscript under communication).

(B) Book Chapters

1. Promita Bhattacharjee, Prerak Gupta, **Joseph Christakiran M.**, Samit K. Nandi, and Biman B. Mandal. *Silk-based matrices for bone tissue engineering applications*, in *Nanostructures for the Engineering of Cells*, Tissues and Organs, pp. 439-472. William Andrew Publishing, 2018.

2. Yogendra Pratap Singh, **Joseph Christakiran Moses**, Ashutosh Bandyopadhyay, Bibrita Bhar, Bhaskar Birru, Nandana Bhardwaj, and Biman B. Mandal. *State-of-the-art strategies and future interventions in bone and cartilage repair for personalized regenerative therapy*, in *Regenerated Organs*, pp. 203-248. Academic Press, 2021.

(C) Patents Filed

1. Biman B. Mandal, Yogendra Pratap Singh, Ashutosh Bandyopadhyay, Shreya Mehrotra, **Joseph Christakiran Moses**, Bibhas Kumar Bhunia, Janani G, and Dimple

Chauhan. *Development of silk based bioinks and use thereof*, Indian Patent Application Number: 201831038727; Filing Date: 12th October, 2018.

2. Biman B. Mandal, **Joseph Christakiran Moses**, and Sayanti Shome. *An in-vitro bone marrow construct mimicking the trabecular endosteum and its use thereof*, Indian Patent Application Number: 202131052636; Filing Date: 16th November, 2021.

3. Biman B. Mandal, and **Joseph Christakiran Moses**. *Silk bioactive nano-composite metal coating and its use thereof*, Indian Patent Application Number: 202131061074; Filing Date: 27th December, 2021.

(D) Conference, Seminar, Workshop Participation/ Presentations

1. **Joseph Christakiran M.** and B. B. Mandal. *Silk-Bioceramic composites for bone tissue engineering applications*, Research conclave 2016, IIT-Guwahati. (Poster presentation)

2. 9th TCS annual event and flow cytometry workshop on "Flow application in basic, applied and clinical biology (FABACTCS 2016)" November 03-05, 2016, Organized by IIT-Guwahati, Guwahati, Assam. (Workshop Participation)

3. **Joseph Christakiran M.**, Philip James Thomas Reardon, Rocktotpal Konwarh, Jonathan C Knowles, and Biman B Mandal. *Biomimetic electrospun silk-bioactive glass composites for osteochondral interfacial tissue engineering*, Research conclave 2017, IIT-Guwahati. (Poster presentation)

4. **Joseph Christakiran M.**, Philip James Thomas Reardon, Rocktotpal Konwarh, Jonathan C Knowles, and Biman B Mandal. *Hierarchically structured electrospun silk-bioactive glass composites for osteochondral interface tissue engineering*. 6th Asian Biomaterial Congress; October, 2017 – Trivandrum, Kerala, India. (Poster presentation)

5. **Joseph Christakiran Moses**, Prerak Gupta and Biman B Mandal. *Osteoinductive and proangiogenic bioactive glass silk composite scaffolds towards resorbable and vascularized bone grafts*. Americas Chapter Meeting of the Tissue Engineering and Regenerative Medicine International Society (TERMIS– Americas); December, 2017 – Charlotte, NC, USA. (Poster presentation)

6. **Joseph Christakiran Moses**, and Biman B Mandal. *Cell instructive silk-bioactive glass composite scaffolding matrices towards osteoinductive, proangiogenic and resorbable bone grafts*, Research conclave 2018, IIT-Guwahati. (Poster presentation)

7. **Joseph Christakiran Moses**, Triya Saha and Biman B. Mandal. *Silk based bioinks for 3D bioprinting of hierarchically relevant osteochondral interface.* Research conclave 2019, IIT-Guwahati. (Poster presentation)

8. **Joseph Christakiran Moses**, Triya Saha and Biman B. Mandal. *Chondroprotective and osteoinductive silk based bioinks for 3D bioprinting stem cell laden biomimetic osteochondral interface*; BioTERM 2019 (International conference on Biomaterial based therapeutic engineering and regenerative medicine), organised by The Society

for Biomaterials and Artificial Organs (India); 27 November - 1 December 2019 – IIT Kanpur. (Bajpai-Saha-Student Oral Presentation)

9. Online workshop on "Flow cytometry techniques & applications" December 2020, Organized by North East Centre for Biological Sciences and Healthcare Engineering (NECBH), IIT-Guwahati, Guwahati, Assam. (Workshop Participation)

10. Online workshop on “Biosafety and biosecurity procedures" June 2021, Organized by Research and Development Section, IIT-Guwahati, Guwahati, Assam. (Workshop Participation)

11. **Joseph Christakiran Moses**, Souradeep Dey, Ashutosh Bandyopadhyay, Manoj Agarwala, and Biman B. Mandal. *Biofabrication of silk-based human diaphyseal bone cross-sectional unit encompassing a tissue engineered bone marrow as potential orthobiologics for atrophic non-union repair*. The Japan-India YNU Symposium 2021 on “Sustainable Transformation (SX), held online and hosted by Sakura Exchange Program (YNU); December 2021 - Yokohama National University. (Poster presentation)

(E) <u>Conference Publications</u>

1. Yogendra Pratap Singh, **Joseph Christakiran M.**, Bibhas K. Bhunia and Biman B. Mandal. *Bi-phasic silk scaffolds for osteochondral tissue engineering*, in ***European Cells & Materials*** (June 2016) 31(1):326.

2. **Joseph Christakiran Moses**, Prerak Gupta and Biman B Mandal. *Osteoinductive and proangiogenic bioactive glass-silk composite scaffolds towards resorbable and vascularized bone grafts*, in ***Tissue Engineering PART A*** (2017), vol. 23, pp. S89-S89.

II. Publications from other collaborative research projects

(A) Journal Publications

1. Prerak Gupta, Mimi Adhikary, **Joseph Christakiran M**., Manishekhar Kumar, Nandana Bhardwaj and Biman B. Mandal. *Investigating the osteogenic potential of hydroxapatite incorporated non-mulberry fiber reinforced tri-composites silk fibroin scaffolds*, ***ACS Applied Materials & Interfaces*** 2016, 8 (25), 15874-15888.

2. Yogendra Pratap Singh, **Joseph Christakiran Moses**, Nandana Bhardwaj, and Biman B. Mandal. *Injectable hydrogels: A new paradigm for osteochondral tissue engineering*, ***Journal of Materials Chemistry B***. 2018, 6(35):5499-529.

3. Yogendra Pratap Singh, **Joseph Christakiran Moses**, Bibhas K. Bhunia, Samit Kumar Nandi, and Biman B. Mandal. *Hierarchically structured seamless silk scaffolds for osteochondral interface tissue engineering*, ***Journal of Materials Chemistry B***. 2018, 6(36):5671-88.

4. Shreya Mehrotra, **Joseph Christakiran Moses**, Ashutosh Bandyopadhyay, and Biman B. Mandal. *3D Printing/Bioprinting based tailoring of in vitro tissue models: Recent advances and challenges*, ***ACS Applied Bio Materials***. 2019, 2 (4), 1385-1405.

5. Prerak Gupta, **Joseph Christakiran Moses**, and Biman B. Mandal. *Surface Patterning and Innate Physicochemical Attributes of Silk Films Concomitantly Govern Vascular Cell Dynamics*, ***ACS Biomaterials Science & Engineering***. 2019, 5 (2), 933-949.

6. Ashutosh Bandyopadhyay, Suvro Kanti Chowdhury, Souradeep Dey, **Joseph Christakiran Moses**, and Biman B. Mandal. *Silk: A promising biomaterial opening new vistas towards affordable healthcare solutions*, ***Journal of the Indian Institute of Science*** 2019, 99(3), 445-487.

7. Guru Janani, Manishekhar Kumar, Dimple Chouhan, **Joseph Christakiran Moses**, Ankit Gangrade, Sohenii Bhattacharjee, and Biman B. Mandal. *Insight into silk-based biomaterials: from physicochemical attributes to recent biomedical applications*, ***ACS Applied Bio Materials*** 2019, 2 (12), 5460-5491.

8. **Joseph Christakiran Moses**, Mainak Dey, K. Bavya Devi, Mangal Roy, Samit Kumar Nandi, and Biman B. Mandal. *Synergistic effects of silicon/zinc doped brushite and silk scaffolding in augmenting the osteogenic and angiogenic potential of composite biomimetic bone grafts*, ***ACS Biomaterials Science & Engineering.*** 2019, 5 (3), 1462-1475.

9. Arpita Shome[§], **Joseph Christakiran Moses**[§], Adil M. Rather, Biman B. Mandal, and Uttam Manna. *Unconventional and facile fabrication of chemically reactive silk fibroin sponges for environmental remediation*, ***ACS Applied Materials & Interfaces***. 2021, 13 (20), 24258–24271.

([§] *denotes equal contribution*)

10. Yogendra Pratap Singh[§], **Joseph Christakiran Moses**[§], Nandana Bhardwaj, and Biman B. Mandal. *Overcoming the dependence on animal models for osteoarthritis therapeutics – The promises and prospects of in-vitro models*, ***Advanced Healthcare Materials***. 2021: 2100961.

11. Yogendra Pratap Singh[§], **Joseph Christakiran Moses**[§], Ashutosh Bandyopadhyay, and Biman B. Mandal. *3D Bioprinted silk-based in vitro osteochondral model for osteoarthritis therapeutics*, ***Advanced Healthcare Materials***. 2022: 2200209.

([§] *denotes equal contribution*)

(B) Book Chapter

1. **Joseph Christakiran Moses**, Ankit Gangrade, and Biman B. Mandal. *Carbon nanotubes and their polymer nanocomposites.* in *Nanomaterials and Polymer Nanocomposites*, pp. 145-175. Elsevier, 2019.

(C) Patent Filed

1. Biman B. Mandal, Yogendra Pratap Singh, **Joseph Christakiran Moses**, and Ashutosh Bandyopadhyay. *3D bioprinted osteochondral in-vitro osteoarthritis model construct and applications thereof*, Indian Patent Application Number: 202131027358; Filing Date: 18th June 2021.